

Fatigue
Crack
Growth
Thresholds,
Endurance Limits,
and Design

JAMES C. NEWMAN
AND ROBERT S. PIASCIK, EDITORS



STP 1372

STP 1372

***Fatigue Crack Growth
Thresholds, Endurance Limits,
and Design***

J. C. Newman, Jr. and R. S. Piascik, editors

ASTM Stock Number: STP1372



ASTM
100 Barr Harbor Drive
West Conshohocken, PA 19428-2959

Printed in the U.S.A.

Library of Congress Cataloging-in-Publication Data

Fatigue crack growth thresholds, endurance limits, and design / J.C. Newman and R.S.

Piasecki, editors.

(STP ; 1372)

"ASTM stock number: STP1372."

Includes bibliographical references and index.

ISBN 0-8031-2624-7

1. Metals—Fatigue. 2. Metals—Cracking. 3. Fracture mechanics. I. Newman, J. C. II. Piasecki, Robert S. III. ASTM special technical publication ; 1372.

TA460.F375 2000

620.1'66—dc21

99-089527

Copyright © 2000 AMERICAN SOCIETY FOR TESTING AND MATERIALS, West Conshohocken, PA. All rights reserved. This material may not be reproduced or copied, in whole or in part, in any printed, mechanical, electronic, film, or other distribution and storage media, without the written consent of the publisher.

Photocopy Rights

Authorization to photocopy items for internal, personal, or educational classroom use, or the internal, personal, or educational classroom use of specific clients, is granted by the American Society for Testing and Materials (ASTM) provided that the appropriate fee is paid to the Copyright Clearance Center, 222 Rosewood Drive, Danvers, MA 01923; Tel: 508-750-8400; online: <http://www.copyright.com/>.

Peer Review Policy

Each paper published in this volume was evaluated by two peer reviewers and at least one editor. The authors addressed all of the reviewers' comments to the satisfaction of both the technical editor(s) and the ASTM Committee on Publications.

To make technical information available as quickly as possible, the peer-reviewed papers in this publication were prepared "camera-ready" as submitted by the authors.

The quality of the papers in this publication reflects not only the obvious efforts of the authors and the technical editor(s), but also the work of the peer reviewers. In keeping with long-standing publication practices, ASTM maintains the anonymity of the peer reviewers. The ASTM Committee on Publications acknowledges with appreciation their dedication and contribution of time and effort on behalf of ASTM.

Foreword

This publication, *Fatigue Crack Growth Thresholds, Endurance Limits, and Design*, contains papers presented at the symposium of the same name held in Norfolk, Virginia, on 4–5 November 1998. The symposium was sponsored by ASTM Committee E8 on Fatigue and Fracture. The symposium co-chairmen were J. C. Newman, Jr. and R. S. Piascik, NASA Langley Research Center.

Contents

Overview	vii
-----------------	------------

MECHANISMS

Mechanisms and Modeling of Near-Threshold Fatigue Crack Propagation— J. PETIT, G. HENAFF, AND C. SARRAZIN-BAUDOUX	3
The Significance of the Intrinsic Threshold—What Is New?— A. HADRBOLETZ, B. WEISS, AND R. STICKLER	31
On the Significance of Crack Tip Shielding in Fatigue Threshold—Theoretical Relations and Experimental Implications— H.-J. SCHINDLER	46
Effects of K_{max} on Fatigue Crack Growth Threshold in Aluminum Alloys— J. A. NEWMAN, JR., W. T. RIDDELL, AND R. S. PIASCIK	63

TEST PROCEDURES

Fatigue Crack Growth Threshold Concept and Test Results for Al- and Ti-Alloys— G. MARCI	81
Resistance Curves for the Threshold of Fatigue Crack Propagation in Particle Reinforced Aluminium Alloys— B. TABERNIG, P. POWELL, AND R. PIPPAN	96
An Indirect Technique for Determining Closure-Free Fatigue Crack Growth Behavior— S. W. SMITH AND R. S. PIASCIK	109
Effect of an Overload on the Threshold Level of Ti-6-22-22— A. J. MCEVILY, M. OHASHI, R. SHOVER, AND A. DECARMINE	123
Relation Between Endurance Limits and Thresholds in the Field of Gigacycle Fatigue— C. BATHIAS	135
A Size Effect on the Fatigue Crack Growth Rate Threshold of Alloy 718— K. R. GARR AND G. C. HRESKO, III	155

Effect of Geometry and Load History on Fatigue Crack Growth in Ti-62222—
H. O. LIKNES AND R. R. STEPHENS 175

**Increases in Fatigue Crack Growth Rate and Reductions in Fatigue Strength
Due to Periodic Overstrains in Biaxial Fatigue Loading—**
A. VARVANI-FARAHANI AND T. H. TOPPER 192

ANALYSIS

Analysis of Fatigue Crack Closure During Simulated Threshold Testing—
R. C. McCLUNG 209

**Analyses of Fatigue Crack Growth and Closure Near Threshold Conditions
for Large-Crack Behavior—**J. C. NEWMAN, JR. 227

The Mechanics of Moderately Stressed Cracks—F. O. RIEMELMOSER AND
R. PIPPAN 252

APPLICATIONS

Pitfalls to Avoid in Threshold Testing and Its Interpretation—R. W. BUSH,
J. K. DONALD, AND R. J. BUCCI 269

**Use of Small Fatigue Crack Growth Analysis in Predicting the S-N Response
of Cast Aluminium Alloys—**M. J. CATON, J. W. JONES, AND J. E. ALLISON 285

**Prediction of Fatigue Limits of Engineering Components Containing Small
Defects—**Y. AKINIWA AND K. TANAKA 304

**Corrosion Fatigue Crack Growth Thresholds for Cast Nickel-Aluminum
Bronze and Welds—**E. J. CZYRYCA 319

**Mean Stress and Environmental Effects on Near-Threshold Fatigue Crack
Propagation on a Ti6246 Alloy at Room Temperature and 500°C—**
C. SARRAZIN-BAUDOUX, Y. CHABANNE, AND J. PETIT 341

Component Design: The Interface Between Threshold and Endurance Limit—
D. TAYLOR AND G. WANG 361

Near-Threshold Fatigue Strength of a Welded Steel Bridge Detail—
P. ALBRECHT AND W. J. WRIGHT 374

Fatigue Crack Growth Thresholds Measurements in Structural Materials—
R. LINDSTRÖM, P. LIDAAR, AND B. ROSBORG 400

Endurance Limit Design of Spheroidal Graphite Cast Iron Components Based on Natural Defects—G. MARQUIS, R. RABB, AND L. SIIVONEN	411
Author Index	427
Subject Index	429

Overview

Mechanisms

The technical session on fatigue-crack growth (FCG) threshold mechanisms was chaired by R. Pippin. Three mechanisms that influence thresholds, crack-tip closure, environment, and K_{\max} effects, were discussed. A simplistic four-parameter model that describes FCG threshold behavior of elastic-plastic materials was presented. The proposed model was capable of predicting the R-ratio effects produced by “intrinsic” mechanisms and “extrinsic” shielding mechanisms. From this research, the basic FCG threshold behavior was characterized by two parameters, $K_{\max/\text{th}}$ and $\Delta K_{\text{th}/\text{int}}$, which can be obtained from two tests conducted on a single specimen. A crack-tip closure concept based on the cyclic plasticity in the vicinity of a fatigue crack under threshold conditions was proposed.

The electron channeling contrast imaging (ECCI) technique was used to characterize crack-tip dislocation configuration and derive crack-tip plastic strain contours. From these results, the lower portion of the load-crack-tip-opening displacement curves was critically evaluated for crack-tip opening loads. This technique was used to study the fatigue-crack-growth-threshold behavior of quasi-two-dimensional structures, such as thin foils and films of various materials. Microstructure and environment based mechanisms and modeling for near-threshold FCG were presented. Here, three crack-growth regimes were suggested: (1) stage I single crystal crack growth, (2) stage II cracking along the normal to the applied load, and (3) a crystallographic stage which prevails near the threshold when the deformation at the crack-tip was localized within a single slip system. The damaging effects of water vapor environment were discussed in terms of hydrogen assisted crack propagation. Near threshold, K_{\max} effects were investigated in ingot and powder metallurgy aluminium alloys. Results suggest that no single value of FCG threshold exist. Observations suggest that K_{\max} -accelerated, closure free, near-threshold FCG was caused by changes in crack-tip process zone damage mechanism(s).

Test Procedures

Two sessions on loading and specimen-type effects were chaired by E. Phillips and R. Piascik. Research showed that the resistance-curve (R-curve) method to determine the threshold for fatigue-crack growth should allow more reliable application of ΔK_{th} values to engineering problems. A very simple technique to measure such R-curves was described and the results were shown to give effective thresholds. Application of the R-curve method leads to the Kitagawa diagram that can be used to estimate the fatigue limit as a function of defect size.

Different interpretations of the influence of K_{\max} on ΔK_{th} were highlighted during the session. Research showed that a constant ΔK_{th} could be established and considered a material property based on the fatigue-crack-growth rates asymptotically approaching zero. While similar behavior was observed by others, a finite decrease in ΔK_{th} was noted for increased K_{\max} ; here, an increased K_{\max} driving force was suggested and no constant FCG threshold was observed. A unique test procedure based upon the increase in threshold level was adopted to determine the maximum level of crack closure resulting from an overload. The

novel observations showed that FCP behavior at distances well beyond the overload plastic zone could be sensitive to prior overloads.

High (gigacycle) cycle fatigue studies showed that fatigue thresholds were about the same in conventional fatigue and in resonant fatigue if the computation of the stress-intensity factor (K) was correct. But there was a very large difference between the endurance limits at 10^6 cycles and 10^9 cycles. Results suggest that a life prediction approach based on ΔK_{th} was not safe because it does not account for an incubation nucleation process. Standard (ASTM E647) fatigue-crack-growth tests on nickel-based superalloy 718 along with crack-closure measurements were instrumental in reconciling data from different laboratories. But, the results did show that standard techniques could not explain increased closure from larger specimens. Similar differences in Ti-6222 threshold fatigue-crack-growth rates were observed using three standard test specimen configurations. Here, differences in threshold FCP rates could not be explained by crack-tip closure, suggesting possible crack length and load reduction procedure dependence on FCP behavior.

FCP under biaxial constant straining and periodic compressive straining was discussed. Accelerated FCP after compressive loading was related to flattening of fracture surface asperities and reduced crack closure. For various biaxiality ratios, the ratios of the effective strain intensity factor range to constant amplitude strain intensity factor range at the threshold were found to be close to the ratios of the closure free fatigue limit obtained from effective strain-life to the constant amplitude fatigue limit.

Analysis

The session on analyses of fatigue-crack-growth-threshold behavior was chaired by T. Nicholas. Three papers in this session analyzed the behavior of fatigue cracks in the threshold regime using several different analysis methods. These methods were the elastic-plastic finite-element method (FEM), the Dugdale-type model, the BCS (Bilby, Cottrell and Swinden) model, and a discrete-dislocation model. Most of these methods only consider plasticity-induced closure in a continuum mechanics framework but the discrete-dislocation model was applied to a two-phase material with alternating regions of different yield stresses to simulate different grain structures.

Test measurements made during load-reduction procedures have indicated that the crack-opening stresses rise as the threshold was approached. In the literature, this rise has been attributed to roughness-, fretting-oxide-debris-, or plasticity-induced closure. These analysis methods were being investigated to see if threshold behavior could be predicted from only the plasticity-induced closure mechanism. Two-dimensional, elastic-plastic, finite-element crack-growth simulations of the load-reduction threshold test show a rise in the crack-opening stress (S_{open}/S_{max}) ratio as the ΔK levels were reduced, only if the initial ΔK level at the start of the load-reduction procedure was high enough. At low initial ΔK levels, the rise in the crack-opening-stress ratio was not predicted. Comparisons made between the FEM and the strip-yield model, FASTRAN, showed good agreement under plane-stress conditions. The rise in the closure level was caused by remote closure at the site of the initiation point for the load-reduction procedure. Because both of these analyses were two-dimensional, in nature, a remaining question was whether three-dimensional effects could cause a rise in closure even at the low ΔK levels due to the plane-stress regions near the free surfaces. The strip-yield model demonstrated that the plastic deformations even with the low ΔK levels were still a dominant factor for crack-face interference near threshold conditions.

The study of a homogeneous material with the dislocation model showed the existence of an intrinsic threshold in the near threshold regime due to the dislocation nature of plasticity. Incorporating micro-structural features (alternating grain structure) into the analysis, it was

shown that the intrinsic threshold value was determined only by the mechanism for dislocation generation and does not depend on micro-structural details like the grain size. However, in the near threshold regime and in the lower Paris regime the plastic deformation and the crack-growth rates are severely influenced by microstructure. Only in the upper Paris regime, where cyclic plastic-zone size exceeds several times the micro-structural length scale, usual continuum plasticity mechanics was appropriate to describe the events at the crack tip.

Applications

R. Rice and G. Marci chaired two sessions on applications of threshold concepts and endurance limits to aerospace and structural materials. The impact of a number of testing variables on the measurement of fatigue-crack-growth thresholds, in particular ASTM E647, was discussed. Applicability of the original E647 recommendations in light of some recent advances was also discussed. In addition, the effects of some commonly overlooked parameters, such as residual stress and environment, on the measurement and interpretation of crack-growth thresholds were presented.

A model using small-crack data to estimate the stress-life ($S-N$) response of cast aluminum alloys tested at high stress levels (50 to 90% of the yield stress) under $R = -1$ conditions was developed. The tradition LEFM model, with small-crack data, was inadequate in predicting the $S-N$ behavior at the high stress levels. Perhaps, the use of non-linear fracture mechanics concepts, such as the cyclic J integral, would have improved the life predictions at the high stress levels. In another paper, the cyclic resistance-curve method was used to correlate fatigue limits for structural carbon steel components with small defects (ranging in length from 0.16 to 4 mm's). The threshold condition of crack growth from these small cracks was given by a constant value of the effective-stress-intensity-factor range irrespective of crack length and stress ratio ($R = 0$ to -2). Haigh (stress amplitude mean stress) diagrams for the endurance limit were successfully derived from the arrest condition of nucleated small cracks in smooth specimens.

Fatigue-crack-growth rate tests on cast nickel-aluminum bronze (NAB) and NAB weld metal specimens were conducted to determine the threshold for fatigue-crack growth (ΔK_{th}), per ASTM E647. Compared to the values for cast NAB, higher ΔK_{th} values and higher crack-closure levels in NAB weld metal tests were noted, due to the residual stresses in the weldment. The cracking behavior of a Ti-6246 alloy under cyclic loading at different levels of mean stress was studied, with special attention to the near-threshold fatigue-crack growth regime, and to possible coupled effects of corrosion and creep. The near-threshold crack growth at low K_{max} (i.e. low R ratio) was shown to be highly sensitive to the environment, and a predominant detrimental influence of water vapor was observed, even under very low partial pressure. This behavior was suspected to be related to a contribution of stress corrosion cracking induced by water vapor when some conditions favoring a localization of the deformation and the attainment of a critical embrittlement are fulfilled.

A method was derived from fracture mechanics to assess the effects of stress concentrations in components. The approach was based on an extension of the well-known critical-distance concept. This concept was tested using data from specimens containing short cracks and circular notches of various sizes and was successfully applied to the analysis of a component in service. In another paper on structural components, fatigue test data were presented for a transverse stiffener specimen made of a typical bridge steel. The specimens were tested under variable-amplitude fatigue loading for up to 250,000,000 cycles. A fracture-mechanics model was used to predict the variable-amplitude fatigue lives of the transverse stiffener specimens.

Fatigue-crack-growth thresholds were determined for 304 stainless steel, nickel-base weld metal alloy 182, nickel-base alloy 600, and low-alloy steel in air at ambient temperature and in high-temperature water and steam. A relatively inexpensive and time-saving method for measuring fatigue-crack-growth thresholds, and fatigue crack growth rates at low ΔK -values, was used in the tests. The method was a ΔK -decreasing test with constant K_{\max} .

Defects in several thick-wall castings made of cast iron were statistically evaluated. A fracture-mechanics based model involving hardness and square-root of the defect area successfully related the defect size to the experimentally observed fatigue limit. The model also correlated the torsion and tension endurance limits. Endurance limits as a function of mean stress were presented in the form of Haigh diagrams.

James C. Newman, Jr.
NASA Langley Research Center
Hampton, VA
symposium co-chairman and editor

Robert S. Piascik
NASA Langley Research Center
Hampton, VA
symposium co-chairman and editor

Mechanisms

J. Petit,¹ G. Henaff,² and C. Sarrazin-Baudoux³

Mechanisms and Modeling of Near-Threshold Fatigue Crack Propagation

Reference: Petit, J., Henaff, G. and Sarrazin-Baudoux, C., “Mechanisms and Modeling of Near-Threshold Fatigue Crack Propagation,” *Fatigue Crack Growth Thresholds, Endurance Limits, and Design*, ASTM STP 1372, J. C. Newman, Jr. and R. S. Piascik, Eds., American Society for Testing and Materials, West Conshohocken, PA, 2000.

Abstract: First, this paper proposes a comprehensive framework for the modeling of the intrinsic FCP (i.e. after elimination of any environmental and closure effects). On the basis of numerous experimental data on Al alloys, steels and Ti alloys, three intrinsic crack growth regimes have been identified:

- i) stage I regime, observed in single crystals or in the early growth phase of short cracks;
- ii) stage II regime, commonly observed when the crack advance proceeds along a plane normal to the load axis and results from the activation of symmetrical slip systems;
- iii) crystallographic stage I-like regime which prevails near the threshold.

Second, this contribution is dedicated to the description of environmentally assisted propagation and specially focused on the understanding of the role of water vapor and the complex interactions existing between environment and microstructure. The effective FCP behavior is described by superimposing two distinct stage II regimes:

- i) a propagation assisted by water vapor adsorption which can be operative under very low partial pressure or at very low frequencies;
- ii) hydrogen-assisted propagation which is operative when some critical conditions are encountered.

Constitutive laws are proposed for both intrinsic propagation and water-vapor assisted propagation.

Keywords: Fatigue, near-threshold crack growth, effective stress intensity factor, modeling, gaseous environment, vacuum, water vapor, adsorption, microstructure.

¹ Directeur de Recherche CNRS, Laboratoire de Mécanique et de Physique des Matériaux, UMR CNRS 6617, ENSMA, 86960 Futuroscope Cedex, France.

² Maître de Conférence, Laboratoire de Mécanique et de Physique des Matériaux, UMR CNRS 6617, ENSMA, 86960 Futuroscope Cedex, France.

³ Chargée de Recherche CNRS, Laboratoire de Mécanique et de Physique des Matériaux, UMR CNRS 6617, ENSMA, 86960 Futuroscope Cedex, France.

Introduction

During the last two decades, the near-threshold fatigue crack propagation has been widely investigated. The ability to define the conditions under which cracks or defects are effectively nonpropagating is a powerful means for design and failure analysis. The threshold stress intensity factor range, ΔK_{th} , was initially assumed to be a material parameter. However, numerous experimental data showed that ΔK_{th} and the near-threshold propagation behavior are dependent on several intrinsic and extrinsic parameters [1,2]. It has been shown that the number of affecting parameters is reduced by taking into account the contribution of the shielding effect of crack closure [3]. Introducing the concept of effective stress intensity factor range, ΔK_{eff} , as defined by Elber [3], leads to the concept of effective fatigue crack propagation which is assumed to be more representative of the intrinsic material properties. The interest in the near-threshold fatigue crack growth and in the threshold concept has been accentuated by the problem of short fatigue cracks. It has been demonstrated that short cracks tend to propagate without closure contribution, which is mainly explained by the absence of closure induced by the crack wake during the early growth [4]. In many cases, the short crack propagation can be described using effective long crack propagation laws (i.e. after closure correction). In such conditions, the effective behavior becomes a more general concept applicable to many kinds of cracks. However, there are still problems that must be solved by reaching a better understanding and hence a comprehensive description of the near-threshold fatigue crack growth. Even after closure correction, at least two main parameters still have a decisive influence: microstructure and environment.

Following the initial work of Dahlberg [5], Hartman [6] and Bradshaw and Wheeler [7], the deleterious effect of ambient air on fatigue crack propagation as compared to an inert environment like high vacuum, has been clearly related to the presence of moisture in the surrounding environment for most of the metallic materials fatigued at room temperature [8-28]. At higher temperature, the respective role of water vapor and oxygen is more disputed [26]. The main difficulty encountered to understand the role of water vapor resides in the complex interactions of an active environment with other parameters which influence the propagation, including intrinsic parameters as alloy composition and microstructure or extrinsic parameters as loading conditions, specimen geometry, crack depth, crack closure and temperature. This paper proposes a survey of studies conducted on the influence of gaseous moist environments on fatigue crack propagation at mid and low rates, on the basis of a framework describing the intrinsic fatigue crack propagation which is essential to uncouple the respective influence of the different factors and to analyze their interactions.

General Evidences of Environmentally Influenced Fatigue Crack Growth

The diagrams plotted in Figures 1 to 4 give illustrations of the influence of ambient atmosphere on the effective near-threshold FCP in different metallic materials at room or moderate temperatures: high purity Al-Zn-Mg single crystal [20], high strength steel used for helicopter rotors [22], Ti-6Al-4V Titanium alloys used in turbine engine at 300°C [27], and an intermetallic compound type Fe-Al under development for aeronautic application [28]. A general trend can be observed in all cases with a growth

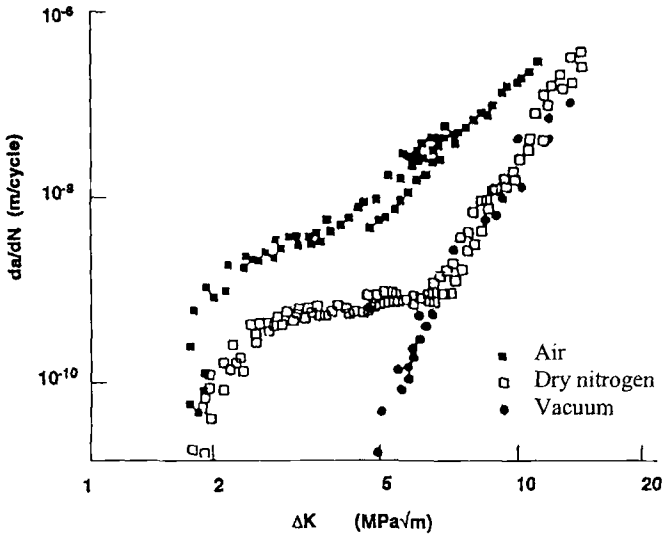


Figure 1 – Fatigue crack propagation in a single crystal of Al-4.5% wt Zn-1.25% wt Mg in ambient air, high vacuum and dry Nitrogen (15 ppm H₂O). R=0.1 and 35 Hz.

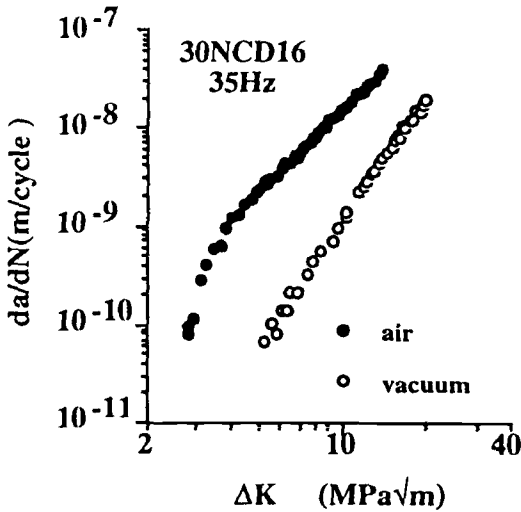


Figure 2 – Comparison of propagation data in ambient air and high vacuum on a high strength steel 30NCD16. R=0.7, 35 Hz.

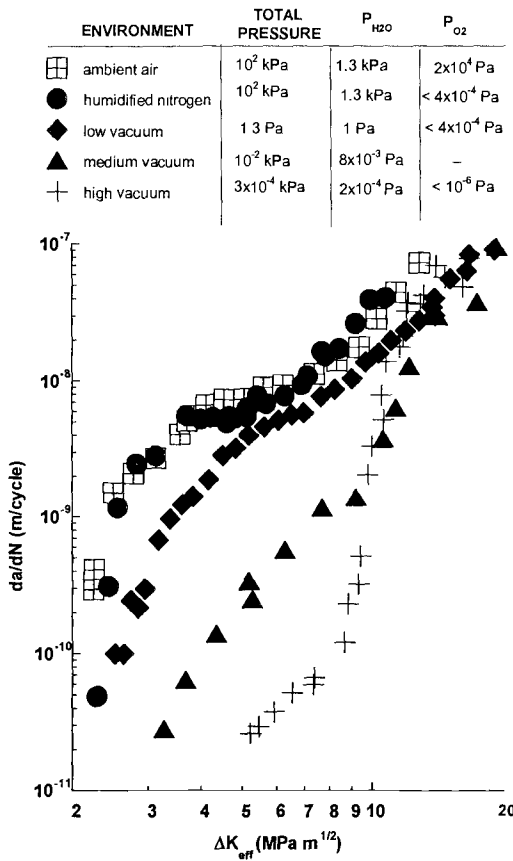


Figure 3 – Influence of partial pressure of water vapor and oxygen on fatigue crack growth in a Ti-6Al-4V alloy at 300°C (Constant K_{max} test performed at 35 Hz).

rate in air substantially accelerated compared to that in vacuum at given effective stress intensity factor ranges. A critical rate range lays about 10⁻⁸ m/cycle for polycrystals (10⁻⁹ m/cycle in Al-Zn-Mg single crystals) for tests run at frequencies ranging between 20 and 50Hz.

Above this critical range, the influence of ambient air is limited while, below, it becomes substantial and more and more accentuated when ΔK_{eff} decreases. Finally the effective threshold range, $\Delta K_{eff,th}$, is significantly lower in air than in high vacuum [18-23]. Another point of importance is the comparison of the crack growth in air to that in an inert gas like nitrogen containing traces of water vapor (Figure 1), or under low pressure of gas being mainly water vapor (Figure 3 and 4). Typically, a few ppm of water vapor is sufficient to induce, in the near-threshold area, a detrimental effect similar to that in air, but is innocuous in the mid-rate range. These observations are in

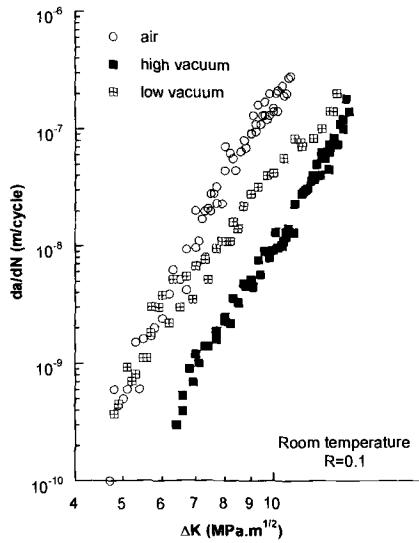


Figure 4 – da/dN vs ΔK curves in a Fe-Al intermetallic compound tested in air, high vacuum (5×10^{-4} Pa) and low vacuum (10^{-2} Pa).

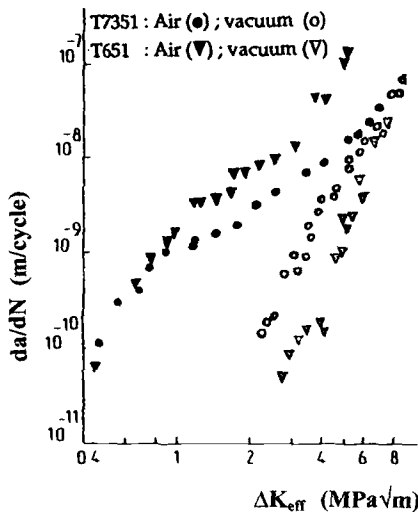


Figure 5 – Interactive influence of microstructure and atmospheric environment on a 7075 alloy in two aged conditions T7351 and T651 tested in ambient air and high vacuum ($R=0.1$, 35 Hz).

accordance with a predominant detrimental effect of water vapor on the growth of fatigue cracks in metallic alloys at room temperature (5-18) and at moderate temperature in Ti alloys (27). Such behavior is analyzed in the followings.

An illustration of the coupled influence of microstructure and environment still existing after closure correction is given in figure 5 on a 7075 alloy in two aged conditions tested in ambient air and high vacuum [21]. The peak-aged matrix contains shareable Guinier-Preston zones and shareable precipitates which promote, at sufficiently low ΔK , a localization of the plastic deformation within a single slip system in each individual grain along the crack front, while the over-aged matrix contains larger and less coherent precipitates which favor a wavy slip mechanism [18, 29-31]. In vacuum, the peak-aged T651 condition leads to a retarded crystallographic crack propagation while the over-aged T7351 condition gives a conventional stage II propagation. The different changes in the slope of the effective curves for both conditions can be interpreted in terms of microstructural barriers to slip-band transmission, as initially suggested by Yoder et al. [32]. But the change in the slope at the level of the critical rate in air are opposite to that in vacuum, and the influence of aging is also completely inverted, the crack growth for the T651 aging being faster in air than that of the T7351 and becoming slower in vacuum. These results support a high sensitivity of slip mechanisms to environment.

From these illustrations of the effect of environment on the fatigue crack propagation behavior, it appears that modeling of crack growth under active atmosphere, such as ambient air, requires a specific approach in term of effective stress intensity factor range (i.e. closure corrected) and accounting with the respective role of embrittling species, surface oxidation and related interactions with closure and all parameters acting on the transport of active molecules up to the crack tip. To finally reach a practical and global description of the nominal propagation, adequate models of the closure contribution should be added as, for example, numerical modelings developed by Newman et al. [33] for plasticity induced closure, or Mc Clung and Sheitoglu et al. for roughness-induced closure [34,35].

Based on studies of the authors and of literature, this paper proposes an overview of studies conducted on various metallic materials and heading to, firstly, a comprehensive framework to describe intrinsic crack propagation in the mid-rate and near-threshold ranges, and secondly, environmentally assisted effective propagation in gaseous moist atmospheres.

Intrinsic Fatigue Crack Propagation

Intrinsic fatigue crack propagation data in the mid-rate range and in the threshold area were obtained in high vacuum and with closure correction or using loading conditions for which crack closure is eliminated (constant K_{max} -tests). In most cases, high vacuum ($<5 \times 10^{-4}$ Pa) has been considered as reference inert environment for tests run at frequencies ranging about 20 to 50 Hz. Tests carried out at low frequency in high vacuum have to be more carefully considered. For example, a substantial acceleration of the growth rates has been observed on a high strength steel tested in high vacuum at 0.2Hz [22] indicating that, even at such low pressure, active species can affect the crack growth process.

Threshold tests were performed using a shedding procedure in accordance with ASTM recommendation. The frequency was generally of 35 Hz and the stress ratio R was from 0.05 to 0.7 or variable (constant K_{max} tests). A furnace was mounted into the environmental chamber allowing experiments at temperatures ranging up to 500°C. Crack advance was optically monitored by mean of a travelling microscope (x10 to 200) at room temperature and measured by the potential drop technique when tests are carried out in controlled atmospheres into the chamber or in the furnace. Closure correction were made using the compliance offset method by mean of back face strain gauges (BFSG) or CTOD gauges clipped at the notch of the specimens when tests are run at room temperature, or using a capacitive detector mounted at the mouth of the notch for tests run into the chamber and at high temperature. Measurements of validation performed at room temperature with the three techniques (CTOD gage, BFSG gage and capacitive detector) were shown in accordance [27]. Numerous experimental data have been obtained on aluminum alloys (Table 1), single crystals of high purity Al-4.5%wtZn-1.25%wt Mg (20), steels (Table 2) and titanium alloys (Table 3) including a γ Ti-48Al-2Mn-2Nb compound.

Table 1—*Properties of Al alloys*

Alloys	Conditions	σ_y (Mpa)	σ_M (Mpa)	Elongation (%)	Grain size (μ m)
2024	T351	320	473	17.5	40 (Equiaxed)
2618	T651	400	460	10.0	40 (Equiaxed)
7075	T351	458	583	10.6	600 x 150 x30
7075	T651	527	590	11.0	600 x 150 x30
7075	T7351	470	539	11.7	600 x 150 x30
7075	24 hours at 200°C	234	338	14.4	600 x 150 x30
X7075	T7351	390	464	16.0	8000 x 350 x 310
7175M	T7351	475	546	9.8	2400 x 500 x 200
7175F	T7351	465	538	11.0	200 x 100 x 20
Al-4.6Cu-1.1Li-Zr	44 hours at 190°C	496	517	-	Partially recrystallized (10%)
Al-4.6Cu-1.1Li-Zr	64 hours at 160°C	531	593	12	Partially recrystallized (10%)

Table 2 – *Mechanical properties of steels*

Steels	σ_y (Mpa)	σ_M (Mpa)	Elongation (%)
30NCD16	1130	1270	13
MARVAL X	1240	1300	14
E 460	460	600	21
METASAFE S 1000	771	1046	14
A 316	220	580	-

Table 3 – *Properties of titanium alloys*

Ti alloys	σ_y (Mpa)	σ_M (Mpa)	Elongation (%)	microstructure
Ti-6Al-4V :				
Room T	975	1035	16	80% of α_p platelets + fine grains
300°C	650	770	20	
Ti 6246 (Room T)	985	1098	10.2	Widmanstätten
Ti-48Al-2Mn-2Nb (Room T)	195/220	286/288	0.25/0.6	Fully lamellar

The intrinsic FCP has been analyzed [36] in accordance to three basic crack propagation regimes:

i) The intrinsic stage I, has been identified on single crystals of peak aged Al-Zn-Mg alloy (Figure 6). Typically, the crack develops within a $\{111\}$ plane pre-oriented for single slip [37]. This regime is also typical of the early growth of microstructural short cracks in polycrystals [38].

ii) The intrinsic stage II is commonly observed on polycrystals and single crystals in the so-called Paris regime when crack propagation proceeds at macroscopic scale along planes normal to the loading direction [39,40]. Such propagation is favored by microstructures which promote homogenous deformation and wavy slip as large or non-coherent precipitates or small grain sizes. Accumulation and tangling of dislocations near the crack tip reduce plastic blunting ability of the material, and result in a

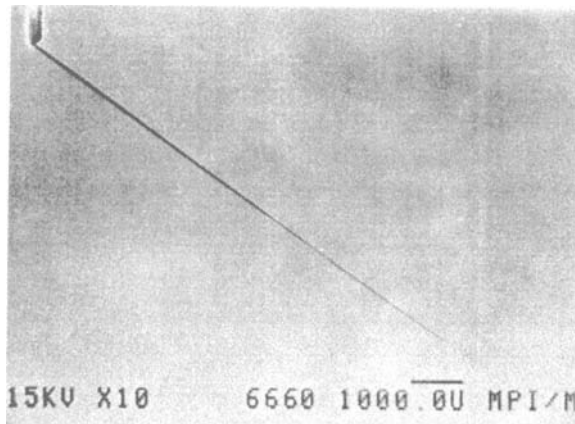


Figure 6 – *Stage I crack growth in high vacuum in a peak aged single crystal of Al-4.5% wt Zn-1.25% wt Mg alloy preoriented for (111) slip.*

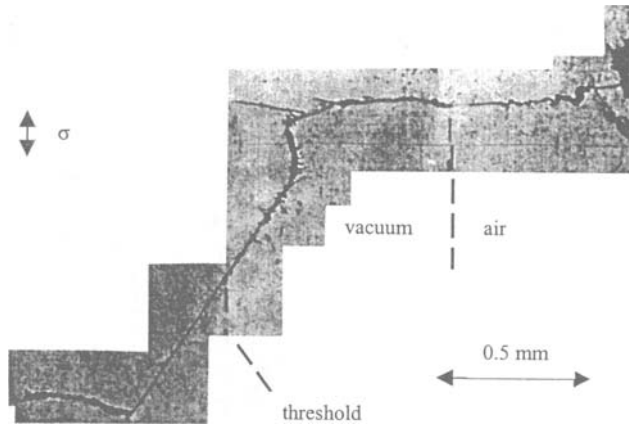


Figure 7a – Crack propagation in high vacuum of an overaged single crystal of Al-4.5% wt Zn-1.25% wt Mg alloy preoriented for easy slip ($R=0.1$, 35 Hz). The initial stage II crack switches to a stage I crack in the near-threshold domain. After threshold, at increasing ΔK , the stage I crack switches again to stage II.

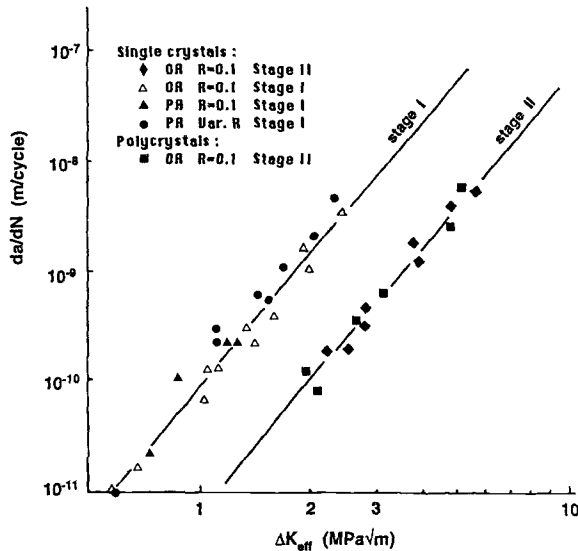


Figure 7b – Crack propagation data in high vacuum of single crystals and polycrystals of Al-4.5% wt Zn-1.25% wt Mg alloy ($R=0.1$, 35 Hz). Only data for well established stage I and stage II have been selected and ΔK values correspond to mode I loading.

discontinuous progression of the crack front as well in the mid-rate range as in the near threshold region [39]. Figure 7a illustrates the change from a near threshold stage I to a mid ΔK stage II propagation in an Al-Zn-Mg single crystal. Figure 7b shows that,

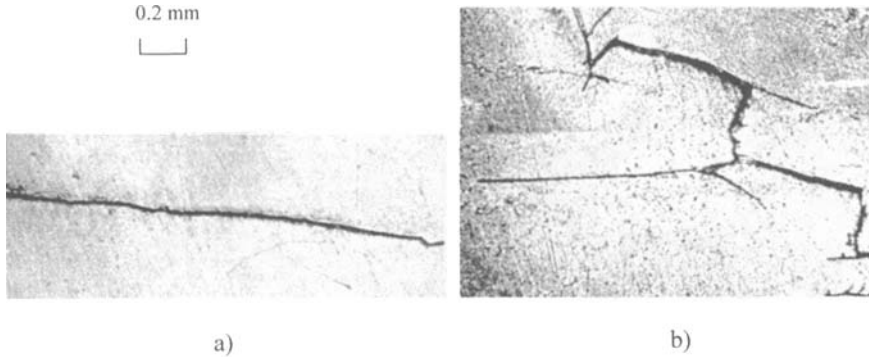


Figure 8 – a) Profile of a stage II crack grown in high vacuum in a Al-1.1% wt Li alloy ($R=0.1$, 35 Hz); b) Profile of a stage I-like crack grown in high vacuum in a Al-1.1% wt Li alloy ($R=0.1$, 35 Hz).

in comparable loading conditions, stage I cracks grow much faster than stage II cracks. This result is specially of importance for the early propagation of microcracks. Figure 8a gives an example of the crack profile of a stage II crack in a technical Al-Li alloy.

iii) The intrinsic stage I-like propagation corresponds to a crystallographic crack path which is observed in polycrystals near the threshold or in the early stage of growth of naturally initiated microcracks [38] when the microstructure favors heterogeneous deformation along single slip systems within individual grains [31,36] (see example in Figure 8b). Crack branching or crack deviation mechanisms [41] and barrier effect of grain boundaries [38], are assumed to lower the stress intensity factor at the crack tip of the main crack and so to induce such retarded propagation compared to the two other stages.

The intrinsic stage II regime for mode I loading is in accordance with a propagation law derived by Petit et al. [18, 22, 40] from the models initially proposed by Rice [42] and Weertman [43] :

$$(da/dN)_{int} = A/D_0^* (\Delta K_{eff}/E)^4 \quad (1)$$

where A is a dimensionless parameter, E the Young modulus and D_0^* the critical cumulated displacement leading to rupture over a crack increment ahead of the crack tip. Intrinsic data for well identified stage II propagation are plotted in Figure 9 in a da/dN vs ΔK_{eff} diagram for a wide selection of Al alloys, and in Figure 10 in a da/dN vs $\Delta K_{eff}/E$ diagram for a selection of steels and Ti alloys in comparison to the mean curve for Al alloys.

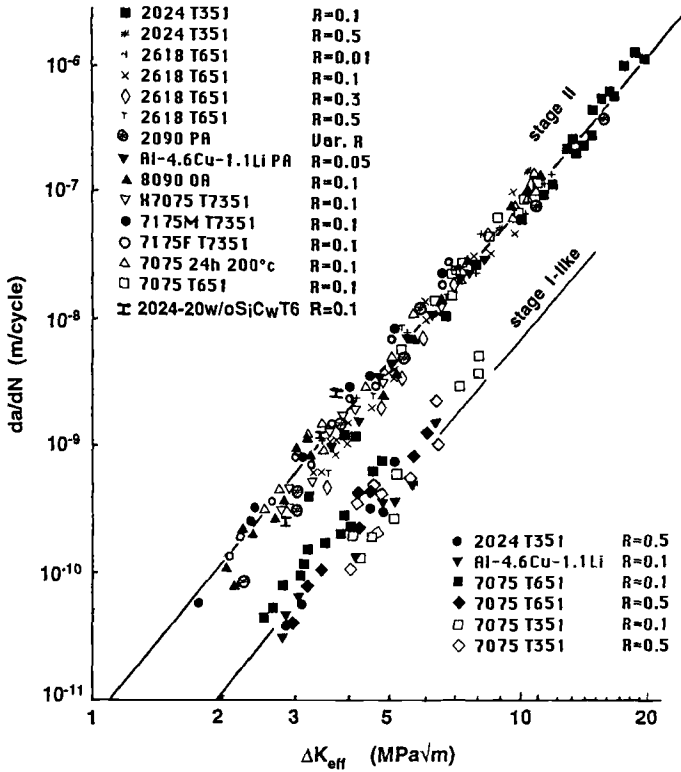


Figure 9 – Intrinsic stage II and stage I-like regimes for a selection of Al based alloys tested at room temperature in high vacuum. Data on 2090PA after [25], 8090 after [62] and 2024-20%SiC_w after [63].

These diagrams constitute an excellent validation of the above relation, specially for growth rates lower than 10^{-7} m/cycle, and confirm that the LEFM concept is very well adapted to describe the intrinsic growth of a stage II crack. This regime clearly appears to be nearly independent on the alloy composition, the microstructure (when it does not induce a localization of the deformation at the crack tip), the grain size, and hence the yield stress. The predominant factor is the Young modulus of the matrix, and the slight differences existing between the three base metals can be interpreted as some limited change in D_0^* according to the alloy ductility [40]. As a consequence, most of the changes observed between the nominal stage II propagation of different alloys in inert environment are inherent to the changes in the Young modulus and in the contribution of crack closure.

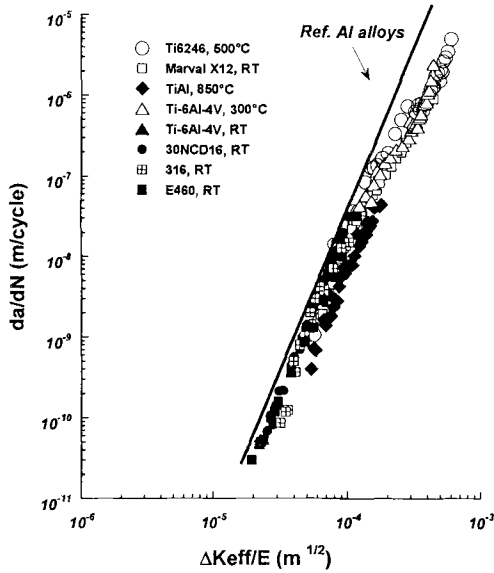


Figure 10 – Intrinsic stage II data plotted in a da/dN vs $\Delta K_{eff}/E$ (E : Young modulus) for a selection of steels and Ti based alloys tested in high vacuum. The straight line is the mean curve for Al alloys (from Fig. 9).

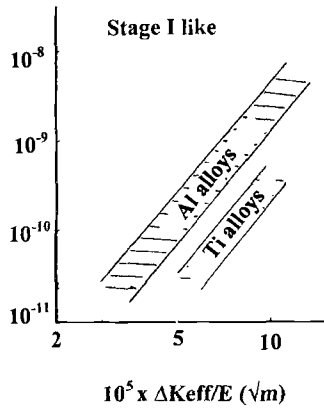
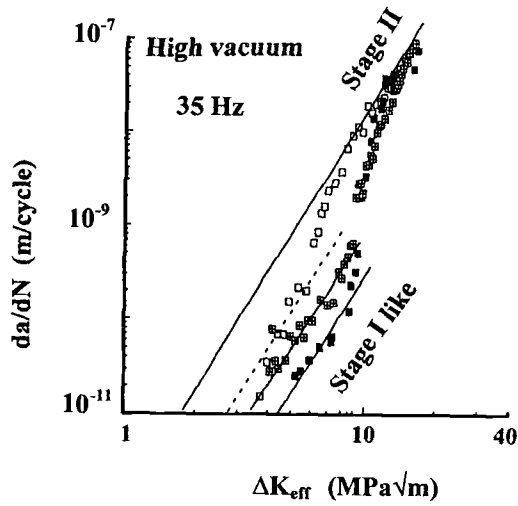
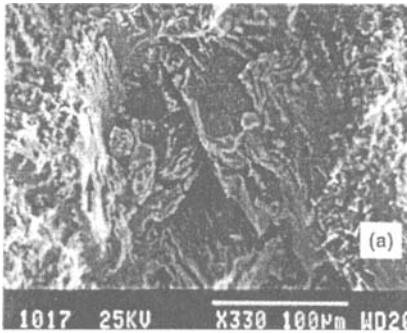


Figure 11 – Scatter bands for intrinsic stage I-like in Al and Ti alloys.

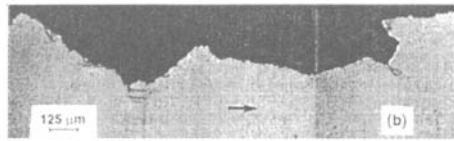
In sharp contrast with the stage II, the stage I-like propagation cannot be rationalized using the above relation (Figures 9 and 11). This regime is highly sensitive to all factors which can favor the strain localization within a single slip system at the microstructural scale. Such localization can occur at very different stress levels with respect to grain size, dimension and shearability of precipitates, thickness and length of lamellae and



a)



b)



c)

Figure 12 – a) Influence of microstructure on intrinsic stage I-like propagation in Ti-6Al-4V alloy tested in high vacuum at 300°C (constant K_{max} tests, 35 Hz):
 bimodal 40% α_p ($\phi=20\mu\text{m}$),
 ■ heterogeneous 80% α_p ($\phi=8\mu\text{m}$ + lamellae of 50 μm),
 ■ globular 75% α_p ($\phi=8\mu\text{m}$);
 b) Microfractographic aspect of a stage I-like crack in heterogeneous microstructure;
 c) profile of stage I-like crack of Figure 12b.

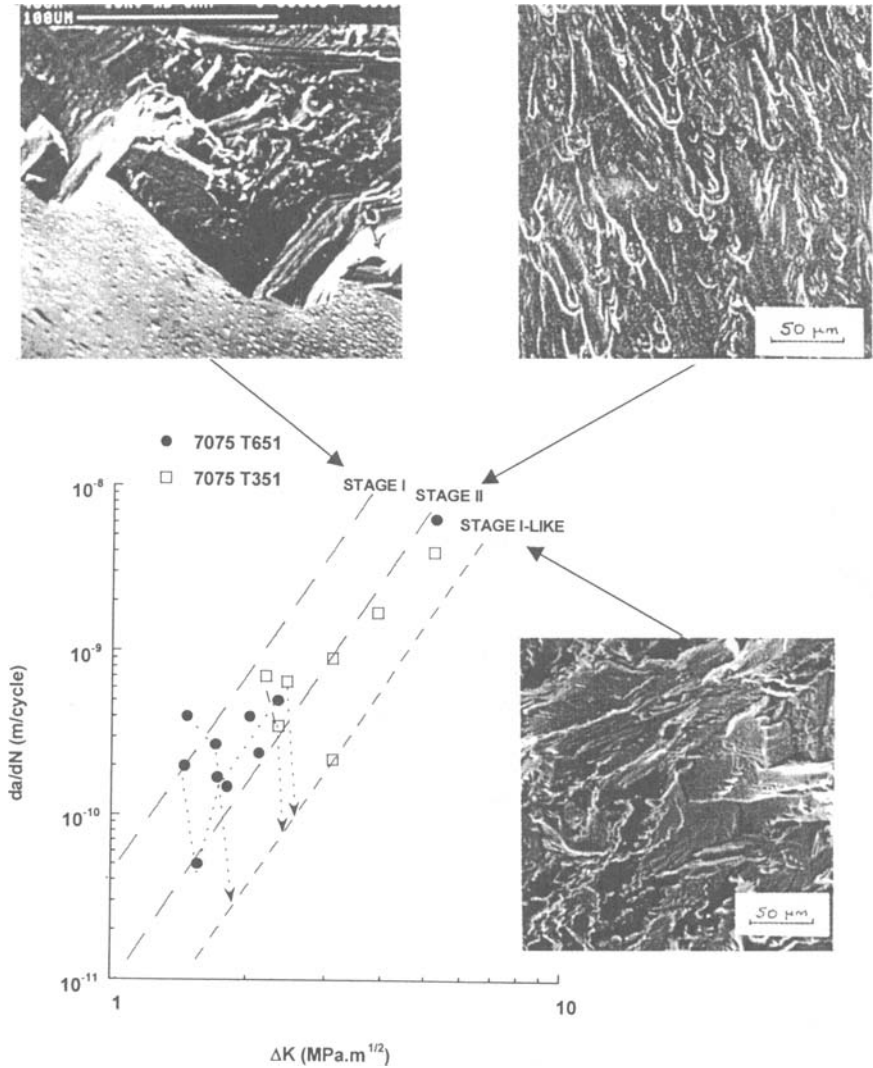


Figure 13 – Comparison with the three intrinsic regime of propagation data of naturally initiated microcracks grown in high vacuum in a 7075 alloy in different aged conditions ($R=0.1$, 35 Hz).

nature and volume fraction of the phase where such localization takes place. For example, the Figure 12a gives an illustration of the influence of the size and of the volumic fraction of primary α_p grains in a TA6V alloy treated in three different conditions. The higher the α_p volume fraction or/and the larger the grain size, the more accentuated the retardation induced by the crystallographic crack path (Fig. 12b and c) which develops within each individual α_p grains along basal planes as identified using the EBSD technique [27]. In addition, the retardation is more well marked when the number of available slip systems is limited (Ti alloys) or is nearly absent when some secondary slip systems can be activated near the boundaries [44] and facilitate the crossing of slip barriers as observed in Al-Li alloys with Lithium addition higher than 2 % wt.

The intrinsic behavior of naturally initiated microcracks has been analyzed on the basis of the above framework consisting of three main crack regimes [45]. An illustration is given in Figure 13.

As observed in illustration (a) of Figure 13, microcracks initiated at the surface of a specimen of a 7075 type alloy in T651 peak aged condition, grow in the stage I regime in the first grain. Such propagation is favored by GP and S' shareable precipitates which promote the localization of the deformation within PSB's [31]. When the crack has crossed several grains, the retarded stage I-like propagation regime with a rough crystallographic surface morphology prevails (illustration (c) of Fig. 13). For larger crack extend and higher ΔK ranges, the propagation switches to the intermediate stage II regime (illustration (b) of Fig. 13). So, it has been shown that, when the relation of the crack propagation with respect to the microstructure is well established, the LEFM concept, i.e. the ΔK concept, can be applied as well for short cracks as for long cracks after correction for closure and when condition for small scale yielding are fulfilled.

Environmentally Assisted Crack Propagation

Following the rationalization of intrinsic stage II propagation presented above, some similar rationalization of FCG in air would be expected after correction for crack closure and Young modulus effects. Figure 14 presents a compilation of stage II propagation data obtained in ambient air for a selection of alloys. Obviously there is no rationalization in air. The sensitivity to atmospheric environment is shown strongly dependent as well on base metals, addition elements, and microstructures (see 7075 alloy in three different conditions) as on R ratio and growth rate. However, as noted above, a typical common critical rate range can be pointed at about 10^{-8} m/cycle (Figure 15). This critical step is associated to stress intensity factor ranges at which the plastic zone size at the crack tip is of the same order as grain or sub-grain diameters. In addition it has been shown that, for growth rates lower than this critical range, crack propagation results from a step-by-step advance mechanism instead of a cycle-by-cycle progression as generally observed in the Paris regime in air [46].

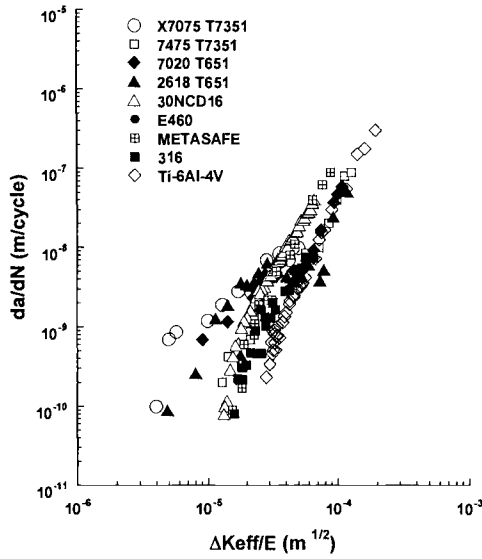


Figure 14 – Comparison of da/dN vs $\Delta K_{eff}/E$ crack growth data in air for various alloys.

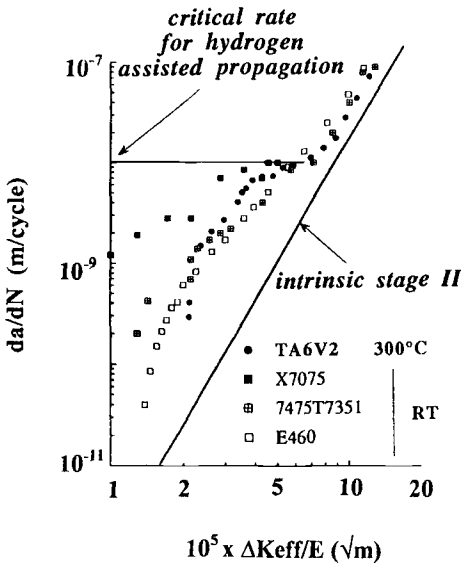


Figure 15 – Critical crack growth rate $(da/dN)_{cr}$ below which enhanced environmental influence is observed.

On the basis of experimental data in air and inert gas containing traces of water vapor, obtained on similar aluminum alloys, steels and Ti alloys than those tested in vacuum, a comprehensive model has been established by Petit et al. [18,21,22] including two different mechanisms for environmentally assisted crack growth as schematically illustrated in Figure 16.

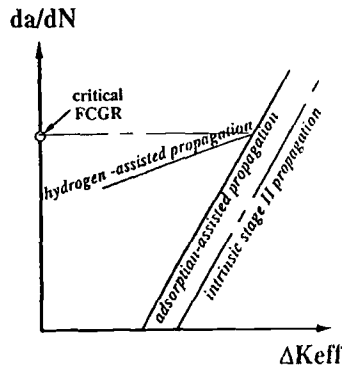


Figure 16 – Schematic illustration of the two different environmentally assisted stage II propagation regimes in comparison to intrinsic stage II propagation.

- at growth rates higher than a critical rate $(da/dN)_{CR}$ which depends upon several factors as surrounding partial pressure of water vapor, load ratio, test frequency, chemical composition and microstructure, the crack growth mechanism is assisted by water vapor adsorption but is still controlled by plasticity as in vacuum;
- at growth rates lower than $(da/dN)_{CR}$, an hydrogen assisted crack growth mechanism becomes operative, hydrogen being provided by adsorbed water vapor when some critical conditions are fulfilled.

Both mechanisms are detailed in the following.

Adsorption Assisted Crack Propagation

Historically, Snowden [47] has first suggested that the environmental effect on fatigue behavior of metals must be described in terms of the number of gas molecules striking the crack tip surface and being adsorbed on fresh metal surface exposed to active species in the part of the loading cycle during which the crack is open. Later, Lynch [10,11] and Bouchet et al. [17] have proposed that active species adsorption or chemisorption on a few atomic layers would be sufficient to enhance fatigue crack propagation by facilitating dislocation nucleation and has demonstrated the detrimental role of water vapor. This approach, based on a surface phenomenon, is close from the description proposed by Petch [48] who derived from Gibbs adsorption equation an expression for the surface energy variation in the case of the adsorption of a diatomic molecule and a Langmuir isotherm [50]:

$$\gamma_1 = \gamma - 2 \Gamma_s k T \ln(1 + (A p)^{1/2}) \quad (2)$$

where γ_1 is the lowered surface energy, A is a constant related to the condensation factor determined by the temperature T , p is the pressure, k the gas constant and Γ_s the number of adsorbed molecules at saturation. According to gas kinetic theory, the number of gas molecules striking a unit area in a unit time is given by the relation:

$$n_0 = NP / (2\pi MkT)^{1/2} \quad (4)$$

where N is the Avogadro number, P the partial gas pressure, M the gas molecular weight. However, assuming that the upper critical pressure in a S-shaped pressure controlled phenomenon corresponds to the value of n_0 at saturation of an adsorbed monolayer, the calculated critical pressures were lower by a factor 100 to 1 compared with experimental data. Similar discrepancies were observed by Bradshaw and Wheeler [7].

A first modification to this approach was proposed by Achter [49] who reconsidered coverage condition at the crack tip and the impedance factor related to the restricted gas flow in the fatigue crack; but substantial discrepancies were still observed between calculated and experimental critical pressure values. These approaches based on correlation between rate variations and pressure of active gas at the crack tip did not settle the actual governing mechanism. In addition unity sticking coefficients were assumed. The influence of R ratio or/and of crack closure was not taken into account, and geometrical crack surfaces were considered instead of physical surfaces which could be much larger.

In accordance with Lynch approach [10, 11] adsorption is considered only to induce change in the cumulated displacement D^* , the basic crack propagation mechanism being similar to that in high vacuum, i.e. in inert environment. Reconsidering the superposition model originally formulated by Wei [12-16], a revised formulation has been proposed in the form [18]:

$$(da/dN)_e = (da/dN)_{int} + \theta[(da/dN)_{e,s} - (da/dN)_{int}] \quad (5)$$

with suffixes e = environmental, int = intrinsic, e,s = saturated environmental effect, θ coverage coefficient of freshly created surfaces by adsorbed water vapor molecules as originally defined by Langmuir [50]. The variation of D^* with respect to θ can be written as follows:

$$1/D^* = [1/D^*_0 + \theta (1/D^*_1 - 1/D^*_0)] \quad (6)$$

where D^*_0 is the intrinsic value of D^* for $\theta = 0$ and D^*_1 the value of D^* when surfaces are saturated ($\theta = 1$).

The adsorption assisted propagation law can be derived from equation (1) as:

$$\begin{aligned} (da/dN)_{ad} &= A/D^* (\Delta K_{eff}/E)^4 \\ &\text{or} \\ (da/dN)_{ad} &= A[1/D^*_0 + \theta (1/D^*_1 - 1/D^*_0)] (\Delta K_{eff}/E)^4 \end{aligned} \quad (7)$$

The knowledge of the dependence of θ upon the frequency and the water vapor pressure is hence essential. Wei et al. [12-16] have proposed to depict this dependence by considering gas transport at the tip and surface reaction kinetics. Two limiting cases are considered:

i) the transport controlled case with:

$$\theta = \frac{F}{SN_0RT} P_0 t \tag{8}$$

where S is the active surface area, N_0 the number of adsorption sites per unit surface area, R the gas constant, T the temperature, P_0 the surrounding pressure, t the time, and F the Knudsen flow parameter.

Because of the rapid reactions of environment with fresh surface (high reaction rate constant k_c) and the limited rate for supply of active species to the crack tip, significant attenuation of the active gas pressure takes place at the crack tip ;

ii) the surface reaction controlled case with:

$$\theta = 1 - \exp(-k_c P_0 t) \tag{9}$$

when the reaction rates are sufficiently slow so that the gas pressure at the crack tip is essentially equal to the external pressure.

It is noticeable that Wei's model for transport controlled regime is in agreement with adsorption controlled propagation. Hence hydrogen assistance is not required to use this mode. But conversely, when hydrogen assistance is operative, specially in near-threshold condition, the Wei's model cannot be used.

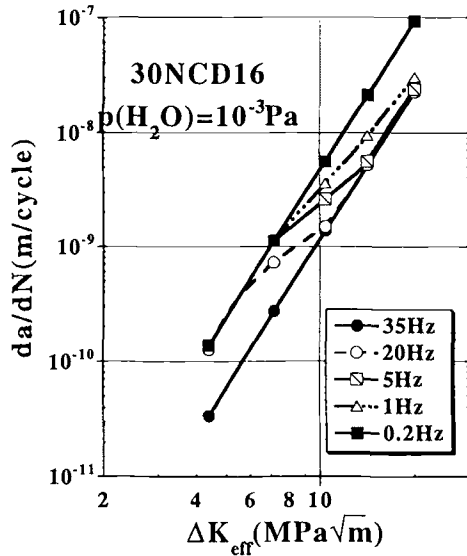


Figure 17 – Influence of test frequency on the effective crack growth in a high strength steel under very low partial pressure of water vapor ($5 \times 10^{-3} Pa$).

An illustration of adsorption assisted propagation is given in Figure 17 for a 30NCD16 steel tested at a total pressure of 1.3×10^{-3} Pa, with a partial pressure of water vapor of 1.0×10^{-3} Pa. At a frequency of 0.2 Hz the prevailing regime is adsorption assisted propagation ($\theta = 1$) while at 35 Hz the intrinsic regime is operative ($\theta = 0$). At intermediate frequency, a transitional behavior is observed, θ varying during the test from 1 to 0 at increasing rates. A reassessment of Wei's model has been done by G. Henaff et al. [22] to describe the low rate range and to account for very low pressures. A critical point has been the formulation of the crack impedance for a quasi-stationary crack and a molecular flow. The S curves drawn in Figure 17 correspond to θ evolutions as computed from the following equation:

$$\alpha S_0 \theta / 4F - \frac{1}{N_s V_a} \log(1 - \theta) = \frac{P_0}{4 N_0 RT} t \quad (10)$$

where α is the surface roughness parameter, V_a the average molecular rate, N_s number of stationary cycles.

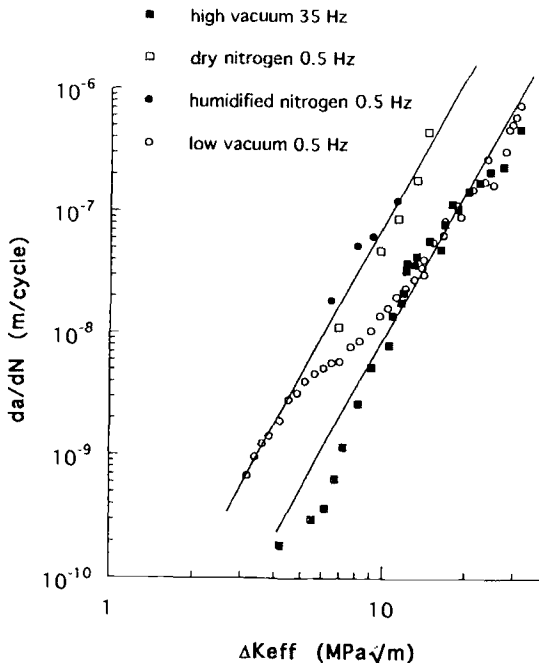


Figure 18 – Adsorption assisted regime in Ti-6Al-4V alloy at 300°C as defined from tests at different frequencies and partial pressure of water vapor and compared to intrinsic crack propagation in high vacuum.

The computations reveal success in accounting for the adsorption-assisted propagation in 30NCD16 steel [22] (Fig. 17) and also on TA6V at 300°C in Ti-6Al-4V (Fig. 18). For the latter alloy a value of the surface roughness parameter α of 173 is used. This value is much higher than that used by Wei et al. [12-16] and Ogawa et al. on titanium alloys [51] lying between 1 and 2. The present value has been obtained considering that the fatigue rupture surface is fractal from a scale of 10^{-1} mm² to a scale 10 mm² (which seems reasonable to evaluate the number of available adsorption sites) and a fractal dimension of 2.2 in agreement with results from Mandelbrot et al. on steels [52] or Bouchaud et al. on Al alloys [53].

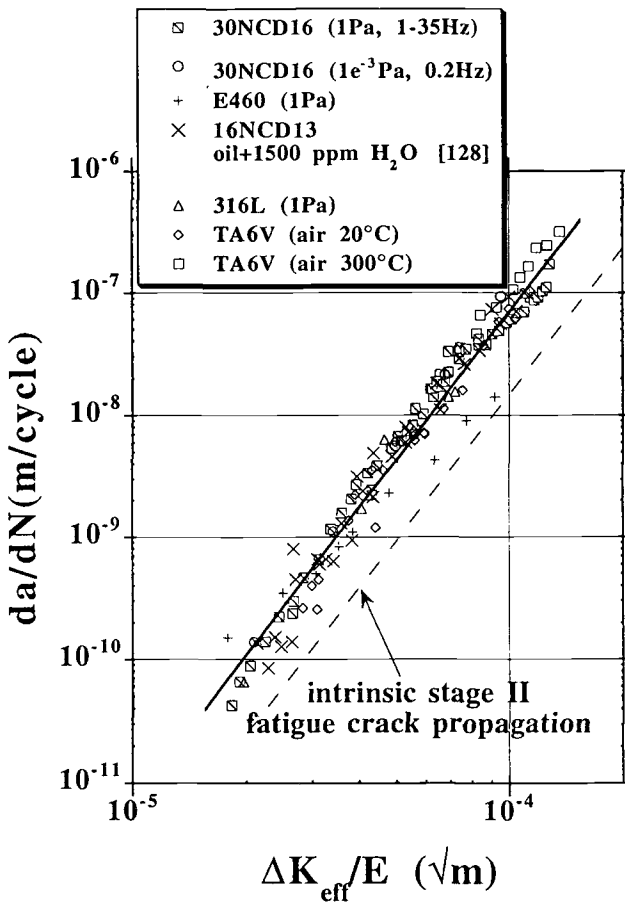


Figure 19 – Adsorption assisted regime on different steels and on Ti-6Al-4V alloy in selected environments.

In Figure 19 are plotted data for adsorption assisted propagation in different steels and in Ti-6Al-4V alloy. It can be seen that a reasonable rationalization of da/dN with respect to $\Delta K_{eff}/E$ is obtained suggesting a comparable acceleration of the growth rates in both types of alloys.

Hydrogen Assisted Propagation

This propagation regime becomes operative when several conditions favoring high hydrogen concentration into the process zone at the crack tip are fulfilled:

conditions of access to the crack tip for active species which lead to sufficient partial pressure of water vapor to create an instantaneous adsorbed monolayer, surrounding pressure, frequency, growth rate, R ratio. In such conditions, the mechanism is reaction-controlled;

- sufficiently low stress intensity factor to reach a regime with a stationary crack and plastic deformation localized in a limited number of slip systems within a single grain at the crack front;

- a long time enough to allow hydrogen to diffuse by dislocation dragging so as to attain a critical hydrogen concentration for metal embrittlement.

Such conditions are encountered in ambient air or in humidified inert gas for growth rates lower than a critical rate $(da/dN)_{CR}$ [49].

The occurrence of the hydrogen assisted regime can be associated to a typical change in the slope of the propagation curves which becomes close to 2 to 1, and the transition from one regime to the other is marked by a more or less well defined plateau range (Fig. 14, 15, 19). A slope of 2 to 1 suggests a $\Delta CTOD$ controlled propagation and using a superposition model, the following expression can be proposed for environmentally assisted propagation :

$$da/dN = (da/dN)_{ad} + (da/dN)_H^2 \quad (11)$$

$$da/dN = 1/D^*_{cs} (\Delta K_{eff}/E)^4 + \Delta K_{eff}^2/E\sigma \quad (12)$$

where σ is the yield stress of the material at the crack tip.

Application of this relation to crack growth in air and of relation (1) in vacuum for Al alloys shows a good agreement with the experimental data (Fig. 20). But it is still an empirical description for hydrogen assistance.

Hydrogen embrittlement of iron-based metal requires the accumulation of a critical hydrogen concentration at some specific spots, unlike aluminum alloys where embrittlement would result from the formation of hydrides whose brittle nature would in turn induce an embrittlement of the bulk material [54]. Nevertheless these two processes would behave in the same way from a kinetic point of view, which might explain a certain analogy in near-threshold fatigue crack growth behavior. However, the embrittling process by itself remains unclear and some authors think it is better to talk about "hydrogen-assisted cracking" rather than "hydrogen embrittlement" [55,56] since the brittle nature of the process is not obvious.

Beachem [56] proposed "microscopic plasticity mechanisms" and "severe, localized crack-tip deformations" to explain this behavior. Some authors have shown by in-situ observations that hydrogen induces an easier motion of the dislocations and a

subsequently earlier rupture as compared to vacuum [57]. This is also consistent with Beachem's theory which suggests that "instead hydrogen locking dislocation in place," it "unlocks them to multiply or move at reduced stresses" [58], so that one might talk about enhanced plasticity.

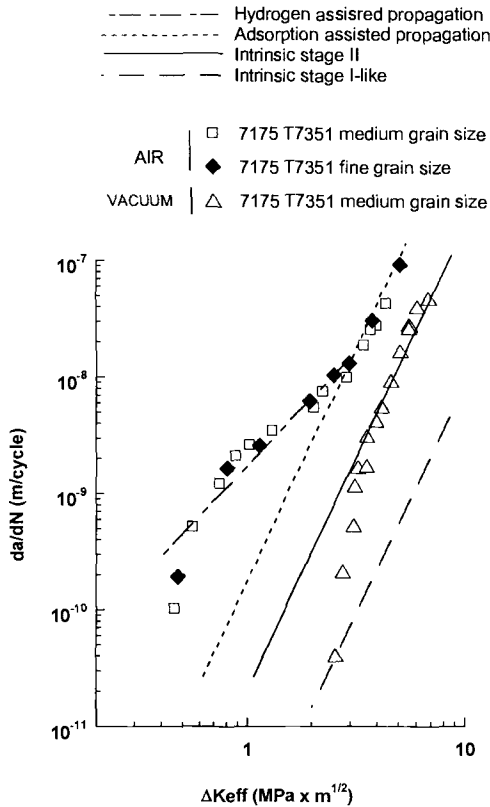


Figure 20 – Application of the superposition model for environmentally assisted propagation in Al alloys.

Strain localization represents an alternative mechanism [58]. In accordance with this mechanism and on the basis of in-situ crack tip observations in air and in vacuum, and as mentioned above, McEvily and Gonzalez Vasquez [59] have proposed a representation of the influence of environment on the blunting process at the crack tip. The higher growth rates in air would result from a lesser blunting as compared to vacuum. This analysis is consistent with Davidson and Lankford's previous findings [60,61]. According to them, as less energy is dissipated in plastic deformation in air, more energy

is available for the growth process. It can be pointed out that the two approaches are not opposed.

Finally, it should be emphasized that further in-depth investigations covering different scientific fields are still required in order to precisely define the hydrogen - assisted mechanism observed in humid atmospheres on metallic alloys.

Conclusions

From studies conducted during the last 25 years on the influence of atmospheric environment on fatigue crack propagation in metallic alloys the following conclusions can be drawn:

1 – Theoretical models developed since the initial works of Mc Clintock, Rice and Weertman do not take into account any potential influence of environment and closure; so any correlation between such models and experiments should be done using intrinsic data provided by experiments conducted in inert environment and corrected for closure.
2 – The concept of inert environment has to be carefully used especially at low growth rates and low frequencies; for example, traces of water vapor of the order of a few ppm inert gas can be active in the near-threshold area.

3 – Based on numerous experiments on a wide selection of metallic alloys, three main intrinsic propagation regimes have been clearly defined:

i) Intrinsic stage I which has been identified on single crystals and is also typical of the early propagation of surface microcracks. Stage I is the fastest regime for given loading conditions.

ii) Intrinsic stage II propagation is observed on most of the metallic alloys in the Paris regime, with a crack path normal to the stress axis. A modeling derived from Weertman and Rice initial models is proposed as: $da/dN = A/D^* \cdot (\Delta K_{eff}/E)^4$

iii) Intrinsic stage I-like propagation corresponds to stage I propagation at the scale of each individual grain along the crack front. But at macroscopic scale, the crack remains normal to the stress axis as a stage II crack. As a consequence of shielding effects (crack branching, crack deviation and microstructural barriers) the stage I-like is generally retarded if compared to stage II, and is very sensitive to microstructure and respective slip localization.

4 – The environmental crack growth enhancement has been analyzed by comparing effective data in gaseous environment containing well-controlled amount of water vapor and oxygen, to intrinsic data:

i) The effective propagation in ambient air is characterized in most cases by a strong environmental enhancement of the crack growth, especially near the threshold, and is much more accentuated for Al alloys than for steels and Ti alloys at room temperature.

ii) In contrast to intrinsic stage II, environmentally-assisted effective stage II is highly sensitive to several factors including alloy composition, microstructure, grain size and yield strength.

5 – The behavior in moist environment of metallic alloys can be described by the superimposing of two distinct processes:

i) Adsorption of water vapor molecules which promotes the growth process without altering the basis intrinsic mechanism of damage accumulation. Adsorption onto fresh surfaces is analyzed as a decrease in the critical cumulated displacement D^* which has been described in term of the surface coverage coefficient θ . This regime is generally

operative in the mid-rate range at atmospheric pressure, but can be operative near-threshold condition at sufficiently low partial pressure of water vapor.

ii) Hydrogen-assisted propagation as initially described by Wei and co-authors in which hydrogen is provided by the dissociation of adsorbed water vapor molecules. Critical conditions for such mechanism depend on water vapor pressure, time (frequency) and temperature. This regime is generally observed in near-threshold conditions, at a growth rate below a critical step ranging about 10^{-8} m/cycle, which corresponds to deformation localized within individual grain.

References

- [1] Bäcklund, J., Blom, A.F. and Beevers, C.J., *Fatigue Thresholds, Fundamentals and Engineering Applications*, Proc. of an International Conference held in Stockholm, June 1-3, 1981. EMAS Pub., U.K., 1982, pp..
- [2] Davidson, D. and Suresh, S., *Fatigue Crack Growth Threshold Concept*, TMS AIME Pub., Warrendale, PA, 1984, pp..
- [3] Newman, Jr., J.C. and Elber, W., *Mechanics of Fatigue Crack Closure*, ASTM STP 982, American Society for Testing and Materials, pub., 1988, pp.
- [4] Lankford J. and Ritchie R.O., *Short fatigue cracks*, Santa Barbara, 1992.
- [5] Dahlberg, E. P. "Fatigue crack propagation in high strength 4340 steel in humid air", *A.S.M. Transactions Quarterly*, Vol. 58, 1965, pp. 46-53.
- [6] Hartman, A., *International Journal Fracture Mechanic*, Vol. 1, 1965, pp.167-187.
- [7] Bradshaw, F.J. and Wheeler, C., *Appl. Mat. Research*, 1966, pp.112-120.
- [8] Enochs, J.S., Devereux, O.F., *Met. Trans.*, 6A, 1975, pp. 391-397
- [9] Buck, O., Fransen, J.D., Marcus, H.L., *Engng. Fract. Mech.*, 7, 1975, pp. 167
- [10] Lynch, S. P., "Mechanisms of Fatigue and Environmentally Assisted Fatigue", *Fatigue Mechanisms*, ASTM STP 675, American Society for Testing and Materials, pub., 1978, pp.174-213.
- [11] Lynch, S. P., "Environmentally-assisted cracking: overview of evidence for an adsorption-induced localised-slip process", *Acta Metallurgica* , 36, 1988, pp.2639-2661.
- [12] Simmons, G. W., Pao, P. S. and Wei, R. P., "Fracture Mechanics and Surface Chemistry Studies of Subcritical Crack Growth in AISI 4340 Steel", *Metallurgical Transactions*, 94, 1978, pp.1147-1158.
- [13] Wei, R. P., "On understanding environment-enhanced fatigue crack growth: a fundamental approach", *ASTM STP 675*, American Society for Testing and Materials, pub., 1979, pp.816-840.
- [14] Wei, R. P., Pao, P. S., Hart, R. G., Weir, T. W. and Simmons, G. W., "Fracture Mechanics and Surface Chemistry Studies of Fatigue Crack Growth in an Aluminum Alloy", *Metallurgical Transactions*, 11A, 1980, pp.151-158.
- [15] Wei, R. P. and Simmons, G. W., "Recent progress in understanding environment-assisted fatigue crack growth", *International Journal of Fatigue*, 17, 1981, pp.235-247.
- [16] Pao, P.S., Gao, M. and Wei, R.P., "Critical assessment of the model for environmentally-assisted fatigue crack growth", *ASTM-STP 924*, Ed. R.P. Wei and R.P. Gangloff, 1988, pp. 182-195.

- [17] Bouchet, B., de Fouquet, J., Aguilon, M., "Influence de l'environnement sur les faciès de rupture par fatigue d'éprouvettes monocristallines et polycristallines d'alliage Al-Cu 4 %", *Acta Metallurgica*, 23, 1976, pp.1325-1336.
- [18] Petit, J., "Some aspects of near-threshold fatigue crack growth: microstructural and environmental effects", *Fatigue Crack growth Thresholds Concepts*, eds Davidson, D. and Suresh, TMS AIME pub., 1983, pp. 3-25.
- [19] Bignonnet, A., Petit, J. and Zeghloul, A., "The influence of environment on fatigue crack growth mechanisms", Ed. P. Scott, *Environment Assisted Fatigue, EGF7*, Mechanical Engineering Publications, 1990, pp.205-222.
- [20] Gudladt, H. J. and Petit, J., "Stage II crack propagation of Al-Zn-Mg single crystals in dry & wet atmospheres", *Scripta Metallurgica & Materialia*, 25, 1993, pp.2507-2512.
- [21] Petit, J. and Hénaff, G., "A survey of near-threshold fatigue crack propagation : mechanisms and modelling", *Proceedings of Fatigue 93* eds. Baïlon, J.P. and Dickson, I.J., EMAS pub., Vol. 1, 1995, pp.503-512.
- [22] Hénaff, G., Marchal, K. and Petit, J., "On Fatigue Crack Propagation Enhancement by a Gaseous Atmosphere: Experimental and Theoretical Aspects", *Acta Metallurgica et Materialia*, 43, 1995, pp. 2931-2942.
- [23] Petit, J. and Mendez, J., "Some aspects of the influence of microstructure on fatigue", *Fatigue '96*, Eds. G. Lütjering and H. Nowack, Pergamon Press, 1, 1996, pp.15-26.
- [24] Enochs, J.S. and Devereux, O.F., "Fatigue crack growth in 5032-H34, Aluminium in vacuum and active gas environments", *Metallurgical Transaction*, 6A, 1975, pp.391-397.
- [25] Piasick, R.S. and Gangloff, R.P., "Environmental fatigue of Al-Li alloy", *Metallurgical Transactions*, Part. I in 22A, pp. 2415-2428 and Part. II in 24 A, 1991, pp. 2751-2762.
- [26] Lesterlin, S., Sarrazin-Baudoux, C. and Petit, J., "Effects of temperature and environment interactions on fatigue crack propagation in a Ti alloy", *Scripta Materialia*, 34, 1996, pp.651-657.
- [27] Sarrazin, C., Lesterlin, S. and Petit, J., "Atmospheric influence on fatigue crack propagation in titanium alloys at elevated temperature", *Elevated temperature effects on fatigue and fracture, ASTM STP 1267*, Eds. R.S. Piasick, R.P. Gangloff and A. Saxena, (ASTM,1997), 1997, pp.117-139.
- [28] Tonneau, A., Henaff, G., Mabru, C. and Petit, J., "Environmentally-assisted fatigue crack propagation in aluminides at room temperature", *Scripta Materialia*, Vol. 39, N° 11, 1998, pp. 1503-1508.
- [29] Kirby, R.B. and Beevers, C.J., *Fat. Engng. and struct.*, Vol. 1, 1979, pp. 203-215.
- [30] Lindigkeit, J., Gysler, A. and Lütjering, G., *Met. Trans.*, Vol. 12A, 1981, pp. 1613-1619
- [31] Selines, R.J., "The fatigue behavior of high strength Aluminum alloys", *Ph. D. Thesis*, MIT, USA, 1971.
- [32] Yoder, G.R., Cooley, Y.A. and Crooker, T.W., "A critical analysis of grain size and yield strength dependence of near-threshold fatigue crack growth in steels", *Fracture Mechanics, ASTM STP 791*, American Society for Testing and Materials, pub., Vol.1, 1983, pp.348-365.

- [33] Fleck, N. A. and Newman, Jr. C. J., "Analysis of crack closure under plane strain conditions", *Mechanics of fatigue crack closure, ASTM STP 982*, Eds J. C. Newman Jr, and W. Elber, 1988, pp.319-341.
- [34] McClung, R. C., "Finite Element Analysis of Specimen Geometry Effects on Fatigue Crack Closure", *Engng Fract. Mech.*, Vol. 17, 1994, pp. 861-872.
- [35] McClung, R. C. and Sheitoglu, H., *Mechanics of fatigue crack closure, ASTM STP 982*, American Society for Testing and Materials, pub.,, 1988, pp.279-299.
- [36] Petit, J., "Modelling of Intrinsic Fatigue Crack Growth", *Theoretical and numerical analysis of fatigue*, Eds. A. F. Blom and C. J. Beevers, EMAS, 1992, pp.131-152.
- [37] Petit, J., Kosche, K. and Gudladt, H. J., " Intrinsic Stage I Crack Propagation in Al-Zn-Mg Single Crystals", *Scripta Metallurgica et Materialia*, 26, 1992, pp.1049-1054.
- [38] de Los Rios, E. R., Mohamed, H. J. and Miller, K. J., "A micro-mechanical analysis for Short Fatigue Crack Growth", *Fatigue & fracture of Engineering Materials and Structures*, 8, 1985, pp.49-63.
- [39] Roven, H. J. and Nes, E., "Cyclic Deformation of Ferritic Steel - II. Stage II Crack Propagation (Overview n°94)", *Acta Metallurgica et Materialia*, 39, 1991, pp.1735-1754.
- [40] Petit, J. and Hénaff, G., "Stage II intrinsic fatigue crack propagation", *Scripta Metallurgica*, 25, 1991, pp. 2683-2687.
- [41] Suresh, S., "Fatigue crack deflection and fracture surface contact : micromechanical models", *Metallurgical Transactions*, 16A, 1985, pp. 249-260.
- [42] Rice, J. R., "Plastic Yielding at a Crack Tip", *International Conference on Fracture*, Sendai Japan, 1965, pp. 283-308.
- [43] Weertman, J., "Rate of Growth of Fatigue Cracks Calculated from the Theory of Infinitesimal Dislocations Distributed on a Plane", *International Journal of Fracture Mechanics*, 2, 1966, pp. 460-467.
- [44] Xu, Y.B., Wang, L., Zhang, Y., Wang, Z.G. and Hu, Q.Z., "Fatigue behavior of an Aluminum-Lithium Alloy 8090-T6 at Ambient and Cryogenic Temperature", *Metallurgical Transactions*, 22A, 1991, pp.723-729.
- [45] Petit, J., "Influence of environment on small fatigue crack growth", Proc. of Int. Conf. on "Small Fatigue Cracks: Mechanics and Mechanisms", 6-11 Dec. 1998, Kona, Hawaii, USA., Engineering Foundation Pub., N.Y., USA., to be published.
- [46] Davidson, D. L. and Lankford, J., "The effect of water vapor on fatigue crack tip stress and strain range and the energy required for crack propagation in low-carbon steel", *International Journal of Fracture*, 17, 1981, pp.257-275.
- [47] Snowden, K. U., "The Effect of Atmosphere on the Fatigue of Lead", *Acta Metallurgica*, 12, 1964, pp.295-303.
- [48] Petch, N. J., "The lowering of fracture stress due to surface adsorption", *Philosophical Magazine*, 1, 1956, pp.331-337.
- [49] Achter, M. R., "The Adsorption Model for Environmental Effects in Fatigue Crack Propagation", *Scripta Metallurgica*, 2, 1968, pp.525-528.
- [50] Langmuir, I., "The adsorption of gases on plane surfaces of glass, mica and platinum", *Journal of the American Chemical Society*, 40, 1918, pp. 1361-1403.
- [51] Ogawa, T., Tokaji, K. and Ohya, K., *Fatigue Fract. Eng. Mat. Str.*, 16, n° 9, 1993, pp. 973-982.

- [52] Mandelbrot, B.B. Passoja, D.E. and Paullay, A.J., *Nature*, 308, 1984, pp.721-722.
- [53] Bouchaud, E., de Arcangelis, L., Lapasset G. and Planes, J., "les fractales dans la rupture des matériaux", *La Recherche* 233, 1991, pp. 808-809.
- [54] H.K. Birnbaum, H.K., "Hydrogen Related Fracture of Metals", *Atomics of Fracture* , 1983, pp. 733-765.
- [55] Thompson, A.W. and Bernstein, I.M., "The Role of Plastic Fracture Processes in Hydrogen Embrittlement", *Proceed ICF4*, 1977, p.249.
- [56] Beachem, C.D., "A new model for hydrogen-assisted cracking (hydrogen embrittlement)", *Met. Trans.*, 3 , 1972, pp. 437-451.
- [57] Tabata, T. and Birnbaum, H.K., "Direct Observations of Hydrogen-Enhanced Crack Propagation in Iron", *Scripta Met.* , 17, 1983, pp. 947-950.
- [58] Louthan, M.R., Jr. , "Strain Localization and Hydrogen Embrittlement", *Scripta Met.* , 17, 1983, pp. 451-454.
- [59] McEvily, A.J. and Gonzalez Velasquez, J.L., , "Fatigue Crack Tip deformation Processes as Influenced by the Environment", *Met. Trans.*, 23A, 1992, pp.2211-2221.
- [60] Davidson, D.L. and Lankford, J.L., "The effect of water vapor on fatigue crack tip mechanics on 7075-T651 aluminum alloy", *Fat. Engng. Mat. Struct.*, Vol. 3 , 1983, pp. 241-256.
- [61] Davidson, D.L. and Lankford, J.L., "Fatigue crack tip mechanics of a powder metallurgy aluminum alloy in vacuum and in humid air", *Fat. Engng. Mat. Struct.*, Vol. 7 , 1984, pp. 29-39.
- [62] Petit, J. and Ranganathan, N., " Fatigue crack propagation at low rate and near threshold in Al-Li alloys", *Aluminium-Lithium*, Eds. M. Peters and P.J. Winkler, DGM pub., Vol. 1, 1992, pp. 521-532.
- [63] Petit, J. and Bertheau, D., "Fatigue crack propagation in Al-SiC Matrix composites", *Mechanical Properties and Applications of MMC*, Proc. Techn'Mat 92, Euro-Japan exchanges on Materials, C. Ed. Bathias, Elsevier A.S. pub., Vol. 1, 1992, pp.93-101.

A. Hadrboletz,¹ B. Weiss,² and R. Stickler³

The Significance of the Intrinsic Threshold - What Is New?

Reference: Hadrboletz, A. Weiss, B., and Stickler, R., “The Significance of the Intrinsic Threshold - What Is New?” *Fatigue Crack Growth Thresholds, Endurance Limits, and Design*, ASTM STP 1372, J. C. Newman, Jr. and R. S. Piascik, Eds., American Society for Testing and Materials, West Conshohocken, PA, 2000.

Abstract: Numerous investigations in the past decades have shown that the fatigue threshold is influenced by several external and internal parameters. The effect of closure as one of the dominating factors indicates the existence of $\Delta K_{th,eff}$ as a material property. Due to the fact that the determination of closure is controversial a modified closure evaluation procedure was used in this investigation.

Using selected materials (dual phase steel, particulate reinforced Al-alloy) this modified closure procedure resulted in $\Delta K_{th,eff}$ values of reduced scatter in comparison to conventional evaluation procedures.

An alternative concept to describe threshold conditions was suggested by introducing characteristic plastic strain contours. The dislocation configuration in the vicinity of a crack tip, revealed by the electron channeling contrast imaging (ECCI) technique in the scanning electron microscope, allowed to deduce such plastic strain values in polycrystalline Cu selected as model material.

The ECCI technique was also applied to quasi two-dimensional structures (thin foils) which may be of interest in microelectronic systems. Results show that for foils of the thickness in the magnitude of the grain size a crack growth behavior is observed which appears not to be affected by closure.

Keywords: fatigue threshold, intrinsic threshold, closure, dislocation configuration, electron channeling contrast, plastic strain amplitude, thin foils

¹ Research Scientist, Institute of Materialphysics, University of Vienna, Strudlhofgasse 4, A-1090 Vienna, Austria.

² Professor, Institute of Materialphysics, University of Vienna, Strudlhofgasse 4, A-1090 Vienna, Austria.

³ Professor, Institute of Physical Chemistry - Material Science, University of Vienna, Wahringerstrasse 42, A-1090 Vienna, Austria.

Introduction

The first case of a fatigue threshold referred to in the literature is the fatigue limit or endurance limit deduced from conventional S-N curves. The high-cycle fatigue limit of polycrystalline metals and alloys is defined as the threshold stress for propagation of cracks which may have nucleated but did not grow further during subsequent cyclic loading at this particular stress amplitude.

In many cases of engineering practice the dimensioning against fatigue failure is based on the concept of admissible defects. This concept makes use of the threshold for the growth of long fatigue cracks as the essential parameter. Thus the question arises which criteria govern the threshold condition for the growth of such fatigue cracks.

The most widely applied concept to describe the long-crack fatigue threshold is based on linear elastic fracture mechanics. With respect to the fatigue threshold considerations under low-amplitude loading (i.e. high-cycle fatigue conditions) a critical ΔK value is defined below which practically no crack growth should occur. This value was termed threshold stress intensity range, ΔK_{th} . The threshold stress intensity range, ΔK_{th} was initially assumed to be a material constant. However, numerous experimental results showed that ΔK_{th} is dependent on several external (e.g. R-ratio, tensile and compressive overload, loading mode, test frequency, temperature and environment) and internal (e.g. grain size, multiphases, composite material and texture) parameters [1,2].

It could be shown that the number of these affecting parameters can be reduced by taking into account various mechanisms thought to be responsible for the prevention of a fatigue crack to close under reduced loads [3]. Introducing the concept of crack closure the threshold stress intensity was replaced by an effective (or intrinsic) fatigue threshold stress intensity which is considered to be a true material constant. As frequently described in the literature the accurate determination of an effective threshold value is problematic and a modified approach was suggested as will be discussed in the following chapter [3,4].

About twenty years ago several special conferences were devoted to the fatigue threshold. However, in the last few years only individual publications appeared in the literature most of them related to engineering aspects, only a limited amount were concerned to more basic considerations [5,6]. In 1994 we have summarized in a review paper the knowledge on fatigue threshold with respect to experimental procedures, theoretical models, long and short crack behavior etc. [7].

We discussed also the numerous parameters influencing the fatigue threshold properties from an engineering and a material science point of view and arrived to the conclusion that due to the complicated nature a quantification of the threshold conditions on basic principles seems to be problematic. In a critical assessment we suggested at a first step to unify the testing and evaluation procedure in order to separate different influencing factors and to introduce alternative criteria to describe the threshold in a more unified manner.

The objective of this investigation is to treat in a more basic approach the following aspects related to the threshold:

- i a modified evaluation of the closure behavior to gain a more fundamental $\Delta K_{th,eff}$ value
- ii the use of plastic strain amplitude to describe the long crack threshold state with a unified quantity, which may also be extended to short crack behavior.
Using the electron channeling contrast imaging technique it was possible to determine the global dislocation structure, which can be related to cyclic plastic strain values and which allows a correlation to the threshold value.
- iii to investigate the fatigue threshold conditions in quasi two-dimensional structures in order to find an alternative way in minimizing closure.

Evaluation of Crack Closure

As a first attempt to rationalize the different influences on ΔK_{th} the phenomenon of crack closure was introduced, resulting in an effective value.

At present various experimental procedures are available for the determination of $\Delta K_{th,eff}$:

One method involves the determination of $\Delta K_{th,eff}$ at high positive R-ratios at which closure is absent (K_{max} -method [7,8]). This method is limited to low-ductility materials since under the required high tensile stresses ductile materials will be subjected to considerable plastic deformation.

The second method involves testing at large negative R-ratios ($-3 < R < -1$) at which $K_{th,max} = \Delta K_{th,eff}$. This method does not require stresses as high as mentioned above, however, it requires a precise alignment of the specimens to prevent buckling [9].

The common method involves the load shedding technique (R = constant, according to ASTM E-647) for the determination of ΔK_{th} . To determine the value of $\Delta K_{th,eff}$ ($\Delta K_{th,eff} = K_{th,max} - K_{cl}$) the closure behavior has to be monitored.

Various procedures have been proposed to determine the closure contribution based on an evaluation of the recorded load (stress) - crack opening displacement (COD) curve [3,4]. Idealized crack opening curves have the form as shown schematically in Figure 1a. This ideal curve consists of two straight-lines. The branch between K_{max} and K_{cl} reflects the closing of the crack with diminishing external load. K_{cl} is alternatively defined in the literature as K_{op} , referring to the opening of the crack under increasing external load. At K_{cl} the ideal crack is completely closed and further unloading corresponds to the elastic behavior of a crack free specimen. The compliance of a specimen with an open crack is larger than that of a specimen containing a closed crack, and thus, the slope of the branch below K_{cl} is steeper. In this idealized case, for $K_{min} < K_{cl}$ the $\Delta K_{th,eff}$ corresponds to the difference between K_{max} and K_{cl} , while ΔK_{th} is usually defined as $K_{max} - K_{min}$.

In a real material the closure behavior is not as abrupt as drawn in Figure 1a, but rather gradual as shown schematically in Figure 1b. By reducing the external load from K_{max} the crack opening is reduced proportionally along the straight line down to K_{cl} , the value at which the crack faces first come into contact at asperities. On further unloading an increasing number of asperities come into contact until at K_{closed} the crack faces are in tight contact and the COD is equal to zero. On further unloading the compliance of the specimen is again nearly that of a defect free material. On reloading the sequence is inverted except that the last contact at asperities on the fracture faces is lost at K_{op} , which is in general slightly larger than K_{cl} [4]. This small difference has been attributed to frictional forces at the fracture surface.

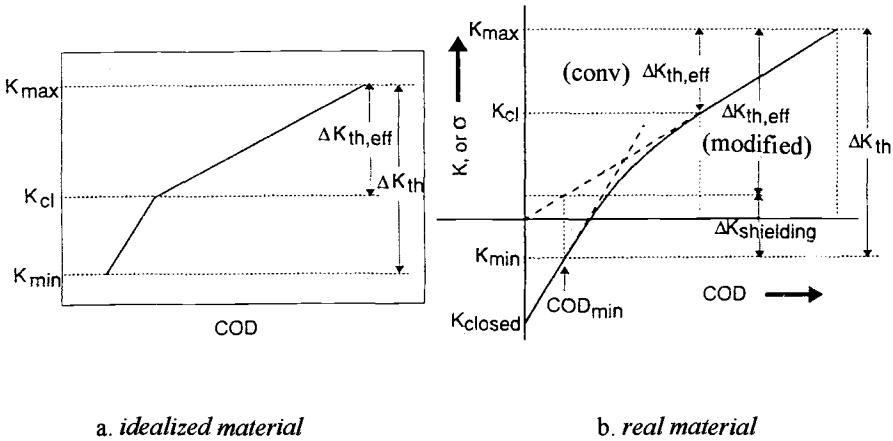


Figure 1 - Load (or K)-COD Curves, Schematic [4]

For the real material the values of K_{cl} (first contact of asperities) and K_{closed} (crack practically closed, COD = 0) differ significantly. For the evaluation of the closure contribution the magnitudes of both K_{max} and K_{min} are essential. In Figure 1b K_{min} was selected so that $K_{min} > K_{closed}$, i.e. the crack never fully closes over the whole K -range.

Although the recording of the load or K -COD curve is experimentally relatively simple, the interpretation of the significance of the various points along the curve is at present controversial. Conventionally, K_{cl} is taken as the point of deviation from linearity of the upper branch of the curve. In view of the asymptotic path of the lower branch, other investigators proposed to deduce the K_{cl} value from the intersection of the tangent of the lower portion with the extrapolation of the straight line of the upper branch [3], as also indicated in Figure 1b. It was pointed out by Chen [4] that, in the

closure evaluation, the effect of the lower portion of the load-COD curve down to K_{min} (or to K_{closed}) must be taken into account.

The proposed procedure to measure crack closure [4] involves, for the case $K_{closed} < K_{min} < K_{cl}$, the determination of the residual crack opening COD_{min} at K_{min} , as indicated in Figure 1b. From this it follows the modified $\Delta K_{th,eff}$:

$$\Delta K_{th,eff} = \Delta K_{th} - \Delta K_{shielding}$$

with $\Delta K_{shielding}$ (taking into account the difference between the closure-free and the closure-affected crack) as defined in Figure 1b. For the case $K_{min} < K_{closed}$ it follows that $\Delta K_{th,eff} = K_{th,max}$.

Significance of Closure

Using the $\Delta K_{th,eff}$ concept the influence of different external and internal parameters on the threshold values can be reduced as shown in Table 1. In this Table a summary of various closure mechanisms explaining the threshold behavior is presented [10].

Table 1 - ΔK_{th} -behavior Related to Closure [10]

Parameter	ΔK_{th} -behavior	Comments
External		
$R = K_{min}/K_{max}$	Max. values of ΔK_{th} at $R=0$ decreasing ΔK_{th} -values with increasing positive and increasing negative R-values significant influence for coarse grained material; ΔK_{th} almost independent of R for fine grained material	roughness induced closure: rough fracture surface at $R = 0$ smooth fracture surface at higher R-values no R-dependency if $K_{min} > K_{cl}$
tensile overload	reduction of near threshold fatigue crack growth	plasticity induced closure (crack has to transmit an enlarged plastic zone)
compressive overload	acceleration of near ΔK_{th} fatigue crack growth	reduced crack closure due to flattening of the fracture surface asperities
loading-mode	Higher ΔK_{th} in bending compared to tension-compression	influence eliminated by closure (inhomogeneous plastic deformation)

Parameter	ΔK_{th} -behavior	Comments
test-frequency	minor increase of ΔK_{th} with increasing frequency	formation of oxides on the crack surfaces
test-temperature	ΔK_{th} increases with raising temperatures	increased closure due to the formation of corrosion products (mainly oxides), predominantly roughness- and oxide induced closure
environment	ΔK_{th} is to be almost independent of R in an inert environment compared to air increased ΔK_{th} in oil compared to inert, gaseous environment	lack of oxide induced closure, absence of roughness induced closure which is enhanced by fretting corrosion (loose particles), viscous induced closure

Internal

grain size	ΔK_{th} increases with increasing grain size	coarser structures exhibit rougher fracture surfaces leading to pronounced roughness induced closure
multi-phases	higher ΔK_{th} -values compared to single-phase materials	roughness induced closure and a meandering crack path (geometrical closure)
metal-matrix composites	ΔK_{th} varies both with volume fraction and the average size of the reinforced hard particles	$\Delta K_{th,eff}$ depends only on the mean particle size; there is no function of its volume fraction
texture	ΔK_{th} depends on the angle between crack plane and crystallographic orientation	fracture surface roughness varies with the crack-orientation (roughness-induced closure), large changes in crack path orientation cause geometrically induced closure

As reported in literature the most prominent external parameter affecting ΔK_{th} is the R-ratio. As an example the influence of R in the range of -10 to + 0,8 on ΔK_{th} of Al 2024-T3 is depicted in Figure 2 which indicates a maximum of ΔK_{th} for R = 0. Using $\Delta K_{th,eff}$ an almost constant value over the whole range of R is derived which may be explained mainly by roughness induced closure [9]. Various other external parameters also affect ΔK_{th} caused by different closure mechanisms [7], however the use of the $\Delta K_{th,eff}$ concept reduces their influence (see Table 1).

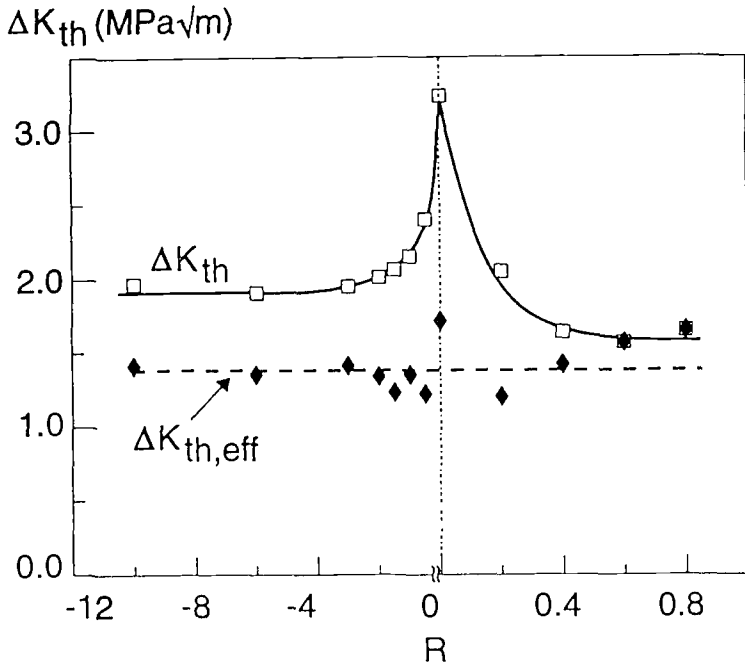


Figure 2 - Influence of an External Parameter (R-ratio) on ΔK_{th} and $\Delta K_{th,eff}$ of Al2024 T3

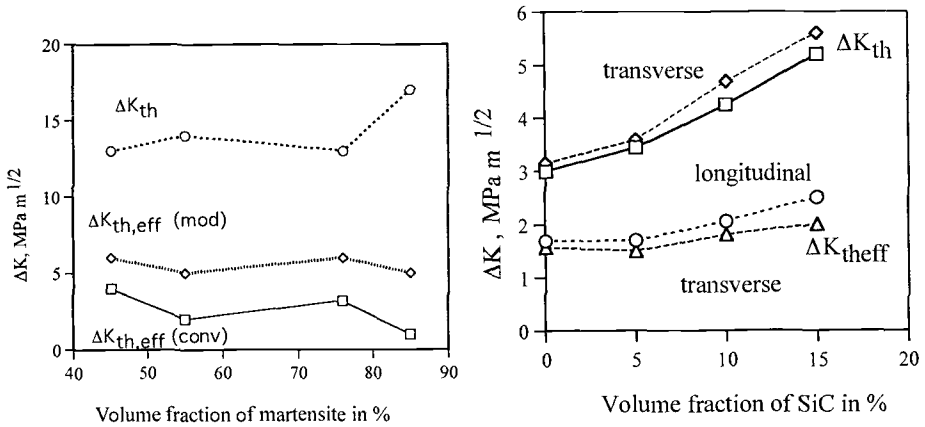


Figure 3a - Influence of an Internal Parameter (Different Volume Fraction of Martensite) on ΔK_{th} and $\Delta K_{th,eff}$ in a Dual Phase Steel with the Following Composition: 0,07 C; 1,46 Si; 0,47 Mo; 0,61 Cr

Figure 3b - Influence of an Internal Parameter on ΔK_{th} and $\Delta K_{th,eff}$ (Different Volume Fraction of SiC Particles with a Size of 5 μm in an Al Composite Material)

Microstructural features as for example different phases, also influence ΔK_{th} in a more complex way, affecting the mechanical properties. Figure 3a depicts the influence of the volume fraction of martensite in a dual phase ferritic-martensitic steel [11]. Introducing $\Delta K_{th,eff}$ determined in two different ways shows that the modified evaluation of closure resulted in almost constant values. The closure behavior may be attributed to mainly geometrically induced closure.

In Figure 3b the dependence on ΔK_{th} as function of the volume fraction of SiC particles with sizes of 5 μm introduced in an Al 6061 matrix is presented. The reduction of the effect of the reinforcing particles is expressed by an almost constant value of $\Delta K_{th,eff}$ [12].

Determination of Plastic Strain in the Crack Tip Region

In view of the experimental efforts and the numerous affecting parameters many authors attempted to calculate the threshold values from basic principles. For a rough estimation of the threshold value, as a first guideline the Young's modulus was used. For a more precise calculation of $\Delta K_{th,eff}$ various models have been introduced which have been classified into two groups: a) models based on stress field or energy considerations and b) models taking into account microstructural parameters (e.g. grain size and dislocation mobility). However a generally applicable quantitative prediction of the threshold behavior seems still problematic [7].

An alternative approach is to relate the threshold value to the cyclic plastic strain, due to the fact that the fatigue response is determined by the amount of plastic strain.

Based on the idea of a direct relationship between a characteristic dislocation structure and plastic strain amplitudes, few studies have been performed on the localized plasticity in the vicinity of a fatigue crack at threshold. The investigations were mainly performed with polycrystalline Cu [13] using transmission electron microscopic (TEM) techniques. As an alternative method the electron channeling contrast imaging (ECCI) technique (ECCI) as a new non-destructive technique was applied. The ECCI technique allows to reveal the global dislocation structure in the near crack tip region [14,15,16].

Typical dislocation structures of recrystallized polycrystalline Cu specimens (which was selected as a model material) near the crack tip are presented in Figure 4a and Figure 4b. The specimens were fatigue tested in a resonance system at 20 kHz and $R = -1$. Threshold values were obtained with the load shedding technique corresponding to a propagation rate of about $1 \cdot 10^{-13}$ m/c. For more experimental details see Ref [14].

Figure 4a shows around the crack tip a heavily deformed zone and after electropolishing it could be revealed that this zone consists of fine dislocation cells (Figure 4b). For higher ΔK values the zone containing dislocation cells is extended (Figures 5a and 5b).

Dislocation cells can also be observed ahead of the crack tip. Beyond this region with cell structures a dense vein structure containing persistent slip bands (PSB's), labyrinth structures or mixtures of these are observed as presented in Figure 6. In this figure characteristic plastic strain values are given.

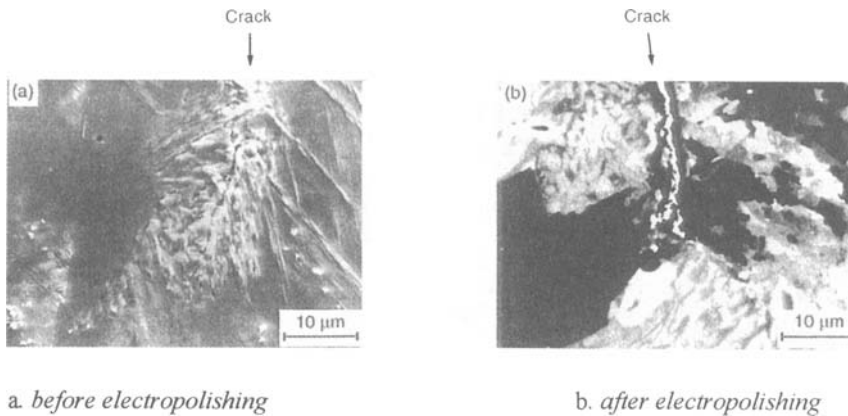


Figure 4 - Dislocation Structures Around the Crack Tip Observed for Polycrystalline Cu Tested at the Fatigue Threshold ($\Delta K_{th} = 2,5 \text{ MPa m}^{1/2}$) at Room Temperature, 20 kHz and $R = -1$; ECCI-micrographs [14]

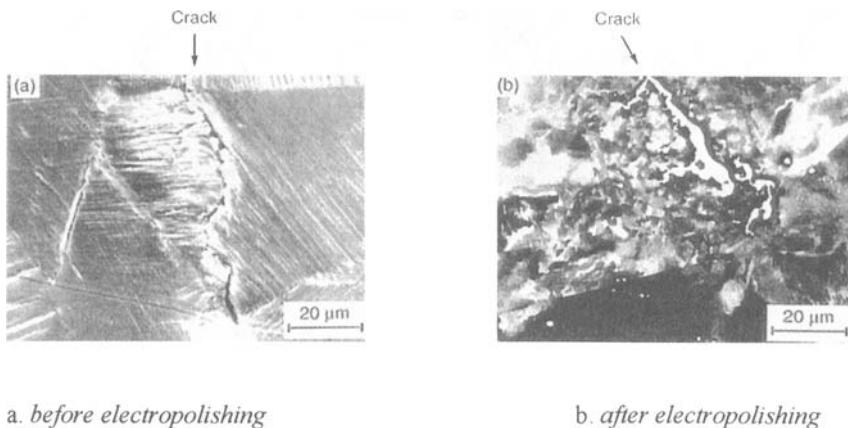


Figure 5 - Dislocation Structures Around the Crack Tip Observed for Polycrystalline Cu Tested at ($\Delta K = 4,8 \text{ MPa m}^{1/2}$) at Room Temperature, 20 kHz and $R = -1$; ECCI-micrographs (14)

To derive at plastic strain amplitudes from these typical dislocation structures the cyclic stress strain response has to be known. According to [17] for polycrystalline Cu dislocation cells can be observed for plastic strain amplitudes exceeding $6 \cdot 10^{-4}$, whereas the structure containing loose veins corresponds to plastic strain amplitudes lower than $2 \cdot 10^{-5}$. In between these two values falls the region containing PSB's and veins. As can be seen from Figure 6 a correlation between observed structures and plastic strain values is possible.

A comparison between calculated values of the plastic zone size [14] and the extent of typical dislocation structures reveals agreement if not only the innermost region containing cells but also the region containing PSB's is considered. Similar observations were reported by [13] who stated that a quantitative description of the plastic strain in the plastic zone might be problematic due to the triaxiality of the stress state. Therefore the fatigue threshold behavior of two dimensional systems was studied.

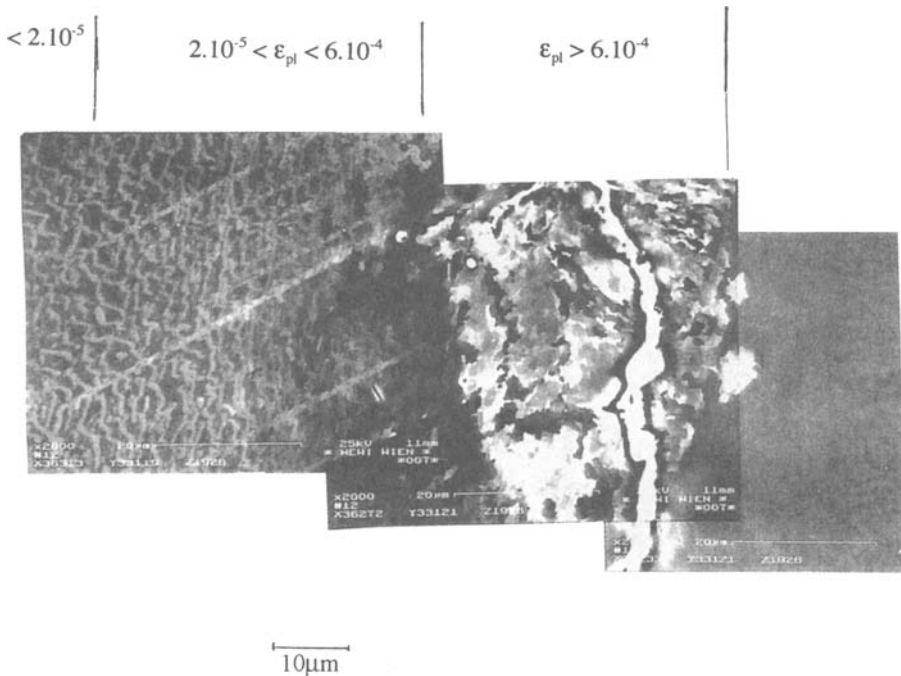


Figure 6 - Dislocation Arrangement in the Vicinity of a Fatigue Crack in Polycrystalline Cu at Room Temperature, 20 kHz, R = -1, Crack Propagation Rate of about $1 \cdot 10^{-10}$ m/c

The Threshold Behavior of Quasi Two Dimensional Systems

The investigation of the threshold behavior of quasi two dimensional systems (thin foils) with grain sizes in the magnitude of the thickness of the foil was performed not only to avoid the problem of stress triaxiality but also because of the interest in properties as essential parts in microelectronic and microelectromechanical systems [18].

For the purpose of comparison of the threshold behavior of bulk material, recrystallized Cu foils (thicknesses ranging between 20 μm and 100 μm) were chosen as testing material. For the determination of the fatigue threshold the foils were attached to a supporting specimen holder loaded in a resonance system operated at 20 kHz and $R = -1$. The end portions of the foils were glued to the supporting holder (bar with cross section of 20 x 6 mm) leaving a free standing middle zone of approximately 4 mm width. A small starting notch was introduced in the mid-section of the foil. For experimental details see [18].

Fatigue crack growth curves (crack length a) as function of the number of loading cycles (N) were determined for constant-strain amplitude loading. First results are presented in Figure 7. As can be seen for the bulk material a typical a - N curve is derived, whereas for the foils the a - N curves show an anomalous behavior which seems to be similar to the growth of short cracks in bulk material characterized by temporary arrests of the crack. These a - N curves of the thin foils appear to approach a saturation value corresponding to a threshold. This behavior may be due to the loading conditions under displacement control.

The ECCI micrographs at different stages of fatigue (A, B, C) are depicted for a 100 μm foil in Figure 7. The micrograph corresponding to condition A shows temporary crack arrest, due to an interaction of the crack with a grain boundary. B indicates also a temporary crack arrest due to formation of a secondary crack surrounded by dislocation cells. C corresponds to the final threshold condition, the crack tip interacts with a twin boundary and is surrounded by a small zone consisting of dislocation cells. PSB's can be observed in the vicinity.

Threshold values were calculated by using the standard LEFM relations for plane stress conditions for a through crack [18]. We consider these values only as a rough approximation not taking into account the effects of displacement controlled test procedure. Based on the observation of the crack growth behavior similar to that of short cracks it may be hypothesized that these calculated threshold values resemble effective threshold data of recrystallized bulk Cu, however they show a large scatter which may be due to the variation of Young's modulus known to be strongly dependent on textures of Cu foils [19].

In comparison to bulk material the plastic zones around the crack are smaller which supports the assumption that the threshold value is considered to be an effective value.

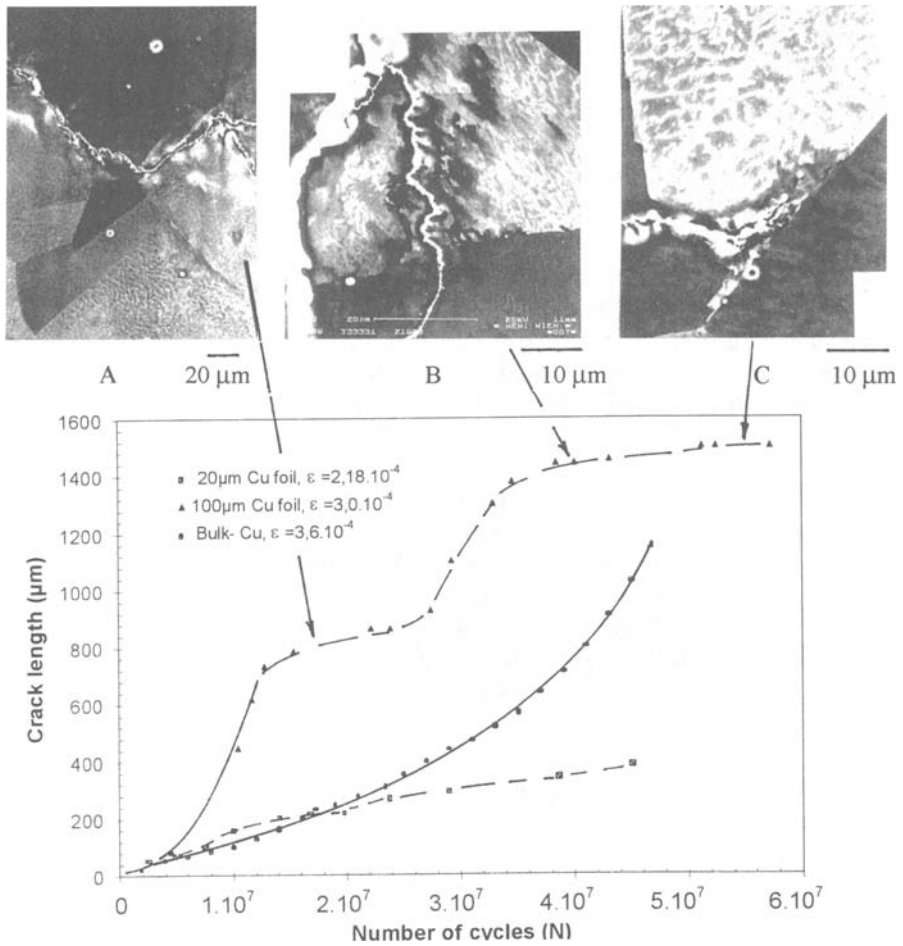


Figure 7 - Changes of Crack Length as Function of Number of Loading Cycles of Recrystallized Cu Foils with Varying Thicknesses and Grain Sizes and for Bulk Material; ECCI Micrographs above Correspond to Different Stages of Fatigue (A, B, C) of the Foil with a Thickness of 100 μm, test Conditions: Room Temperature, 20 kHz and R = -1

Summary and Conclusions

Based on the alternative concepts to describe threshold behavior it may be summarized:

The fatigue threshold is influenced by several external and internal parameters. Taking into account the effect of closure as one of the dominating factors, the experimental

findings indicate the existence of $\Delta K_{th,eff}$ as an almost material constant. Due to the fact that the determination of closure is controversial a modified closure evaluation procedure was used which takes into account the lower portion of the load-COD curve.

For selected materials this procedure resulted in $\Delta K_{th,eff}$ values of reduced scatter in comparison to conventional evaluation procedures, so that these values may be regarded as a true material constant.

A concept based on the cyclic plasticity in the vicinity of a fatigue crack under threshold conditions was proposed. This requires to study the dislocation configurations by using the essentially non-destructive ECCI- method, which allows to identify the changes in mesoscopic dislocation structures between surface layers and the interior of specimens over large specimen areas. From this information it was possible to derive plastic strain contours for various critical strain values of the deformed regions around the fatigue crack. This method should also be applicable to analyse the plastic strain contours along the crack path revealing the load history. The ECCI technique may be successfully applied to other single phase materials and simple alloy systems.

This proposed plastic strain concept may be applied to both short cracks (which are influenced by the fatigue limit known to be directly related to the plastic strain) and long cracks ($\Delta K_{th,eff}$ is a function of plastic strain). Thus it seems feasible to present a modified Kitagawa diagram in terms of plastic strain instead of stress. These considerations should permit to define the characteristic behavior of cracks with varying length by the use of a basic physical parameter.

A new method was introduced to study the fatigue threshold behavior of quasi two-dimensional structures such as thin foils and films of various materials. The observed crack growth properties (similar to those of short cracks in bulk material) in polycrystalline Cu foils indicate only a limited amount of closure. This is due to the lack of microstructural constraint if the thickness of the foils is in the magnitude of the grain size. The observed characteristic plastically deformed regions are smaller than in bulk materials indicating a true effective threshold value.

References

- [1] *Fatigue Threshold*, Proc. International Conference Stockholm, Sweden, 1981, J. Bäcklund, A. Blom and C. J. Beevers, Eds., EMAS, Warley, UK, 1982.
- [2] Taylor, D., *Fatigue Thresholds*, Butterworths, London, UK, 1989.
- [3] *Mechanics of Fatigue Crack Closure*, ASTM STP 982, Proc. Conf. Charleston, South Carolina, USA, 1986, J. C. Newman and W. Elber, Eds., Philadelphia, Pa, USA, 1988.

- [4] Chen, D. L., Weiss, B., and Stickler, R., "Effect of Stress Ratio and Loading Condition on the Fatigue Threshold," *International Journal of Fatigue*, 14, 1992, pp. 325–329.
- [5] Marci, G., "Fatigue Crack Propagation Threshold: What Is It and How It Is Measured," *Journal of Testing and Evaluation*, JTEVA, Vol. 26, No. 3, May 1998, pp. 220–233.
- [6] Kujawski, D., and Ellyin, F., "A Unified Approach to Mean Stress Effect on Fatigue Threshold Conditions," *International Journal of Fatigue*, Vol. 17, No. 2, Feb. 1995, pp. 101–106.
- [7] Hadrboletz, A., Weiss, B., and Stickler, R., "Fatigue Threshold of Metallic Materials—A review," *Handbook of Fatigue Crack Propagation in Metallic Structure*, A. Carpinteri, Ed., Elsevier Science B.V., Amsterdam, 1994, Vol. 1, pp. 847–882.
- [8] Marci, G., "A Fatigue Crack Growth Threshold," *Engineering Fracture Mechanics*, Vol. 41, No. 4, 1992, pp. 367–385.
- [9] Kemper, H., Weiss, B., and Stickler, R., "An Alternative Presentation of the Effects of the Stress-ratio on the Fatigue Threshold," *Engineering Fracture Mechanics*, Vol. 32, 1989, pp. 591–600.
- [10] Hadrboletz, A., Weiss, B., and Stickler, R., "The Significance of the Fatigue Threshold for Metallic Materials," *Localized Damage IV*, H. Nisitani, M. H. Aliabadi, S. J. Nishida, D. J. Cartwright, Eds., Computational Mechanics Publications, Southampton, UK, 1996.
- [11] Chen, D. L., Weiss, B., Stickler, R., and Wang, Z. G., "Effective Fatigue Threshold of a Dual-Phase Steel," *Euromat 94*, Proc. of 15th Conf. on Materials Testing in Metallurgy, 11th Congress on Materials Testing, B. Vorsatz and E. Szöke, Eds., Vol. 3, pp. 722–726.
- [12] Sun, Z. M., Weiss, B., Chen, D. L., Stickler, R., Wang, Z. G., and Bi, J., "Small and Long Fatigue Cracks in SiC Particulate Reinforced Al-Alloys," *Fatigue 93*, Proc. of the 5th International Conf. on Fatigue and Fatigue Thresholds, Montreal, Canada, 1993, J. P. Bailon and J. I. Dickson, Eds., EMAS, Warley, UK, 1993, Vol. 2, pp. 1117–1122.
- [13] Tong, Z. X., and Bailon, J. P., "Dislocation Structures Near the Fatigue Crack Tip in Copper," *Fatigue and Fracture of Engineering Materials and Structures*, 1995, 18, pp. 847–859.

- [14] Chen, D. L., Melisova, D., Weiss, B., and Stickler, R., "The Electron Channelling Contrast Technique Applied to the Characterization of Dislocation Structures in the Vicinity of a Fatigue Crack," *Fatigue and Fracture of Engineering Materials and Structures*, 1997, Vol. 20, pp. 1551–1561.
- [15] Zauter, R., Petry, F., Bayerlein, M., Sommer, C., Christ, H. J., and Mughrabi, H., "Electron Channelling Contrast as a Supplementary Method for Microstructural Investigations in Deformed Metals," *Philosophical Magazine*, A 66, 1992, pp. 425–436.
- [16] Joy, D. C., and Booker, G. R., "Recent Developments in Electron Channelling Techniques," *Scanning Electron Microscopy*, 1973, pp. 137–144.
- [17] Lukas, P., and Kunz, L., "Influence of Low Temperature on Dislocation Structures and Fatigue Behavior of Copper," *Basic Mechanisms in Fatigue*, Proc. International Colloq. on Basic Mechanisms in Fatigue, 1988, Brno, CSSR, P. Lukas and J. Polak, Eds., Akademia, Prague, CSSR, 1988, pp. 161–168.
- [18] Hadrboletz, A., Kathibi, G., Weiss, B., and Stickler, R., "Fatigue Threshold Behavior of Thin Metallic Foils," *Fracture From Defects*, Proc. of the 12th European Conf. on Fracture, Brown, M. W., de los Rios, E., and Miller, K. J., Eds., EMAS Publ, Sheffield, September 1998, pp. 247–252.
- [19] *Landolt-Börnstein, Zahlenwerte und Funktionen aus Physik, Chemie, Astronomie, Geophysik und Technik*, Borchers, H., Hansen, H., Hellwege, K. H., Schäfer, K., and Schmidt, E., Eds., Springer Verlag, Berlin, 1971.

Hans-Jakob Schindler ¹

On the Significance of Crack Tip Shielding in Fatigue Threshold - Theoretical Relations and Experimental Implications

Reference: Schindler, H. J., “On the Significance of Crack Tip Shielding in Fatigue Threshold—Theoretical Relations and Experimental Implications,” *Fatigue Crack Growth Thresholds, Endurance Limits, and Design*, ASTM STP 1372, J. C. Newman, Jr. and R. S. Piascik, Eds., American Society for Testing and Materials, West Conshohocken, PA, 2000.

Abstract: The fatigue crack growth (FCG) threshold behavior of elastic-plastic materials is analyzed theoretically by simplistic mechanical considerations. Emphasis was laid upon two of the key aspects of threshold, which are both still controversially discussed in the literature: intrinsic threshold and extrinsic crack tip shielding. The analytical relations derived from the model confirm experimental indications, that at R-ratios beyond a certain limit FCG and its threshold is governed by intrinsic mechanisms, whereas at lower R it is crucially influenced by extrinsic shielding mechanisms. The latter are postulated to consist of a crack-closure and a non-closure part, which is confirmed by preliminary experimental data as well as data from the literature. To measure crack closure independently, a new experimental technique, the so-called cut compliance method, is proposed, which is shown by some preliminary tests to work well even in the threshold regime. The model and the derived mathematical relations also enable one to distinguish between those parts of the threshold that are inherently associated with FCG, and the ones that are geometry- or load-history-dependent. Therewith conservatively transferable threshold data can be obtained.

Keywords: crack tip shielding, crack closure, intrinsic threshold, experimental, residual stress, influence functions, cut compliance method, threshold chart, R-effect

Nomenclature

a	crack length and cut length, respectively
a _n , a _f	depth of initial notch and final length of fatigue crack, respectively
C	constant in the crack-growth equation
C _{op/pl}	= K _{op/pl} / K _{max}
CC	cut compliance (-method)
ΔK	SIF range, ΔK=K _{max} -K _{min}

¹ Senior research engineer, Swiss Federal Labs. for Materials Testing and Research (EMPA), CH-8600 Dübendorf, Switzerland.

ΔK_{eff}	range of SIF that produces plastic strains in the vicinity of the crack-tip
ΔK_{th}	value of ΔK below which no FCG occurs
$\Delta K_{\text{th/int}}$	intrinsic component of ΔK_{th}
ϵ_M	strain at measurement point M
FCG	fatigue crack growth
K_i	SIF at initiation of ductile tearing
K_{frs}	SIF due to residual stresses or crack closure stresses
$K_{\text{max/th}}$	threshold value of K_{max} for low R
$K_{\text{min}}, K_{\text{max}}$	minimum and maximum SIF of a load cycle, respectively
K_{nc}	extrinsic shielding of the crack tip other than crack closure, in terms of SIF
K_{op}	SIF required to overcome the contact stresses acting between the crack faces
$K_{\text{op/pl}}$	plasticity induced crack closure SIF
$K_{\text{op/ext}}$	SIF due to crack closure remote from the crack tip
K_{sh}	extrinsic shielding of the crack tip loading in terms of SIF
n	exponent in the crack-growth equation
R	load or SIF ratio, $R=K_{\text{min}}/K_{\text{max}}$
R_{op}	$R_{\text{op}}=K_{\text{op}}/K_{\text{max}}$
R_p, R_m	yield stress and ultimate tensile strength, resp.
R_{sh}	value of R at the transition between shielded and non-shielded crack tip
SIF	stress intensity factor
Z	influence function

The existence of a threshold of the stress intensity range, ΔK_{th} , below which no crack propagation occurs, was postulated shortly after fracture mechanics parameters were first used to correlate the rates of fatigue crack growth (FCG) [1]. Enabling safe life calculations to be simplified, fatigue tests to be shortened, and giving some theoretical support to the widely used concept of fatigue strength and endurance limits, the FCG-threshold plays an important role in engineering fatigue. However, most of the knowledge about this phenomenon is of empirical nature, and the underlying mechanisms are far from being satisfactorily understood. The FCG-threshold is known to be affected by several parameters, like the R-ratio, stress history, environment, frequency, crack length, and geometry of the specimen or structural component [2]. So it is no surprise that there is a pronounced scatter in the experimental data reported in the literature [3]. Since threshold concepts applied in safe life calculations of structural components only make sense if there is no doubt that the data used are conservative, relatively high safety margins have to be applied when using experimental data in practical applications.

Regarding the number of influencing factors on the one hand and the experimental effort and costs to determine reliable threshold data according to ASTM E647 on the other, a mainly empirical approach to account for the threshold behavior in safe life predictions is not adequate. Neither is a purely theoretical one, since the physical processes involved are much too complex to be treatable purely theoretically. Thus, as in other fields of fracture mechanics, the most efficient way to come to quantitative

predictions appears to be a semi-empirical one, which means using simplistic mechanical models in combination with experimental data to determine the inevitable open parameters of the model. Whilst it should be general and flexible enough to reproduce the major experimental features and phenomena of the process, it also has to be simple enough to be analytically solvable. The above mentioned open constants should be as few as possible, physically well defined and experimentally easily measurable. However, at least as important as choosing an appropriate model is using it consistently in the evaluation of test data and in the FCG-prediction of a given structural component.

A key factor in FCG and threshold is crack closure [4-8]. Although this phenomenon has been known for more than two decades now and is in principle generally accepted as a typical feature of FCG, there still is no consensus about its physical relevance, its magnitude, its experimental and computational determination and the definition of characteristic parameters [9-13]. A variety of models and empirical formulas have been proposed in the literature to quantify this effect. The controversy especially concerns the threshold regime, where plane strain conditions prevail and the plasticity induced crack closure is relatively small. Another important question is the transferability of threshold values measured on a test specimen to structural components of other shapes and sizes. In the present paper some of these questions are tried to be further clarified by simplistic models and considerations. They allow to sort out transferable and non-transferable components of the threshold.

Probably one of the main reasons why a common view on this subject has not yet been achieved in the scientific community are the difficulties encountered when quantifying crack closure experimentally, since the usually applied compliance methods become inaccurate at low load ranges. In the present paper a new method, the cut compliance method, is proposed. The preliminary experimental results show the applicability of this method even in the threshold regime. The data obtained give additional information about the physical processes involved in the threshold behavior and allows one to distinguish between those components of the FCG-threshold, which are affected by the test specimen geometry and the testing conditions and those, which are inherently connected with the fatigue process. This differentiation is essential when dealing with the question of the transferability of the threshold data from the test specimen to a structural component.

Fatigue Crack Growth Law

FCG results from local damage due to the repetitive plastic strains in the vicinity of the crack tip that result from a cyclic stress intensity factor (SIF) [3,4,14]. The latter, called the effective SIF-range ΔK_{eff} , is formed by the external load reduced by the local crack-tip shielding effects like crack closure [5, 6]. It is an experimental fact, that there is a threshold of the effective SIF-range, $\Delta K_{th/int}$, where the crack ceases to grow. A suitable modification of Paris' law to account for this behavior is

$$\frac{da}{dN} = C \cdot (\Delta K_{eff}^n - \Delta K_{th/int}^n) \quad (1)$$

$\Delta K_{th/int}$ results from mechanisms that prevent micro-plastic effects to occur in the vicinity of the crack tip, like dislocations caught at grain boundaries, slip bands interrupted by inclusions, microscopically finite crack tip radii, etc., so it is called the intrinsic FCG-threshold. $\Delta K_{th/int}$ is considered to be a material property. Nevertheless it can be affected by factors like the environment and the loading frequency. The mathematical form of (1) assures that $\Delta K_{th/int}$ has the awaited minor effect on the FCG-rate da/dN at higher SIF-ranges.

ΔK_{eff} is generally given by

$$\Delta K_{eff} = \begin{cases} K_{max} - K_{sh} & \text{for } R < R_{sh} \\ \Delta K & \text{for } R > R_{sh} \end{cases} \quad (2)$$

where

$$R = \frac{K_{min}}{K_{max}} = 1 - \frac{\Delta K}{K_{max}} \quad (3)$$

$$R_{sh} = K_{sh}/K_{max} \quad (4)$$

K_{sh} represents the total extrinsic shielding in terms of SIF, the term "extrinsic" meaning due to secondary mechanical forces acting at or near the crack surfaces [12, 15], such as the well known crack closure K_{op} . However, directly measured crack closure values K_{op} often are significantly lower than the ones determined indirectly by crack growth observation [11, 17], which implies that crack closure might be not the only shielding effect of a fatigue crack tip in the threshold regime. Therefore, we assume K_{sh} to be composed of crack-closure K_{op} and an additional component, K_{nc} , i.e.

$$K_{sh} = K_{op} + K_{nc} \quad (5)$$

Since extrinsic shielding of other type than crack closure is hardly possible in a 2D-system, K_{nc} is likely to be associated with 3D-effects such as the crack curvature, which in general deviates from a straight line, and local non-planar crack-growth caused by microstructural features, leading to crack surface roughness. Regarding the former and the particularly local nature of closure effects at small load ranges (where a substantial part of the closure SIF is formed by contact stresses within a few tenths of a millimeter behind the crack-tip), it is obvious that closure effects can not be completely captured by the usual 2D-considerations. The latter results in local friction, Mode-II- and Mode-III effects that can contribute to crack-tip shielding but not to crack closure as measured by direct 2D-methods such as ASTM E 647 or the CC-method discussed later on. According to these considerations, K_{nc} is likely to depend on the micro-structure of the material and the specimen or component thickness.

Concerning K_{op} , it is suitable to distinguish between two components,

$$K_{op} = K_{op/pl} + K_{op/ext} \quad (6)$$

The first, $K_{op/pl}$, represents the closure-SIF due to the inevitable local plastic deformation at the crack tip. The second, $K_{op/ext}$, results from additional closure effects such as corrosion products stuck to the crack faces, asperities and roughness of the crack surface, including plasticity-induced closure of the crack-faces remote from the crack-tip, due to overloads at earlier stages of the crack. Thus, $K_{op/pl}$ can be considered to be inherently associated with FCG in elastic-plastic materials, whereas $K_{op/ext}$ depends on system-specific conditions.

An analytical or a Finite-Element model is required to split K_{op} according to (6). In [4], $K_{op/pl}$ was calculated by means of a strip yield model from the condition that closure-free crack-growth requires the slope of the crack contour at the physical crack tip to be zero, which led to

$$K_{op/pl} = C_{op/pl} K_{max} \tag{7}$$

with

$$C_{op/pl} \equiv \frac{R_p}{R_p + R_m} \quad \text{for plane stress} \tag{8}$$

where R_p and R_m denote the yield strength and the ultimate tensile strength, respectively. Physically, $C_{op/pl}$ represents the ratio of a representative flow stress in tension to the one for subsequent compression. The approximation (8) holds for plane stress. In plane strain, which often prevails in the threshold regime, the strip yield model as used in [4] is less accurate. Due to triaxiality, the local flow stress is increased, the strain correspondingly decreased, and the ratio of tensile to compressive flow stress is lower [16], resulting in a considerably reduced crack closure [7]. Following roughly pattern of the derivation in [4] and regarding the results of [16], we account for these effects roughly by replacing in (8) R_m by $2R_m$, thus

$$C_{op/pl} \equiv \frac{R_p}{R_p + 2R_m} \quad \text{for plane strain} \tag{9}$$

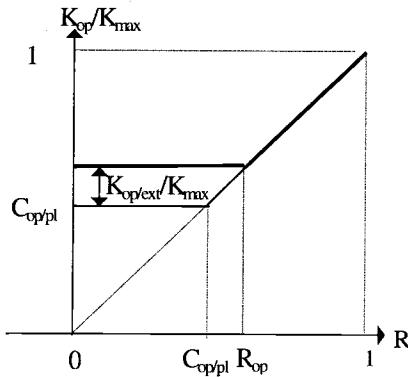


Fig. 1 - General behavior of the opening SIF as a function of R according to the present model

The general behavior of K_{op} as given by (6) - (9) is shown in Fig. 1 as a function of R which is in good agreement with empirical and numerical behavior [5-8]. In Fig. 2, K_{op} is shown as a function of K_{max} , which also is in qualitative agreement with the behavior of experimental data [8]. Fig. 2 also shows a possible way to estimate $C_{op/pl}$ experimentally.

Actually, as shown in [13, 16], $K_{op/pl}$ depends not only on K_{max} as stated by (6a-6c), but, at least to some degree, also on K_{min} , since low or negative values of K_{min} tend to reduce the closure effect by additional plastic compression of the crack surface. This effect is disregarded here for the sake of simplicity (see [18] for further discussion).

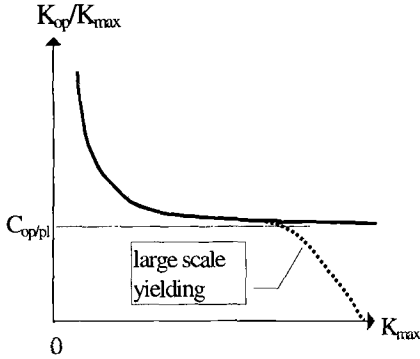


Fig. 2 - General behavior of K_{op} as a function of K_{max} for $R < R_{sh}$

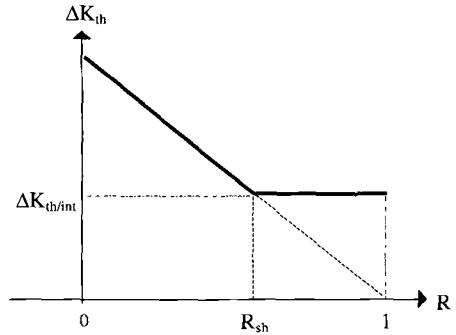


Fig. 3 - Dependence of K_{th} on R .

With (5) - (9), (2) becomes

$$\Delta K_{eff} = \begin{cases} (1 - C_{op/pl}) \cdot K_{max} - K_{op/ext} - K_{nc} & \text{for } R < R_{sh} \\ \Delta K & \text{for } R > R_{sh} \end{cases} \quad (10)$$

where

$$R_{sh} = (K_{op} + K_{nc})/K_{max} \quad (11)$$

Threshold Behavior

The FCG-threshold in terms of ΔK , ΔK_{th} , is obtained by inserting (10) and (11) in (1) and setting $da/dN=0$. One obtains

$$\Delta K_{th} = \Delta K_{th0} \cdot (1 - R) \quad \text{for } R < R_{sh} \quad (12a)$$

$$\Delta K_{th} = \Delta K_{th/int} \quad \text{for } R > R_{sh} \quad (12b)$$

where

$$\Delta K_{th0} = \frac{\Delta K_{th/int} + K_{op/ext} + K_{nc}}{1 - C_{op/pl}} \quad (13)$$

ΔK_{th} as given by (12a) and (12b) is shown in Fig. 3. It compares well with experimental data (see Fig. 7 below and e.g. [12, 17, 19]), indicating that the model used here is able to reproduce the main characteristics of the FCG and the corresponding threshold. Inserting (3) in (12) and (13) leads to

$$K_{max/th} = \frac{\Delta K_{th/int} + K_{op/ext} + K_{nc}}{1 - C_{op/pl}} \quad \text{for } R < R_{sh} \quad (14a)$$

$$\Delta K_{th} = \Delta K_{th/int} \quad \text{for } R > R_{sh} \quad (14b)$$

The conditions for non-propagation corresponding to (14a) and (14b), i.e. $K_{max} < K_{max/th}$ for $R < R_{sh}$ and $\Delta K < \Delta K_{th}$ for $R > R_{sh}$, respectively, form the shaded area in the K_{max} -vs.- ΔK -plane (Fig. 4), confirming experimental and theoretical findings of other authors [15, 16, 17, 19]. This area, called in the following the threshold-chart, characterizes the threshold behavior of a certain test specimen or component. It is defined by only two parameters, $\Delta K_{th/int}$ and $K_{max/th}$. Correspondingly, only two threshold tests are required to establish the threshold chart: One at $R < R_{sh}$, e.g. $R=0.1$, to deliver $K_{max/th}$, the other at

$R > R_{sh}$, e.g. $R=0.7$, to deliver $\Delta K_{th/int}$. By performing first the former at a constant (low) R-value, and then - using the same specimen - the other at a constant K_{max} (as described in [11], with K_{max} chosen to be about the mean value of K_{Ic} and K_{max} of the previous test), the complete threshold chart can in principle be obtained from just one single specimen.

Of course, neither K_{max} nor ΔK are unbounded, but limited by additional conditions of fracture mechanics and strength of materials. For example, K_{max} is obviously limited to $K_{max} < K_c$, or, in case of stress corrosion cracking or creep, to $K_{max} < K_{Isc}$ or $K_{max} < K_{creep}$,

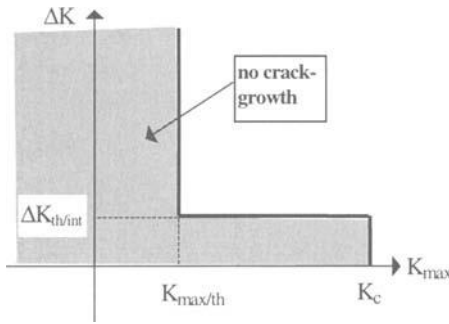


Fig. 4 - Conditions for no crack propagation in the test specimen ("threshold chart").

respectively (Fig. 4). Similar limits are imposed on the ΔK -values by the condition of general yielding under compression. The corresponding upper and left-hand boundary of the shaded area, which turns out to be system- and crack-length-dependent [18], is not further considered here.

From (3) and (14a, b) one obtains an equation to determine R_{sh} or K_{sh} , respectively, from experimentally determined $\Delta K_{th/int}$ and $K_{max/th}$ i.e.

$$R_{sh} = \frac{K_{sh}}{K_{max/th}} = 1 - \frac{\Delta K_{th/int}}{K_{max/th}} \tag{15}$$

According to (11), R_{sh} represents an upper bound of $R_{op}=K_{op}/K_{max}$, thus

$$K_{op} \leq R_{sh} \cdot K_{max} \tag{16}$$

Lower-Bound FCG-Thresholds

The relations (12a, b) and (14a, b), respectively, exhibit the various ingredients of the FCG-threshold. According to their definition and the discussion above, only $\Delta K_{th/int}$ is a "pure" material property (though affected by additional factors like loading frequency and environment). $C_{op/pl}$ is process- and thickness-dependent. $K_{op/ext}$ depends definitely at least on the crack- and specimen-geometry, the environment and the load-history. K_{nc} is expected to depend on the thickness of the specimen or component, respectively, increasing with increasing thickness. Thus, for a structural component of the same thickness as the specimen, a lower bound of $K_{max/th}$, which can be conservatively used to predict the fatigue behavior of a structure, is obtained by setting K_{nc} and $K_{op/ext}$ equal to zero in (13) or (14a), i.e.

$$\Delta K_{max/th/min} = \frac{\Delta K_{th/int} + K_{nc}}{1 - C_{op/pl}} \tag{17}$$

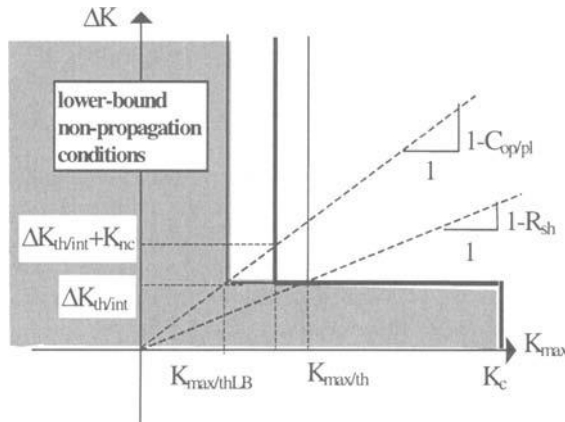


Fig. 5 - Lower-bound- threshold chart and its relation to the chart of non-propagation in the specimen (Fig. 4). The dark-shaded area represents its conservative part ($K_{nc} = 0$).

A lower bound of $K_{max/th}$, which can be used as a conservative threshold for any component- and crack.geometry, is obtained by neglecting K_{nc} as well and using the plane strain approximation of $C_{op/pl}$, thus

$$K_{max/th/LB} = \frac{\Delta K_{th/int} \cdot (R_p + 2R_m)}{2R_m} \tag{18}$$

The graphical representation of the conservative threshold charts according to (17) and (18) as well as the graphical determination of R_{sh} is shown in Fig. 5.

In order to determine $K_{max/th/min}$ according to (17), K_{nc} is required. By (5) and (15), it is found to be

$$K_{nc} = K_{max/th} - \Delta K_{th/int} - K_{op} \tag{19}$$

(for $R < R_{sh}$)

where K_{op} has to be measured. For this purpose the cut compliance method is proposed in the next section.

Measurement of K_{op} by the Cut-Compliance Method

The cut compliance (CC-) method was primarily developed to measure residual stresses [19]. Its idea is to release the latter by introducing a cut into the considered body. From the strain change at a suitably chosen point M due to progressive cutting it is

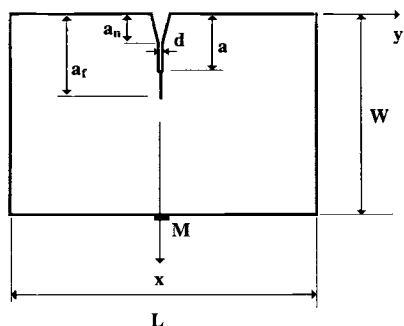


Fig. 6 - A cut of length a introduced in the plane of the fatigue crack of length a_f .

possible to calculate the distribution of the released stresses. Since fracture mechanics principles are used to establish the corresponding mathematical relations, the stress intensity factor due to residual stresses is delivered as well [21]. As shown in [22] it also enables the residual stresses in front of the crack-tip as well as the corresponding SIF to be measured in a rather simple way.

Briefly, the CC-method applied to crack closure measurements works as follows: A cut is progressively introduced along the plane of the fatigue crack. As an example, Fig. 6 shows the case of a rectangular plate containing a fatigue crack of a length a_f , which was initiated at the tip of a notch of length a_n . The actual length of the cut is denoted by a , its width by d . As derived in [21] the SIF at the tip of the cut due to the residual stresses is obtained from the strain $\epsilon_M(a)$ measured at M by

$$K_{rs}(a) = \frac{E'}{Z(a)} \frac{d\epsilon_M}{da} \tag{20}$$

where E' denotes the generalized Young's modulus ($E' = E$ for plane stress and $E' = E/(1-\nu^2)$ for plane strain) and $Z(a)$ the so-called influence function [21]. The latter is a unique

function that depends on the component geometry, on the cut plane and on the location of the strain gage, but not on the residual stress distribution. For a relatively deeply cracked rectangular plate ($a > W/4$, $L > 2W$) (see Fig. 6), there is a simple exact solution for Z [22, 23]:

$$Z(a) = -\frac{7.952}{\pi \cdot (W - a)^{3/2}} \quad (21)$$

The strain $\epsilon_M(a)$ is suitably measured by strain gages and recorded as a function of the cut depth a . Then, this curve has to be processed according to (20) and (21), which can be done by means of a simple spreadsheet computation. For $a \geq a_f$ this gives the SIF due to closure stresses acting on the crack faces and the residual stresses in the ligament. At $a = a_f$ equation (20) represents the required quantity K_{op} ,

$$K_{op} = K_{Irs}(a=a_f) \quad (22)$$

(Note that in the range $a < a_f$, $K_{Irs}(a)$ as delivered by (20) represents not the contact stresses acting on the crack-faces, but an upper bound thereof.) In cases of small cyclic loads like near the FCG-threshold, the compressive plastic zone is rather small and may probably neglected in most cases. Thus, the maximum (negative) value of K_{Irs} obtained by (20) from specimens loaded near the FCG-threshold represents an upper bound for K_{op} , which can be considered to be a good approximation of the actual K_{op} . Thus we assume

$$K_{op} \cong \max(|K_{Irs}|) \quad (23)$$

Preliminary Experimental Results

To demonstrate the applicability of the CC-method and to give some examples of obtained closure and threshold data, the results of some tests performed within a feasibility-study [24] are given in the following. Four single edge notch specimens (Fig. 6; $W=14$ mm, $L=55$ mm and thickness $B=10$ mm) of a structural steel of the type FeE460 ($R_p=420$ N/mm², $R_m=550$ N/mm²) were loaded under cyclic pure bending. To obtain near-threshold data they were fatigued at constant R-values ($R=0.1, 0.3, 0.5$ and 0.7) and a frequency of about 230 Hz by decreasing load range ΔK until the growth rate was less than about 10^{-7} mm/cycle. The measured near-threshold data are shown in Table 1 and in Fig. 7 as a function of R, and in the $K_{max/th}$ -vs.- ΔK_{th} -plane, confirming the theoretical behavior of the model as shown in Fig. 1 and 3, respectively.

From the data in Table 1, the following characteristic threshold values are obtained:

$$\Delta K_{th/int} = 132 \text{ N/mm}^{3/2}, \quad K_{max/th} \approx 309 \text{ N/mm}^{3/2}, \quad (24a)$$

which results with (15) and (18) in

$$R_{sh} = 0.573, \quad K_{max/th/LB} = 182 \text{ N/mm}^{3/2} \quad (24b)$$

For the tensile properties given above, (7) and (9) deliver the local plasticity-induced crack closure $K_{op/pl}$ in plane strain (which prevails in the present case) to be

$$K_{op/pl} = 0.276 \cdot K_{max} \tag{25}$$

To measure K_{op} by the CC-method the fatigued specimens were cut in two halves of $W = 14 \text{ mm}$ and $B = 4.9\text{mm}$ thickness resulted, in order to obtain two more or less identically fatigued specimens. One of them was used to measure crack closure by the CC-method, and the other to measure the actual length of the fatigue crack. The cuts required for the CC-method were introduced by electric discharge machining (EDM). A typical strain signal as a function of the cut depth is shown in Fig. 8. To handle the noise that is typical for EDM-cutting, $\epsilon_M(a)$ was fitted to a polynomial of 6th order before (20) was applied, so the corresponding derivative could be taken analytically. The SIF obtained by using (20) and (21) on these polynomials are shown in Fig. 9. As expected, the maximum (actually minimum, since they are always negative) values of K_{Irs} , which are considered to be K_{op} , are located quite close to $a=a_f$ (see Table 2 for a_f), which confirms the assumption that led to (23).

Table 1 - Results of fatigue tests in the threshold regime

Specimen	L1	L2	L3	L4
R	0.1	0.3	0.5	0.7
$\Delta K_{th} [\text{N/mm}^{3/2}]$	274	226	153	132
$K_{max/th} [\text{N/mm}^{3/2}]$	305	315	307	440
$K_{sh} [\text{N/mm}^{3/2}]$ ¹⁾	173	183	175	-

¹⁾ determined by (15)

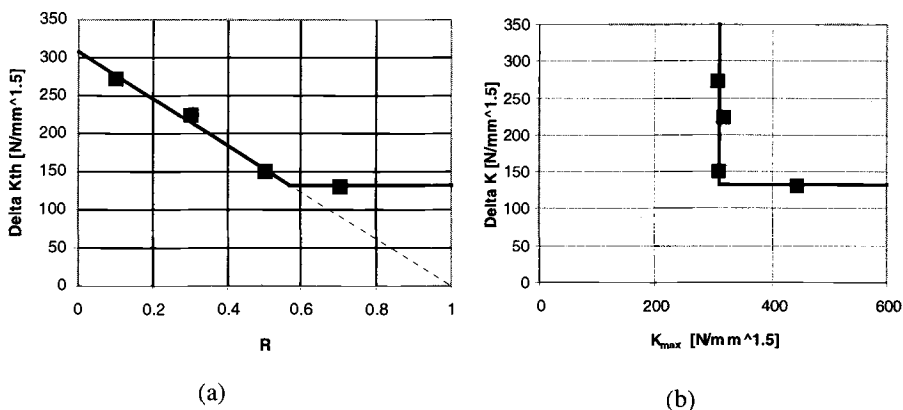


Fig. 7 - Experimental threshold values as a function of R (a) and K_{max} (b) in comparison with the behavior of the theoretical model (full lines).

After crack-length measurement the second halves of the described twin-specimens were used to determine K_{op} in the same way, but by mechanical sawing instead of EDM. As expected, the noise in the strain signal was considerably lower [24]. Qualitatively, the results were the same as the ones shown in Fig. 9. However, as shown in Table 2, there were considerable differences between the measured K_{op} of the twins, indicating that the fatigue process was not perfectly symmetrical.

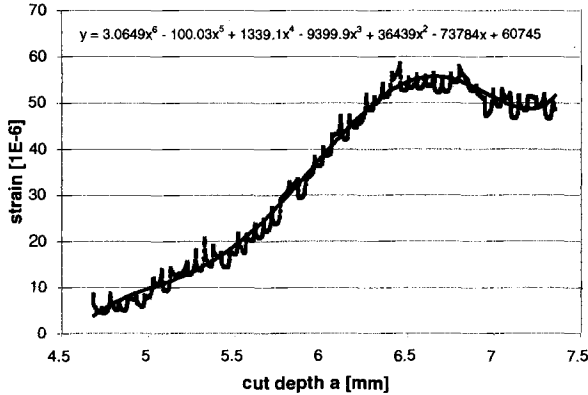


Fig. 8 - Measured strain ϵ_M at the rear surface of specimen L2 as a function of cut depth, and the corresponding fitting polynomial

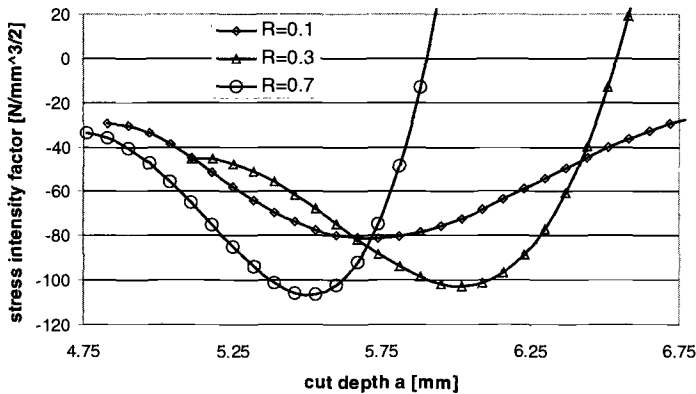


Fig. 9 - Measured stress intensity factor due to closure stresses and residual stresses as a function of cut depth

These preliminary experimental results show that K_{op} can be indeed significantly smaller than K_{sh} , indicating that there is a considerable amount of non-closure shielding. The analytically calculated $K_{op/pl}$ are relatively close to the measured K_{op} in both cases, which

means that either $K_{op/ext}$ is relatively small in the present specimens, or that (7) and (9) give somewhat too high predictions.

Table 2 - Experimental data obtained from the CC-Method

Specimen	L1	L2	L3	L4
R	0.1	0.3	0.5	0.7
a_f [mm]	5.9	6.1	5.9	5.5
K_{op} [$N/mm^{3/2}$] ¹⁾	81/139	103/119	- ²⁾	107/223

¹⁾ values for twin-specimens, determined according to (23); ²⁾ measurement failed because of a disconnection;

Table 3 - Experimental crack shielding parameters for $R < R_{sh}$ (specimen L1 and L2)

Specimen	K_{sh} ¹⁾ [$N/mm^{1.5}$]	K_{op} ²⁾ [$N/mm^{1.5}$]	K_{nc} ³⁾ [$N/mm^{1.5}$]	$K_{op/pl}$ ⁴⁾ [$N/mm^{1.5}$]	$K_{op/ext}$ ⁵⁾ [$N/mm^{1.5}$]	$K_{max/th/min}$ ⁶⁾ [$N/mm^{1.5}$]
L1	173	110	63	84	26	269
L2	183	111	72	87	24	282

¹⁾ determined by (15); ²⁾ see Table 2(mean values); ³⁾ by (19); ⁴⁾ by (26); ⁵⁾ by (5); ⁶⁾ by (17) and (19)

Discussion and Conclusions

The mechanics of FCG in the threshold regime are analyzed by means of a simplistic analytical model. It is shown that the conditions for non-propagation of a crack in a test specimen or a structural component is essentially characterized by two parameters, $K_{max/th}$ and $K_{th/int}$. To determine these two parameters, basically two threshold tests are required: The first one is suitably performed at a low and constant R-ratio, and the second at a constant K_{max} which has to be considerably higher than K_{max} of the first test. Both these measurements can be performed on the same specimen.

Only one of these two threshold parameters, $K_{th/int}$, represents an independent material property. The other one, $K_{max/th}$, consists of several intrinsic and extrinsic components. With respect to their transferability, three types of contributions to $K_{max/th}$ can be distinguished: intrinsic (material-dependent), inherent (material- and process-dependent), and system-dependent ones, as schematically shown in Fig. 10. These various contributions to the threshold explain why there often is a significant scatter in experimental threshold data reported in the literature. When applied to predict the behavior of a crack in a structural component, only the intrinsic and the process-inherent components should be taken into account. The present model offers the possibility to sort

out these components and, therewith, to determine conservative lower bound thresholds from a few experimental results, in principle just from one threshold test at a high R-ratio. It is up to further experimental investigations to explore the accuracy and conservatism of this approach.

To fill the often observed gap between the effective stress range obtained by direct K_{op} - measurements and the one obtained indirectly from crack-growth measurements a so-called "non-closure" shielding was introduced. Its physical nature and influencing factors need further investigation. The preliminary experimental results indicate that the introduced "non-closure" shielding effect K_{nc} is of relevant size in the threshold regime, about one third of the total extrinsic shielding. The physical origin of K_{nc} is not quite clear yet. It seems to be mainly due to local closure, crack front curvature and other 3D-effects that can not be captured with a 2D-consideration of crack closure. Correspondingly, K_{nc} is expected to increase with increasing specimen thickness. Whereas crack closure is higher in plane stress than in plane strain, the non-closure shielding is likely to behave in the opposite way. Thus, these two effects tend to compensate each other.

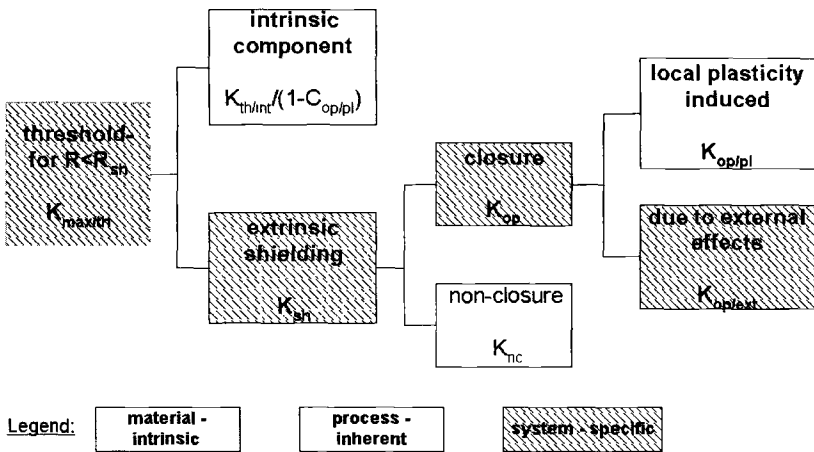


Fig. 10 - Composition of the threshold parameter for $R < R_{sh}$, $K_{max/th}$

Summarizing, the main conclusions that can be drawn from the present theoretical and experimental investigation are the following:

- The simplistic 4-parameter model presented here is able to reproduce the main features of FCG and threshold.
- The basic behavior of the threshold is characterized by two parameters, $K_{max/th}$ and $\Delta K_{th/int}$, which can be obtained in principle from two tests performed on one single specimen.
- The cut compliance method is applicable to determine the crack closure SIF K_{op} even in the threshold range. It provides some additional information about crack closure.

- Significant crack closure (about $0.3 \cdot K_{\max}$ in the considered structural steel) is present even in the threshold regime
- Besides crack closure as measured by the CC-method, there are additional extrinsic shielding effects of nearly the same magnitude, which have similar effects on crack retardation and threshold as crack closure. These additional effects are expected to be less pronounced at the higher loads outside the threshold regime.
- The existence of "non-closure" shielding effects explains why opening loads determined by direct methods, are usually significantly smaller than the ones determined by indirect methods.

References

- [1] Paris, P.C., "The fracture mechanics approach to fatigue," *Fatigue - an interdisciplinary approach*, J.J. Burke, N.L. Reed, V. Weiss, Eds., Syracuse University Press, NY, 1964, pp. 107-132.
- [2] Klesnil, M, Lucas, P., "Effect of Stress Cycle Asymmetry on Fatigue Crack Growth," *Materials Science and Engineering*, Vol. 9, 1972, pp. 231-240.
- [3] Wu, S., Mai, Y-W., Cotterell, B., "A Model of Fatigue Crack Growth Based on Dugdale Model and Damage Accumulation," *Int. J. Fracture*, Vol. 57, 1992, pp. 253-267.
- [4] Schindler, H.J. "Analytisches Modell zur Berechnung der Rissausbreitungs-geschwindigkeit unter Ermüdungsbeanspruchung," *Proc. 30. Tagung des DVM AK Bruchvorgänge*, DVM-Bericht 230, Deutscher Verband für Materialforschung und -prüfung, Berlin, 1998, 333-343 (in German).
- [5] Elber, W., "The significance of fatigue crack closure ," *Damage Tolerance in Aircraft Structures*, ASTM STP 486, American Society for Testing and Materials, Philadelphia, 1971, pp. 230-242.
- [6] Newman, J.C., "A crack closure model for predicting fatigue crack growth under aircraft spectrum loading," ASTM STP 748, American Society for Testing and Materials, Philadelphia, 1981, pp. 53-84.
- [7] Schijve, J., "Fatigue Crack Closure: Observations and Technical Significance," *Mechanics of Fatigue Crack Growth*, ASTM STP 982, J.C. Newman and W. Elber, Eds., ASTM, Philadelphia, 1988, pp. 5-34.
- [8] McClung, R.C., "The Influence of Applied Stress, Crack Length, and Stress Intensity Factor on Crack Closure," *Metallurgical Transactions A*, Vol. 22A, 1991, pp. 1559-1571.
- [9] James, M.N., "Some unresolved issues with fatigue crack closure-measurement, mechanism and interpretation problems," *Advances in Fracture Research*, ed. B.L. Karihaaloo, et al., Pergamon, Amsterdam, Vol. 5, 1997, pp. 2403-2413.

- [10] Louat, N., Sadananda, K., Duesbury, M., Vasudevan, A.K., "A theoretical Evaluation of Crack Closure," *Metall. Transactions A*, Vol. 24A, 1993, pp. 2225-2232.
- [11] Marci, G., "Determination of the Partitioning Point Dividing ΔK into ΔK_{eff} ," *Engineering Fracture Mechanics*, Vol. 53, 1995, pp 23-36.
- [12] Mc Evily, A.J., Ritchie, R.O., "Crack Closure and the Fatigue Crack Propagation Threshold as a Function of Load Ratio," *Fatigue and Fracture of Engineering Materials and Structures*, Vol. 21, 1998, pp. 847-855.
- [13] McClung, R.C., "Finite Element Analysis of Specimen Geometry Effects on Fatigue Crack Closure," *Fatigue and Fracture of Engineering Materials and Structures*, Vol. 17, 1994, pp. 861-872.
- [14] Rice, J.R., "Mechanics of Crack Tip Deformation and Extension by Fatigue," *ASTM STP 415*, American Society for Testing and Materials, Philadelphia, 1967, pp. 247-309.
- [15] Ritchie, R.O., and Yu, W., "Short crack effects in fatigue: a consequence of crack tip shielding," *The Metallurgical Society of AIME*, 1986, 167-189.
- [16] de Koning, A.U. and Liefing, G., "Analysis of Crack Opening Behaviour by Application of a Discretized Strip Yield Model," *ASTM STP 982*, J.C. Newman and W. Elber, Eds., ASTM, Philadelphia, 1988, pp. 437-458.
- [17] H. Döker, V. Bachmann, "Determination of Crack Opening Load by Use of Threshold Behaviour," *Mechanics of Fatigue Crack Growth*, ASTM STP 982, American Society for Testing and Materials, Philadelphia, 1988, pp. 274-259.
- [18] Schindler, H.J., "Charakterisierung und Abschätzung des Ermüdungsverhaltens im Bereich des Schwellenwerts," *DVM-Bericht 231*, Deutscher Verband für Materialforschung und -prüfung, Berlin, 1999, pp. 121-130 (in German).
- [19] Schmitt, R.A., Paris, P.C., "Threshold for Fatigue Crack Propagation ...," *ASTM STP 536*, American Society for Testing and Materials, Philadelphia, 1973, pp. 79-94.
- [20] Cheng, W., Finnie, I., "An Overview of the Crack Compliance Method For Residual Stress Measurement," *Proc. 4th Int Conf. On Residual Stress*, Baltimore, Soc. Experimental Mechanics, 1994, pp. 449-458.
- [21] Schindler, H.J., Cheng, W., Finnie, I., "Experimental Determination of Stress Intensity Factors due to Residual Stresses," *Experimental Mechanics*, Vol. 37, No. 3, 1997, pp. 272-279.
- [22] Schindler, H.J., "Experimental Determination of Crack Closure by the Cut Compliance Technique," to be published in: *Advances in Fatigue Crack Closure Measurement and Analysis*, ASTM STP 1343, R.C. McClung and J.C. Newman, Jr., Eds., American Society for Testing and Materials, West Conshohocken, 1999.

- [23] Schindler, H.J., Finnie, I., "Determination of Residual Stresses and the Resulting Stress Intensity Factors in the Ligament of Pre-cracked Components," *Advances in Fracture Research*, B.L. Karihaaloo, et al., eds.(Proceedings of 9th Int. Conf. on Fracture), Sydney, Pergamon, Amsterdam, Vol. 1, 1997, pp. 523-530.
- [24] Bertschinger, P, Schindler, H.J., Soyka, G., "Experimentelle Ermittlung der Risschliessung an Baustahl und Schweisseisen im Bereich des Schwellenwerts," *DVM-Bericht 231*, Deutscher Verband für Materialforschung und -prüfung, Berlin, 1999, pp. 153-161 (in German).

J. A. Newman,¹ W. T. Riddell,² and R. S. Piascik³

Effects of K_{max} on Fatigue Crack Growth Threshold in Aluminum Alloys

Reference: Newman, J. A., Riddell, W. T., and Piascik, R. S., “Effects of K_{max} on Fatigue Crack Growth Threshold in Aluminum Alloys,” *Fatigue Crack Growth Thresholds, Endurance Limits, and Design, ASTM STP 1372*, J. C. Newman, Jr. and R. S. Piascik, Eds., American Society for Testing and Materials, West Conshohocken, PA, 2000.

Abstract: Effects of K_{max} on closure-free, near-threshold fatigue crack growth are examined in ingot metallurgy aluminum alloys 2024 and 7050, and powder metallurgy aluminum alloy 8009. Significantly lower closure-free fatigue crack growth thresholds, as well as accelerated fatigue crack growth rates, were observed as K_{max} increased. Results indicate that no single value of fatigue crack growth threshold exists, because near-threshold fatigue crack growth is dependent on both K_{max} and ΔK . The near-threshold K_{max} effect is linked to an increase in crack-tip void production. Experimental observations suggest that K_{max} -accelerated, closure-free, near-threshold fatigue crack growth rates were caused by changes in crack-tip process zone damage mechanism(s) that are a result of increased crack-tip driving force.

Keywords: fatigue crack growth, threshold, aluminum alloys, K_{max} , load ratio, R , fractography

Introduction

From the time Paris related fatigue crack growth rates to the cyclic stress intensity factor range, ΔK [I], researchers have sought an explanation for the secondary effect of stress ratio (R) or K_{max} on fatigue crack growth rates. Forman [2] and Walker [3] have proposed empirical relationships. Although useful from a design standpoint, such relations do not identify the mechanism(s) responsible for the effects of K_{max} , or R , on fatigue crack growth. Elber's concept of plasticity-induced crack closure was a major breakthrough in

¹ Graduate Student, Department of Engineering Science and Mechanics, Virginia Tech, Blacksburg, VA 24061.

² Formerly: National Research Council, NASA-Langley Research Center, Mechanics of Materials Branch, Hampton, VA 23681; Currently: Mechanical Engineer, U. S. Dept. of Transportation, Volpe National Transportation Systems Center, Cambridge, MA 02142.

³ Senior Scientist, NASA-Langley Research Center, Mechanics of Materials Branch, Hampton, VA 23681.

mechanism-based fatigue crack growth modeling of R -effects [4]. Elber proposed that fatigue damage occurs only during the portion of loading in which the crack faces are completely open. Thus, fatigue crack growth rate is described in terms of effective ΔK , as defined in Equations 1 and 2, where K_{op} is the stress intensity above which the crack is open.

$$\Delta K_{eff} = K_{max} - K_{op} \quad (1)$$

$$\frac{da}{dN} = f(\Delta K_{eff}) \quad (2)$$

Other researchers have expanded and refined the crack closure concept. For example, closure has been used to explain load-history effects [5] and mechanisms other than plasticity have been proposed to contribute to crack wake contact [6, 7]. Nearly all fatigue crack growth models that account for crack closure assume it is the sole cause of stress ratio effects. However, some research has suggested that crack closure does not account for all stress ratio effects, especially at high values of R [8]. This suggests that intrinsic mechanism(s) (*i.e.* independent of crack closure), dependent on K_{max} , or R , also influence fatigue crack growth rates. Effects of K_{max} on fatigue crack growth rates tend to be more dramatic in the near-threshold regime than in the Paris regime [9]. The near-threshold regime of fatigue crack growth governs the fatigue lives of many engineering structures. Therefore, understanding K_{max} effects is important, especially when designing components for a tensile mean load subject to small amplitude oscillatory loads. The objective of this paper is to determine the effects of K_{max} on near-threshold fatigue crack growth.

Test Method

To study the effect of K_{max} on near-threshold fatigue crack growth, three aluminum alloys (2024, 7050, and 8009) were selected. Alloy 7050-T6 plate (S-L orientation), and powder metallurgy (PM) 8009 sheet (L-T orientation) were selected because accelerated near-threshold fatigue crack growth rates are observed at increased stress ratio [10]. This behavior is not explained satisfactorily by plasticity-induced crack closure models. Aluminum alloy 2024-T3 sheet (L-T orientation) was selected because its fatigue crack growth behavior is relatively well characterized and crack-tip closure models successfully describe near-threshold behavior at a variety of load ratios. A list of relevant material properties and testing parameters are presented in Table 1 for all three alloys.

Fatigue crack growth tests were performed using closed loop servo-hydraulic testing machines, with constant amplitude sinusoidal wave loading. As summarized in Table 1, alloy 7050 tests were conducted using the ASTM Standard Test Method for Measurement of Fatigue Crack Growth Rates (E 647) compact tension (C(T)) specimen, while alloys 8009 and 2024 were tested using the eccentricity loaded single edge notch tension (ESE(T)) specimen (formerly the extended compact tension specimen) [11]. A computer controlled system [12] was used to continuously monitor crack length throughout testing using either the back-face strain [13] or the front-face displacement [14] compliance technique. This system automatically adjusts loads as the crack grows to ensure that programmed stress intensity factors are applied throughout the tests. Fatigue crack

Table 1 - *Mechanical properties and specimen configurations.*

	Alloy (orientation)		
	2024-T3 (L-T)	7050-T6 (S-L)	8009 (L-T)
E, GPa	72.4	71.7	88.4
σ_y , MPa	345	248	420
K_{IC} , MPa \sqrt{m}	34	29	30
grain size, μm	70-150	30-100	0.3-1.0
orientation	L-T	S-L	L-T
specimen geometry	ESE(T)	C(T)	ESE(T)
thickness (B), mm	2.3	2.5	2.3
width (W), mm	38.1	30.5	38.1

growth rates were evaluated after crack growth increments of $a/W = 0.001$. Periodically, crack lengths were verified by visual measurements. Testing was performed in accordance with ASTM standards (E 647), where applicable. For the constant- K_{\max} threshold tests performed in this study, $C = -0.8 \text{ mm}^{-1}$ was used. Although ASTM standards (E 647) recommend using $C = -0.08 \text{ mm}^{-1}$ for constant- R threshold tests, a steeper K -gradient can be used for constant- K_{\max} testing because the crack-tip monotonic plastic zone does not change as the crack grows. The maximum applied loads during testing were at, or above, 50% of the load capacity. At threshold, the load range always exceeded 1% of the total load range. Use of a 16 bit data acquisition board allowed sufficient resolution of load under all test conditions.

Testing was performed at sufficiently high load ratios ($0.5 < R < 1.0$) so that crack-tip closure was eliminated. The reduced displacement technique [15], applied to compliance measurements, did not indicate the presence of crack closure in the near-threshold regime. However, remote means of detecting crack closure, including the reduced displacement technique, might not be sensitive enough to detect crack closure in the near-threshold regime. Therefore, a novel, near-tip, and non-contacting measurement technique named Digital Image Displacement System (DIDS) [16] was also used to check for closure. Here, a thin film of tantalum is deposited in a random pattern of $4 \mu m$ speckles on the surface of a specimen near the crack-tip. A long-focal-length microscope acquired a series of digital near-crack-tip images during a load cycle. After the images were obtained, pairs of speckled regions (one below and one above the crack) were selected. An image correlation algorithm [17] was used to calculate relative displacements for each pair of speckled regions selected, for each acquired image. The near-crack-tip closure behavior can be studied from the resulting load versus relative displacement traces. Due to the complexities involved in using DIDS, only a few tests in which crack closure was deemed most likely were analyzed this way. Constant- $K_{\max} = 5.5 \text{ MPa}\sqrt{m}$ tests were deemed most likely to exhibit closure, but no closure was detected using DIDS in the near-threshold regime.

Effect of K_{max} on Fatigue Crack Growth Rate

Figure 1 shows the near-threshold fatigue crack growth characteristics of alloy 2024 for threshold tests conducted at a constant- K_{max} of 5.5, 11.0, 16.5, and 22.0 $\text{MPa}\sqrt{\text{m}}$. The ASTM suggested crack growth threshold rate (10^{-10} m/cycle) is shown as a horizontal dotted line in Figure 1. Fatigue crack growth, if affected by crack-tip closure, would lie in the shaded region. The test data indicate that increased K_{max} causes an increase in fatigue crack growth rates, especially as threshold is approached. The constant- K_{max} test results reveal two subtle, but important, characteristics for alloy 2024: (1) K_{max} effects exist on near-threshold fatigue crack growth behavior (e.g. increasing K_{max} from 5.5 to 22 $\text{MPa}\sqrt{\text{m}}$, produced a 13% reduction in ΔK_{th}) and (2) no true threshold was reached due to a (subtle) finite slope in the da/dN versus ΔK data at the suggested threshold rate.

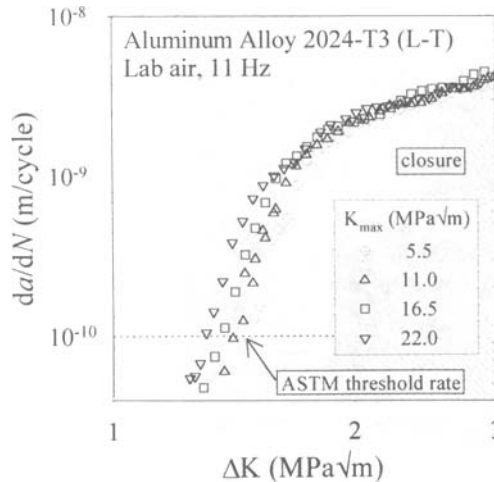


Figure 1 - Fatigue crack growth rate versus ΔK data of alloy 2024-T3 for constant- K_{max} threshold tests.

The near-threshold fatigue crack growth characteristics of 7050 are shown in Figure 2 for constant- K_{max} threshold tests of 5.5, 11.0, 16.5, and 22.0 $\text{MPa}\sqrt{\text{m}}$. The ASTM suggested threshold crack growth rate is shown as a horizontal dotted line in Figure 2 and fatigue crack growth, if affected by crack-tip closure would lie in the shaded region. Fatigue crack growth rates of 7050 aluminum increase with increasing K_{max} . As K_{max} increases from 5.5 to 22.0 $\text{MPa}\sqrt{\text{m}}$, the ASTM suggested threshold decreased from $\Delta K_{th} = 1.1$ to 0.73 $\text{MPa}\sqrt{\text{m}}$ (a 34% reduction). No true threshold was reached for this material because a (subtle) finite slope in the fatigue crack growth data existed about the suggested threshold rate.

Near-threshold fatigue crack growth data for PM alloy 8009 is shown in Figure 3. The ASTM suggested crack growth threshold rate is shown as a horizontal dotted line in Figure 3 and fatigue crack growth, if affected by crack-tip closure would lie in the shaded region. A comparison of constant- K_{max} (5.5 and 11.0 $\text{MPa}\sqrt{\text{m}}$) tests results for 8009

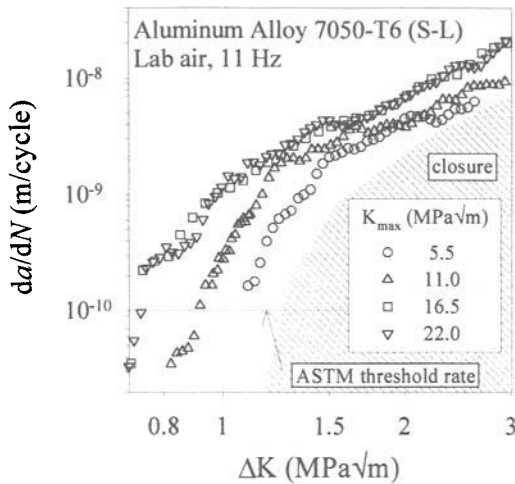


Figure 2 - Fatigue crack growth rate versus ΔK data of alloy 7050-T6 for constant- K_{max} threshold tests.

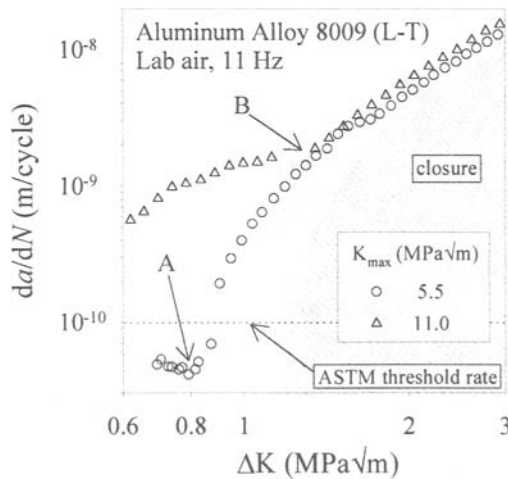


Figure 3 - Fatigue crack growth rate versus ΔK data of alloy 8009 for constant- K_{max} threshold tests.

reveal distinctly different near-threshold behavior when compared with typical fatigue crack growth curves (*i.e.* 2024 and 7050). Abrupt transitions in slope, followed by accelerated fatigue crack growth behavior, were observed in the fatigue crack growth curves of Figure 3 at points A and B for $K_{max} = 5.5$ and 11.0 MPa \sqrt{m} , respectively. The constant- $K_{max} = 5.5$ MPa \sqrt{m} test data intersected the ASTM suggested threshold rate at $\Delta K = 0.9$ MPa \sqrt{m} , but nearly- ΔK -independent da/dN is observed at 4 to 5×10^{-11} m/cycle (point A in Figure 3). For the constant- $K_{max} = 11.0$ MPa \sqrt{m} threshold test, the test data

never intersected the ASTM suggested threshold rate for $\Delta K > 0.6 \text{ MPa}\sqrt{\text{m}}$, but a similar transition in fatigue crack growth behavior did occur (point B in Figure 3)

Additional tests were conducted to investigate the pronounced acceleration in near-threshold fatigue crack growth rates observed during constant- K_{max} threshold tests, shown in Figure 3. To study the accelerated fatigue crack growth behavior noted by point A in Figure 3, a constant ΔK test ($0.77 \text{ MPa}\sqrt{\text{m}}$) was conducted at a $K_{\text{max}} = 5.5 \text{ MPa}\sqrt{\text{m}}$ with loading frequencies of 11, 5, and 1 Hz. The results shown in Figure 4a reveal that increased fatigue crack growth rates (da/dN) were obtained with decreasing loading frequency. Replotting the data of Figure 4a versus time reveals these fatigue crack growth rates are time dependent, as indicated by the nearly constant slope (da/dt) for all three frequencies (see Figure 4b). To investigate the possibility that creep crack growth or stress corrosion cracking is superimposed on fatigue crack growth, a constant load corresponding to $K = 5.5 \text{ MPa}\sqrt{\text{m}}$ (equivalent to the K_{max} applied in Figure 4) was held immediately following the 1 Hz test. No crack growth was detected after 1 week (168 hours) of constant load testing. Had the time-dependent crack growth rate (da/dt) of Figure 4b persisted, approximately 0.3 mm of crack growth would have occurred during the 1 week test.

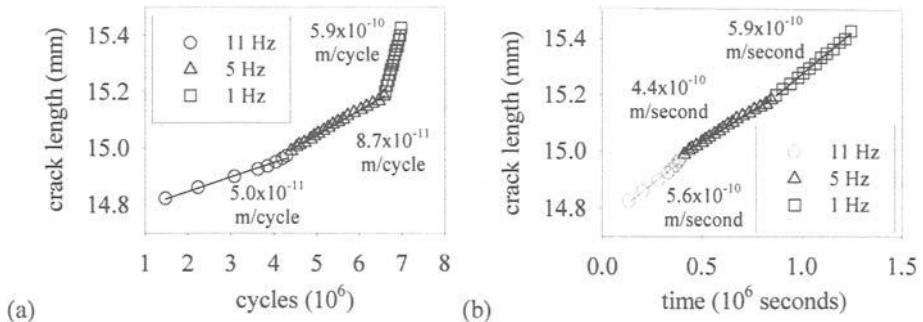


Figure 4 - Crack length as a function of (a) cycles and (b) time for alloy 8009 subject to constant $K_{\text{max}} = 5.5$ and $\Delta K = 0.77 \text{ MPa}\sqrt{\text{m}}$ loading in lab air at 11, 5, and 1 Hz.

To determine whether the time dependent behavior that was noted in air was a result of environment, similar tests were conducted in vacuum ($<5 \times 10^{-7} \text{ Pa}$). Comparison of constant- K_{max} (5.5 and 11.0 $\text{MPa}\sqrt{\text{m}}$) threshold tests conducted in air and vacuum under identical mechanical loading are shown in Figure 5. In general, the air rates are faster than those in vacuum. However, both vacuum and air data exhibit transitions in fatigue crack growth behavior at A_{vac} and A_{air} , respectively, for $K_{\text{max}} = 5.5 \text{ MPa}\sqrt{\text{m}}$, and for B_{vac} and B_{air} , respectively, for $K_{\text{max}} = 11.0 \text{ MPa}\sqrt{\text{m}}$. Similar to the frequency effect noted in lab air, increased fatigue crack growth rates (da/dN) were observed as the loading frequency decreased (11, 5, and 1 Hz) in high vacuum (see Figure 6a) for testing at constant ΔK ($1.21 \text{ MPa}\sqrt{\text{m}}$) and $K_{\text{max}} = 5.5 \text{ MPa}\sqrt{\text{m}}$ (a loading condition near A_{vac} in Figure 5). Data of Figure 6b is similar in character to Figure 4b, where da/dt remains nearly constant as frequency changes. The vacuum data indicate that K_{max} -dependent accelerated fatigue crack growth behavior in 8009 is not induced by environmental effects.

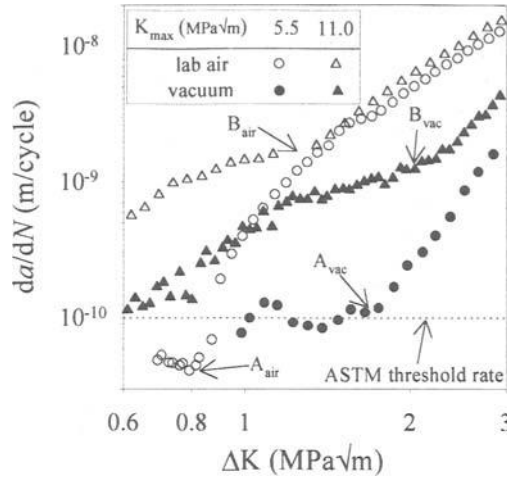


Figure 5 - Fatigue crack growth rate versus ΔK data for constant- $K_{max} = 5.5$ and 11.0 $MPa\sqrt{m}$ threshold tests on 8099 aluminum, loaded at 11 Hz, in both lab air (open symbols) and high vacuum ($<5 \times 10^{-7}$ Pa, as closed symbols).

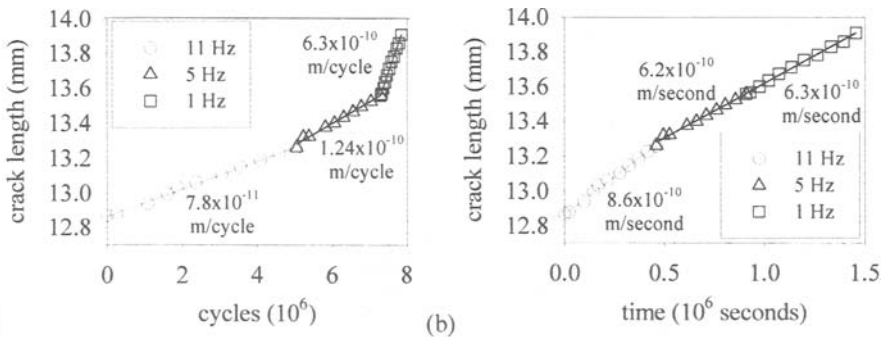


Figure 6 - Crack length as a function of (a) cycles and (b) time for alloy 8099 subject to constant $K_{max} = 5.5$ and $\Delta K = 1.21$ $MPa\sqrt{m}$ loading in high vacuum ($<5 \times 10^{-7}$ Pa) at 11, 5, and 1 Hz.

Fractography

Increasing (closure free) fatigue crack growth rates with increasing K_{max} suggest additional crack tip damage occurs at higher K_{max} . Examination of crack surfaces produced during constant- K_{max} testing was done to identify and characterize possible K_{max} -enhanced damage. Alloy 2024 fatigue crack surface micrographs are shown in Figures 7a and 7b for tests conducted at constant- $K_{max} = 5.5$ and 22.0 $MPa\sqrt{m}$, respectively. The figures correspond to the crack surface generated at a minimum ΔK ($da/dN = 5 \times 10^{-11}$ m/cycle), as shown in Figure 1. The direction of fatigue crack growth (FCG) is always

left to right, indicated by an arrow. Transgranular crack paths are shown in Figures 7a and 7b (flat featureless regions) with widely dispersed voids (a few are labeled A). On the right side of the figures, voids are marked by white circles, while the left side remains unmarked. A more detailed comparison shows that as K_{\max} is increased from 5.5 to 22.0 $\text{MPa}\sqrt{\text{m}}$, the number of microvoids per unit area increased nearly 25% [18]. Void formation is the dominant mechanism of quasi-static fracture, shown in Figure 7c ($K_c = 42 \text{ MPa}\sqrt{\text{m}}$); voids (labeled A in Figure 7c) are larger and more numerous than those observed on both fatigue crack surfaces (Figures 7a and 7b). Figure 7d is a micrograph at high magnification showing a typical microvoid observed on the fatigue crack surface in Figure 7b. At high magnification, particles (labeled B) are revealed at the bottom of the void. Energy dispersive X-ray (EDX) analysis identified these particles as an undissolved phase, Al_2CuMg .

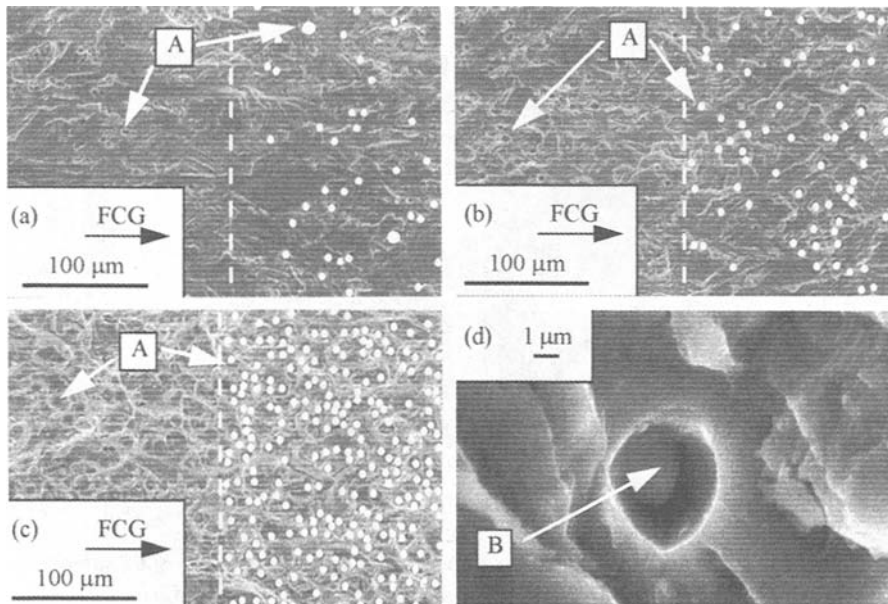


Figure 7 - SEM fractographs of alloy 2024-T3 fatigue crack surfaces produced by constant- K_{\max} = (a) 5.5 and (b) 22.0 $\text{MPa}\sqrt{\text{m}}$ threshold tests, (c) quasi-static fracture ($K_c = 42 \text{ MPa}\sqrt{\text{m}}$), and (d) a high magnification fractograph of a typical microvoid produced on the fatigue crack surface of Figure 7b. For Figures 7a-c, microvoids are marked by white circle (or ovals) on the right, but unmarked on the left.

Figures 8a and 8b are micrographs showing the fatigue crack surface of alloy 7050 generated at constant $K_{\max} = 5.5 \text{ MPa}\sqrt{\text{m}}$ ($\Delta K = 1.1 \text{ MPa}\sqrt{\text{m}}$ and $da/dN = 1.5 \times 10^{-10}$ m/cycle) and constant $K_{\max} = 22.0 \text{ MPa}\sqrt{\text{m}}$ ($\Delta K = 0.7 \text{ MPa}\sqrt{\text{m}}$ and $da/dN = 3 \times 10^{-11}$ m/cycle, respectively (refer to Figure 2). These micrographs show transgranular crack paths (flat featureless regions labeled B) and regions that exhibit a rough surface (outlined in white and labeled A). As K_{\max} increases, the percent of crack surface covered by rough

regions increases. At monotonic fracture ($K_c = 35 \text{ MPa}\sqrt{\text{m}}$), nearly the entire crack surface is consumed with these rough regions, as shown in Figure 8c. Figure 8d is a high magnification micrograph showing a typical rough region observed on the fatigue crack surface in Figure 8b. Closer examination of the rough regions revealed clusters of microvoids, each containing a small particle, labeled C in Figure 8d. EDX analysis of these particles identified these regions as $\text{Al}_7\text{Cu}_2\text{Fe}$ constituent particles. Further study of Figure 8d reveals faint white lines surround most of particles, which is evidence of ductile lips marking the outer regions of microvoids. A comparison of fatigue crack surfaces produced at 5.5, 11.0, 16.5, and 22.0 $\text{MPa}\sqrt{\text{m}}$ revealed an increase in constituent particle microvoids as K_{max} increased.

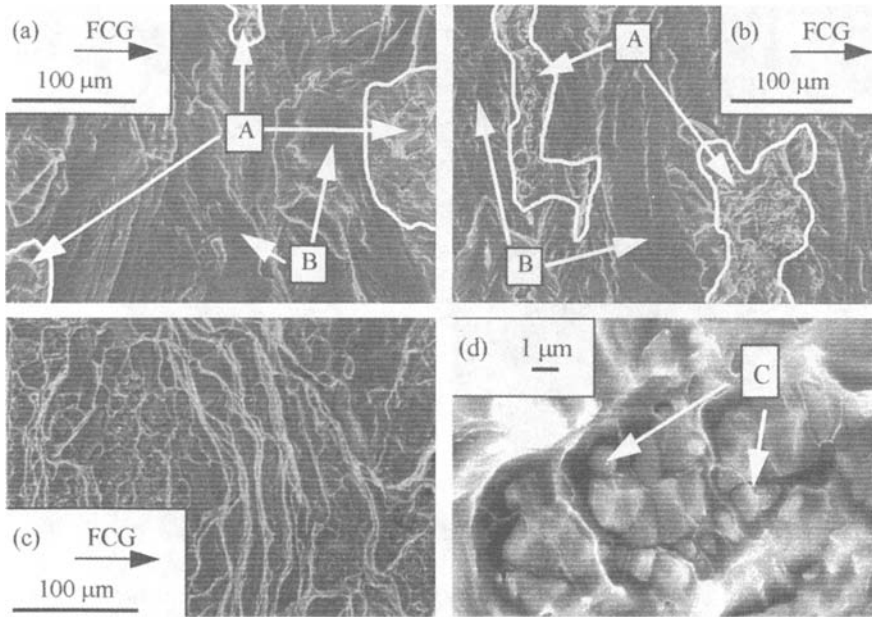


Figure 8 - SEM fractographs of alloy 7050-T6 fatigue crack surfaces produced by constant- K_{max} = (a) 5.5 and (b) 22.0 $\text{MPa}\sqrt{\text{m}}$ threshold tests, (c) quasi-static fracture ($K_c = 35 \text{ MPa}\sqrt{\text{m}}$), and (d) a high magnification fractograph of a typical region labeled A on the fatigue crack surface shown in Figure 8b. Regions labeled A in Figures 8a and 8b are outlined in white, while regions B in the figures remain unmarked. Figure 8c is almost completely consumed with regions previously denoted as A.

Figure 9a is a photograph showing the through-the-thickness fatigue crack surface of an alloy 8009 specimen tested at a constant $K_{max} = 5.5 \text{ MPa}\sqrt{\text{m}}$. The near vertical fatigue crack surface transition in the center of Figure 9a (between the dark and light regions) marks the change in fatigue crack morphology that coincides with the transition to accelerated fatigue crack growth rates (point A in Figure 3). The feature (vertical curved line) on the far right of Figure 9a marks the final crack front of the fatigue crack surface.

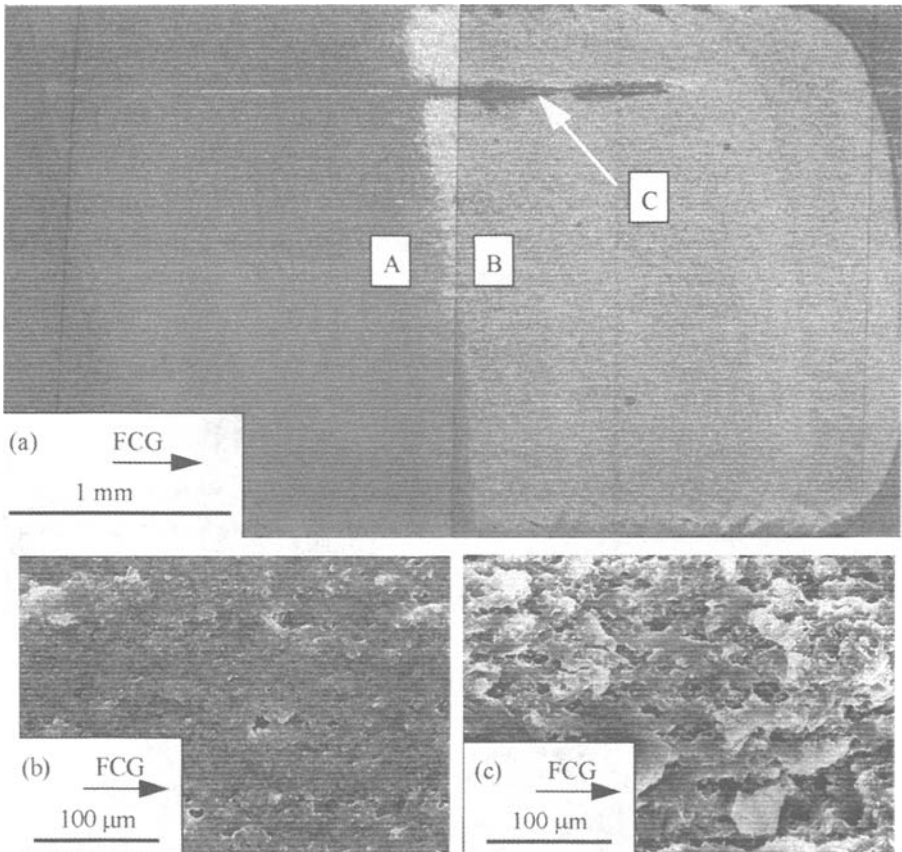


Figure 9 - SEM fractographs of alloy 8009 fatigue crack surfaces produced by a constant- $K_{max} = 5.5 \text{ MPa}\sqrt{\text{m}}$ threshold test; (a) the entire fatigue crack surface, (b) high magnification fractograph of region A in Figure 9a, and (c) high magnification fractograph of region B in Figure 9a. Figures 9b and 9c correspond to fatigue crack growth rates just before and just after point A in Figure 3. (Recall threshold tests performed with decreasing ΔK .)

A delamination crack parallel to the direction of FCG and normal to the fatigue crack surface is labeled C in Figure 9a. During fatigue cracking, delamination occurred along ribbon surface oxides that were produced during processing of the sheet [19]. Figures 9b and 9c are micrographs showing regions A and B in Figure 9a, respectively, at higher magnification. Prior to the transition (Figure 9b), the crack surface is somewhat featureless with widely spaced voids. After the transition (Figure 9c), the rougher crack surface contains many voids. Figures 10a and 10b are micrographs showing the fatigue crack surface morphology of alloy 8009 at a $K_{max} = 11.0 \text{ MPa}\sqrt{\text{m}}$. Figure 10a shows the fatigue crack surface just prior to accelerated da/dN (to the right of point B in Figure 3)

and Figure 10b shows the accelerated fatigue crack growth surface morphology (to the left of point B in Figure 3). Here, accelerated fatigue crack growth rates are correlated with a distinct increase in void formation. Careful examination of fatigue crack surfaces similar to that shown in Figure 10b show that only microvoids, with no mating convex surfaces, are present. This observation strongly suggests a microvoid nucleation process similar to that observed by other researchers [19]. No EDX analysis was performed on alloy 8009 due to the extremely fine microstructure. However, it is suggested that void formation occurs about small (40-80 nm diameter) dispersoids of $Al_{13}(Fe,V)_3Si$ [20].

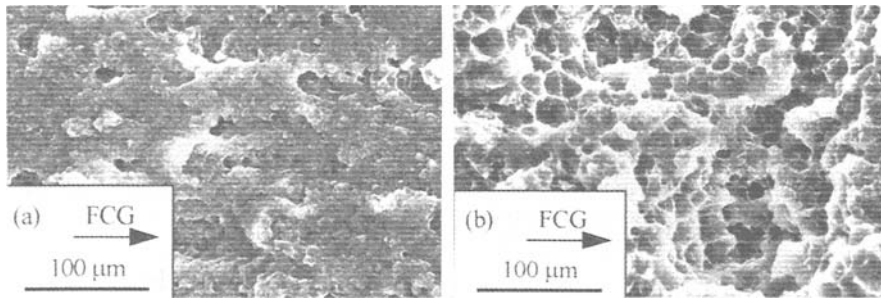


Figure 10 - SEM fractographs of alloy 8009 fatigue crack surfaces produced by a constant- $K_{max} = 11.0 \text{ MPa}\sqrt{\text{m}}$ threshold test; high magnification fractographs of crack surfaces produced (a) just before and (b) just after fatigue crack growth conditions of point B in Figure 3. (Recall threshold tests performed with decreasing ΔK .)

Discussion

Results show that near-threshold fatigue crack growth is dependent on both ΔK and K_{max} . Accelerated fatigue crack growth rates are correlated with increasing levels of K_{max} causing increasing levels of crack-tip process zone damage. The increase in damage, manifested as voids, is related to microvoid nucleation at secondary phase particles (Al_2CuMg excess phase in alloy 2024, Al_7Cu_2Fe constituent particle in alloy 7050 and possibly $Al_{13}(Fe,V)_3Si$ dispersoid particles in 8009). The effect of increasing K_{max} on ΔK_{th} is summarized in Table 2. The table lists the decrease in ΔK_{th} (ASTM suggested definition) for corresponding increased levels of K_{max} . For example, ΔK_{th} for alloy 7050 decreased from $1.3 \text{ MPa}\sqrt{\text{m}}$ to $0.73 \text{ MPa}\sqrt{\text{m}}$ as K_{max} was increased from $5.5 \text{ MPa}\sqrt{\text{m}}$ to $22.0 \text{ MPa}\sqrt{\text{m}}$. To relate the fatigue crack growth test results to a meaningful fracture parameter, K_{max} is normalized with K_{Ic} , the linear-elastic (plane-strain) fracture toughness. Table 2 shows that the K_{max} levels used in this study are well below the monotonic toughness: $K_{max}/K_{Ic} \leq 0.65$ for 2024, ≤ 0.57 for 7050, and ≤ 0.37 for 8009.

Results indicate that for low to moderate levels of K_{max} ($K_{max}/K_{Ic} \leq 0.65$) near threshold transgranular fatigue crack growth in alloys 2024 and 7050 exhibited increased void production with increased K_{max} . Similar to voids produced at fracture, the voids produced during fatigue crack growth nucleate at secondary phase particles. At high K_{max} , this behavior might be explained by “static modes” where isolated regions of the microstructure exhibit low toughness properties and fail during a single loading cycle

Table 2 - Changes in ΔK_{th} with K_{max} .

	Alloy (orientation)		
	2024-T3 (L-T)	7050-T6 (S-L)	8009 (L-T)
Change in K_{max} (MPa \sqrt{m})	5.5 \rightarrow 22.0	5.5 \rightarrow 22.0	5.5 \rightarrow 11.0
Change in ΔK_{th} (MPa \sqrt{m})	1.5 \rightarrow 1.3	1.3 \rightarrow 0.73	1.15 \rightarrow < 0.6
K_{max}/K_{IC}	0.16 \rightarrow 0.65	0.19 \rightarrow 0.57	0.18 \rightarrow 0.37
Void initiation sites	Al ₂ CuMg particles	Al ₇ Cu ₂ Fe particles	Al ₁₃ (Fe,V) ₃ Si particles*
Particle size (μm)	2 to 3	1 to 3	0.04 to 0.08

* not determined by EDX

(monotonic loading). Because void production occurs especially in the near threshold regime and can occur at relatively low K_{max} levels, a more subtle but important alternative rationalization, in terms of process zone fatigue damage, might be needed to explain this behavior. The preexisting state of damage (dislocation cell structure) contained in a cyclic process zone is greater than that contained in a monotonic process zone. For a given cyclic load, an increase in K_{max} driving force promotes further dislocation motion allowing additional dislocations accumulate at barriers (incoherent particle-matrix interface) promoting void growth. Potential barriers about which voids might form are precipitate-matrix interfaces, dispersoids, and/or constituent particles.

The ultra-fine microstructure of powder metallurgy (PM) alloy 8009 requires further mechanistic considerations. Because 8009 contains a submicron grain size, it is unlikely that crack-tip process zone dislocation cell structures are developed [21, 22]. From previous research, the fracture properties of alloy 8009 are apparently governed by microvoid damage produced from dislocation interactions with dispersoids [20]. The similar microvoid morphology noted on fatigue crack surfaces in this study compared to room temperature fracture surfaces of 8009 produced by previous researchers [20] suggest that accelerated near threshold fatigue crack growth is a result of "dispersoid type" microvoid damage. Increased fatigue crack growth rates with decreased loading frequency in vacuum also suggests a further influence by time dependent processes. The fact that no crack growth was observed during constant load testing suggests that pure creep is not operative. Based on these observations, it is speculated that accelerated near threshold fatigue crack propagation by void growth is promoted by a room temperature creep-fatigue process. Here, fatigue loading is required to generate an abundance of mobile dislocations that are driven by K_{max} to dislocation sinks (dispersoids). The accelerated near threshold fatigue crack growth rate characteristics shown in Figure 3 are consistent with a vacancy transport mechanism. Figure 11 is a linear plot of the critical values (ΔK_{trans} , da/dN_{trans} , and K_{max}) shown in Figure 3 (points A and B), which correspond to the change in crack surface appearance and unusual threshold behavior previously noted. Transition points for constant- K_{max} threshold tests of 16.5 and 22.0 MPa \sqrt{m} are shown in Figure 11, although the associated fatigue crack growth data and fractography are not presented. The data in Figure 11 suggest that as fatigue crack growth rates increase, additional K_{max} driving force is required to produce sufficient mobile vacancies to support microvoid crack propagation.

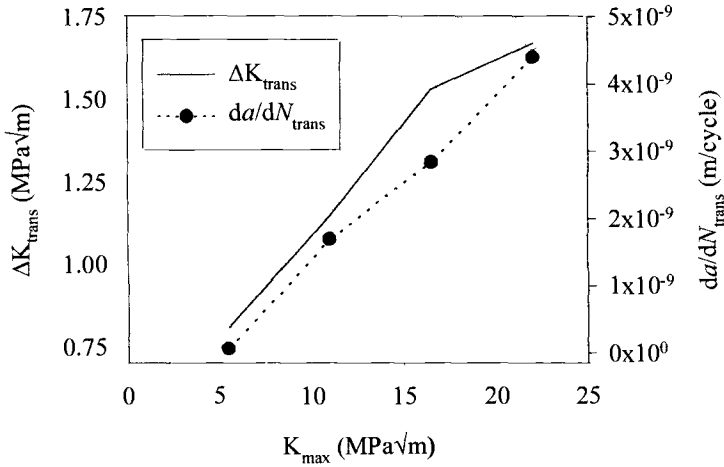


Figure 11 - Linear plot of ΔK_{trans} (open symbols) and corresponding fatigue crack growth rates, da/dN_{trans} (closed symbols), versus K_{max} for alloy 8009.

Conclusions

Results show that (1) closure-free near-threshold fatigue crack growth rate is a function of both ΔK and K_{max} and (2) no single value of closure-free ΔK_{th} exists. For well-behaved alloys, such as alloy 2024, the effect of K_{max} is relatively small and the variation in ΔK_{th} is minimal. However, engineering alloys (e.g. alloy 7050 S-L orientation) can exhibit significant variations in ΔK_{th} for K_{max} -sensitive orientations. Results also show that fine-grained microstructures, similar to alloy 8009, can be greatly influenced by K_{max} , resulting in profound variations in near-threshold crack growth characteristics.

Accelerated near threshold fatigue crack growth rates are correlated with increasing levels of crack-tip process zone damage. The increase in damage is related to microvoid nucleation at dispersoid or precipitate particles. It is speculated that the increase in K_{max} driving force promotes void growth by altering the process zone cyclic dislocation structure and by forcing additional dislocations/vacancies to accumulate at microstructural barriers (e.g. incoherent particle-matrix interface).

Acknowledgments

This research was performed while one author (JAN) held a Virginia Tech-NASA Langley Graduate Student Researchers Program (GSRP) appointment, and another author (WTR) held a National Research Council - NASA Langley Research Associateship.

References

- [1] Paris, P., and Erdogan, F., "A Critical Analysis of Crack Propagation Laws," *Journal of Basic Engineering*, Transactions of the ASME, Dec. 1963, pp. 528-534.

- [2] Forman, R. G., Kearney, V. E., and Engle, R. M., "Numerical Analysis of Crack Propagation in Cyclic-Loaded Structures," *Journal of Basic Engineering*, Transactions of the ASME, Sept. 1967, pp. 459-464.
- [3] Walker, K., "The Effect of Stress Ratio During Crack Propagation and Fatigue for 2024-T3 and 7075-T6 Aluminum," *Effects of Environment and Complex Load History on Fatigue Life, ASTM STP 462*, American Society for Testing and Materials, Philadelphia, PA, 1970, pp. 1-14.
- [4] Elber, W., "Fatigue Crack Closure Under Cyclic Tension," *Engineering Fracture Mechanics*, v. 2, 1970, pp. 37-45.
- [5] Ward-Close, C. M. and Ritchie, R. O., "On the Role of Crack Closure Mechanisms in Influencing Fatigue Crack Growth Following Tensile Overloads in a Titanium Alloy: Near Threshold Versus Higher ΔK Behavior," *Mechanics of Fatigue Crack Closure, ASTM STP 982*, J. C. Newman, Jr. and W. Elber, Eds., American Society for Testing and Materials, Philadelphia, PA, 1988, pp. 93-111.
- [6] Purushothaman, S. and Tien, J. K., "A Fatigue Crack Growth Mechanism for Ductile Materials," *Scripta Metallurgica*, v. 9, 1975, pp. 923-926.
- [7] Suresh, S., Zaminski, G. F., and Ritchie, R. O., "Oxide Induced Crack Closure: An Explanation for Near-threshold Corrosion Fatigue Crack Growth Behavior," *Metallurgical Transactions*, v. 12A, 1981, pp. 1435-1443.
- [8] Gan, D. and Weertman, J., "Crack closure and crack propagation rates in 7050 Aluminum," *Engineering Fracture Mechanics*, v. 15, 1981, pp. 87-106.
- [9] Beevers, C. J., "Fatigue Crack Growth Characteristics at Low Stress Intensities of Metals and Alloys," *Metals Science*, The Metals Society, Aug./Sept., 1977, pp. 362-367.
- [10] NASA-Johnson Space Center, 1994, *Derivation of Crack Growth Properties of Materials for NASA/FLAGRO 2.0*, Vol. 1, NASA-Johnson Space Center, JSC-26254.
- [11] Piascik, R. S., Newman, J. C., Jr., and Underwood, J. H., "The Extended Compact Tension Specimen," *Fatigue and Fracture of Engineering Materials and Structures*, v. 20, 1997, pp. 559-563.
- [12] Fracture Technology Associates, *User's Reference Manual for Automated Fatigue Crack Growth (Compliance)*, version 2.43, Fracture Technology Associates, Bethlehem, PA.
- [13] Deans, W. F., Jolly, C. B., Poyton, W. A., and Watson, W., "A Strain Gauging Technique for Monitoring Fracture Mechanics Specimens During Environmental Testing," *Strain*, v. 13, 1977, pp. 152-154.
- [14] Saxena, A., Hudak, S. J., Jr., Donald, J. K., and Schmidt, D. W., "Computer-Controlled Decreasing Stress Intensity Technique for Low Rate Fatigue Crack Growth Testing," *Journal of Testing and Evaluation*, v. 6, 1978, pp. 167-174.
- [15] Elber, W., "Crack Closure and Crack Growth Measurements in Surface-Flawed Titanium Alloy Ti-6Al-4V," NASA TN D-8010, 1975.

- [16] Sutton, M. A., Zhao, W., McNeill, S. R., Helm, J. D., Piascik, R. S., and Riddell, W. T., "Local Crack Closure Measurements: Development of a Measurement System Using Computer Vision and a Far Field Microscope," *Second Symposium on Crack Closure Measurement and Analysis, ASTM STP 1343*, R. C. McClung and J. C. Newman, Jr., Eds., American Society for Testing and Materials, West Conshohocken, PA, 1999 (in press).
- [17] Sutton, M. A., Chao, Y. J., and Lyons, J. S., "Computer Vision Methods for Surface Deformation Measurements in Fracture Mechanics," *Novel Experimental Techniques in Fracture Mechanics*, AMD-Vol.176, American Society for Mechanical Engineers, 1993, pp. 203-217.
- [18] Riddell, W. T. and Piascik, R. S., "Stress Ratio Effects on Crack Opening Loads and Crack Growth Rates in Aluminum Alloy 2024," *Fatigue and Fracture Mechanics: Twenty-Ninth Volume, ASTM STP 1332*, T. L. Panontin and S. D. Sheppard, Eds., American Society for Testing and Materials, West Conshohocken, PA, 1999, pp. 407-425.
- [19] Kim, S.-S., Haynes, M. J., and Gangloff, R. P., "Localized Deformation and Elevated-Temperature Fracture of Submicron-Grain Aluminum with Dispersoids," *Materials Science and Engineering*, v. A203, 1995, pp. 256-271.
- [20] Jata, K. V., Maxwell, D., and Nicholas, T., "Influence of Environment and Creep on Fatigue Crack Growth in a High Temperature Aluminum Alloy 8009," *Journal of Engineering Materials and Technology*, v. 116, 1994, pp. 45-53.
- [21] Lloyd, D. J., "Deformation of Fine-Grained Aluminum Alloys," *Metal Science*, May 1980, pp. 193-198.
- [22] Westengen, H., "Tensile Deformation of a Fine-Grained Al-Alloy," *Strength of Metals and Alloys*, R. C. Gifskins, Ed., Pergamon Press, New York, NY, 1983, pp. 461-466.

Test Procedures

Günter Marci¹

Fatigue Crack Growth Threshold Concept and Test Results for Al- and Ti-Alloys

Reference: Marci, G., “Fatigue Crack Growth Threshold Concept and Test Results for Al- and Ti-Alloys,” *Fatigue Crack Growth Thresholds, Endurance Limits, and Design*, ASTM STP 1372, J. C. Newman, Jr. and R. S. Piascik, Eds., American Society for Testing and Materials, West Conshohocken, PA, 2000.

Abstract: The fact that fatigue crack propagation (FCP) rates approach zero asymptotically as the fracture mechanics loading parameter ΔK decreases toward certain limiting values is the reason for the scientific interest in these so-called ‘threshold’ values. In respect to the practical use of these ‘limiting values’, the author divides them into two groups, namely in ‘non-propagation conditions’ ΔK_{th} and in a material property ‘FCP-threshold’ ΔK_T . It is shown that ΔK_T must be an integral part in the functional correlation between FCP-rates and the cyclic loading conditions expressed in ΔK_{eff} . The experimental determination of ΔK_{th} on six Al-alloys and four Ti-compressor disk alloys show that ΔK_T exists for all the alloys investigated. The effect of temperature on ΔK_T was investigated on one Ti 6Al 4V- and one Ti 8Al 1V 1Mo disk material at room temperature (RT) and 260°C and at RT, 260°C and 360°C, respectively. No temperature effect on ΔK_T was found for the temperature range investigated.

Keywords: fatigue crack propagation, threshold, non-propagation condition, material property

Nomenclature

FCP	Fatigue crack propagation
K_{min}, K_{max}	Minimum and maximum stress intensity factor of a cycle
$\Delta K = K_{max} - K_{min}$	Stress intensity range
$R = K_{min} / K_{max}$	Stress- or stress intensity factor ratio
ΔK_{th}	Fatigue crack - non-propagation condition
ΔK_T	FCP-threshold, material property, maximum ΔK causing no continuous FCP under arbitrary cyclic loading
K^{\wedge}	Partitioning stress intensity factor dividing ΔK in an

¹ Senior Scientist, Institute for Materials Research, DLR - German Aerospace Research Center, D-51170 Cologne, Germany

ΔK_{eff}	effective and a non-effective part
da/dN	Effective part of ΔK
LT, TL, CR, RC	FCP-rate
	Crack orientation as defined in ASTM E 399-97, Standard Test Method for Plane-Strain Fracture Toughness of Metallic Materials, Figs. 1 through 3

Introduction

It is known from experience that FCP-rates decrease with decreasing cyclic loading amplitudes ΔK in such a way that FCP-rates asymptotically approach zero as ΔK approaches a certain limit value. This limit value ΔK depends on the subject material. In other words, there is a stress intensity range for a given material below which cyclic loading does not propagate a crack. This is of eminent technological importance for structural design as well as for the correct understanding and description of the FCP-process.

For practical use we would like to have something like the 'fatigue strength' in Wöhler-type fatigue or preferably, a material property similar to K_{IC} . A material property 'FCP-threshold' would mean that for a given material this FCP-threshold is a single-valued property, such that any ΔK equal or smaller than this material property 'threshold' would not produce FCP under any circumstances. Which kind of threshold exists under cyclic loading conditions must be shown by experimental investigations. To precisely define the two possibly usable parameters in fracture mechanical terms, the following definitions are made:

- 1) any 'non-propagation condition' is denoted as ΔK_{th}
(comparable to the fatigue strength),
- 2) the material property 'FCP-threshold' is denoted as ΔK_T
(comparable to the yield strength $R_{P 0.2}$ or K_{IC}).

The existence of a material property 'FCP-threshold' ΔK_T had been shown previously by the author [1]. ΔK_T is independent of the R-ratio, K_{max} and load history effects.

The Fracture Mechanics Concept of a FCP-Threshold

When we consider the fracture mechanics description of FCP, then we are dealing with a cycle-by-cycle correspondence between FCP-rates and the cyclic loading conditions ΔK . Beyond a cycle-by-cycle correspondence between da/dN and ΔK , the fracture mechanics methodology as presently in use is not valid. For the threshold this can only imply that a threshold corresponds to conditions that mark the lower end of this cycle by cycle correspondence. The physical limit for a cycle-by-cycle correspondence is the system of Burger's vectors of the respective metallic material, i.e., is in the range between 10^{-7} to 5×10^{-7} mm/cycle. Because of our technical limitation to measure such small FCP-rates, the lower limit for cycle-by-cycle FCP is set at 10^{-7} mm/cycle in [2, ASTM E 647]. From a

fracture mechanics stand-point, zero FCP-rates corresponds to growth rates $< 10^{-7}$ mm/cycle. More arguments for setting the lower limit of cycle-by-cycle FCP at 10^{-7} mm/cycle are found in [1].

A further question relates to the metallurgical meaning of a material property 'FCP-threshold'. FCP is a damaging mechanism to the material due to cyclic loading conditions. If no damage occurs under cyclic loading condition, i.e., $\Delta K \leq \Delta K_T$, then the dislocation movement in the near-region of the crack front has to be purely elastic. If dislocations could pass over obstacles under the influence of external loading conditions ΔK_T , then fatigue damage would accumulate in the crack front region and FCP would follow. The metallurgical interpretation of a 'FCP-threshold' ΔK_T is graphically shown in Fig. 1 as the 2-dimensional yield surface (plane strain) for the near-region of the crack front. ΔK_T ($\Delta K_T = K_{I1} - K_{I2}$) which can be experimentally measured corresponds to the changing external loading conditions ($K_{I1} \geq K_{I1} \geq K_{I2}$) which result in the near-region of the crack front in stress- ($\Delta\sigma_{ii}$) and strain excursions ($\Delta\varepsilon_{ii}$) between the tensile- and the compression yield surface.

In previous publications, it was pointed out that the practical use of 'non-propagation conditions' ΔK_{th} in the design of structural parts is very limited. Only in special cases can a certain benefit be obtained by consideration of ΔK_{th} in the design process. Yet, for the ΔK_{eff} concept a material property 'FCP-threshold' is necessary merely from a formal, mathematical view-point. In the correlation $da/dN = \text{function of } \Delta K_{eff}$, the condition $da/dN = \text{zero}$ requires ΔK_{eff} to be zero simultaneously (remember: in the fracture mechanics concept, $da/dN = \text{zero}$ is identical to 10^{-7} mm/cycle growth rate). In order to transfer ΔK to ΔK_{eff}

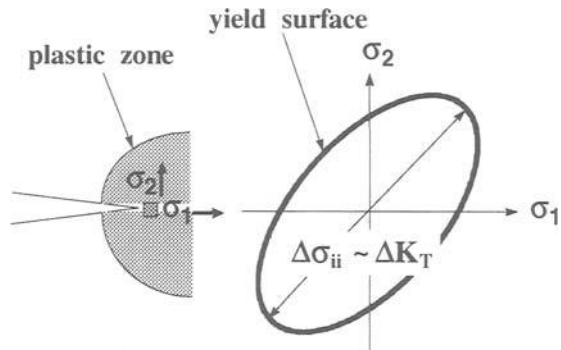


Fig. 1-Graphical Definition of a FCP- threshold.

a partitioning point is required. To prevent any discussion about the physical meaning and the measurement of this partitioning point, a partitioning point is postulated and here denoted as K^{\wedge} , but no further definitions or descriptions are imposed² [3] [4]. For the sake simplicity, assume a constant R test in accordance with ASTM E 647. Then, K^{\wedge} must be a continuous function of (K_{max} and K_{min}), i.e., $K_{max} > K^{\wedge} > K_{min}$. It follows that always

² For the arguments leading to Eq. (2b), the existence of a partitioning point for ΔK and acceptance ΔK_{eff} as driving force for FCP is required. The physical cause for the partitioning point (closure versus hydro-static stress) is unimportant for ΔK_T being constant.

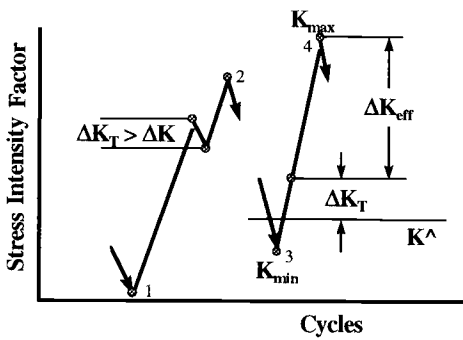
$$\Delta K_{eff} = K_{max} - K^{\wedge} \neq 0 \tag{1}$$

Equation (1) contradicts the requirement “ $\Delta K_{eff} = \text{zero when } da/dN = \text{zero}$ ”. The following definition of ΔK_{eff} is the simplest functional form to get Eq. (1) in agreement with this requirement (and with experimental facts):

$$\Delta K_{eff} = (K_{max} - K^{\wedge}) - \Delta K_x \tag{2a}$$

For Eq. (2a) to be correct and meaningful requires that ΔK_x being of constant value, independent of the particular cyclic loading condition in question. It is easy to guess that ΔK_x is actually the material property ‘FCP-threshold’ ΔK_T . Therefore, Eq. (2a) has to be written as:

$$\Delta K_{eff} = (K_{max} - K^{\wedge}) - \Delta K_T \tag{2b}$$



$K^{\wedge} = \text{partitioning point of } \Delta K$

Fig. 2-Graphical Description of the Relevance of the 'FCP-threshold' for FCP.

Equation (2b) shows the importance of the material property ‘FCP-threshold’ in the fracture mechanics methodology of FCP prediction. This is graphically illustrated in Fig. 2. Consider the stress intensity factor excursion from point ‘1’ to point ‘2’; this excursion has to be considered as one cycle, since the unloading corresponds to a $\Delta K < \Delta K_T$ and is - per definition given in Fig. 1 - merely elastic. The cycle, i.e., the stress intensity factor excursion from point ‘3’ to ‘4’, illustrates Eq. (2b) graphically. Every stress intensity factor excursion has to surpass K^{\wedge} by ΔK_T before FCP can commence.

Test Methods for the Experimental Determination of the ‘FCP-Threshold’

The most commonly used test methods for the determination of a ‘FCP-threshold’ are shown in Fig. 3, namely the R-constant method as specified in ASTM E 647 and the K_{max} -constant method. In the present investigation, the FCP-rates as well as the threshold had been determined for a crack growth increment of 0.1 mm. For each of these increments Δa , the ΔK was reduced by 6%. Details on the experimental procedures can be found in Refs. [1], [5], [6], [7]. The K_{max} -constant test method was originally reported by Davenport and Brook [8] and later Bailon et al. [9], Marci [10] and Hertzberg et al. [11].

Some remarks related to the crack length measurements should be of general interest. Microscopically, the crack front is never absolutely straight and the crack is not absolutely flat and FCP occurs by a system of Burger’s vectors. At growth rates of 10^{-7} to 5×10^{-7}

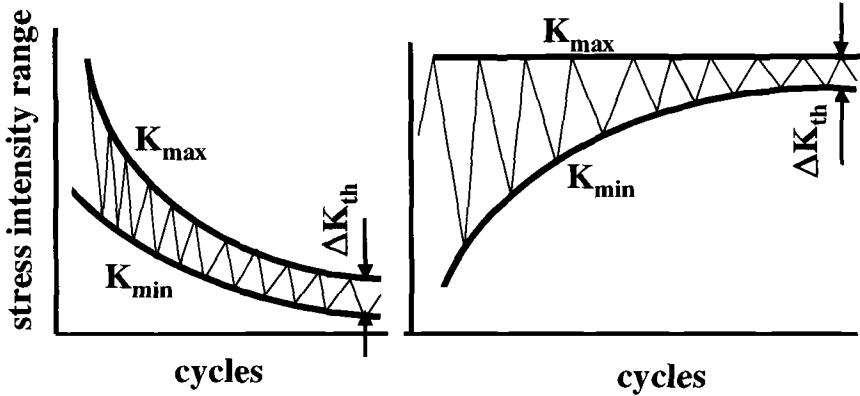


Fig. 3 R - Constant Test Method, (ASTM E 647).

K_{max} - constant Test Method

mm/cycle the conditions of non-propagation by a cycle-by cycle process might be attained microscopically along parts of the crack front. A stationary non-propagation condition along the total crack front is not achieved under such conditions. Yet, for a fatigue crack to achieve equilibrium along its crack front, the crack has to grow microscopically in a discontinuous manner to straighten the crack front and to make the fracture surfaces more flat. Such are the conditions when a fatigue crack propagates with FCP-rates in the range of 10^{-7} and 5×10^{-7} mm/cycle. In contrast to the microscopic conditions of the crack, the crack length, and therewith the growth rates, are measured macroscopically by electrical potential drop methods. Our experience shows that the DC potential drop method we use in our experiments measures a "quasi" continuous FCP down to approximately 8×10^{-8} mm/cycle FCP-rate. Below these FCP-rates, even the potential drop method clearly measures discontinuous crack propagation.

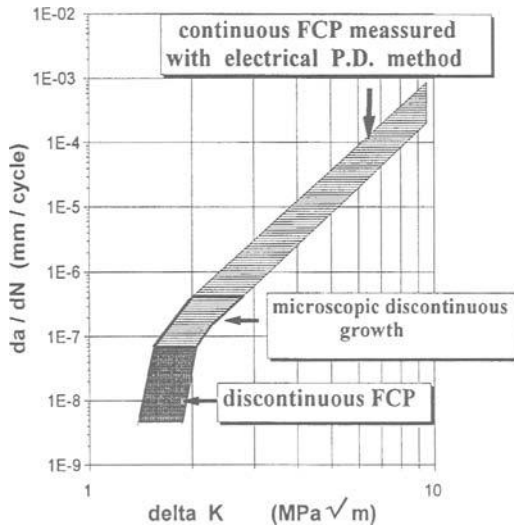


Fig. 4 Fatigue Crack Propagation Behavior (Schematically).

Below these FCP-rates, even the potential drop method clearly measures discontinuous crack propagation.

Materials Investigated

The 'non-propagation conditions' (ΔK_{th}) and the material property 'FCP-threshold' (ΔK_T) were determined on aluminum - and titanium alloys. All aluminum alloys were plate materials of 10 mm thickness from which C(T) specimens with $B = 10$ mm and $W = 50$ mm were fabricated. The following Al-alloys were investigated at room temperature, laboratory air environment and with a test frequency of 50 Hz :

2219-T851, 2024-T351, 6061-T651, 6082-T651, 7075-T7351 and 7475-T7351.

The C(T) specimens of 2219-T851 were side-grooved in order to keep the FCP in the desired direction. The effective thickness of the specimens was close to 8.5 mm.

Three titanium alloys investigated consisted of 'end of life' compressor disks of different stages of the compressor and different air craft engines. Two disks were fabricated from the alloy Ti 6Al 4V and one disk from Ti 8Al 1V 1Mo. The effect of temperature on ΔK_T and ΔK_{th} were determined on one Ti 6Al 4V - and one Ti 8Al 1V 1Mo disk by comparison of the results obtained at room temperature, 533K and 633K. The results from a previous investigation on IMI 834 turbine disk material are included [12]. Tests were run on C(T) specimens with a test frequency of 50 Hz. Dimension of the specimens and crack orientations are given with the respective results. On all materials investigated, ΔK_{th} and ΔK_T were determined by the R-constant as well as K_{max} -constant test method.

Results and Discussion

Non-propagation Conditions ΔK_{th} and FCP-threshold ΔK_T

Figure 5 shows the results obtained from the compressor disk of Ti 6Al 4V. Indiscriminately, all conditions with 9×10^{-8} mm/cycle $< da/dN \leq 1.1 \times 10^{-7}$ mm/cycle are considered non-propagation conditions ΔK_{th} , at first. The right side of Fig. 5 shows the ΔK_{th} values plotted

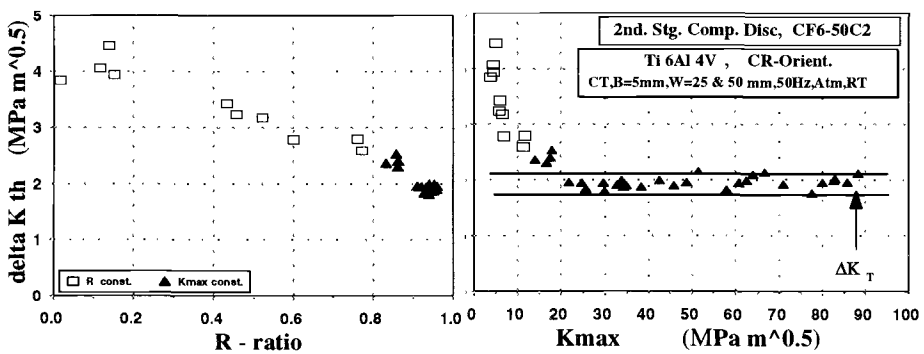


Fig. 5-Non-propagation Conditions and Material Property 'FCP-threshold' for "End of Life" Ti 6Al 4V Compressor Disk at Room Temperature.

versus the respective K_{\max} , whilst in the left side ΔK_{th} is plotted versus the respective R-ratio. The word 'respective' refers to ΔK_{th} which is clearly defined by any two of the parameters: R, K_{\max} , K_{\min} and ΔK . It can be seen in Fig. 5 that each of the figures emphasizes a different aspect of the ΔK_{th} . The right side of Fig. 5 shows the dominating effect of non-propagation conditions which are not any more influenced by the R-ratio or K_{\max} . From $K_{\max} = 20 \text{ MPa } \sqrt{\text{m}}$ to nearly $K_{\max} = 90 \text{ MPa } \sqrt{\text{m}}$, a constant ΔK_{th} between 1.7 to 2.1 $\text{MPa } \sqrt{\text{m}}$ is measured. The scatter of $\pm 0.2 \text{ MPa } \sqrt{\text{m}}$ is considered by the author the limit of measurement capability of present day servo-hydraulic testing equipment. Similar scatter bands were obtained in [13]. Here we have - in the limits of measurement capabilities - a constant value. Only because the data in this large K_{\max} range are constant - not influenced by K_{\max} or the R-ratio - allows to define them as material property ' ΔK_T '. It has to be realized that ΔK_T can not be measured 'a priori'. ΔK_T is determined based on the property of the measured ΔK_{th} values.

There is a task left which can not be fulfilled by the author or any other individual scientist, namely to define exactly what a material property 'FCP-threshold' ΔK_T should be. As possibilities there are:

1. the average value of all ΔK_{th} values falling in the scatter band between 1.7 to 2.1 $\text{MPa } \sqrt{\text{m}}$ (approximately $\Delta K_T = 1.9 \text{ MPa } \sqrt{\text{m}}$),
2. the lower bound value of the scatter band (approximately $\Delta K_T = 1.7 \text{ MPa } \sqrt{\text{m}}$),
3. define a value statistically, such that 90 % of the data in the scatter band lie above the defined value,
4. how many ΔK_{th} values and under what conditions must be determined such that the material property 'FCP-threshold' ΔK_T can be extracted.

The scientific community, particularly the designers of damage tolerant structures, have to decide on the exact definition of the material property 'FCP-threshold' ΔK_T .

In the right side of Fig. 5, no such definition is made. The author simply indicates the data band by two solid lines where the measured values of the material property 'FCP-threshold' ΔK_T are located. For the ΔK_{th} values in the K_{\max} -range between $K_{\max} = 4.4 \text{ MPa } \sqrt{\text{m}}$ and $K_{\max} = 20 \text{ MPa } \sqrt{\text{m}}$, the material property 'FCP-threshold' ΔK_T must exist, too (based on the definition given in Fig. 1). But in this K_{\max} -range, neither the K_{\max} -constant- nor the R-constant test method is able to measure ΔK_T . Only the 'jump-in test method' [4] could measure the ΔK_T values in this K_{\max} -range. The left side of Fig. 5 emphasizes the effect of closure (wedging action to separate the fracture surfaces) and/or the effect of the partitioning point (dividing ΔK in an effective part) on the ΔK_{th} values measured. No conclusion in respect to a material property 'FCP-threshold' can be obtained from such a figure, i.e., from a ΔK_{th} - R plot. The K_{\max} -range in which ΔK_T can not be measured by either of the two test methods in Fig. 3 varies from approximately 2 to 6 $\text{MPa } \sqrt{\text{m}}$ (Fig. 6) and 3 to 20 $\text{MPa } \sqrt{\text{m}}$ (Fig. 5) depending on the particular material. The K_{\max} ranges indicated comprise the R-ratios between $0 < R < 0.8$ and therewith the K_{\max} range in which closure has the most pronounced effect on the FCP-behavior. The consequence for the experimental determination of ΔK_{th} is that all metallurgical features affecting closure influence the ΔK_{th} values for $0 < R < 0.4$ strongly. It is therefore a matter of number of tests how the trend of data looks like, compare Figs. 6 and 7.

A qualitative definition of the non-propagation conditions and the material property 'FCP-threshold' should be given here. It should be realized that for any given K_{\max} -value,

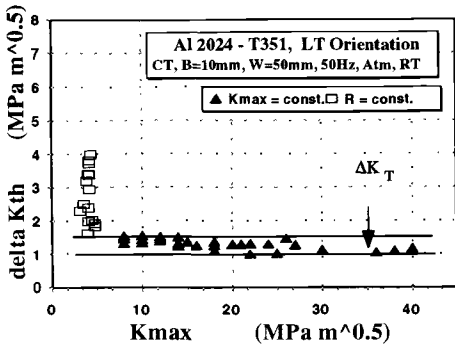


Fig. 6-Non-propagation Conditions and Material Property 'FCP-threshold' for Al 2024 - T351 Plotted Versus K_{max} .

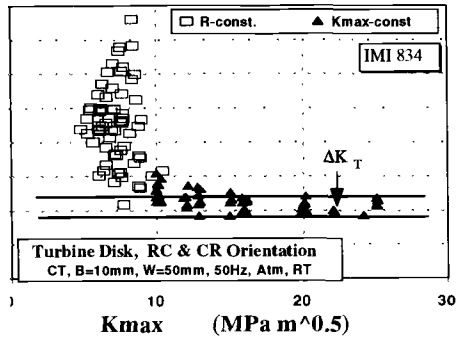


Fig. 7-Non-propagation Conditions and Material Property 'FCP-threshold' for IMI 834 Plotted Versus K_{max} .

any $\Delta K < \Delta K_{th}$ is a non-propagation condition, too. Therefore, ΔK_{th} is the upper bound value of all such ΔK for a given K_{max} , i.e., ΔK_{th} is the largest ΔK value for a given K_{max} condition that does not produce FCP. In line with this definition of ΔK_{th} , the material property 'FCP-threshold' ΔK_T is defined as the largest stress intensity factor excursion ΔK that does not produce FCP under any cyclic loading condition.

The Range of Measurement for ΔK_{th}

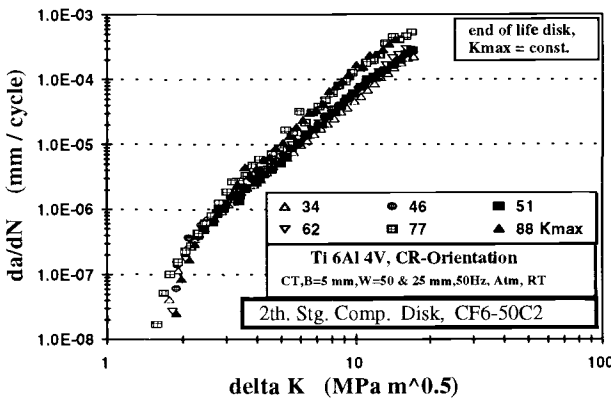


Fig. 8- da/dN Versus Delta K from K_{max} Constant Test for the K_{max} -range up to Instant Failure.

As a general rule, one wishes to measure ΔK_{th} and determine ΔK_T in the stress intensity range from 'zero' to the point of fracture of the respective material. Since this is not possible in all cases, the following clarifications are necessary. The lowest point of measurement corresponds to ΔK_{th} at $R = 0$ and the corresponding K_{max} ($\Delta K_{th} = K_{max} - 0$), let us say $K_{max, th}$. The upper end for the measurements of ΔK_{th}

can be the point of specimen fracture K_c , if no subcritical crack growth under static load or no abnormal FCP occurs. This is the case for the Ti 6Al 4V disk material from which the ΔK_{th} values shown in Fig. 5 were obtained. In Fig. 8, the da/dN versus ΔK curves

obtained with the K_{max} -constant method for this disk material are shown. The ΔK_{th} data in Fig. 5 comprise the data points corresponding to FCP-rates of 10^{-7} mm/cycle of each of the da/dN versus ΔK curves shown in Fig. 8. The essence of Fig. 8 is that over the entire K_{max} -range up to specimen fracture (practically) identical da/dN versus ΔK curves are obtained. Consequently, the material property 'FCP-threshold' is identical, too.

Now, compare Fig. 8 with Fig. 9. Both figures show da/dN versus ΔK curves obtained with the K_{max} -constant method.

Figure 9 shows the da/dN versus ΔK curves for the Ti-disk alloy IMI 834. This material and other Ti-alloys [13] [14] show an abnormal FCP-behavior when K_{max} reaches a certain (high) limiting value. For materials exhibiting such "abnormal FCP behavior", the upper end of the measuring range for ΔK_{th} is the point where "abnormal FCP" starts. In case of IMI 834 in Fig. 9, the limiting K_{max} value is 27 MPa \sqrt{m} (see Ref. [12]). The causes for this abnormal FCP-behavior in Ti-alloys are presently unknown. This abnormal FCP-behavior manifests itself such that in the range from 27 to 29 MPa \sqrt{m} the ΔK_{th} ($da/dN = 10^{-7}$ mm/cycle) becomes smaller than the ΔK_T measured at lower K_{max} values, and that the more, the more K_{max} exceeds 27 MPa \sqrt{m} . For K_{max} values of 29 MPa \sqrt{m} and higher, the FCP-rates initially decrease with decreasing ΔK . But, upon reaching FCP-rates in the range of 10^{-6} mm/cycle, the FCP-rates stay either constant or increase with decreasing ΔK . Presently, this abnormal FCP-behavior has been observed only on Ti-alloys.

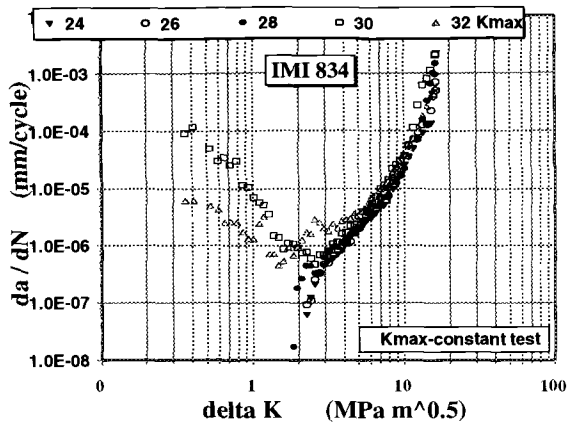


Fig. 9- da/dN Versus Delta K Curves Obtained with the K_{max} -constant Test Method over the K_{max} Range up to and Including Abnormal FCP Behavior.

Comparison of Results from the R-constant- and K_{max} -constant Test Methods

There exists a question concerning the equivalence of results obtained by the R-constant- and the K_{max} -constant test methods. Independent of the practical usage of each method, the question is: are the results obtained identical? In Fig. 10, the R-constant test method was applied up to $R = 0.92$. Thus, the results from both test methods can be compared with each other over most of the K_{max} range (right side of Fig. 10). As can be seen in this figure, both test methods deliver equivalent results.

The non-propagation condition ΔK_{th} is determined as the point at which in a certain Δa (chosen by the investigator) a FCP-rate $da/dN = 10^{-7}$ mm/cycle is measured. It is the general practice (and a necessity for the ΔK_{th} determination) to use several steps of decreasing ΔK and decreasing da/dN , the end-point of this series of steps is than the ΔK_{th} with $da/dN =$

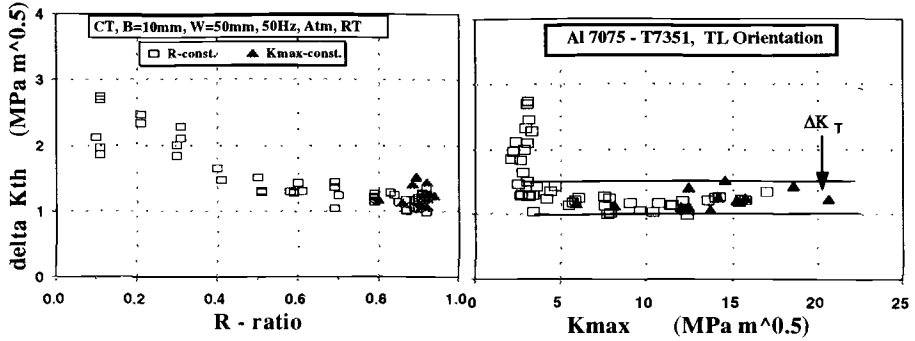


Fig. 10-Non-propagation Conditions and Material Property 'FCP-threshold' Obtained on Al-7075-T7351, left: Plotted Versus R, right: Plotted Versus Kmax.

10^{-7} mm/cycle. Because of this practice, the K_{max} -constant test method can not be used for the lowest part of the total K_{max} range, while the R-constant test method can not be used for the highest part of the total K_{max} range.

Results obtained for Al-Alloys at Room Temperature

The ΔK_T values determined for the Al-alloys are in the range, for:

- Al 2024-T351: (Fig. 6) --- $1.0 \text{ MPa}\sqrt{\text{m}} \leq \Delta K_T \leq 1.5 \text{ MPa}\sqrt{\text{m}}$
- Al 2219-T851: (Fig. 11) --- $1.15 \text{ MPa}\sqrt{\text{m}} \leq \Delta K_T \leq 1.4 \text{ MPa}\sqrt{\text{m}}$
- Al 6061-T651: (Fig. 11) --- $1 \text{ MPa}\sqrt{\text{m}} \leq \Delta K_T \leq 1.25 \text{ MPa}\sqrt{\text{m}}$
- Al 6082-T651: (Fig. 12) --- $0.9 \text{ MPa}\sqrt{\text{m}} \leq \Delta K_T \leq 1.15 \text{ MPa}\sqrt{\text{m}}$

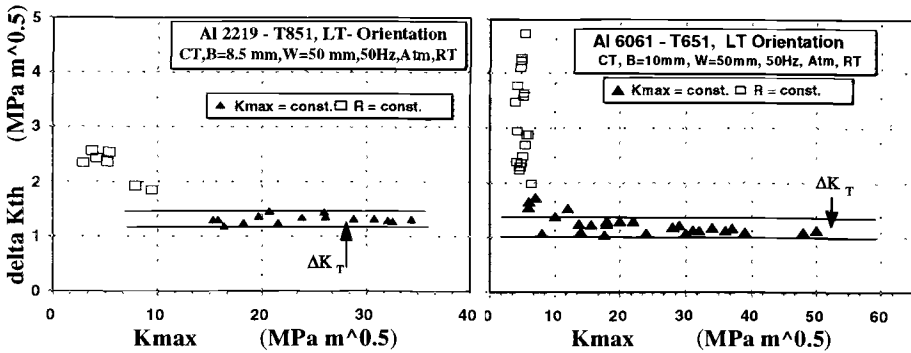


Fig. 11-Non-propagation Conditions and Material Property 'FCP-threshold' Obtained on Al 2219-T851 and Al 6061-T651, Plotted Versus Kmax.

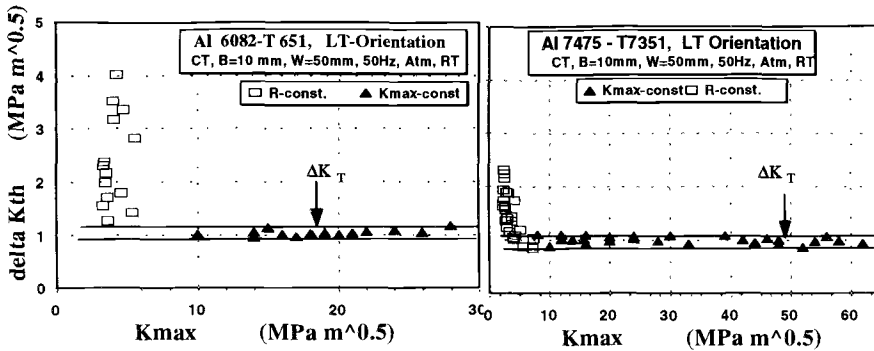


Fig. 12-Non-propagation Conditions and Material Property 'FCP-threshold'. Al 6082-T651 and Al 7475-T7351, Plotted Versus K_{max}.

- Al 7075-T7351: (Fig. 10) --- $1.0 \text{ MPa}\sqrt{\text{m}} \leq \Delta K_T \leq 1.5 \text{ MPa}\sqrt{\text{m}}$
- Al 7475-T7351: (Fig. 12) --- $0.85 \text{ MPa}\sqrt{\text{m}} \leq \Delta K_T \leq 1.1 \text{ MPa}\sqrt{\text{m}}$.

The Al- C(T) specimens were made from large plates of 10 mm thickness. The C(T) specimens of the 7475-T7351 were taken out of the plate at one location. For the other alloys, the location at which the specimens were taken out of the plate could vary over the total of the respective plates. Actually, the C(T) specimens were fabricated out of broken M(T) specimens, which were supplied in several batches. But for one material they came all out of one plate. To what degree the different specimen locations in the plate could have influenced the scatter band of ΔK_T values, has not been investigated. The non-propagation conditions ΔK_{th} for low R-ratios are known to be affected by the metallurgical conditions in the surface region of the specimens. Numerous investigations concerned with the effect of metallurgical parameters on ΔK_{th} are limited to low R-ratios. In addition, the experimental techniques used are often not up to date. Therefore, little information is available in the scientific literature which allows judgment on the scatter band of ΔK_T as obtained in the present investigation. The experimental technique is of particular importance, if the - possibly minute - influence of metallurgical variables is to be systematically investigated. In the author's opinion, the ΔK_{th} and ΔK_T results obtained from Al-alloys can be generalized:

The lower bound value of the material property 'FCP-threshold' ΔK_T for Al-alloys is in the range of: $0.8 \text{ MPa}\sqrt{\text{m}} \leq \Delta K_T \leq 1.2 \text{ MPa}\sqrt{\text{m}}$. A scatter band $\pm 0.2 \text{ MPa}\sqrt{\text{m}}$ should be a realistic aim for the experimental determination of ΔK_{th} .

Results for Ti-Compressor Disk Materials at Room-Temperature and Higher Temperature

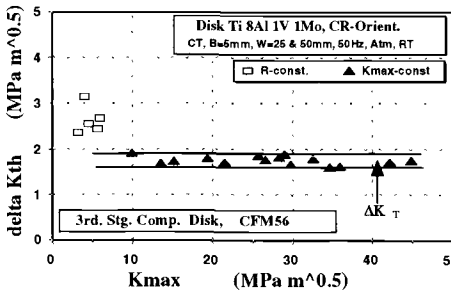


Fig. 13-Non-propagation Conditions and Material Property 'FCP-threshold'. Plotted Versus Kmax for (End of Life) Ti 8Al 1V 1Mo Compressor Disk.

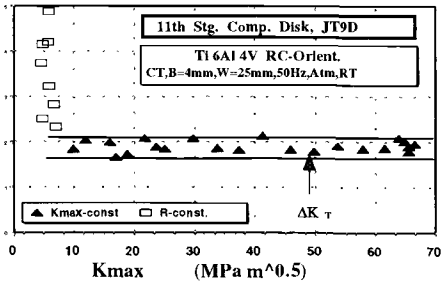


Fig. 14-Non-propagation Conditions and Material Property 'FCP-threshold'. Obtained at RT on a Ti 6Al 4V Disk and Plotted Versus Kmax.

At room temperature, the ΔK_T determination furnished the value-ranges for:
 'first' (end of life) Ti 6Al 4V disk (Fig. 5), $1.7 \text{ MPa}\sqrt{\text{m}} \leq \Delta K_T \leq 2.15 \text{ MPa}\sqrt{\text{m}}$,
 IMI 834 disk forging (Fig. 7), $1.8 \text{ MPa}\sqrt{\text{m}} \leq \Delta K_T \leq 2.5 \text{ MPa}\sqrt{\text{m}}$,
 (end of life) Ti 8Al 1V 1Mo disk (Fig. 13), $1.6 \text{ MPa}\sqrt{\text{m}} \leq \Delta K_T \leq 1.9 \text{ MPa}\sqrt{\text{m}}$,
 'second' (end of life) Ti 6Al 4V disk (Fig. 14), $1.65 \text{ MPa}\sqrt{\text{m}} \leq \Delta K_T \leq 2.1 \text{ MPa}\sqrt{\text{m}}$.

At 260°C, the ΔK_T determination (Fig. 15) supplied the following value-ranges for:
 'first' (End of Life) Ti 6Al 4V disk (left side), $1.9 \text{ MPa}\sqrt{\text{m}} \leq \Delta K_T \leq 2.5 \text{ MPa}\sqrt{\text{m}}$,
 and the (end of life) Ti 8Al 1V 1Mo (right side) $1.5 \text{ MPa}\sqrt{\text{m}} \leq \Delta K_T \leq 1.9 \text{ MPa}\sqrt{\text{m}}$.

At 360°C, the ΔK_T determination for a Ti 8Al 1V 1Mo compressor disk (Fig. 16) resulted in the value-range, $1.7 \text{ MPa}\sqrt{\text{m}} \leq \Delta K_T \leq 1.9 \text{ MPa}\sqrt{\text{m}}$.

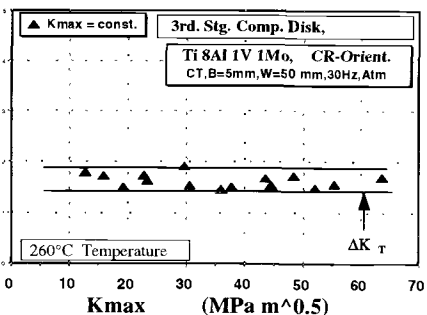
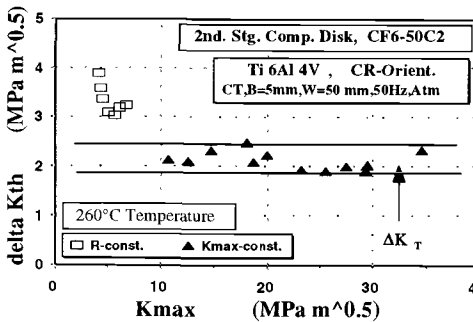


Fig. 15-Non-propagation Conditions and Material Property 'FCP-threshold' for (End of Life) Compressor Disks at 260°C, left: 'first' Ti 6Al 4V Disk and right: Ti 8Al 1V 1Mo Disk.

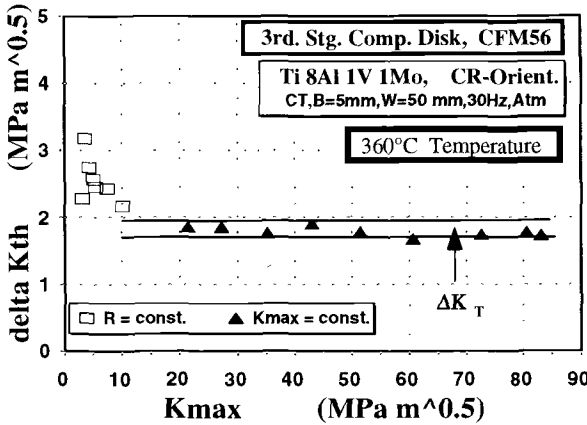


Fig. 16-Non-propagation Conditions and Material Property 'FCP-threshold' for a Ti 8Al 1V 1Mo Compressor Disk at 360°C.

The ΔK_{th} and ΔK_T for the (end of life) Ti 8Al 1V 1Mo compressor disk were obtained at RT, 260°C, and 360°C. On the 'first' (end of life) Ti 6Al 4V compressor disk the ΔK_{th} and ΔK_T values were obtained at room temperature and 260°C, too. A comparison of the ΔK_T values in the temperature ranges investigated for each of these Ti-disks, indicates no significant influence of temperature on the ΔK_T values. One should be aware that at slightly higher temperatures than these investigated in the present investigation, a temperature effect on ΔK_T might turn out to be significant.

Based on the limited number of test results ΔK_{th} with $R < 0.8$, no conclusion can be reached for the Ti – disk materials as to functional dependence of ΔK_{th} on the R-ratio. Again, a scatter band $\pm 0.2 \text{ MPa}\sqrt{\text{m}}$ should be a realistic aim for the experimental determinations of ΔK_T and ΔK_{th} with Ti-alloys.

Conclusions

1. All Al- and Ti-alloys investigated showed the existence of a material property 'FCP-threshold' ΔK_T . This agrees with previous results obtained by the author.
2. The material property 'FCP-threshold' ΔK_T values for the Al- and Ti-alloys were determined within a scatter band of approximately $\pm 0.2 \text{ MPa}\sqrt{\text{m}}$.
3. The average ΔK_T values at room temperature for the Al-alloys, 2024-T351, 2219-T851, 6061-T651, 6082-T651, 7075-T7351, and 7475-T7351 are roughly in between:

$$0.95 \text{ MPa}\sqrt{\text{m}} \leq \Delta K_T \leq 1.25 \text{ MPa}\sqrt{\text{m}}$$
4. At room temperature, the average ΔK_T values for the (end of life) Ti-compressor disks two different disks of Ti 6Al 4V and one of Ti 8Al 1V 1Mo] and for a Ti- disk forging [IMI 834] are roughly in between:

$$1.9 \text{ MPa}\sqrt{\text{m}} \leq \Delta K_T \leq 2.15 \text{ MPa}\sqrt{\text{m}}$$
5. At 260°C, the average ΔK_T values for the two (end of life) Ti-compressor disks [one disk of Ti 6Al 4V and one of Ti 8Al 1V 1Mo] are:

$$2.2 \text{ MPa}\sqrt{\text{m}} \text{ and } 1.7 \text{ MPa}\sqrt{\text{m}}, \text{ respectively.}$$

6. At 360°C, the average ΔK_T value for the end of life compressor disks of Ti 8Al 1V 1Mo is 1.8 MPa \sqrt{m} .
7. No influence of temperature in the range from room temperature to 260°C or 360°C for the Ti 6Al 4V or Ti 8Al 1V 1Mo, respectively, was found in this investigation. This conclusion must be considered preliminary.
8. The non-propagation conditions ΔK_{th} for R-ratios below $R = 0.8$ for the Al- and Ti-alloys investigated did not show a definite functional dependence on the respective R-ratio.

Acknowledgment

The author owes a special thanks to Mr. Uwe Fuchs for the careful and diligent execution of the tests reported on and to Lufthansa - Technik - Hamburg (WU 534) for supplying the spent Ti-compressor disks.

References

- [1] Marci, G., "Fatigue Crack Propagation Threshold: What Is It and How Is It Measured ?" *Journal of Testing and Evaluation*, JTEVA, Vol. 26, No. 3, May 1998, pp. 220-233.
- [2] ASTM E 647 - 95a, Standard Test Method for Measurement of Fatigue Crack Growth Rates, Annual Book of ASTM Standards, Section 3, Vol. 03.01.
- [3] Marci, G., "Determination of the Partitioning Point dividing ΔK into ΔK_{eff} ," *Engineering Fracture Mechanics*, Vol. 53, No. 1, 1996, pp. 23-36.
- [4] Lang, M. and Marci, G., "Reflecting on the Mechanical Driving Force of Fatigue Crack Propagation," *Fatigue and Fracture Mechanics: 29th Volume*, ASTM STP 1332, T. L. Panontin and S. D. Sheppard, Eds., American Society for Testing and Materials, 1998.
- [5] Marci, G., Castro, D.E., and Bachmann, V., "Fatigue Crack Propagation Threshold," *Journal of Testing and Evaluation*, JTEVA, Vol. 17, No. 1, 1989, pp. 28 -39.
- [6] Marci, G., "A Fatigue Crack Growth Threshold," *Engineering Fracture Mechanics*, Vol. 41, No. 3, 1992, pp. 367 - 385.
- [7] Marci, G., "Non-propagation Conditions (ΔK_{th}) and Fatigue Crack Propagation Threshold (ΔK_T)," *Fatigue and Fracture of Engineering Materials and Structures*, Vol. 17, No. 8, 1994, pp. 891 - 907.
- [8] Davenport, R. T. and Brook, R., "The Stress Intensity Range in Fatigue," *Fatigue and Fracture of Engineering Materials and Structures*, Vol. 1, 1979, pp. 151 - 158.
- [9] Bailon, J.-P., Dickson, J. I., Masounave, J., and Bathias, C., "Technical Note: Comments on the Threshold Stress Intensity Range in Fatigue," *Fatigue and Fracture of Engineering Materials and Structures*, Vol. 3, 1981, pp. 277 - 283.
- [10] Marci, G., "Effect of the active Plastic zone on Fatigue Crack Growth Rates,"

- Fracture Mechanics*, ASTM STP 677, C. W. Smith, Ed., American Society for Testing and Materials, 1979, pp. 168 - 186.
- [11] Hertzberg, R. W., Herman, W. A., and Ritchie, R. O., "Use of a Constant K_{max} Test Procedure to Predict Small Crack Growth Behavior in 2090-T8E41 Aluminum-Lithium Alloy," *Scripta Metallurgica*, Vol. 21, 1987, pp. 1541 - 1546.
- [12] Marci, G., "Comparison of fatigue crack propagation Thresholds of two Ti turbine-disk materials," *Fatigue*, Vol. 16, August 1994, pp. 409 - 412.
- [13] Marci, G., "Abnormal $da/dN - \Delta K$ curves: New failure mode with Ti - alloys," *Mat. -wiss. u. Werkstofftech.*, Vol. 28, 1997, pp. 51 - 58.
- [14] Lang, M., Hartman, G. A., and Larsen, J. M., "Investigation of an Abnormality in Fatigue Crack Growth Curves - the Marci Effect," *Scripta Metallurgica*, Vol. 38, No. 12, 1998, pp. 1803 - 1810.

Bernhard Tabernig,¹ Phil Powell,² and Reinhard Pippan¹

Resistance Curves for the Threshold of Fatigue Crack Propagation in Particle Reinforced Aluminium Alloys

Reference: Tabernig, B., Powell, P., and Pippan, R., “Resistance Curves for the Threshold of Fatigue Crack Propagation in Particle Reinforced Aluminum Alloys,” *Fatigue Crack Growth Thresholds, Endurance Limits, and Design, ASTM STP 1372*, J. C. Newman, Jr. and R. S. Piascik, Eds., American Society for Testing and Materials, West Conshohocken, PA, 2000.

Abstract: The threshold of stress intensity factor range ΔK_{th} increases with increasing crack extension until it reaches the constant value of long cracks. Such curves can be interpreted as resistance curves for the threshold of fatigue crack propagation.

In the paper a very simple method to measure such R-curves is presented and a concept based on the R-curve is used to describe the propagation/non-propagation behavior of physically small cracks. The application of the R-curve technique results in the Kitagawa diagram where one can estimate the fatigue limit of components containing “small” flaws. R-curve tests and standard fatigue experiments at different stress ratios were performed on a 20 vol% SiC particle reinforced 359 T6 cast aluminum alloy which contains naturally small flaws up to 400 μm . Application of the R-curve concept is demonstrated and the estimations are compared with experimental results of the fatigue tests. Good agreement between the predicted and measured failure behavior was found.

Keywords: fatigue threshold, resistance curve, physically small crack, fatigue limit prediction, Kitagawa diagram

Introduction

Modern defect tolerant design philosophy is based on the premise that all engineering structures are inherently flawed. Assuming that small-scale yielding prevails, the linear

¹Research assistant and senior scientist, respectively, Erich Schmid Institut für Materialwissenschaft der Österreichischen Akademie der Wissenschaften und Institut für Metallphysik der Montanuniversität Leoben, Jahnstr. 12, 8700 Leoben, Austria.

²Research scientist, Structural Materials Centre, Defence Evaluation and Research Agency, Farnborough, Hampshire, GU14 6TD, UK.

elastic fracture mechanics provide the parameter threshold of stress intensity factor range ΔK_{th} as a characteristic value to determine the condition for propagation/non-propagation of existing flaws. Fatigue cracks should not grow at stress intensity ranges smaller than ΔK_{th} . In fact this is only correct for long cracks. Many works show that the similitude concept of fracture mechanics, i.e. that cracks with the same crack tip condition (characterised by ΔK) will propagate at the same rate, does not hold for small cracks. They even grow at values of ΔK below that of the threshold value determined in a standard crack growth test which is called the threshold of long cracks. Hence a fatigue limit estimation of a component which contains a small flaw based on the long crack threshold is nonconservative. Furthermore the minimum necessary crack length for application of the long crack behaviour is usually unknown. Therefore a damage tolerant concept based on ΔK_{th} is not commonly used in engineering fatigue design. Different authors [1-3] have proposed to apply a R-curve technique to fatigue to overcome this problem. The purpose of this paper is to present a simple technique to measure resistance curves for fatigue, to describe results obtained on a 20 vol% SiC particle reinforced 359 T6 aluminum alloy and to compare failure prediction based on the R-curve method with experimental results of fatigue tests.

R-curve Method

The R-curve is defined as the plot of the resistance of a material to crack propagation versus crack extension. In this context the R – curve can be defined as the resistance of a material against fatigue crack propagation (characterised by ΔK_{th}) versus crack extension. Romaniv et al. [4], Tanaka et al. [2], Pippan et al. [5], Pineau [6] and others show that the threshold of stress intensity factor range increases with increasing crack length until it reaches a constant value at a certain extension of crack. This value is called the long crack threshold. Many authors [2,4-8] explain this increase of the threshold by an increase of the contribution of crack tip shielding, mostly caused by an increase of the crack closure stress intensity [9].

Till now there exists no standard technique to measure R-curves. Suresh [10], Pippan [11] and Novack and Marissen [12] proposed to measure the long crack threshold on specimens precracked in cyclic compression. In addition it was shown [3, 13] that this method also permits to determine the R-curve for ΔK_{th} . Figure 1 shows schematically the loading procedure of a R-curve test and the resulting crack extension vs. number of cycles.

The specimen is pre-cracked in cyclic compression. The crack emanates from the notch similar to the crack initiation in cyclic tension, but in cyclic compression the crack growth then decreases progressively until the crack stops propagating completely. In front of a pre-crack initiated in cyclic compression there is a small region with residual tensile stresses. The advantage of pre-cracking the specimen in cyclic compression is that the pre-crack is surely open when unloaded and consequently that the stress intensity where the crack closes is below zero at the beginning of the fatigue crack growth test. One can perform the threshold test for a constant load ratio by increasing the load amplitude in steps until the threshold value of the long crack is reached [3, 7, 10, 12, 13].

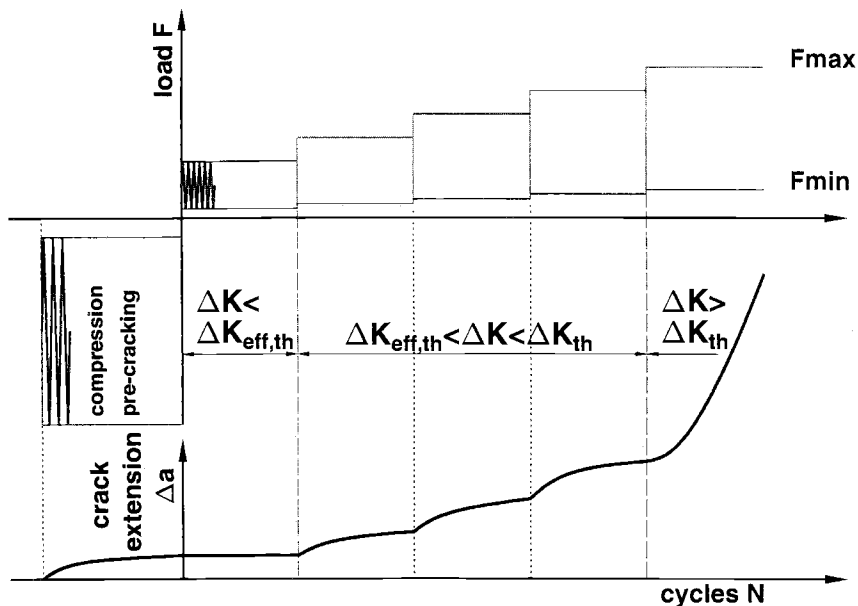


Figure 1- Schematic illustration of the loading procedure of a test to determine the R – curve for fatigue crack propagation threshold and the fatigue crack growth curve for a constant load ratio.

If the load amplitude corresponds to a ΔK which is smaller than the effective threshold $\Delta K_{eff,th}$ (the threshold of a crack without contact shielding), the crack will not grow. The first propagation is observed if ΔK is larger than $\Delta K_{eff,th}$. Therefore this technique allows one to determine an upper and a lower bound for $\Delta K_{eff,th}$. At the load steps where the amplitudes correspond to a ΔK which is larger than $\Delta K_{eff,th}$ and smaller than the long crack threshold, the crack starts to grow and stops at a certain extension. The decrease of the crack growth rate until arrest occurs is caused by the increase of crack closure or other shielding mechanisms. Finally there is a step where the crack does not stop. At this load amplitude the increase of the maximum stress intensity factor K_{max} by crack extension is larger than the increase of the crack closure stress intensity K_{cl} . From there on the test can be continued to measure the conventional da/dN versus ΔK diagram. The stress intensity factor ranges ΔK where the crack arrests for the last time and where the crack does not stop growing provide a upper and a lower bound for the long crack threshold of stress intensity range. If one plots the extension of the crack where it stops growing versus the corresponding ΔK , one obtains in addition the R -curve for the threshold of stress intensity factor range. Such an example performed at a load ratio $R = 0.6$ on a 20 vol% SiC particle reinforced 359 T6 aluminium alloy is shown in Figure 2.

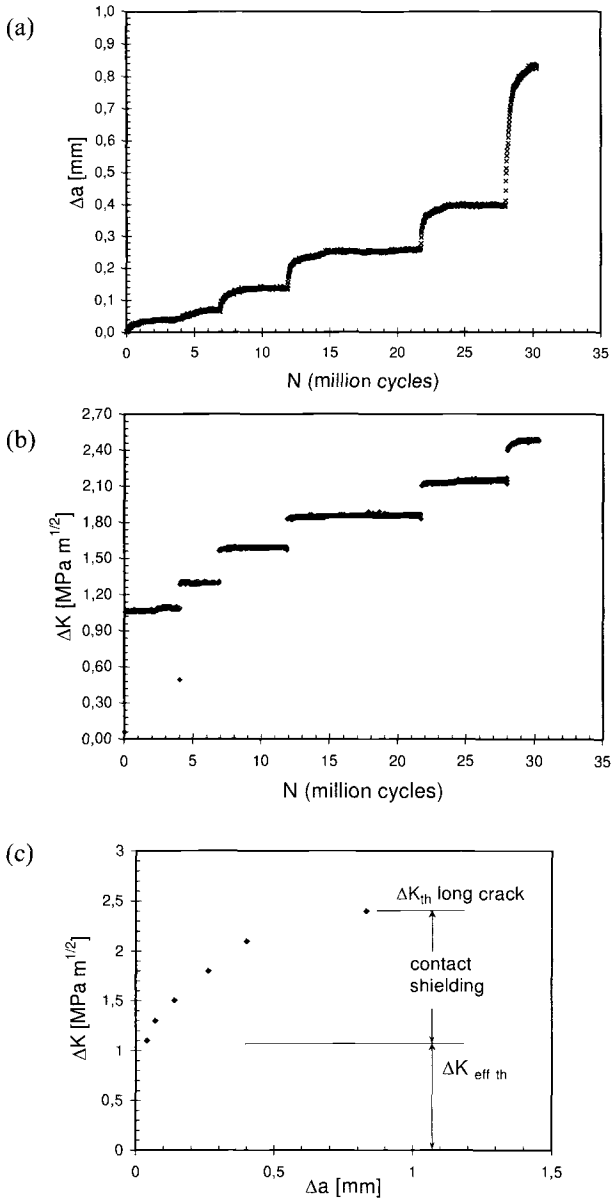


Figure 2 - Typical experimental result of the first steps of a rising load amplitude experiment in a 359 + 20% SiC (T6) alloy at a constant load ratio $R = 0.6$
 (a) change of crack extension,
 (b) change of stress intensity factor range,
 (c) R - curve for the threshold of fatigue propagation.

Experimental

The material examined in this study is a 20 vol% SiC particle reinforced 359 T6 cast aluminium alloy (Young's modulus 97 GPa and tensile strength 247 MPa). In microstructural investigations a large number of porosity was found. The mean size of the particles was about 7 μm .

Crack Growth Tests

Crack growth testing was carried out for three different load ratios (0.1, 0.6, -1) according the procedure described in Fig. 1. Two different types of test piece design have been used: a compact tension specimen (CT40: width $W = 40$ mm, thickness $B = 10$ mm, depth of the notch $a_N = 10$ mm) for $R > 0$ and a standard eight point single edge notched bend test specimen (SENB8: $W = 25$ mm, $B = 8$ mm, $a_N = 5$ mm) for $R = -1$. The notches for all specimens were machined by spark erosion. Furthermore a special razor blade cutting technique was performed in order to get extremely sharp notches (notch radii between 10 and 20 μm). The sharper the notch, the smaller the loads for prefatigue and the tensile residual stress field at the crack tip at the start of the crack growth test. The specimen were prefatigued in cyclic compression (load ratio $R = 20$) at a $\Delta K = 8 \text{ MPa m}^{1/2}$ to initiate a crack of about 50 μm length measured from the notch root. The experiments were performed on a electromechanic resonance machine at a cyclic frequency of about 100 Hz (only a few tests were done in a servohydraulic machine at 50 Hz). The tests were conducted in air at room temperature. During crack growth testing the crack length was monitored by DC – potential drop technique. The accuracy to measure a change in crack length was $\pm 5 \mu\text{m}$ for crack extensions of the first millimeter.

Fatigue Testing

Additionally fatigue testing on the same material was performed in accordance with ASTM Standard Practice for Conducting Force Controlled Constant Amplitude Axial Fatigue Tests of Metallic Materials (E 466-96) using Vibrophore resonant fatigue testing machines fitted with 20 kN load cells. The test frequency was nominally 100 Hz. Tests were carried out on plain test pieces ($K_t = 1.035$) at the two stress ratios $R = 0.1$ and $R = -1$ at RT. The test pieces had a round test section ($d = 3.99\text{mm}$). Tests were run to test piece fracture or to run-out at 10^7 cycles nominal. The S/N data exhibited much scatter which was attributed to the presence of large pores [14]. Therefore microscale examinations in the SEM of the fracture surfaces have been performed to reveal the effect of porosity on the fatigue properties and to determine the initial defect sizes. Some runners-out were also available for microscale examination. They were broken in a tensile test and their fracture surfaces were studied with specific reference to the presence of defects.

Results and Discussion

Resistance Curves

In the threshold test the load amplitude was increased in steps and the change of crack extension and stress intensity factor range was measured. Plotting the extension of the crack where it arrests versus the corresponding ΔK , the R-curve for fatigue propagation is obtained. Figures 3a, b, c show the R-curves for fatigue threshold of the investigated alloy for the three different load ratios $R = 0.1, 0.6$ and -1 .

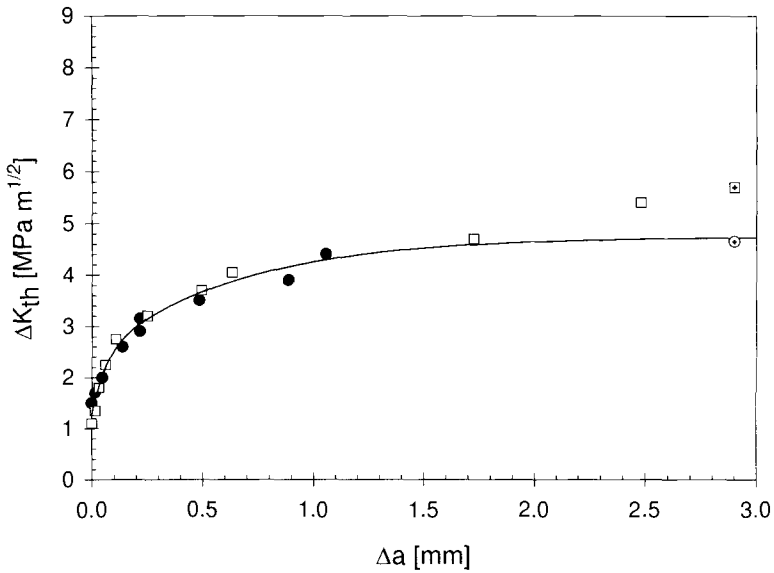


Figure 3a - R-curve for fatigue crack growth threshold of a 20% SiC particle reinforced 359 T6 aluminum alloy at the load ratio $R = 0.1$.

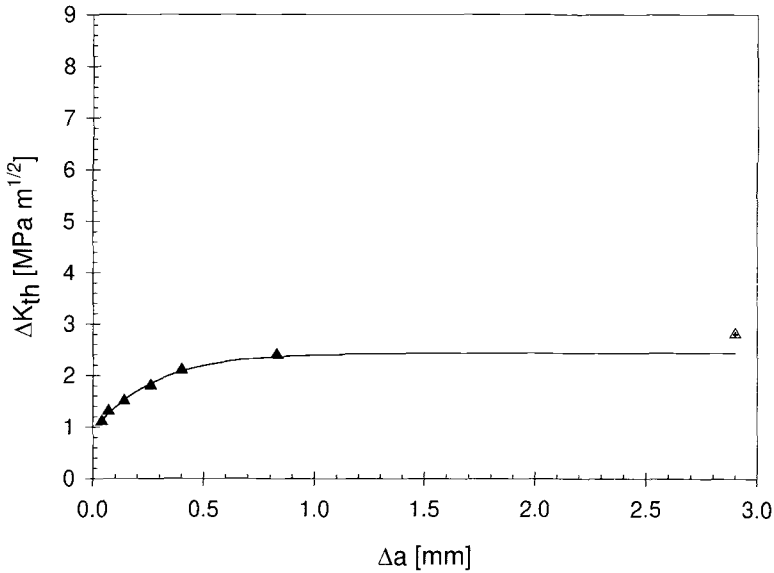


Figure 3b - *R-curve for fatigue crack growth threshold of a 20% SiC particle reinforced 359 T6 aluminum alloy at the load ratio $R = 0.6$.*

The open, black and gray symbols refer to different experiments where the crack stopped at certain extensions. The symbols with a x-hair are not data points of the R-curve, they only indicate the load level where the crack did not arrest (starting point of the measurement of the da/dN versus ΔK curve). They have also been used to fit the R-curve in a conservative way. Initially the crack grew at a load amplitude which corresponds to a ΔK of around $1.2 \text{ MPa } m^{1/2}$ irrespective of the different load ratios. Hence the effective threshold $\Delta K_{eff\ th}$ for this material lies between 1.1 and $1.3 \text{ MPa } m^{1/2}$. The thresholds increase with crack extension at all three load ratios, but by a different amount. It is obvious that the contribution of the effect of crack closure (crack tip shielding) is much higher at $R = -1$ and $R = 0.1$ than at $R = 0.6$. It should be pointed out that ΔK was determined by the difference of K_{max} and K_{min} (hence at the crack growth test at $R = -1$ also the compressive part was counted). The extension of the crack where the long crack threshold is reached is significantly larger at $R = 0.1$ than at $R = 0.6$ and $R = -1$. The long crack threshold for $R = 0.1$ is at $4.5 \text{ MPa } m^{1/2}$ and is reached at a crack extension of 2 mm . This is a surprising large value, but it should be noted that 80% of shielding contribution is built up within the first half millimeter of crack extension. The

threshold values for $R = 0.6$ ($2.4 \text{ MPa m}^{1/2}$) and for $R = -1$ ($8.1 \text{ MPa m}^{1/2}$) are constant for cracks extensions larger than 1 mm. The rough fracture surfaces of the tested specimens indicate that the increase of the threshold in the investigated alloy may mainly be caused by an increase of roughness induced crack closure.

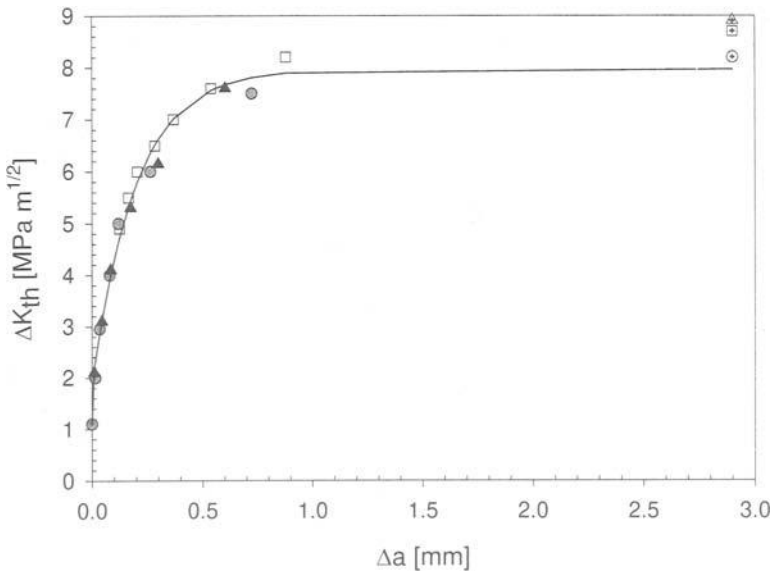


Figure 3c - *R*-curve for fatigue crack growth threshold of a 20% SiC particle reinforced 359 T6 aluminum alloy at the load ratio $R = -1$.

S/N Data and Defect Sizes

Standard fatigue experiments were carried out to measure the S/N curves of the 359 + 20% SiC aluminium alloy at the load ratios $R = 0.1$ and -1 . The S/N data [14], presented in Table 1, exhibited much scatter. While the specimen XA06410, for example, was a run – out, the test pieces XA06415 and XA06419 failed within 70 000 cycles, although they were tested at the same stress level and the same load ratio.

The SEM examinations of the fracture surface of the 359 MMC gave evidence of presence of large pores (up to 400 μm) in the area of fatigue origin. Most of the critical pores were located at or near the surface of the test pieces. The pores were characterized

as idealised elliptic flaws, shown in Figure 4 [15] and their defect sizes a_0 determined (see Table 1). The fatigue limit appears to be controlled by growth/non-growth of cracks initiated early at these pores.

Table 1 - S/N data and defect sizes a_0 in 359 T6 + 20% SiC for $R = -1$ and 0.1 .

	DERA specimen No	$\Delta\sigma$ [MPa]	Numbers of cycles	defect size [mm]	Status
R = -1	XA06410	144.9	10784000	0.075	Run – out
	XA06412	165.6	1472400	0.11	Failure
	XA06413	165.6	39907300	0.05	run – out
	XA06414	176.0	47300	0.07	Failure
	XA06415	144.9	69700	0.22	Failure
	XA06416	155.3	9700	0.4	Failure
	XA06417	134.6	2914000	0.25	Failure
	XA06419	144.9	<50000	0.24	Failure
R = 0.1	XA06397	102.5	197600	0.1	Failure
	XA06398	102.5	17400	0.18	Failure
	XA06401	83.8	10540300	not available	run – out
	XA06402	93.2	10851900	0.05	run – out
	XA06403	121.1	276300	0.04	Failure
	XA06404	121.1	88900	0.09	Failure
	XA06405	102.5	10882000	not available	run – out
	XA06406	139.7	97200	0.06	Failure
	XA06407	139.7	1283000	0.04	Failure

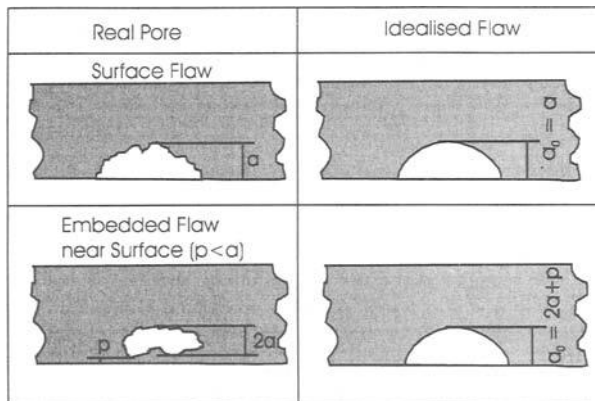


Figure 4 - Idealisation of real pore.

Application of the R-curve Concept

Using the example of the 359 MMC aluminium alloy the application of the R-curve concept is now demonstrated and the estimations are compared with the experimental results of fatigue tests.

One can draw the resistance-curves into a crack driving force diagram (ΔK versus a), see Figure 5. Assuming a surface defect and that the component width is much larger than the defect size, the crack driving force is given by $\Delta K = 1.12 \Delta\sigma (\pi a)^{1/2}$. The crack driving forces for different constant stress amplitudes are also drawn in the diagram. The difference between the origin of the R-curve and the origin of the driving force diagram is set equal to the initial defect size a_0 .

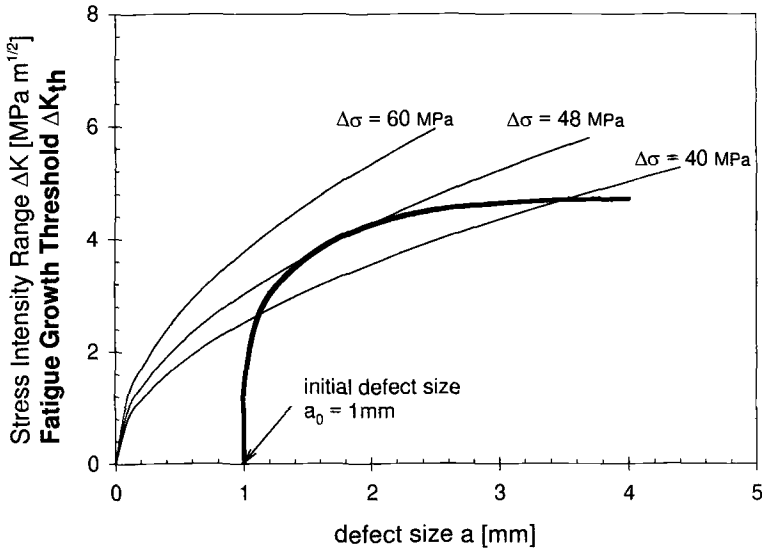


Figure 5 - Crack driving force diagram with the R-curve of 359 + 20% SiC for $R = 0.1$.

- At smaller stress amplitudes the crack may propagate at first but it should arrest after a certain extension which is determined by the intersection of the two curves.
- At larger load amplitudes the driving force is always larger than the resistance (threshold). Hence, such a component should fail.
- The ΔK vs. crack length curve which is tangential to the R-curve gives the fatigue limit for the given defect size.

If one assumes that the shape of the R-curve is independent of the initial crack length, one can shift the R-curve in the crack driving force diagram to different defect sizes in order to simulate the influence of defect size on the fatigue limit. Hence application of the R-curve results in the Kitagawa diagram which gives the fatigue limit of a material containing “small” flaws. Figures 6a and b show the Kitagawa – diagrams for the 359 + 20% SiC aluminum alloy for the load ratios $R = -1$ and 0.1 .

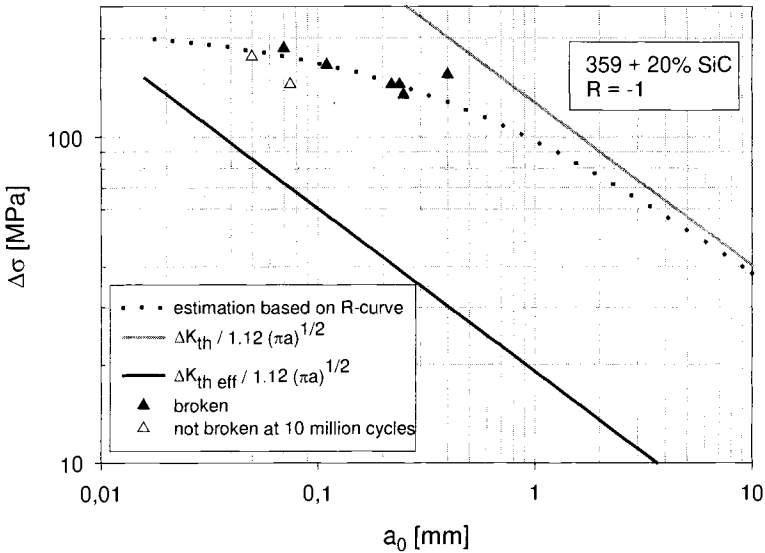


Fig. 6a - Kitagawa diagram (fatigue limit vs. defect size) for the 359 + 20% SiC aluminum alloy for load ratio $R = -1$.

The dotted line represents the estimation obtained by the application of the R-curve concept. The region below this line should be the safe regime where no failure occur. One can now draw the S/N data (white symbols for run – out, dark symbols for failure, gray symbols for specimens not available for determining defect size) in the Kitagawa diagrams, in order to compare these experimental results with the predictions based on the R-curve concept. It is evident that the experimental results are in good agreement with the estimations of the R-curve technique. Furthermore the strong influence of load ratio on the fatigue limit vs. initial crack size at $R = 0.1$ and $R = -1$ is obvious. In addition the limit curves of the effective threshold $\Delta K_{\text{eff th}}$ and the long crack threshold ΔK_{th} are plotted in the diagrams. While the effective threshold always gives a safe lower fatigue limit, the long crack threshold ΔK_{th} determines the fatigue limit of the material only in case of large defects.

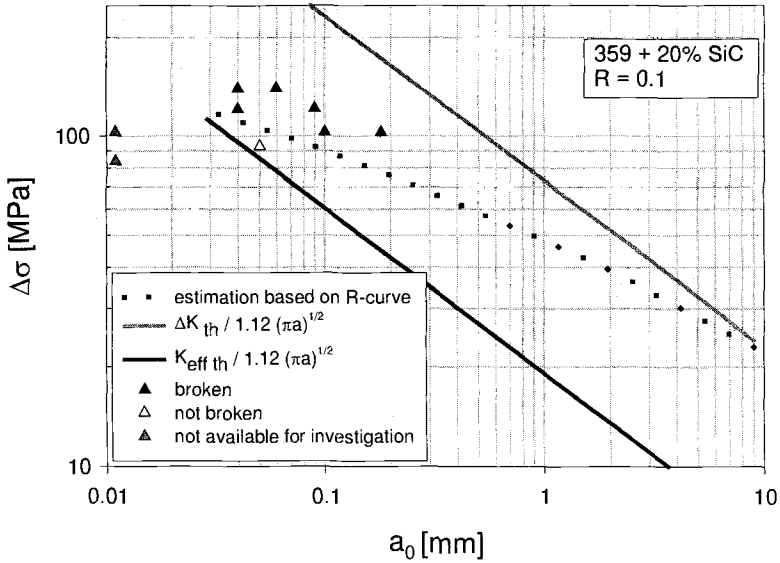


Figure 6b - Kitagawa diagram (fatigue limit vs. defect size) for the 359 + 20% SiC aluminum alloy for load ratio $R = 0.1$.

Conclusion

Resistance curves for the threshold of fatigue propagation should allow a more reliable application of ΔK_{th} values to engineering problems. A very simple technique to measure such R-curves is the step-wise increase of the load amplitude on specimens precracked in cyclic compression. The resulting R-curves give the effective threshold for crack propagation, the minimum crack extension where one expects long crack behaviour and the increase of shielding as a function of crack extension. Application of the R-curve leads to the Kitagawa diagram which can be used to estimate the fatigue limit as a function of defect size. It was shown that the load ratio has a strong influence on the shape of the R-curve and hence on the fatigue limit vs. initial crack size diagram. Good agreement was found between experimental results of fatigue tests and estimations based on the R-curve in the investigated case of a 20 vol% SiC particle reinforced aluminum alloy.

Acknowledgments

The authors thank all partners of the BRITE – EURAM project MISPOM (Aerospatale, Teksid, Defence Evaluation and Research Agency, Universitat Politècnica de Catalunya, Università di Ancona, Erich Schmid Institut, National University Galway) for collaboration. They are indebted to the European Community for financial support.

References

1. Pook, L.P., “The Role of Crack Growth in Metal Fatigue”, *The Metals Society London*, 1983, p. 101.
2. Tanaka, K., and Akinawa, Y., “Resistance-curve Method for Predicting Propagation Threshold of Short Fatigue Cracks at Notches”, *Engineering, Fracture Mechanics*, 30, 1988, pp. 863-876.
3. Pippan, R and Stüwe H. P., “Fatigue Crack Growth Behavior in Constant-Amplitude and Constant- ΔK Tests on Notched Specimens”, In: *ECF6*, H. C. Elst and A. Bakker (Eds), EMAS, Warley, UK, 1986, pp. 1269-1277.
4. Romaniv, O., Siminkovich, V.N. and Tkach, A.N., *Fatigue Thresholds*, J. Bäcklund, A. F. Blom and C.J. Beevers (Eds), EMAS, Warley, UK, 1981, pp. 588-594.
5. Pippan, R., Berger, M. and Stüwe, H. P., “The Influence of Crack Length on Fatigue Crack Growth in Deep Sharp Notches”, *Metallurgical Transactions*, 18a, 1987, pp. 429-435.
6. Pineau, A., In Proceedings: *Small Fatigue Cracks*, R. O. Ritchie and J. Lankford (Eds), AIME, 1986, pp. 191-212.
7. Suresh, S., *Fatigue of Materials*, Cambridge University Press, 1991.
8. McEvily, A. J. and Yang, Z., “The Growth of Short Fatigue Cracks under Compression and/or Tensile Cyclic Loading”, *Metallurgical Transactions*, 22A, 1991, pp. 1079-1082.
9. Ritchie, R. O., “Mechanisms of Fatigue Crack Propagation in Metals, Ceramics and Composites: Role of Crack Tip Shielding”, *Materials Science and Engineering*, 103, 1988, pp. 15-28.
10. Suresh, S., “Crack Initiation in Cyclic Compression and its Application”, *Engineering Fracture Mechanics*, 21, 1985, pp. 453-463.
11. Pippan, R., “The Growth of Short Cracks under Cyclic Compression”, *Fatigue Fracture Engineering Materials Structures*, 9, 1987, pp. 319-328.
12. Nowack, H. and Marissen, R., “Fatigue Crack Propagation of Short and Long Cracks”, In Proceedings: *Fatigue 87*, R. O. Ritchie and E. A. Stark (Eds), EMAS, Warley, UK, 1987, pp. 207-230.
13. Pippan, R., Plöchl, L., Klammer, F. and Stüwe H. P., “The Use of Fatigue Specimens Pre-cracked in Compression for Measuring Threshold Values and Crack Growth”, *Journal of Testing and Evaluation*, 22, 1994, pp. 98-103.
14. Powell, P., In working paper DERA/WP/2.3/2 in BRITE-EURAM project MISPOM (n° BE96-3168), 1998.
15. WES 2805, *Japan Welding Society standard*, 1980.

Stephen W. Smith¹ and Robert S. Piascik²

An Indirect Technique for Determining Closure-Free Fatigue Crack Growth Behavior

Reference: Smith, S. W. and Piascik, R. S., “An Indirect Technique for Determining Closure-Free Fatigue Crack Growth Behavior,” *Fatigue Crack Growth Thresholds, Endurance Limits, and Design, ASTM STP 1372*, J. C. Newman, Jr. and R. S. Piascik, Eds., American Society for Testing and Materials, West Conshohocken, PA, 2000.

Abstract: The effects of stress ratio (R) and maximum applied stress-intensity factor (K_{\max}) on fatigue crack growth rate (da/dN) have been investigated. Fatigue crack growth behavior was analyzed by plotting applied cyclic stress-intensity factor (ΔK) versus applied K_{\max} for an $\alpha+\beta$ titanium alloy (Ti 6-2-2-2-2) at several values of da/dN . This analysis revealed two distinct regions of fatigue crack growth behavior. At threshold da/dN ($\approx 10^{-10}$ m/cycle) and for $K_{\max} < 4.6$ MPa \sqrt{m} the threshold cyclic stress-intensity factor (ΔK_{th}) is greatly influenced by crack closure. For closure free fatigue crack growth ($K_{\max} > 4.6$ MPa \sqrt{m}), a subtle but distinct decrease in ΔK_{th} is observed with increasing K_{\max} . Plots of ΔK versus K_{\max} were also generated for AA 2024 test data produced in two different studies. These data also revealed two distinct regions of fatigue crack growth behavior consistent with the Ti 6-2-2-2-2 results. This methodology can be used to determine closure free fatigue crack growth and to monitor subtle changes in ΔK_{th} .

Keywords: fatigue crack growth, fatigue crack growth threshold, crack closure, K_{\max} effects, stress ratio effects

¹ Senior Engineer, Lockheed Martin Engineering & Sciences, Hampton, VA 23681, formerly Resident Research Associate, National Research Council, Hampton, VA 23681.

² Senior Scientist, Mechanics of Materials Branch, NASA-Langley Research Center, Hampton, VA 23681.

Introduction

Research has shown that stress ratio effects are dominated by fatigue crack closure, particularly in the near-threshold regime [1-5]. To determine values of cyclic stress-intensity factor (ΔK) corrected for closure (ΔK_{eff}), the crack opening stress-intensity (K_{op}) must be determined ($\Delta K_{\text{eff}} = K_{\text{max}} - K_{\text{op}}$) [2]. However, the experimental determination of an opening load is difficult and can result in a high degree of scatter for near-threshold fatigue crack growth. These difficulties are not surprising when one considers the available tools to determine opening loads. The most common measurement techniques rely on determining a deviation in a load-displacement trace [2, 6], where the displacement is measured using a remote strain gage or crack mouth opening gage. Typically, crack-tip displacements in the near-threshold regime are very small. Therefore, measurements with a far-field displacement gage may lack the required fidelity to accurately determine crack opening loads within the threshold regime. Other techniques require the measurement of surface displacements near a crack tip [7, 8]. However, these measurements may not accurately reflect the opening behavior along the entire crack front.

With the current limitations of crack closure measurements, it is desirable to develop indirect techniques to determine the effects of crack closure. Schmidt and Paris [3] were the first to analyze fatigue crack growth rate data by plotting ΔK_{th} versus R . They observed a distinct transition in the data which was attributed to the presence of crack closure. Later, Döker and Bachmann [4] modified this analysis by plotting data as ΔK_{th} versus K_{max} , to more accurately reflect trends in fatigue crack growth behavior. Analyses of this nature have attempted to determine intrinsic ΔK_{th} values by identifying data which are free of crack closure [3, 4, 9-11]. Within this paper, the area of focus is expanded to include the lower Paris to threshold regime, in order to characterize near-threshold stress ratio (K_{max}) effects.

Materials and Testing

The alloy used in this study is an $\alpha+\beta$ titanium alloy, Ti 6-2-2-2 (Ti-5.60 Al-1.81 Zr-1.79 Cr-1.88 Sn-1.96 Mo-0.23 Si, wt.%) received in sheet form cross rolled to a final thickness of 1.65 mm (0.065 inch). The alloy was hot rolled at 927 °C (1700 °F) and solution annealed at 899 °C (1650 °F) for 30 minutes, followed by an aging treatment at 510 °C (950 °F) for 10 hours (the material was processed in packs of several sheets which were air cooled following all heat treatments). The solution treated and aged product contains primary α grains less than 10 μm , with transformed β colonies. For comparison, the fatigue crack growth rate data for aluminum alloy (AA) 2024-T3 from two separate studies will also be presented [3, 12].

All fatigue crack growth rate testing was performed using closed loop servo-hydraulic machines, operated under load control, with sinusoidal waveform loading. Eccentrically loaded single edge notch tensile (ESE(T)) specimens, formally known as extended compact tension (EC(T)) [13], were used for fatigue crack growth rate testing. All Ti 6-2-2-2 data presented, was acquired using 38.1 mm wide T-L oriented specimens tested at 5 Hz. A strain gage (bonded to the back-face surface of each specimen) located directly opposite the machined notch, was used to determine crack

length and crack opening loads. The calculated crack length and stress-intensity factor (K) solution [13] were used with an automated system to perform K control testing. The computer controlled system made it possible to perform variable ΔK tests with very smooth profiles free of stepped load sheds. Visual crack length measurements were performed periodically during fatigue testing and were used along with a final fracture surface crack length to make small (typically 0.5 % error) corrections (by linear interpolation) to the compliance based crack length determinations.

Fatigue crack growth rate tests were performed by applying a constant R or constant K_{\max} , in accordance with ASTM Test Method for Measurement of Fatigue Crack Growth Rates (E 647). Constant R tests were performed with a decreasing ΔK ($C = -0.08 \text{ mm}^{-1}$) in the near-threshold regime and increasing ΔK ($C = +0.16 \text{ mm}^{-1}$) in the Paris regime and higher. Constant K_{\max} tests were performed using a decreasing ΔK ($C = -0.40 \text{ mm}^{-1}$ or -0.80 mm^{-1}) starting at low R , with R increasing as the fatigue threshold is approached. A schematic of the applied stress-intensity profile for each of these techniques is represented in Figure 1. The constant R decreasing ΔK test, represented by Figure 1a, results in a decreasing K_{\max} and minimum stress-intensity factor (K_{\min}) to reduce ΔK . If K_{\min} is reduced to a level less than K_{op} , crack closure will be present, reducing the crack tip driving force resulting in decreased fatigue crack growth rates. For constant K_{\max} decreasing ΔK tests, represented by Figure 1b, an increasing K_{\min} produces a reduction in ΔK . This increasing R procedure makes it easier to maintain a K_{\min} which is greater than K_{op} , consequently free of closure, as threshold is approached.

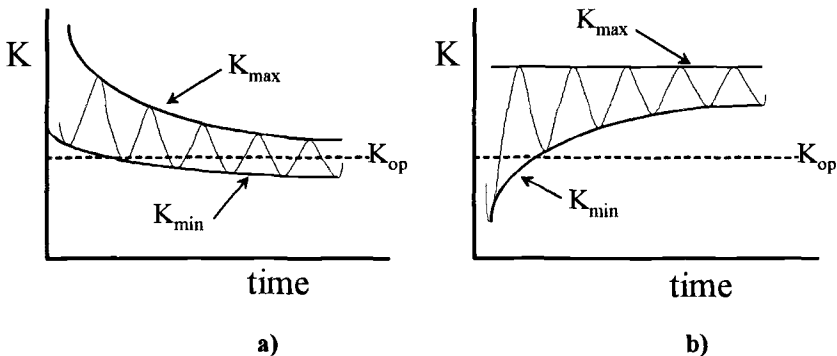


Figure 1. Schematic diagrams for the a) constant R decreasing ΔK test and b) constant K_{\max} decreasing ΔK test.

Throughout the fatigue crack growth rate tests, load-displacement measurements were evaluated to determine crack closure using the offset technique described in ASTM E 647. Opening loads corresponding to several offset levels (1, 2, 4, 8 and 16 %) were continuously determined. Periodically, load-displacement data were acquired and analyzed independently to determine crack opening levels using Elber's reduced displacement technique [2]. The results for crack opening load measurements using each of these techniques were compared and the offset level which produced crack opening

levels agreeing most favorably with results from Elber's technique was used to determine ΔK_{eff} . For all of the results presented, a 1 % offset level resulted in the best agreement with results from Elber's technique.

Results

Fatigue crack growth rate data for tests performed in room temperature laboratory air at two constant stress ratios are presented in Figure 2. These tests were conducted at $R = 0.1$ (circle symbols) and $R = 0.5$ (square symbols). Also plotted in Figure 2 is the closure corrected (ΔK_{eff}) data for $R = 0.1$ (diamond symbols). The ΔK_{eff} data shown in Figure 2 were calculated using opening loads at a load-displacement offset of 1 %. For the $R = 0.5$ results shown in Figure 2, no crack closure was detected using either the offset technique or Elber's reduced displacement technique. Here, very good agreement between the ΔK_{eff} result ($R = 0.1$) and $R = 0.5$ data were observed in the near-threshold regime.

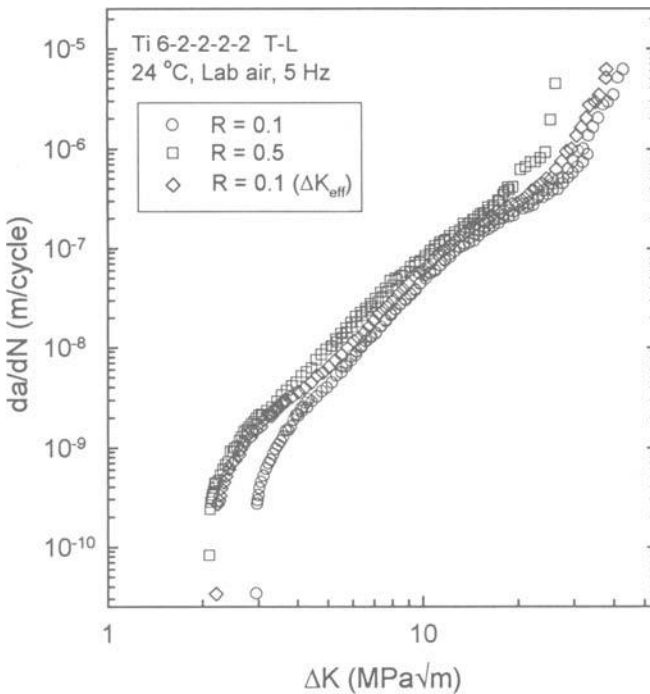


Figure 2. Fatigue crack growth rate data for Ti 6-2-2-2 in room temperature laboratory air using constant R testing.

Constant K_{max} tests were conducted to produce near-threshold fatigue crack growth rate data at very high stress ratios [14, 15]. Figure 3 shows lower Paris to threshold regime fatigue crack growth rate data for the two constant R tests, previously shown in Figure 2, as well as three constant K_{max} tests ($K_{max} = 11.0, 16.5, 22.0 \text{ MPa}\sqrt{\text{m}}$). Three points for ΔK between 5.5 and 9.5 $\text{MPa}\sqrt{\text{m}}$ are identified in Figure 3 where the loading parameters for a constant K_{max} test and a constant R test are similar; the fatigue crack growth rates determined using both test methods for the similar loading conditions are in excellent agreement. This confirms that when identical loading parameters are applied for constant K_{max} and constant R tests, consistent results are obtained. At very low values of ΔK , the three constant K_{max} tests shown in Figure 3 produce accelerated da/dN compared to the two constant R tests. The three values of ΔK identified along the x-axis in Figure 3 represent the intercept of the fatigue crack growth test results ($K_{max} = 16.5 \text{ MPa}\sqrt{\text{m}}$, $R = 0.5$, and $R = 0.1$) with da/dN at $1 \times 10^{-10} \text{ m/cycle}$. These values are estimates of ΔK_{th} , per ASTM E 647. As shown in Figure 2, the difference in ΔK_{th} for $R = 0.1$ and 0.5 appears to be a result of crack closure. However, the further decrease in ΔK_{th} observed for the three K_{max} tests presented in Figure 3 is not consistent with the view of a single intrinsic fatigue crack growth rate curve [2].

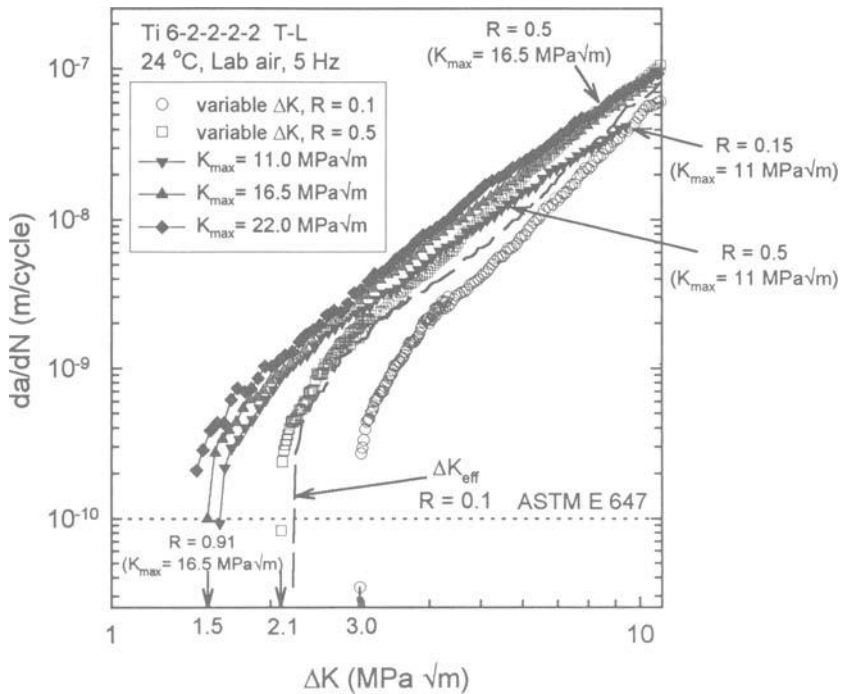


Figure 3. Lower Paris to threshold regime fatigue crack growth rate data for Ti 6-2-2-2 for constant R and constant K_{max} tests.

Discussion

Fatigue Crack Growth Behavior

Fatigue crack growth rate data (shown in Figure 3) were evaluated using an analysis developed by Schmidt and Paris [3]. Shown in Figure 4 are values of ΔK versus R at 1×10^{-10} m/cycle from two constant R (open symbols) and five constant K_{max} tests (solid symbols). These seven data points represent values of ΔK and R obtained by performing linear regression analysis for the five test conditions presented in Figure 3 as well as constant K_{max} tests at 3.85 and 6.6 $\text{MPa}\sqrt{\text{m}}$. Two distinct regions can be identified [3]. For $R < 0.5$, ΔK_{th} increases sharply with decreasing R . For $R > 0.75$, the Schmidt and Paris analysis assumes no change in the observed ΔK_{th} with increasing R . For R less than a critical stress ratio ($R_{cl} \approx 0.73$), increasing ΔK_{th} with decreasing R was attributed to fatigue crack closure. Fatigue crack closure was confirmed to exist at $R = 0.1$ using both the offset technique and Elber's reduced displacement techniques. For stress ratios greater than R_{cl} , an average ΔK is chosen to represent a constant ΔK_{th} (ΔK_{eff} in Figure 4). While the two linear fits shown in Figure 4 appear to result in a fairly good representation of the data, a line of constant ΔK does not appear to accurately represent the trends in the data. The apparent limitation of this technique is in assuming a constant ΔK_{th} exists for $R > R_{cl}$.

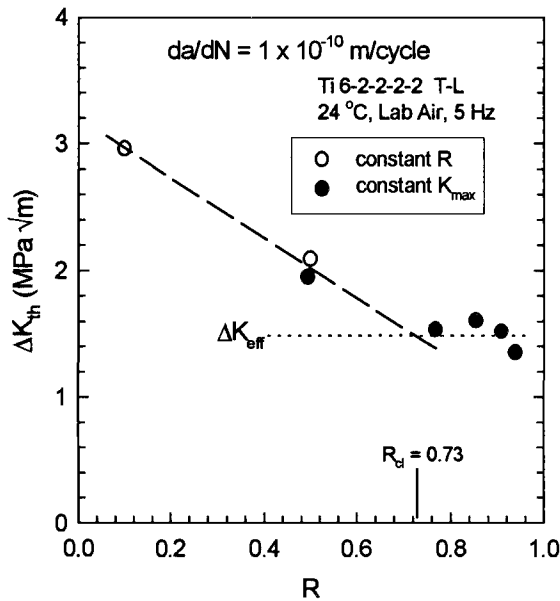


Figure 4. ΔK_{th} versus R data at 1×10^{-10} m/cycle for Ti 6-2-2-2 (using Schmidt-Paris plotting method).

The data presented in Figure 4 are plotted as ΔK_{th} versus K_{max} in Figure 5. For low values of K_{max} ($< 4.6 \text{ MPa}\sqrt{\text{m}}$), a relatively large increase in ΔK_{th} is observed with decreasing K_{max} (dashed linear regression line). As noted previously, this region is dominated by fatigue crack closure. For values of K_{max} greater than approximately $4.6 \text{ MPa}\sqrt{\text{m}}$, a more subtle yet distinct decrease in ΔK_{th} is observed for increasing K_{max} (dotted linear regression line). This behavior extends to very high values of R (> 0.9), suggesting that fatigue crack closure is not influencing the fatigue crack growth behavior for $K_{max} > 4.6 \text{ MPa}\sqrt{\text{m}}$. The shallow slope indicates that fatigue crack growth behavior is affected by applied K_{max} , even when the growing fatigue crack is not affected by crack closure processes. Therefore, the use of a line of constant ΔK to represent the high R data does not accurately represent the observed trends. The results in Figure 5 are consistent with the AA 2024-T3 data of Schmidt and Paris [3] when plotted as ΔK_{th} versus K_{max} (Figure 6). Here, a linear regression fit of the data for $K_{max} > 4 \text{ MPa}\sqrt{\text{m}}$ (dotted line in Figure 6) reveals a distinct decrease in ΔK_{th} with increasing K_{max} . More recent AA 2024-T3 data [12] (shown in Figure 7) confirm the trends shown in Figures 5 and 6. For each of these sets of data, no discrete value of ΔK_{th} is observed and the threshold regime is described by two linear curves which represent a closure dominated region and a K_{max} affected region. Examination of the fatigue surfaces for the K_{max} affected data presented in Figure 7 has revealed an increase in size and density of voids formed with increasing K_{max} [12]. These observations indicate that the fatigue processes are affected by the applied K_{max} and that the change in ΔK with applied K_{max} is not solely due to crack closure.

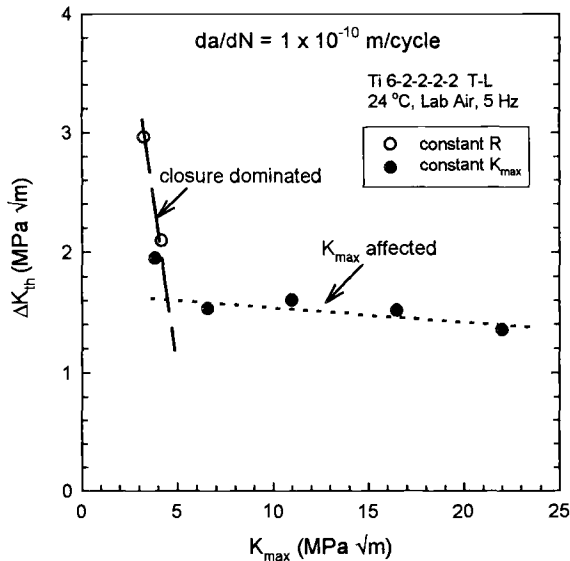


Figure 5. ΔK_{th} versus K_{max} data at 1×10^{-10} m/cycle for Ti 6-2-2-2, showing two distinct fatigue crack growth regions.

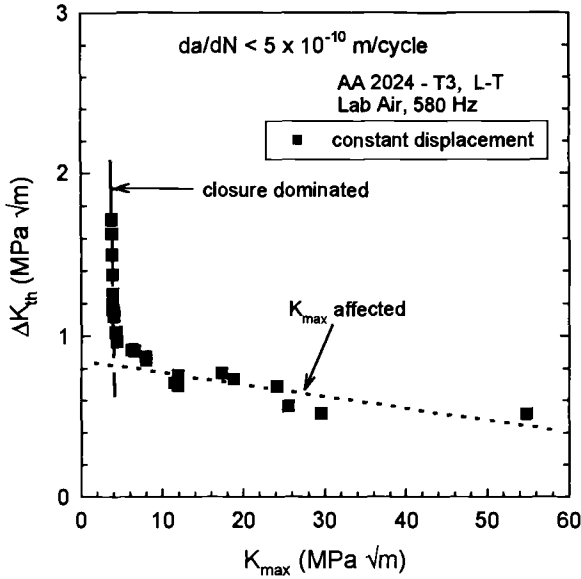


Figure 6. ΔK_{th} versus K_{max} data at $da/dN < 5 \times 10^{-10}$ m/cycle for AA 2024-T3, showing two distinct fatigue crack growth regions (from Schmidt and Paris [3]).

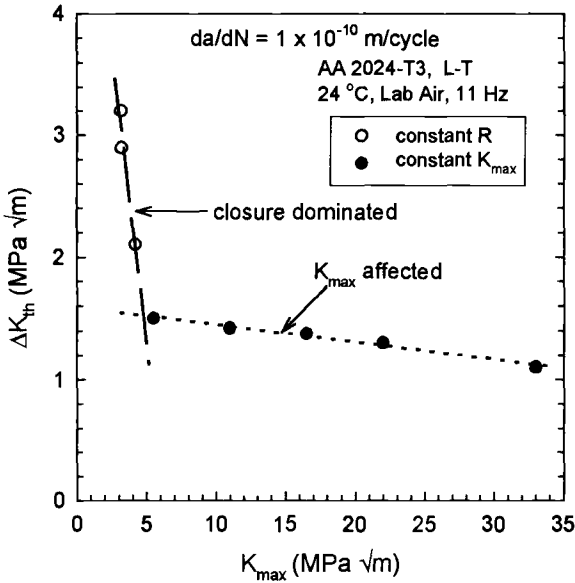


Figure 7. ΔK_{th} versus K_{max} data at 1×10^{-10} m/cycle for AA 2024-T3, showing two distinct fatigue crack growth regions (from J. A. Newman, et al. [12]).

Plots of ΔK versus K_{max} were used to determine a single da/dN versus ΔK curve that represents the boundary between crack closure dominated and K_{max} affected fatigue crack growth behavior. Figure 8 is a plot of ΔK versus K_{max} at four values of constant da/dN for constant R and constant K_{max} tests. Curves of ΔK versus K_{max} were generated for a total of twenty values of da/dN from 1×10^{-10} to 1×10^{-7} m/cycle for Ti 6-2-2-2-2. Data presented for each value of da/dN can be fit using two linear regressions, representing a closure dominated region A (dashed lines) and a K_{max} affected region B (dotted lines). The absolute value of the slope for the K_{max} affected regime, B in Figure 8, is seen to increase with increasing da/dN . The slope of the linear regression fit for the K_{max} affected regime for twenty values of da/dN examined are plotted in Figure 9. Here, the absolute value of the slope is observed to decrease with decreasing da/dN to a crack growth rate of approximately 5×10^{-10} m/cycle. For values of da/dN less than 5×10^{-10} the slope of the K_{max} affected regime remains fairly constant and is not zero as previously suggested [3]. The intercept of the two linear regressions for each value of da/dN represents the boundary between regions A and B; the boundary is marked by line segments connecting the intercepts in Figure 8. The intercepts are used to develop a fatigue crack growth rate curve which distinguishes between the region A closure dominated and region B K_{max} affected data (solid line in Figure 10). Any fatigue crack growth rate data to the left of the solid line in Figure 10 is free of crack closure, while data within the shaded region are affected by crack closure.

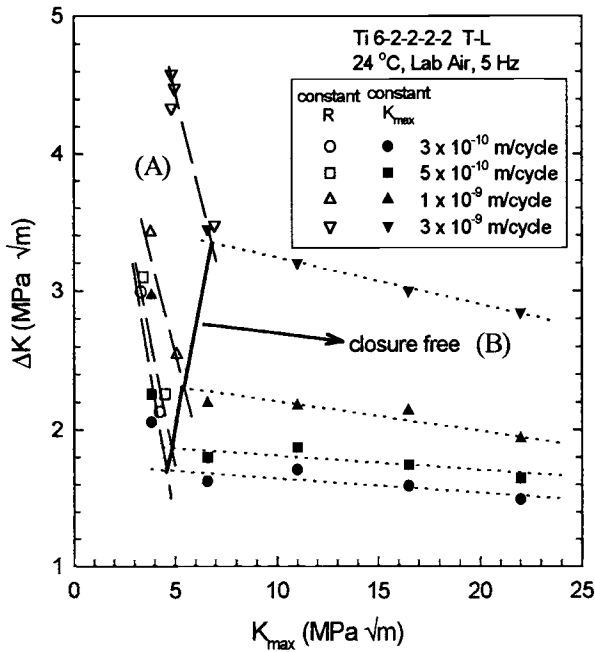


Figure 8. ΔK versus K_{max} data for Ti 6-2-2-2-2 at several fatigue crack growth rates, showing two distinct fatigue crack growth regions.

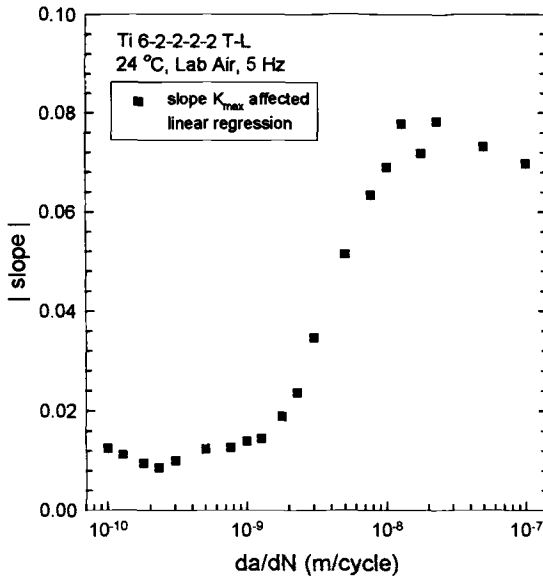


Figure 9. Absolute value of slope versus log da/dN for the linear regression fit of the K_{max} affected data of Ti 6-2-2-2-2 at room temperature for twenty selected values of da/dN .

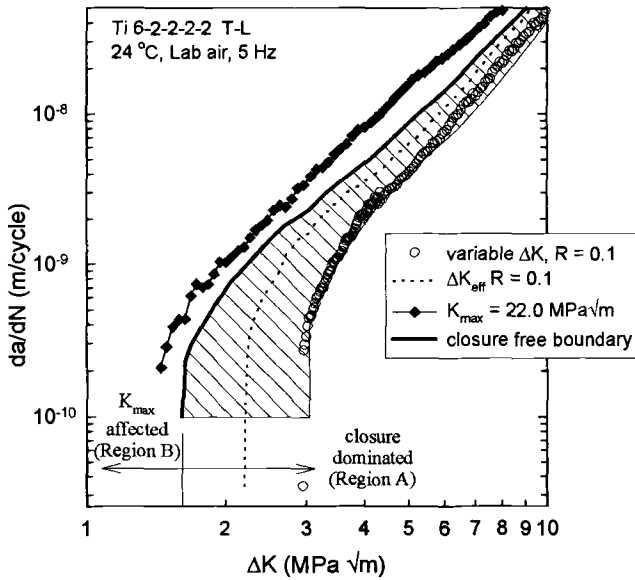


Figure 10. Lower Paris to threshold regime fatigue crack growth rate data for Ti 6-2-2-2-2 showing regions affected by crack closure and free from crack closure.

Crack Opening Behavior

The closure-free boundary does not coincide with the closure corrected ΔK_{eff} curve, dashed line shown in Figure 10, suggesting a discrepancy between the two methods used to establish closure-free fatigue crack growth rate data. Based on the bilinear ΔK versus K_{max} plots shown in Figure 8, the closure corrections performed to establish the ΔK_{eff} curve for the $R = 0.1$ data do not fully account for crack closure. Also, the $R = 0.5$ data is contained in the closure dominated regime for each of the values of da/dN presented in Figure 8. However, far-field closure measurements did not resolve any closure for $R = 0.5$. This suggests that the far-field measurements lack the necessary resolution to accurately determine crack-tip opening loads. Additionally, far-field load-displacement traces have been shown to be highly dependent upon interpretation, which can result in large differences in reported crack-tip opening levels [6, 16].

The plots of ΔK versus K_{max} (Figure 5 and 8) can be used to develop a better understanding of the crack opening behavior for Ti 6-2-2-2-2. Assuming K_{max} influences fatigue crack growth behavior in the closure dominated region, the K_{max} affected linear regression line (dotted line in Figure 11) can be extended into the closure dominated region. Selecting a data point within the closure affected regime ($R = 0.1$ is noted as point 1 in Figure 11), a vertical line can be extended to the x-axis (solid line). The solid line intercepts the K_{max} affected linear regression (dotted line) at ΔK_{eff} and the x-axis at the applied K_{max} (noted as $K_{max, app}$ in Figure 11). K_{op} is calculated by subtracting ΔK_{eff} from the applied K_{max} , resulting in a $K_{op} = 1.6 \text{ MPa}\sqrt{\text{m}}$ for $R = 0.1$ at $1 \times 10^{-10} \text{ m/cycle}$.

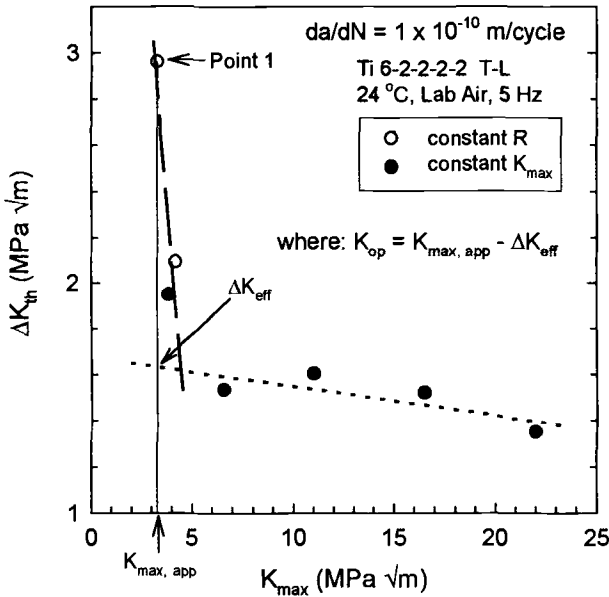


Figure 11. ΔK_{th} versus K_{max} data for Ti 6-2-2-2-2 at $1 \times 10^{-10} \text{ m/cycle}$, showing K_{op} determination.

Figure 12 is a comparison of opening ratio (K_{op}/K_{max}) versus ΔK for $R = 0.1$ using the ΔK versus K_{max} data (square symbols) and the ASTM offset technique at an offset level of 1% with a far-field strain gage to measure displacement (triangle symbols). No data for $K_{op}/K_{max} < 0.175$ are presented for the far-field technique due to the limited load-displacement data acquired below this level which makes it impractical to determine fatigue crack closure using the offset technique. The two curves indicate a similar trend; decreasing K_{op}/K_{max} with increasing ΔK . However, the directly measured opening ratios are lower in value than those determined using the ΔK versus K_{max} curves, particularly as threshold is approached. This discrepancy suggests that the far-field strain gages used in this study are not able to fully resolve the closure events occurring at the crack tip. This also suggests that the ΔK_{eff} curve presented in Figure 2 does not accurately reflect an effective fatigue crack growth behavior for Ti 6-2-2-2-2 under the conditions examined.

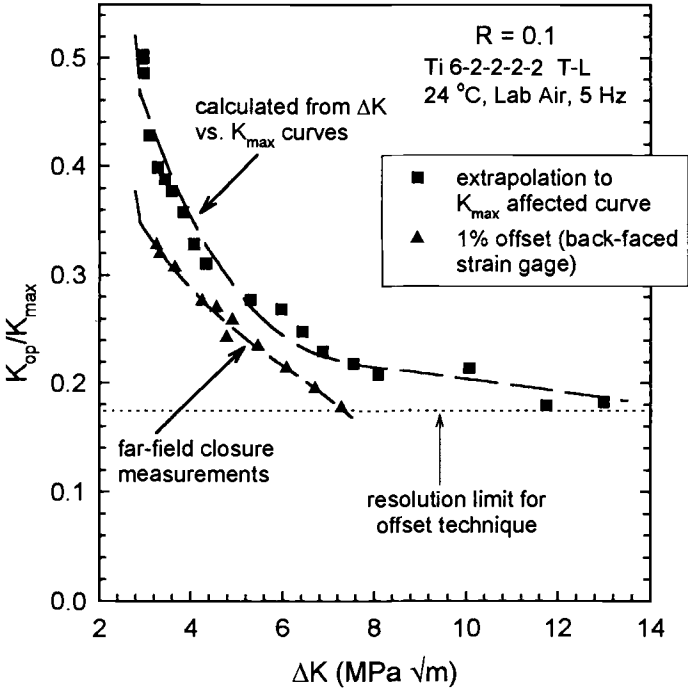


Figure 12. Opening stress-intensity ratio versus ΔK comparing calculated values and experimentally measured values for Ti 6-2-2-2-2 for $R = 0.1$.

Conclusions

The methodology outlined in this paper has been used to identify closure free fatigue crack growth and to monitor subtle changes in ΔK_{th} . Fatigue crack growth behavior of Ti 6-2-2-2 has been evaluated by plotting values of ΔK and K_{max} for several values of da/dN from constant R and constant K_{max} tests. Plots of ΔK versus K_{max} for each value of da/dN examined reveal a closure dominated regime and a closure free K_{max} affected regime. The slope of the K_{max} affected regime approaches zero as da/dN approaches 1×10^{-10} m/cycle. However, a finite slope was measured for all values of da/dN , suggesting that no single intrinsic ΔK_{th} is present. This behavior was also observed for AA 2024 in the near-threshold regime. Estimates of K_{op} determined with this methodology can be used in conjunction with conventional compliance techniques to more accurately interpret crack-tip closure processes.

References

- [1] Couper, M.J. and Griffiths, J.R., "Effects of Crack Closure and Mean Stress on the Threshold Stress Intensity Factor for Fatigue of an Aluminum Casting Alloy," *Fatigue and Fracture of Engineering Materials and Structures*, Vol. 13, No. 6, 1990, pp. 615-624.
- [2] Elber, W., "The Significance of Fatigue Crack Closure," *Damage Tolerance in Aircraft Structures, ASTM STP 486*, American Society for Testing and Materials, Philadelphia, PA, 1971, pp. 230-242.
- [3] Schmidt, R.A. and Paris, P.C., "Threshold for Fatigue Crack Propagation and the Effects of Load Ratio and Frequency," *Progress in Flaw Growth and Fracture Toughness Testing, ASTM STP 536*, American Society for Testing and Materials, Philadelphia, PA, 1973, pp. 79-94.
- [4] Döker, H. and Bachmann, V., "Determination of Crack Opening Load by Use of Threshold Behavior," *Mechanics of Fatigue Crack Closure, ASTM STP 982*, J.C. Newman, Jr. and W. Elber, Eds., American Society for Testing and Materials, Philadelphia, PA, 1988, pp. 247-259.
- [5] Musuva, J.K. and Radon, J.C., "Threshold of Fatigue Crack Growth in a Low Alloy Steel," *Advances in Fracture Research (Fracture 81)*, D. Francois Ed., Pergamon Press, Oxford, 1982, pp. 1365-1372.
- [6] Donald, J.K., "A Procedure for Standardizing Crack Closure Levels," *Mechanics of Fatigue Crack Closure, ASTM STP 982*, J.C. Newman, Jr. and W. Elber, Eds., American Society for Testing and Materials, Philadelphia, PA, 1988, pp. 222-229.
- [7] Davidson, D.L. and Lankford, J., "High Resolution Techniques for the Study of Small Cracks," *Small Fatigue Cracks*, R.O. Ritchie and J. Lankford, Eds., TMS, Warrenton, PA, 1986, pp. 455-470.
- [8] Sutton, M.A., Zhao, W., McNeill, S.R., Helm, J.D., Piascik, R.S., Riddell, W.T., "Local Crack Closure Measurements: Development of a Measurement System Using Computer Vision and a Far-Field Microscope," *Advances in Fatigue Crack Closure Measurements and Analysis, ASTM STP 1343*, R.C. McClung and J.C.

- Newman, Jr., Eds., American Society for Testing and Materials, West Conshohocken, PA, to be published.
- [9] Suresh, S., *Fatigue of Materials*, Cambridge University Press, Cambridge, UK, 1991, pp. 203-215.
- [10] Liaw, P.K., Leax, T.R., and Logsdon, W.A., "Near-Threshold Fatigue Crack Growth Behavior in Metals," *Acta Metallurgica*, Vol. 31, No. 10, 1983, pp. 1581-1587.
- [11] Vasudévan, A.K. and Sadananda, K., "Classification of Fatigue Crack Growth Behavior," *Metallurgical and Materials Transactions, A*, Vol. 26A, 1995, pp. 1221-1234.
- [12] Newman, J.A., Riddell, W.T., and Piascik, R.S., "Effects of K_{max} on Fatigue Crack Growth Threshold in Aluminum Alloys" accepted for publication in *Fatigue Crack Growth Thresholds, Endurance Limits, and Design, ASTM STP 1372*, J.C. Newman and R.S. Piascik, Eds., American Society for Testing and Materials, West Conshohocken, PA, 1999.
- [13] Piascik, R.S. and Newman, J.C., Jr., "An Extended Compact Tension Specimen for Fatigue Crack Growth and Fracture Testing," *International Journal of Fracture*, Vol. 76, 1995, pp. R43-R48.
- [14] Herman, W.A., Hertzberg, R.W., and Jaccard, R., "A Simplified Laboratory Approach for the Prediction of Short Crack Behavior in Engineering Structures," *Fatigue and Fracture of Engineering Materials and Structures*, Vol. 11, No. 4, 1988, pp. 303-320.
- [15] Hertzberg, R., Herman, W.A., Clark, T., and Jaccard, R., "Simulation of Short Crack and Other Low Closure Loading Conditions Utilizing Constant K_{max} ΔK -Decreasing Fatigue Crack Growth Procedures," *Small-Crack Test Methods, ASTM STP 1149*, J.M. Larsen and J.E. Allison, Eds., American Society for Testing and Materials, Philadelphia, PA, 1992, pp. 197-220.
- [16] Riddell, W.T., Piascik, R.S., Sutton, M.A., Zhao, W., McNeill, S.R., Helm, J.D., "Determining Fatigue Crack Opening Loads from Near-Crack-Tip Displacement Measurements," *Advances in Fatigue Crack Closure Measurements and Analysis, ASTM STP 1343*, R.C. McClung and J.C. Newman, Jr., Eds., American Society for Testing and Materials, West Conshohocken, PA, to be published.

A. J. McEvily,¹ M. Ohashi,² R. Shover,¹ and A. DeCarminé¹

Effect of an Overload on the Threshold Level of Ti-6-22-22

Reference: McEvily, A. J., Ohashi, M., Shover, R., and DeCarminé, A., “Effect of an Overload on the Threshold Level of Ti-6-22-22,” *Fatigue Crack Growth Thresholds, Endurance Limits, and Design*, ASTM STP, 1372, J. C. Newman, Jr. and R. S. Piascik, Eds., American Society for Testing and Materials, West Conshohocken, PA, 2000.

Abstract: The effects of overloads on the fatigue crack growth behavior of the high strength α / β titanium alloy Ti-6-22-22 have been investigated. Fatigue cracks were grown at a baseline R level of 0.1, and single overloads, ranging in magnitude from 2-3 times the baseline level, were applied to determine the effect of the overloads on subsequent fatigue crack growth behavior. Because of the high yield strength of the alloy, 1225 MPa, the number of delay cycles following an overload was not as pronounced as in alloys of lesser strength. A principal effect of an overload in this titanium alloy was to increase the threshold for fatigue crack growth. An experimental procedure based upon the increase in threshold level was adopted to determine the maximum level of crack closure resulting from an overload.

The novel observation was made that following a sufficiently high overload the process of further crack growth involved the emergence of a surface crack ahead of the preexisting crack. It was also observed that the crack growth behavior at distances well beyond the overload plastic zone size could be sensitive to prior overload history.

Keywords: Fatigue crack growth, fatigue threshold, overloads, titanium.

Ti-6-22-22 (Ti-6Al-2Sn-2Zr-2Mo-2Cr) is a high strength α / β titanium alloy of interest for advanced aircraft applications such as the High Speed Civilian Transport and the U. S. Air Force F-22 fighter aircraft [1]. Although the alloy has been available for over 20 years, only in recent years have detailed assessments of the fatigue crack growth characteristics of Ti-6-22-22 in thin sheet form been made, e.g., Stephens et al. [2]. The purpose of the present paper is to add to the information on fatigue crack growth behavior of this alloy, and in particular to consider the effects of overloads on subsequent crack growth behavior. This latter aspect is of interest because of the high yield strength of the alloy, 1225 MPa (175 ksi). Since the number of delay cycles, N_d , following an overload is inversely proportional to the square of the yield strength [3,4] it is to be expected that an overload will result in a lower value of N_d than in alloys of lower yield strength. An overload will also result in an increase in the threshold level, and the magnitude of this increase will be a matter of interest.

¹ Metallurgy Dept., U. of Connecticut, Storrs, CT 06269.

² National Research Institute of Police Science, Tokyo, Japan

Materials and Tests

The Ti-6-22-22 alloy for these tests was supplied by NASA Langley in 1.65 mm thick sheet form, and is from the same batch tested by Stephens et al. [2]. The alloy had been solution heat treated at 732° C for 1/2 hour, aged at 510° C for 10 hours, and then air cooled. The resultant microstructure consisted of an equiaxed α -phase dispersed evenly throughout an $\alpha + \beta$ -matrix with an estimated grain size less than 10 μm (Stephens et al. [2]).

ASTM type compact specimens (CT) in the LT orientation were used for the fatigue crack growth studies ($W = 57.2$ mm, $H = 34.5$ mm). (An ECT specimen was also tested for comparison purposes.) To facilitate the observation of the crack tip, the specimen surface under observation was polished to a mirror-like finish prior to testing. Strain gauges were affixed to the front surface at the back edge for the purpose of determining the crack opening level, K_{op} , by the subtracted-displacement technique. With some specimens two gauges, one on each face, were used to amplify the displacement signal. A manually decreasing ΔK procedure was used to determine the rate of fatigue crack growth as a function of ΔK ($R = 0.1$, frequency 30 Hz or less), and the crack tip position was determined with the aid of a low-power microscope. In these decreasing ΔK tests the normalized K -gradient was equal to -0.08 mm^{-1} in accord with ASTM Designation E 647. After fatigue crack growth, the roughness of the fatigue fracture surfaces was measured with a Tencor Alpha-Step 200 Surface Profiler.

In the overload tests the crack was grown at a given baseline level, ΔK_b , and the overload was applied after the base line growth rate had stabilized. The % overload was defined as

$$\%overload = \frac{K_{\max ol} - K_{\max b}}{K_{\max b} - K_{\min b}} \times 100 \quad (1)$$

where $K_{\max ol}$ is the maximum stress intensity factor at the overload level, $K_{\max b}$ is the maximum stress intensity factor at the baseline level, and $K_{\min b}$ is the minimum stress intensity factor at the baseline level. Single overloads were applied at different baseline levels ranging from 6 to 18 $\text{MPa}\sqrt{\text{m}}$, with the % overload being either 100, 150 or 200. The number of delay cycles following an overload was determined by noting the total number of cycles needed to advance the crack through the overload-affected zone at a constant ΔK and then subtracting the number of cycles required to grow the crack this same increment in the absence of an overload.

In preliminary testing it was found that the residual tensile stresses induced during the machining of the starter notch could result in crack development ahead of the notch, as shown in Fig. 1. These residual stresses also affected crack growth behavior. For example, in one case a crack was developed at the starter notch at a ΔK_b level of 12 $\text{MPa}\sqrt{\text{m}}$, and a high baseline closure level of 9.0 $\text{MPa}\sqrt{\text{m}}$ was found after 1 mm of crack growth. The closure level gradually reduced to 4.1 $\text{MPa}\sqrt{\text{m}}$, after an additional 12 mm of crack growth at the 12 $\text{MPa}\sqrt{\text{m}}$ ΔK_b level. There was also evidence of a strong loading-history effect in this Ti-6-22-22 alloy. For example, in one test sequence a 200% overload was applied at $\Delta K_b = 12 \text{ MPa}\sqrt{\text{m}}$, where the baseline crack growth rate was $3 \times 10^{-5} \text{ mm/cycle}$. After 1.8 mm of additional crack growth at the baseline level, a distance

well beyond the overload plastic zone size, the crack growth rate was only one half of its original value. This and similar observations indicated that there were long-range history effects following a high overload. Because of such large history effects, in the overload tests if the crack wake contained an overload-affected zone it was machined away before conducting another overload test on the same specimen.

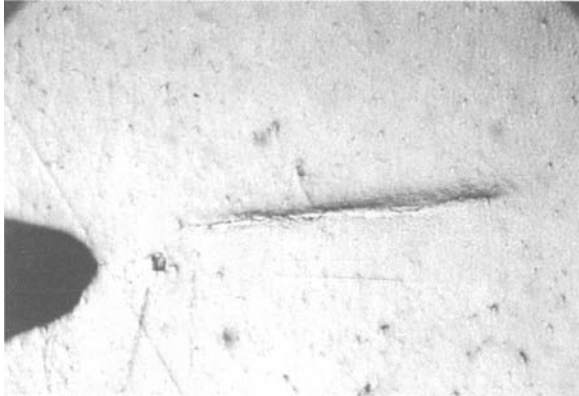


Fig. 1. Appearance of crack ahead of starter notch.

Results

Baseline Data

Fig. 2. is a plot of da/dN as a function of ΔK . The threshold value, corresponding to a crack growth rate of 10^{-10} m/cycle for the data shown, was $4.6 \text{ MPa}\sqrt{m}$. (In this test the crack length before conducting the decreasing ΔK test was 15 mm, so that any residual stress problems associated with the starter notch were avoided.) In a second specimen the threshold level was higher, $5.5 \text{ MPa}\sqrt{m}$. Fig. 3 is a plot of the crack opening levels as a function of ΔK for both a CT specimen and an ECT specimen. It is seen that the crack opening level is fairly independent of the ΔK level for both types of specimen, an indication that in this high strength material crack closure is of the roughness-induced type. The average value of the closure level was $2.6 \text{ MPa}\sqrt{m}$ for the CT specimen, but for the ECT specimen a lower value was obtained. It is noted that crack closure level at threshold for $R = 0.1$ loading of an ECT specimen obtained by Stephens et al. [2] was also lower than for the present CT results, i.e. $1.6 \text{ MPa}\sqrt{m}$ vs. $2.6 \text{ MPa}\sqrt{m}$. In our tests the fracture surface roughness values, R_a , for both types of specimens were similar, i.e., $1-2 \mu\text{m}$ but the crack path in the ECT specimen was straighter than in the CT specimen. We surmise that the higher H/W ratio of the ECT specimen (1.875 vs. 1.2) led to better specimen alignment, which resulted in less crack-path wandering and lower closure levels. (In a subsequent study the loading pins were mounted in bearings, and the closure levels observed for a CT specimen were similar to those reported herein for the ECT specimen.)

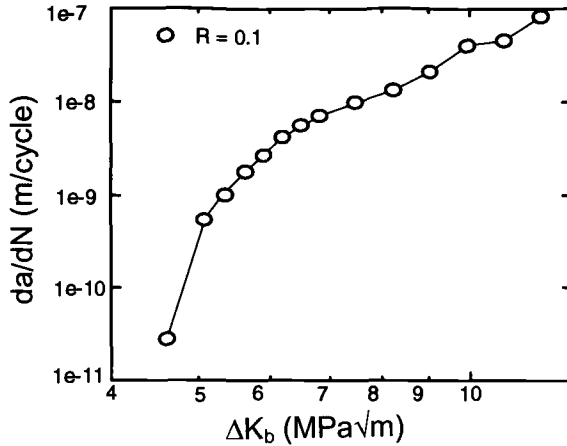


Fig. 2. The rate of fatigue crack growth for Ti-6-22-22 as a function of ΔK at $R = 0.1$.

In the subsequent analysis of the effect of an overload, the following constitutive relationship will be used

$$\frac{da}{dN} = A(\Delta K_{eff} - \Delta K_{effth})^2 \tag{2}$$

where A is a material constant, $\Delta K_{eff} = K_{max} - K_{op}$, and ΔK_{effth} is the value of ΔK at the threshold level. Fig. 4 is a plot of this relationship. From this figure it is observed that the value of the material constant A equal to $1.0 \times 10^{-9} (\text{MPa})^{-2}$ when da/dN is expressed in m/cycle.

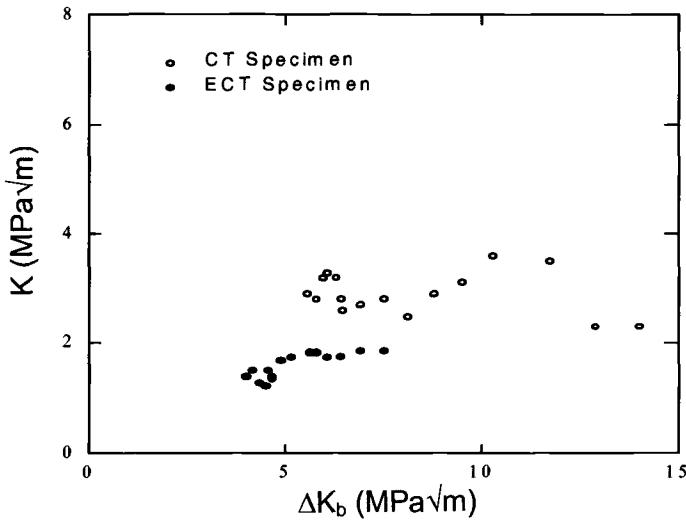


Fig. 3. Crack opening levels for Ti-6-22-22 as a function of ΔK at $R = 0.1$.

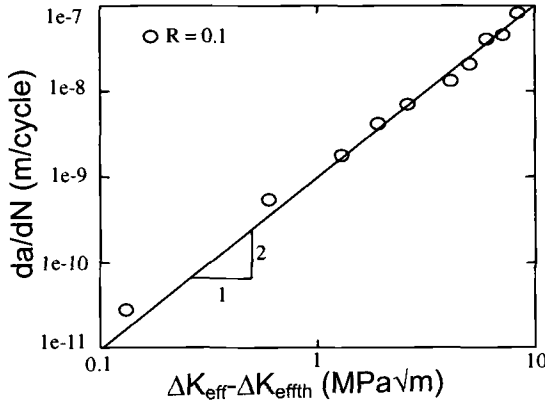


Fig 4. The rate of fatigue crack growth as a function of $\Delta K_{eff} - \Delta K_{effth}$ for Ti-6-22-22.

Overload Studies

Review: In previous studies we have found, as first observed by Paris and Hermann [5], that two crack opening events take place following an overload. The lower of these opening levels is designated K_{op1} and represents the crack opening level everywhere except in the overload zone at the surface of the specimen. The higher of the two opening levels is designated K_{op2} , and represents the opening of the crack within the surface overload zone itself [3]. Fig. 5 shows for a 9Cr-1Mo steel ($\sigma_y = 530$ MPa) how these two levels can be detected using a compliance method together with an offset displacement technique [4]. (Here $K_{op2,i}$ is the level at which crack opening in the surface overload zone initiates). It is noted that the crack must advance a sufficient distance into the overload zone before a sufficient change in compliance has occurred to render the second opening level detectable. However, the higher the yield strength of a material as with Ti-6-22-22, the smaller will be the overload plastic zone size, which renders the detection of K_{op2} more difficult.

The following expression has been developed to determine the number of excess cycles (delay cycles, N_d) over the number of cycles required at constant amplitude for the crack to transit the overload affected zone [4]:

$$N_d = \frac{r_{pol}}{A(K_{maxb} - K_{opb} - \Delta K_{effth})^2} \left[\frac{K_{maxb} - K_{opb} - \Delta K_{effth}}{K_{maxb} - K_{op2max} - \Delta K_{effth}} - 1 \right] \tag{3}$$

where A is a material constant defined above, r_{pol} is the size of the overload plastic zone, K_{maxb} is the maximum value of K at the baseline level, K_{opb} is the crack opening level at the baseline level, ΔK_{effth} is the effective value of ΔK at the threshold level, and K_{op2max} is the maximum value that K_{op2} attains as the fatigue crack traverses the overload zone. In Eq. 3, the term before the brackets represents the number of cycles required to traverse the overload zone if there were no retardation effect, and the term in brackets is a multiplying factor which reflects the severity of the overload. The value of r_{pol} for plane stress is approximated by

$$r_{pol} = \frac{K_{ol}^2}{\pi \sigma_y^2} \tag{4}$$

Fig.6 compares experimental and calculated values of N_d for two thicknesses of the 9Cr-1Mo steel, with K_{op2max} from load-displacement plots expressed as

$$K_{op2max} = 0.8\left(\frac{0.3}{B}\right)^{0.15} \tag{5}$$

A reasonably good correlation between the experimental and calculated values of N_d is apparent.

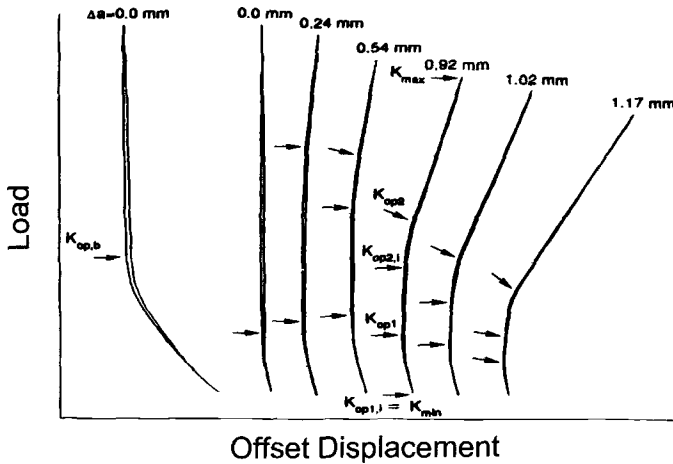


Fig. 5. Load -offset displacement plots before and after a 100% overload ($\Delta K_b = 14.5 \text{ MPa}\sqrt{m}$) for a 0.3 mm thick specimen of 9Cr-1Mo steel at various increments of crack length measured from the point of overload application. After Bao and McEvily (4).

As the result of an overload a new threshold level, ΔK_{thol} , will be established. The magnitude of ΔK_{thol} can be estimated for the 9Cr-1Mo steel subjected to a 100% overload by noting from Eq. 3 that when

$$K_{maxbth} - K_{op2max} - \Delta K_{effh} = 0 \tag{6}$$

we have the condition for the non-propagation of a fatigue crack after an overload. Eqs. 5 and 6 can then be combined to yield the following expression for ΔK_{thol} , noting that $K_{maxbth} = \Delta K_{thol} / (1 - R)$:

$$\Delta K_{thol} = \frac{\Delta K_{effh}}{\frac{1}{1 - R} - 0.8\left(\frac{0.3}{B}\right)^{0.15}} \tag{7}$$

For the 9Cr-1Mo steel ΔK_{effh} was $3.5 \text{ MPa}\sqrt{m}$ and R was 0.05, so that for B equal to 6.35 mm, the estimated value of ΔK_{thol} is $6.5 \text{ MPa}\sqrt{m}$; for B equal to 0.3 mm the estimated value of ΔK_{thol} is $14.0 \text{ MPa}\sqrt{m}$. In contrast, the constant amplitude threshold was $6.0 \text{ MPa}\sqrt{m}$ for the 6.35 mm thick specimen, and $7.5 \text{ MPa}\sqrt{m}$ for the 0.3 mm thick

specimen, so that the change in threshold level due to a 100% overload was much more pronounced in the thinner specimen.

We will employ a similar type of analysis in dealing with overload effects in Ti-6-22-22.

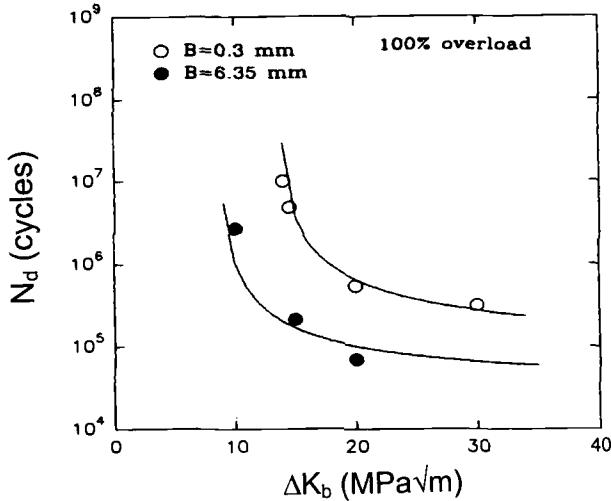


Fig. 6. Comparison of the calculated number of delay cycles with experimental results as a function of ΔK_b for both 0.3 mm and 6.35 mm thick specimens of 9 Cr-1Mo steel. After Bao and McEvely (4).

Present Results:

Next we consider the effect of an overload on Ti-6-22-22. Because of its high yield strength, 1225 MPa, for a given overload r_{pol} is smaller by a factor of five as compared to the 9Cr-1Mo steel. We have found that over the small plastic zone sizes resulting from overloads in Ti-6-22-22 at ΔK_b levels similar to that shown in Fig.5 that the change in the compliance of the specimen was generally insufficient to clearly resolve the upper opening level in the 1.65 mm thick specimens. Preliminary results also confirmed the expectation that the number of delay cycles following an overload was much smaller for Ti-6-22-22 than for the 9Cr-1Mo steel. We therefore directed our attention to the determination of ΔK_{thol} and adopted an indirect approach to estimating the value of K_{op2max} . The assumption was made that after an overload a new threshold would be established subject to the condition

$$K_{max\ thol} - K_{op2\ max} = \Delta K_{effh} \tag{8}$$

where $K_{max\ thol}$ is the value of K_{max} at the new threshold following an overload. From Eq. 8 the value of K_{op2max} is given as

$$K_{op2\ max} = K_{max\ thol} - \Delta K_{effh} \tag{9}$$

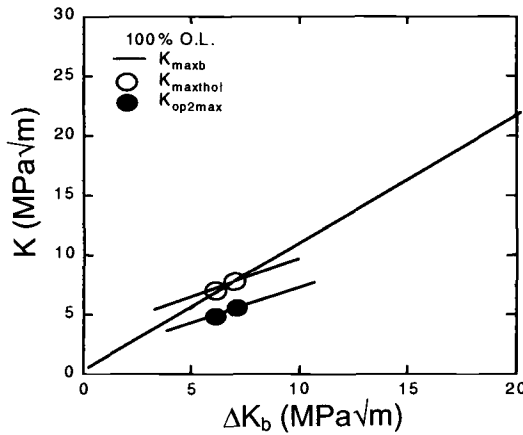


Fig. 7. $K_{maxthol}$, K_{op2max} and K_{maxb} as a function of ΔK_b for Ti-6-22-22 as a function of ΔK_n after a 100% overload.

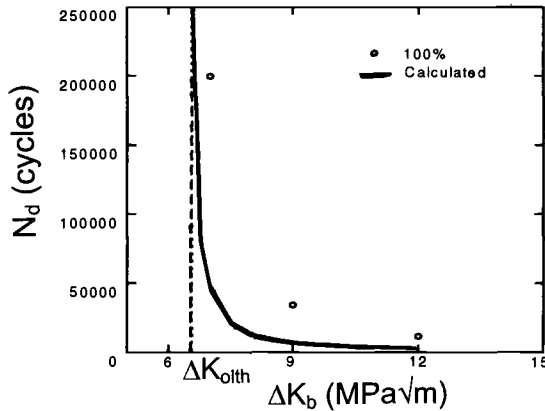


Fig. 8. The number of delay cycles after a 100% overload as a function of ΔK_b for Ti-6-22-22.

From the constant amplitude tests ΔK_{effth} was known to have a value of $2.4 \text{ MPa} \sqrt{m}$, so that only the value of $K_{maxthol}$ at which the crack would propagate had to be established to obtain K_{op2max} . This was done by using the following experimental procedure. After an overload the specimen was cycled at the original baseline level. If the crack did not propagate after 10^6 cycles, the ΔK level was increased by 0.5-1.0 $\text{MPa} \sqrt{m}$ and the specimen was again cycled to determine if crack propagation would occur at the new ΔK level. If propagation did not occur after 10^6 cycles the ΔK level was again increased. This procedure was followed until a ΔK level was reached at which the crack propagated, with this ΔK level corresponding to a new threshold level, ΔK_{thol} , as influenced by the application of the overload. Based upon these experimental results corresponding values for $K_{maxthol}$ and K_{op2max} can then be determined with the aid of Eq. 7, and a plot of K_{op2max} as a function of ΔK_b can be made. Fig. 7 gives the values for $K_{maxthol}$ and K_{op2max} as a function of ΔK_b , for the case of the 100% overload. Also shown

in Fig.7 is a line which represents K_{maxb} for $R = 0.1$ loading. Propagation can only occur at the baseline level when K_{maxb} exceeds $K_{maxthol}$.

Once the K_{op2max} level had been established, the number of delay cycles, N_d , can be determined using Eq.3. This was done for the 100% overload case, and the results are shown in Fig 8, with reasonably good agreement being found between the trends of the experimental and calculated values. It was observed that after an overload the crack deflected slightly and this may account for the number of delay cycles being somewhat higher than predicted. It is noted that the numbers of delay cycles in this high strength titanium alloy are small in contrast to those in 9Cr-1Mo steel at comparable ΔK levels. A main effect of an overload in Ti-6-22-22 is therefore to increase the threshold level rather than to develop large numbers of delay cycles above the new threshold.

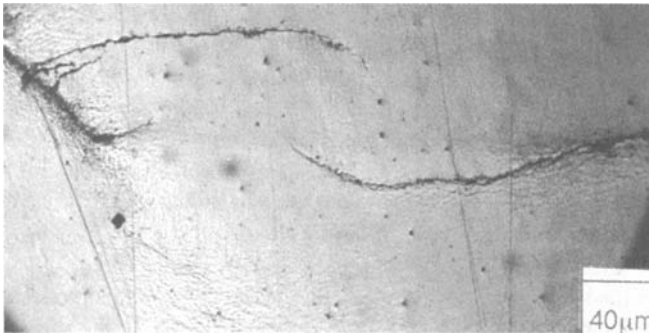


Fig. 9. Appearance of fatigue crack after 150% overload.

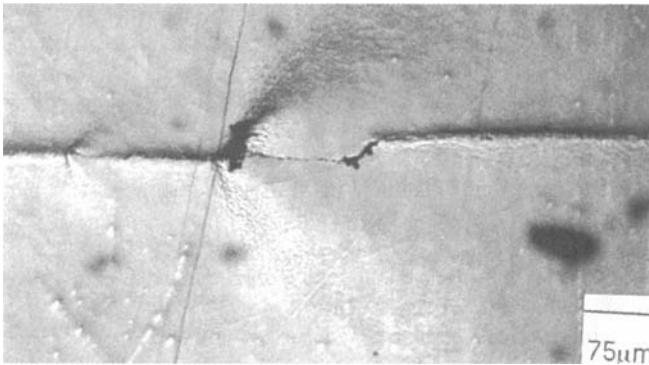


Fig. 10. Appearance of fatigue crack after 200% overload.

For the 150% and 200% overload cases, however, a different mode of crack growth following an overload took place which precluded an analysis for the number of delay cycles similar to that carried out for the 100% overload case. Upon increasing the baseline level after an overload to the $K_{maxthol}$ level, instead of the original crack propagating through the overload zone as in the case of the 100% overload, a new crack appeared at the surface ahead of the original crack and eventually linked up with the original crack. This surface cracking process was similar to that for the notched specimens shown in Fig. 1. Examples of this type of discontinuous growth after an overload are given in Figs.9

and 10. In these figures the overall direction of crack growth is from left to right. In Fig. 9 the site of the overload is at the extreme left of the figure. The main crack appeared to have been arrested within the overload plastic zone. A new surface crack ahead of the overload point had formed at the right of the figure, but had not yet linked up with the main crack at the left. The overload plastic zone size is also detectable in Fig. 9, and it is noted that the size of this zone is in agreement with the size estimated by Eq. 4.

In Fig. 10 the site of the overload is at the heavy, dark vertical line in the left center of the figure. The ridged region at the right is the new surface crack, and it is similar in appearance to the crack shown in Fig. 1. This ridging is a form of extrusion associated with the emergence of the new surface new crack. The size of the overload plastic zone in this case is also in agreement with the size estimated by Eq. 4.

There is the possibility that the new surface crack is a manifestation of the growth of a tunneling, subsurface crack, which, being in plane strain, is not significantly affected by an overload. The highest value of $K_{\max_{ol}}$ in these tests was $50.4 \text{ MPa} \sqrt{m}$. The corresponding plane stress plastic zone size is 0.54 mm. If the depth of this plastic zone is taken to be equal to its extent, then roughly 0.7 mm of the 1.7 mm thickness would be in plane strain, and more so for lower values of $K_{\max_{ol}}$. To check on the possibility of subsurface crack growth, the following experiment was carried out. A specimen at ΔK_b equal to $18 \text{ MPa} \sqrt{m}$ was subjected to a 200% overload, and cycling was resumed at the original baseline level. After 800,000 cycles a surface crack appeared ahead of the main crack and in less than 7,500 additional cycles it joined with the main crack. Cyclic loading was terminated at this point, and $10 \mu\text{m}$ were polished from the surface. No crack could be observed within the overload plastic zone. The absence of surface cracking at a depth of $10 \mu\text{m}$ may be due to the curvature associated with the lateral contraction in which occurs in the overload zone. At a free surface in this region there can be no residual compressive stress normal to the plane of crack growth. In order to avoid regions of high compressive residual stress, a surface crack initially should be shallow and grow along a line slightly away from the line of maximum contraction, as observed.

In the next stage of this experiment, an additional 0.75 mm of material was removed from the surface to reach the mid-thickness region. After polishing it was found that a crack was present which was continuous from the position of the overload through the overload zone. On the basis of this experiment it appears that the surface cracks which appear ahead of the overload plastic zone and the main surface crack are indeed manifestations of subsurface fatigue crack growth.

Since the discontinuous surface crack growth process differed from that modeled for the 100% overload case, the value of $K_{op2\max}$ and the number of delay cycles were not determined for the 150% and 200% overload cases. A plot of $K_{\max_{thol}}$ as a function of ΔK_b is shown in Fig. 11 for each of these overload levels. From these plots it is seen that the threshold level following an overload was $15.0 \text{ MPa} \sqrt{m}$ for the 150% overload, and $18.0 \text{ MPa} \sqrt{m}$ for the 200% overload.

As a result of an overload a new threshold is established which increases from the original value of $4.6 \text{ MPa} \sqrt{m}$ to a higher level, with the magnitude of the increase

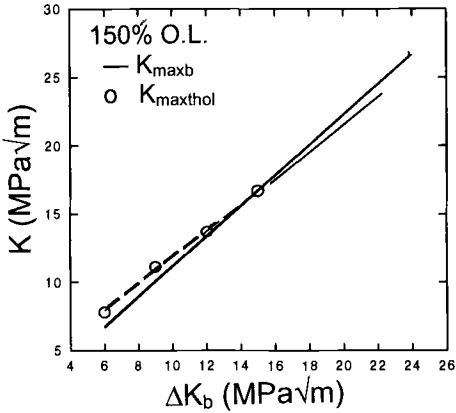


Fig. 11a. $K_{maxthol}$ and K_{maxb} as a function ΔK_b for 150% overloads.

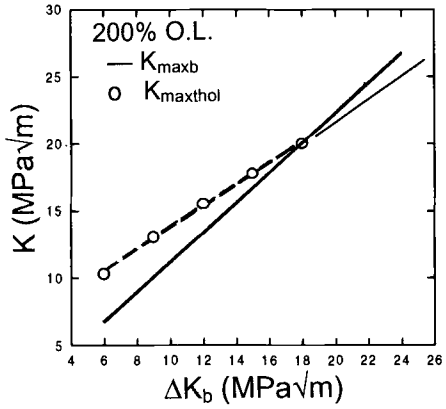


Fig. 11b. $K_{maxthol}$ and K_{maxb} as a function ΔK_b for 200% overloads.

depending upon the severity of the overload, as indicated in Fig. 12. It is noted that for the 100% overload case the increase in threshold level is relatively small. This is consistent with the work of Phillips and Newman [6], who found that for spike overloads applied to Ti-6-22-22 specimens every 2500 cycles in otherwise constant amplitude cycling at a $\Delta\sigma$ of 124 MPa and an R of 0.1, there was little effect on total lifetime for overload levels of 83% or less.

Other Observations: Since a dwell at maximum load is known to have an adverse affect on the fatigue behavior of some titanium alloys, we explored the effect of a 72 hour hold at a 200% overload level, 37.3 MPa \sqrt{m} ($r_{pol} = 0.3$ mm) No crack growth occurred during this hold time, or in subsequent cycling at the baseline ΔK level, 12 MPa \sqrt{m} . The K_{op1} crack opening level subsequent to the overload was 2.3 MPa \sqrt{m} , whereas just prior to the overload K_{opt} had been 3.3 MPa \sqrt{m} . This decrease was due to the blunting of the crack tip that occurred during the overload. It is noted that when the overload was applied without a dwell being involved that a decrease of the same order of magnitude in K_{op1} took place, therefore very little happened during the dwell at room temperature to affect the fatigue crack growth process.

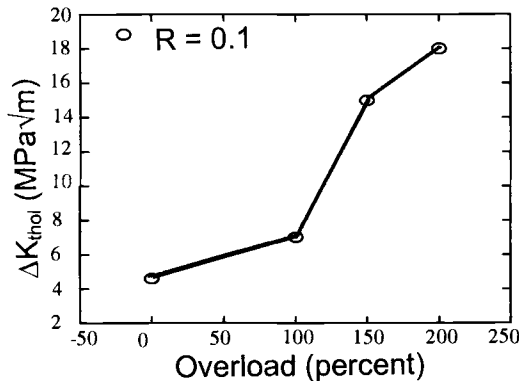


Fig. 12. Effect of magnitude of the overload on the subsequent threshold level.

Concluding Remarks

1. There is a significant increase in threshold level at the 150 and 200% overload levels in 1.6 mm thick specimens of Ti-6-22-22.
2. After 150% and 200% overloads, the main fatigue crack at the surface was either completely arrested or propagated at an extremely low rate. The emergence of a new surface fatigue crack ahead of the arrested or slowly growing surface fatigue crack was a manifestation of the subsurface growth of a fatigue crack.
3. At the 100% overload level the increase in threshold level due to an overload is much less than at higher overload levels. For overloads of 100% or less, their effect on the subsequent rate of propagation in this alloy is relatively small. Reasonably good agreement was found between the experimental and calculated trends of the delay cycles at the 100% overload level.
4. Fatigue crack growth behavior in this alloy was strongly influenced by the residual stresses associated with the starter-notch-machining process, as well as by load history effects.

Acknowledgment

The financial support provided by the National Aeronautics and Space Administration (NASA Research Grant No. NAG 1 1382) is gratefully acknowledged. Appreciation is also expressed to Dr. J. C. Newman for helpful discussions throughout the course of this investigation.

References

- [1] Lineberger, L., "Titanium Aerospace Alloy," *Advanced Materials and Processes*, ASM, Vol. 153, No.5, May 1998, pp. 45-46.
- [2] Stephens, R. R., Stephens, R. I., Veit, A. L. and Anderson, T. P., "Fatigue Crack Growth of Ti-62222 Titanium Alloy under Constant Amplitude and MiniTwist Flight Spectra at 25° C and 175°," *Int. J. Fatigue*, Vol. 19, 1997, pp. 301-308.
- [3] McEvily, A. J. and Yang, Z., "The Nature of the Two Opening Levels Following an Overload in Fatigue Crack Growth," *Met. Trans*, Vol. 21A, 1990, pp. 2717-27.
- [4] Bao, H. and McEvily, A. J., "The Effect of an Overload on the Rate of Fatigue Crack Propagation under Plane Stress Conditions," *Met. Trans.*, Vol. 26A, 1995, pp. 1725-33.
- [5] Paris, P. C. and Hermann, L., *Fatigue Thresholds*. J. Backlund, A. F. Blom, and C. J. Beevers, Eds., EMAS, Warley, UK, Vol. 1, 1985, p.11.
- [6] Phillips, E. P. and Newman, J. C., Jr., Private communication, 1998.

Claude Bathias¹

Relation Between Endurance Limits and Thresholds in the Field of Gigacycle Fatigue

Reference: Bathias, C., “**Relation Between Endurance Limits and Thresholds in the Field of Gigacycle Fatigue,**” *Fatigue Crack Growth Thresholds, Endurance Limits, and Design, ASTM STP 1372*, J. C. Newman, Jr. and R. S. Piascik, Eds., American Society for Testing and Materials, West Conshohocken, PA, 2000.

Abstract: In order to predict fatigue crack propagation at very long life a piezoelectric fatigue machine was built in our laboratory. This device is able to fail specimen at 10^{10} cycles and to determine thresholds up to 10^{-9} mm/cycle. The originality of this machine resides in the possibility to apply simultaneously to a specimen a constant tension effect and longitudinal ultrasonic vibratory effort with adjustable amplitude. That is to say, the R ratio can be varied from -1 to 0.9.

It appears that the fatigue thresholds are about the same in conventional fatigue and in resonant fatigue if the computation of the stress intensity factor K is correct. But there is a very large difference between the endurance limits at 10^6 cycles and 10^9 cycles. It means about 10% for steels and 30% for aluminium and nickel-based alloys.

To improve the relation between thresholds and fatigue limits, the gigacycle fatigue is studied in a Ni alloy manufactured by powder metallurgy with two sizes of inclusions. The testing temperature is 450°C. The first conclusion is that there is not any infinite fatigue limit until 10^9 cycles. The second conclusion is a possible correlation between the fatigue limit and the threshold at R ratio = 0. This relation is much more improbable for R = -1 because an incubation phenomenon exists around an inclusion or a porosity loaded at low stress level.

Keywords: gigacycle fatigue, threshold , prediction

It is of great importance to understand and predict a fatigue life in terms of crack initiation and small crack propagation. It has been generally accepted that at

¹ Professor, CNAM - ITMA, 2 rue Conté, 75003 Paris, FRANCE

high stress levels, fatigue life is determined primarily by crack growth, while at low stress levels, most of the life is consumed by the process of crack initiation. Several authors demonstrated that the portion of life attributed to crack nucleation is the upper 90% in the high cycle regime (10^6 to 10^7 cycles) for steel, aluminum, titanium and nickel alloys. In the case for which the crack nucleates from a defect, such as inclusion, pore, it is said that a relation must exist between the fatigue limit and the crack growth thresholds.

However, the relation between crack growth and initiation is not obvious for many reasons. First, it is not sure that a fatigue crack grows immediately at the first cycle from a sharp defect. Second, when a defect is small, a short crack does not grow as a long crack. Specially the effect of R ratio or the closure effect depends of the crack length. Thus, the relation between ΔK_{th} and σ_D is still to be discussed.

Another important aspect is the concept of infinite fatigue life. It is understood that below ΔK_{th} and below σ_D the fatigue life is infinite. In fact, the fatigue limit σ_D is usually determined for $N_f = 10^7$ cycles. Recently, it was shown by several authors [7-6] that fatigue failure can appear up to 10^9 cycles and may be beyond 10^9 . The fatigue strength difference at 10^7 and 10^9 cycles could be more than 100 MPa. It means the relation σ_D versus ΔK_{th} must be established in the gigacycle regime if any relation exists.

In order to discuss this problem we have carried out some tests in the gigacycle regime using a piezo-electric fatigue machine working at 20 KHz. In what follows we report the results of the fatigue behavior of two types of alloys:

- the first type is characterized by inclusions and porosities such as Ni base alloys processed by powder metallurgy;
- the second one is characterized by structural defects as Ti alloys without inclusion.

The experiments show that there are several mechanisms depending on the alloys and defects. It seems that there is no general relation between ΔK_{th} and σ_D even at 10^9 cycles. But, in the case where initiation depends of inclusions, a Murakami type model appears efficient.

Experimental Device

Principale

Since the first 20 KHz machine was constructed in 1950 by Mason [7], ultrasonic fatigue testing is less time consuming.

A schematic view of our USF system of this study is shown in Figure 1. The machine is essentially an ultrasonic machine constituted of a Branson power generator whose frequency is held at 20 KHz. The vibration of the specimen is induced with a piezo-ceramic transducer which generates acoustical wave to the specimen through a power concentrator (horn) in order to obtain more important stress and an amplification of the displacement. The resonant length of the specimen and concentrator is calculated at a frequency of 20 KHz. The dynamic displacement amplitude of the specimen extremity U_0 is measured by an optic fiber sensor, which

permits to measure the displacement from $1\ \mu\text{m}$ to $199.9\ \mu\text{m}$, with a resolution of $0.1\ \mu\text{m}$. A system of video-camera / television is used for the detection of crack initiation with a magnification of 140-200 times.

For crack propagation a single edge notched specimen is used. For our specimen, the stress intensity factor K was calculated correctly by Wu by finite element method [8].

For crack initiation an axisymetrical specimen is chosen. Both specimens are discribed in other papers [4,5,6,8].

Stress Intensity Factor Calculation

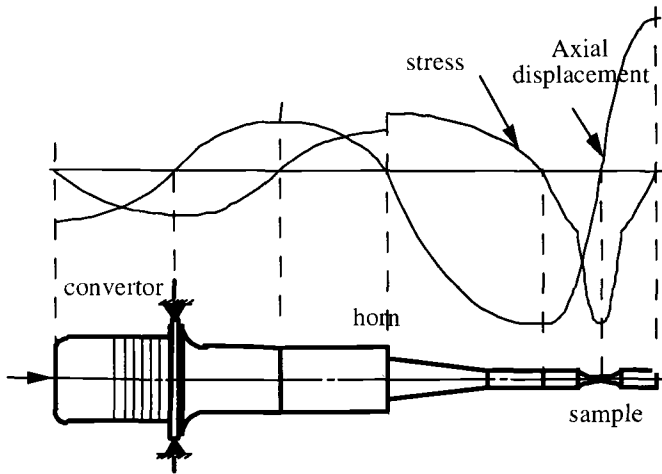


Figure 1 – Schematic of a Piezo-Electric Fatigue Machine

In the usual domain of fracture mechanics, a lot of relations are proposed to calculate the stress intensity factor K in specimens. But it is generally believed that all formulates are established for static or cyclic loading, not for the vibration excitation. In a vibratory system, the situation becomes more complex in the presence of inertia force and the absence of nominal force that is necessary to the classical fracture approach.

As the specimen used in ultrasonic fatigue testing is often special, the FEM is the only suitable method to derived different specific problems:

- the presence of a crack in the vibrating specimen;
- non constant thickness;
- elevated order mode of vibration;
- influence of temperature on the experiments.

For our specimen, K was correctly calculated by finite element method for $R = -1$, singular elements were used at the crack tip to resolve K . The computation is based on the FEM using the linear elasticity theory for the plane-strain problem. The eight-

node isoparametric quadratic elements are employed. K was also calculated by FEM when ultrasonic specimen are use for conventional fatigue [8].

Computer Control

The stress intensity factor of the specimen was obtain by measuring the displacement amplitude at the extremity of sample. The voltage that the high frequency generator applied to the transducer ceramic sets the displacement amplitude. To avoid any sensor, we have developed a computer system which control the tension using a D/A and A/D card. In the generator, a DC tension output has been set up giving 0 to 10 volts response corresponding strictly proportional to 0 to 100% of axial amplitude displacement of the transducer.

This output is calibrated with the displacement of the horn end by a optical displacement amplitude measurement system. This sensor enables to evaluate the maximum stress and strain value at the middle of a virgin specimen (without crack). This maximum strain value is checked and confirmed to be exact, using an electric strain gauge during tests.

The displacement amplitude control by computer was more reproducible and permit test even when it is impossible to measure directly the displacement amplitude (cryogenic endurance test for example).

The displacement amplitude for certain specimens can be modified not only by changing output power but also by replacing the horn (Figure 2).

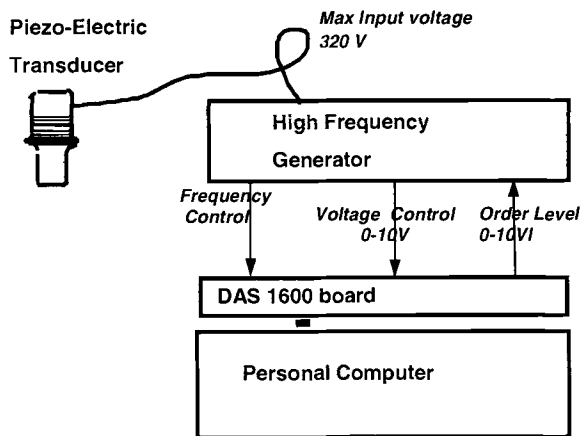


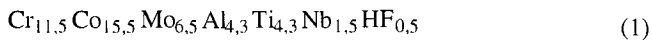
Figure 2 – Schematic of Amplitude Control by Computer

Fatigue of Alloys with Inclusions

Fatigue of PM Nickel Base Alloys (N18)

In order to study the application of ΔK thresholds to the initiation of fatigue crack from defects, we have chosen a nickel base alloy (N18) with and without seeding of inclusions to reveal the role of inclusions in the gigacycle domain [9].

The chemical composition of N18 nickel base alloy is:



The principal mechanical properties are:

$$\sigma_y = 1050 \text{ MPa} \quad \text{UTS} = 1500 \text{ MPa}$$

In order to reveal the effect of defects, a pollution with ceramic inclusions (80 to 150 μm diameter) was made, using 30 000 inclusions for 1 kilogram of alloy. A comparison is done between N 18 alloy with and without inclusions. Nevertheless, it is observed that when the rate of ceramic particles increases, the porosity is also increased, that is to say, a competition exists between particles and pores for crack nucleation.

Fatigue Crack Growth of N18 Alloy

Figure 3 presents the results at high frequency to $R = -1$. We could see that the threshold is smaller at high temperature than at ambient temperature. Normally we could wait a fall of threshold with the increase of the temperature. But in Figure 3 the threshold is smaller at 400°C than at 650°C and 750°C. The curves at 400°C, 650°C and 750°C cut the vicinities 10^{-5} mm/cycle. The observed gaps are explained by the phenomenon of oxidization to the bottom of the crack. On the crack surface of the sample used in our tests, the oxidization at 650°C and at 750°C was observed. At high temperature, normally propagation crack rate increases with the temperature. But the oxidization could slow down propagation to the neighborhood threshold to a small load when the temperature is rather elevated.

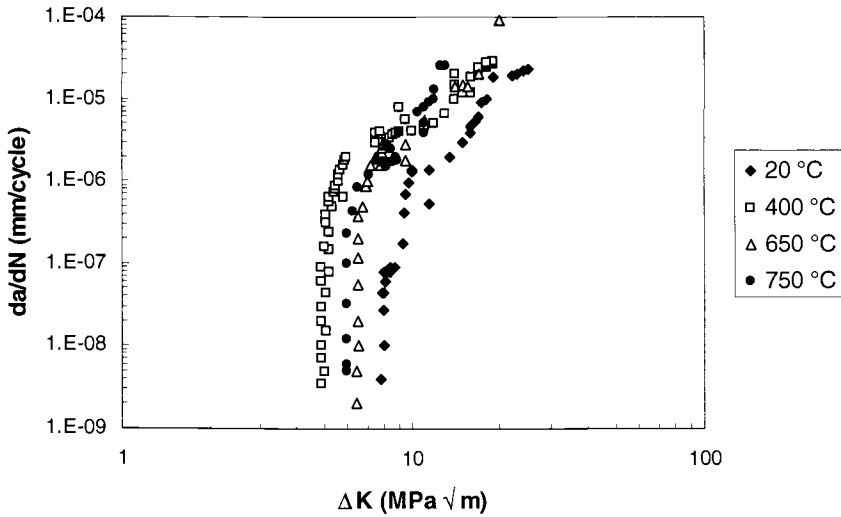


Figure 3 – Fatigue Threshold for N18 at $R = -1$

At 450°C, the effect of R ratio is given in Figure 4. We found that the ΔK thresholds for $R = -1$, $R = 0$, $R = 0.8$ are respectively 5.5 $\text{MPa}\sqrt{\text{m}}$, 8 and 4.5.

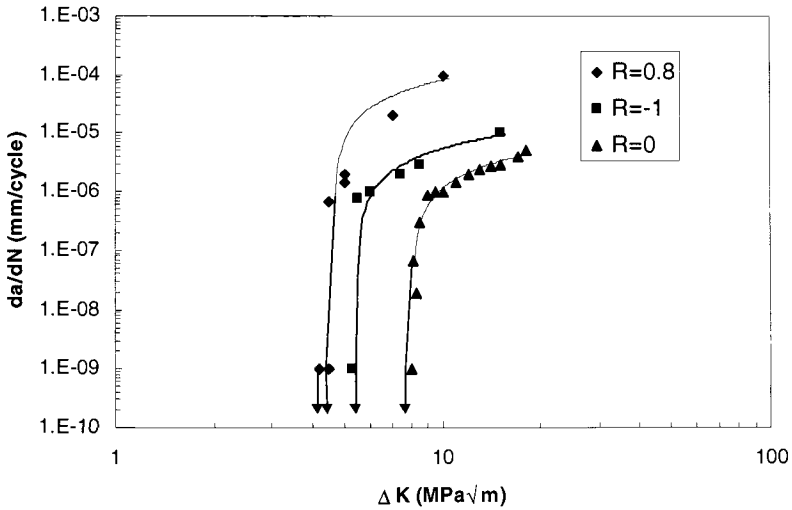


Figure 4 – Fatigue Threshold for N18 at 450°C

but in presence of inclusions the fatigue limit can drop until 400 MPa. Initiation small pores can not be attributed to the absence of other defect because ceramic inclusions have been observed on the surface and inside this sample. No crack nucleation at the surface ceramic inclusions can be observed after the fatigue test.

A surface artificial defect of 100 μm diameter comparable at inclusion size, makes by an electrical arc, generates a fatigue life shorter than a natural defect (only 1% of usual fatigue life). This fact could indicate that incubation phase was important in the case of natural porosities.

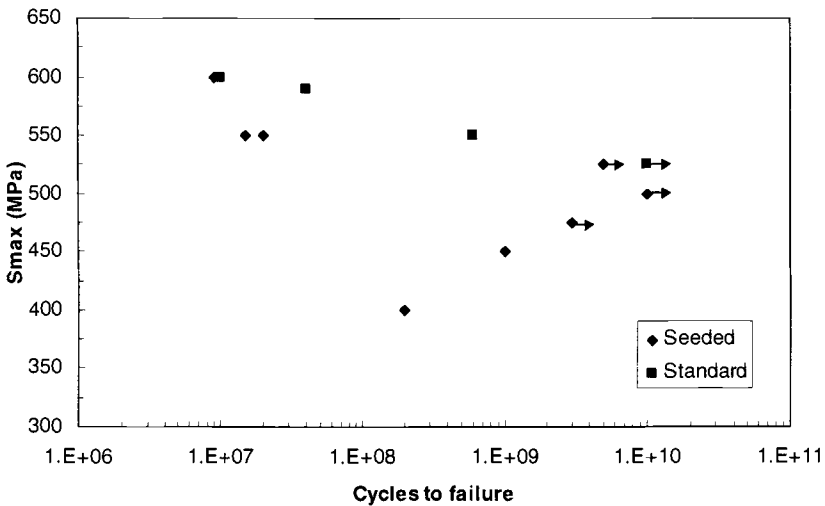


Figure 6 – SN Curves for N18 at R = -1 and 450°C

Gigacycle Fatigue of N18 at 450°C with R Ratio Equal to 0

The curve of standard and polluted N18 with R = 0 are shown Figure 5. Initiation sites are mainly porosities for the standard N18 and ceramics inclusions for polluted material inside the sample and not on surface (Figure 7). The data scattering for seeded material is higher than standard because of the size, shape and interfaces with matrix of porosities are more constant than inclusions. But it is outstanding that fatigue limits are not so different (540 MPa for standard material and 520 MPa for seeded one) although that the average size of porosities and inclusions are quite different (23 μm for standard and 98 μm for seeded).

We also observe that for standard SN curve, the fatigue limit at 10⁹ cycles is 75 MPa lower than fatigue limit a 10⁷ cycles.

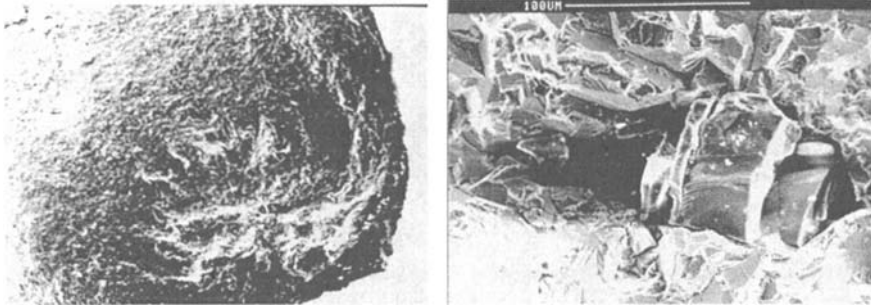


Figure 7 – Fatigue crack initiation on inclusion
 $N=9.7 \cdot 10^7$ - $1/2\sigma=260\text{MPa}$
 $R=0$ - 450°C
N18 seeded - $f=20\text{kHz}$

Gigacycle Fatigue of N18 at 450°C with R Ratio Equal to 0.8

In this case all initiation sites are internal but the SN curves of standard and polluted materials are clearly different (Figure 5).

The fatigue limit of seeded material is 25 MPa lower than standard material (125 MPa for standard and 150 MPa for seeded). A large mean stress value increases the ceramic inclusion nocivity.

Modeling of the Gigacyclic Fatigue and Discussion

Initiation Zones at 10^9 Cycles - In specialized literature, few results are given on this topic. According to our own observations and those of Murakami [10], the gigacyclic fatigue crack initiation seems to occur essentially inside the sample and not at the surface as it is observed for some shorter life.

So we can modelize three types of crack initiation in a cylindrical sample of which the surface was polished depending on whether it is low (10^4 cycles), megacyclic (10^6 cycles) or gigacyclic (10^9 cycles) fatigue. Let's say that for the smallest numbers of cycles to rupture, the crack initiation sites are multiple and on the surface, according to the standard, at 10^6 cycles, there is only one initiation site but, for the higher number of cycles to rupture, the initiation is located at an internal zone.

Integration of the da/dn Curve - Considering $da/dn = C \Delta K^m$ and $\Delta K = (\pi/2) \Delta\sigma \sqrt{\pi a}$ where $\Delta\sigma$ is the fatigue limit at 10^9 cycles for a given R ratio and a is the maximum size of the radius of the internal propagation. We compute the initial value of ΔK at the tip of the inclusion or at the pore. The average ΔK initial is given below:

R ratio	ΔK_{th}	ΔK_i particle MPa \sqrt{m}	ΔK_i pore MPa \sqrt{m}
-1	5.5	8.5	6
0	8	12	6.25
0,8	4.5	6.7	3.3

Concerning the particles, for a given ΔK_i the crack growth rate is always higher than 10^{-6} mm/cycle. It means the fatigue life of the specimens should be less than 10^6 cycles instead of 10^9 cycles. Thus, it is not realistic to say the crack grows as soon as the first cycle is applied. A nucleation time is operating.

Concerning the pores, ΔK_i is smaller than ΔK_{th} for the same R ratio, but ΔK_{th} is determined in air and for a long crack. In vacuum ΔK_{th} is higher than in air. In this respect, it is reasonable to think the crack initiates without nucleation from a pore.

Prediction of Fatigue Limit at 10^9 Cycles - Murakami [10] has proposed a fatigue model to predict the fatigue limit of steels depending of hardness and defect size.

According Murakami [10], it seems the fatigue strength at 10^9 cycles can be predicted using his model with few modifications. From the present data we have verified this relation :

$$\sigma_w = \frac{C \cdot (Hv + 120)}{(\sqrt{area})^{1/6}} \cdot \left[\frac{(1 - R^3)^\alpha}{2} \right]$$

where :

C = 1.78 for internal and external defects

Hv : Vickers hardness

\sqrt{area} : Defect surface

σ_w : MPa

R : Load ratio

α : $0.878 + Hv \cdot 10^{-4}$

α : $0.878 + Hv \cdot 10^{-4}$

Table 1 - Application of Murakami Model to N18 Alloy

R	-1	-1	0	0	0,8	0,8
Defect	Mixed	Inclusion	Porosity	Inclusion	Porosity	Inclusion
Localisation	Surface	Internal	Internal	Internal	Internal	Internal
\sqrt{area} (μm)	50	100	25	100	25	100
σ_w (MPa)	524	466	309	246	160	126
σ experimental (MPa)	525	400	280	270	160	130
Error %	0	+14	0	-9	0	-3

Comparing the effect of inclusions and porosities, it is interesting to point out the following:

The role of the inclusions is sometimes hidden by the role of porosities when the R load ratio is equal to -1 or to 0. The scattering of the results for R = 0 in a N18 polluted of inclusions is very important. Since for a N18 standard, the scattering is low.

It is very remarkable that when R = 0 or R = -1, the resistance to the gigacyclic fatigue at 450°C is 250 MPa in the N18 with or without inclusions.

On the contrary, when the static stress of the fatigue cycle is very high, for R = 0,8, the role of inclusions becomes preponderant. Without inclusions, the N18 fatigue limit, at 450 °C, is 155 MPa at 10⁹ cycles. However, it is 125 MPa with inclusions. This is the case of damage done by the vibrations on the turbine disks.

For a rough application, it seems better to use Murakami approach than a short crack growth modeling.

Spring steels - Two kinds of ultrahigh strength spring steel wires for automotive use were tested in this study [11]: a Chromium-Vanadium steel of valve spring quality (VSQ) (ASTM A232) and a Chromium-Silicon steel VSQ wire (ASTM A877), which were supplied in the form of normalized hot-coiled 6.5 mm diameter wire. The Cr-V and Cr-Si spring wires are suitable for shock loads and moderately elevated temperature service, the latter has better relaxation resistance than the Cr-V alloy steel and can be used at temperatures as high as 245°C. The chemical composition (in wt%) and tensile properties of the materials were listed in Tables 2 and 3 respectively.

The fatigue strength was determined in the life range of 10⁶ - 10⁹ cycles as shown in Figures 8 and 9.

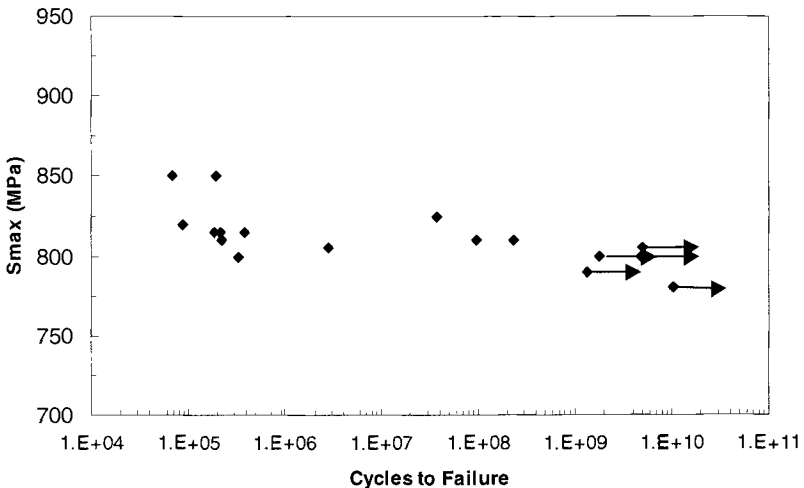


Figure 8 – SN Curve for the Steel 60 CV2 at R = -1

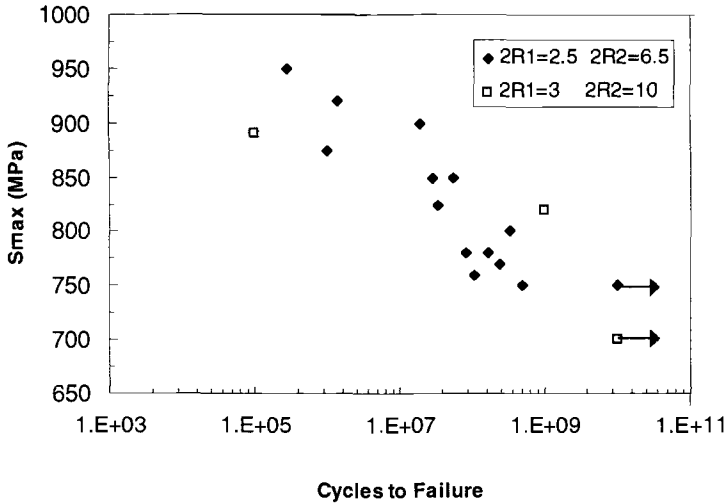


Figure 9 – SN curve for the Steel 55SC7 at R = -1

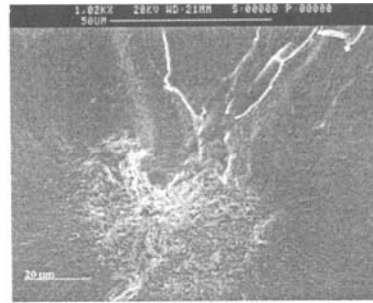
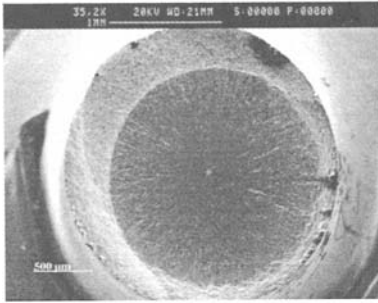
The experimental results show that fatigue fracture can occur in the high strength steel wires beyond 10^7 cycles. The fatigue strength at 10^7 cycles is 860 MPa for Cr-Si steel, better than 810 MPa for Cr-V steel. Instead, at 10^9 cycles is about 800 MPa for Cr-V steel, and better than 770 MPa for Cr-Si steel.

Two typical S-N curves are obtained, for Cr-V steel, the S-N curve becomes horizontal beyond 10^6 cycles at a limiting stress (about 800 MPa), known as fatigue limit, and the S-N curve of Cr-Si steel does not generally exhibit a horizontal asymptote beyond 10^6 cycles as it was admit according to the standard. Fatigue crack initiations were observed in internal defects (Figure 10), in the case of fatigue life is beyond 10^7 cycles. On the other hand, the fatigue initiation occurs in the surface.

Depending of the transition between the two operating mechanisms a stepwise S-N curve can appear with a plateau at $10^6 - 10^7$ cycles. This type of behavior is reported in the literature by K. Miller and S. Nishijima [12].

Table 2 Chemical composition

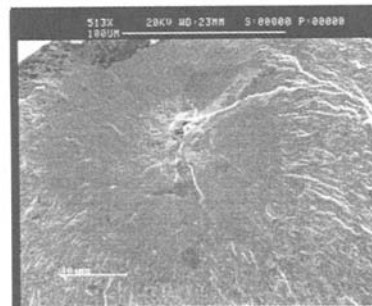
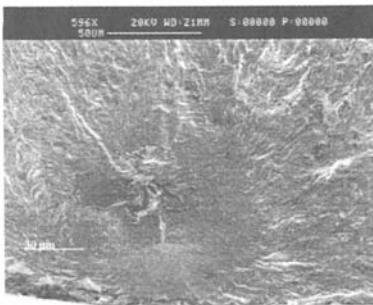
Alloy	C	Si	Cr	V	Mn	S	P	Ni
60CV2	0.48-0.53	0.1-0.4	0.8-1.1	0.15min	0.7-1.0	0.04max	0.035max	
55SC7	0.51-0.58	1.2-1.6	0.6-0.8		0.6-0.8	0.04max	0.035max	
54SC6	0.535	1.400	0.635		0.629	0.016	0.006	0.056



Specimen: Cr-Si Spring Steel Wire
N°1

$\sqrt{a_{area}} = 38 \mu\text{m}$, $h = 1150\mu\text{m}$,
 $a_i = 150\mu\text{m}$

$a_c = 900\mu\text{m}$, $S_{max} = 800 \text{ MPa}$, $R = -1$, $N_f = 3.3 \times 10^8$ cycles, $N_i/N_f = 99.91\%$



Specimen: Cr-Si Spring Wire N°13

$\sqrt{a_{area}} = 46 \mu\text{m}$, $h = 60 \mu\text{m}$

$a_i = 50\mu\text{m}$, $a_c = 1250\mu\text{m}$

$S_{max} = 760 \text{ MPa}$, $R = -1$, $N_f = 1.1 \times 10^8$

Specimen: Cr-Si Spring Wire N°16

$\sqrt{a_{area}} = 22 \mu\text{m}$, $h = 75 \mu\text{m}$

$a_i = 60\mu\text{m}$, $a_c = 1410\mu\text{m}$

$S_{max} = 875 \text{ MPa}$, $R = -1$, $N_f = 6.6 \times 10^7$

Figure 10 – Internal Initiation on Spring Steel

Our experimental and analytical techniques show the portion of fatigue life attributed to crack nucleation is higher than 99% N_f when N_f is 10^8 cycles.

An other example with a stepwise S-N curve is given for 4142 steels.

Gigacycle Fatigue of 4142 Steels - For this investigation, a kind of low alloy high strength steel (42CrMo4 or 4142) was used. Four different 42CrMo4 steel specimens, characterized by two compositions viz S - 0.024 wt% for 42CrMo4U, S - 0.087 wt% for 42CrMo4R (shown in Table 4) and two tempering temperatures 600°C for reception B and 425°C for reception C (shown in Table 5), were provided. In Table 6 the mechanical properties of the four 42CrMo4 steels are given.

Table 4 - Chemical Composition (%)

	C	Mn	P	S	Si	Al	Ni	Cr	Cu	Mo
42CrMo4U	0.428	0.827	0.012	0.024	0.254	0.023	0.173	1.026	0.210	0.224
42CrMo4R	0.412	0.836	0.015	0.087	0.242	0.023	0.186	1.032	0.209	0.164

Table 5 - Heat Treatment

	Heat treatment
Rep B	Austenitization : 950°C ; Oil quenching; Temper : 600°C
Rep C	Austénitisation : 950°C ; Oil quenching; Temper : 425°C

The high strength steels were tested in ultrasonic fatigue tests ($f = 20\text{KHz}$) with a stress ratio $R = -1$ under load control. The specimens were polished by grinding using # 500, 1200, 2400, 4000 papers. All experiments were performed at ambient temperature. During testing, the middle section of the specimen was cooled by compressed air and the temperature was controlled at about 70°C. The fatigue strength was determined in the life range of $10^6 - 10^9$ cycles as shown in Figure 11.

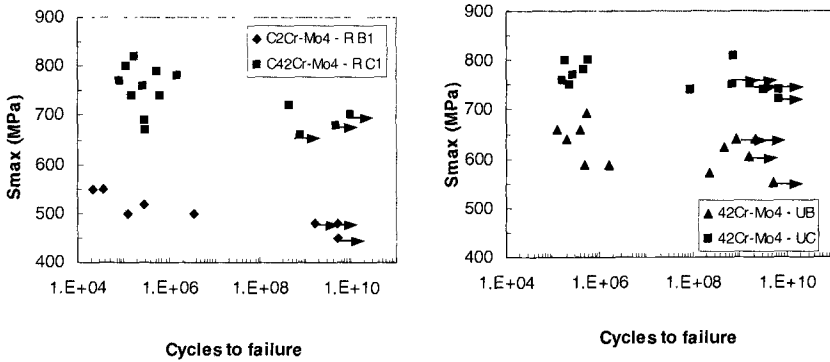


Figure 11 - S-N Curve for the 42CrMo4 Steels $R = -1$

The experimental results show that fatigue rupture can occur in the high strength steels over 10^7 cycles. The S-N curve of Cr-Mo steel does not generally exhibit a horizontal asymptote beyond 10^6 cycles as it was admitted according to the standard. Fatigue crack initiations were observed on internal defects, in the case of fatigue life is beyond 10^7 cycles. A stepwise curve is well defined in this case, depending of two nucleation mechanisms.

Fracture surfaces were observed after testing by SEM. The stages of crack initiation, stable crack propagation, unstable crack propagation and final failure are well defined. In the high cycle range regime ($> 10^7$ cycles), the initiation sites were founded at nonmetallic inclusions located in the interior of the specimen as far as 900 μm . The origin was identified by the use of energy dispersive analysis, the typical

composition of the inclusion is sulfide. In the low cycle range regime ($< 10^7$ cycles), the initiation sites were found at surface.

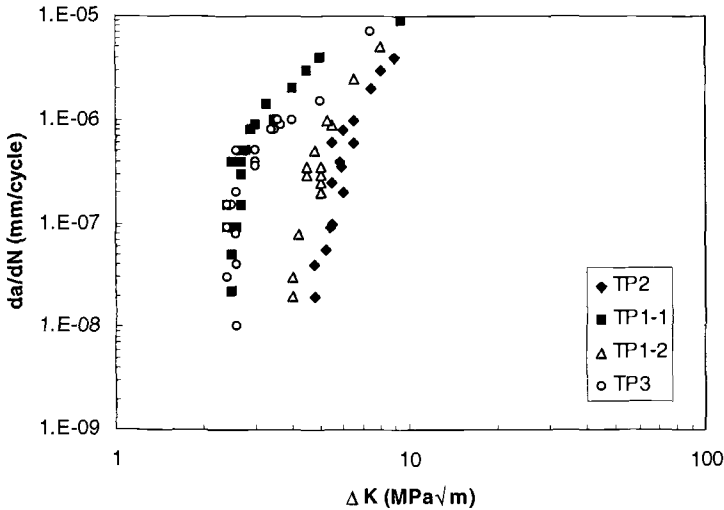


Figure 12 – Fatigue Threshold of Ti6246 in Function of Thermal Processing Conditions $R = -1$

Fatigue of Alloys Without Inclusion

What does happen in alloys without inclusion in the gigacycle fatigue regime?

To answer this question, titanium alloys were tested in crack propagation and in crack initiation. It is well known that in titanium alloys there is not any inclusion or porosity. In this condition, nucleation of fatigue crack cannot nucleate from defects.

Fatigue Threshold of Ti Alloys

The Ti-6.2.4.6 alloy was supplied by the RMI Company: the chemical composition is shown in Table 6. Four Thermomechanical Processes (TP) routes (TP1(1) TP1(2) TP2 and TP3) were used to produce the forgings with different microstructures and

attendant mechanical properties (Table 7). The β -processed microstructures present similar lamellar α -phase morphology with different primary α volume fraction and grain size in a transformed β matrix. The $\alpha+\beta$ process conduces to a bi-modal structure with duplex lamellar and globular primary alpha phase.

Table 6 - Chemical Composition of Ti-6.2.4.6. Alloy Investigated (in wt%)

TP number	Al	Sn	Zr	Mo	C ppm	Cu ppm	Si ppm	Fe ppm	O ₂ ppm	H ₂ ppm	N ₂ ppm
1(1)	5.68	1.98	3.96	6.25	90	<50	<50	400	930	44	80
1(2); 2 & 3	5.70	2.04	4.08	6.43	83	<50	<50	300	1100	28	70

Table 7 - TP Routes Variables and Associated Microstructures

T.P. Number	Forging condition	Thermal treatment	Final microstructure type
1(1) and 1(2)	955°C/WQ ¹ (Tβ + 10°C)	935°C/2H/WQ + 905°C/1H/Air + 595°C/8H/Air	α platelets and β-transformed matrix
2	955°C/WQ (Tβ + 10°C)	935°C/2H/Slow Cool. --> Room T. + 595°C/8H/Air	coarse α platelets and β-transformed matrix
3	905°C/Air (Tβ - 40°C)	935°C/2H/WQ + 905°C/1H/Air + 595°C/8H/Air	bi-modal structure (α platelets and α nodular) and β-transformed matrix

¹Water Quench

Quantification of the morphological aspects has been performed to provide a complete description of various microstructures. Two orthogonal metallographic surfaces were examined, the number of detected whole particles being more than 2000. A global image analysis was used to measure primary α-phase volume fraction (f_{αP}), total α-phase volume fraction (f_{αT}), thickness of primary alpha platelets (d_{αP}) and mode distance between coarser particles (d_β). Sizing and shape measurements were performed in individual analyses way. This procedure provides, for example, the perimeter (P_{αP}), the area (S_{αP}) and the longest dimension (L_{αP}) of each particle.

For the low crack growth rate, an effect of microstructure has been found on the threshold. The results given in the Figure 12 show that the fatigue threshold is higher for coarse lamellar microstructure than for fine globular microstructure (TP 3). Quantitative microstructure fractures are given in the Table 8.

Table 3 Mechanical properties

Alloy	UTS MPa	E Gpa	ρ Kg/m ³	A %	HV
60CV2	1800	210	7850		435
55SC7	1800	210	7850	35	500
55SC7-TT2	1800	210	7850	35	590
54SC6	1692	210	7850		510

Table 8 - Image Analysis Results for the Four TP Microstructures

TP Condition	$f_{\alpha P}$		$f_{\alpha S}$		$d_{\alpha P}$		d_{β}		$P_{\alpha P}/S_{\alpha P}$	
	lam	glob	lam	glob	lam	glob	lam	glob	lam	glob
		%	%		μm		μm		μm^{-1}	
1(1)	54		13		1.7		0.8		2.9	
Axial view	± 2		± 4		± 0.2		± 0.2		± 0.9	
1(1)	37		15.8		1.7		2.5		2.6	
Radial view	± 2		± 4		± 0.2		± 0.2		± 0.8	
1(1)	42		14.8		1.7		1.9		2.7	
Volume	± 4		± 8		± 0.4		± 0.4		± 1.7	
1(2)	43.9		14.1		1.9		2.4		2.2	
	± 4		± 8		± 0.4		± 0.4		± 1.5	
2	66.2		7.3		2.2		0.74		1.7	
	± 4		± 8		± 0.4		± 0.4		± 1.6	
3	20	27.3	20		1.0	3.1	1.6	4.3	1.16	4.5
	± 4	± 4	± 8		± 0.4	± 0.4	± 0.4	± 0.4	± 0.8	± 3.2

Fatigue Initiation of Ti Alloys

With the same alloys it is found that crack initiation and fatigue can occur up to 10^9 cycles in spite there is not any inclusion or pore. Figure 13 presents SN curves depending on the thermal processing.

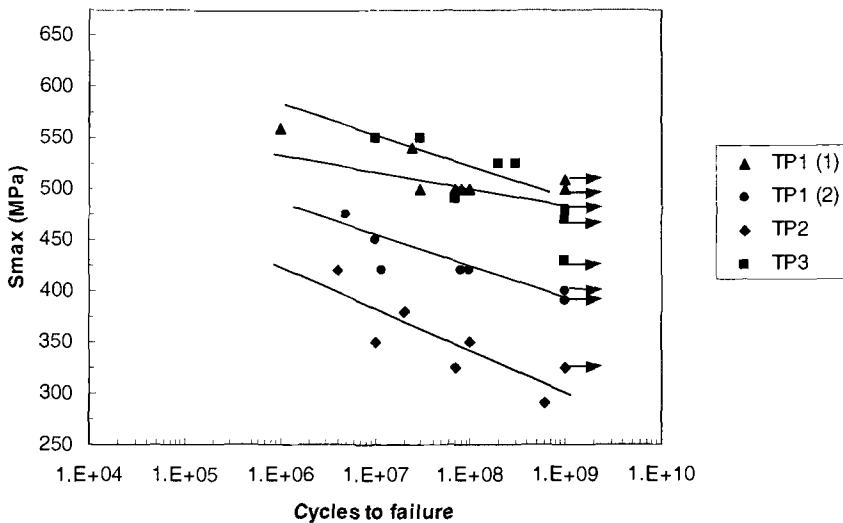


Figure 13 - Gigacycle SN Curve for Ti 6246 at 300 K and R = -1

At room temperature, a significant difference can be observed in S-N curves between the different TP conditions. Thus, the TP3 material have comparatively the best fatigue resistance (510MPa), the TP1(1) and TP1(2) materials exhibit a lower response with a fatigue-limit estimated respectively at 490MPa and 400MPa for 10^9 cycles and TP2 material has the worse fatigue-limit resistance with only 325MPa.

We must notice the TP3 alloy gives the lowest ΔK threshold and the best fatigue limit.

The SEM fractographic observations indicate than all the TP1(1) broken samples have systematic surface initiation (less than $40\mu\text{m}$ of the external surface) whereas TP1(2), TP2 and TP3 have systematic internal fatigue crack site. Internal initiation sites were identified by tracking back along the fracture surface markings which radiated from the point of origin. In TP2 conditions, microstructure and more particularly colonies of primary alpha phase (αp) is showing through the fracture surface by backscattered electrons observations and form a sort of facet (Figure 12). It can be seen that the facets are oriented to the fracture plane: a feature common to all samples specimen. In the duplex structure and mainly at low temperature, fracture initiate on coarse globular primary alpha phase (Figure 14).

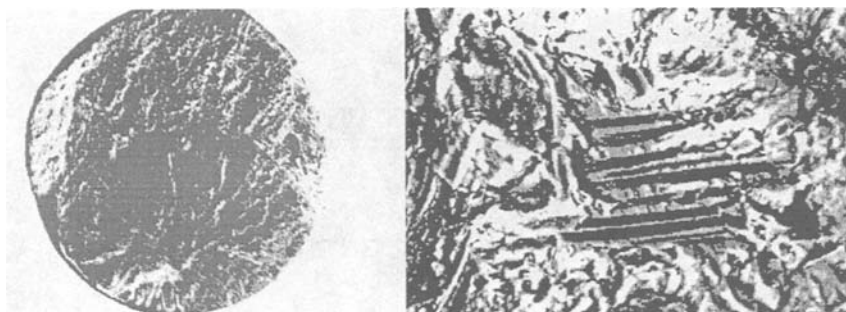


Figure 14 – *Fatigue Crack Initiation on α Primary Phase*

In conclusion, it is emphasised that gigacycle fatigue regime is not always correlated at defects such as inclusions or pores. For Ti 6246, the gigacycle fatigue limit is associated with transformed amount and secondary alpha volume fraction. Internal fatigue initiation with quasi-cleavage facets in primary alpha phase has been shows.

In this conditions, it is very difficult to get a general relation between ΔK_{th} and $\Delta\sigma_D$. A nucleation process must exist.

General Discussion of the Gigacyclic Fatigue

Initiation Zones at 10^9 Cycles

In specialized literature, few results are given on this topic [1]. According to our own observations and those of Murakami [10], the gigacyclic fatigue crack initiation seems to occur essentially inside the sample and not at the surface as it is observed for some shorter life.

So we can modelize three types of crack initiation in a cylindrical sample with polished surface depending on whether it is low cycle (10^4 cycles), megacyclic (10^6 cycles) or gigacyclic (10^9 cycles) fatigue. For the smallest numbers of cycles to rupture, the crack initiation sites are multiple and on the surface, according to the general opinion, at 10^6 cycles, there is only one initiation site but, for the higher number of cycles to rupture, the initiation is located at an internal zone. What remains is to specify how and why some fatigue cracks can initiate inside the metal in gigacyclic fatigue.

Initiation Mechanisms at 10^9 Cycles

The explanation of the phenomenon is not obvious. It seems that the cyclic plastic deformation in plane stress condition becomes very small in the gigacyclic regime. In this case, internal defects or large grain size play a role, in competition with surface damage. It means also the effect of environment is quite small in the gigacyclic regime since the initiation of short cracks is inside the specimen. Thus, the surface plays a minor role if it is smooth. The effect of plane stress plasticity is evanescent compared to microplasticity due to defects or microstructure misfits. It means that internal initiation is correlated with stress concentration or load transfer.

Role of the Inclusions - The inclusions can be some privileged crack initiation sites, especially if the R load ratio is high. Figure 7 presents an example of the N18 alloys. If the crack initiates from an inclusion or from a pore, it seems a relation between ΔK_{th} and σ_D at 10^9 cycles can exist. But it is not a general relation.

Role of the Porosities - The porosities can initiate crack in competition with inclusions, so much that the load ratio is low, particularly in tension compression.

Role of the Grains Size - In titanium alloys, the inclusions and the porosities are not important. They are only grain anomalies which initiate cracks. In the T6A4V and 6246 alloys, the internal initiation often occurs near long primary α platelettes. Nevertheless, the secondary phase seems to play a role also important in the resistance at gigacyclic fatigue enhancing more or less the $\alpha P/b$ platelette cracking [5]. The important influence of the microstructure on the fatigue resistance at a high

number of cycles has already been mentioned in the above paragraph. In this case, the relation between ΔK_{th} and σ_D is difficult to justify.

Conclusions

Experimentally we have shown that beyond 10^7 cycles, fatigue rupture can occur in a large number of alloy. In some cases, the difference of fatigue resistance can decrease by 100, even 200 MPa, between 10^6 and 10^9 cycles. According to our observations, the concept of infinite fatigue life on an asymptotic SN curve is not correct. Under these conditions, the fatigue limit defined with a statistical analysis between 10^6 and 10^7 cycles cannot guarantee an infinite fatigue life. In the range of gigacycle fatigue a piezo-electric fatigue machine has been used at 20 KHz.

Assuming that the fatigue life of machines, such as engines are ranging about 10^8 cycles, it is very interesting to determine a safe fatigue limit for 10^9 cycles. From a practical point of view, the only way is piezo-electric fatigue machine. A relation between ΔK_{th} and $\Delta\sigma_D$ is not general.

The very high fatigue life, called gigacyclic, requires more attention for the choice of the alloys or for the prediction of endurance. An approach based ΔK_{th} and that crack concept is not safe because an incubation nucleation process is often operating.

Reference:

- [1] S. Stanzl-Tschegg, "Ultrasonic Fatigue", *Fatigue 96* - pp 1886-1887, 1996
- [2] J.M. Wells, "Ultrasonic Fatigue" *AIME* - ISBN member 0-89520-397-9, 1982
- [3] C. Bathias, "A review of fatigue of Aluminum" Matrix Reinforced by Particules and Short Fibers *Sciences Forum* 217-222, 1407 - 1412, 1996
- [4] J. Ni, "Mechanical behavior of alloys in ultrasonic fatigue" *Thèse de doctorat* CNAM, 1991
- [5] G. Jago "Relation between microstructure and properties in Ti alloys" *Thèse de doctorat*- CNAM, 1996
- [6] H. Tao, "Ultrasonic fatigue of Ti and alloys at cryogenic temperature" *Thèse de doctorat* , CNAM (1996)
- [7] Mason, W.P "Piezoelectric crystals and their applications" *ultrasonics*, pp 161-164, 1950
- [8] T. Wu and C. Bathias., "Application of fracture mechanics concept in ultrasonic fatigue" *Engng. Fract. Mech.*, Vol. 47, No 5, pp 683-690, 1994.
- [9] J. Bonis, *Thèse de doctorat*, Univ. Paris-Sud, 1997
- [10] Y. Murakami and M. Endo., "Effects of defects, inclusions and inhomogeneities on fatigue strength", *Fatigue*, Vol. 16, 163-182, 1994
- [11] Q. Wang, *Thèse de doctorat*, CNAM (1998)
- [12] Euromech 382 on gigacycle fatigue, To be published by *FFEMS on may 1999*, Paris, 1-2 July 1998

K. R. Garr¹ and G. C. Hresko, III²

A Size Effect on the Fatigue Crack Growth Rate Threshold of Alloy 718

Reference: Garr, K. R., and Hresko, G. C., III, "A Size Effect on the Fatigue Crack Growth Rate Threshold of Alloy 718," *Fatigue Crack Growth Thresholds, Endurance Limits, and Design*, ASTM STP 1372, J. C. Newman, Jr. and R. S. Piascik, Eds., American Society for Testing and Materials, West Conshohocken, PA, 2000.

Abstract: Fatigue crack growth rate (FCGR) tests were conducted on Nickel-based superalloy 718 in the solution annealed and aged condition at room temperature. In each test, the FCGR threshold was measured using the K-decreasing constant R method. Initial testing was at two facilities, one of which used C(T) specimens with $W = 127$ mm. Previous data at the other facility had been obtained with specimens with $W = 50.8$ mm. A comparison of test results at $R = 0.1$ showed that the threshold for the 127 mm specimen was considerably higher than that of the 50.8 mm specimen. A check showed that this difference was not due to a heat-to-heat or lab-to-lab variation. Additional tests were conducted on specimens with $W = 25.4$ mm and at other R values. Data for the various specimens is presented along with parameters usually used to describe threshold behavior.

Keywords: Alloy 718, crack propagation, crack closure, specimen size effect, fatigue crack growth rate threshold, Biaxiality ratio, T stress, constraint

Introduction

Two test laboratories were used during the course of obtaining fatigue crack growth rate (FCGR) data on Nickel-based superalloy 718. Considerable testing had been conducted at one facility, laboratory A, on C(T) specimens with a width, $W = 50.8$ mm. The second laboratory, laboratory B, used a larger specimen, $W = 127$ mm.

The FCGR threshold at room temperature with $R = 0.1$ from laboratory B was considerably higher than the previous values obtained at laboratory A. A heat-to-heat

¹ Engineering Specialist, The Boeing Company, Rocketdyne Propulsion & Power, 6633 Canoga Ave., PO Box 7922, Canoga Park, CA 91309-7922.

² Associated with Fracture Systems Research, 3135 Essex Road, Allentown, PA 18103.

variation was ruled out as the data at laboratory A agreed with data from a different heat of Alloy 718 previously tested at that facility. To check out the potential for a laboratory variation, specimens were exchanged between the two facilities. The results from each of these tests agreed with the earlier data based on specimen size. Thus, the disparity in FCGR thresholds could not be attributed to either a heat-to-heat or laboratory variation. Further tests were conducted on specimens with $W = 25.4$ mm at $R = 0.1$ and at 0.7 . The report presented here gives the results of the tests conducted at laboratory A on different size specimens at room temperature with additional data from an earlier test series using the same heat of material tested at R values from 0.1 to 0.9 .

Material

The material tested was Nickel-based superalloy 718 with composition as shown in Table 1. All specimens were of the C(T) configuration with varying width, W , machined from 12.7 mm plate. The plate was milled down to the final thickness and the specimens electric-discharge machined to the final planer dimensions with the crack oriented in the T-L direction. The thickness varied slightly. Specimens originally fabricated for laboratory A were roughly 7.6 mm thick while those for laboratory B were about 9.4 mm.

Table 1 – Alloy 718 Composition (wt %)

C	Mo	Cr	Ni + Co	Ti	Al	Nb + Ta	Co
0.050	2.98	18.26	53.40	1.00	0.48	5.10	<0.10

After fabrication, the specimens were given a solution anneal and age heat treatment as follows: solution annealed at 1038 °C for 10 min to 30 min in Argon, followed by an air cool to room temperature. They were then aged at 760 °C for 10 h, then furnace cooled to 649 °C and held at that temperature until the total aging plus furnace cooling time was equal to 20 h. The average room temperature mechanical properties are: yield strength = 1071.4 MPa, ultimate tensile strength = 1330.7 MPa, elongation = 24 %, and RA = 37.3 %. The grain size taken on specimen 5W1 was ASTM 2.5.

Experimental Procedure

The FCGR testing methodology used was in accordance with ASTM Test Method for Measurement of Fatigue Crack Growth Rates (E647-88) except for the pin and clevis arrangement. The 50.8 mm specimens had a 12.7 mm OD metal bushing inserted in the pin hole with a 9.53 mm diameter pin. The hole in the clevis was standard size, $W/4$, but did not have a flat bottom; thus, the clevis hole is oversize for this pin. The

25.4 mm specimens had a similar arrangement. The 127 mm specimen used a 25.4 mm diameter pin in a needle roller bearing.

All tests were conducted at room temperature on C(T) specimens with W equal to 25.4 mm, 50.8 mm, and 127 mm. These will be referred to as 1W, 2W, and 5W, respectively, as these represent the relative size variation. Specimens 1W1, 1W2, 1W3, 1W4, 2W1, and 2W5 were electric-discharge machined from the tested halves of specimen 5W1.

Fatigue precracking was performed on all specimens. With one exception, precrack growth rates for tests conducted at or below $R = 0.7$ were less than 10^{-5} mm/cy. Although specimen 2W6, tested at $R = 0.7$, had a maximum crack growth rate of 1.52×10^{-5} mm/cy, the crack growth rate was below 10^{-5} mm/cy for the last 1.65 mm of precracking. Specimens tested at $R = 0.8$ and 0.9 had crack growth rates above 10^{-5} mm/cy in the initial portion of the precracking. The crack growth rate was below 10^{-5} mm/cy for at least the last 1.52 mm.

A closed-loop servo-hydraulic machine was used for all tests. Frequencies in the threshold region were in the range of 100 Hz to 150 Hz. The threshold segment was performed using the automated K-decreasing constant R test procedures [1,2]. Generally, the threshold portion was terminated when the crack growth rate was 1×10^{-8} mm/cycle or lower, or the crack showed no further growth after cycling for 12 h to 24 h, indicating that the crack had arrested. This was followed by a K-increasing procedure for verification and to obtain growth rates at higher ΔK 's. In some tests a second decreasing ΔK segment was conducted.

Crack length was measured by Direct Current Potential Drop (DCPD). The current leads were placed at the midpoint of the specimen width, W. The potential leads were on the front face, positioned across the specimen crack mouth. The crack length was related to the normalized change in potential difference by Johnson's equation [3]. All the data, except the closure measurements, were obtained digitally. After testing, the specimen was broken open and a visual measurement made of the final crack length. If the visual measurement differed from the DCPD value, the DCPD data were adjusted.

The signal cancellation technique was used to measure crack closure using a front face clip gage [4]. Frequency was reduced to the 20 to 30 Hz range and the clip gage attached to the specimen. Closure was determined using an oscilloscope. An analog conditioner modified the load and displacement signals to produce a nulled oscilloscope trace that displayed the distinct nonlinear behavior associated with crack closure. Through signal conditioning, the load displacement curve was made to be vertical. This nulled load versus displacement curve was then amplified and the signal monitored on an oscilloscope. Photographs of the oscilloscope trace were taken with a Polaroid SX 70 camera with automatic exposure. Crack closure levels were estimated from the photographs of the oscilloscope trace where deviation from the vertical occurred. See references [4-7] for discussions of the method. Typically, closure measurements are taken several times during a test. The load percentage corresponding to the closure point was entered into the analysis program with the corresponding electric potential value. The analysis program performed a least squares fit to all the closure data and linearly distributed the closure over the FCGR curve.

Crack length versus cycle data was reduced to da/dN data by the modified secant method. In this method, the Δa and ΔN increments are sequenced to every other data

point but incremented by each data point. Successive Δa increments overlap each other. The stress intensity range, ΔK , is calculated from the equation given in the standard using a crack length midway through the increment. The equations for da/dN and a_i are

$$(da/dN)_i = \frac{[a_{i+1} - a_{i-1}]}{[N_{i+1} - N_{i-1}]} \quad \text{and} \quad a_i = \frac{1}{2} [a_{i+1} + a_{i-1}] \quad (1)$$

where:

$(da/dN)_i$ = crack growth rate of the i^{th} increment

a_i = crack length midway through the increment

N_i = cycle number of the i^{th} increment.

Surface roughness measurements were made on several specimens using a Mitutoyo Surftest 402 instrument. Roughness was measured over a 0.762 mm stroke. The instrument was set on either the 10.2 or 50.8 μm range depending on the ability of the instrument to obtain a measurement. Most measurements were made using the 50.8 μm scale. Roughness average, defined as the arithmetical average of deviations from the center line, was measured. Two measurements were taken at each location and the average value used. Measurements were taken at various locations in the central region of the fracture surface with the instrument stroke parallel to the crack growth direction. The specimens were mounted on a movable table with a digital micrometer that was used to set the measurement position. The center of the stroke was used in calculating the roughness position.

Results and Discussion

The da/dN versus ΔK and ΔK effective curves for specimens tested at $R = 0.1$ and 0.7 are shown in figures 1a through 1d. The thresholds and other data are given in Table 2. As seen in Fig. 1a and in Table 2, the threshold varies with specimen width. Specimen 5W1 has a much higher threshold than the 1W and 2W specimens, outside the scatter the authors generally observed. More on this point later. A similar result is seen in Fig. 1b for tests at $R = 0.7$, except that the thresholds for the 1W and 2W specimens are essentially the same. Note, the decreasing portion of specimen 2W5 was terminated at the value shown without achieving arrest.

Figures 1c and 1d, show the same data plotted as a function of ΔK effective. In Fig. 1c, ΔK effective tends to reconcile the $R = 0.1$ data except near the lowest ΔK effective region. Note, the lowest point for 2W1 is below $1\text{MPa}\sqrt{\text{m}}$, see Table 2. Figure 1d shows the data for the $R = 0.7$ tests. Closure measurements were made on both the 1W

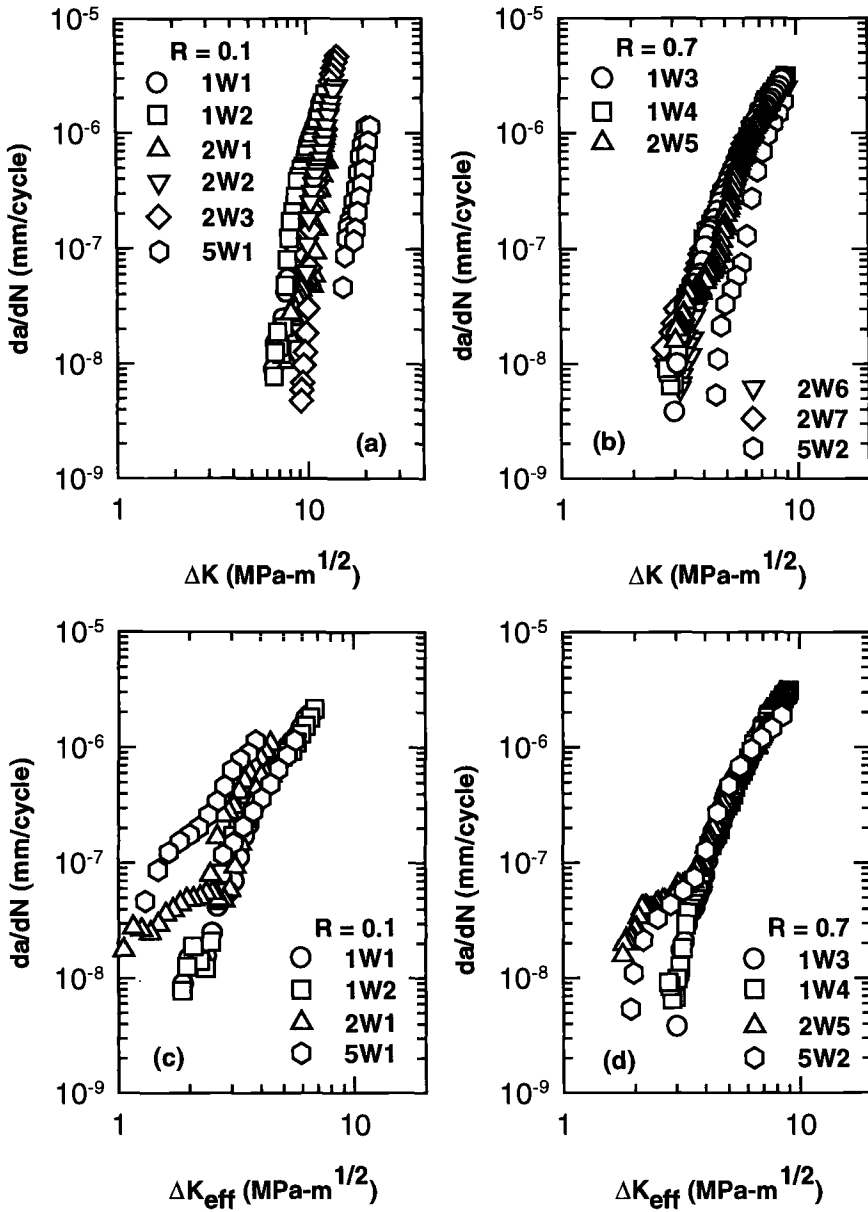


Figure 1 - (a) da/dN vs. ΔK for $R = 0.1$, (b) da/dN vs. ΔK for $R = 0.7$, (c) da/dN vs. ΔK effective for $R = 0.1$, (d) da/dN vs. ΔK effective for $R = 0.7$

Table 2 - Summary of Threshold Data

Specimen	Width (mm)	Thickness (mm)	R	Applied ΔK (th) (MPa·m ^{1/2})	da/dN at Threshold (mm/cy)	Effective ΔK (th) (MPa·m ^{1/2})	a at Threshold (mm)	a/W at Threshold	C (mm ⁻¹)
1W1	25.425	9.398	0.1	6.54	8.94 X 10 ⁻⁹	1.88	9.789	0.385	-0.20
1W2	25.349	9.423	0.1	6.56	7.80 X 10 ⁻⁹	1.86	9.708	0.383	-0.20
2W1	50.825	9.398	0.1	10.13	7.87 X 10 ⁻⁸	2.45	15.796	0.311	-0.08
2W1 (a)	50.825	9.398	0.1	7.79	1.04 X 10 ⁻⁸	0.97	25.842	0.508	-0.08
2W2	50.698	7.747	0.1	9.86	6.30 X 10 ⁻⁸		17.943	0.354	-0.08
2W3	50.698	7.823	0.1	9.13	4.78 X 10 ⁻⁹		18.636	0.368	-0.08
5W1	126.873	9.271	0.1	15.37	4.67 X 10 ⁻⁸	1.30	36.695	0.289	-0.08
5W1 (a)	126.873	9.271	0.1	17.72	1.18 X 10 ⁻⁷	2.78	45.095	0.355	-0.08
2W4	50.749	7.747	0.4	7.60	3.94 X 10 ⁻⁸		18.306	0.361	-0.08
2W4 (a)	50.749	7.747	0.4	6.05	2.43 X 10 ⁻⁸		27.658	0.545	-0.08
1W3	25.375	9.398	0.7	3.00	3.81 X 10 ⁻⁹	(b)	12.377	0.488	-0.20
1W4	25.425	9.423	0.7	2.78	9.14 X 10 ⁻⁹	(b)	14.059	0.553	-0.08
2W5 (c)	50.775	9.423	0.7	3.03	1.58 X 10 ⁻⁸	1.78	25.618	0.505	-0.08/-0.16
2W6	50.698	7.849	0.7	3.15	6.10 X 10 ⁻⁹		25.517	0.503	-0.08
2W7	50.724	7.823	0.7	2.69	1.38 X 10 ⁻⁸		26.861	0.530	-0.08
5W2	126.949	9.550	0.7	4.48	5.41 X 10 ⁻⁹	1.91	36.101	0.284	-0.08
2W8	50.724	7.569	0.8	2.85	2.05 X 10 ⁻⁹		27.318	0.539	-0.08
2W9	50.876	7.696	0.9	2.51	5.28 X 10 ⁻⁹		20.610	0.405	-0.08
2W10	51.054	7.798	0.9	3.30	8.97 X 10 ⁻⁹		17.318	0.339	-0.08

(a) Indicates a second decreasing ΔK test on the same specimen.

(b) Closure measurements were taken, however, no evidence of closure was found in this specimen.

(c) No arrest; decreasing segment terminated at threshold value shown. Last 11 points were with the steeper gradient.

specimens but no closure was observed, as noted in Table 2. Specimen 2W5 and 5W2 are in good agreement.

Table 2 gives the specimen dimensions, the R value, and stress gradient, C , used in the test, the applied ΔK , da/dN , crack length, and a/W at threshold, and, if closure measurements were taken, the ΔK effective threshold. Looking at all the 2W specimens tested at $R = 0.1$, it is noted that the spread in ΔK_{th} is from 7.79 to 10.13 $\text{MPa}\sqrt{\text{m}}$, a difference of 2.34 $\text{MPa}\sqrt{\text{m}}$. This includes specimens of both thickness. Now consider the minimum difference between ΔK_{th} for specimens 2W1 and 5W1, 15.37 and 10.13 $\text{MPa}\sqrt{\text{m}}$, respectively. This is a difference of 5.24 $\text{MPa}\sqrt{\text{m}}$. For the 2W specimens tested at $R = 0.7$, the difference between the highest and lowest values of ΔK_{th} is less than 0.5 $\text{MPa}\sqrt{\text{m}}$, again including specimens of both thickness. The minimum difference between ΔK_{th} for specimens 2W6 and 5W2 is 1.33 $\text{MPa}\sqrt{\text{m}}$ (3.15 and 4.48 $\text{MPa}\sqrt{\text{m}}$, respectively). Also, comparing only the values of ΔK_{th} for specimens with thickness equal to roughly 9.4 mm shows the variation in threshold to be due to specimen width and not thickness.

Based on these observations, the authors consider the increased value of ΔK_{th} for the 5W specimens to be outside the variability generally observed. Further, it is concluded that the higher value of ΔK_{th} in the 5W specimens is due to specimen width and not due to thickness.

It should be pointed out that the stress gradient, C , of the 1W specimens tested at $R = 0.1$ and specimen 1W3 tested at $R = 0.7$ was higher than that of the other specimens. The authors do not believe that this difference influenced the values of ΔK_{th} obtained. This is based on the good agreement in ΔK_{th} values for specimens 1W3 and 1W4 and the results of Zawada and Nicholas [8]. Their results showed no effect of the load shedding constant between -0.08 mm^{-1} and -1.2 mm^{-1} on the values of ΔK_{th} . Also, the steeper stress gradient should produce a higher, not lower, threshold value.

Figures 2a and 2b, respectively show the ΔK_{th} and K_{max-th} plotted as a function of R . Included are data for 2W specimens of the same heat of material tested at $R = 0.4, 0.8,$ and 0.9 in an earlier program, none of which had closure measurements taken during the test. Figure 2a, shows the effect of mean stress on the threshold stress intensity. There is a variation in response of the threshold stress intensity with R that is a function of specimen size, as shown by the different slopes. Included in Fig. 2a are the ΔK effective thresholds. The average value of ΔK effective thresholds between $R = 0.1$ and 0.7 appears to be independent of mean stress and specimen width.

The lines drawn in Fig. 2a are from the average value of the threshold at $R = 0.1$ to the average value at $R = 0.7$. For the 2W specimens, the line then connects to the average of the 0.9 data. The data at $R = 0.4$ and 0.8 were not used in determining the lines.

Figure 2b shows K_{max-th} versus R confirming the observations made in Fig. 2a. Figures 2a and 2b indicate that the region where the threshold is controlled by either K_{max} or ΔK varies with specimen width. In Fig 2b, the 5W specimens have a negative slope between $R = 0.1$ and 0.7 while the 1W specimens have a positive slope.

As closure was not found in the 1W specimens tested at $R = 0.7$, it is possible that the transition where the threshold is controlled by either K_{max} or ΔK is at an R value lower than 0.7 . Assuming that ΔK_{th} at $R = 0.6$ is the same as at $R = 0.7$ would result in

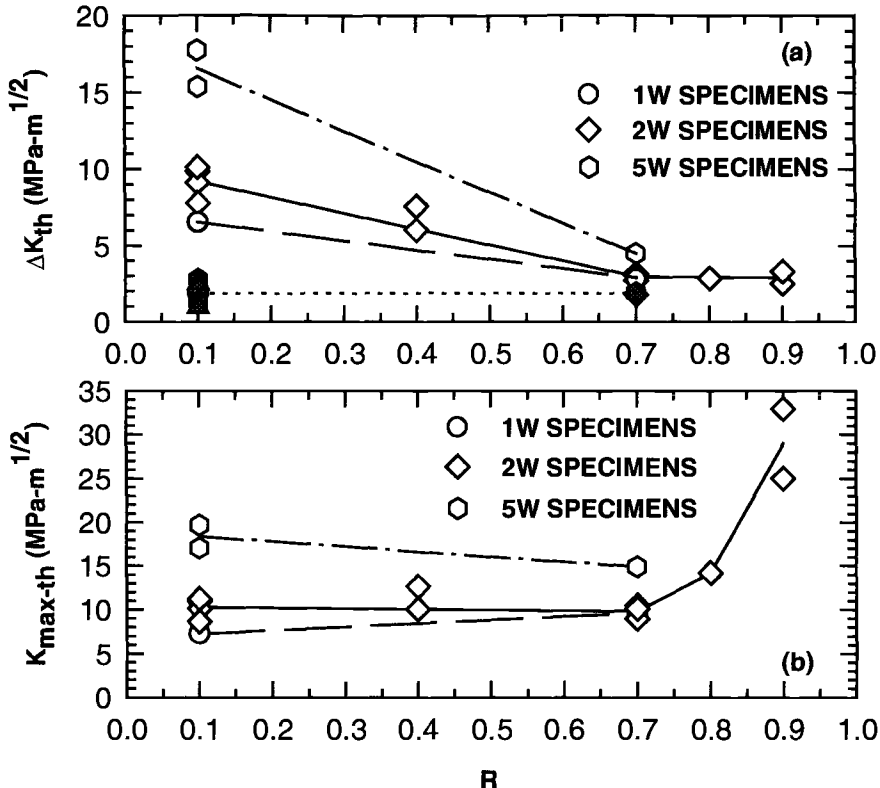


Figure 2 - (a) ΔK_{th} vs. R . Open symbols are ΔK applied. Closed symbols are ΔK effective, (b) K_{max-th} vs. R . All data are at threshold

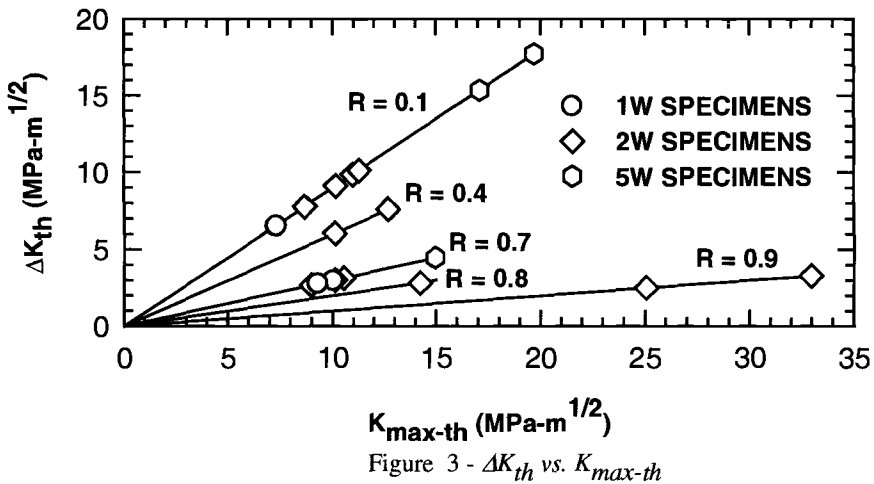


Figure 3 - ΔK_{th} vs. K_{max-th}

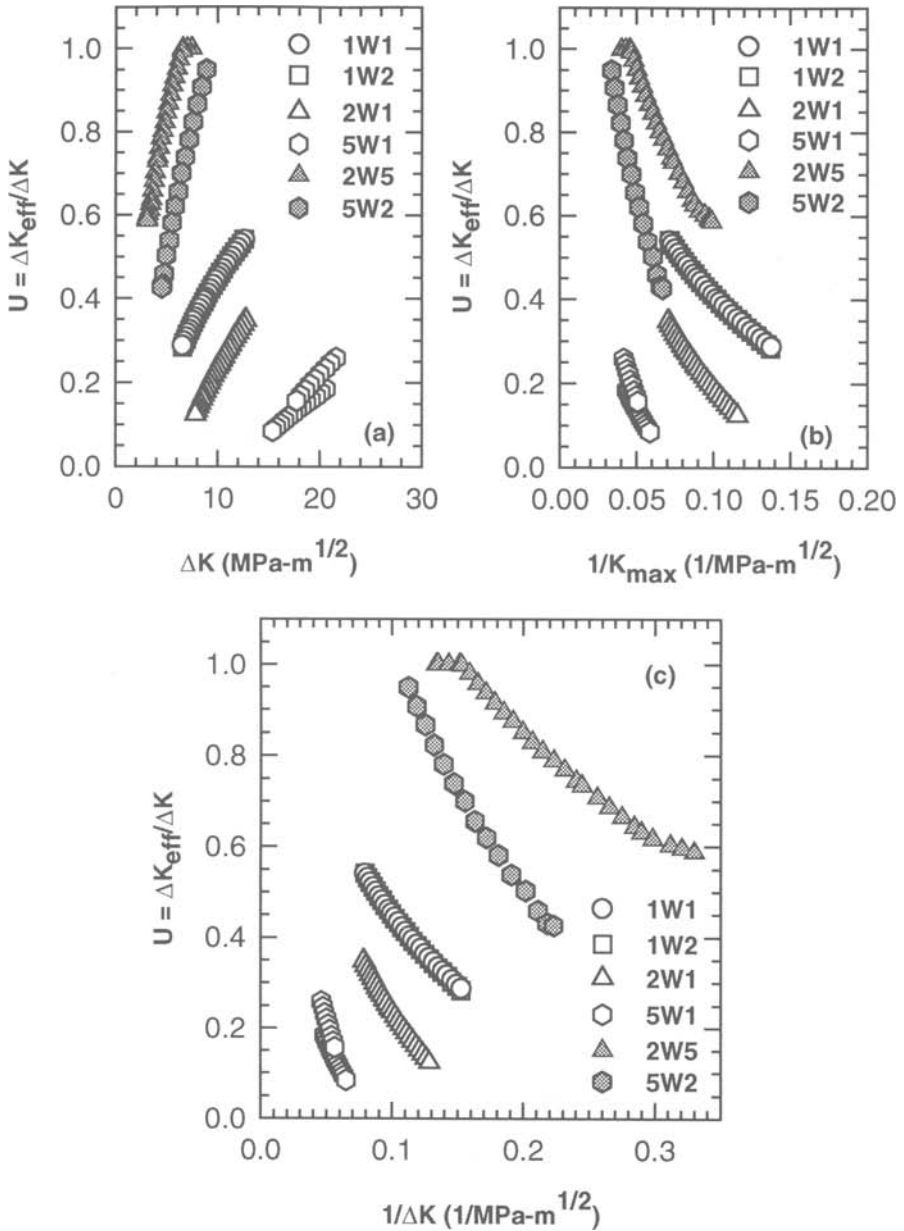


Figure 4 - (a) U vs. ΔK , (b) U vs. $1/K_{max}$, (c) U vs. $1/\Delta K$.
 Open symbols $R = 0.1$, closed symbols $R = 0.7$

the same value of $K_{\max\text{-th}}$ at both $R = 0.1$ and 0.6 . This would produce a line with zero slope in Fig. 2b with the transition where the threshold is controlled by either K_{\max} or ΔK at $R = 0.6$. It would also make the slope of the 1W line in Fig. 2a slightly steeper. Rectifying the 5W data requires an increase in the average value of ΔK_{th} at $R = 0.7$. More data with closure are needed for specimens with different widths at different R values.

Doker, et al., [9] appears to have first suggested plotting threshold data as ΔK_{th} vs. $K_{\max\text{-th}}$. More recently in a series of papers, Vasudevan, et al. [10,11], and Sadananda and Vasudevan [12], have expanded the use of the two parameter approach. Figure 3 is a plot of ΔK_{th} versus $K_{\max\text{-th}}$. The data for the different width specimens tested at the same R value fall on the same line. All the same R value data fall on their respective lines with slopes of $(1-R)$. The lowest value of ΔK_{th} is defined as ΔK_{th}^* in Vasudevan, et al.'s notation. The lowest ΔK_{th} value is $2.51 \text{ MPa}\cdot\text{m}^{1/2}$ for the 2W specimen at $R = 0.9$. Based on the trend of the data in Fig. 2a, this value appears to be independent of specimen width. Although negative R value tests were not conducted, it appears that the lowest value of $K_{\max\text{-th}}$, defined as $K_{\max\text{-th}}^*$, would depend on specimen width.

An estimate of the $K_{\max\text{-th}}$ for each specimen width was made. For each specimen width, the lowest ΔK_{th} at $R = 0.1$ and the highest ΔK_{th} at $R = 0.7$ were used to estimate the lowest ΔK_{th} at $R = 0.0$. Using data given by Usami [13], an estimate of the ΔK_{th} at $R = -1$ was made and $K_{\max\text{-th}}$ calculated. The $K_{\max\text{-th}}$ values for the 1W, 2W, and 5W specimens are 6.21, 7.46, and $14.97 \text{ MPa}\sqrt{\text{m}}$, respectively. According to Vasudevan, et al [10,11] and Sadananda and Vasudevan [12], crack growth will occur when $K_{\max} > K_{\max\text{-th}}^*$ and $\Delta K > \Delta K_{\text{th}}^*$. Based on this, the 5W data would not have predicted crack growth at the values observed in the 1W and 2W specimens, and the 2W data would not have predicted the 1W data, tested at R equal to 0.1.

Figures 4a and 4c show the trend in closure level, $U = \Delta K_{\text{eff}}/\Delta K$, as a function of various parameters. The shaded symbols represent $R = 0.7$ data, the open symbols are for $R = 0.1$ data. Figures 4a to 4c show that the fraction of the load cycle over which the crack is open decreases as threshold is approached, i.e., closure increases. In all cases, the closure levels varies with specimen width with the larger width specimen having the higher closure level, particularly in the $R = 0.1$ data.

These results are consistent with those of Zawada and Nicholas [8]. They tested C(T) specimens of Rene 95 of different sizes at 650°C in vacuum and lab air at $R = 0.1$ in the near threshold region. They also tested at different values of C , the load shedding constant. As mentioned earlier, their results showed no effect of the load shedding constant between -0.08 mm^{-1} and -1.2 mm^{-1} , and no effect of specimen thickness for $W = 40 \text{ mm}$ with thickness of 5 mm and 10 mm. They did, however, observe a difference in the closure level between the $W = 40 \text{ mm}$ and 20 mm specimens with thickness equal to 5 mm. The smaller specimen had lower values of K_{cl} . Zawada and Nicholas [8] considered the difference in closure levels between the two sizes to be outside the "specimen-to-specimen variability" and "beyond the uncertainty in determining closure loads".

In a study of the effect of load history and specimen geometry on the value of the crack closure load, Ashbaugh [14] observed a size effect. Ashbaugh tested Rene 95 at room temperature and $R = 0.1$. Crack closure was measured by CMOD, back face strain gage, and interferometric displacement gage (IDG) on three different size C(T)

specimens. Two specimens had $W = 40$ mm, one with thickness, $t = 10$ mm (standard) and the other with $t = 5$ mm (thin), and one specimen with $W = 20$ mm and $t = 5$ mm (half size). In constant amplitude tests, the half size specimen had lower values of closure than did the standard and thin specimens, which were essentially the same. The difference in closure levels was considered to be outside the normally observed scatter in the data by Ashbaugh [14].

The results shown in Fig. 4a are in agreement with the data of Shercliff and Fleck [15] on BS 4360 50B steel. The increase in R value for both the 2W and 5W specimens increased da/dN , see Fig. 1, and increased U. They attributed the near threshold behavior to oxide or roughness induced closure.

Davidson [16] measured the closure by a stereo technique that allowed him to determine the mode I and mode II closure levels. He plotted U versus $1/\Delta K$ and showed that the opening load in mode II was lower than in mode I at low values of ΔK . The mode I closure was linear while the mode II closure was nonlinear in the low ΔK region. Figure 4c is a similar plot for our data. However, our closure measurements do not differentiate between mode I and mode II closure.

Figures 5a and 5b show K_{op}/K_{max} versus ΔK or K_{max} , respectively, again exhibit that closure increases with specimen width. Considering Fig. 5a, Shercliff and Fleck [15] observed a similar behavior in the 6082 Al they tested and attributed this to roughness induced closure.

To summarize the results, the threshold and the degree of closure vary with specimen width. The question is what causes the differences?

Several parameters were investigated in an attempt to answer that question. The plastic zone size, the biaxiality ratio (B), the T stress, and the specimen roughness. Table 3 gives the plastic zone size, PZS, divided by the specimen thickness, t , and PZS divided by the remaining ligament, $(W-a)$, at the start of the decreasing ΔK segment and at ΔK_{th} . Also included in the table are values of B and T at the start and at the ΔK_{th} . The plastic zone size, PZS, was calculated using the equation

$$PZS = (1/2\pi)(K_{max}/\sigma_y) \quad (2)$$

where

σ_y = yield strength.

As seen in Table 3, the value of PZS/thickness increases with specimen width for specimens tested at $R = 0.1$, compare specimens 1W1, 1W2, 2W1, and 5W1. This holds for both at the start and at threshold. This trend does not appear to hold for specimens tested at $R = 0.7$, compare specimens 1W3, 1W4, 2W5, and 5W2. The reverse trend occurs when PZS/(W-a) is compared. Here the larger specimens have the smaller value, particularly at the start. Newman [17] stated that as long as the PZS divided by crack length and PZS divided by the remaining ligament are less than 0.1, small scale yielding conditions exist. All the specimens met this criteria.

Leevers and Radon [18] gave tabulated values of B, the biaxiality ratio, for the C(T) configuration as a function of a/W . Their case b data were fitted to a 5th order

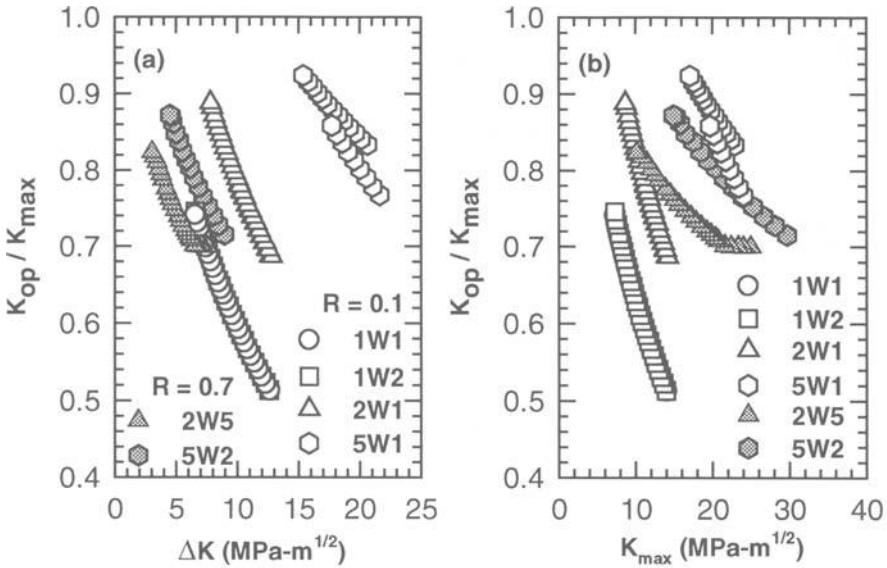


Figure 5 - (a) K_{op}/K_{max} vs. ΔK , (b) K_{op}/K_{max} vs. K_{max}

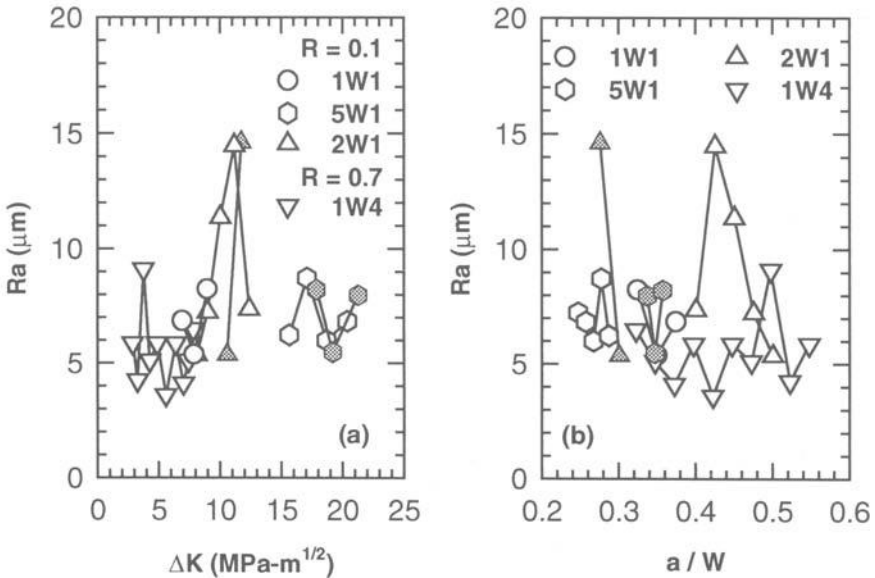


Figure 6 - Roughness measurements (a) vs. ΔK and (b) vs. a/W . Measured parallel to the growth direction. Closed symbols are for the decreasing ΔK mode with the higher threshold

Table 3. - Summary of Various Parameters at the Start of a Decreasing ΔK Segment and at Threshold

Specimen	R	PZS/t Start	PZS/t at ΔK_{th}	PZS/ (W-a) at Start	PZS/ (W-a) at ΔK_{th}	B at Start (b)	B at ΔK_{th} (b)	T at Start (MPa)	T at ΔK_{th} (MPa)
1W1	0.1	2.89×10^{-3}	7.79×10^4	1.44×10^{-3}	4.68×10^{-4}	0.344	0.523	33.61	21.68
1W2	0.1	2.88×10^{-3}	7.82×10^4	1.44×10^{-3}	4.71×10^{-4}	0.342	0.521	33.44	21.75
2W1	0.1	2.91×10^{-3}	1.87×10^3	7.25×10^{-4}	5.02×10^{-4}	0.342	0.429	23.77	21.69
2W1 (a)	0.1	2.97×10^{-3}	1.11×10^3	9.06×10^{-4}	4.16×10^{-4}	0.531	0.599	30.11	18.20
2W2	0.1	4.59×10^{-3}	2.15×10^3	9.49×10^{-4}	5.08×10^{-4}	0.349	0.488	27.44	22.51
2W3	0.1	4.57×10^{-3}	1.82×10^3	9.48×10^{-4}	4.45×10^{-4}	0.342	0.504	27.18	21.14
5W1	0.1	7.85×10^{-3}	4.36×10^3	7.71×10^{-4}	4.49×10^{-4}	0.341	0.396	24.47	19.93
5W1 (a)	0.1	8.62×10^{-3}	5.80×10^3	9.49×10^{-4}	6.58×10^{-4}	0.465	0.490	30.51	25.63
2W4	0.4	6.74×10^{-3}	2.87×10^3	1.39×10^{-3}	6.86×10^{-4}	0.343	0.496	32.91	26.22
2W4 (a)	0.4	6.48×10^{-3}	1.82×10^3	1.63×10^{-3}	6.11×10^{-4}	0.533	0.603	40.42	20.64
1W3	0.7	1.24×10^{-2}	1.48×10^3	6.40×10^{-3}	1.07×10^{-3}	0.384	0.593	74.38	30.09
1W4	0.7	1.33×10^{-2}	1.26×10^3	6.60×10^{-3}	1.05×10^{-3}	0.339	0.603	71.37	26.59
2W5	0.7	9.15×10^{-3}	1.50×10^3	2.28×10^{-3}	5.63×10^{-4}	0.341	0.598	42.09	21.31
2W6	0.7	1.59×10^{-2}	1.95×10^3	3.32×10^{-3}	6.08×10^{-4}	0.343	0.598	50.90	22.20
2W7	0.7	1.35×10^{-2}	1.43×10^3	2.79×10^{-3}	4.68×10^{-4}	0.341	0.602	46.53	18.60
5W2	0.7	1.28×10^{-2}	3.24×10^3	1.26×10^{-3}	3.41×10^{-4}	0.306	0.388	29.61	17.24
2W8	0.8	3.49×10^{-2}	3.71×10^3	7.03×10^{-3}	1.20×10^{-3}	0.344	0.603	74.17	29.28
2W9	0.9	3.27×10^{-2}	1.13×10^2	6.88×10^{-3}	2.88×10^{-3}	0.382	0.543	76.90	53.43
2W10	0.9	3.17×10^{-2}	1.93×10^2	6.73×10^{-3}	4.47×10^{-3}	0.383	0.469	76.17	66.30

(a) Indicates a second decreasing ΔK test on the same specimen.

polynomial, equation 3, and the coefficients used to calculate B at the start of the decreasing ΔK test and at ΔK_{th} . As all the specimens started the first decreasing ΔK section at an a/W of about 0.25, there was essentially no variation in B. Also, most of the specimens reached threshold at a/W of between 0.35 and 0.4, again producing little variation in B. Only those specimens that had a second decreasing ΔK segment had larger values of B.

$$B = -0.209 + 2.758\alpha - 4.479\alpha^2 + 15\alpha^3 - 32.083\alpha^4 + 21.667\alpha^5 \quad (3)$$

Where

$$\alpha = a/W.$$

The T stress has been used to explain the differences in crack growth rates of specimens with different geometry [15,19,20]. It was thought that the T stress may also be used to explain the differences observed in the present work. The equation used to calculate the T stress was that given by Leever and Radon [18], equation 4, with K_{max} being used in all cases. As seen in Table 3, the T stress showed some variation at the start of the decreasing ΔK segment for specimens tested at $R = 0.1$, but essentially no variation at ΔK_{th} , particularly when only the first decreasing ΔK segment is considered.

$$T = BK/\sqrt{\pi a} \quad (4)$$

Where

a = crack length.

Roughness measurements were taken on several specimens. Figure 6 shows the roughness variation for specimens on which closure was measured. The data shown are only for the decreasing ΔK segments. Although there is considerable variation in the roughness of an individual specimen, most of the measurements were in the 4 to 9 μm range independent of specimen width or R value at which tested. The roughness of the specimens originally fabricated for testing at laboratory A have essentially the same roughness range regardless of R value, 4 to 10 μm .

Figure 7 shows the trend in some of the parameters investigated as a function of specimen width for specimens tested at $R = 0.1$. The open symbols are for the start of the test and the closed symbols at ΔK_{th} . Data for the 50.8 mm and 127 mm specimens are for the first decreasing ΔK segment. In Fig. 7a, K_{op}/K_{max} increases with W with the commensurate decrease in U, Fig. 7b. Figure 7c shows the biaxiality ratio. The variation in the value of B at threshold is due to the variation in a/W at which threshold occurred. The T stress, Fig. 7d, shows some variation at the start of the test but essentially none at threshold.

Constraint was also considered as a possible reason for the difference in ΔK_{th} with specimen width. Fig. 8a and 8b show da/dN versus ΔK for the 2W and 5W specimens tested at $R = 0.1$ and 0.7, respectively. In Fig. 8a, note that a very small shift in the $R = 0.7$ curve would bring the Paris section in line with the Paris region of the $R = 0.1$

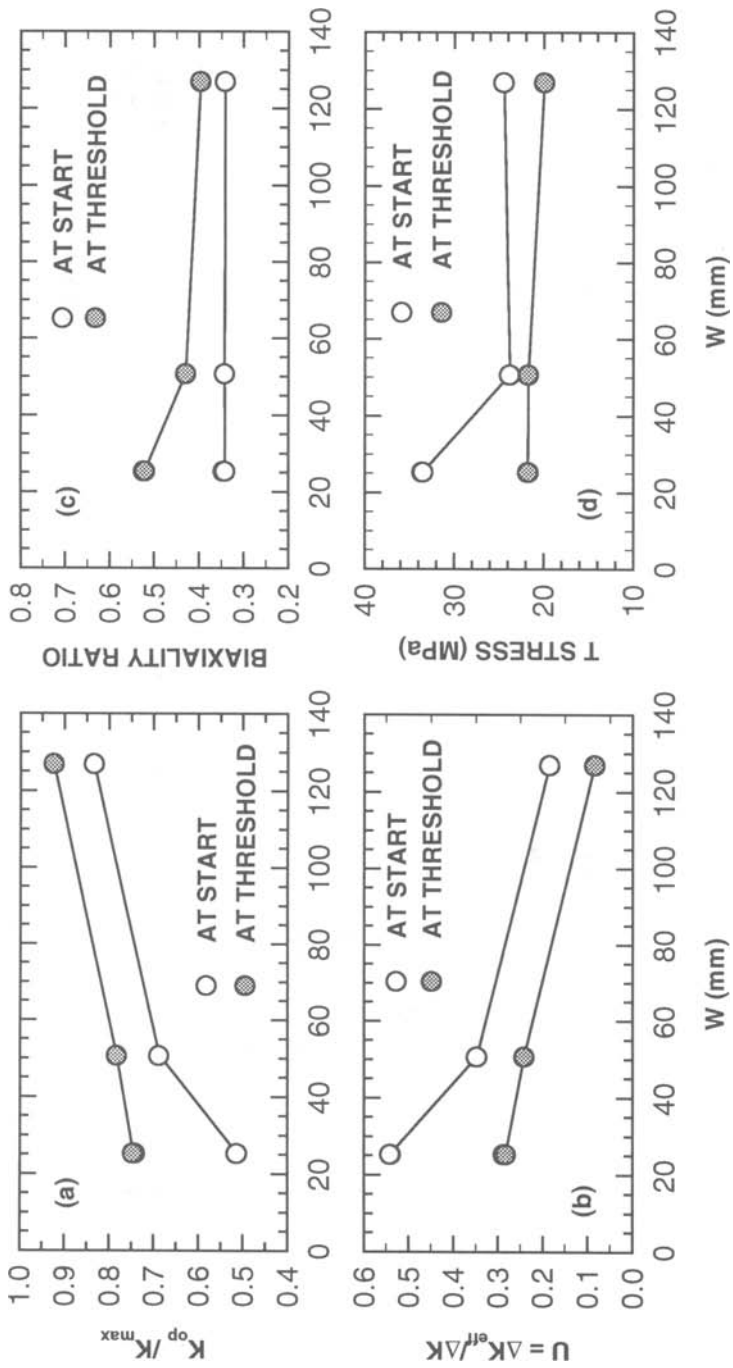


Figure 7 - (a) K_{op} / K_{max} vs W , (b) U vs W , (c) Biaxiality ratio vs. W , (d) T stress vs. W . Open symbols are at start, closed symbols are at threshold. All data are for $R = 0.1$

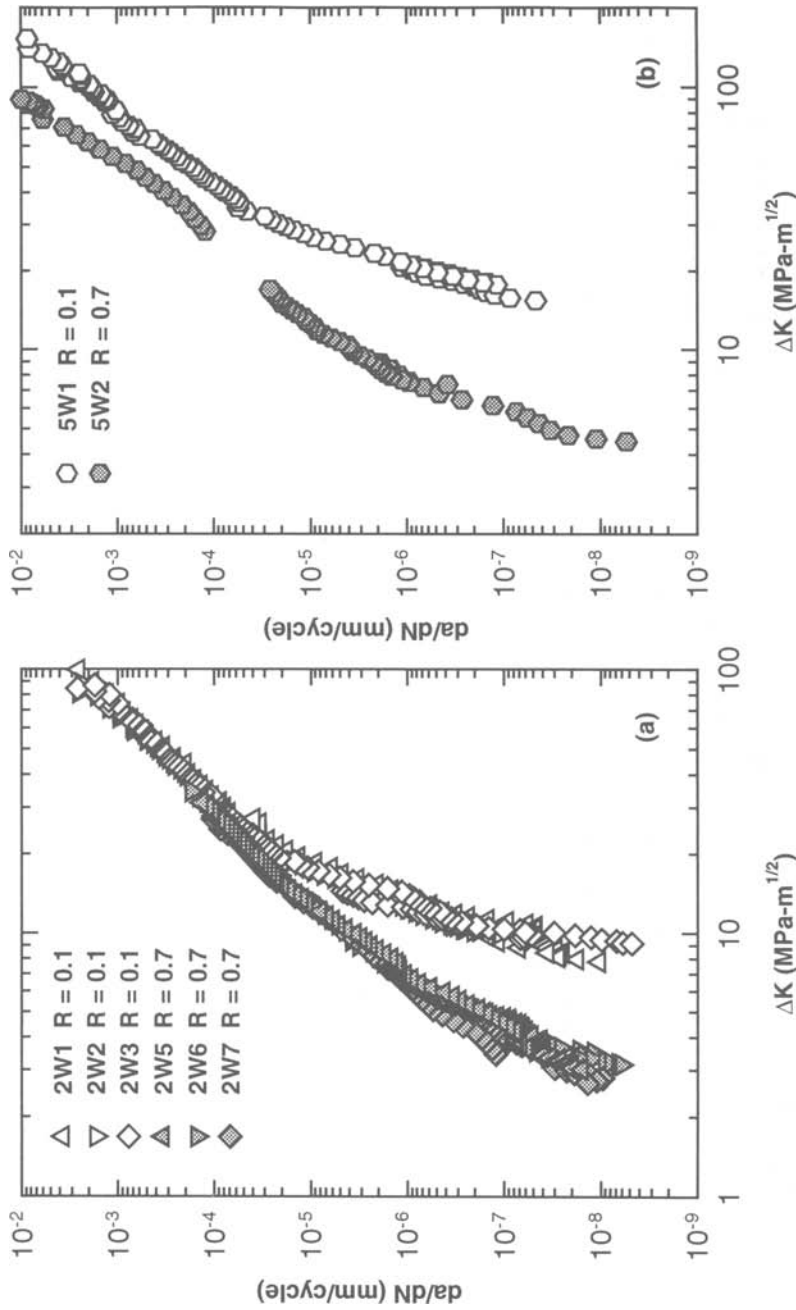


Figure 8a - da/dN vs. ΔK for 2W Specimens

Figure 8b - da/dN vs. ΔK for 5W Specimens

curve. In Fig. 8b, for the 5W specimens, a much larger separation is seen. Newman's closure model [21] with the maximum stress divided by the flow stress, S_{\max}/σ_o , of 0.2 was used to estimate the Paris region constraint factor. S_{\max} and σ_o were calculated using equations (5) and (6), respectively. The values of P_{\max} and a/W were obtained from the test records.

$$S_{\max} = [P_{\max}/(tW(1-\alpha))][1+3(1+\alpha)/(1-\alpha)] \quad (5)$$

$$\sigma_o = (\sigma_y + \sigma_u)/2 \quad (6)$$

Where

P_{\max} = maximum load

t = thickness

W = width

α = a/W

σ_y = yield strength

σ_u = ultimate tensile strength.

The constraint factor was 3 for the 1W and 2W specimens and 1.2 for the 5W specimens. Newman's model [21] is based on plasticity and applies to the Paris region and is not applicable to the threshold region. Also, in these tests the Paris region is obtained after the threshold has been determined and thus, can't influence directly the threshold behavior. However, it is included here as it gives an indication that the constraint is different in the larger specimen and that constraint may be a factor in controlling the threshold behavior. At present the authors are not aware of a constraint model for the threshold region for nickel base superalloys.

Some speculation by the authors is offered. Roughness is essentially the same regardless of specimen size and the R value tested. Assuming that the curvature seen in Fig. 4b is indicative of mode II, as seen by Davidson [16], a possible explanation for the different values of ΔK_{th} is that the amount of mode II in a specimen is a function of specimen width. An alternative explanation may be made on the basis of the difference in constraint with specimen size, as seen in Figure 8.

Conclusion

Fatigue crack growth rate tests were conducted on Nickel-based superalloy 718 at room temperature at $R = 0.1$ and 0.7 on C(T) specimens with W of 25.4 mm, 50.8 mm, and 127 mm. Additional data on 50.8 mm specimens was obtained from a separate test program. The FCGR threshold varied with specimen width, particularly at $R = 0.1$, with the highest threshold resulting from the widest specimen. Closure was measured on some specimens and the ΔK effective threshold obtained. Although this was instrumental in reconciling the data, it did not explain why there is more closure in the larger specimen. The biaxiality ratio and T stress were calculated but did not show a

difference that could explain the data. Roughness measurements were taken on specific specimens, again with no significant difference between the specimens. Most of the roughness measurements were between 4 and 10 μm regardless of R value or specimen width. At this time there does not appear to be an obvious explanation for the different thresholds due to the specimen width. Differences in constraint or mode II stresses with specimen width are possible mechanisms that may explain the different values of ΔK_{th} observed. Additional FCGR data are needed over a wide range of R values and specimen widths to better describe the boundary of this effect and the variables controlling the behavior.

Acknowledgments

This paper is based on work performed under NASA Contracts NAS8-40000 and NAS8-45000. We are pleased to acknowledge the contribution of P. Stirling for fractography, the assistance of R. Ball with the roughness measurements, and the helpful discussions with J. C. Newman, Jr., D. W. Schmidt, and D. Russell.

References

- [1] Saxena, A., Hudak, Jr., S. J., Donald, J. K., and Schmidt, D. W., "Computer-Controlled Decreasing Stress Intensity Technique for Low Rate Fatigue Crack Growth Testing," *Journal of Testing and Evaluation*, Vol. 6, No. 3, 1978, pp. 167-174.
- [2] Donald, J. K., and Schmidt, D. W., "Computer-Controlled Stress Intensity Gradient Technique for High Rate Fatigue Crack Growth Testing," *Journal of Testing and Evaluation*, Vol. 8, No. 1, Jan. 1980, pp. 19-24.
- [3] Schwalbe, K. H. and Hellmann, D., "Application of the Electrical Potential Method to Crack Lengths Measurements Using Johnson's Formula," *Journal for Testing and Evaluation*, Vol. 9, No. 3, May 1981, pp. 218-221.
- [4] Clark, G. A., Andrews, W. R., Paris, P. C., and Schmidt, D. W., "Single Specimen Tests for J_{IC} Determination", *Mechanics of Crack Growth*, ASTM STP 590, American Society for Testing and Materials, 1976, pp. 27-42.
- [5] Allison, J. E., "The Measurement of Crack Closure During Fatigue Crack Growth", *Fracture Mechanics: Eighteenth Symposium, ASTM STP 945*, D. T. Read and R. P. Reed, Eds., American Society for Testing and Materials, Philadelphia, 1988, pp. 913-933.
- [6] Suresh, S., *Fatigue of Materials*, Press Syndicate of the University of Cambridge, Cambridge, England, 1991, pp. 225-228.

- [7] Hertzberg R. W., Newton, C. H., and Jaccard, R., "Crack closure: Correlation and Confusion", *Mechanics of Crack Closure, ASTM STP 982*, J. C. Newman, Jr., and W. Elber, Eds., American Society for Testing and Materials, Philadelphia, 1988, pp. 139-148.
- [8] Zawada, L. P. and Nicholas, T., "The Effect of Closure on the Near-Threshold Fatigue Crack Propagation Rates of a Nickel Base Superalloy," *Mechanics of Fatigue Crack Closure, ASTM STP 982*, J. C. Newman, Jr. and W. Elbers, Eds. American Society for Testing and Materials, Philadelphia, 1988, pp. 548-567.
- [9] Doker, H., Bachmann, V., and Marci, G., "A Comparison of Different Methods of Determination of the Threshold for Fatigue Crack Propagation", *Fatigue Thresholds, Vol. I*, J. Backlund, A. F. Blom, and C. J. Beevers, Eds. Engineering Materials Advisory Services, Inc., Warley, West Midlands, United Kingdom, 1982, pp. 45-57.
- [10] Vasudeven, A. K., Sadananda, K., and Louat, N., "Two Critical Stress Intensities for Threshold Fatigue Crack Propagation", *Scripta Metallurgica et Materialia*, Vol. 28, 1993, pp. 65-70.
- [11] Vasudeven, A. K., Sadananda, K., and Louat, N., "A Review of Crack Closure, Fatigue Crack Threshold and Related Phenomena", *Material Science and Engineering*, Vol. A188, 1994, pp. 1-22.
- [12] Sadananda, K. and Vasudeven, A. K., "Analysis of Fatigue Crack Closure and Thresholds," *Fracture Mechanics: 25th Volume, ASTM STP 1220*, F. Erodgan, Ed., American Society for Testing and Materials, Philadelphia, 1995, pp. 484-501.
- [13] Usami, S., "Applications of Threshold Cyclic-Plastic-Zone-Size Criterion to some Fatigue Limit Problems", *Fatigue Thresholds, Vol. I*, J. Backlund, A. F. Blom, and C. J. Beevers, Eds. Engineering Materials Advisory Services, Inc., Warley, West Midlands, United Kingdom, 1982, pp.205-238
- [14] Ashbaugh, N. E., "Effects of Load History and Specimen Geometry on Fatigue Crack Closure Measurements," *Mechanics of Fatigue Crack Closure, ASTM STP 982*, J. C. Newman, Jr. and W. Elbers, Eds. American Society for Testing and Materials, Philadelphia, 1988, pp. 186-189.
- [15] Shercliff, H. R., and Fleck, N. A., "Effect of Specimen Geometry on Fatigue Crack Growth in Plane Strain-I. Constant Amplitude Response.", *Fatigue and Fracture of Engineering Materials and Structures*, Vol.13, 1990, pp. 287-296.
- [16] Davidson, D. L., "Plasticity Induced Fatigue Crack Closure," *Mechanics of Fatigue Crack Closure, ASTM STP 982*, J. C. Newman, Jr. and W. Elbers, Eds. American Society for Testing and Materials, Philadelphia, 1988, pp. 186-189.

- [17] Newman, J. C. Jr., "Prediction of Stable Crack Growth and Instability Using the V_R -Curve Method", *Elastic-Plastic Fracture Mechanics Technology*, ASTM STP 896, J. C. Newman, Jr., and F.J. Loss, Eds., American Society for Testing and Materials, Philadelphia, 1985, pp. 135-166.
- [18] Leever, P. S. and Radon, J. C., "Inherent Stress Biaxiality in Various Fracture Specimen Geometries", *International Journal of Fracture*, Vol. 19, 1982, pp. 311-325.
- [19] Shercliff, H. R., and Fleck, N. A., "Effect of Specimen Geometry on Fatigue Crack Growth in Plane Strain-II. Overload Response.", *Fatigue and Fracture of Engineering Materials and Structures*, Vol.13, 1990, pp. 297-310.
- [20] Liknes, H. O., and Stephens, R. P., "Effect of Geometry and Load History on Fatigue Crack Growth in Ti-62222", *Fatigue Crack Growth Thresholds, Endurance Limits, and Design*, ASTM STP 1372, J. C. Newman, Jr., and R. S. Piascik, Eds., American Society for Testing and Materials, West Conshohocken, PA, 1999, pp.
- [21] Newman, J. C. Jr., "A Crack Opening Stress Equation for Fatigue Crack Growth", *International Journal of Fracture*, Vol. 24, 1984, pp. R131-R135.

Haakon O. Liknes¹ and Robert R. Stephens²

Effect of Geometry and Load History on Fatigue Crack Growth in Ti-62222

Reference: Liknes, H. O. and Stephens, R. R., “Effect of Geometry and Load History on Fatigue Crack Growth in Ti-62222,” *Fatigue Crack Growth Thresholds, Endurance Limits, and Design*, ASTM STP 1372, J. C. Newman, Jr. and R. S. Piascik, Eds., American Society for Testing and Materials, West Conshohocken, PA, 2000.

Abstract: Fatigue crack growth behavior of Ti-62222 mill-annealed material in sheet form was examined as a function of specimen geometry. The geometries investigated were the eccentrically loaded single edge-notch tension (ESE(T)), the compact tension (C(T)), and the middle tension (M(T)). Tests were conducted at room temperature at two load ratios ($R=0.1$ and 0.7) and covered a broad range of crack growth rates ranging from 10^{-7} to 10^{-2} mm/cycle. The same precracking and threshold test procedures were used for all geometries as each threshold test was started at the same crack length and continuous load shedding was applied at a K -gradient of $C=-0.08$ mm⁻¹. As a result, the same stress intensity-crack length (K - a) history was maintained throughout all of the threshold tests. Experimental results showed differences in fatigue crack growth behavior at the lowest crack growth rates while higher crack growth rates were similar. Surface roughness differences at lower crack growth rates were observed at the same nominal ΔK for the three geometries, suggesting differing crack growth mechanisms. Discrepancies observed in specimen behavior are assessed in terms of the crack tip stress field distribution which include both y -direction and T -stresses. In addition, supplemental fatigue crack growth tests showed a dependence on crack length and load reduction procedure.

Keywords: fatigue crack growth, near threshold, load ratio, roughness, geometry, crack closure, T -stress, biaxiality, y -stresses, titanium, load history

For damage-tolerant design, it is important to be able to accurately determine the threshold stress intensity range, ΔK_{th} , as this value identifies the point below which a crack is not expected to grow when subjected to cyclic loads. Previous studies have examined the effect of biaxial stresses and specimen geometry on fatigue crack growth and threshold behavior [1-7]. Conventional fracture theories assume the state of stress and strain in the vicinity of a crack tip is characterized by a single parameter, the stress intensity factor K . However, in recent years, researchers have attempted to describe the fracture behavior in terms of two parameters [8-10], where the second parameter is the elastic T -stress. The T -stress is the second term of the Williams [11] series expansion for linear elastic crack tip fields, as shown in equation (1).

¹ Graduate Assistant, Mechanical Engineering, University of Idaho, Moscow, ID 83843

² Associate Professor, Mechanical Engineering, University of Idaho, Moscow, ID 83843

$$\begin{bmatrix} \sigma_{11} & \sigma_{12} \\ \sigma_{21} & \sigma_{22} \end{bmatrix} = \frac{K}{\sqrt{2\pi r}} \begin{bmatrix} f_{11}(\theta) & f_{12}(\theta) \\ f_{21}(\theta) & f_{22}(\theta) \end{bmatrix} + \begin{bmatrix} T & 0 \\ 0 & 0 \end{bmatrix} \quad (1)$$

Although the T -stress is neglected in linear elastic fracture mechanics (LEFM), researchers have found the sign and magnitude of the T -stress can effect the size and shape of the plastic zone at loading levels corresponding to small-scale yielding [12,13]. The magnitude of T varies with the applied stress, thus it is commonly described in terms of the stress biaxiality parameter, B , as shown in equation (2). This notation was introduced by Leever and Radon [14] and has become widely used. Sherry *et al.* [15] have provided a compendium of T -stress solutions for two and three dimensional cracked geometries.

$$B = \frac{T\sqrt{\pi a}}{K} \quad (2)$$

Numerous reports of geometry and biaxiality effects on fatigue crack growth have been documented in the literature, primarily for threshold and near threshold behavior. Although Liu *et al.* [1] reported that stress biaxiality ratios (σ_x/σ_y) between -1.5 and 1.75 did not effect fatigue crack growth rates in aluminum alloys using a cruciform specimen, many other researchers have identified effects. Leever *et al.* [2] showed that fatigue crack growth rates in PMMA were reduced by a factor of 2 or 3 as the stress biaxiality ratio was varied between 0 and 2. Shercliff and Fleck [3] showed that for tests on aluminum and steel specimens in the C(T) and M(T) configurations (under plane strain conditions), greater retardation was observed after an overload in M(T) specimens than in C(T) specimens. This was attributed to the T -stress and its effect on the plastic zone size.

Several studies have reported higher crack growth rates in the more symmetrically loaded (with respect to the load line) specimens such as the M(T) than in asymmetrically loaded specimens such as the single edge-notch tension (SE(T)), wedge-opening loading (WOL), and C(T) [4-7]. Differences were attributed to the mode I stress distribution ahead of the crack tip and the microstructural/crack tip interaction. Lang *et al.* [4] found that fatigue crack growth rates using the M(T) specimen were consistently higher at all frequencies than those using the WOL specimen. Horng and Fine [5] observed a higher threshold stress intensity with the SE(T) specimen than with the M(T) specimen. They also found that when corrected for closure, fatigue crack growth data for both specimen types matched within experimental error. Surface roughness-induced crack closure was reported as the origin of the specimen geometry effect. Vecchio *et al.* [6] observed higher fatigue crack growth rates in the M(T) specimen than in the C(T) specimen for an aluminum alloy and a nickel-base superalloy. They noted that the specimen with the greatest load symmetry yielded the lowest threshold stress intensity level. Saxena *et al.* [7] showed that the fatigue crack growth rate for the SE(T) specimen was higher than the C(T) specimen in the early stages of crack growth, while in the latter stages no difference was observed. From these studies, it is apparent a complex interaction exists between the crack tip, microstructure, and surrounding stress field.

Recently, High Speed Civil Transport and Aging Aircraft research programs have begun utilizing a relatively new specimen geometry, the ESE(T). The elongated specimen configuration provides many distinct advantages over the SE(T), M(T), and

C(T) [16]. These include lower applied loads than the SE(T) and M(T), reduced T -stresses in comparison to the C(T), a tendency to maintain crack planarity in materials whose texture and microstructure tend to cause out-of-plane growth, and additional working room within the elongated section to allow the use of environmental chambers or complex transducers. Furthermore, the stress intensity factor solution for the ESE(T) specimen has the advantage of being valid to essentially $a/W=0$. There is also substantial interest in standardizing the ESE(T) specimen in the ASTM Test Method for Measurement of Fatigue Crack Growth Rates (E647-95a), but additional analysis of this geometry is needed before this step is taken.

This paper contains a description and analysis of a research program involving geometry effects observed between the ESE(T), C(T), and M(T) specimens in Ti-62222 mill-annealed sheet material. This material is a relatively high strength α/β titanium alloy of interest for advanced aircraft applications. It is of paramount importance for damage tolerant design applications that the fatigue crack growth behavior be properly evaluated. This need led to the objectives of this research which were to compare fatigue crack growth behavior between three specimen geometries and to evaluate the factors that effect the near threshold fatigue crack growth behavior.

Experimental Details

Material and Specimen Detail

The material used in this investigation was Ti-62222 (Ti-6Al-2Sn-2Zr-2Mo-2Cr) mill-annealed (as-received) material. This material has an alpha phase dispersed throughout an alpha plus beta matrix, with an estimated grain size of approximately 10 μm (Figure 1). Fatigue crack growth tests were performed in the L-T orientation, with the following tensile properties: ultimate tensile strength of 1 164 MPa, yield strength of 1 112 MPa, and an elongation of 12.9% for a 50 mm gage section. ESE(T), C(T), and M(T)

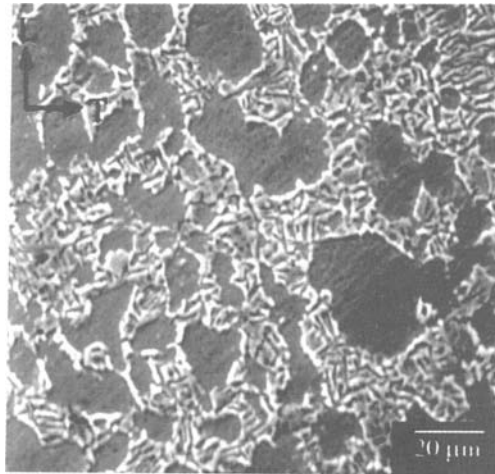


Figure 1 – SEM micrograph of Ti-62222 mill-annealed microstructure.

specimens were machined from approximately 1.6 mm thick sheet, where the specimen thickness was maintained at 1.6 mm. The width of the specimens was 38.1 mm for the ESE(T) and C(T), and 76.2 mm for the M(T). Initial notch lengths for each geometry were 5.1 mm for the ESE(T), and 7.6 mm for the C(T) and M(T) specimens (Figure 2).

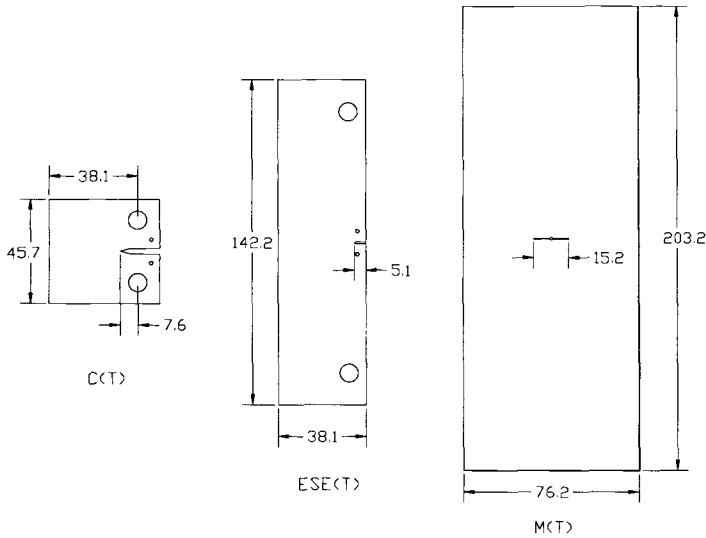


Figure 2 – Schematic of C(T), ESE(T), and M(T) specimen geometries. All dimensions in mm.

Test Procedure

Fatigue crack growth tests were performed without interruption on computer controlled closed-loop servohydraulic test systems under load control, in accordance with E647-95a. Tests were performed using a sinusoidal waveform at frequencies between 20-30 Hz. A consistent precracking history between specimens was maintained so that the threshold tests could be started at the same crack length, as defined by the stress intensity factor solution, and the same nominal ΔK for each geometry, regardless of stress ratio. This approach allowed application of the same K - a history throughout the test. At $R=0.1$, precracking was started at $a=7.6$ mm and $\Delta K=14.2$ MPa \sqrt{m} , and finished at $a=12$ mm and $\Delta K=10$ MPa \sqrt{m} . Load shedding was applied at a K -gradient of $C=-0.08$ mm $^{-1}$, according to

$$\Delta K = \Delta K_0 \exp[C(a-a_0)] \tag{3}$$

where ΔK_0 was the initial stress intensity range and a_0 was the initial crack length. Since the ESE(T) specimen had a notch only 5.1 mm long, it was cycled at a constant $\Delta K=14.2$

MPa $\sqrt{\text{m}}$ until the crack length was 7.6 mm, at which time the load was shed at a rate of $C=-0.08 \text{ mm}^{-1}$. At $R=0.7$, the notches were precracked to a length of 12 mm at a constant $\Delta K=10 \text{ MPa}\sqrt{\text{m}}$. Therefore, all threshold tests, regardless of the specimen geometry, were started after the precracking procedure at an initial crack length of $a=12 \text{ mm}$ and $\Delta K=10 \text{ MPa}\sqrt{\text{m}}$. Duplicate tests were performed to verify repeatability of fatigue crack growth behavior.

The procedure for testing at higher crack growth rates varied slightly between geometries. Specimens were precracked by load shedding to approximately $\Delta K=7 \text{ MPa}\sqrt{\text{m}}$ and then cycled at constant load. However, for the M(T) specimen, a K -gradient of $C=0.10 \text{ mm}^{-1}$ was used to assure that sufficient data were collected prior to specimen failure.

Crack length was monitored using the compliance method and verified visually with a 50X travelling microscope marked in increments of 0.01 mm. Tests using the M(T) specimen utilized a clip-gage that had a compressive force of approximately 25 N. This compressive force was required to insert the clip-gage into the specimen knife edges. However, because of the relatively low loads encountered using the thin ESE(T) and C(T) specimens during threshold tests, an extensometer with a compressive force of 0.4 N was used in an effort to perform the low stress ratio tests at a true stress ratio of 0.1. The force required to compress a clip-gage for insertion into specimen knife edges can act to increase the actual stress ratio seen at the crack tip if the applied cyclic loads are of the magnitude of the compression force of the clip-gage. The low-force extensometer was attached to the specimens via rubber bands wrapped around dowel pins positioned through the specimen. The 1.6 mm diameter dowel pins were inserted through holes located $\pm 5.1 \text{ mm}$ from the crack line, and 3.8 mm from the front face of the specimens (Figure 2). Ninety degree notches 0.25 mm deep were machined on the front face of the ESE(T) specimens to hold the extensometer knife edges in place. To address concerns over the effect of the dowel pin holes on the accuracy of the stress intensity solution, finite element analysis was performed on ESE(T) specimens with and without dowel pin holes. At a crack length of 12 mm, the difference in stress intensity was only about 0.3%, and decreased rapidly at longer crack lengths. Since the dowel pin holes were farther away from the notch tip in the C(T) specimen than in the ESE(T) specimen, it was assumed that the influence of the holes for the dowel pins in the C(T) specimen would be similar or less.

The C(T) specimen was modified slightly from the design specified in E647-95a in order for the specimen to fit in the clevis grips that were used. If the standard specimen design had been used, the clevis grips would have interfered with the dowel pins. Therefore, the pin hole location was moved from $0.275W$ to $0.358W$ from the centerline, where W was the specimen width. Additionally, a $0.208W$ diameter hole was used rather than $0.25W$. The influence of these changes on the stress intensity was also analyzed via finite element analysis. At $a=12 \text{ mm}$, the stress intensity calculated for the modified specimen was approximately 2% higher, but dropped off rapidly to approximately 0.5% lower than the standard specimen at longer crack lengths, which was deemed acceptable. C(T) specimens were measured before and after notching with a micrometer to see if any residual stresses were present that might effect fatigue crack growth behavior, but no differences were observed. Additionally, custom washers were used to keep the C(T) and

ESE(T) specimens centered in the clevis grips in an effort to avoid misalignment that could induce shear loading across the faces.

For the $R=0.1$ tests, crack closure data were collected automatically at the same time the nominal data were collected by the computer. For the M(T) specimen tests, crack opening data were collected using a clip-gage only. For the ESE(T) and C(T) specimen tests, crack opening data were collected at both the front face (using an extensometer) and at the back face by means of a small strain gage. This was done to verify crack opening measurements using both methods and to assess crack opening load as a function of measurement technique. Crack opening data were analyzed using the offset method outlined in E647-95a with a 2% offset criterion.

Results and Discussion

The fatigue crack growth tests performed at $R=0.1$ and 0.7 using the three specimen geometries are presented in Figures 3 and 4. Duplicate tests for each geometry showed good repeatability for nominal crack growth data in all regions. However, some variability was seen in crack closure data even in cases where the nominal data were indistinguishable between duplicate tests. Data presented for the various geometries are representative of the typical crack growth behavior. Comparison of crack opening loads obtained at the front face with those obtained at the back face generally showed little difference. The most extreme difference was in the C(T) specimen, where data from the back face showed about 6% less closure than data from the front face. The crack closure data presented in this paper for the C(T) specimen are the average of the back face and front face compliance measurements, while for the other geometries crack closure data presented are based on the front face compliance.

For higher crack growth rates at $R=0.1$, the fatigue crack growth behavior was consistent between the three specimen geometries, with no discernible differences (Figure 3). At $R=0.7$, crack growth behavior was also similar, with the M(T) specimen showing slightly higher crack growth rates, however the difference was very small (Figure 3).

For near-threshold tests (region I) at $R=0.7$, there was no crack closure observed based on compliance plots since the minimum load was found to be greater than the apparent crack opening load, thus $\Delta K = \Delta K_{\text{eff}}$. There was not a significant difference in crack growth behavior between the three specimen geometries except for the lowest decade of crack growth rate (Figure 4a). Over this range, the M(T) specimen showed slightly higher crack growth rates and a lower threshold value than the other two geometries.

For $R=0.1$, at an intermediate ΔK value of approximately $10 \text{ MPa}\sqrt{\text{m}}$ or greater, the nominal crack growth rates observed for the three specimen geometries were similar (Figure 4b). However, as ΔK values approached threshold, the C(T) specimen exhibited lower nominal crack growth rates and a higher nominal threshold value ($\Delta K_{\text{th,nom}}=4.5 \text{ MPa}\sqrt{\text{m}}$) than observed for the M(T) and ESE(T) specimens ($\Delta K_{\text{th,nom}}=3.3 \text{ MPa}\sqrt{\text{m}}$ and $3.1 \text{ MPa}\sqrt{\text{m}}$, respectively). The difference observed between the ESE(T) and M(T) fatigue crack growth curves was small, with the M(T) specimen showing slightly lower crack growth rates than the ESE(T). When corrected for crack closure, the nominal curves for all three specimen geometries shifted to the left to various degrees depending on the extent of crack closure observed. The C(T) specimen experienced the greatest

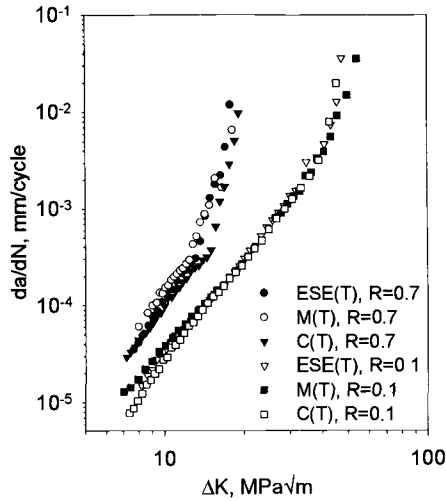


Figure 3 – Region II and region III fatigue crack growth behavior.

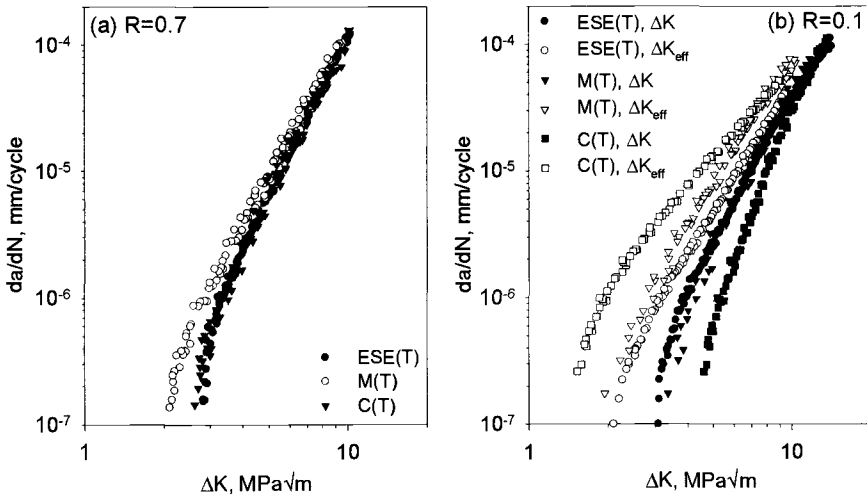


Figure 4 – Region I fatigue crack growth behavior; (a) R=0.7, (b) R=0.1.

degree of crack closure while the ESE(T) specimen experienced the least. Crack closure levels for the M(T) specimen fell between the other two geometries but closer to the ESE(T). The large shift observed for the C(T) specimen is a result of the significantly higher crack opening loads observed in comparison to those observed for the other two

geometries (Figure 5). This figure compares the ratio of the crack opening stress intensity and maximum stress intensity (K_{op}/K_{max}) to the stress intensity range (ΔK). During load shedding, as ΔK decreased and approached threshold, the opening load to maximum load ratio increased significantly for the C(T) specimen and to a lesser extent for the ESE(T) and the M(T), although the M(T) crack opening load was always greater than that observed for the ESE(T). The general trend for the C(T) specimen was a moderate increase in K_{op}/K_{max} which leveled off as threshold conditions were approached. For the M(T) and ESE(T) specimens, K_{op}/K_{max} showed a very gradual increase followed by a rapid increase as the stress intensity range approached threshold. A summary of the threshold values is shown in Table 1.

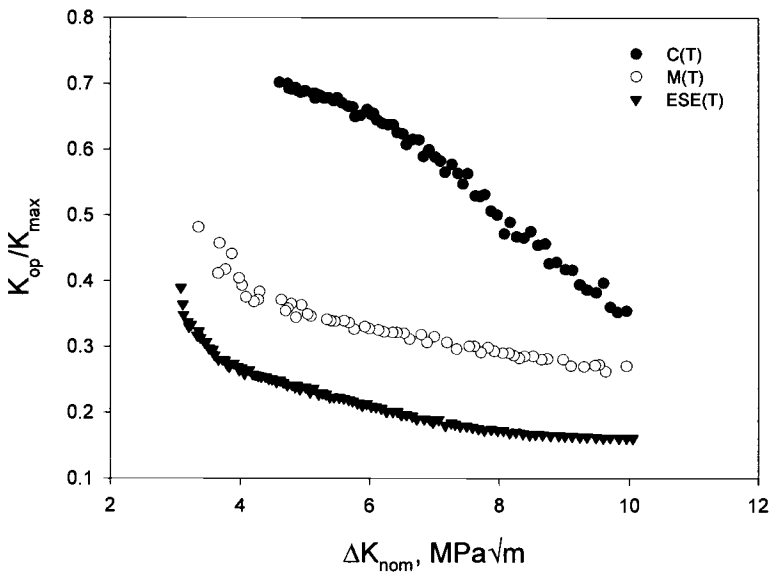


Figure 5 – K_{op}/K_{max} vs. ΔK for constant amplitude near threshold loading, $R=0.1$.

Table 1 – Fatigue Crack Growth Threshold Values

Specimen Type	$R=0.1$	$R=0.1$	$R=0.7$
	$\Delta K_{th,nom}$ (MPa√m)	$\Delta K_{th,eff}$ (MPa√m)	ΔK_{th} (MPa√m)
M(T)	3.3	1.9	2.1
ESE(T)	3.1	2.1	2.8
C(T)	4.5	1.5	2.6

For $R=0.1$, crack growth rates decreased as the loading was changed from being symmetric with respect to the load line (M(T)) to an asymmetric condition (C(T)). One might expect the fatigue crack growth rates observed for the ESE(T) specimen to fall between the M(T) and C(T) crack growth rate curves inasmuch as it is also asymmetrically loaded, although to a lesser extent than the C(T) specimen. However, this was not the case, which will be discussed in detail later.

Nominal fatigue crack growth data for the three specimen geometries, when plotted in terms of ΔK_{eff} , did not improve the correlation in the fatigue crack growth data, as reported by Horng and Fine [5]. In addition, at $R=0.7$, where crack closure contributions were minimal, there was still a small difference in the fatigue crack growth behavior. However, the higher crack opening loads observed for the C(T) specimen in comparison to the other geometries were consistent with that reported by Horng and Fine [5], Vecchio *et al.* [6], and Saxena *et al.* [7]. Lang *et al.* [4] attributed specimen closure differences observed to the inherent stress gradient of the specimens. In more symmetrically loaded specimens, the stress gradient away from the crack across the specimen width is very small, while for more asymmetrically loaded specimens there exists a higher stress gradient due to the bending component. A uniform stress distribution tends to keep the crack open for a major part of the fatigue cycle, while a higher stress gradient leads to early closure of the crack [4]. This argument helps account for the higher crack opening loads observed in the C(T) specimen in comparison to the ESE(T) and M(T) specimens.

In general, the lower ΔK_{th} values and higher crack growth rates for more symmetrically loaded specimens are consistent with other studies [3-7] when compared with asymmetrically loaded specimens. Higher crack growth rates and a lower threshold stress intensity value for the ESE(T) specimen in comparison to the C(T) specimen are consistent with comparisons made between the SE(T) and the C(T) [5, 7]. The SE(T) and ESE(T) geometries have similarities, with the main difference being the location of the load line. The asymmetric loading of the C(T) specimen is greater in magnitude than with the ESE(T) specimen, thus the crack growth behavior observed for these two geometries is consistent with previous findings.

An examination of the fracture surfaces for the intermediate and higher crack growth rates revealed similar characteristics for the different geometries. The fracture surfaces were relatively smooth with evidence of both faceting and fatigue striations. For the intermediate crack growth rates, there were no discernible differences between the fracture surfaces of the three specimen geometries. For the near-threshold tests, as the applied ΔK level was reduced below approximately $10 \text{ MPa}\sqrt{\text{m}}$ to near-threshold conditions, the fracture surface morphology became more crystallographic in nature with more facets present, as observed in SEM fractographs. The observed increase in fracture surface roughness with decreasing ΔK level for all three specimen types supports the crack opening measurements (Figure 5), as the measured $K_{\text{op}}/K_{\text{max}}$ ratio increased with decreasing ΔK . An increase in surface roughness with decreasing ΔK was observed for all three specimen geometries, as determined from SEM fractographs. However, it was observed that the fracture surface roughness was greatest for the C(T) specimen and approximately the same for the ESE(T) and M(T) specimens (Figure 6). The corresponding ΔK_{th} associated with these fractographs was between approximately 3 and

4.5 MPa \sqrt{m} , depending on geometry. A rougher fracture surface would tend to lead to greater mode II displacement during crack growth. This would in turn lead to higher crack opening loads, which is consistent with the observations made in this study for the three geometries, and especially for the C(T) specimen. The variation in surface roughness observed between the three specimen geometries does not explain all of the differences observed in the fatigue crack growth behavior. These remaining differences suggest that other conditions existed that may have influenced the crack tip/microstructure interaction. A discussion of possible contributing factors follows.

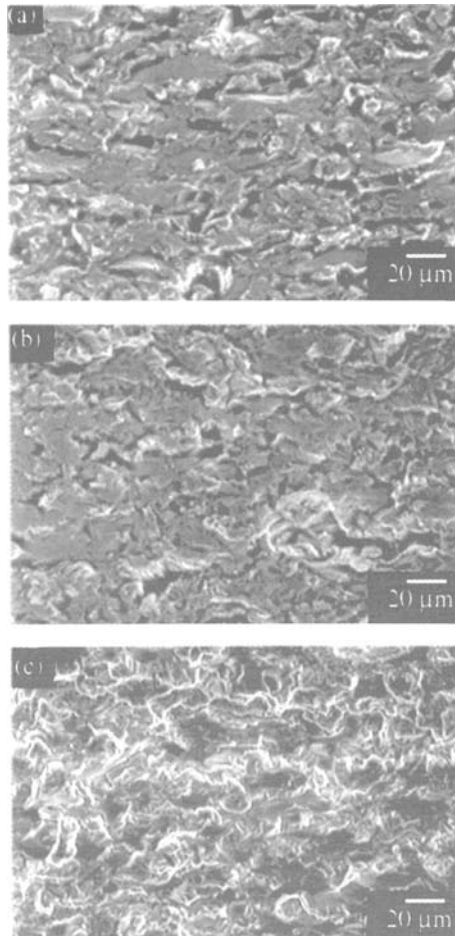


Figure 6 – SEM fractographs showing surface morphology at near threshold conditions; (a) M(T), (b) ESE(T), (c) C(T).

Crack Tip Stress Field

Previous studies [4,6] have shown that at a given ΔK the y -direction stress distribution ahead of the crack tip is higher in the M(T) specimen than in the C(T) and WOL specimens. Based on finite element analysis, Vecchio *et al.* [6] showed the y -direction stress is very similar for the M(T) and C(T) specimens close to the crack tip (within 0.02 mm), yet increases for the M(T) at distances farther away from the crack tip. It is reasonable to assume that the y -direction stress for the ESE(T) specimen is also similar to the M(T) and C(T) specimens close to the crack tip. It was also reported that the higher y -direction stress distribution observed in the M(T) specimen resulted in a larger process zone (the cyclic plastic zone) in the M(T) specimen than in the C(T) specimen. These studies concluded that because of the higher y -stress distribution, more damage accumulated (as a result of the larger process zone) in the M(T) specimen precipitating higher crack growth rates. The material used in this study has a yield strength of 1112 MPa. For $R=0.1$ at $\Delta K=10$ MPa $\sqrt{\text{m}}$, the monotonic plastic zone size in the crack plane based on plane stress conditions was calculated to be approximately 32 μm ($2r_y=(K_{\text{max}}/\sigma_{ys})^2/\pi$). The cyclic plastic zone was calculated to be roughly 8 μm . At the threshold value for the C(T) specimen ($\Delta K_{\text{th}}=4.5$ MPa $\sqrt{\text{m}}$), the monotonic and cyclic plastic zone sizes were approximately 6.4 μm and 1.6 μm , respectively. Because of lower threshold values, the plastic zone sizes for the M(T) and ESE(T) specimens at threshold were even smaller. Therefore, the cyclic plastic zone size associated with the threshold and near threshold conditions presented in this study are contained within the distance ahead of the crack tip (≤ 20 μm) where the y -direction stress is similar for the three geometries. Therefore, similar y -direction stresses just ahead of the crack tip would result in similar plastic zone sizes. Because of the high strength and small plastic zones observed in this material for near threshold conditions at $R=0.1$, it is assumed the differences in crack growth behavior are not associated with the difference in the y -direction stress distribution for the three specimen geometries.

What appears to be of greater significance in this study at $R=0.1$ is the effect of the additional biaxial stress (the T -stress) developed at the crack tip. Previous studies reported that the size and shape of the plastic zone is effected by the level of remotely applied biaxial stress, where higher biaxial stress ratios result in smaller plastic zones [1,17,18]. Larsson and Carlsson [13] also showed similar behavior for uniaxially loaded M(T) and C(T) specimens due to the inherent stress biaxiality in these geometries. Joshi and Shewchuk [19] explained that when a positive biaxial stress is applied to a uniaxially loaded specimen, additional plastic constraint is placed on the crack tip, reducing the plastic zone size, and contributing to slower crack growth. While T -stress solutions for the C(T) and M(T) specimens have been extensively published [14-15, 20-21], a solution for the ESE(T) specimen was performed by the present authors over an a/W range of 0.2 to 0.7 using finite element analysis for comparison. As a verification of the method and model used, an analysis was also performed on the C(T) geometry to compare results with previously published solutions (Figure 7). The T -stress solution for the M(T) specimen is always negative ($B\approx-1$), and only changes slightly as a function of crack length. For the ESE(T) specimen, the T -stress is negative until an a/W ratio of approximately 0.45 and then becomes positive. At a given a/W ratio, B is always lower

in the ESE(T) specimen than in the C(T) specimen. Because of similar crack growth behavior for the M(T) and ESE(T) specimens and the lower T -stresses in these geometries, it is suggested that in this study there was a dependence of the fatigue crack growth behavior on the T -stress.

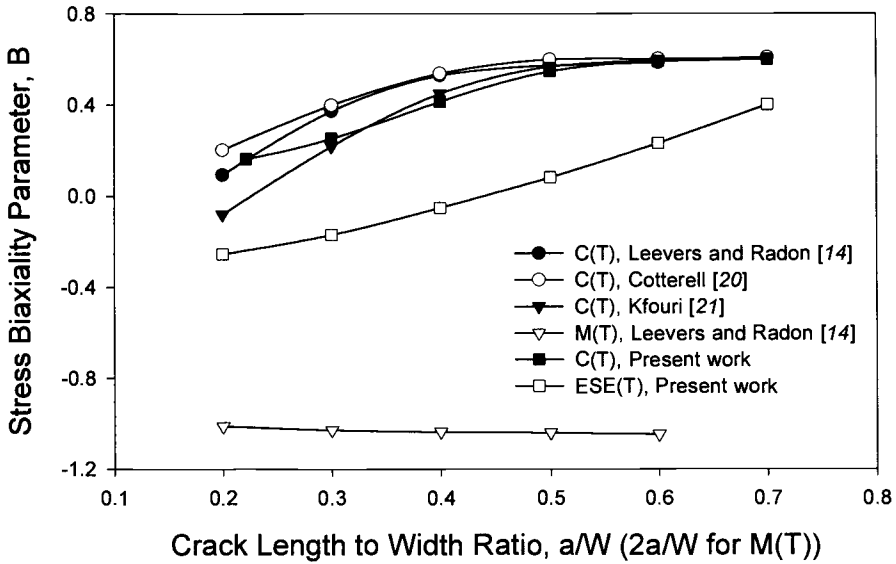


Figure 7 – Comparison of stress biaxiality parameter (B) vs. crack length to width ratio (a/W) for C(T), ESE(T), and M(T) specimen geometries.

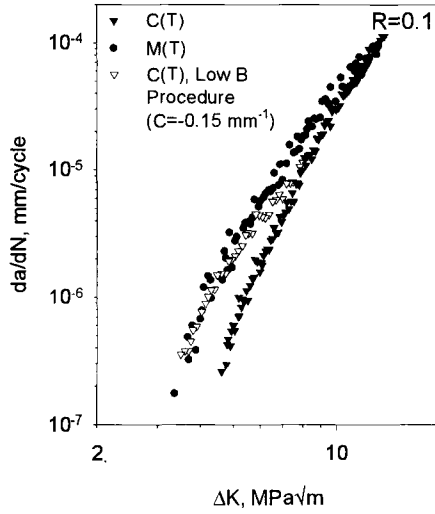
The reduced specimen geometry effect observed at $R=0.7$ is believed to be related to a correlation between the cyclic plastic zone size and the grain size of the material. At $R=0.7$, K_{max} is much larger in comparison to that observed at $R=0.1$ for the same ΔK . Therefore, at given ΔK levels, the cyclic plastic zone size is much larger at $R=0.7$ than at $R=0.1$. At $\Delta K=10 \text{ MPa}\sqrt{\text{m}}$, the cyclic plastic zones were approximately $8 \mu\text{m}$ and $70 \mu\text{m}$ for $R=0.1$ and 0.7 , respectively. Also, at $\Delta K=4 \text{ MPa}\sqrt{\text{m}}$, the cyclic plastic zone size is roughly $10 \mu\text{m}$ for $R=0.7$, the typical grain size dimension for this material. Several studies [22-24] have shown a good correlation between material grain size and cyclic plastic zone as a transition from a structure-sensitive mode of fatigue crack growth to a structure-insensitive one. These studies support the argument that when the plastic zone size is greater than the microstructural dimension, material damage is fairly homogeneous and relatively structure-insensitive. This is associated with region II type growth. As the cyclic plastic zone becomes smaller than the grain size, structure-sensitive crack growth occurs, corresponding to region I type growth. This occurs at approximately $\Delta K=4 \text{ MPa}\sqrt{\text{m}}$ for $R=0.7$, which also corresponds to the small divergence in crack growth behavior (Figure 4a). Therefore, at $R=0.7$, region II type growth is extended to lower ΔK

values in comparison to $R=0.1$, which accounts for the similar fatigue crack growth behavior observed between the three geometry types at $R=0.7$. At $R=0.1$, where the cyclic plastic zone is much smaller and on the order or less than the material grain size, crack growth is more dictated by the crack tip/microstructure/stress field interaction.

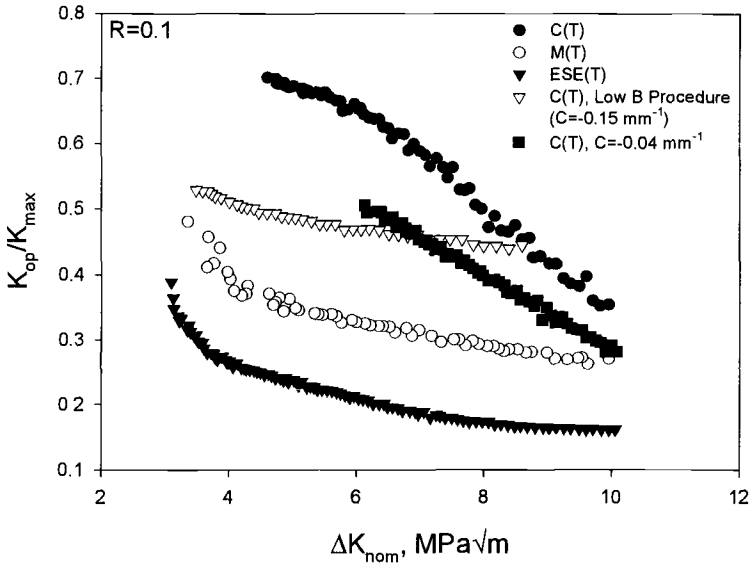
Load Reduction Procedure

Considering stress biaxiality effects on crack growth behavior, it follows logically that a similar trend (higher crack growth rate for lower B) may exist in uniaxially loaded specimens where the level of stress biaxiality varies with crack length, as in the ESE(T) and C(T). To examine this theory, a modified test procedure was devised that would result in B values of approximately one half the B values observed in the test procedure previously described for the C(T) specimen. This was achieved by starting the threshold test at a different ΔK and crack length, and load shedding at a different rate. The procedure consisted of a rapid precrack at $C=-0.52 \text{ mm}^{-1}$ ending at $a=9 \text{ mm}$ and $\Delta K=8 \text{ MPa}\sqrt{\text{m}}$. The threshold test was then started and the load was shed at $C=-0.15 \text{ mm}^{-1}$. The results show that the nominal fatigue crack growth curve gradually shifted to match the fatigue crack growth curve of the M(T) specimen (Figure 8a). Crack opening loads were still higher for the C(T) than in the ESE(T) or M(T), but lower than the baseline C(T) experiment (Figure 8b). Higher crack growth rates were seen despite the fact that this test was performed at a steeper K -gradient. This suggests a crack growth dependence on test procedure, and in particular, the level of stress biaxiality seen at the crack tip as a result of the test procedure. In addition, with the C(T) and ESE(T) specimens, it is difficult to separate the effects of the K -gradient and biaxiality level on crack growth because each is influenced by the other. This may not be the case in the M(T) specimen, where B changes only slightly as a function of crack length.

For practical reasons, the ASTM load reduction procedure is based on the nominal stress intensity range ΔK , although ΔK_{eff} has been shown to more effectively rationalize differences in crack growth behavior under conditions where closure levels vary. To evaluate the effective load shedding rate, an "effective" K -gradient, C_{eff} , was calculated for each threshold test. Average C_{eff} values for the M(T) and ESE(T) specimens were approximately -0.10 mm^{-1} . However, the C(T) specimen, which exhibited higher levels of closure, had C_{eff} values of nearly -0.15 mm^{-1} through most of the test. Based on these observations, an additional C(T) threshold test was performed with a K -gradient of $C=-0.04 \text{ mm}^{-1}$. The precracking procedure for this test was the same as for the test performed at $C=-0.08 \text{ mm}^{-1}$. Due to the low load shedding rate, ΔK levels below approximately $6 \text{ MPa}\sqrt{\text{m}}$ were not attained because the crack length exceeded the specimen width, leading to premature specimen failure. However, a general trend was established. The average C_{eff} value for this test was about -0.07 mm^{-1} . The nominal crack growth behavior was unchanged, but the ΔK_{eff} curve more closely matched the ΔK_{eff} curves for the M(T) and EC(T) specimens. Based on this study, it would appear that the ASTM recommended load shedding rate of -0.08 mm^{-1} may not be appropriate for some materials and specimen geometries, as variations from the recommended load shedding rate can influence closure levels and can lead to more conservative (lower) threshold values.



(a)



(b)

Figure 8 – Comparison of various load-history conditions; (a) fatigue crack growth behavior, (b) K_{op}/K_{max} vs. ΔK .

Conclusions

Based upon the nominal stress intensity factor range for $R=0.1$, fatigue crack growth rates were found to be higher in the M(T) and ESE(T) specimens than in the C(T) specimen for lower crack growth rates. Correcting for crack closure, growth rates were higher in the C(T) specimen than in the M(T) and ESE(T) specimen. Crack opening load differences were attributed to variations in fracture surface roughness for the three specimen geometries, with the C(T) specimen developing the roughest fracture surface as indicated by fractographic observations. At $R=0.7$, where crack closure contributions were minimized, differences were still observed in crack growth behavior, yet to a lesser extent.

At $R=0.1$, the plastic zone sizes calculated for near threshold conditions were found to be contained within the dimension ahead of the crack tip where the y -direction stress for the three geometries is similar. Therefore, the y -stress distribution ahead of the crack tip was assumed to have little influence on the fatigue crack growth behavior at $R=0.1$. Similar fatigue crack growth behavior for the symmetrically loaded M(T) and asymmetrically loaded ESE(T) specimen also supports this claim.

Crack growth differences at $R=0.1$ were attributed to the stress biaxiality inherent to the specimen geometries studied. Generally, lower B values corresponded to higher crack growth rates. This was also found to be true for the C(T) specimen when the test procedure was changed, resulting in lower B values and thus an increase in the crack growth rate.

Variations explored in the K - a history for the C(T) specimen suggest a crack length dependence on the fatigue crack growth behavior. It is felt that the ASTM recommended load shedding rate of -0.08 mm^{-1} may be inappropriate for certain specimen geometries, as changes in the load shedding rate produced shifts in both the nominal and effective fatigue crack growth curves, resulting in more conservative threshold values.

Acknowledgments

The authors gratefully acknowledge research funding from Lockheed-Martin Aeronautical Systems Company. Special thanks are due to the Idaho Space Grant Consortium as well as the State of Idaho for financial assistance of this research program. The authors would also like to thank J. C. Newman, Jr. and E. P. Phillips for helpful discussions regarding this study.

References

- [1] Liu, A. F., Allison, J. E., Dittmer, D. F., and Yamane, J. R., "Effect of Biaxial Stresses on Crack Growth," *Fracture Mechanics, ASTM STP 677*, C. W. Smith, Ed., American Society for Testing and Materials, 1979, pp. 5-22.
- [2] Leever, P. S., Culver, L. E., and Radon, J. C., "Fatigue Crack Growth in PMMA and Rigid PVC under Biaxial Stress," *Engineering Fracture Mechanics*, Vol. 11, 1979, pp. 487-498.

- [3] Shercliff, H. R. and Fleck, N. A., "Effect of Specimen Geometry on Fatigue Crack Growth in Plain Strain – II. Overload Response," *Fatigue and Fracture of Engineering Materials and Structures*, Vol. 13, 1990, pp. 297-310.
- [4] Lang, R. W., Hahn, M. T., Hertzberg, R. W., and Manson, J. A., "Effects of Specimen Configuration and Frequency on Fatigue Crack Propagation in Nylon 66," *Fracture Mechanics: Fifteenth Symposium, ASTM STP 833*, R. J. Sanford, Ed., American Society for Testing and Materials, Philadelphia, 1984, pp. 266-283.
- [5] Horng, J. L. and Fine, M. E., "Near-threshold Fatigue Crack Propagation Rates of Dual-phase Steels," *Materials Science and Engineering*, Vol. 67, 1984, pp. 185-195.
- [6] Vecchio, R. S., Crompton, J. S., and Hertzberg, R. W., "The Influence of Specimen Geometry on Near Threshold Fatigue Crack Growth," *Fatigue and Fracture of Engineering Materials and Structures*, Vol. 10, 1987, pp. 333-342.
- [7] Saxena, V. K., Malakondaiah, G., and Radhakrishnan, V. M., "Influence of Specimen Configuration and Loading History on Fatigue Crack Growth Behaviour of 2024-T3 Clad Aluminum Alloy," *Engineering Fracture Mechanics*, Vol. 49, 1994, pp. 153-157.
- [8] Betegón, C. and Hancock, J. W., "Two-Parameter Characterization of Elastic-Plastic Crack-Tip Fields," *Journal of Applied Mechanics*, Vol. 58, 1991, pp. 104-110.
- [9] Wang, Y.-Y., "On the Two-Parameter Characterization of Elastic-Plastic Crack-Front Fields in Surface-Cracked Plates," *Constraint Effects in Fracture, ASTM STP 1171*, E. M. Hackett, K.-H. Schwalbe, and R. H. Dodds, Eds., American Society for Testing and Materials, 1993, pp. 120-138.
- [10] Sumpter, J. D. G., "An Experimental Investigation of the T Stress Approach," *Constraint Effects in Fracture, ASTM STP 1171*, E. M. Hackett, K.-H. Schwalbe, and R. H. Dodds, Eds., American Society for Testing and Materials, 1993, pp. 492-502.
- [11] Williams, M. L., "On the Stress Distribution at the Base of a Stationary Crack," *Journal of Applied Mechanics*, Vol. 24, 1957, pp. 109-114.
- [12] Rice, J. R., "Limitations to the Small Scale Yielding Approximation for Crack Tip Plasticity," *Journal of Mechanics and Physics of Solids*, Vol. 22, 1974, pp. 17-26.
- [13] Larsson, S. G. and Carlsson, A. J., "Influence of Non-Singular Stress Terms and

Specimen Geometry on Small-Scale Yielding at Crack Tips in Elastic-Plastic Materials," *Journal of Mechanics and Physics of Solids*, Vol. 21, 1973, pp. 263-277.

- [14] Leevers, P. S. and Radon, J. C., "Inherent Stress Biaxiality in Various Fracture Specimen Geometries," *International Journal of Fracture*, Vol. 19, 1982, pp. 311-325.
- [15] Sherry, A. H., France, C. C., and Goldthorpe, M. R., "Compendium of T -Stress Solutions for Two and Three Dimensional Cracked Geometries," *Fatigue and Fracture of Engineering Materials and Structures*, Vol. 18, 1995, pp. 141-155.
- [16] Piascik, R. S., Newman Jr., J. C., and Underwood, J. H., "The Extended Compact Tension Specimen," *Fatigue and Fracture of Engineering Materials and Structures*, Vol. 20, 1997, pp. 449-563.
- [17] Adams, N. J. I., "Some Comments on the Effect of Biaxial Stress on Fatigue Crack Growth and Fracture," *Engineering Fracture Mechanics*, Vol. 5, 1973, pp. 983-991.
- [18] McClung, R. C., "Closure and Growth of Mode I Cracks in Biaxial Fatigue," *Fatigue and Fracture of Engineering Materials and Structures*, Vol. 12, 1989, pp. 447-460.
- [19] Joshi, S. R. and Shewchuk, J., "Fatigue-crack Propagation in a Biaxial-stress Field," *Experimental Mechanics*, Vol. 10, 1970, pp. 529-533.
- [20] Cotterell, B., "On Fracture Path Stability in the Compact Tension Test," *International Journal of Fracture Mechanics*, Vol. 6, 1970, pp. 189-192.
- [21] Kfourri, A. P., "Some Evaluations of the Elastic T -term Using Eshelby's Method," *International Journal of Fracture*, Vol. 30, 1986, pp. 301-315.
- [22] Yoder, G. R., Cooley, L. A., and Crooker, T. W., "Quantitative Analysis of Microstructural Effects on Fatigue Crack Growth in Widmanstätten Ti-6Al-4V and Ti-8Al-1Mo-1V," *Engineering Fracture Mechanics*, Vol. 11, 1979, pp. 805-816.
- [23] Irving, P. E. and Beevers, C. J., "Microstructural Influences on Fatigue Crack Growth in Ti-6Al-4V," *Materials Science and Engineering*, Vol. 14, 1974, pp. 229-238.
- [24] Yuen, A., Hopkins, S. W., Leverant, G. R., and Rau, C. A., "Correlations Between Fracture Surface Appearance and Fracture Mechanics Parameters for Stage II Fatigue Crack Propagation in Ti-6Al-4V," *Metallurgical Transactions*, Vol. 5, 1974, pp. 1833-1842.

A. Varvani-Farahani¹ and T. H. Topper²

Increases in Fatigue Crack Growth Rate and Reductions in Fatigue Strength due to Periodic Overstrains in Biaxial Fatigue Loading

Reference: Varvani-Farahani, A. and Topper, T. H., “Increases in Fatigue Crack Growth Rate and Reductions in Fatigue Strength due to Periodic Overstrains in Biaxial Fatigue Loading,” *Fatigue Crack Growth Thresholds, Endurance Limits, and Design, ASTM STP 1372*, J. C. Newman, Jr. and R. S. Piascik, Eds., American Society for Testing and Materials, West Conshohocken, PA, 2000.

Abstract: Fatigue crack growth under biaxial constant amplitude straining (CAS) and a strain history having periodic compressive overstrains (PCO) were investigated.

A comparison of the growth of fatigue cracks under constant amplitude straining and under strain histories having periodic compressive overstrains revealed that the morphology of the fracture surface near the crack tip and the crack growth rate changed dramatically with the application of the compressive overstrains. When the magnitude of the compressive overstrains was increased, the height of the fracture surface irregularities was reduced as the increasing overstrain progressively flattened fracture surface asperities near the crack tip. The reduced asperity height was accompanied by drastic increases in crack growth rate and decreases in fatigue strength.

Crack opening stress measurements for biaxial fatigue cracks made using confocal scanning laser microscopy (CSLM) image processing of the crack profile, showed that the biaxial cracks were fully open at zero internal pressure for block strain histories containing in-phase periodic compressive overstrains of yield point magnitude. Therefore, for the shear strained samples there was no crack face interference and the strain intensity range was fully effective. For PCO tests with biaxial strain ratios of -0.625, and +1, effective strain intensity data were obtained from tests with positive stress ratios for which cracks did not close. The strain intensity factor ranges derived from popular fatigue life parameters were used to correlate fatigue crack growth rates for the various strain ratios investigated. These parameters all involved the shear strain range, and the normal strain range acting on the maximum shear strain plane. For various biaxiality ratios, the ratios of the effective strain intensity factor range to the constant amplitude strain intensity factor range at the threshold were found to be close to the ratios of the closure free fatigue limit obtained from effective strain-life to the constant amplitude fatigue limit.

Keywords: Biaxial fatigue, periodic compressive overstrain, confocal scanning laser microscopy technique, closure-free fatigue life, crack growth rate, intensity factor range

Many investigations [1-3] have shown that, for both short and long fatigue cracks, periodic compressive overstrains of near yield stress magnitude drastically accelerate both crack initiation and crack propagation.

¹Professor- Department of Mechanical Engineering, Ryerson Polytechnic University, Toronto, M5B 2K3 Canada

²Professor- Civil Engineering Department, University of Waterloo, N2L 3G1 Canada

At near threshold stress intensities, these effects are thought to be due to a flattening of crack tip asperities by the high compressive stress which leads to a reduction in crack closure and an acceleration in crack growth. The results of Topper and Yu [1] showed that increased propagation rates and decreased threshold stress intensities accompanied the application of periodic compressive overstrains for various metals. Their findings also revealed crack opening stress levels below zero for large compressive overstrains. Similarly, Zaiken and Ritchie [4] proposed two mechanisms responsible for the decreased opening stress level: (i) the flattening of fracture surface asperities and (ii) a change in the residual stresses ahead of the crack tip. However, they argued that the contribution of the residual stress ahead of the crack tip would not be significant.

Previous studies [3, 5] investigated the growth of short fatigue cracks under constant amplitude straining and strain histories having periodic compressive overstrains of various magnitudes. They reported that the fracture surface near the crack tip and the crack growth rate changed dramatically with the magnitude of the compressive overstrain. The height of the surface irregularities reduced as the compressive overstrain increased and progressively flattened fracture surface asperities near the crack tip. This resulted in a reduced crack closure stress and a higher crack growth rate. Varvani-Farahani and Topper [6] developed a model of the plastic deformation of the fracture surface asperities at the crack tip to relate the crushing of the asperities to crack closure and crack growth rate. They correlated the magnitude of the periodic compressive overstrain, the fracture surface asperity height and the plastically flattened area to the fully effective strain intensity factor range (ΔK_{eff}).

This study provides quantitative information concerning crack growth rates as a crack grows into the interior of the specimen under biaxial strain ratios (hoop strain/axial strain) of $\lambda = -1, -v, -0.625$ and $+1$ obtained using a Confocal Scanning Laser Microscopy (CSLM) image processing technique. CSLM also provided accurate measurements of the height of asperities for constant amplitude straining and for periodic compressive overstrain histories. The effect of periodic compressive overstrains on fracture surface asperities, crack growth rate, and fatigue life for uniaxial and biaxial fatigue straining conditions were studied. A number of strain intensity parameters derived from popular critical shear plane parameters were used to correlate fatigue lives and crack growth rates for the various strain ratios investigated. These parameters all involved the shear strain range, the normal strain range and the crack depth on the maximum shear strain plane. The following critical plane approaches were examined in this study.

1. Shear strain parameter (Tresca)- the earliest shear plane theory used the shear strain amplitude on the plane of maximum shear strain amplitude to correlate fatigue lives for different biaxial strain ratios.

$$\gamma_{max} = \text{Max} [|\epsilon_a - \epsilon_r| \text{ or } |\epsilon_a - \epsilon_h| \text{ or } |\epsilon_h - \epsilon_r|] \tag{1}$$

where ϵ_a , ϵ_h , and ϵ_r are axial, hoop, and radial strain on tubular specimen respectively.

2. Brown and Miller [7] proposed that fatigue cracks initiate on the planes of maximum shear strain and hypothesized that the maximum shear strain amplitude (γ_{max}) and the amplitude of the strain normal to the plane of maximum shear strain (ϵ_n) were the critical parameters governing fatigue damage. The Brown-Miller life parameter is defined as

$$\frac{\Delta\gamma_{max}}{2} + C \Delta\epsilon_n = \text{Constant} \tag{2}$$

where $\Delta\gamma_{max}$ and $\Delta\epsilon_n$ are the maximum shear strain range and normal strain range on the maximum shear strain plane, respectively.

The value of the constant C of 0.30 was chosen to best fit the fatigue data presented in this study.

3. Kandil et al. [8] derived the following equivalent shear strain parameter for correlating multiaxial fatigue data

$$\bar{\gamma} = 2 \left[\left(\frac{\gamma_{\max}}{2} \right)^{\kappa} + S \varepsilon_n^{\kappa} \right]^{\frac{1}{\kappa}} \quad (3)$$

The values of the constants $\kappa=0.50$ and $S=0.20$ were chosen to give the best fit curve to the present fatigue data.

4. Fatemi and Socie [9] have demonstrated a robust correlation of fatigue data for various stress states with and without mean stress, based on the assumption that the peak normal stress to the plane of maximum shear strain range directly affects the Stage I shear-dominated propagation of small cracks. They proposed the following parameter

$$\frac{\Delta\gamma_{\max}}{2} \left[1 + k \frac{\sigma_n}{\sigma_y} \right] = f(N_f) \quad (4)$$

where k is a constant equal to 0.60 for 1045 steel [9], N_f is the number of cycles to failure, and σ_n and σ_y are the normal stress and yield stress, respectively.

Experimental Procedure

Material, Properties, and Specimen Design

The material examined in this investigation was a SAE 1045 Steel in the form of 63.5 mm diameter bar stock with the following chemical composition (Wt %): 0.46 C, 0.17 Si, 0.81 Mn, 0.027 P, 0.023 S, and the remainder Fe. This material is a medium carbon heat treatable steel which is widely used in the automotive industry. The microstructure of the SAE 1045 steel after final polishing showed pearlitic-ferritic features containing up to 30 μm long sulfide inclusions in the rolling direction. The modulus of elasticity is 206 GPa, the cyclic yield stress is 448 MPa. Fig. 1 shows the solid uniaxial and tubular biaxial fatigue specimens used in this study.

Fatigue Crack Tests

Uniaxial Fatigue Tests—Uniaxial fatigue crack growth rate tests were performed in axial strain control in an MTS servo-hydraulic test machine with a load-cell capacity of 25000 lb (111.20 kN). The crack growth tests under uniaxial constant amplitude straining (CAS) were performed with a strain amplitude of $\pm 0.075\%$. Periodic compressive overstrain crack growth tests were performed with compressive overstrains of -0.17% , -0.24% , and -0.38% followed by numbers of small cycles n equal to 50, 200, 500, and 1000 [3]. Figs. 2a-b illustrate the crack growth test strain histories for uniaxial constant amplitude straining and a uniaxial strain history containing periodic compressive overstrains.

Biaxial Fatigue Tests—Thin-walled tubular specimens were cyclically strained in the axial direction in the strain frame while pressure was alternately applied to the inside and

outside of the specimen during each cycle. The biaxial fatigue machine is described in Ref. [5].

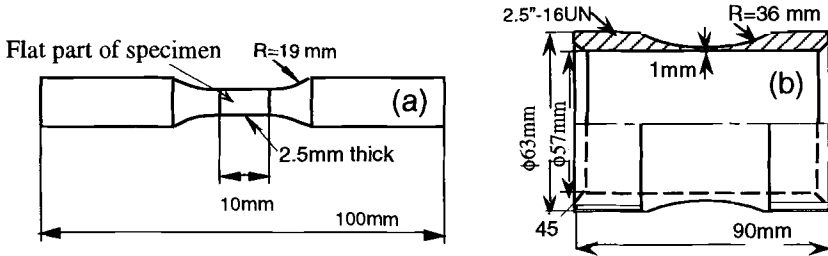


Figure 1 - Uniaxial Plate Specimen, and b) Biaxial Tubular Specimen

Three biaxial principal strain ratios (hoop strain/axial strain) were used $\lambda=-1$ (pure shear straining), a biaxial strain ratio of $\lambda=-0.625$, and $\lambda=+1$ (equibiaxial straining).

Constant amplitude biaxial fatigue tests and tests with strain histories containing periodic compressive overstrains (PCO) were performed in strain control at a frequency of 0.5 Hz. The axial strain (ϵ_a) and transverse (hoop) strain (ϵ_h) were controlled to provide the 180° out-of-phase biaxial strain ratio of $\lambda=-1$ and a strain ratio of -0.625 . The strain histories used for biaxial shear fatigue tests for strain ratios of -1 , and -0.625 , respectively are shown in Figs. 2c-d and 2e-f. One of the strain histories for each strain ratio is constant amplitude straining and the other has blocks of a periodic compressive overstrain followed by n small cycles. Equibiaxial fatigue ($\lambda=+1$) tests were performed under strain control for both constant amplitude straining and for strain histories containing periodic overstrains. The axial strain and hoop strain were controlled to provide an in-phase biaxial strain ratio of $\lambda=+1$. The strain histories used in equibiaxial fatigue are shown in Figs. 2g-h. The number of small cycles per block at each strain level was chosen so that the overstrain damage was about 20% of the total damage.

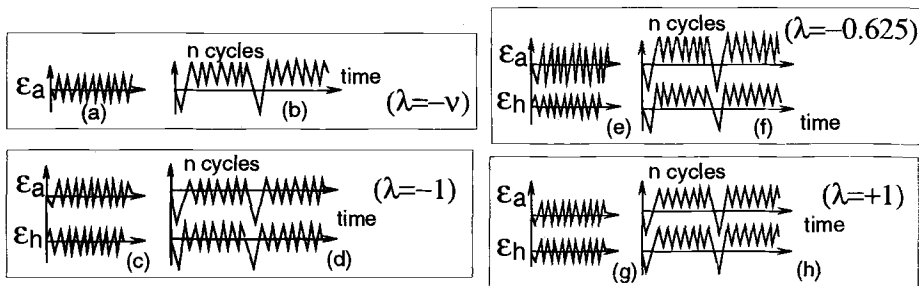


Figure 2 - Straining Histories for various Uniaxial and Biaxial CAS and PCO Conditions

Uniaxial and Biaxial Crack Depth and Crack Opening Measurements

Under uniaxial straining, a confocal scanning laser microscopy (CSLM) image processing technique was used to measure the crack depth of small cracks in the early stage

of growth (Stage I) as the number of cycles increased. The CSLM system which is described in detail in previous studies [10-11] has a resolution of 0.25 μm . Crack growth in Stage II was measured on the surface of the plate specimen shown in Fig. 1a using an optical microscope with a 500X magnification. Similarly, shear and equibiaxial fatigue crack lengths were measured using an optical microscope at the same intervals as the depth measurements were performed using CSLM.

Using a tensometer (tension machine) and a pressurizing device respectively for uniaxial and biaxial cracked specimens, cracked specimens were pulled to open the crack mouth under the CSLM system [11]. Then a laser beam was centered on the crack by direct observation through an attached optical microscope. The cracked specimen was scanned by the laser beam which was then reflected to a detector. Images from different levels of crack depth were obtained by changing the specimen height using a piezo-electric stage. A set of confocal image slices at depth steps of 1 μm were acquired. Post image processing was later used to combine all the images. Optical sectioning using post-image-processed crack data provided the crack depth and the crack mouth width at every point along the crack length for each tensile stress/internal pressure system employed. Fatigue crack growth tests under strain histories presented in Fig. 2 were performed by measuring the crack depth and crack length at intervals of 1000-5000 cycles.

Fracture Surface Asperity Height Measurements

A fractographic examination of the fracture surface of short fatigue cracks was carried out after breaking the 1045 Steel specimens in liquid nitrogen. The fracture surface and the variation in the height of asperities on the fracture surface were observed using a confocal scanning laser microscope. First, the laser beam was centered on the area of the fracture surface adjoining the crack tip by direct observation through an attached optical microscope. An area of 1 mm^2 of fracture surface at the crack tip was scanned by the laser beam and reflected to the detector. In order to obtain a three dimensional profile of fracture surface asperities, a piezo-electric stage, was used. The piezo-electric stage controls the distance between specimen and microscope. This provides successive images of level contours of the asperities from their peaks to their valleys. All images were combined to create an image of the configuration of the fracture surface profile. Taking different slices through this profile and determining an average value of fracture surface asperity height in each slice, revealed that the asperity height is dramatically influenced by the magnitude of the compressive overstrain. In this study the fracture surface asperity heights of specimens under both constant amplitude straining and strain histories containing periodic compressive overstrain cycles were measured. The CSLM measurements of the fracture surfaces of small cracks revealed that there was little variation of asperity heights across the fracture surfaces. The maximum variation of asperity height in an area of 1 mm^2 did not exceed 10%. The fracture surface asperity heights reported in the results section of this study are the average values of asperity height measured on a 1 mm^2 area of the fracture surface.

Results and Discussion

Cracking Behaviour for various Biaxiality Ratios

Uniaxial Fatigue Straining ($\lambda=-v$)—Under uniaxial straining, cracks first initiated and grew into the specimen on the maximum shear plane at 45° to the specimen surface (Stage I growth). After growing through one or two grains into the specimen (in the depth direction) in Stage I, the crack plane (in the depth direction) rotated to become normal to the axis of straining (Stage II growth). The plane of crack growth in Stage II was observed

from the fracture surface of the specimen after failure. Aspect ratios (a/c) of cracks which experienced fatigue straining just above the fatigue limit stress were found to be approximately 0.80. Using the CSLM technique [10], the crack depth profile (in Stage I crack growth) was found to be semi-elliptical in shape.

Equibiaxial Fatigue Cracks ($\lambda=+1$)—In equibiaxial (in-phase biaxial) fatigue tests on tubular specimens, cracks initiated and grew along the specimen surface on the two maximum shear planes parallel to and perpendicular to the specimen axis and propagated through the wall thickness on planes at 45° to the specimen axis. About two thirds of the equibiaxial fatigue cracks initiated parallel to the axial direction of the tubular specimen. The greater number of cracks in this direction which coincides with the direction of rolling is attributed to elongated sulfide inclusions parallel to the rolling direction. Equibiaxial fatigue cracks initiated at a few points on the tubular specimen and propagated along and into the specimen. In most tests, failure defined by oil leaking through the specimen thickness occurred when the crack length exceeded 2 mm.

Biaxial Shear Cracks of ($\lambda=-1$) and ($\lambda=-0.625$)—In 180° out-of-phase biaxial straining tests on tubular specimens, cracks initially nucleated on an active slip band system which coincided with the maximum shear planes at ± 45 degrees to the axial direction of the specimen. Microcracks (shear planes) propagated into the surface of the specimen while their length remained unchanged.

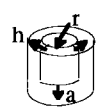
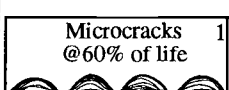
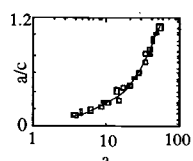
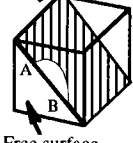

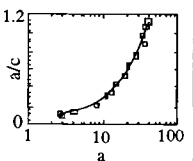
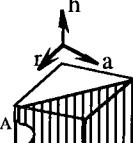
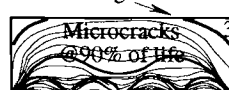
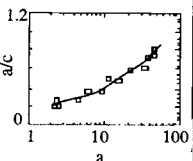
To measure the depth of microcracks, fatigued tubular specimens were pressurized internally using a hydraulic device in the confocal scanning laser microscope. Hoop and longitudinal stresses due to a progressive increase in the static internal pressure opened the crack along the maximum shear plane and three dimensional images of the crack were acquired. The crack opened and the crack depth increased with internal pressure until it was fully open. Under both shear straining ($\lambda=-1$) and a biaxial straining of $\lambda=-0.625$, many microcracks initiated and grew into the specimens. In each specimen, about 10 microcracks were marked and the depth and length of these microcracks were measured as the number of cycles progressed. Then the average crack length and depth of the ten microcracks at given cycle numbers from initiation to failure was calculated. The scatter in the measured length and depth of cracks in a specimen did not exceed 15%. The propagation of microcracks can be characterized as R-system crack behavior using the terminology introduced first by Marco and Starkey [12]. In this system, cracks start at many points on a specimen and progress toward the interior of the material (depth direction). The number of microcracks increased as cycling progressed. Once a crack initiated it grew into the specimen as the number of cycles increased but, its surface length did not increase much until the specimen reached about 90% of its fatigue life. The microcracks were uniformly distributed on the surface of specimen. At 60%-70% of the fatigue life, linking up of a few microcracks was observed. At 90%-95% of the fatigue life when the shape ratio of crack depth to half crack length reached unity, the microcracks began to grow in the length as well as in the depth direction and began linking up on shear planes. This linking up of microcracks led to failure shortly thereafter. Typically during failure inclined microcracks linked up in the longitudinal direction of a specimen to form a 2.0 mm to 5.0 mm crack. Table 1 presents the crack plane, the crack growth mechanisms for Stage I and Stage II crack growth, the variation of crack aspect ratio, and the ratio of N_i/N_f (crack initiation life to the fatigue failure life) for biaxial strain ratios of -0.625, -1, and +1.

The Effects of Periodic Compressive Overstrains on Fracture Surface Asperity Height

Uniaxial Fatigue Straining ($\lambda=-v$)—An examination of the growth of short fatigue cracks under constant amplitude straining and during strain histories having periodic

compressive overstrains of various magnitudes revealed that the fracture surface near the crack tip and the crack growth rate changed dramatically with the magnitude of the compressive overstrain. The height of the surface irregularities reduced as the compressive overstrain increased progressively flattening fracture surface asperities near the crack tip.

Table 1-Crack Plane, Stage I and II Crack Growth, Aspect Ratio, and N_i/N_f Ratio for various Biaxiality Ratios λ .

λ	(ϵ_w, ϵ_n) (%)	Crack Plane	Stage I and II Crack Growth	Aspect Ratio	$\frac{N_i}{N_f}$
-0.625	(0.128, -0.08)				0.088
	(0.16, -0.1)				0.074
	(0.2, -0.125)				0.078
	(0.24, -0.15)				0.068
	(0.29, -0.18)				0.070
-1	(0.15, -0.15)				0.050
	(0.20, -0.20)				0.110
	(0.30, -0.30)				0.095
	(0.50, -0.50)				0.090
+1	(0.10, 0.10)				0.074
	(0.135, 0.135)				0.088
	(0.15, 0.15)				0.086
	(0.22, 0.22)				0.083
	(0.30, 0.30)				0.085

CSLM image processing of the fracture surface in an area immediately behind the fatigue crack tip was used to measure the height of asperities for constant amplitude straining and for periodic compressive overstrains of -0.17%, -0.24%, and -0.38% (followed by 50 small fatigue cycles). Asperity height decreased from 28 μm in constant amplitude straining to 18, 13, and 8 μm for -0.17%, -0.24%, and -0.38% overstrains, respectively. A complementary investigation using a Scanning Electron Microscope (SEM) revealed compression-induced abrasion marks. The abrasion marks corresponded to the region close to the crack tip location when the compressive overstrains of -0.38% were applied [3].

Fig. 3a shows crack depth versus number of cycle plots for cracks for various magnitudes of the compressive overstrains. Fig. 3b shows that as the magnitude of periodic compressive overstrain increases the height of fracture surface asperities reduces.

The crack growth rate of short fatigue cracks in 1045 steel increases dramatically as the magnitude of compressive overstrain increases. A compressive overstrain led to a flattening of roughness asperities and therefore a reduction in closure stress. In this regard, Henkener et al. [13] reported that the crack growth rate increased as the magnitude of a compressive overload increased. The increased compressive overload led to an increase in the range of the effective intensity factor. Herman et al. [14] and Hertzberg et al. [15] also showed that a low closure stress (due to compressive loads) is associated with the crushing of asperities in the crack wake.

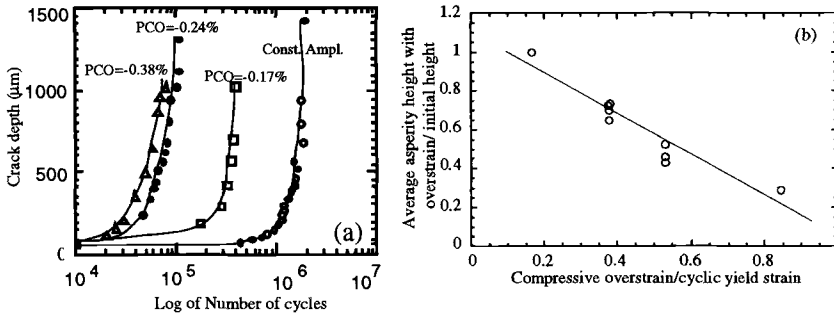


Figure 3- a) Crack Growth behavior under CAS and various PCO Histories, and b) Asperity Height versus various PCO Magnitudes

The crack growth behavior of short fatigue cracks under three periodic compressive overstrains (Fig. 3a) shows that the increase in crack growth rate from -0.17% to -0.24% compressive overstrain is much higher than that for an interval from -0.24% to -0.38% compressive overstrain. For a 1 mm increase in crack depth in this figure, a test at a -0.17% overstrain level requires 8000 blocks ($50 \times 8000 = 400,000$ cycles) while the tests with -0.24% and -0.38% overstrains correspond to about 1800 and 1500 blocks respectively. In this regard, Kemper et al. [16] and Tack and Beevers [17] observed a similar saturation effect in which increases in compressive overstrain beyond a certain level did not result in additional increases in crack growth rate.

Biaxial Fatigue Straining—CSLM measurements and SEM examinations of crack fracture surfaces, which had experienced in-phase periodic compressive overstrains, revealed that for all strain ratios the fracture surface asperities at the crack tip were severely flattened suggesting that the decreases in fatigue lives are mainly due to the crushing of fracture surface asperities by in-phase compressive overstrains. A typical SEM fractograph of a specimen subjected to an in-phase biaxial compressive overstrain of -0.3% followed by 19 small $\lambda = -1$ (shear straining) tension-compression cycles of $\pm 0.15\%$ strain is shown in Fig. 4b. A noticeable feature of the flattened asperities on the fracture surface of the in-phase PCO tests is the parallel abrasion lines. The deduction, that these lines are induced by the abrasion between crack flanks due to the compressive overstrain, is substantiated by the observation that parallel lines are formed in the same direction in all flattened areas. Similar reductions of asperity heights were observed for all other strain ratios.

For shear straining ($\lambda = -1$), CSLM observations showed that the application of a -0.3% compressive overstrain crushed the fracture surface asperities and resulted in fully open crack growth with no crack face interference. Thus, the full range of applied strain intensity

was effective. For uniaxial straining ($\lambda=-\nu$) and equibiaxial straining ($\lambda=+1$), PCO cycles increase the portion of a fatigue cycle that is effective (see Figs 5a-5b).

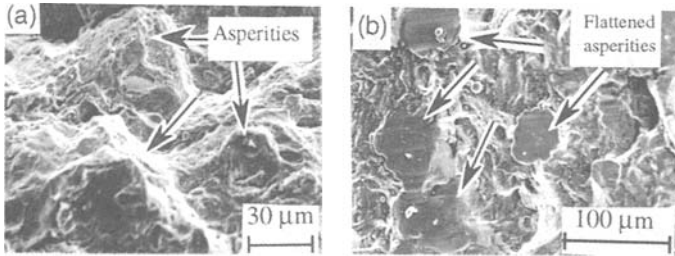


Figure 4- SEM Microphotographs of Fracture Surface Asperities a) before, and b) after Application of PCO Shear Straining History

Small cycle numbers were chosen so that the crack opening stress remained below the minimum stress and the whole strain cycle was effective. For PCO biaxial fatigue straining of -0.625 , there is both a decrease in crack face interference in the shear mode, and an increase in the effective portion of the opening mode due to overstrains. Again small cycle numbers were chosen so that the crack faces did not touch and the whole strain cycle was effective (see Fig 5c).

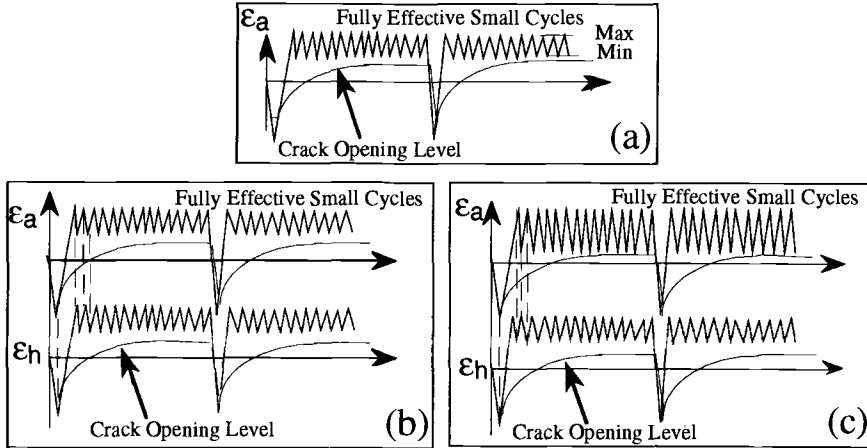


Figure 5- Fully Effective Small Cycles when the Crack Opening Level is less than Minimum Strain Level: a) Uniaxial Straining, b) Equibiaxial Straining, and c) Biaxial Straining of $\lambda=-0.625$

Fatigue Life Parameters based on Critical Shear Plane Approaches

Under both constant amplitude straining and strain histories containing periodic compressive overstrains, fatigue failure defined by oil leaking through the specimen

thickness occurred when the crack length exceeded 2.0 mm. Figs. 6a-6d plot the fatigue lives versus i) the maximum shear strain parameter (SSP), ii) the Brown and Miller parameter (BMP), iii) the Kandil et al. parameter (K et al. P), and iv) the Fatemi and Socie parameter (FSP) for various strain ratios. The upper data (open symbols) give fatigue lives under constant amplitude straining and the lower data (solid symbols) give equivalent small cycles to failure for strain histories containing periodic compressive overstrains in which the crack remained open during the small cycles.

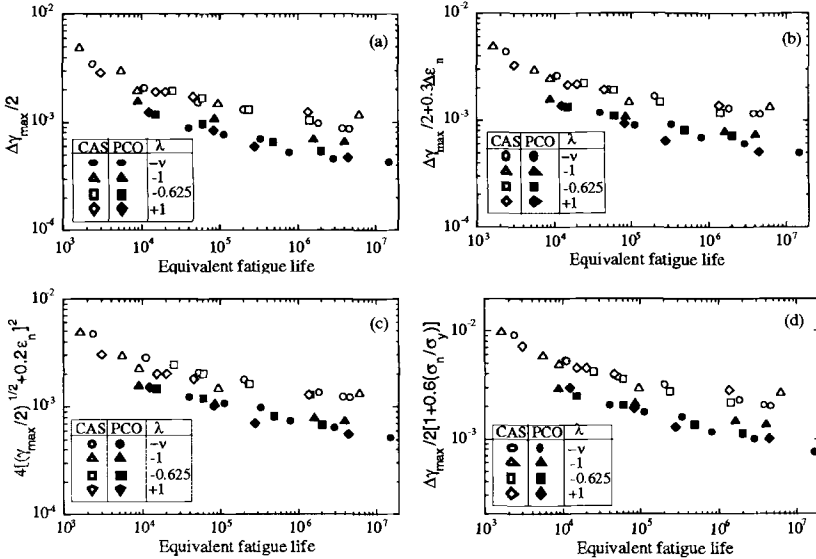


Figure 6- Fatigue Lives for Tests at various Strain Ratios versus Life Parameters of a)the Maximum Shear Strain. b) Brown and Miller, c) Kandil et al., and d) Fatemi and Socie for Constant Amplitude Straining and Periodic Compressive Overstrain Histories

For instance, Fig. 6a plots fatigue lives versus the maximum shear strain parameter for various strain ratios of $-v, -0.625, -1, +1$. These figures show a significant decrease in the fatigue strength of specimens which were subjected to periodic compressive overstrains of yield point magnitude. Under uniaxial straining, the fatigue strength was reduced by a factor that ranged from 1.50 at short lives (10^4 cycles) to 2.7 at the fatigue limit when periodic compressive overstrains of -0.38% were applied. The fatigue strength reduction due to the overstrains for $\lambda = -1$ straining varies from 1.40 at short lives (10^4 cycles) to 1.75 at the fatigue limit, for biaxial tests with a strain ratio of $\lambda = -0.625$ the reduction varied from 1.50 at short lives (10^4 cycles) to 1.90 at the fatigue limit, and for equibiaxial tests the reduction varied from 1.75 at short lives (10^4 cycles) to 2.80 at the fatigue limit when in-phase periodic compressive overstrains of -0.30% were applied. In Fig. 6 fatigue lives are given as an equivalent number of small cycles which is calculated as

$$N_{eq, SM} = N_T \left(1 - \frac{1}{n}\right) \bigg/ \left[1 - \left(\frac{N_T}{n N_{fOS}}\right)\right] \tag{5}$$

where

n = the number of small cycles following a compressive overstrain in a block history,
 N_T = the total number of cycles, and
 N_{fos} = the number of overstrain cycles to failure.

Figures 6a-6d show that the fatigue lives obtained under constant amplitude straining (with closure) and various biaxial strain ratios are collapsed onto one curve when they are plotted against the shear strain parameter, the Brown and Miller parameter, the Kandil, Miller and Brown parameter, and the Fatemi and Socie parameter. Fully effective (closure-free) fatigue life data obtained for the periodic compressive overstrain tests were correlated reasonably well for all strain ratios by the shear strain and the Brown-Miller (BM) approaches for lives less than 10^6 cycles. The Kandil-Miller-Brown parameter (KMB) and the Fatemi-Socie parameter (FS) show better correlations over the whole of the low cycle fatigue (LCF) and high cycle fatigue (HCF) regions.

Strain Intensity Factor Range Formulations based on Critical Shear Plane Components

Strain intensity factor range values [19] were calculated for a semi-elliptical surface crack under tensile mode straining, and shear mode straining using,

$$\Delta K_I = F_I Q E \Delta \varepsilon \sqrt{\pi a} \quad (6a)$$

$$\Delta K_{II} = F_{II} Q \Delta \gamma G \sqrt{\pi a} \quad (6b)$$

where

ΔK_I = the strain intensity factor range for the opening mode,
 ΔK_{II} = the strain intensity factor range for shear straining,
 F_I = the shape factor for a semi-elliptical opening mode crack,
 F_{II} = the shape factor for a semi-elliptical shear crack,
 Q = the surface strain concentration factor,
 $\Delta \varepsilon$ = the cyclic normal strain range,
 $\Delta \gamma$ = the cyclic shear strain range,
 E = the elastic modulus
 G = the shear modulus, and
 a = the crack depth on the plane of maximum shear strain.

The strain concentration factor Q [19] is a function of crack depth, a , and grain size, D , given by eqn (7)

$$Q = 1 + 5.3 \exp\left(-\alpha \frac{a}{D}\right) \quad (7)$$

where α/D is used as a constant which fits the measured fatigue limit strain $\Delta \varepsilon_n$ to the maximum strain calculated from

$$\Delta \varepsilon_{th} = \frac{\Delta K_{th}}{F Q E \sqrt{\pi a}} \quad (8)$$

In eqn (8), for uniaxial straining and pure shear straining, the shape factor F corresponds to F_I and F_{II} [18] respectively.

The effective strain based intensity factor range was modeled based on critical plane strain components. Critical plane approaches postulate that cracks initiate and propagate on the maximum shear strain plane and that the normal strain on this plane assists in the fatigue crack growth process. The components of this model consist of the maximum shear strain range and the normal strain range acting on the maximum shear strain plane [18]. Equations (9a-9c) provide the effective strain intensity factor ranges based on i) the shear strain parameter, ii) the Brown and Miller parameter, and iii) the Kandil et al. parameter, respectively.

$$\Delta K_{eff}^S = F_{II} Q G \Delta \gamma_{max} \sqrt{\pi a} \tag{9a}$$

$$\Delta K_{eff}^{BM} = Q G (F_{II} \Delta \gamma_{max} + 0.78 F_I \Delta \epsilon_n) \sqrt{\pi a} \tag{9b}$$

$$\Delta K_{eff}^K = Q G \left[F_{II} (\Delta \gamma_{max})^{0.5} + 0.73 F_I (\Delta \epsilon_n)^{0.5} \right]^2 \sqrt{\pi a} \tag{9c}$$

where shear modulus $G=E/2(1+\nu)$ and Poisson’s ratio (ν) in this study is $\nu=0.3$. The derivation of equations (9a-9c) are given in Ref. 20.

These parameters showed roughly the same ability to correlate fatigue crack growth rates. As mentioned earlier closure free crack growth was achieved in PCO tests by choosing a number of small cycles that maintained the measured crack opening stress below the minimum stress of the small cycles (see Fig. 5).

Closure Free Crack Growth Rate versus the Effective Strain Intensity Factor Ranges

Crack growth rates for biaxial strain ratios of $-\nu$, -0.625 , -1 , and $+1$ versus the effective strain intensity factor range values (ΔK_{eff}) -formulated based on the maximum shear strain parameter, the Brown and Miller parameter, and the Kandil et al. parameter- are plotted in Figs. 7a-c. In these figures, (da/dN) is the crack growth rate for the small cycles in PCO histories which is obtained by subtracting the crack growth due to the compressive overstrain cycles from the growth per block due to the periodic compressive overstrains followed by n small cycles and dividing by the number of small cycles per block.

$$\left(\frac{da}{dN} \right) = \frac{(n + m) \left(\frac{da}{dN} \right)_T - m \left(\frac{da}{dN} \right)_{os}}{n} \tag{10}$$

where

- $(da/dN)_{os}$ = crack growth rate due to overstrain cycles in a block history
- $(da/dN)_T$ = crack growth rate due to both small cycles and overstrain cycles in a block history
- n = the number of small cycles between two overstrains in a PCO block history, and
- m = the number of overstrain cycles in a PCO block history.

The constant amplitude strain intensity factor range (ΔK) at the threshold level for strain ratios of $-\nu$ and $+1$ was found to be about 9.0 and 8.9 $MPa\sqrt{m}$ respectively, and for strain ratios of -0.625 and -1 was found to be about 5.0 and 5.20 $MPa\sqrt{m}$ respectively.

Table 2 presents the ratios U_1 (the effective strain parameter range at the fatigue limit/the strain parameter range at the fatigue limit), and $U_2=\Delta K_{eff}/\Delta K$ at the threshold intensity level for various strain ratios and parameters.

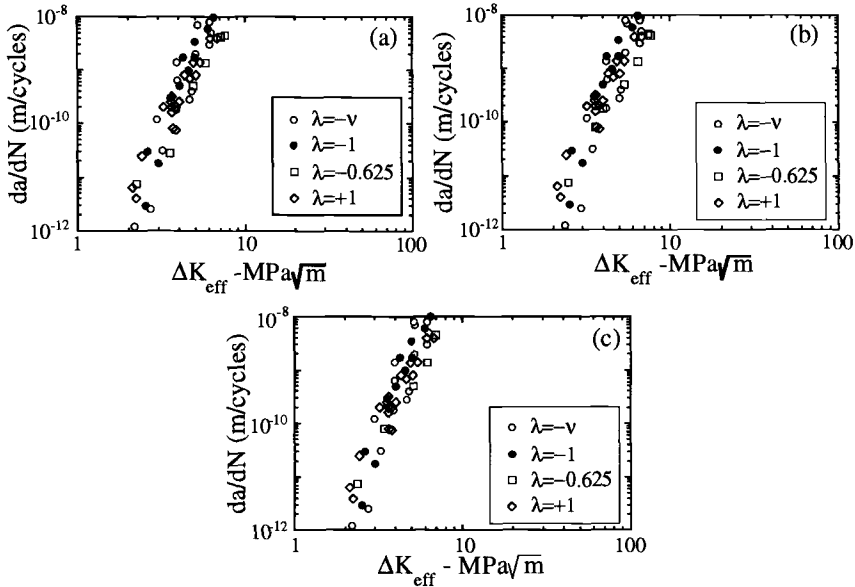


Figure 7- Crack Growth Rate versus Effective Strain Intensity Factor Range based on: a) the Shear Strain Parameter, b) the Brown and Miller Parameter, and c) the Kandil et al. Parameter

Table 2- U_1 and U_2 ratios for various strain ratios and critical shear plane parameters.

λ	U_1 Ratio at fatigue limit				U_2 Ratio at threshold level		
	SSP	BMP	K et al. P	FSP	SSP	BMP	K et al. P
- ν	0.37	0.38	0.38	0.325	0.30	0.32	0.30
-0.625	0.50	0.54	0.50	0.52	0.50	0.50	0.49
-1	0.50	0.50	0.51	0.50	0.48	0.48	0.48
+1	0.37	0.33	0.38	0.34	0.30	0.30	0.30

For various biaxiality ratios, the ratios of the effective strain intensity factor range at the threshold intensity to the constant amplitude strain intensity factor range at the threshold level were found to be close to the ratios of the closure free fatigue limit to the constant amplitude fatigue limit.

Conclusions

In this paper crack growth rates and fatigue lives under constant amplitude straining and periodic compressive overstrain histories were studied. Four principal strain ratios of - ν , -0.625, -1, and +1 were chosen.

1. In uniaxial straining ($\lambda=-\nu$), cracks initiated along the maximum shear plane at 45° to the surface of the specimen (Stage I growth) and failure then took place by Stage II growth perpendicular to the axis of the specimen. In equibiaxial fatigue straining ($\lambda=+1$), cracks

nucleated on the two maximum shear planes parallel and perpendicular to the specimen axis and initially propagated into the specimen on planes at 45° to the specimen surface (Stage I growth). They then propagated normal to the stress axis (Stage II growth). In both uniaxial and equibiaxial fatigue straining, a crack once initiated, grew in the length and depth directions until failure took place.

In tests with biaxial strain ratios of $\lambda=-1$ and $\lambda=-0.625$, surface cracks initially nucleated on slip bands at $40^\circ-45^\circ$ to the axis of the specimen. Then the growth of microcracks on shear planes into the specimen occupied up to 90% of the fatigue life during which time the surface length of the microcracks remained nearly constant. The microcracks started increasing in length after the crack became semi-circular ($a/c=1$) at about 90% of fatigue life. Failure then occurred by a rapid linking of microcracks.

2. CSLM measurements and an SEM examination of the growth of short fatigue cracks under uniaxial and biaxial constant amplitude straining and during strain histories having periodic compressive overstrains revealed that the crack growth rate increased dramatically with the magnitude of the compressive overstrain. The height of the fracture surface irregularities reduced progressively as the compressive overstrain increased, and flattened fracture surface asperities near the crack tip. This resulted in a reduced crack closure stress as well as fatigue strength and caused faster crack growth.

The magnitude and frequency of application of the periodic compressive overstrain cycles in the second test series was chosen to reduce the crack opening stress to a level below the minimum stress level of the constant amplitude cycles so that there was closure free crack growth. The compressive overstrains significantly increased crack growth rates and decreased the threshold strain intensity for the smaller constant amplitude cycles. They also caused a large decrease in the small cycle fatigue resistance as measured by their equivalent strain-life curves.

3. Fatigue lives obtained under constant amplitude straining (with closure) and various biaxial strain ratios were collapsed onto one curve when they were plotted against the shear strain parameter, the Brown and Miller parameter, the Kandil, Miller and Brown parameter, and the Fatemi and Socie parameter. Fully effective (closure-free) fatigue life data obtained for the periodic compressive overstrain tests were correlated reasonably well for all strain ratios by the shear strain and the Brown-Miller (BM) approaches for lives less than 10^6 cycles. The Kandil-Miller-Brown parameter (KMB) and the Fatemi-Socie parameter (FS) showed better correlations over the whole of the low cycle fatigue (LCF) and high cycle fatigue (HCF) regions. The effective strain intensity factor range was modeled based on critical plane strain components. For various biaxiality ratios, the ratios of the effective strain intensity factor range at the threshold intensity to the constant amplitude strain intensity factor range at the threshold level were found to be close to the ratios of the closure free fatigue limit to the constant amplitude fatigue limit.

References

- [1] Topper, T. H., and Yu, M. T., "The Effect of Overloads on Threshold and Crack Closure," *International Journal of Fatigue*, Vol.7, 1985, pp.159-164.
- [2] Yu, W., and Ritchie, R. O., "Fatigue Crack Propagation in 2090 Aluminum-Lithium Alloy: Effect of Compression Overload Cycles," *Journal of Engineering Materials and Technology*, Vol. 109, 1987, pp.81-85.
- [3] Varvani-Farahani, A., and Topper, T. H., "The Effect of Periodic Compressive Overloads on the Crack Surface Roughness and Crack Growth Rate of Short Fatigue Cracks in 1045 Steel," *Proceedings of Sixth International Fatigue Congress, Fatigue 96*, Berlin, Germany, Vol.I, 1996, pp.295-300.
- [4] Zaiken, E., and Ritchie, R. O., "On the Role of Compression Overloads in Influencing Crack Closure and Threshold Condition for Fatigue Crack Growth in 7150 Aluminum Alloy," *Engineering Fracture Mechanics*, Vol.22, 1986, pp.35-48.

- [5] Varvani-Farahani, A., and Topper, T. H., "Crack Growth and Closure Mechanisms of Shear Cracks under Constant Amplitude Biaxial Straining and Periodic Compressive Overstraining in 1045 Steel," *Int. J. Fatigue*, 1997, Vol.19, No.7, pp.589-596.
- [6] Varvani-Farahani, A., and Topper, T. H., "The Effect of Periodic Compressive Overstrain Excursions on Crack Closure and Crack Growth Rates of Short Fatigue Cracks—Measurements and Modelling," *the Second Symposium on Advances in Fatigue Crack Closure Measurements and Analysis. (ASTM STP 1343)*, Accepted for publication, 1999.
- [7] Brown, M. W. and Miller, K. J., "A Theory for Fatigue Failure under Multiaxial Stress-Strain Conditions," *Proceedings of the Institution Mechanical Engineering*, 1973, Vol.187, pp.745-755.
- [8] Kandil, F. A., Miller, K. J., and Brown, M. W., "Creep and aging interactions in biaxial fatigue of type 316 stainless steel," *Multiaxial Fatigue, ASTM STP 853*, K.J. Miller and M. W. Brown, Eds., 1985, pp.651-668.
- [9] Fatemi, A., and Socie, D. F., "A Critical Plane Approach to Multiaxial Fatigue Damage including Out of Phase Loading," *Fatigue Fract. Engng Mater. Struct.*, 1988, Vol.11, No.3, pp.149-165.
- [10] Varvani-Farahani, A., Topper, T. H., and Plumtree, A., "Confocal Scanning Laser Microscopy Measurements of the Growth and Morphology of Microstructurally Short Fatigue Cracks in Al 2024-T351 Alloy," *Fatigue Fract. Engng Mater. Struct.*, 1996, Vol.19, No.9, pp.1153-1159.
- [11] Varvani-Farahani, A., and Topper, T. H., "Short Fatigue Crack Characterization and Detection using Confocal Scanning Laser Microscopy (CSLM)," *Nontraditional Methods of Sensing Stress, Strain, and Damage in Materials and Structures*, ASTM STP 1318, G. F. Lucas, D. A. Stubbs, Eds., 1997, Florida, pp.43-55.
- [12] Marco, S. M., and Starkey, W. L., "A Concept of Fatigue Damage," *Transaction of ASME*, 1954, Vol.76, pp.627-632.
- [13] Henkener, J. A., Scheumann, T. D., and Grandt, A. F., "Fatigue Crack Growth Behaviour of Peakaged Al-2.6LI-0.09ZR Alloy," *Proc. 4th Int. Conf. on Fatigue and Fracture Threshold*, Honolulu, 1990, pp.957-962.
- [14] Herman, W. A., Hertzberg, R. W., and Jaccard, R., "Prediction and Simulation of Fatigue Crack Growth under Conditions of Low Cycle Closure," *Advance Fracture Research, 7th Int. Conf. on Fracture*, Houston, 1989, pp.1417.
- [15] Hertzberg, R. W., Herman, W. A., Clark, T., and Jaccard, R., "Simulation of Short Fatigue Crack and other Low Closure Loading Conditions utilizing Constant K_{max} ΔK -decreasing Fatigue Crack Growth Procedures," *Small-Crack Test Methods, ASTM STP 1149*, 1992, pp.197-220.
- [16] Kemper, H., Weiss, B., and Stickler, R., "An Alternative Prediction of the Effect of the Stress-Ratio on the Fatigue Threshold," *Engng Fract. Mech.*, 1989, Vol.4, pp.591-600.
- [17] Tack, A. J., and Beevers, C. J., "The Influence of Compressive Loading on Fatigue Crack Propagation in three Aerospace Bearing Steels," *Proceedings of the 4th International Conference on Fracture and Fatigue Thresholds*, Honolulu, 1990, pp.1179-1184.
- [18] Varvani-Farahani, A., *Biaxial Fatigue Crack Growth and Crack Closure under Constant Amplitude and Periodic Compressive Overload Histories in 1045 Steel*, A Ph.D. Thesis, University of Waterloo, Canada, 1998
- [19] Abdel-Raouf, DuQuesnay, D. L., Topper, T. H., and Plumtree, A., "Notch-Size Effects in Fatigue based on Surface Strain Redistribution and Crack Closure," *Int. J. Fatigue*, 1992, Vol.14, pp.57-62.

Analysis

R. Craig McClung¹

Analysis of Fatigue Crack Closure During Simulated Threshold Testing

Reference: McClung, R. C., “Analysis of Fatigue Crack Closure During Simulated Threshold Testing,” *Fatigue Crack Growth Thresholds, Endurance Limits, and Design*, ASTM STP 1372, J. C. Newman, Jr. and R. S. Piascik, Eds., American Society for Testing and Materials, West Conshohocken, PA, 2000.

Abstract: Load shedding procedures during fatigue crack growth threshold testing can, under some conditions, induce significant changes in fatigue crack closure levels, which can in turn artificially influence the apparent threshold level. In this paper, mechanics analyses of growing fatigue cracks that account for plasticity-induced closure are used to study load shed effects on crack opening levels during simulated threshold testing. Both finite element and FASTRAN strip yield models are employed, and the two approaches are compared. The current ASTM standard test method for determining thresholds is evaluated. Analyses explore the effects of initial stress, initial stress intensity factor, specimen size, material flow strength, and load shed rates on crack closure.

Keywords: fatigue crack growth, fatigue crack closure, threshold testing, finite element model, FASTRAN, strip yield model, load shedding

Background

Fatigue crack growth (FCG) thresholds are an important element of many practical fatigue design systems, characterizing conditions under which FCG is not expected to occur at perceptible rates. Reliable experimental measurement of the threshold for a given material is therefore a critical component of the materials testing needed to support these design systems. Although many different methods for determining the threshold have been proposed, one of the most common methods in current use is the one recommended in ASTM E 647, “Standard Test Method for Measurement of Fatigue Crack Growth Rates.” This method, based on research published by Saxena, Hudak, Donald, and Schmidt in 1978 [1], steadily decreases the load range of the fatigue cycle while maintaining the chosen stress ratio, R , constant, thereby steadily decreasing the applied range of the stress intensity factor, ΔK . The stress intensity factor threshold, ΔK_{th} , is determined from the resulting FCG data as the value of ΔK corresponding to a

¹ Manager, Materials Integrity Section, Southwest Research Institute, San Antonio, TX 78228-0510

specified slow growth rate, operationally defined in the ASTM test method as 10^{-10} m/cycle.

The ASTM method specifies the rate of load shedding in terms of the normalized K -gradient, C , such that C is limited to a value algebraically greater than -0.08 mm^{-1} (-2 in.^{-1}):

$$C = \frac{1}{K} \frac{dK}{da} \quad (1)$$

The relationship between ΔK and crack length, a , is therefore given by

$$\Delta K = \Delta K_0 \exp[C(a - a_0)] \quad (2)$$

where ΔK_0 is the initial ΔK at the start of the load shed, and a_0 is the corresponding crack length.

Threshold tests conducted by this method, at this specified load shed rate, can be relatively slow and expensive, especially when slower cycling frequencies are required. Faster load shed rates are attractive as a means of saving time and money. Furthermore, the recommended ASTM rate of $C = -0.08 \text{ mm}^{-1}$ is not feasible for some small specimen geometries, because the crack may effectively run out of specimen before the threshold is reached. For example, the surface-crack tension specimen (sometimes called the Kb bar specimen) commonly used in the aircraft gas turbine engine industry [2] can have a thickness as small as 6.35 mm (0.25 in.).

Some experience suggests that shed rates faster than those recommended by the ASTM test method can be employed without ill effect. This was observed by Saxena et al. [1] in their original work, and faster rates have been employed in the gas turbine engine industry for many years. Sheldon, Bain, and Donald [3] have recently completed a systematic study of the effects of shed rate and other parameters on measured values of ΔK_{th} determined from tests on Kb and compact tension specimens of Ti-6Al-4V. They obtained nearly identical threshold values for shed rates ranging from -0.24 mm^{-1} (-6 in.^{-1}) up to -1.6 mm^{-1} (-40 in.^{-1}) at $R = 0.1$ when starting K_{max} values were less than $11 \text{ MPa}\sqrt{\text{m}}$ ($10 \text{ ksi}\sqrt{\text{in.}}$). At a higher stress ratio of $R = 0.8$, gradients ranging from -0.3 mm^{-1} (-7.5 in.^{-1}) to -0.8 mm^{-1} (-20 in.^{-1}) had no effect on measured threshold, although gradients of -1.2 mm^{-1} (-30 in.^{-1}) did exhibit distinctly higher thresholds. When initial K_{max} values were higher, ranging from 8.8 to 44 $\text{MPa}\sqrt{\text{m}}$ (8 to 40 $\text{ksi}\sqrt{\text{in.}}$), faster shed rates also led to higher thresholds. Representative data from this study are shown in Figure 1, which illustrates the increase in measured threshold with increasing initial K_{max} values for two different ASTM load shed rates. In these data, thresholds are unchanged with initial K_{max} until initial K_{max} exceeds 20 $\text{MPa}\sqrt{\text{m}}$ (18 $\text{ksi}\sqrt{\text{in.}}$). The artificial elevation in threshold is more pronounced for -0.8 mm^{-1} ($C = -20 \text{ in.}^{-1}$), but still occurs at -0.4 mm^{-1} ($C = -10 \text{ in.}^{-1}$).

It is not completely surprising that load sheds much faster than recommended by the ASTM standard can sometimes cause anomalous results. However, load sheds conducted at the recommended ASTM load shed rates can also cause difficulties when initial ΔK values are too high. Fleck [4] has documented a particularly good example of this

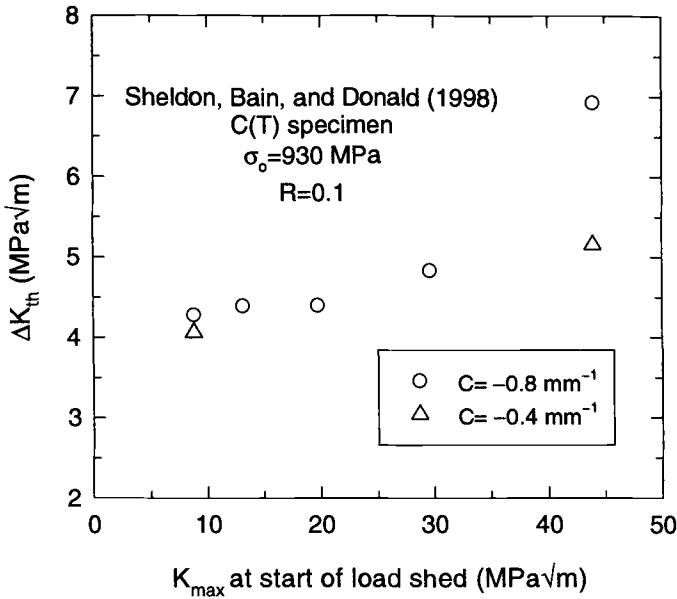


Figure 1 – Experimentally determined [3] effect of K_{max} at start of load shed on measured threshold for different load shed rates

phenomenon from companion threshold tests at $R = 0.05$ with 3 mm (0.12 in.) thick compact tension specimens of BS4360 steel. A “conventional test” employed an ASTM load shed with $C = -0.08 \text{ mm}^{-1}$ (-2 in.^{-1}) and ΔK_0 about 10 MPa√m (9 ksi√in.). Crack growth data at higher ΔK values were approximately the same for C values of 0 or $+0.08 \text{ mm}^{-1}$. Another test employed an ASTM load shed with $C = -0.08 \text{ mm}^{-1}$ but a much higher value of $\Delta K_0 = 51.4 \text{ MPa}\sqrt{\text{m}}$ (47 ksi√in.). While the conventional test gave a threshold value around $\Delta K_{th} = 6 \text{ MPa}\sqrt{\text{m}}$ (5.5 ksi√in.), the test with a load shed from a large ΔK_0 indicated a much higher threshold of 12.9 MPa√m (11.7 ksi√in.) (see Figure 2).

One potential reason for the observed effects of rapid load shed and high initial ΔK on apparent threshold is fatigue crack closure. Plasticity-induced closure is dependent on the prior load history, which influences the plastic wake behind the crack as well as the residual stresses ahead of the crack. Since the prior load history in a threshold load shed has a larger amplitude than the current load history, the residual displacements behind the crack will be relatively larger, which could lead to artificially increased levels of closure. Increased closure, in turn, would reduce the effective range of the stress intensity factor, leading to threshold crack arrest at somewhat higher ΔK levels than under constant amplitude loading.

Fleck [4] provided some experimental evidence for this argument. He measured closure in the tests referenced previously using a crack mouth gage, back face strain gage, and replicas. As shown in Figure 3, in the “conventional test” with a load shed beginning

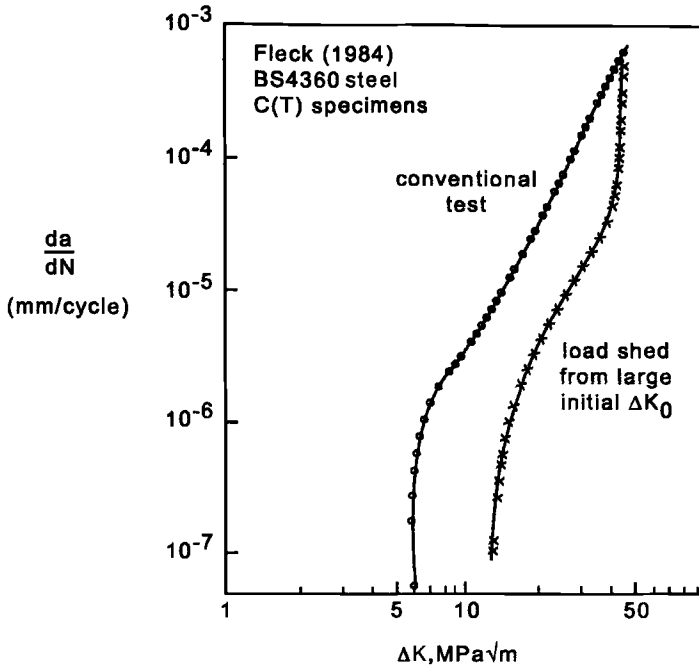


Figure 2 – Fleck [4] FCG data for test with a conventional load shed from an initial $\Delta K_0 = 10 \text{ MPa}\sqrt{\text{m}}$ and another test with a load shed from an initial $\Delta K_0 = 51.4 \text{ MPa}\sqrt{\text{m}}$

at ΔK_0 about $10 \text{ MPa}\sqrt{\text{m}}$, the effective stress range ratio $U = (S_{\max} - S_{\text{open}})/(S_{\max} - S_{\min})$ remained about 0.70, decreasing only very near the threshold. However, in the test where the load shed began at $\Delta K_0 = 51.4 \text{ MPa}\sqrt{\text{m}}$, U decreased (closure increased) sharply to 0.40 as ΔK decreased to $40 \text{ MPa}\sqrt{\text{m}}$, and further decreased below 0.20 as threshold was approached. This substantial increase in closure could easily explain the sharp increase in apparent threshold.

In this paper, two different mechanics models of plasticity-induced crack closure are employed to study the potential effect of load sheds on closure. The first model is an elastic-plastic finite element (FE) simulation of fatigue crack growth, and the second model is based on a Dugdale strip yield analysis of a fatigue crack. The effects of load shed rate, initial ΔK_0 , and material strength on crack closure during simulated ASTM load sheds are characterized, and the implications of the results for threshold testing are explored.

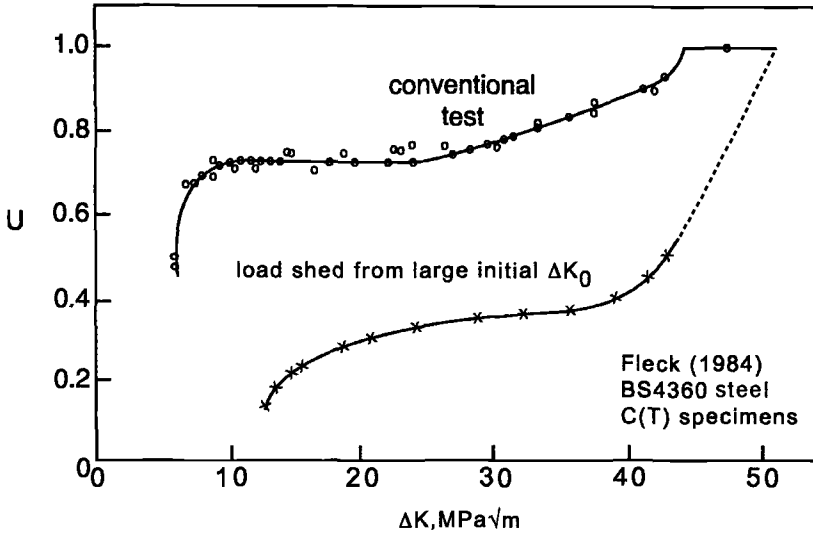


Figure 3 – Fleck [4] crack closure measurements for test with a conventional load shed from an initial $\Delta K_0 = 10 \text{ MPa}\sqrt{\text{m}}$ and another test with a load shed from an initial $\Delta K_0 = 51.4 \text{ MPa}\sqrt{\text{m}}$

Finite Element Modeling

Elastic-plastic finite element models of growing fatigue cracks have been used to study crack closure for over twenty-five years [5]. The model employed in this study [6] has been used for over ten years to address a wide range of problems. In this model, the meshes were composed of four-noded linear strain elements arranged to form a center-crack geometry, employing quarter-symmetry. At each occurrence of minimum load in a cycle, the boundary conditions at the crack-tip node were changed to allow the crack to grow by one element length through a group of very small, uniformly-sized elements along the crack line. Remote stresses were applied in many small steps, stresses and displacements along the crack line behind the crack tip were closely monitored on each load step, and boundary conditions on the crack surfaces were appropriately changed as the crack opened or closed. The constitutive model followed linear kinematic hardening characterized by $H/E = 0.01$, where E is the elastic modulus and H is the slope of the plastic line. The flow stress, σ_0 , is the intersection of the elastic and plastic lines. The material simulated in this research was either an aluminum alloy with $E = 70\,000 \text{ MPa}$ (10 154 ksi) and $\sigma_0 = 430 \text{ MPa}$ (62.4 ksi), or Ti-6Al-4V with $E = 116\,000 \text{ MPa}$ (16 800 ksi) and $\sigma_0 = 930 \text{ MPa}$ (135 ksi). All analyses were plane stress. Further information on the FE model is available in [6].

In this study, applied loads were chosen to simulate threshold load reduction schedules. The crack was first grown at a constant applied stress range until a full wake

had developed and closure levels had stabilized. Then, at some predetermined crack length, stress amplitudes were reduced in accordance with Eqn (2) while keeping the stress ratio constant at $R = 0$. The load reduction continued until the crack had grown out of the fine mesh region.

Note that strictly speaking, the finite element mesh is dimensionless, because “loads” are applied in normalized form as remote traction stresses on the top boundary. The mesh geometry is adequately described in mesh coordinates, and physical dimensions do not have to be assigned to the mesh in order to perform fatigue crack growth simulations. However, since the ASTM threshold load shed specification is dimensional, a physical length scale must be assigned to the mesh in order to define the load schedule. This seemingly minor detail turns out to provide an important insight into the ASTM threshold method, as will be discussed later.

A detailed FE study of the threshold load shed problem has been reported previously [7]. Representative results are reproduced in Figure 4. In this simulation, the mesh was assigned a length scale of 0.05 mm, so the specimen half-width W (1000 mesh units) was 50 mm or roughly 2 inches. The initial applied maximum stress (S_{\max}) in the fatigue cycle was set equal to $0.4\sigma_0$, where $\sigma_0 = 430$ MPa (62.4 ksi), and the initial crack size was $a_0 = 14$ mm (0.55 in.), so ΔK_0 at the start of the load shed was approximately 38 MPa \sqrt{m} . The load shed followed the ASTM method with $C = -0.08$ mm $^{-1}$, the ASTM recommended value. The simulation was stopped when the crack ran out of the fine mesh region ($a = 330$ mesh units = 16.5 mm), at which time the applied stress was $0.3\sigma_0$. In Figure 4, the stress history (S_{\max}/σ_0 , bottom curves) and closure history (S_{open}/S_{\max} , top curves) are shown for the threshold load shed (solid lines) and for two corresponding constant amplitude stress histories (dashed lines). The constant amplitude simulations were conducted at maximum stresses of $0.4\sigma_0$ and $0.3\sigma_0$, which were the beginning and ending stresses in the threshold simulation.

The constant amplitude simulations show the usual small maximum stress effect on closure behavior, such that S_{open}/S_{\max} was slightly higher for the slightly lower S_{\max}/σ_0 value. The striking result, however, is that the closure level during the load shed simulation increased substantially (S_{open}/S_{\max} rose from 0.48 to 0.64), ending much higher than the corresponding constant amplitude closure level for the final maximum stress. This behavior is qualitatively consistent with the earlier cited experimental results of Fleck, who saw a sharp initial increase in closure when starting an ASTM load shed from a relatively high initial ΔK_0 .

Additional FE simulations reported in [7] investigated the effects of different assigned specimen sizes. The initial maximum stress S_{\max}/σ_0 was kept the same, but the initial ΔK_0 values were higher (55 MPa \sqrt{m}) or lower (27 MPa \sqrt{m}) since the specimen dimensions were different. Since the ASTM schedule is dimensional, the rate of decrease of the applied stress was also different. Closure increased more sharply for the higher initial ΔK_0 and less sharply for the lower initial ΔK_0 .

The FE simulations permit detailed investigations of the stress, strain, and displacement fields associated with growing fatigue cracks. Studies in [7] found that the load shed process caused changes in the crack opening displacements, the cumulative axial plastic strains behind the crack tip, and the residual stresses both ahead of and behind the crack tip. As postulated above, the residual plasticity from earlier in the load

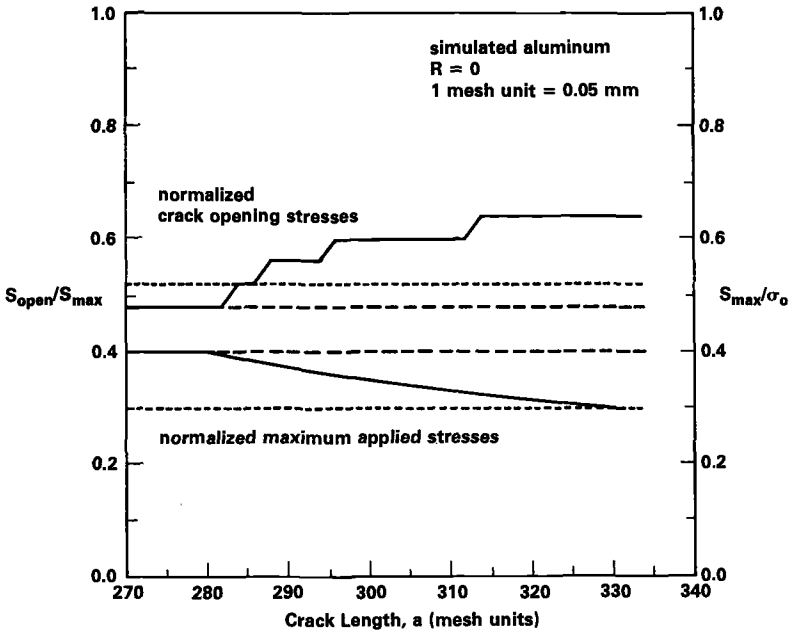


Figure 4 – Applied stress histories and crack closure histories for finite element simulation of threshold load shed test and two constant amplitude tests [7]

history, when applied stresses were larger, caused increased crack closure later in the load history, when applied stresses were smaller. The crack opening process was still a continuous “unzipping” of the crack except at the highest initial ΔK_0 values, when discontinuous closure was observed. The discontinuous closure was associated with a “hump” of residual deformation at the location of the crack tip at the beginning of the load shed.

However, the FE model is not the ideal tool to study closure during threshold load sheds. The FE mesh along the crack line must be fine enough to capture reversed yielding at the crack tip in order to give reliable results [5], and this causes problems at low stress amplitudes, when plastic zone sizes become very small. The logical solution—to make near-tip elements smaller—either dramatically increases the number of elements, thereby making execution times impractically long, or requires a decrease in the length of the fine mesh region, limiting the distance over which loads can be shed. As a result, the threshold test simulations reported above addressed only the early portion of the load shed and were terminated before the applied stress intensity factor reached true near-threshold levels. For example, ΔK at the end of the load shed in Figure 4 was still about 29 MPa \sqrt{m} . Therefore, although the FE studies clearly show the tendencies for closure artifacts under some load sheds, they cannot simulate the entire load shed process.

FASTRAN Modeling

An alternative mechanics model of fatigue crack closure that is free of these limitations is one based on a strip yield crack model. Although several such models have been published, the most well-known and widely-used is the FASTRAN model of Newman [8, 9]. FASTRAN is an analytical crack closure model based on the Dugdale model, but modified to leave plastically deformed material in the wake of the crack. In this model, the plastic-zone size and crack-surface displacements are obtained by superposition of two elastic problems—a crack in a plate subjected to a remote uniform stress and a crack in a plate subjected to uniform stress acting over a segment of the crack surface. The FASTRAN model was developed for a central crack in a finite-width specimen subjected to uniform stresses, or through cracks emanating from a circular hole in a finite width specimen also subjected to uniform applied stresses. The model is composed of rigid-perfectly plastic regions ahead of the crack tip and in the crack wake, and a linear elastic region elsewhere. The flow stress σ_0 in the plastic regions is taken as the average between the yield and ultimate strength of the material as a first-order approximation for strain hardening.

The primary advantages of FASTRAN are that it is much faster than the FE model, and that there are no mesh limitations on the extent of crack growth or the stress magnitudes applied. The disadvantages are that FASTRAN employs a much simpler representation of the stress, strain, and displacement fields both ahead of the crack and behind the crack (in its wake); much simpler formulations for material constitutive response and constraint; and the model is limited to only two geometries.

FASTRAN has been used previously to study crack closure during threshold load sheds. Newman [10] simulated several different threshold load shed procedures and found anomalously high levels of closure very near threshold in some cases. More recently, Newman [11] has employed the current version of the model, FASTRAN-II [9], to investigate load shed closure behavior in more detail.

Because FASTRAN is a simpler and more approximate model of closure, it is important to verify its accuracy by comparison to more sophisticated models. In this case, it is relatively simple to compare the current FASTRAN-II code to the FE simulations of load shedding in the regime where the FE model can be reliably exercised. A sample comparison is shown in Figure 5. These simulations are for a middle-crack tension specimen (ASTM designation M(T)) of total width $2W = 12.7$ mm (0.5 in.). The simulated material is Ti-6Al-4V with a flow stress of $\sigma_0 = 930$ MPa (135 ksi). The applied maximum stress at the beginning of the load shed was $S_{\max}/\sigma_0 = 0.4$, and the corresponding crack length was $2a = 3.8$ mm (0.15 in.), so the initial ΔK_0 was 30.4 MPa $\sqrt{\text{m}}$ (27.6 ksi $\sqrt{\text{in.}}$). The load shed followed the ASTM protocol with $R = 0$ but at an accelerated load shed rate with $C = -0.8$ mm $^{-1}$ (-20 in. $^{-1}$).

The predicted closure levels in the FASTRAN and FE simulations agree remarkably closely in the region where the two overlap. Stable opening levels under constant amplitude loading prior to the load shed are similar, and both models indicate a sharp increase in closure immediately after the start of the load shed, followed by a leveling-out of opening stresses. Since the FASTRAN simulation is not mesh-limited, however, it provides a more complete picture of the closure history as the load shed continues: in this

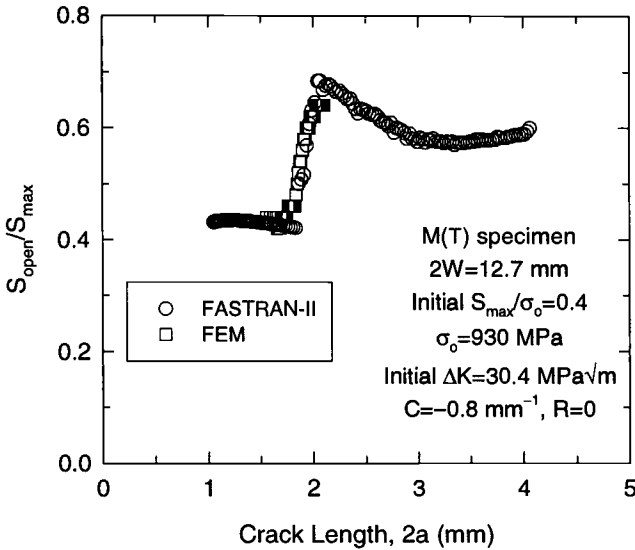


Figure 5 – Comparison of calculated closure stresses during simulated threshold load sheds with FASTRAN-II and finite element models

case, the high opening level decreases slightly but remains artificially elevated and even begins to increase again near the end of the load shed. In this particular simulation, the final ΔK is about 4.4 MPa \sqrt{m} (4 ksi $\sqrt{in.}$).

Based on these validations, the FASTRAN model can now be used with some confidence to study how different parameters influence closure behavior during threshold load sheds. Figure 6 shows results for three simulations with the same geometry, material, stress ratio, and normalized K -gradient, but different initial maximum stresses at the start of the load shed. The initial ΔK values at the start of the load shed ranged from 11.8 to 35.3 MPa \sqrt{m} (10.7 to 32.1 ksi $\sqrt{in.}$). The simulations show the usual stress level effect on closure before the start of the load shed. At the highest S_{max}/σ_0 value, the closure history is much like that shown in Figure 5: a sharp immediate increase in closure when the load shed commences, followed by some decrease in closure as the load shed continues, but then a further rise in closure near the end of the load shed. At the lowest S_{max}/σ_0 value, the initial rise in closure is relatively small, and additional increases in closure are not observed near the end of the test. The final normalized closure level S_{open}/S_{max} is slightly higher than S_{open}/S_{max} just before the load shed, but this is to be expected; the S_{max}/σ_0 value at the end of the test is lower than at the start of the test, and the stress level effect on constant amplitude closure has already been noted.

Figure 6 demonstrates that closure levels can change in complex ways during a threshold load shed. For the purposes of determining the FCG threshold itself, the most important closure level is probably the closure level at near-threshold values of ΔK . In

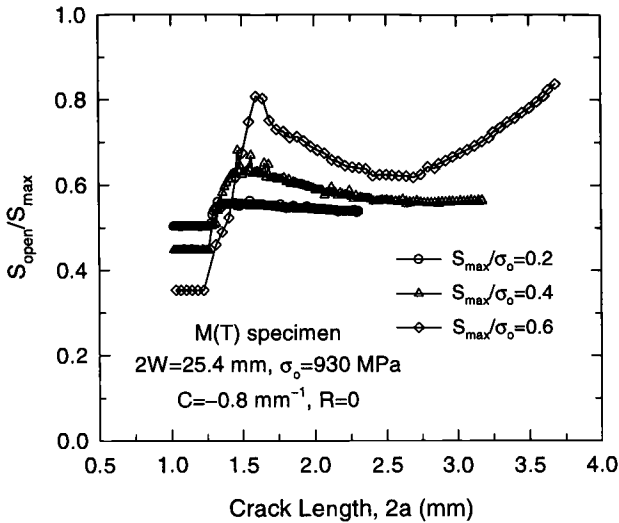


Figure 6 – Calculated crack opening stresses during simulated threshold load sheds for different maximum stresses at start of load shed

this study, the value of $\Delta K = 5.5 \text{ MPa}\sqrt{\text{m}}$ ($5 \text{ ksi}\sqrt{\text{in.}}$) was chosen as a representative near-threshold condition. In the graphs of results that follow, then, the closure behavior during a threshold load shed is characterized by the $S_{\text{open}}/S_{\text{max}}$ value when ΔK has decreased to $5.5 \text{ MPa}\sqrt{\text{m}}$, irrespective of the starting ΔK value. This provides a convenient one-parameter indication of load shed closure.

Figure 7 summarizes the results of numerous simulations for the same material, load shed rate, and a/W value, but six different specimen sizes and six different initial maximum stresses, leading to a wide range of initial ΔK values at the start of the load shed. The results demonstrate the effect of the initial ΔK value on anomalous closure behavior during threshold load sheds. When the initial ΔK value was relatively small, the load shed had little or no effect on crack closure; the $S_{\text{open}}/S_{\text{max}}$ value at $\Delta K = 5.5 \text{ MPa}\sqrt{\text{m}}$ was within a few percent of the corresponding $S_{\text{open}}/S_{\text{max}}$ value during constant amplitude cycling at the final S_{max}/σ_0 value. As the initial ΔK increased, however, an increasing closure artifact was observed, with $S_{\text{open}}/S_{\text{max}}$ values even approaching 1 as the initial ΔK approached $44 \text{ MPa}\sqrt{\text{m}}$ ($40 \text{ ksi}\sqrt{\text{in.}}$). This increase was consistently observed whether the higher ΔK value was due to a larger specimen size or a higher initial stress, suggesting that initial ΔK is an appropriate correlating parameter.

However, ΔK alone is an inadequate indication of whether or not a closure artifact is observed. The results in Figure 8 demonstrate that material strength is also a critical variable. The two sets of simulations in Figure 8 differed only in the material flow strength; all other loading and geometry parameters were the same. The material with the lower flow stress exhibited closure artifacts at substantially lower values of initial ΔK .

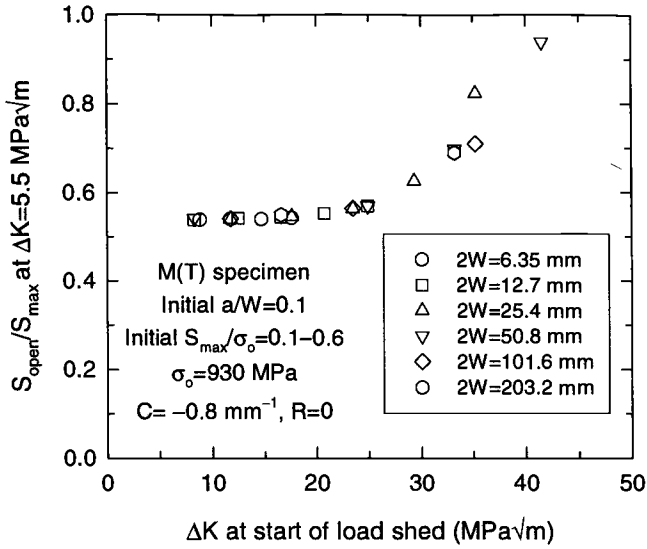


Figure 7 – Calculated effect of ΔK at start of load shed on crack opening stress near threshold for different specimen sizes and initial maximum stresses

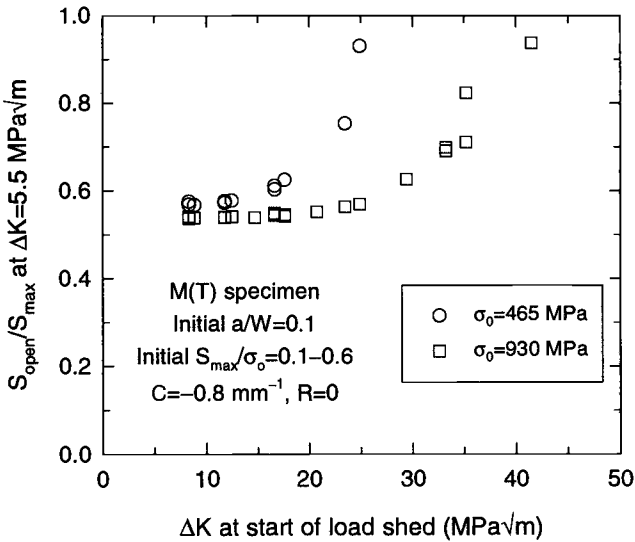


Figure 8 – Calculated effect of ΔK at start of load shed on crack opening stress near threshold for different material flow strengths

All of the simulations in Figures 7 and 8 maintained the same value of the ASTM normalized K -gradient, $C = -0.8 \text{ mm}^{-1}$ (-20 in.^{-1}). The results in Figure 9 show the effects of load shed rate: closure artifacts were observed at much lower initial ΔK values for faster shed rates. At the recommended ASTM rate ($C = -0.08 \text{ mm}^{-1} = -2 \text{ in.}^{-1}$), larger initial ΔK values could be tolerated even in this weaker material, but a closure artifact was observed eventually as initial ΔK continued to increase. These simulation results in Figure 9 are entirely consistent with the experimental data shown earlier in Figure 1: higher values of initial ΔK led to anomalously high closure and anomalously high thresholds, and these anomalous effects occurred at lower values of initial ΔK for faster load shed rates. No direct comparisons between the experiments and the analysis are provided because closure measurements were not reported for the experiments, and it is not immediately obvious how to calculate the quantitative effect of increased closure on apparent threshold in the simulations.

Discussion

Evaluation of the ASTM Load Shed Scheme

The mechanics analyses conducted in this study indicate that the ASTM threshold test scheme can effectively reduce cyclic load amplitudes without inducing significant closure artifacts under some conditions; in particular, when the initial ΔK_0 is relatively small. Furthermore, the analyses suggest that load shedding can be performed at much faster normalized K -gradients without introducing closure artifacts if the initial ΔK_0 is adequately small. However, the analyses indicate that the ASTM scheme can lead to artificially increased levels of crack closure, and hence yield artificially high apparent thresholds, when the initial ΔK_0 is too high for the particular normalized K -gradient selected. This problem appears to be more pronounced for materials with lower flow strengths.

The ASTM standard itself attempts to address some of these concerns by suggesting a limit, not on the initial ΔK_0 value, but on the upper bound da/dN value (10^{-8} m/cycle) for the K -decreasing procedure. While this appears to be a useful guideline, it is not clear how this upper bound da/dN value can be linked directly to the mechanics of the fatigue crack that govern closure behavior. Is this upper bound da/dN value sometimes too restrictive? How might it change with different material strengths? Is it sometimes an inadequate limit?

The inherent dimensionality of the current ASTM method raises other concerns. The normalized K -gradient must be expressed in terms of a physical length dimension. In contrast, a mechanics perspective on the fatigue crack reveals that the crack-tip deformation fields are inherently nondimensional. That is, the crack tip fields can be completely characterized by an appropriate set of nondimensional parameters that can then be scaled to describe any particular (dimensional) application. For example, Figure 10 shows the contours of residual plastic strain around a growing fatigue crack that were calculated from the FE closure model. This figure is a “snapshot” of the plastic strains at zero load after the crack has grown a long distance through the member. The

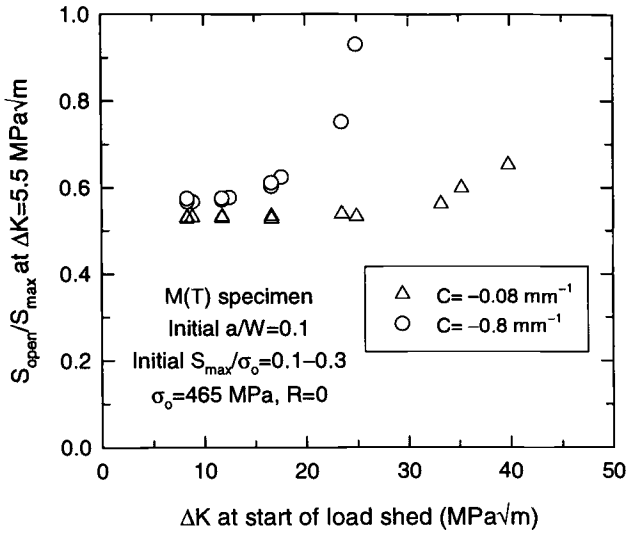


Figure 9 – Calculated effect of ΔK at start of load shed on crack opening stress near threshold for different load shed rates

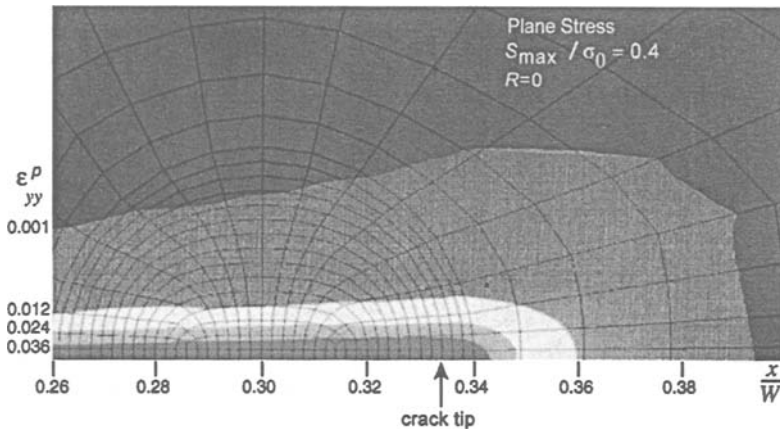


Figure 10 – Contours of residual axial plastic strain around a growing fatigue crack, as calculated by a finite element model of crack closure

plastic strains ahead of the current crack tip represent the crack-tip plastic zone that was formed at the maximum load in the previous cycle. The plastic strains behind the crack tip represent the residual plastic wake that leads directly to crack closure. This particular set of plastic strain contours is characterized completely by the normalized applied stress, S_{\max}/σ_0 , the normalized plastic hardening modulus, H/E , and the normalized crack length, a/W . As long as these ratios remain the same, the same set of plastic strain contours would be obtained no matter what value of maximum stress or specimen width was chosen.

Instinctively, an acceptable rate of load shedding should somehow be related to crack growth through these crack-tip strain fields. If the load is shed too rapidly relative to the crack-tip deformation fields, then closure artifacts could be expected. Therefore, it might be reasoned that an appropriate expression for the acceptable rate of load shedding ought to be somehow nondimensional in keeping with the nondimensional crack-tip fields.

However, the ASTM method is dimensional, and this can lead to potential difficulty. As noted previously, the FE closure model itself captures some of the inherent nondimensionality of the fatigue crack, because loads are applied in partially normalized form as remote stresses, and no length scale is required for the FE mesh. But since the ASTM method is dimensional, some length scale must be assigned in order to carry out the analysis. Consider a somewhat ridiculous set of choices of that length scale. Consider, on the one extreme, a length scale of 1 mesh unit = 1 micron. Then consider, on the other extreme, a length scale of 1 mesh unit = 1 mile. The nondimensional contours of Figure 10 apply equally to either length scale, since a scales with W . But the ASTM method does not similarly scale. Figure 11 shows the stress history required to satisfy the ASTM schedule for a normalized K -gradient of -0.08 mm^{-1} . The specimen with the 1 mile length scale will experience a precipitous drop in applied stress relative to the crack tip fields, while the specimen with the 1 micron length scale will experience a negligible drop in applied stress relative to the crack tip fields. The mile specimen will inevitably show a massive closure artifact, while the micron specimen will experience effectively no load reduction before the crack grows all the way through the specimen.

The initial ΔK values in these two absurd examples are also clearly extreme: $\Delta K_0 = 5.6 \text{ MPa}\sqrt{\text{m}}$ for the micron specimen, and $\Delta K_0 = 224\,000 \text{ MPa}\sqrt{\text{m}}$ for the mile specimen. In keeping with the more realistic analyses summarized earlier, the closure artifact arises for large initial ΔK_0 . For small initial ΔK_0 , more rapid load sheds are possible without introducing closure artifacts. But it is possible that this indicates a potential difficulty with the fundamental form of the ASTM normalized K -gradient itself: $(1/K)(dK/da)$. When K is very large, dK/da is also permitted to be very large. The results of the closure analyses presented in this paper indicate that when ΔK is relatively large, the ASTM load shed scheme produces closure artifacts. In contrast, it would seem that an ideal load shed scheme should give an artifact-free closure response at all ΔK levels.

Speculation About Improved Load Shed Schemes

Perhaps a more fundamental concern about the current ASTM load shed scheme, and in particular the current functional form of the normalized K -gradient, is simply that it sometimes works, sometimes doesn't work, and sometimes introduces unnecessary and

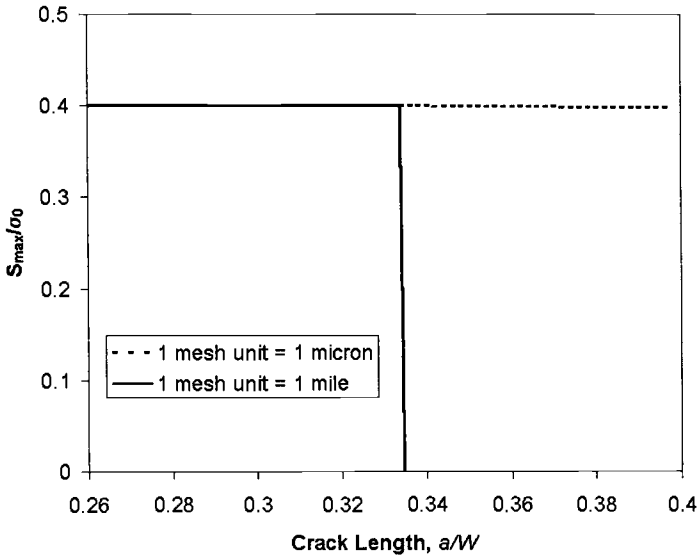


Figure 11 – Applied stress history for finite element simulated ASTM load sheds with two extreme values of assigned mesh scale

expensive conservatism, without providing any *a priori* indication of when it will or will not work efficiently. Perhaps something better is possible. Perhaps it is possible, as noted in the previous paragraph, to have a load shed scheme that will give an artifact-free closure response at all ΔK levels.

The investigations reported in this paper have identified some important features of such an improved load shed scheme, if it exists. An optimum load shed scheme should be somehow nondimensional, in keeping with the inherent mechanics of the fatigue crack. An optimum load shed scheme should somehow account for material strength, perhaps employing the material flow strength or yield strength in the nondimensionalization somehow. An optimum load shed should permit the load shed to be carried out at the fastest rate that is safely possible, to minimize the time and cost of the test. And an optimum load shed scheme should avoid closure artifacts. These closure artifacts appear to occur most often at very large ΔK values, but it must be noted that some additional closure artifacts were observed in some of the FASTRAN simulations at the very lowest ΔK values, very near the end of the threshold test.

It is not clear if such an improved load shed scheme exists, and the search for such a scheme is well beyond the scope of the current investigation. And it should be noted that the optimum load shed scheme will likely need to address issues other than the mechanics of plasticity-induced closure. Many lessons were learned in the early days of threshold test method development, and any search for improved methods should incorporate those

lessons learned and not repeat earlier mistakes. The ASTM method itself emerged as the best among several competing methods, based on thorough experimental investigations.

And it must be emphasized strongly that the current ASTM method appears to give satisfactory threshold results under many conditions from the perspective of plasticity-induced crack closure, particularly when the specified limit on da/dN is observed. The primary practical drawback of the current method is more likely that it recommends shed rates that are impractically slow for some applications, and the method itself provides no guidance on how and when to safely increase the shed rate. However, the analyses reported in this paper indicate some key factors to be considered when experimentally determining limits on shed rates: initial ΔK value and material strength.

Limitations of this Investigation

Several limitations of this investigation should be noted. First, all of the reported FE and FASTRAN-II results were for plane stress conditions ($\alpha = 1$ in the FASTRAN-II code). In contrast, near-threshold FCG conditions are often more nearly plane strain in nature, since loads and plastic zone sizes are small. However, additional FASTRAN threshold load shed simulations, not shown here, were conducted in full plane strain ($\alpha = 3$), where crack closure still occurs even in baseline constant amplitude behavior [6]. The results were qualitatively similar, although anomalous increases in closure were somewhat less pronounced and occurred at slightly higher values of initial ΔK . The plane stress results were shown here because they illustrated the phenomena more clearly, and because large numbers of plane stress analyses were computationally much faster than plane strain analyses. However, it should not be hastily concluded that threshold load shed closure effects are strictly a plane strain phenomenon. Thresholds may be significantly influenced by crack closure that occurs at the specimen surface, which will be more nearly in plane stress. Furthermore, remember that the most striking closure artifacts occurred very early in the load shed, when applied stresses were significantly higher and the constraint state could more nearly approximate plane stress. These artifacts may still influence closure later in the load shed after the stress state has transitioned to plane strain.

Second, these investigations were limited to plasticity-induced crack closure. Near the threshold, other closure mechanisms such as crack surface roughness or crack surface oxides may become important. However, the plasticity-induced closure mechanism is still operative near the threshold (perhaps under plane strain conditions, as discussed in the previous paragraph), and can make independent contributions to the interference of mating surfaces behind the crack tip. In other words, the contributions of different closure mechanisms may be additive, and so artificially elevated levels of plasticity-induced closure can influence the total closure level, even if the contributions of roughness- or oxide-induced closure are substantial. And again, remember that some closure artifacts are associated with the early load shed history, when applied stresses are significantly higher and plasticity-induced closure is likely of even greater relative significance.

Finally, the results of this simple analytical investigation are necessarily qualitative in nature. Although quantitative trends are clear, it is not yet possible to fix specific quantitative criteria for “safe” threshold load sheds from analytical modeling alone, due to ambiguities about the stress state and the potential contributions of other closure mechanisms. Experiments are still needed to calibrate the analyses and/or to determine specific numerical limits on load shed rates and initial ΔK values. What these analyses do provide is evidence that any empirically-derived criteria for reliable threshold testing according to the current ASTM method must consider not only the normalized K -gradient but also the initial ΔK value and the material strength. Further analyses should be useful in interpreting and extending new experimental investigations of the current ASTM method, and also in developing and validating potential new threshold load shed schemes employing alternative K -gradient forms.

Conclusions

1. Mechanics modeling of growing fatigue cracks indicate that closure artifacts that could influence apparent thresholds can arise during load shedding procedures specified by the ASTM test method.
2. Load shedding can sometimes occur at rates faster than recommended by the ASTM test method without introducing closure artifacts or inducing artificially high thresholds. Faster load shed rates are acceptable when values of ΔK at the start of the load shed are relatively lower, but faster rates can cause difficulties when values of ΔK at the start of the load shed are relatively higher.
3. Load shedding at rates recommended by the ASTM test method can still produce closure artifacts when the initial ΔK at the start of the load shed is too high.
4. Specified values of initial ΔK at the start of the load shed are insufficient, by themselves, to determine if closure artifacts will occur. Material flow strength can also play a key role, such that weaker materials exhibit closure artifacts at smaller initial values of ΔK .
5. Safe use of the current ASTM test method requires experimentally confirmed limits on the value of ΔK at the beginning of the load shed, taking material yield strength into account.
6. It may be possible to develop an improved, dimensionless load shed method based on principles of crack-tip mechanics that takes material strength into account and is independent of initial ΔK .

References

- [1] Saxena, A., Hudak, S. J., Jr., Donald, J. K., and Schmidt, D. W., "Computer-Controlled Decreasing Stress Intensity Technique for Low Rate Fatigue Crack Growth Testing," *Journal of Testing and Evaluation*, Vol. 6, 1978, pp. 167-174.
- [2] Van Stone, R. H., and Richardson, T. L., "Potential-Drop Monitoring of Cracks in Surface-Flawed Specimens," *Automated Test Methods for Fracture and Fatigue Crack Growth, ASTM STP 877*, American Society for Testing and Materials, 1985, pp. 148-166.
- [3] Sheldon, J. W., Bain, K. R., and Donald, J. K., "Investigation of the Effects of Shed-rate, Initial K_{max} , and Geometric Constraint on ΔK_{th} in Ti-6Al-4V at Room Temperature," to be published in *International Journal of Fatigue*.
- [4] Fleck, N. A., "An Investigation of Fatigue Crack Closure," CUED/C-MATS/TR.104, Cambridge University Engineering Department, 1984.
- [5] McClung, R. C., "Finite Element Analysis of Fatigue Crack Closure: A Historical and Critical Review," FATIGUE '99, Seventh International Fatigue Conference, Beijing, China, June 1999, in press.
- [6] McClung, R. C., Thacker, B. H., and Roy, S., "Visualization of Fatigue Crack Closure in Plane Stress and Plane Strain," *International Journal of Fracture*, Vol. 50, 1991, pp. 27-49.
- [7] McClung, R. C., "Finite Element Modeling of Crack Closure During Simulated Fatigue Threshold Testing," *International Journal of Fracture*, Vol. 52, 1991, pp. 145-157.
- [8] Newman, J. C., Jr., "A Crack-Closure Model for Predicting Fatigue Crack Growth Under Aircraft Spectrum Loading," *Methods and Models for Predicting Fatigue Crack Growth Under Random Loading, ASTM STP 748*, American Society for Testing and Materials, 1981, pp. 53-84.
- [9] Newman, J. C., Jr., "FASTRAN-II – A Fatigue Crack Growth Structural Analysis Program," NASA TM 104159, February 1992.
- [10] Newman, J. C., Jr., "A Nonlinear Fracture Mechanics Approach to the Growth of Small Cracks," *Behavior of Short Cracks in Airframe Components*, AGARD Conference Proceedings No. 328, 1982, pp. 6.1-6.26.
- [11] Newman, J. C., Jr., "Analyses of Fatigue Crack Growth and Closure Near Threshold for Large-Crack Behavior," this publication.

J. C. Newman, Jr.¹

Analyses of Fatigue Crack Growth and Closure Near Threshold Conditions for Large-Crack Behavior

Reference: Newman, J. C., Jr., “Analyses of Fatigue Crack Growth and Closure Near Threshold Conditions for Large-Crack Behavior,” *Fatigue Crack Growth Thresholds, Endurance Limits, and Design, ASTM STP 1372*, J. C. Newman, Jr. and R. S. Piascik, Eds., American Society for Testing and Materials, West Conshohocken, PA, 2000.

Abstract: A plasticity-induced crack-closure model was used to study fatigue crack growth and closure in a thin-sheet 2024-T3 aluminum alloy under threshold and constant- K_{max} testing procedures. Two methods of calculating crack-opening stresses were compared: one based on contact-K analyses and the other on contact crack-opening-displacement (COD) analyses. These methods gave nearly identical results under constant-amplitude loading but under load-reduction (threshold) simulations the contact-K analyses gave lower crack-opening stresses than the contact-COD method. Crack-growth load-reduction simulations showed that remote closure (crack surface contact away from the crack tip) can cause a rapid rise in opening stresses in the near threshold regime for low-constraint (plane-stress) conditions and high applied stress levels for both low and high stress ratios. Under low applied stress levels and high constraint (near plane-strain) conditions, a rise in crack-opening stresses was not observed near the threshold regime. But the residual crack-tip-opening displacements (CTOD) were of the order of measured oxide thicknesses in the 2024 alloy. In contrast, under constant- K_{max} testing, the CTOD near threshold were an order-of-magnitude larger than measured oxide thicknesses. Residual-plastic deformations were much larger than the expected oxide thicknesses. Thus, residual-plastic deformations, in addition to oxides and roughness, play an integral part in threshold development.

Keywords: fatigue crack growth, thresholds, fracture mechanics, cracks, stress-intensity factor, crack closure, plasticity, constraint

In 1970, Paris [1] proposed a method to determine very slow fatigue-crack-growth rates and showed the development of a fatigue-crack-growth threshold, ΔK_{th} . Later, Saxena et al [2] and an ASTM Task Group developed a standard test method for near-threshold crack-growth-rate measurements. The use of thresholds in the design of structures subjected to cyclic loading has greatly increased over the past 20 years. Especially in components subjected to high-cyclic loading, such as engines or propellers, crack propagation to failure occurs very rapidly and thresholds play a large role in life

¹ Senior Scientist, NASA Langley Research Center, Hampton, Virginia, 23681-2199.

prediction. Damage tolerance methods are currently being proposed for use under high-cyclic fatigue conditions and large-crack thresholds are controlling the design of these components. However, continued work in the threshold regime over the past decade suggests that current methods of defining the fatigue-crack-growth threshold are influenced by the test method [3-5] and reveal significant differences between fatigue-life predictions based on small-crack growth rate behavior compared to that based on large-crack (threshold) behavior [6]. These issues raise questions about the use of the thresholds in the design of structures subjected to cyclic loads. Various forms of fatigue-crack closure (plasticity, roughness and oxide debris) have all been proposed to occur during the threshold development. Thus, a complete understanding of thresholds must address all of the possible forms of closure.

Elber [7] observed that fatigue-crack surfaces contact each other even during tension-tension cyclic loading and he subsequently developed the crack-closure concept. This observation and the explanation of crack-closure behavior revolutionized damage-tolerance analyses and began to rationally explain many crack-growth characteristics, such as crack-growth retardation and acceleration. Since the discovery of plasticity-induced crack closure, several other closure mechanisms have been identified, such as oxide- [8] and roughness-induced [9] closure, which appear from the literature to be more relevant in the near-threshold regime. However, observations of fatigue-crack surfaces near threshold conditions, which show roughness and/or oxides, do not readily show the extent of the residual-plastic deformations (without strain measurements or X-ray diffraction) in relation to oxide thicknesses and roughness contributions.

The objective of this paper is to use a two-dimensional, plasticity-induced crack-closure model [10, 11] to study fatigue-crack growth and closure in a thin-sheet 2024-T3 aluminum alloy under threshold (load-reduction) and constant- K_{max} testing procedures. Analyses were made on a middle-crack tension, $M(T)$, specimen using the modified strip-yield model, as shown in Figure 1. Two methods of calculating crack-opening stresses were compared: one based on contact- K analysis and the other on contact crack-opening-displacement (COD) analyses. Results from these two methods and values determined

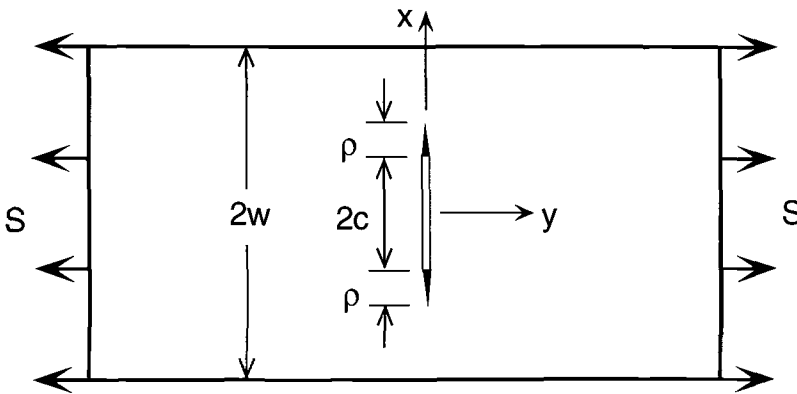


Figure 1 – Crack configuration analyzed with strip-yield model.

from remote crack-mouth-opening displacements (CMOD) using the 1 or 2% compliance offset method are compared. Crack-growth simulations, using the crack-closure model, under threshold and constant- K_{\max} testing procedures were made under a variety of conditions. The effects of constraint (plane-stress or plane-strain conditions), stress ratio, stress level, and load-shedding rates on crack growth and closure were studied. The crack-tip-surface displacements were computed to show the extent of the residual-plastic deformations near threshold conditions. An assessment of the role of plasticity-induced closure and residual-plastic deformations, in addition to oxide debris, in threshold development was made.

Plasticity-Induced Crack Closure Model

The plasticity-induced crack-closure model, shown in Figure 2, was developed for a through crack in a finite-width plate subjected to remote applied stress. The model was based on the Dugdale strip-yield model [12] but modified to leave plastically deformed material in the wake of the crack. The details of the model are given elsewhere and will not be presented here (see Newman [10, 11]). One of the most important features of the model is the ability to model three-dimensional constraint effects. A constraint factor, α , is used to elevate the flow stress (σ_o) at the crack tip to account for the influence of stress state ($\alpha\sigma_o$) on plastic-zone sizes and crack-surface displacements. (The flow stress σ_o is taken as the average between the yield stress σ_{ys} and ultimate tensile strength σ_u of the material, as a first approximation for strain hardening.) For plane-stress conditions, α is equal to unity (original Dugdale model); and for simulated plane-strain conditions, α is equal to 3. Although the strip-yield model does not model the correct yield-zone shape for plane-strain conditions, the model with a high constraint factor is able to produce crack-surface displacements and crack-opening stresses quite similar to those calculated from three-dimensional, elastic-plastic, finite-element analyses of crack growth and closure for finite-thickness plates [13].

The calculations performed herein were made with FASTRAN Version 3.0. Modifications were made to FASTRAN-II (Version 2.0 described in reference 11) to improve the crack-opening stress calculations under variable-amplitude loading, to improve the element "lumping" procedure to maintain the residual-plastic deformation history, and to improve computational efficiency. From the model, CMOD was calculated at the centerline of the model ($x = 0$). In the application of the model, about 25 to 30 elements are created along the crack surface during threshold and constant- K_{\max} test simulations. There were 10 elements in the plastic zone (crack-tip element, $j = 1$, is 1% of the plastic-zone size). The crack-tip-surface element ($j = n$) was 2% of the cyclic plastic zone (ω). Crack-surface displacements were calculated from the elements along the crack surface, as shown in Figure 2(a). The crack-opening stress is normally calculated from the contact stresses, shown in Figure 2(b), by equating the applied stress-intensity factor at S_o to the stress-intensity factor caused by the contact stresses [10]. This value is denoted as $(S_o)_k$. Herein, the crack-opening stress was also calculated from the

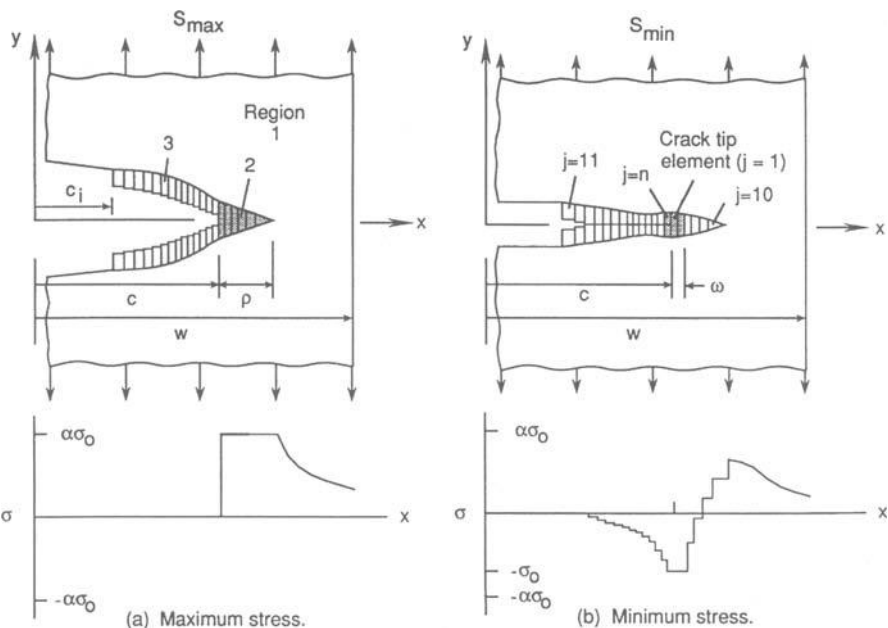


Figure 2 – Schematic of strip-yield model at maximum and minimum applied loading.

contact-COD analysis [4]. From a displacement analysis, the applied stress required to “fully” open the crack surfaces, $(S_o)_d$, was calculated.

Effective Stress-Intensity Factor Range against Crack-Growth Rate Relations

The linear-elastic effective stress-intensity factor range developed by Elber [7] is

$$\Delta K_{eff} = (S_{max} - S_o) F \sqrt{(\pi c)} \tag{1}$$

where S_{max} is the maximum stress, S_o is the crack-opening stress and F is the boundary-correction factor. The crack-growth rate equation proposed by Elber states that the crack-growth rate is a power function of the effective stress-intensity factor range (like the Paris equation). However, fatigue crack-growth rate data plotted against the ΔK or ΔK_{eff} , commonly show a “sigmoidal” shape. To account for this shape, the power relation was modified by Newman [10] to

$$dc/dN = C (\Delta K_{eff})^n G / H \tag{2}$$

where $G = 1 - (\Delta K_o / \Delta K_{eff})^p$ and $H = 1 - (K_{max} / C_5)^q$. The function G accounts for threshold variations with stress ratio (ΔK_o is a function of stress ratio) and the function H

accounts for the rapid crack-growth rates approaching fracture. The parameter C_5 is the cyclic fracture toughness. As cracked specimens are cycled to failure, the fracture toughness is generally higher than the toughness for cracks grown at a low load and then pulled to failure. This is caused by the shielding effect of the plastic wake [14]. The cyclic fracture toughness (C_5), like the elastic fracture toughness (K_{Ic}), is a function of crack length, specimen width, and specimen type. A two-parameter fracture criterion [15] was used to model the fracture process (predict C_5 as a function of crack length and specimen width). Although the fracture term, H , was originally selected to fit high-rate data approaching fracture, the term has recently been used to help explain some K_{max} effects at low rates [16].

The threshold function, G , was originally selected because crack-opening stresses from constant-amplitude loading could not collapse the low-rate data onto a unique ΔK_{eff} against rate curve. The $(\Delta K_{eff})_{th}$ values, denoted as ΔK_o , were a function of stress ratio, R . Developing models to predict threshold behavior would allow better correlation of data and the determination of intrinsic material crack-growth properties in the near-threshold regime. Many investigators (see for example, refs. 17-18) have shown experimentally that the stress-intensity factor threshold under load-reduction schemes can be explained by crack-closure behavior (or a rise in crack-opening loads as the threshold is approached). Recently, Donald and Paris [19], using a remote displacement gage, have shown that the measured crack-opening loads were "not" able to correlate low stress-ratio test data with high stress-ratio (non-closure) data because the measured opening loads were much too high. But what caused the rise in opening loads from the threshold tests? And why does the remote displacement gage method fail to measure the appropriate opening value to correlate crack-growth rate data? A number of suggestions have been advanced to explain the rise in opening loads. Among these are the mismatch of crack-surface features observed by Walker and Beevers [9]; the corrosion product formation on the crack surfaces, as observed by Paris et al [8] and measured by Vasudevan and Suresh [20]; and plasticity-induced crack-closure during load reduction, as calculated by Newman [4]. The mismatch of crack-surface features and corrosion products on the crack surfaces can cause the surfaces to come into contact at a higher load than the load for a crack without mismatch or corrosion products. The mode of crack growth near the threshold is a combination of Mode I and II (tensile and shear). The mixed-mode crack growth, and permanent plastic deformations, causes an irregular crack-surface profile and mismatch, and, consequently, the possibility of premature crack-surface contact. The analytical treatment of crack closure due to crack-surface mismatch or corrosion products on the crack surface is beyond the scope of the present paper. Only the effects of residual-plastic deformations were considered in this paper. However, an assessment of the effects of oxide-debris thickness in relation to computed crack-tip-surface displacements are made for threshold and constant- K_{max} testing. A possible reason for the remote displacement gage measuring the incorrect opening load during threshold testing will be addressed in the next section.

Crack Growth and Plasticity-Induced Closure Analyses

In the following sections, the plasticity-induced crack-closure model, FASTRAN, was used to simulate fatigue-crack growth under constant-amplitude loading and the ASTM Standard Test Method for Measurement of Fatigue Crack Growth Rates (E-647) load-reduction (threshold) testing procedure. The local crack-tip and remote (CMOD) displacements near thresholds were studied under low (plane-stress) and high (plane-strain) constraint conditions. The two methods (contact-K and COD) used to calculate crack-opening stress levels were compared. Using the contact-K analyses, the effects of constraint, stress ratio, stress level and load-shedding rates on crack-opening stresses were studied. A brief discussion of possible three-dimensional residual-plastic-deformation effects on closure is presented.

Constant-Amplitude Loading

The original crack-closure model [10] used the contact-K analysis to calculate crack-opening stresses under constant-amplitude loading. But under variable-amplitude loading, remote or intermittent closure occurs, such as after a single-spike overload, leaving an open gap between the closed surfaces and the crack tip. Thus, a crack-opening displacement (COD) method to calculate crack-opening stresses was also developed by Newman [4]. Here the opening stress was the applied stress level required to “fully” open the crack surfaces. A comparison of the two methods for constant-amplitude loading is shown in Figure 3 for three levels of constraint at $S_{\max}/\sigma_o = 0.2$. Here the two methods gave essentially the same results. The solid curves are the crack-opening stress equations developed to fit these results [21]. Comparisons of crack-growth predictions with test data under variable-amplitude loading tend to support the use of the contact-K analysis method [10]. But the contact-COD method may have bearing on crack-opening measurements recently made by Donald and Paris [19]. This will be presented and discussed later.

Load-Reduction Method

As previously mentioned, Saxena et al [2] and other ASTM colleagues developed a standard test method for near-threshold fatigue-crack-growth-rate measurement. The load-reduction procedure was based on stress-intensity factors changing at an exponential rate. A typical load-reduction example is shown in Figure 4. The ratio of the current applied stress, S_{\max} , to the initial applied stress, $(S_{\max})_i$, is plotted against crack length. The crack length (c_i) at the initiation of the load-reduction procedure was 20 mm in a large middle-crack tension specimen. The smooth curves are based on a constant rate of change in normalized plastic-zone size with crack extension. The normalized K-gradient, $(dK/dc)/K$, was -0.08 mm^{-1} for the upper solid curve, as recommended. This is equivalent to about a 5% change in stress every 0.5 mm of crack extension, as shown by the stair-step lines. The standard also allows a 10% change every 0.5 mm of crack extension, if computerized, smooth load-reduction capability is not available. This is

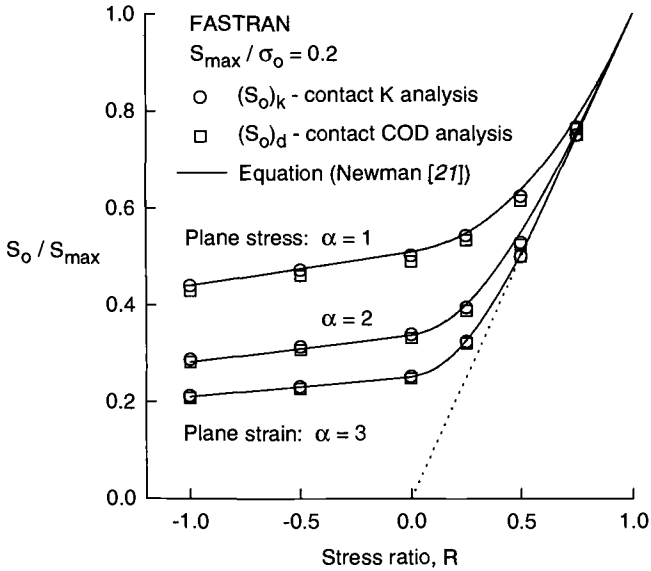


Figure 3 – Calculated crack-opening stresses from contact-K and contact-COD analyses under constant-amplitude loading.

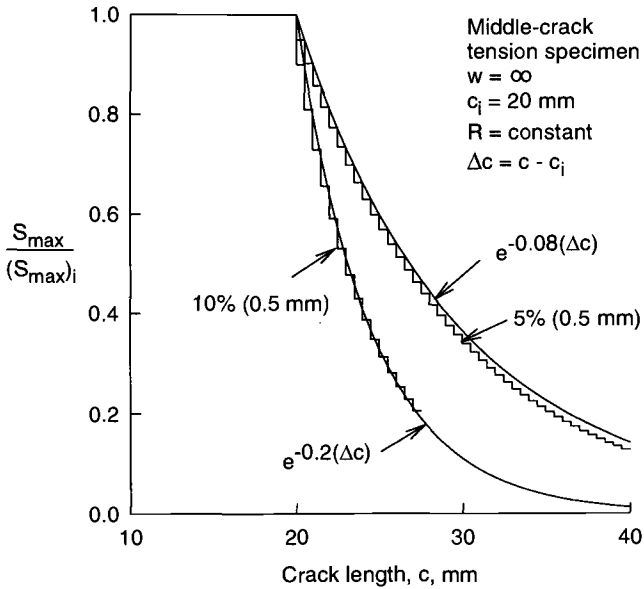


Figure 4 – Load-reduction procedures for low-crack-growth rates.

equivalent to a normalized K-gradient of -0.2 mm^{-1} , as shown by the lower solid curve. The standard load-reduction scheme (upper solid curve) will be used unless otherwise noted.

Local and Remote Displacements – Simulated crack-growth analyses under the standard ASTM load-reduction procedure were made after precracking an M(T) specimen for about 13 mm from a sawcut of 13 mm in length. These analyses were conducted at low and high constraint for low ($R = 0$) and high ($R = 0.7$) stress-ratio conditions. The applied stress level was chosen so that a high stress-intensity factor condition would exist at the start of the load-reduction procedure. The reason that this level was chosen was because some recent threshold testing results in the literature appear to have initiated the load-reduction test at high K levels and the resulting ΔK_{th} values are showing specimen-size and specimen-type effects [19].

Plane-stress conditions – Figure 5 shows the local COD along the crack surfaces for a plane-stress simulation at $R = 0$. The sawcut, fatigue precracking (constant-amplitude loading at $(S_{max})_{CA} = 115 \text{ MPa}$), and load-reduction regions are as indicated along the x-axis. The solid and dashed curves show the results at maximum and minimum applied stress, respectively. These results show that even at the maximum applied stress (9 MPa) the crack surfaces were still in contact near the start of the load-reduction regime. The solid symbols show the displacement at the centroid of the elements in the model. Although not apparent from the figure, the crack surfaces at the crack tip ($c = 51 \text{ mm}$) are closed at minimum load.

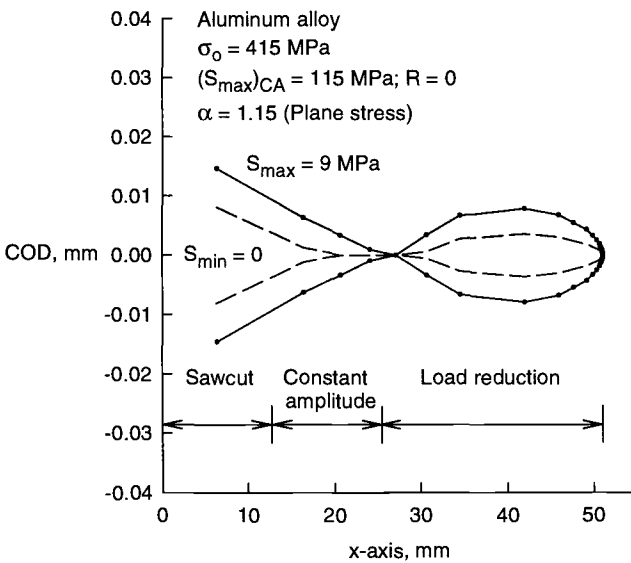


Figure 5 – Crack-surface displacements after load reduction under plane-stress conditions.

The remote cyclic CMOD results at $c = 51$ mm are shown in Figure 6 as the solid curve. Loading and unloading followed the same curve. The dotted line is the linear-elastic behavior. Of course, the contact-COD method gave an opening-stress ratio of 1.0 (crack surfaces never opened) but the contact-K analysis gave a value $(S_o)_k/S_{max}$ of about 0.68. The open symbol denotes when the crack tip opened. The dashed line shows the $(S_o)_{kCA}$ results from a constant-amplitude simulation at the same stress-intensity factor. In an effort to assess whether the value from the contact-K analysis was appropriate to use in a crack-growth analysis, the cyclic crack-tip displacements for both the load-reduction (solid curve) and constant-amplitude (dashed curve) simulations are shown in Figure 7. These results show that the crack-tip-cyclic displacement (or cyclic strain) for the load-reduction case was less than that for the constant-amplitude case. Of course, the contact-COD value, $(S_o)_d$, is not appropriate because the crack tip experienced cyclic plastic deformations and, presumably crack-tip damage and crack growth. Thus, the appropriate opening value to use would be higher than the constant-amplitude case, but whether the $(S_o)_k$ value is appropriate would require further study of crack-growth rates against cyclic displacements or cyclic hysteresis energies. This is beyond the scope of the present study. However, reference 16 showed a close relationship between the traditional ΔK_{eff} approach and the cyclic crack-tip displacements for a steel and an aluminum alloy for constant-amplitude loading, which would support the use of the $(S_o)_k$ values.

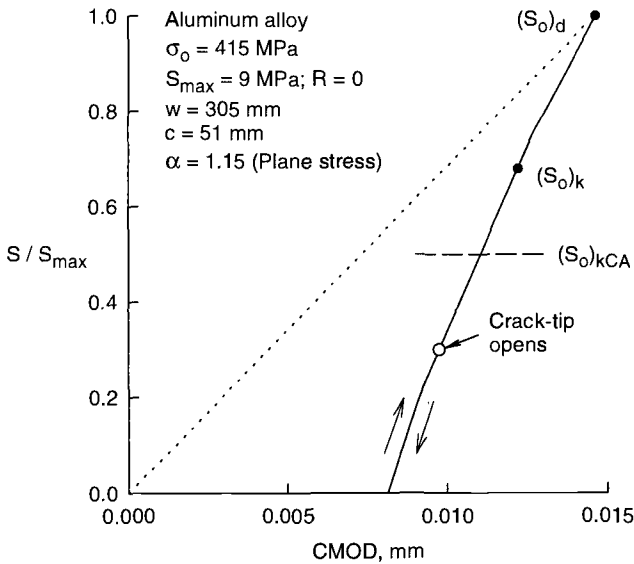


Figure 6 – Remote crack-mouth-opening displacements after load reduction under plane-stress conditions.

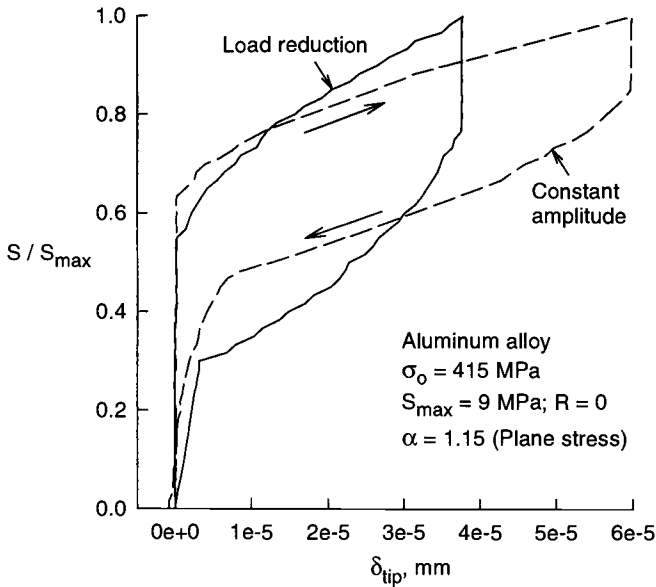


Figure 7 – Crack-tip deformations for a cycle of loading during constant-amplitude loading and load-reduction crack-growth simulations.

High-constraint conditions – To simulate more realistic crack-tip conditions, a higher constraint factor ($\alpha = 2$) was used in the same load-reduction case ($R = 0$) as previously shown. The local COD along the crack surfaces are shown in Figure 8. Again, the solid and dashed curves show the results at maximum and minimum applied stress, respectively. In contrast to the plane-stress case, these results show that the crack surfaces were not in contact at the maximum applied stress (7 MPa). But at minimum load, the crack surfaces near the start of the load-reduction procedure and at the crack tip ($c = 54$ mm) were closed.

The remote cyclic CMOD results at $c = 54$ mm are shown in Figure 9 as the solid curves. Loading and unloading, again, followed the same curve and the dotted line is the linear-elastic behavior. The dashed line shows the $(S_o)_{kCA}$ results from a constant-amplitude simulation at the same stress-intensity factor. Here the contact-COD method gave an opening-stress ratio of about 0.62 and the contact-K analysis gave a value $(S_o)_k/S_{max}$ of about 0.4 (slightly higher than the constant-amplitude value). Using these remote displacements and the 1 or 2% compliance-offset method gave an opening stress value very nearly equal to the $(S_o)_d$ value. This may be why the remote displacement gage may measure an incorrect opening load during threshold testing.

Incidentally, the work of Paris et al [22] has indicated that under conditions of remote (or partial) closure, such as that shown in Figure 8, the appropriate opening stress to use in calculating the effective stress is $(2/\pi) S_{op}$. The value of S_{op} was measured using the 1 or 2% compliance-offset method. As shown herein, S_{op} is nearly equivalent to $(S_o)_d$

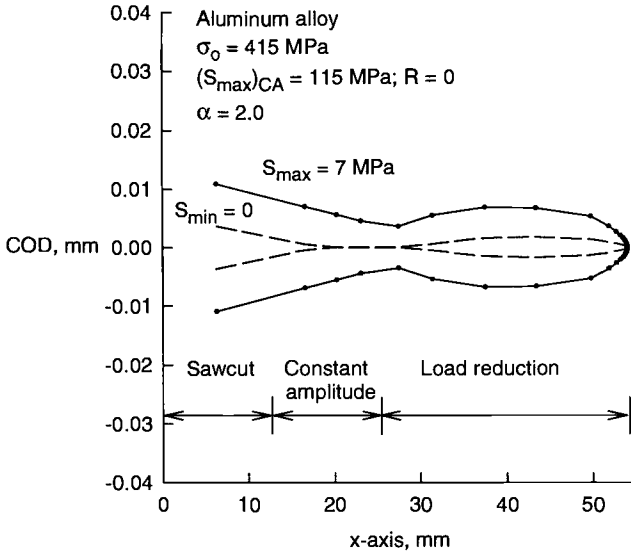


Figure 8 – Crack-surface displacements after load reduction under high-constraint conditions.

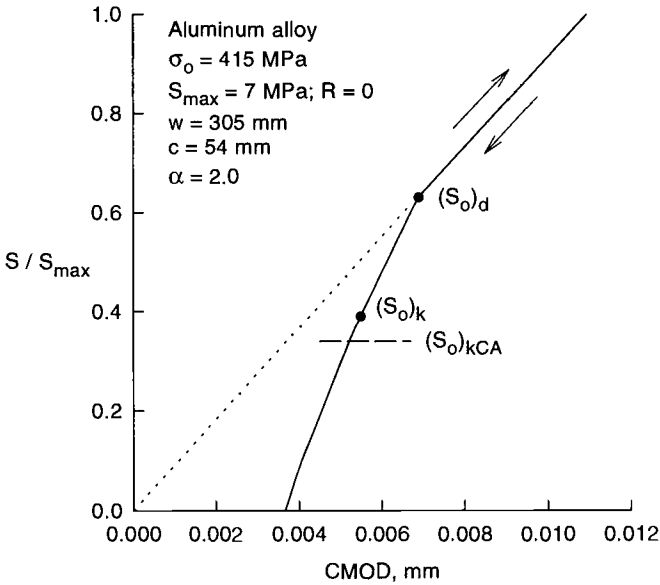


Figure 9 – Remote crack-mouth-opening displacements after load reduction under high-constraint conditions.

determined from the COD analyses. Note that the ratio of $(S_o)_k$ to $(S_o)_d$ is 0.62, close to $2/\pi$ (a value of 0.64).

Crack-Opening-Stress Behavior – In the following, realistic crack-growth properties for the 2024-T3 aluminum alloy are chosen to study the effects of constraint, stress ratios, stress levels, and load-reduction rates on crack-opening stress behavior during threshold testing. For the thin-sheet alloy analyzed herein, a constraint factor of 2 was selected for low rates and 1.15 for high rates. A constraint-loss regime was assumed to occur in the crack-growth rate regime of 1×10^{-7} to 2×10^{-6} m/cycle. The contact-K analyses were used to calculate crack-opening stresses. A brief discussion of three-dimensional effects is also given.

Constraint effects – An M(T) specimen was subjected to simulated fatigue precracking at a maximum applied stress of 115 MPa at $R = 0$ under three conditions of constraint. First, analyses were conducted under constant constraint of 2 and 1.15; and then under a more realistic condition of variable constraint ($\alpha = 2$ to 1.15 during the transition from flat-to-slant crack growth). For $\alpha = 2$, the crack-opening stresses during the precracking stage are shown as the dashed curve in Figure 10. The solid triangular symbol shows the initial ΔK value for the sawcut (no prior plastic history). After a small amount of crack growth, the S_o/S_{max} value stabilized and the load-reduction test were initiated at a ΔK of $30 \text{ MPa}\sqrt{\text{m}}$. The crack-opening stresses during the load-reduction phase are shown as the lower solid curve. A rise in opening stresses (and threshold development) occurred at low values of

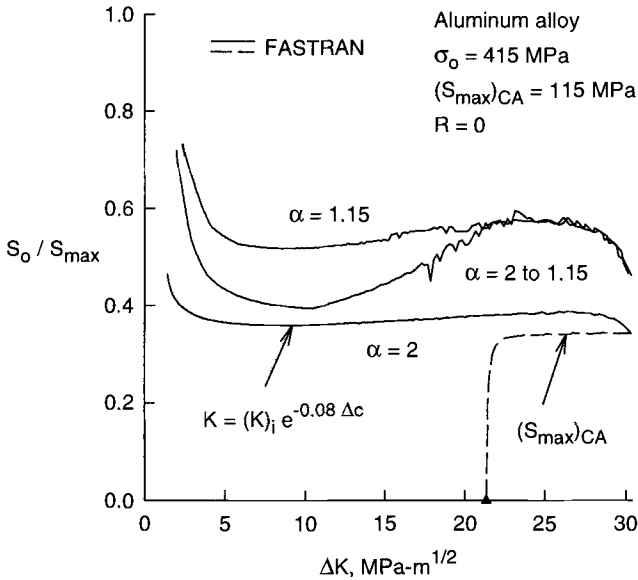


Figure 10 – Calculated crack-opening-stress ratios from simulated threshold tests showing effects of crack-tip constraint.

ΔK . For the other constraint cases, the precracking stage was not shown for clarity. For $\alpha = 1.15$, the results are similar to the previous case, except that the opening values are higher and the rapid rise in opening stresses occurred at a higher ΔK . The more realistic case shows a mixture of the other two cases. At $R = 0$, the threshold in 2024 aluminum alloys generally occurs at a ΔK_{th} value of about $3 \text{ MPa}\sqrt{\text{m}}$.

Stress-ratio effects – Figure 11 shows the precracking stage for the more realistic crack-growth properties ($\alpha = 2$ to 1.15) under constant-amplitude loading at $R = 0$ and 0.7 (dashed curves). Again, the triangular symbols show the initial value of ΔK at the start of the test simulation. The results for the load-reduction phase at $R = 0$ are identical to that shown in the previous figure. It must be noted that the crack-growth simulation at $R = 0$ violates the threshold testing procedure, in that the initial ΔK value at the start of the load-reduction scheme is too high. However, this may be the source of some of the high values of thresholds and specimen-size effects being reported in the literature. On the other hand, the results at $R = 0.7$ seem to be a more realistic test condition. To initiate cracks from sawcuts in aluminum alloys, a ΔK value of about 4 to $6 \text{ MPa}\sqrt{\text{m}}$ is generally required. The crack was precracked at $(S_{max})_{CA}$ of 135 MPa and the ΔK value at the start of load-reduction phase was about $10.5 \text{ MPa}\sqrt{\text{m}}$. The crack-opening stresses are generally near the minimum applied stress but the analyses show a rapid rise at a ΔK of about $2 \text{ MPa}\sqrt{\text{m}}$. This corresponds quite closely to the development of the threshold value at $R = 0.7$ for the 2024 alloy [25].

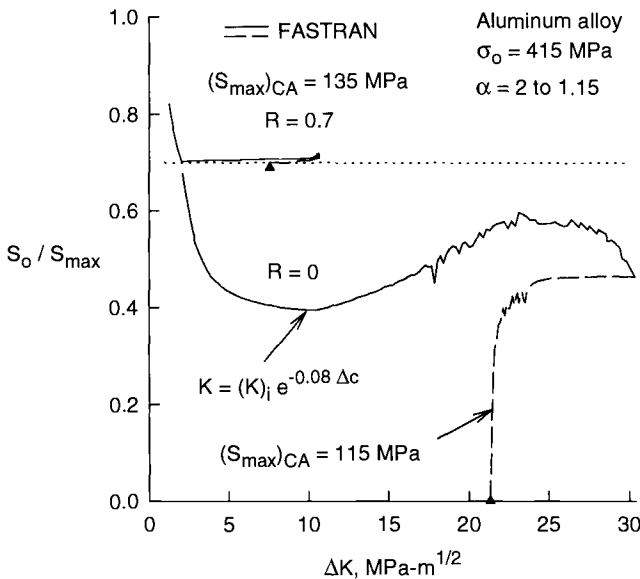


Figure 11 – Calculated crack-opening-stress ratios from simulated threshold tests showing effects of stress ratio.

Stress-level effects – Because the previous low stress ratio test simulation was conducted at a very high precracking stress level, a much lower applied stress level was chosen for the second test simulation at $R = 0$. Again, the $(S_{max})_{CA} = 115$ MPa results shown in Figure 12 are identical to that previously shown. But precracking at a low stress level (45 MPa), before the load-reduction phase, resulted in a stabilized crack-opening stress level even down to very low ΔK values. Thus, under the low applied stress levels, a threshold does not develop solely due to the residual-plastic deformations. Here oxide and/or roughness contributions are needed to predict threshold development. However, residual-plastic deformations still play an important part in threshold development at low stress ratios because it is the combination of the various forms of closure that ultimately contribute to thresholds.

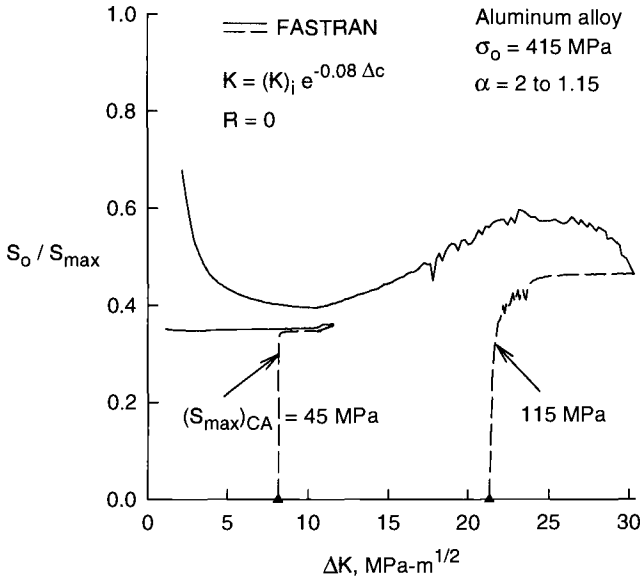


Figure 12 – Calculated crack-opening-stress ratios from simulated threshold tests showing effects of stress level.

Load-shedding effects – Crack-growth simulations were conducted at $R = 0.7$ at a precracking level 135 MPa using two load-decay rates ($\gamma = -0.08$ or -0.2 mm^{-1}). The results are shown in Figure 13. The solid triangle shows the initial ΔK value for each simulation. The specimens were precracked to a ΔK value of about $11 \text{ MPa}\sqrt{\text{m}}$ before the load-reduction simulation began. These results show that the faster decay rate caused a rise to threshold to occur at a higher ΔK value than the standard decay rate. The arrows indicate the value of the constraint factor. The precracking stage was conducted in the constraint-loss regime and the minimum α value was about 1.5. The rise in crack-opening stresses at low ΔK values was caused by remote closure due to residual-plastic deformations.

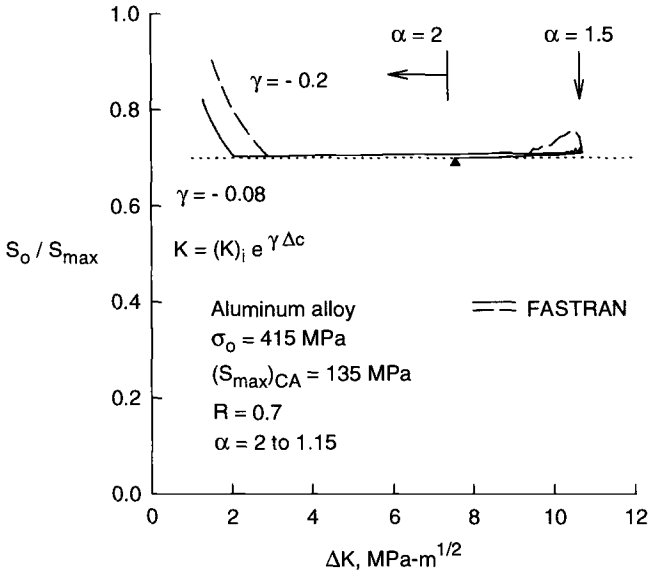


Figure 13 – Calculated crack-opening-stress ratios from simulated threshold tests showing effects of load-reduction rates.

Three-dimensional effects – The previous results show that in-plane plasticity can cause remote or intermittent closure under plane-stress conditions or under high applied stress levels. The use of the constraint factor in a two-dimensional model is “averaging” the effects of three-dimensional plastic stress states at the crack front and in the plastic wake. Three-dimensional crack-growth and closure simulations [23] under constant-amplitude loading show that substantially more closure occurs in the plane-stress regions than in the interior of a finite-thickness body.

Apparently, the plane-stress regions near the free surfaces of a specimen also play an important role in crack-closure behavior under variable-amplitude loading. McEvily [24] found in a test on a 6061 aluminum alloy ($B \approx 13$ mm) that a spike overload caused significant crack-growth delay. When he machined 25% of the thickness from each surface (after the application of the spike overload), he found very little crack-growth delay. Thus, the crack-closure effect under spike overloads is predominantly a surface phenomenon. Do the plane-stress regions cause more contact in a threshold test? To help answer this question, three-dimensional elastic-plastic analyses are required and this must await a future study.

Application of Crack Closure Analyses to Test Data

The crack-closure model analysis will be applied to test data on thin-sheet 2024-T3 aluminum alloy. The threshold tests were conducted on M(T) specimens using the ASTM

load-reduction procedure [19, 25]. In addition, test and analyses will also be compared for a constant- K_{\max} test [19].

Constant-Amplitude/Load-Reduction Tests and Analyses

Hudson [26] conducted constant-amplitude fatigue-crack-growth rate tests on a 2024-T3 aluminum alloy ($B = 2.3$ mm) material over a wide range in stress ratio. Later, Phillips [25] conducted threshold tests on the same material to obtain test data at very low crack-growth rates. Recently, Donald and Paris [19] conducted a test on a similar thin-sheet 2024 alloy using a constant- K_{\max} test. The constant-amplitude crack-opening stress equations [21] with a constraint factor of 1.73 (rates less than 1×10^{-7} m/cycle) [27] were used to calculate the effective stress-intensity factor for these data. The results from Hudson and Phillips' data are plotted on Figure 14 and show that the data correlates quite well, even down to threshold. The constant- K_{\max} test of Donald and Paris (solid diamonds) agreed with the other data for rates greater than about 2×10^{-9} m/cycle, but resulted in lower ΔK_{eff} values than the constant-R tests as the threshold was approached. The constant-R tests showed a slight trend with stress ratio at threshold. The higher stress ratio test had a lower ΔK_{th} (based on full range) than the low stress ratio tests. Phillips [25] measured a rise in crack-opening stresses for the low R tests, but he did not measure a rise for the $R = 0.7$ test. However, he observed in all cases that a higher load was required to re-initiate growth of the dormant crack even at the high stress ratios. This may indicate that an accumulation of oxide raised the opening load even for the high stress ratio test. Interestingly, the solid lines on Figure 14, below rates of 1×10^{-9} m/cycle, is a baseline fit to small-crack data for this alloy [28]; and these results generally agree with the constant- K_{\max} test data. (The baseline curve is fit to small-crack data below rates of 1×10^{-9} m/cycle and large-crack data above 1×10^{-9} m/cycle, ignoring the large-crack threshold data [28].)

A comparison of measured and calculated crack-opening stresses at $R = 0$ are shown in Figure 15. The solid symbols are measured values from Phillips [25] using the Elber method [29] and the open symbols are opening values determined from Hudson's data using an indirect method [10]. (The indirect method finds the value of opening stress at $R = 0$ to correlate with the baseline ΔK_{eff} - rate curve.) The solid curve shows the predicted K_o values from the closure model. Because the precracking ΔK levels were less than about $5 \text{ MPa}\sqrt{\text{m}}$, the analysis did not predict a threshold from residual-plastic deformations. The sharp knee shown by the test data at a ΔK of about $4 \text{ MPa}\sqrt{\text{m}}$ is the development of the threshold. Based on the literature, oxide accumulation is suspected to cause threshold development. The dotted lines are based on constant constraint calculations from plane-stress to plane-strain conditions. The sharp knee at a ΔK level of about $12 \text{ MPa}\sqrt{\text{m}}$ is associated with the beginning of the constraint-loss regime.

Figure 16 shows the crack-opening values from the Donald-Paris data [19] at $R = 0$ and 0.7 using the indirect method (symbols). The constant- K_{\max} test results at rates lower than about 2×10^{-9} m/cycle and the baseline ΔK_{eff} - rate curve (Figure 14) at higher rates were used as the baseline data. Because the $R = 0.7$ and constant- K_{\max} results differed at low rates, the indirect method produced a sharp rise in opening stresses near the threshold for

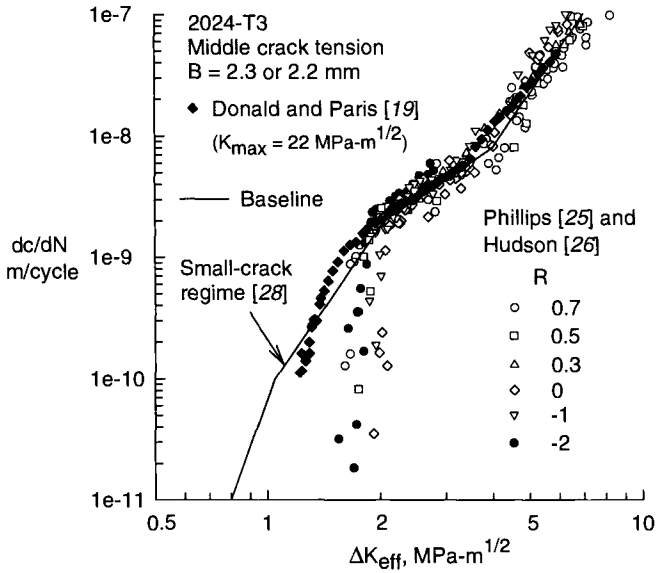


Figure 14 – Effective stress-intensity factor against crack-growth rates for 2024-T3 at very low rates showing small-crack regime and constant- K_{max} test results.

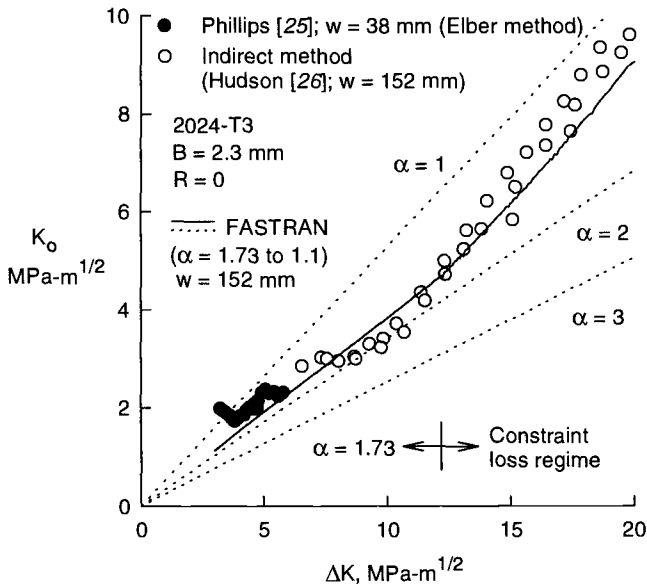


Figure 15 – Crack-opening stress-intensity factors for 2024-T3 aluminum alloy at $R = 0$ from measured, indirect method, and model calculations.

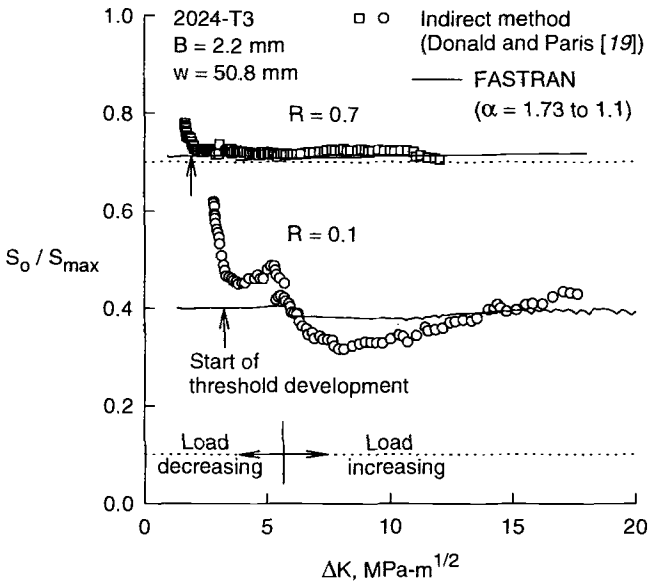
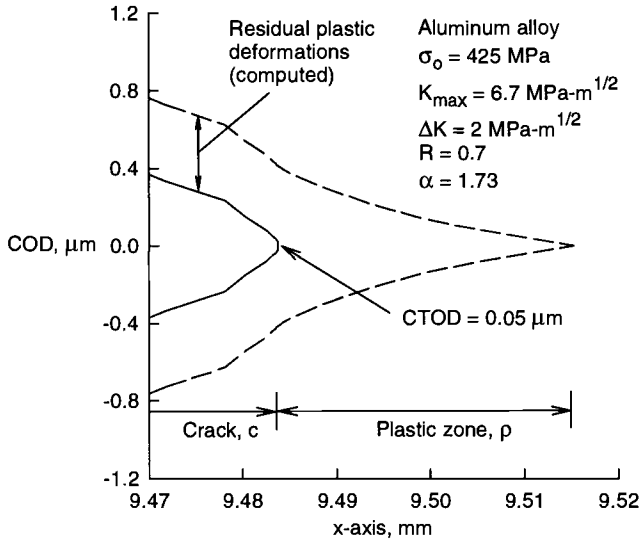


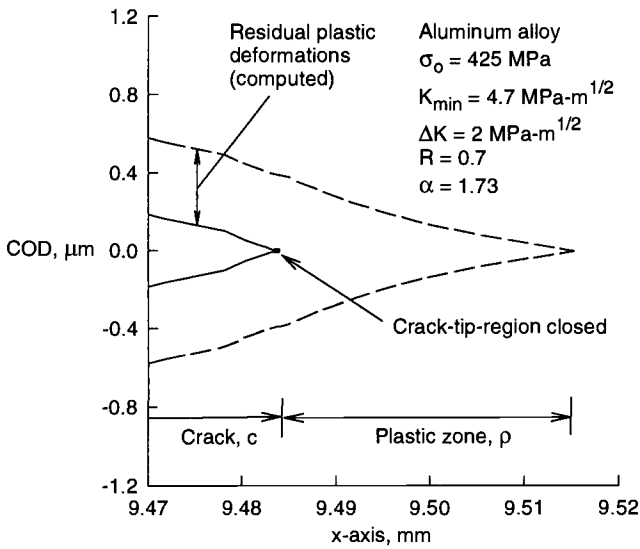
Figure 16 – Crack-opening stress ratios for 2024-T3 aluminum alloy at low and high stress ratios from indirect method and model calculations.

the $R = 0.7$ data (square symbols). The low R results also showed a sharp rise near threshold. The solid curves show the calculations from the closure model for load-decreasing and load-increasing tests. Again, the model did not show a rise in opening loads because the ΔK level at the start of each test was low (about $6 \text{ MPa}\sqrt{\text{m}}$). For these cases, the contact- K and COD analyses gave essentially the same results. Remote displacement gages are most likely unable to measure the very small amount of closure for the high-stress ratio tests. But under high- R conditions, the calculated opening load is very near to the minimum applied stress level. Thus, a small amount of interference from roughness or oxide-accumulation may cause a threshold to develop. (Donald and Paris [19] did not measure any opening loads under the $R = 0.7$ test but measured a rapid rise on the $R = 0.1$ test.)

To study why the model did not predict a rise in the opening stresses, the near crack-tip-opening displacements at the start of the test threshold development (shown by the vertical arrows in Figure 16) are shown in Figures 17 and 18. The local COD values are shown in Figure 17(a) at maximum load and Figure 17(b) at minimum load. The stress-intensity factor range ΔK ($2 \text{ MPa}\sqrt{\text{m}}$) was slightly higher than the $R = 0.7$ threshold value that would have developed for the 2024-T3 alloy (about $1.56 \text{ MPa}\sqrt{\text{m}}$ [19, 25]). The crack length and plastic-zone size are as indicated on the figure. The solid curve shows the crack-surface profile. The dashed curve shows the boundary between elastic and plastic material. Even under the high-constraint conditions and at the low stress-intensity factor level, the residual-plastic deformations contribute greatly to the final crack-surface profile. The



(a) Maximum load



(b) Minimum load

Figure 17 – Crack-tip-surface displacements showing residual-plastic deformations and plastic-zone size near threshold conditions at high-stress ratio.

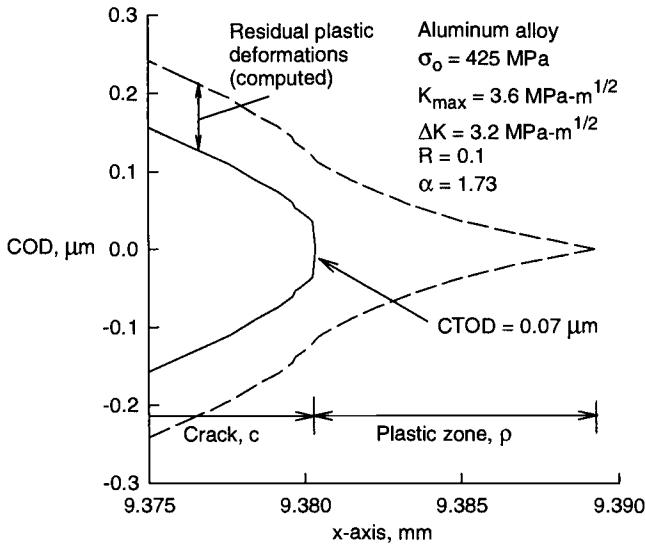


Figure 18 – Crack-tip-surface displacements at maximum load showing residual-plastic deformations and plastic-zone size near threshold conditions at a low stress ratio.

CTOD at maximum load was $0.05 \mu\text{m}$. At minimum load, the crack-tip region is closed over a very small area ($S_0/S_{\text{max}} = 0.71$). Because tests indicate that a threshold would have developed under these conditions, the other forms of closure may be contributing to threshold development. In considering oxide-induced closure, what oxide-layer thickness would have been required to influence crack closure at minimum load? For the 2024-T3 aluminum alloy at a high relative humidity (95%), Vasudevan and Suresh [20] measured peak oxide thicknesses of $0.02 \mu\text{m}$ at $R = 0.33$. But oxide-layer thicknesses are expected to be smaller at the high stress ratio condition because crack-surface contact is minimal and oxide layers are less likely to be crushed or broken to create fresh crack surface. However, the crack-surface displacements would also have been smaller than those shown in the figure at ΔK_{th} . Thus, residual-plastic deformations and oxide accumulation could be plausible explanations for threshold development. The relative contribution of crack-surface roughness to threshold development is difficult to assess.

The crack-tip-surface displacements at maximum load for the $R = 0.1$ test simulation are shown in Figure 18. The CTOD was $0.07 \mu\text{m}$. The residual-plastic deformations (difference between solid and dashed curves) were of the same order-of-magnitude as the near crack-tip COD. At minimum load, the crack surfaces were closed over a large region (not shown). Thus, a peak oxide-layer thickness of $0.02 \mu\text{m}$ [20], in combination with the residual-plastic deformations, would have had a large influence on calculated crack-opening loads and threshold development.

Constant- K_{max} Test and Analysis

The constant- K_{max} test [30] has been proposed as an alternative test to obtain low crack-growth rate data. A crack-growth and closure analysis of the constant- K_{max} test conducted by Donald and Paris [19] is shown in Figure 19. The upper dashed line is the K_{max} ($22 \text{ MPa}\sqrt{\text{m}}$) value and the lower dashed curve is the K_{min} value. The initial notch half-length was c_n and the crack half-length c_i denotes the start of the increasing K_{min} test. The solid curve shows the calculations from the model. At a stress ratio of about 0.8, the crack surfaces became fully open at the minimum stress-intensity factor (solid symbol).

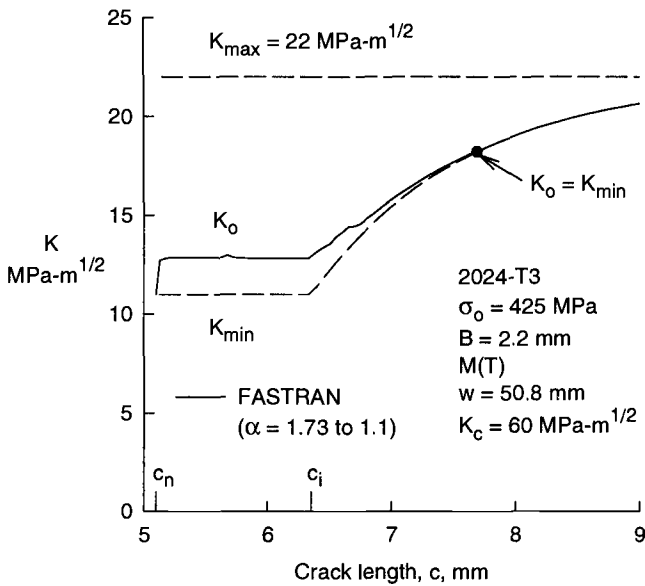


Figure 19 – Calculated crack-opening stress-intensity factors for constant- K_{max} test.

At the end of the test simulation, the R value was about 0.95 and the ΔK value was $1.2 \text{ MPa}\sqrt{\text{m}}$. Figure 20 shows the local crack-tip-surface displacements at the minimum load under these conditions. The solid curves are the crack surfaces and the dashed curves show the boundary between the elastic and plastic regions. The crack-tip-opening displacement was about $0.14 \mu\text{m}$, nearly an order-of-magnitude larger than the expected peak oxide thicknesses [20] even under a relatively high humidity. Thus, oxide-induced closure should not be an issue. Again the contribution of crack-surface roughness is difficult to assess. But the constant- K_{max} test results agreed reasonably well with the small-crack data on this alloy (see Figure 14). Note that the residual-plastic deformations were about 50 times larger than the crack-tip-opening displacement.

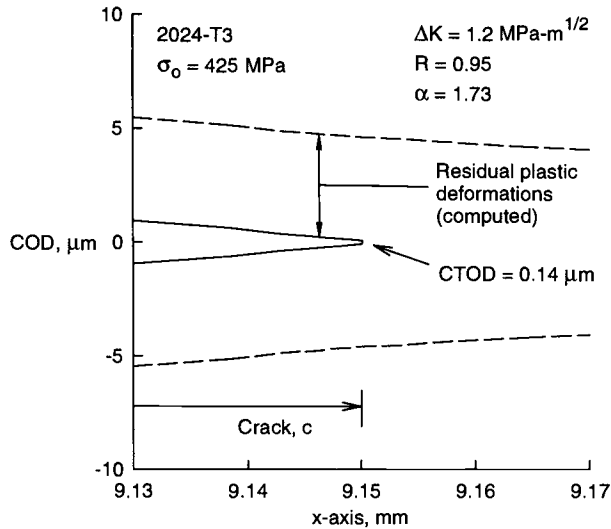


Figure 20 – Crack-tip-surface displacements at minimum load under constant- K_{max} testing near threshold conditions.

Conclusions

A plasticity-induced crack-closure model was used to simulate fatigue-crack growth and closure under constant-amplitude, load-reduction, load-increasing, and constant- K_{max} testing on thin-sheet 2024-T3 aluminum alloy. The following conclusions were made:

(1) Crack-opening stresses under constant-amplitude loading computed from contact- K analyses were nearly equal to those computed from a contact crack-opening displacement (COD) method, but under threshold testing (load-reduction) simulations, the opening stresses from the contact- K analyses were equal to or lower than those from the contact-COD analyses.

(2) For some remote (partial) closure situations, crack-opening stresses computed from remote displacements, using the 1 or 2% compliance-offset method, agreed with the values computed from the contact-COD method. But comparisons of crack-growth predictions with measurements tend to support crack-opening stresses from the contact- K analyses.

(3) Under low ($R = 0$) and high ($R = 0.7$) stress-ratio load-reduction simulations, analyses produce residual-plastic deformations that cause remote closure and threshold development for low-constraint (plane-stress) behavior and at high applied stress levels (applied-stress-to-flow-stress ratios greater than about 0.25). For plane-strain conditions and low applied stress levels, remote closure and threshold development were not observed.

(4) Under low ($R = 0$) and high ($R = 0.7$) stress-ratio load-reduction simulations, analyses produce residual-plastic deformations near threshold conditions that were of the same order-of-magnitude as the crack-tip-opening displacements. But additional contributions from roughness and/or oxide-fretting debris are required to develop thresholds.

(5) Constant- K_{\max} test simulations produce closure-free crack surfaces from residual-plastic deformations at the high stress ratio ($R > 0.8$) conditions; and the crack-tip opening displacements at minimum loads were an order-of-magnitude larger than expected peak oxide thicknesses for 2024 aluminum alloys. Thus, contributions from oxide-fretting debris may not have an influence on threshold development.

References

- [1] Paris, P. C., "Testing for Very Slow Growth of Fatigue Cracks," *Closed Loop Magazine*, MTS Systems Corporation, Vol. 2, No. 5, 1970.
- [2] Saxena, A., Hudak, S. J., Jr., Donald, J. K., and Schmidt, D. W., "Computer-Controlled Decreasing Stress Intensity Technique for Low Rate Fatigue Crack Growth Testing," *Journal of Testing and Evaluation*, Vol. 6, No. 3, 1978, pp. 167-174.
- [3] Minakawa, K. and McEvily, A. J., "On Near-Threshold Fatigue Crack Growth in Steels and Aluminum Alloys," Proceedings of the International Conference on Fatigue Thresholds, Vol. 2, Stockholm, Sweden, 1981, pp. 373-390.
- [4] Newman, J. C., Jr., "A Nonlinear Fracture Mechanics Approach to the Growth of Small Cracks," *Behaviour of Short Cracks in Airframe Materials*, AGARD CP-328, 1983, pp. 6.1-6.26.
- [5] Donald, J. K., Bray, G. H., and Bush, R. W., "An Evaluation of the Adjusted Compliance Ratio Technique for Determining the Effective Stress Intensity Factor," *Fatigue and Fracture Mechanics: Twenty-Ninth Volume, ASTM STP 1332*, T. L. Panontin and S. D. Sheppard, Eds., American Society for Testing and Materials, West Conshohocken, PA, 1999, pp. 674-695.
- [6] Newman, J. C., Jr., Phillips, E. P., Swain, M. H., and Everett, R. A., Jr., "Fatigue Mechanics: An Assessment of a Unified Approach to Life Prediction," *Advances in Fatigue Lifetime Predictive Techniques, ASTM STP 1122*, M. R. Mitchell and R. W. Landgraf, Eds., American Society for Testing and Materials, Philadelphia, 1992, pp. 5-27.
- [7] Elber, W., "The Significance of Fatigue Crack Closure," *Damage Tolerance in Aircraft Structures, ASTM STP 486*, American Society for Testing and Materials, 1971, pp. 230-242.
- [8] Paris, P. C., Bucci, R. J., Wessel, E. T., Clark, W. G., and Mager, T. R., "Extensive Study of Low Fatigue Crack Growth Rates in A533 and A508 Steels," *ASTM STP-513*, 1972, pp. 141-176.
- [9] Walker, N. and Beevers, C. J., "A Fatigue Crack Closure Mechanism in Titanium," *Fatigue of Engineering Materials and Structures*, Vol. 1, No. 1, 1979, pp. 135-148.
- [10] Newman, J. C., Jr., "A Crack-Closure Model for Predicting Fatigue Crack Growth under Aircraft Spectrum Loading," *Methods and Models for Predicting Fatigue*

- Crack Growth under Random Loading*, ASTM STP 748, J. B. Chang and C. M. Hudson, Eds., American Society for Testing and Materials, 1981, pp. 53-84.
- [11] Newman, J. C., Jr., "FASTRAN-II - A Fatigue Crack Growth Structural Analysis Program," NASA TM 104159, February 1992.
- [12] Dugdale, D. S., "Yielding of Steel Sheets containing Slits," *Journal of the Mechanics and Physics of Solids*, Vol. 8, 1960, pp. 100-104.
- [13] Blom, A., Wang, G. S., and Chermahini, R. G., "Comparison of Crack Closure Results Obtained by 3D Elastic-Plastic FEM and Modified Dugdale Model," *Localized Damage: Computer-Aided Assessment and Control*, M. H. Aliabadi et al, Eds., Computational Mechanics Publications, Springer-Verlag, Berlin, 1990, pp. 57-68.
- [14] Newman, J. C., Jr., "Finite-Element Analysis of Crack Growth under Monotonic and Cyclic Loading," *Cyclic Stress-Strain and Plastic Deformation Aspects of Fatigue Crack Growth*, ASTM STP 637, American Society for Testing and Materials, 1977, pp. 56-80.
- [15] Newman, J. C., Jr., "Fracture Analysis of Various Cracked Configurations in Sheet and Plate Materials," *Properties Related to Fracture Toughness*, ASTM STP 605, American Society for Testing and Materials, 1976, pp. 104-123.
- [16] Newman, J. C., Jr., "An Evaluation of Plasticity-Induced Crack-Closure Concept and Measurement Methods," *Advances in Fatigue Crack Closure Measurement and Analysis*, ASTM STP 1343, R. C. McClung and J. C. Newman, Jr., Eds., American Society for Testing and Materials, 1999.
- [17] Ohta, A., Kosuge, M., and Sasake, E., "Fatigue Crack Closure Over the Range of Stress Ratios from -1 to 0.8 Down to Stress Intensity Factor Threshold Level in HT80 Steel and SUS 304 Stainless Steel," *International Journal of Fracture*, Vol. 14, No. 3, 1978, pp. 251-264.
- [18] Minakawa, K. and McEvily, A. J., "On Crack Closure in the Near-Threshold Region," *Scripta Metallurgica*, Vol. 15, 1981, pp. 633-636.
- [19] Donald, J. K. and Paris, P. C., "An Evaluation of ΔK_{eff} Estimation Procedures on 6061-T6 and 2024-T3 Aluminum Alloys," Proceedings of Fatigue Damage of Structural Materials II, Cape Cod, MA, September 7-11, 1998.
- [20] Vasudevan, A. K. and Suresh, S., "Influence of Corrosion Deposits on Near-Threshold Fatigue Crack Growth Behavior in 2XXX and 7XXX Series Aluminum Alloys," *Metallurgical Transactions A*, Vol. 13A, December 1982, pp. 2271-2280.
- [21] Newman, J. C., Jr., "A Crack Opening Stress Equation for Fatigue Crack Growth," *International Journal of Fracture*, Vol. 24, 1984, R131-R135.
- [22] Paris, P. C., Tada, H., and Donald, J. K., "Service Load Fatigue Damage - A Historical Perspective," Proceedings of Fatigue Damage of Structural Materials II, Cape Cod, MA, September 7-11, 1998.
- [23] Chermahini, R. G., Shivakumar, K. N., and Newman, J. C., Jr., "Three-Dimensional Finite-Element Simulation of Fatigue Crack Growth and Closure," *Mechanics of Fatigue Crack Closure*, ASTM STP 982, J. C. Newman, Jr. and W. Elber, Eds., American Society for Testing and Materials, 1988, pp. 398-413.
- [24] McEvily, A. J., "Current Aspects of Fatigue," *Metal Science*, August/September 1977, p. 284.

- [25] Phillips, E. P., "The Influence of Crack Closure on Fatigue Crack Growth Thresholds in 2024-T3 Aluminum Alloy," *Mechanics of Fatigue Crack Closure, ASTM STP 982*, J. C. Newman, Jr. and W. Elber, Eds., American Society for Testing and Materials, 1988, pp. 505-515.
- [26] Hudson, C. M., "Effect of Stress Ratio on Fatigue-Crack Growth in 7075-T6 and 2024-T3 Aluminum Alloy Specimens," NASA TN D-5390, 1969.
- [27] Newman, J. C., Jr., Swain, M. H., and Phillips, E. P., "An Assessment of the Small-Crack Effect for 2024-T3 Aluminum Alloy," *Small Fatigue Cracks*, R. O. Ritchie and J. Lankford, eds., The Metallurgical Society, Inc., 1986, pp. 427-451.
- [28] Newman, J. C., Jr., Harris, C. E., James, M. A., and Shivakumar, K. N., "Fatigue-Life Prediction of Riveted Lap-Splice Joints using Small-Crack Theory," *Fatigue in New and Ageing Aircraft*, R. Cook and P. Poole, eds., EMAS Publishing, UK, 1997, pp. 523-552.
- [29] Elber, W., "Crack-Closure and Crack-Growth Measurements in Surface-Flawed Titanium Alloy Ti-6Al-4V," NASA TN D-8010, September 1975.
- [30] Herman, W. A., Hertzberg, R. W., Newton, C. H., and Jaccard, R., "A Re-evaluation of Fatigue Threshold Test Methods," *Fatigue '87, Third International Conference on Fatigue and Fatigue Thresholds, Vol. II*, 1987, pp. 819-828.

Franz O. Riemelmoser¹ and Reinhard Pippan¹

The Mechanics of Moderately Stressed Cracks

Reference: Riemelmoser, F. O. and Pippan, R., “The Mechanics of Moderately Stressed Cracks,” *Fatigue Crack Growth Thresholds, Endurance Limits, and Design*, ASTM STP 1372, J. C. Newman, Jr. and R. S. Piascik, Eds., American Society for Testing and Materials, West Conshohocken, PA, 2000.

Abstract: The intrinsic behaviour of fatigue cracks is discussed by a discrete dislocation model and by a BCS-type continuum mechanics approximation. The investigation of a homogeneous material shows that the near threshold regime and the existence of an intrinsic threshold itself can be ascribed to the dislocation nature of plasticity. By incorporating microstructural features in the analysis it is then shown that the intrinsic threshold value is determined only by the mechanism for the dislocation generation and does not depend on microstructural details like the grain size. However, in the near threshold regime and in the lower Paris regime the plastic deformation and the crack growth rates are severely influenced by microstructure. Therefore, a micromechanics approach should be used for the predictions of the plastic response of materials. Only in the upper Paris regime, where the cyclic plastic zone size exceeds several times the microstructural length scale usual continuum plasticity mechanics is appropriate to describe the events at the crack tip. Macroscopic quantities like the yield stress of materials cannot be used to describe moderately stressed fatigue cracks.

Keywords: intrinsic material behaviour, threshold, dislocation mechanics, BCS model, computer simulation

Introduction

Fatigue crack propagation in metals is at all amplitudes of stress the result of some non-reversible plastic deformation. It is characterised by two length parameters: the cyclic crack tip opening displacement $\Delta CTOD$ and the cyclic plastic zone size $\Delta\omega$. Opposed to these mechanical length scales are the material inherent ones such as the Burgers vector of a lattice dislocation and the mean distance between dislocation obstacles, the thickness of lamellars in perlitic materials, the size and the spacing of particles in metal matrix compounds and the grain size in monolithic metals.

It is reasonable to assume that the use of standard continuum mechanics to de-

¹ Research assistant and senior scientist, respectively, Erich Schmid Institute for Material Science of the Austrian Academy of Sciences and Institute of Metal Physics of The University Leoben, A - 8700 Leoben, Austria.

scribe fatigue crack propagation and its accompanying plasticity implies that the mechanical lengths scales involved are large in comparison to material length scales which would only be the case in the upper Paris regime where the cyclic plastic zone is a few tenths of millimeters in size. In the lower Paris regime and in the near threshold regime the cyclic plastic zone size decreases to the microstructural length scales and $\Delta CTOD$ is in the order of a Burgers vector of lattice dislocations such that standard continuum mechanics is no longer appropriate to describe the mechanical response of the material.

There are some papers of ours dealing with related questions where plasticity has been described as motion of discrete dislocations. For instance, Pippan [1] has shown by the simulation of the dislocation motion at cyclically loaded mode III and mode II cracks that the intrinsic threshold of homogeneous materials can be explained by the stress intensity factor necessary to generate the dislocations at the crack tip. Later he has incorporated dislocation obstacles in the simulations [2] where it turned out that the calculated intrinsic threshold value does surprisingly neither depend on the obstacle distribution nor on their strength such that the intrinsic threshold, also for such more complicated microstructures, is only a function of the dislocation generation mechanism. Similar calculations have been performed by Riemelmoser et al. [3] for mode I cracks. It was found that many characteristic features of fatigue crack growth in the near threshold regime including the anomaly of the constancy of striation spacing at low ΔK values, can be explained by discrete dislocation models. These investigations put forward an argument that in the near threshold regime the crack grows similar to the Paris regime in each and every cycle.

The aim of the present paper is to study the mechanical response of homogeneous and more complicated materials as a function of the stress intensity factor range. It is shown that only at large ΔK values materials behave in coincidence with macroscopic continuum mechanics. At intermediate stress intensity ranges the plastic deformation at the crack tip is severely influenced by the actual position of the crack tip in relation to the microstructure and at very small ΔK values the discrete (dislocation) nature of plasticity becomes the dominating factor influencing the plastic response of cyclically loaded cracks.

Three examples of materials are discussed which are

1. a homogenous material without microstructural features,
2. a homogenous material with a grain boundary, and
3. a duplex material.

Subsequently a short description of the simulation techniques used is given and then the results are discussed.

The Cyclic Crack Tip Opening Displacement and the Intrinsic Threshold in a Homogeneous Material

In the following we study the plastic response of materials when they are loaded in mode II under plane strain conditions. Let us assume that the plastic zone size is small in comparison to the overall specimen dimensions. In this case it is sufficient to consider a semi-infinite crack along the negative x -axis where the remote stresses are characterized by the stress intensity factor K_{II} . The plasticity is modelled as a dislocation arrangement ahead of the crack tip in a plane coplanar to the crack plane as schematically shown in Fig. 1. The mechanical properties of the material are characterized by the shear modulus μ , by Poisson's ratio ν and by the critical resolved shear stress σ_{crit} which acts against the motion of the dislocations.

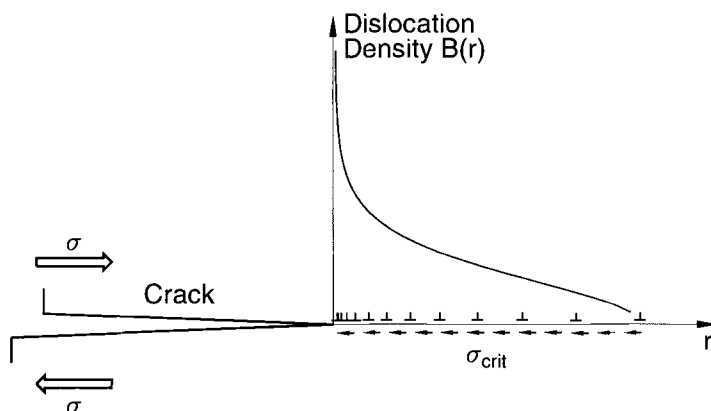


Figure 1: A schematic of the dislocation density in front of a mode II crack.

The force, $F(r)$, on a dislocation with the Burgers vector b at the position r ahead of the crack tip has been derived in [4] as follows:

$$F(r) = \frac{K_{II}b}{\sqrt{2\pi r}} - \frac{\mu b^2}{4\pi r(1-\nu)} + \sum_{b'} \frac{\mu b b'}{2\pi(1-\nu)} \sqrt{\frac{r'}{r}} \frac{1}{r-r'} \quad (1)$$

In case of dislocations with a positive Burgers vector the first term in this equation is the repulsive force caused by remote loading, the second term is the attractive dislocation image force which is due to the free surface of the crack and the third term expresses the reaction of the dislocation with the stress field induced by the other dislocations at the positions r' with the Burgers vectors b' .

In the following we use two different ways to solve Eq. 1. The direct method is to compute the force on the dislocations and to simulate the motion of the discrete dislocations. This is a convenient method when only a small number of dislocations is generated. At large stress intensity ranges many dislocations are cyclically moved

and the straightforward simulation of the dislocation motion becomes too cumbersome. Here it is preferable to make a continuum mechanics approximation of Eq. 1 in the spirit of the BCS theory [5] of cracks (named after the pioneers in elasto-plastic fracture mechanics Bilby, Cottrell and Swinden). The Burgers vectors of the dislocations are smeared out by setting $b = B(r) dr$. This leads to the singular integral equation:

$$\frac{1}{B(r)} \frac{dF(r)}{dr} = \frac{K}{\sqrt{2\pi r}} - \frac{\mu B(r) dr}{4\pi r(1-\nu)} + \frac{\mu}{2\pi(1-\nu)} \int_0^\omega \sqrt{\frac{r'}{r-r'}} \frac{B(r')}{r-r'} dr' = -\sigma_{crit}(r) \quad (2)$$

where the integration in the third term between the equality signs is performed over the entire plastic zone of size ω . The second term between the equality signs, which is of a higher order can be dropped. The benefit of doing this continuum mechanics approximation is that the remaining integral equation can now be solved analytically – at least for a crack in a homogeneous material where the critical resolved shear stress is constant throughout the plastic zone [6].

By a method as introduced by Rice [7] also cyclic plasticity problems, i.e. cracks unloaded with a certain ΔK , can be solved. Here the dislocation arrangement at the crack at maximum load is sought as discussed above. Then the solution of a second crack in a material with a critical resolved shear stress which is twice as large as σ_{crit} of the former material is computed. The dislocation arrangement, i.e. the distribution of the Burgers vector, of the partially unloaded crack is now obtained by subtracting the solution of this second crack from the first one. The cyclic crack tip opening displacement, $\Delta CTOD$, is equal to the amount of Burgers vectors leaving the body at the crack tip during unloading. For a homogeneous material the well known expression Eq. 3 is derived as follows:

$$\Delta CTOD = \frac{\Delta K_{II}^2(1-\nu)}{4\mu\sigma_{crit}} \quad (3)$$

The result of this and the forthcoming analyses is given in terms of the $\Delta CTOD$ rather than in the crack growth increment per loading cycle $\frac{da}{dN}$. However, in metals there is a close relationship between these parameters which can be written as:

$$\frac{da}{dN} = \beta \Delta CTOD^\alpha \quad (4)$$

where α equals to unity for materials when the crack propagates in a striation formation mechanism, i.e. by crack tip blunting and resharpening. For materials where additional damage mechanisms like micro cracking in front of the crack tip occurs the exponent α is larger than unity. The factor β is about 0.5 when the plastic shearing at the crack tip produces a V-notch as proposed by Pelloux [8]. For our mode II crack the factor β equals unity when the crack growth process is due to irreversible plastic shearing at the crack tip.

Let us now consider the direct method of solving Eq. 1 by means of the discrete dislocation model as explained in [1]. Here the crack is loaded in steps. The dislocations are generated at the crack tip whenever the local stress intensity factor reaches

a critical value k_e [9]. The equilibrium arrangement of the dislocations is found by shifting the dislocations along the slip plane as long as the force acting on them (given by Eq. 1) is larger than the critical resolved shear stress.

In Fig. 2 the BCS continuum mechanics solution (Eq. 3) and the result of the dislocation modelling are compared for two different critical resolved shear stresses $\sigma_{crit,1} = \mu/700$ and $\sigma_{crit,2} = \mu/350$. The stress intensity k_e to generate dislocations at the crack tip is in both cases the same $k_e = 0.29\mu\sqrt{b}$. The stress ratio K_{min}/K_{max} is set $R = 0.1$.

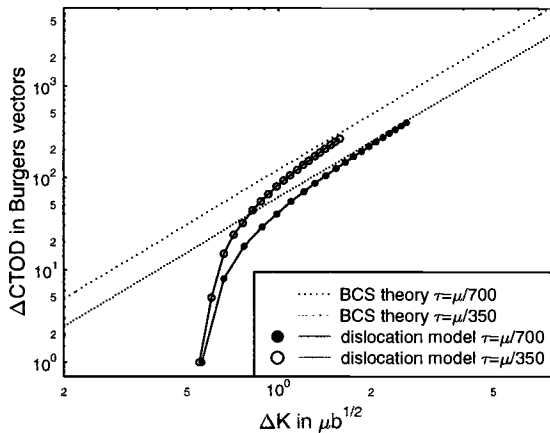


Figure 2: Comparison of the discrete dislocation mechanics solution of the Eq. 2 with the BCS continuum mechanics approximation for two different critical resolved shear stresses.

In the BCS continuum solution, Eq. 3, the $\Delta CTOD$ is proportional to the second power of the stress intensity factor range. Therefore the solutions of both the plastically harder and the plastically softer material appear as a straight line with a slope of 2 in the $\log \Delta CTOD - \log \Delta K$ -diagram.

At large stress intensity ranges, in the Paris regime, where many dislocations are cyclically moved the discrete dislocation model leads to the same result. As expected, here the continuum mechanics approximation and the discrete dislocation modelling are equivalent. At small ΔK values the curves of the discrete dislocation model bend down leading to an intrinsic threshold of the plastic deformation which is at a $\Delta CTOD$ of 1 Burgers vector per cycle. Clearly, plastic deformations smaller than 1 Burgers vector cannot occur.

In our opinion this is the reason why many measured crack growth curves show a knee in the range about a crack propagation rate of 1 Burgers vector per cycle, where these curves become very steep. Crack growth increments below 1 Burgers vector per cycle can be explained, as David L. Davidson [10] mentioned, as follows: When the global stress intensity range is somewhat above the threshold then it is likely that due to irregularities along the crack front the local driving force in some grains is above

and in the other grains it is below the threshold. The crack propagates then only in these few grains where the local driving force exceeds the threshold. This leads to a change in the microscopic crack shape and, in turn, to a stress redistribution along with crack propagation in neighboured grains. As a result of this grain-by-grain crack propagation the growth rate averaged over the entire crack front might be smaller than 1 Burgers vector per cycle.

Again consider Fig. 2. In the Paris regime the crack growth curves for the two materials are different because they have different critical shear stresses σ_{crit} . It is interesting that in the near threshold regime the curves of the two materials come closer and finally meet at $\Delta CTOD = 1b$, i.e. at the intrinsic threshold of the material. This clearly shows that the intrinsic threshold obviously does not depend on the resistance against dislocation motion. It depends, in this case, on the dislocation generation mechanism, i.e. on k_e , only. In the simulations the intrinsic threshold turned out to be about $\Delta K_{th,intr} \approx 1.9 k_e$. From Fig. 2 it can be seen that the continuum mechanics approximation overestimates the $\Delta CTOD$ near the threshold by a factor of 10 or even more depending on the critical shear stress.

In agreement with real measured crack growth curves we find by simulation, as depicted in Fig. 2, that the transition between the near threshold regime and the Paris regime is gradual. The border between the Paris and the near threshold regime can be drawn at a $\Delta CTOD$ of about 150 Burgers vectors per cycle [3].

From the standpoint of discrete dislocation mechanics the Burgers vector of the dislocation could be considered as information inherent in the material. It reminds the material that a small but nevertheless finite stress intensity factor has to be overcome to generate the dislocations and the plastic flow. By smearing out the Burgers vector, i.e. by continuum mechanics approximation, this information is lost. For that reason continuum mechanics is not capable (without any additional assumptions) to reproduce the near threshold behaviour of fatigue cracks.

The Cyclic Crack Tip Opening Displacement and the Intrinsic Threshold in a Material with a Dislocation Obstacle

Let us now study the effect of a dislocation obstacle on the intrinsic near threshold behaviour. The investigated scenario is sketched in Fig. 3. Here a single dislocation obstacle is located at a distance D in front of the crack tip. The dislocations pile up against the obstacle until the shear stress on the dislocation closest to the obstacle overcomes a characteristic stress value, $\sigma_{barrier}$. When this critical stress is reached the dislocation passes the obstacle and penetrates into the second grain.

The material characteristic length scales are now the microstructural length parameter D as well as the Burgers vector b of the lattice dislocations. Five cases were simulated with $D/b = 100; 300; 1000; 3000$ and 10000 , i.e. in all these cases D is large in comparison to b . The critical shear stress in the matrix is set $\sigma_{crit} = \mu/700$ and $\sigma_{barrier} = \mu/70$.

The predicted $\Delta CTOD$ curves computed with the discrete dislocation model are depicted in Fig. 4. In the high stress intensity range regime the plastic zone size

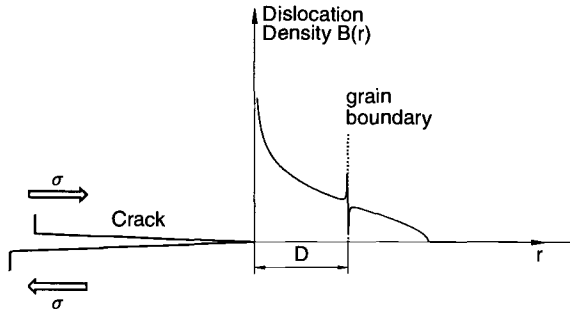


Figure 3: A schematic of the dislocation arrangement when a grain boundary acts as a dislocation obstacle.

is much larger than even the largest D considered. Here all the computed results collapse into a single curve. This confirms, what we expected, namely, when the plastic zone is much larger than the grain size then the crack propagation does not depend on microstructural features but only on the macroscopic yield strength.

The picture changes for intermediate stress intensity ranges. Now the plastic zone size is on the order of D and the crack propagation is severely influenced by the microstructure. The BCS type continuum mechanics predicts larger $\Delta CTOD$ for increasing D given equal ΔK values. Roughly the same tendency is found by the discrete dislocation modelling. For instance, the curve due to the simulation with the smallest D , indicated by the diamonds is generally below the curve with the largest D (circle). On the other hand, in the region of ΔK between 4 and 5 times $\mu\sqrt{b}$ the curve with squares pertaining to intermediate D values is below the curve with the smallest D . This trend which is opposite to the continuum mechanics prediction is affected by the interaction of both involved material length parameters D and b .

At very small stress intensity ranges near the threshold the crack behaviour is then dominated by the second length scale only, by the Burgers vector of the dislocation. All the computed curves meet at $\Delta CTOD = 1b$. In Fig. 4 it is seen that the predicted intrinsic threshold for the considered cases is always about $\Delta K_{th,intr} \approx 1.9k_e$, which is the same value as found previously for the homogeneous materials. This reveals, in accordance with [2], that the intrinsic threshold is not only independent from the critical shear stress for dislocation motion, as shown in the previous section, but also from microstructural details such as the location and, as pointed out in [2], by the strength of dislocation obstacles.

These findings are in a qualitative agreement with experimental results reported in [11]. There it has been shown that precracks formed under compression-compression cycles, where no extrinsic crack closure occurs, do stop after a certain crack growth increment with no obvious relation to the microstructure. This is a reasonable indication that here the threshold, which is the intrinsic threshold because of the lack of crack closure, does not depend on the position of the crack tip in respect to the grain boundaries and other dislocation obstacles. In pure tension fatigue loading crack

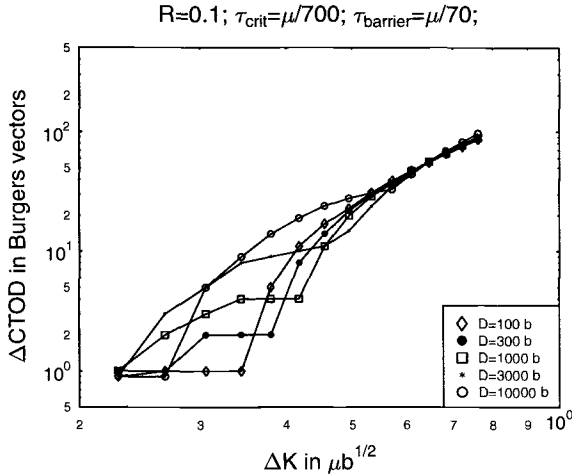


Figure 4: *The cyclic plastic deformation in dependence on the stress intensity range for various D when a single obstacle is located in front of a fatigue crack tip.*

closure occurs and this is, in our opinion, the reason why these fatigue cracks often interact with the microstructure, especially at and near the threshold.

A second experimental support of our results has been given by Liaw et al. [12] and by Hertzberg [13] and [14]. The former have summarized many threshold data, where they have found that the closure corrected thresholds of many materials are proportional to their elastic modulus. To the same conclusion came Hertzberg. For a wide range of materials (Al, Ni and Fe alloys) he compared the stress intensity factor, K_b , corresponding to a crack growth rate of 1 Burgers vector per cycle (which is very close to the threshold). He found that this stress intensity factor is given by $K_b = E\sqrt{b}$.

This is easily explained by our calculations that show that the intrinsic threshold is proportional to the critical stress intensity for dislocation generation which, in turn, is given by $k_e \propto \mu\sqrt{b}$ as found by Rice and Thomson [9].

A Fatigue Crack in a Two-Phase Material with Different Yield Stresses

In Fig. 5 a composite material with alternating layers of two ductile phases α and β is sketched. For both phases the thickness of these layers is equal $T = 4.5\mu\text{m}$. Both phases have equal elastic constants given by the shear modulus $\mu = 80\text{GPa}$ and the Poisson ratio $\nu = 0.3$. The plastic properties of the phases are different. In the phase α the critical shear stress is equal to $\sigma_\alpha = \mu/700$ and in β it is $\sigma_\beta = \mu/350$. It is assumed that there is no barrier stress to transfer the plasticity from one phase into the other.

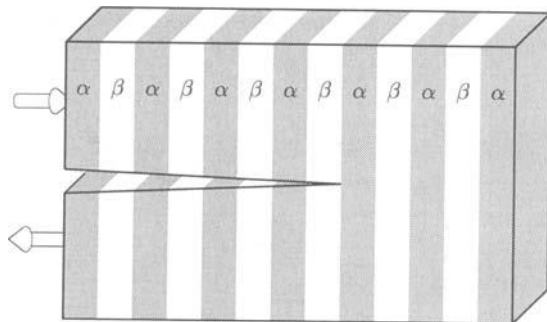


Figure 5: *The investigated layered material. The yield stress of the phase β is twice as large as the yield stress of phase α .*

Again we have computed the $\Delta CTOD$ by means of the direct simulation of the dislocation motion as well as by the continuum mechanics BCS type method. The singular integral equation for the given problem is so complicated that an analytical BCS solution is hardly achievable. We have solved it numerically by a procedure, as explained in [15], where the plastic zone is discretised into uniform displacement elements. In such an element the crystal above the element is displaced in respect to the crystal below it by an amount d . The displacement d in each element is then, as we have shown, determined by the linear algebraic equation system:

$$\sum_j d_j g_{ij} + \sigma_{\text{applied}} = -\sigma_{\text{crit}} \quad (5)$$

where the influence functions g_{ij} are derived in [15]. The distribution of the Burgers vector, $B(r)$, is obtained by

$$B(r) = -\frac{\partial d}{\partial r} \quad (6)$$

A computed example of the dislocation distribution is depicted in Fig. 6. It is seen that the dislocations pile up when they leave the softer and enter into the harder phase. At the interface from the harder to the softer material an inverse pile up is formed.

We have considered 4 different locations of the crack tip as shown in Fig. 7. The results of these simulations are shown in Fig. 8. The full line with black circles pertains to simulation I where the crack tip is on the left-hand boundary of the softer α -phase. In the second simulation (full line, white circles) the crack tip is in the center of the α -phase. In the third and fourth simulation (dashed line; black and white circles respectively) the crack tip is on the left-hand side respectively in the center of the harder β -phase.

Consider that in Fig. 8 three regimes have been identified. The large ΔK regime where macro mechanics applies, the micro mechanics regime at intermediate stress intensity ranges and the dislocation mechanics regime at ΔK_{eff} values which are smaller than about 2 times the intrinsic threshold.

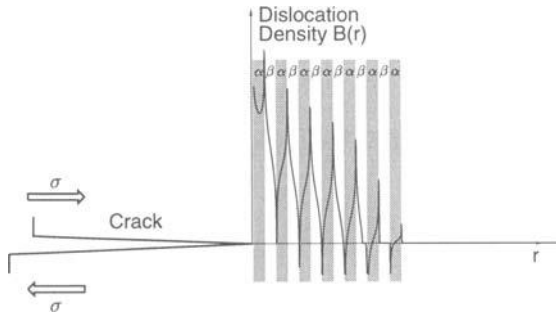


Figure 6: *The dislocation distribution at maximum load ($K = 15\text{MPa}\sqrt{\text{m}}$) in the duplex material. Material data are in the text.*

In the macro mechanics regime the four computed crack growth curves collapse into a single curve which shows that here the crack propagation rate obviously does not depend on the location of the crack tip in respect to the microstructure. This single curve is described by the macroscopically averaged critical shear stress. In our example where the α and β lamellars have the same thickness and where no barrier stress is assumed this macroscopic critical stress is simply the arithmetic average of the critical shear stresses of either component.

At intermediate stress intensity ranges the predicted crack growth rate is very strongly influenced by the microstructure. It can be seen that the largest crack growth rates appear in simulation I where the crack tip is at the interface at the left side of the plastically softer component. The crack growth rate is smaller in the other cases and the smallest crack propagation rate is predicted for simulation III. Here the crack tip is at the interface at the left-hand side of the harder β phase. This suggests that the larger the volume percentage of the harder phase within the plastic zone the smaller the crack growth rate.

For the discussion of this result it is important to remember that the four predicted $\Delta CTOD$ curves have been obtained for the same macroscopic compound material. It is seen that the plastic deformation at intermediate stress intensity ranges is not only a function of the applied loading, but it is also sensitive to the actual position of the crack tip in respect to the α and β platelets. This means that in a given macroscopic material equal changes of the stress intensity factor for different positions of the crack tip does not lead to equal plastic deformations. The principle of similitude is violated in the micro-mechanics regime.

This is also true at small stress intensity ranges where the discreteness of the plasticity becomes important. Here the various curves come closer and meet again at the intrinsic threshold, which once more shows that the intrinsic threshold value itself does not depend on the microstructure.

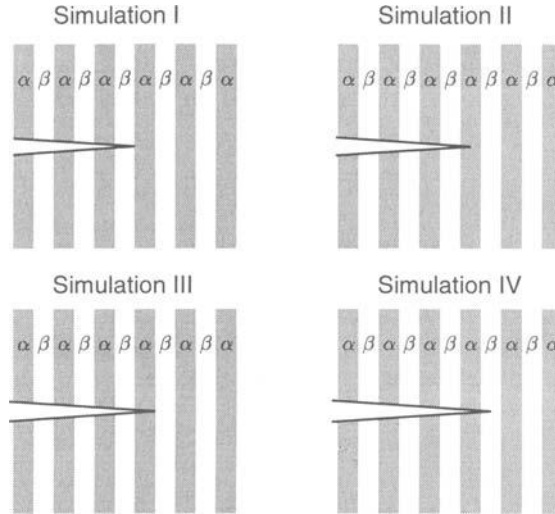


Figure 7: *The position of the crack tip in the four simulations.*

Conclusion

In this paper we consider the intrinsic behaviour of moderately loaded cracks by means of a discrete dislocation model and by a BCS type continuum mechanics solution. We have started the discussion with homogeneous materials and then we have considered microstructural features like grain boundaries and plastically dissimilar phases.

Before we summarize our results it should be emphasized that we have considered only the intrinsic material behaviour. Some extrinsic effects, especially crack closure [16] are also very important. For instance, it is often reported that the dependence of the threshold of stress intensity range on grain size can be ascribed to roughness induced crack closure. Furthermore we want to note that residual stresses caused by an elastic mismatch of different phases or even of differently oriented grains in the microstructure could also influence the threshold value. But even if in future times more refined investigations become possible, the following results should be valid in a very general character.

- At large stress intensity ranges, in the upper Paris regime, when the cyclic plastic zone encircles many grains the crack propagation is determined by macroscopic quantities like the yield strength and the Young's modulus of the material.
- At intermediate stress intensity ranges, in the lower Paris regime when the cyclic plastic zone size shrinks to the scale of microstructural features as, e.g., the grain size the plastic deformation and the crack propagation rate is strongly

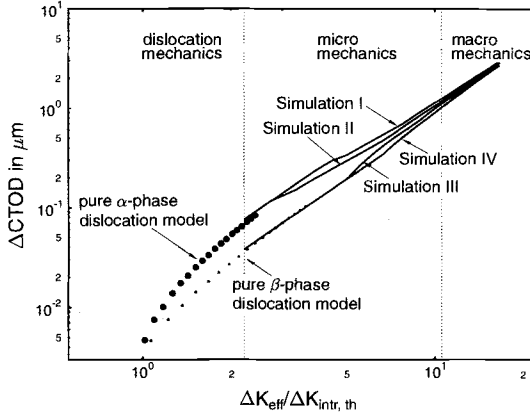


Figure 8: The $\Delta CTOD$ -curves for 4 different locations of the crack tip as sketched on the right upper corner pertaining to crack tip a) on the left side of α , b) in the center of α , c) on the left side of β and d) in the center of β . Dots pertain to the result of the discrete dislocation modelling.

influenced by the microstructure. Then a micromechanical approach should be used. Many laws known from macro continuum mechanics as, e.g., the principle of similitude, do no longer hold in the lower Paris regime.

- Below a crack growth rate of about 150 Burgers vector per cycle, i.e., in the near threshold regime, the plastic deformations are influenced by the discreteness of plasticity. The difference in the predicted crack growth rate between continuum mechanics and the discrete description of plasticity is more than 1 order of magnitude. Furthermore, the discrete dislocation mechanics sometimes lead to unexpected results. We have discussed the example of a grain boundary in front of the crack tip where in the near threshold regime the material behaves opposite to the predictions of classical continuum mechanics.
- The intrinsic threshold does not depend on microstructure. It is a function of the dislocation generation mechanism, only. Therefore it is proportional to the stress intensity factor necessary to generate dislocations. When the dislocations are generated at the crack tip this critical stress intensity factor is proportional to the shear modulus according to Rice and Thomson: $k_e \propto \mu\sqrt{b}$. This is in line with the observations of Liaw et al. and it explains the experimental findings of Hertzberg.

Acknowledgment

This work was financially supported by the FWF (Fonds zur Förderung der wissenschaftlichen Forschung), Project Nr. P 11622 TEC.

References

- [1] R. Pippan, *Acta Metallurgica et Materialia*, Vol.39, 1991, pp.255-262.
- [2] R. Pippan, *International Journal of Fracture*, Vol.58, 1992, pp.305-318.
- [3] F.O. Riemelmoser, R. Pippan and H.P. Stüwe, *Acta Materialia*, Vol.46, 1998, pp.1793.
- [4] R. Thomson and J. Sinclair, *Acta Metallurgica*, Vol.30, 1982, pp.1325.
- [5] B.A. Bilby, A.H. Cottrell and K.H. Swinden, *Proceeding of the Royal Society London.*, Vol.A272, 1963, pp.304-314.
- [6] J. Weertman, I. H. Lin and R. Thomson, *Acta Metallurgica*, Vol.31, 1983, pp.473-482.
- [7] J.R. Rice, *ASTM STP 415, American Society of Testing and Materials*, 1967, pp.247-311.
- [8] R.M.N. Pelloux, *Transactions of the American Society of Metals*, Vol.62, 1969, pp.281-285.
- [9] J.R. Rice and R. Thomson, *Philosophical Magazine A*, Vol.29A, 1974, pp.73-97.
- [10] David L. Davidson, private communication (1998).
- [11] R. Pippan, *Philosophical Magazine A*, Vol.77A, 1998, pp.861-873.
- [12] P.K. Liaw, T.R. Leax, W.A. Logsdon, *Acta Materialia*, Vol.31, 1983, pp.1581-1587.
- [13] Richard W. Hertzberg, *International Journal of Fracture*, Vol.64, 1993, pp.R53 - R58.
- [14] Richard W. Hertzberg, *Materials Science and Engineering*, Vol.A190, 1995, pp.25-32.

- [15] F.O. Riemelmoser and R. Pippan, An inclined strip yield model for describing monotonic and cyclic plasticity, *Proceedings ICES'98, Modelling and Simulation Based Engineering II* Eds. S.N. Atluri and P.E. O'Donoghue, 1998, pp. 1456-1461.
- [16] R.O. Ritchie, Mechanisms of fatigue crack propagation in metals, ceramics and composites: Role of crack tip shielding. *Material Science and Engineering A*, Vol.103, 1988, pp.15-28.

Applications

Ralph W. Bush,¹ J. Keith Donald,² and Robert J. Bucci³

Pitfalls to Avoid in Threshold Testing and its Interpretation

Reference: Bush, R. W., Donald, J. K., and Bucci, R. J., “**Pitfalls to Avoid in Threshold Testing and its Interpretation**,” *Fatigue Crack Growth Thresholds, Endurance Limits, and Design*, ASTM STP 1372, J. C. Newman, Jr. and R. S. Piascik, Eds., American Society for Testing and Materials, West Conshohocken, PA, 2000.

Abstract: The impact of a number of testing variables on the measurement of fatigue crack growth thresholds is discussed. References are made to the original works from which the current recommendations for measurement of threshold in ASTM E 647 were derived. The applicability of these original recommendations in light of advances made since that time is discussed. In addition, the effects of some commonly overlooked parameters and features, such as residual stress and environment, on the measurement and interpretation of crack growth thresholds are presented.

Keywords: fatigue, crack growth, threshold

Nomenclature

ΔK	stress intensity factor range
ΔK_{th}	stress intensity factor range at threshold
K_{max}	maximum stress intensity in stress intensity factor range
ΔK_o	initial ΔK in K-gradient expression
K_o	initial K_{max} in K-gradient expression
C	K-gradient
a	crack length
a_o	initial crack length in K-gradient expression

¹Assistant Professor, Department of Engineering Mechanics, US Air Force Academy, 2354 Fairchild Dr., Suite 6H2, USAF Academy, CO 80840.

²Director, Fracture Technology Associates, 2001 Stonestrow Rd., Bethlehem, PA 18015.

³Technical Consultant, Alcoa Technical Center, Aluminum Company of America, Alcoa Center, PA 15069.

Experience has often indicated that fatigue crack growth (FCG) rate data from standard long crack specimens may be either non-conservative or overly conservative. The reliability of near-threshold FCG data are influenced by many factors, such as measurement and control issues, decreasing K-gradient, starting K level, specimen residual stresses, and environmental issues. The original authors of ASTM Test Method for Measurement of Fatigue Crack Growth Rates (E 647) recognized the importance of these factors on the determination of threshold (ΔK_{th}) and incorporated several guidelines in the standard dealing with these issues. However, these guidelines stem from experience gathered fifteen to twenty years ago when manual control and visual observation of cracks were the norm. During the ensuing time period a new generation engineers and technicians have arisen that may not be aware of the basis for and limitations of these guidelines. In addition, automated test machines and data acquisition systems have largely replaced the manual and visual systems used twenty years ago. These newer systems provide for decreasing scatter in test results through better test control and make it easier to perform tests under alternative methods of control, such as constant K_{max} decreasing ΔK . Given these advances in testing technology and the passage of time since current threshold testing guidelines were introduced, it makes sense to review the basis and limitations of these guidelines. We should also remind ourselves of some of the more common pitfalls that lead to erroneous fatigue crack growth threshold measurement and interpretation.

Decreasing K-gradient

The most common method of determining threshold (ΔK_{th}) utilizes a method of reducing the applied ΔK values from an initial level in a controlled fashion as the crack length increases. This process is termed load shedding. The rate of load shedding needs to be slow enough to avoid anomalous growth rates due to transient behavior and to allow at least 5 crack growth data points to be measured per decade of crack growth rate [1]. This can be done by controlling the test such that $\Delta K = \Delta K_0 \exp[C(a-a_0)]$. The present standard limits the normalized K-gradient, C, to values algebraically greater than -0.08 mm^{-1} (-2 in.^{-1}) in order to avoid spurious threshold measurements. Steeper gradients can be used in any particular case if it is shown that the threshold is unaffected by use of that gradient.

It is instructive to look back for the origin of this guideline. The guideline was instituted to minimize crack growth transients based on the observation that “where the monotonic plastic zone size was small relative to the crack increment (Δa) between crack length observations, the effect of overload transient was small” [2]. In References 1 and 2, a number of tests were performed over a range of stress ratios from -1.0 to $+0.8$ using one aluminum alloy (2219-T851) and one steel alloy (10 Ni steel). The ΔK required to generate a given crack growth rate was measured for several specimens. The ratio of this ΔK for a given specimen and the mean ΔK at the same FCG rate and stress ratio for a group of specimens was plotted versus K-gradient. K-gradients up to four times steeper than those in the current guideline were used. These results are reproduced in Figures 1 and 2. Except for the tests conducted at a stress ratio of $+0.1$, all ΔK values were within 7.5% of the mean. This indicates that for these two alloys the measured threshold is a function of C only at low positive values of R. Figures 3 and 4 provide another partial

view of this data set. In these figures valid fatigue crack growth curves for 2219-T851 are compared to curves exhibiting unusually low threshold values obtained during tests with steep decreasing K-gradients.

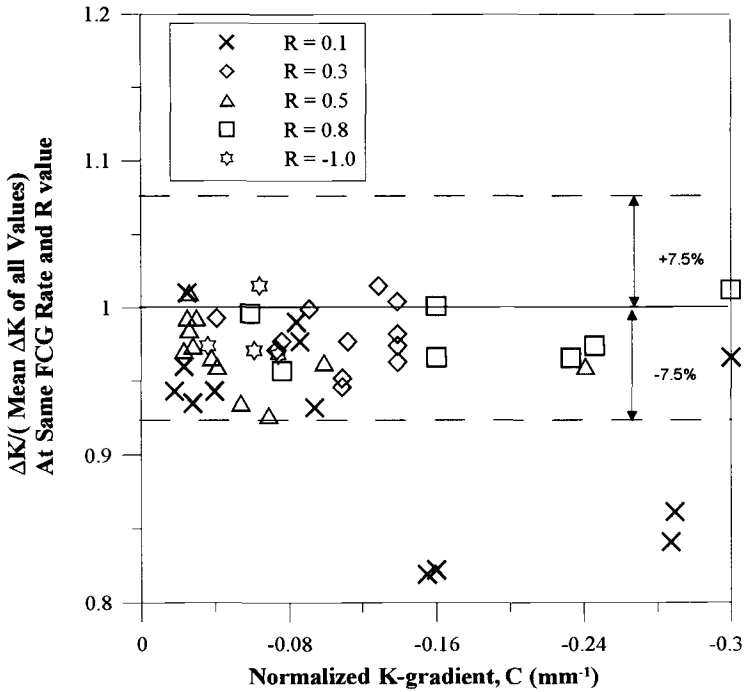


Figure 1 - Effect of normalized K-gradient on near-threshold FCG rates for 2219-T851 aluminum alloy [1]

These earlier experiments utilized visual observations for crack length measurement and manual “stepped” load reduction sequences. It is reasonable to assume that the K-gradient guidelines were, in part, based on limitations in crack length precision and transients associated with discrete load shedding increments. Today, automation provides greater crack length precision and more precise load shedding control. As such, data for both a 2024-T3 and a Ti-6Al-4V alloy tested at a stress ratio of + 0.1 in Figures 5 and 6 respectively demonstrate a lack of sensitivity of the measured threshold to decreasing K-gradient. This is so even with K-gradients up to ten times steeper than recommended in E 647.

The data set on which the current guideline in E 647 was based clearly indicates that the measured fatigue crack growth threshold depends in a complex manner on the decreasing K-gradient and a number of other variables. Hence, the guideline is a conservative and simplified extrapolation of one data set based on two alloys that may not be representative of the broad range of materials tested today. This guideline was

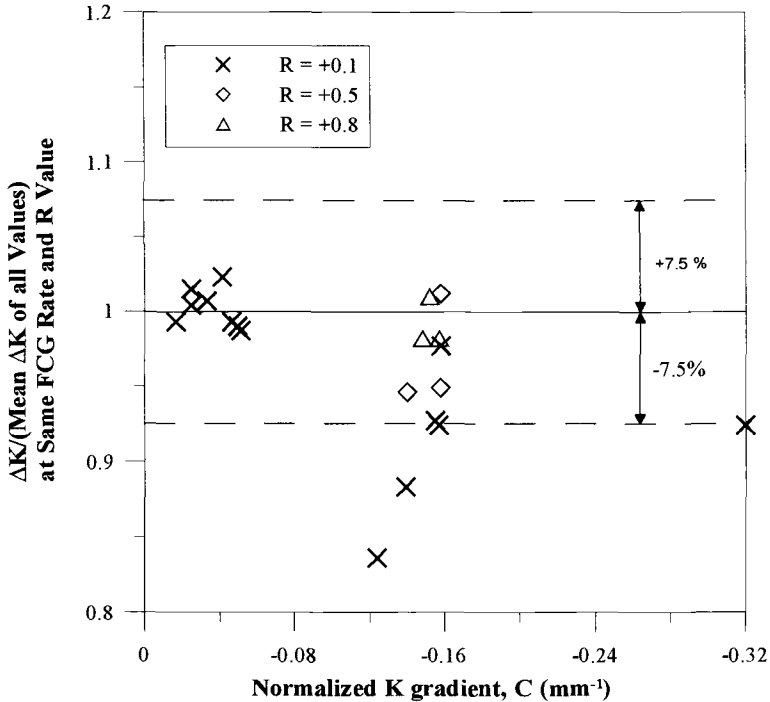


Figure 2 - Effect of normalized K-gradient on near threshold FCG rates for 10Ni steel alloy [1]

never meant to be all-inclusive, nor was it intended to cover all situations. It is now well understood that a certain amount of flexibility is desirable in establishing the optimum K-gradient. For example, even the recommended K-gradient according to E 647 may not be appropriate for small samples because of the limited material available for the required range of crack extension. Therefore, the optimum K-gradient is influenced by a number of considerations including crack length measurement precision, load control precision, and specimen size.

Initial K level

The K level at which a threshold test is started has been shown to have an effect on the measured crack growth threshold. E 647 recommends not using the K-decreasing procedure at crack growth rates greater than 10⁻⁸ m/cycle (3.9 x 10⁻⁷ in/cycle). In the event that a K-decreasing test is initiated at a K_{max} level sufficiently high to be partially or predominantly plane stress, the resulting ΔK_{th} may be elevated above the “true” long crack threshold and is sensitive to both the starting K_{max} level and the magnitude of the

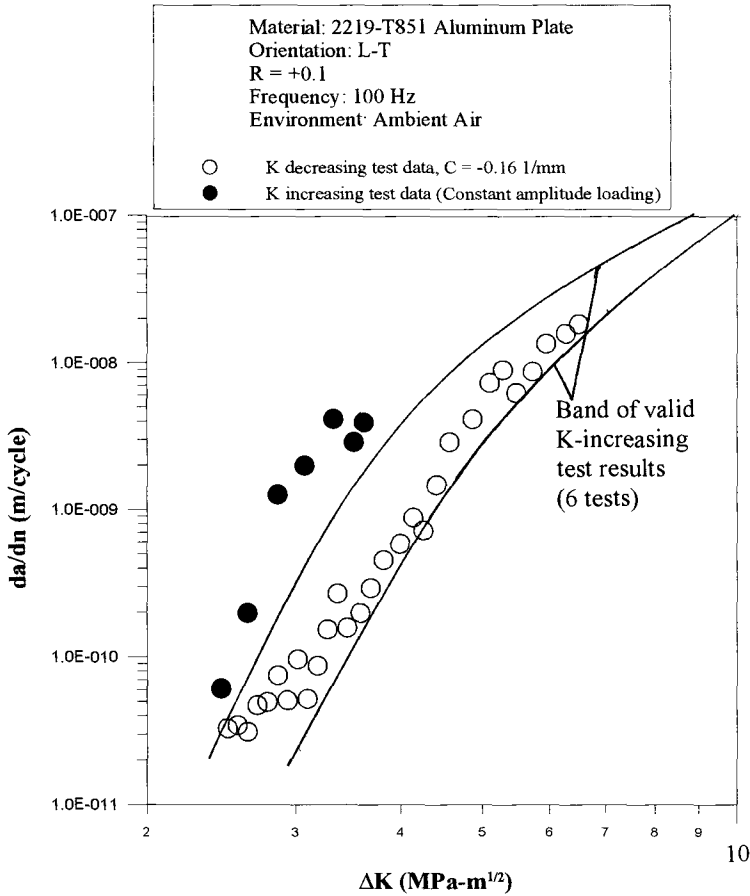


Figure 3 - Examples of anomalous fatigue crack growth rates at $R = +0.1$ obtained when rate of K -decrease with crack extension is high ($C = -0.16 \text{ mm}^{-1}$) [1]

decreasing K -gradient. This is the result of plasticity induced closure in the crack wake. As ΔK is decreased, the plasticity induced interference remains in the crack wake and reduces the cyclic stress intensity at the crack tip. A demonstration of this phenomenon is shown in Figures 7 and 8 for two different specimen types using a 2024-T3 and a Ti-6Al-4V alloy respectively. The results shown in these figures indicate a trend towards increasing measured threshold as the initial K_{max} increases, to a point where the threshold can not be measured for the highest starting K_{max} level due to the high plasticity-induced crack closure level.

Alternative Method of K -Control

In theory, stress analysis should allow for the determination of a ΔK_{th} material

property independent of crack size and geometry. In practice, this is often not the case. The standard practice determines ΔK_{th} at a crack length that is longer than typical of small cracks at similar stress intensities. At a low stress ratio, interference in the crack wake (crack closure) can reduce the range of ΔK and is considered one reason why the ΔK_{th} determined from a long crack may be non-conservative for small crack behavior. A constant K_{max} decreasing ΔK test provides near-threshold FCG rate data at a high stress ratio free from the influence of crack closure. [3-5] Steep decreasing K-gradients can be used without causing crack growth rate retardation because K_{max} remains constant. One issue that remains unresolved is the influence of K_{max} on the resulting threshold. Although this test procedure is permitted under the existing E 647 standard, details regarding K-gradients, K_{max} limitations and application are non-existent.

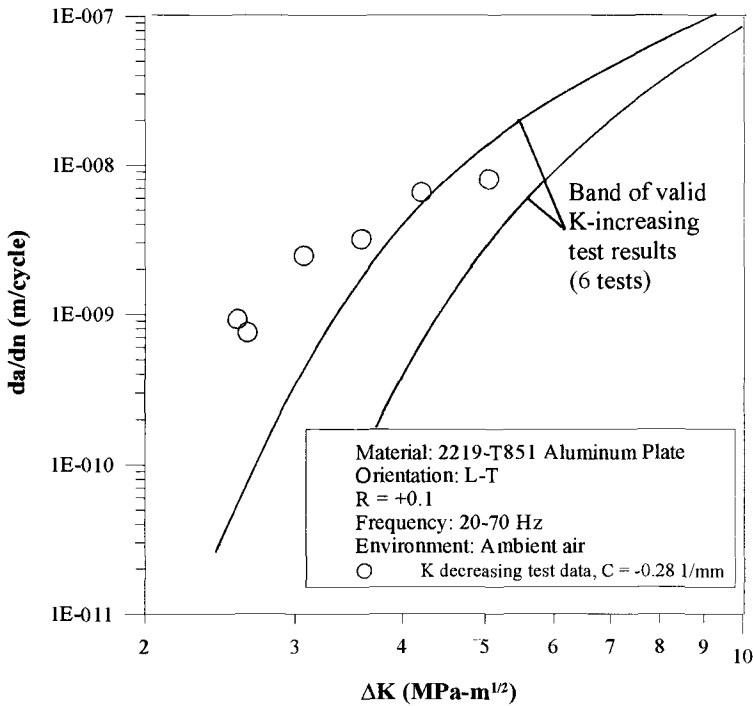


Figure 4 - Examples of anomalous fatigue crack growth rate at $R = +0.1$ obtained when rate of K-decrease with crack extension is high ($C = -0.28 \text{ mm}^{-1}$) [1]

Other Load Transients

Other load transients that can affect threshold measurement are typically due to human error, inexperienced test operators, and/or software/hardware malfunction during the test. Two examples of these transient effects are inadvertent overloads and prolonged test interruptions. Overloads of sufficient magnitude result in increased levels of

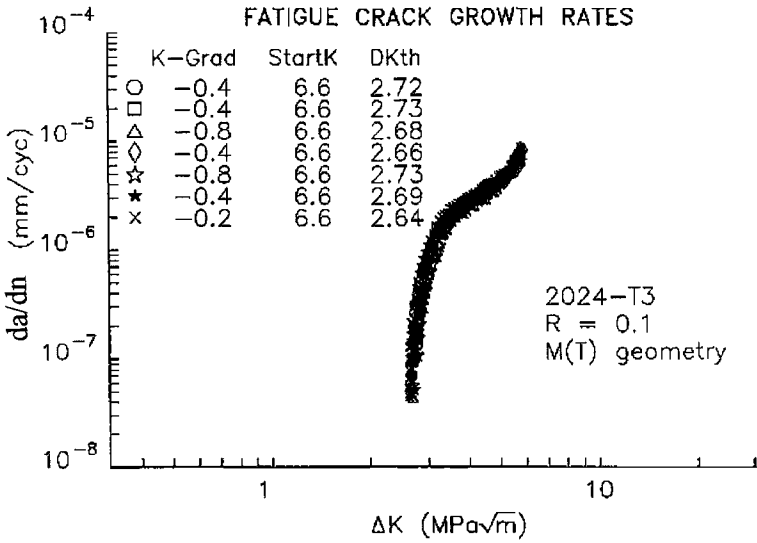


Figure 5 - Fatigue crack growth rate plot showing the effect of decreasing K-gradient for 2024-T3.

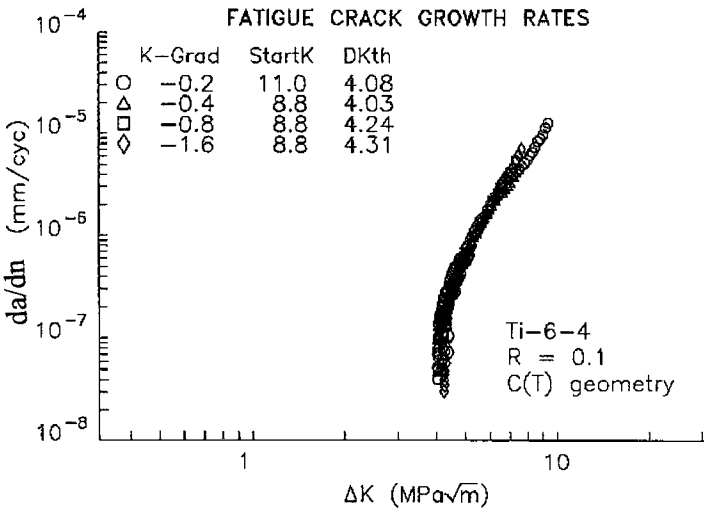


Figure 6 - Fatigue crack growth rate plot showing the effect of decreasing K-gradient for Ti-6-4

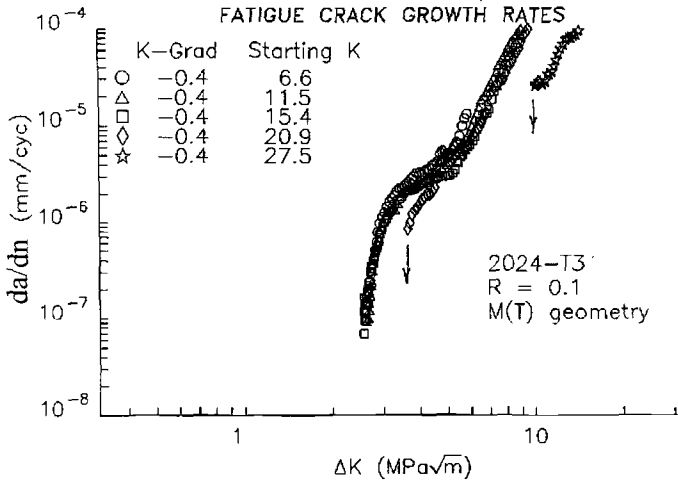


Figure 7 – Fatigue crack growth rate plot showing the effect of the starting K_{max} level for 2024-T3

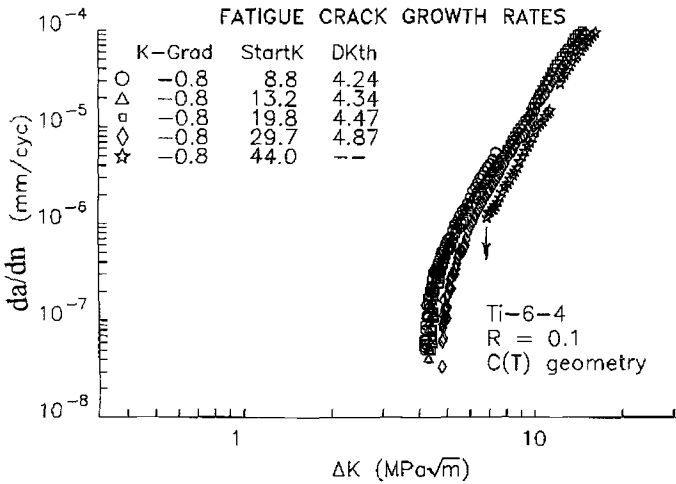


Figure 8 – Fatigue crack growth plot showing the effect of the starting K_{max} level for Ti-6-4

plasticity induced crack closure levels and reduced levels of ΔK_{eff} at the crack tip. This increased crack closure can cause crack retardation, resulting in thresholds that are greater than expected. [2,6-8] On the other hand, prolonged test interruptions may result

in thresholds that are either greater than or less than expected. This behavior can be often attributed to the interaction of the crack tip material with the lab environment during the test interruption. [9,10]. The atomic species most commonly associated with this behavior is hydrogen from water vapor contained in the lab environment. A mechanism commonly used to explain a threshold less than that expected is that the hydrogen atoms diffuse into the plastic zone ahead of the crack tip, reducing cyclic ductility and resulting in increased crack growth rates at a given ΔK level. [11-14] If, however, a film of corrosion product builds up on the fracture surface behind the crack tip during the test interruption the amount of crack closure will increase after restarting the test. The ΔK_{eff} at the crack tip will now be reduced, resulting in a greater than expected threshold. The mechanism that operates during the test interruption is primarily a function of the corrosion susceptibility of the material. For example, in 7XXX aluminum alloys, overaging is performed to enhance the corrosion resistance of the material. Hence, overaged tempers tend to exhibit greater thresholds than underaged tempers. [15-17]

Specimen Preparation and Precrack Procedure

Both specimen preparation and precracking procedures are addressed in E 647. However, given the length of the standard, some inexperienced users may not grasp the significance of these sections. In some cases it has been noted that machining a specimen notch with a dull tool can affect the growth rate of a fatigue crack at a significant distance from the notch tip. The use of a dull tool can produce plastic deformation and residual stresses at the notch root of the specimen. The residual stresses can accentuate crack closure levels at the low load levels and short crack lengths at which thresholds are generally measured. Even if the crack is grown to a greater length than normal, the effects of the plastic deformation are still present in the crack wake and may yet alter threshold behavior.

In other cases, in an effort to save time, precracking loads are selected that are too high and the K-decreasing portion of the test is begun at loads less than those used for precracking. This is equivalent to imposing a block overload sequence on the specimen prior to measuring threshold. It is well known that an overload of sufficient magnitude results in lower crack growth rates than those measured during steady state. [2, 6-8] Hence, precracking at loads greater than those used to begin the K-decreasing portion of the test can result in measured thresholds greater than that measured from a steady state test.

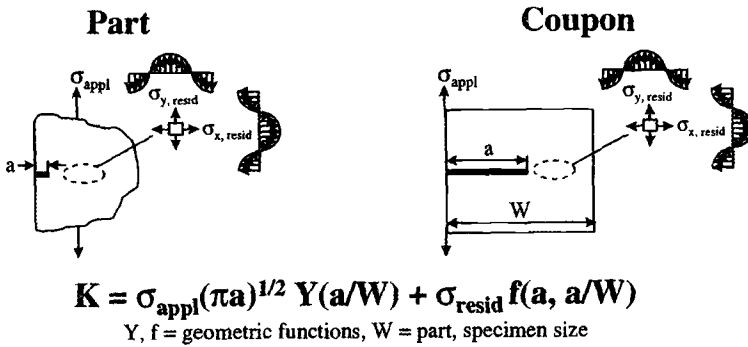
While both of these issues are addressed in the standard, the authors have seen instances where improper precracking and machining procedures have resulted in spurious thresholds.

Residual Stresses

The effects of residual stresses on FCG rate measurement were first brought to light in 1981 [18]. When residual stresses are present in test coupons, an additional internal loading component is added to the applied load that is not accounted for during data analysis. The schematic in Figure 9 illustrates this concept. Classical linear elastic

fracture mechanics similitude breaks down when the additional loading component due to residual stress is appreciable as compared to the external applied load. Residual stress influence can masquerade as a specimen geometry effect or as a false microstructural effect [18,19]. Among the most common test specimen geometries, the compact tension specimen has been shown to be the most susceptible to residual stress bias. An example of a residual stress bias in an aluminum alloy is shown in Figure 10. In this case a new processing method was used to fabricate the product. The initial conclusion reached was that the new processing method increased the fatigue crack growth threshold of the alloy substantially. However, the material made with the new processing method had not been stress relieved. Subsequent testing using stress relieved material fabricated with the new process demonstrated that the apparent increase in threshold was entirely due to residual stresses.

An effective method for detecting residual stress influences in compact tension specimens has been described previously [20]. In this method the height of the compact tension specimen is measured about the location where the clip gauge is to be affixed to the specimen both before and after machining the specimen notch. A change in height greater than a certain amount indicates that residual stresses of sufficient magnitude to create a significant shift in the threshold measurement exist within the specimen. For example, in a compact tension specimen with a width of 50 mm, a change in the height of 0.05 mm or greater would indicate a potential problem.



	Part	Coupon
σ_{appl}	large	small
a	small	large
$\sigma_{\text{resid}}/\sigma_{\text{appl}}$	small	large

Residual stress induced bias is magnified in the coupon test.

Figure 9 – Schematic of residual stress effects on fracture mechanics test measurements [20]

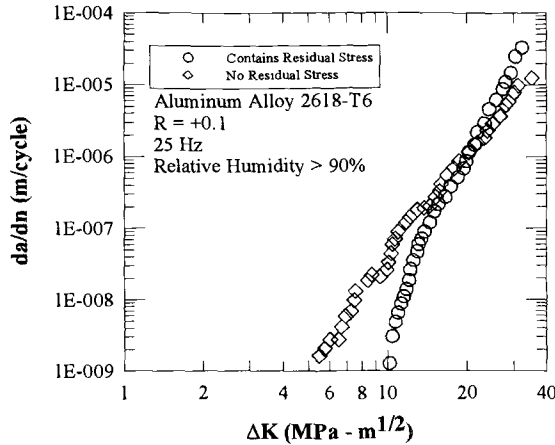


Figure 10 – Comparison of valid and anomalous FCG rate measurements for specimens with and without residual stress

Environmental Interactions

Environmental interactions during fatigue crack growth testing can produce either increases or decreases in crack growth rates depending on the rate of crack growth and mechanism involved. Chemical interactions at the crack tip tend to increase crack growth rates [12-14, 21, 22] and can result in decreasing thresholds. On the other hand, corrosion material may build up on exposed fracture surfaces, increasing crack closure, and resulting in a decrease in crack growth rates, especially when crack opening displacements are low. This may actually result in greater thresholds than expected in an inert environment [23]. An example of this latter type of behavior is illustrated in Figure 11. In the experiment depicted, a constant crack growth rate was obtained in ambient air for aluminum alloy 7475-T7351. When sump water was introduced, the crack growth rate gradually decreased and eventually the crack stalled completely due to buildup of corrosion product on the fracture surface.

It could be argued that a threshold measured in an aggressive environment is not necessarily a material property, as it has a time dependency as well. It could also be argued that the authors of E 647 did not intend for the threshold methods described in the standard to apply to testing in these types of environments. One can also ask the question: how aggressive an environment is required to cause a significant change in the crack growth threshold? For many aluminum alloys, the most common “aggressive” environment required is often termed “lab air”. An example of this for the aluminum alloy 7050-T7451 is shown in Figure 12. In this figure the $da/dn - \Delta K$ curves compared were obtained in low (<10% RH) and high (>90% RH) humidity air. The low humidity air curve is representative of lab air during the cold winter months, whereas the high humidity curve is representative of lab air during the hot, humid summer months. Hence, depending on the time of year the crack growth threshold can vary significantly when measured in lab or ambient air.

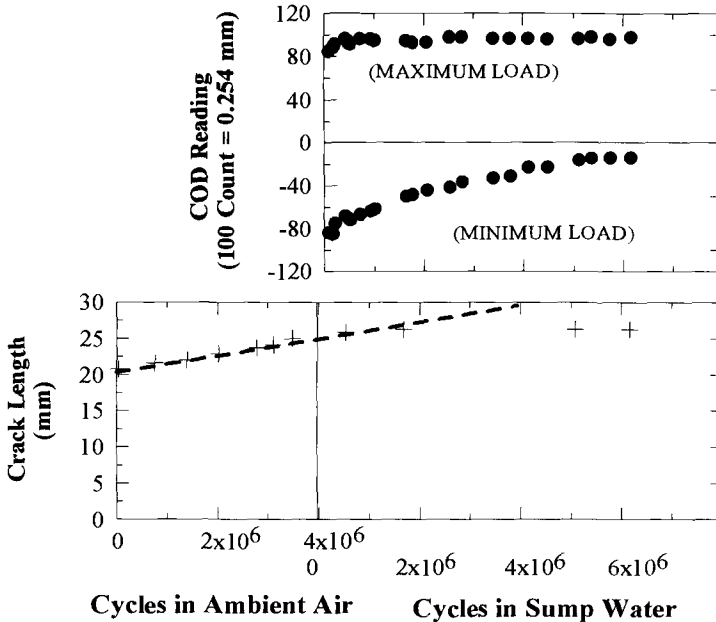


Figure 11 – Crack opening displacement measurements showing that crack arrest occurs in 7475-T7351 CT specimens tested in sump water because of gradual buildup of closure forces caused by corrosion products on crack surfaces [23]

A second manifestation of the non-uniqueness of crack growth threshold in humid lab air for certain materials is demonstrated schematically in Figure 13. This figure contrasts the behavior of SCC (stress corrosion cracking) susceptible and resistant aluminum alloy tempers when the loading sequence is cycled between K-decreasing and K-increasing in the near threshold region of a FCG test. Fracture surface oxide layers in SCC susceptible aluminum alloy tempers have a tendency to be thicker than in SCC resistant tempers, thus increasing the amount of crack closure and decreasing crack tip ΔK values. Formation of this oxide layer is time dependent, as is attainment of crack growth threshold conditions. Until the oxide layer and corrosion debris formed attain their equilibrium thickness in the test environment the crack closure levels and threshold continue to increase. If insufficient time is given for this equilibrium thickness to form, the behavior depicted in Figure 13 can be observed. That is, the threshold of an SCC susceptible product may increase with successive cycles until steady state behavior is reached, as opposed to an SCC resistant product in which the equilibrium oxide layer thickness is thinner and achieved rapidly. Therefore, steady state behavior is generally attained during the first K-decreasing segment. The time dependence of the threshold of the SCC susceptible alloy-temper is related to the time required for a layer of corrosion product to form to a steady state thickness. In an SCC resistant product the thickness of this layer is insufficient to produce a time dependent threshold in lab air. [15,16]

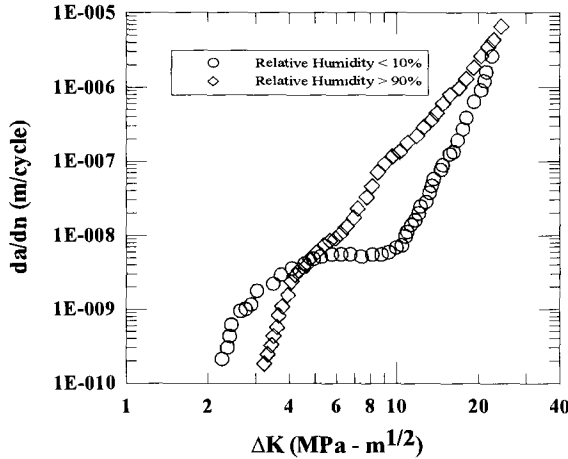


Figure 12 - Fatigue crack growth rate plot showing the effect of relative humidity for 7050-T7451

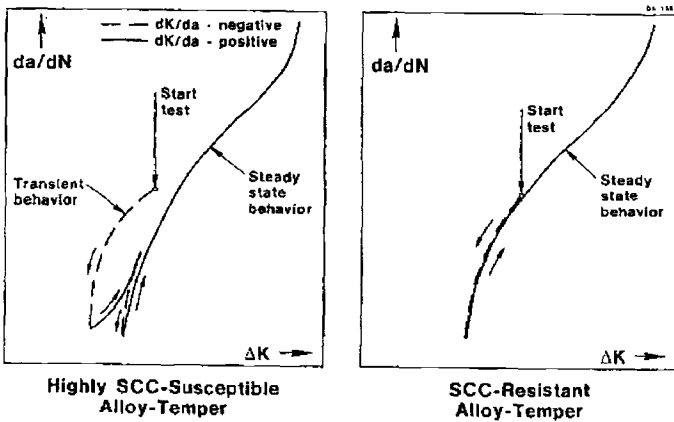


Figure 13 - Typical response to positive and negative *K*-gradients observed during early stages of near-threshold FCG tests on aluminum alloy tempers with high and low resistance to SCC

Conclusions

Technology, fundamental understanding of crack growth thresholds, and testing techniques have made substantial advances since E 647 was originally drafted. In fact, E 647 has been extensively modified for non-visual crack length determination although

test procedure guidelines are still based on twenty-year-old experience. However, the importance of careful experimental technique and specimen preparation has not diminished. One of the important recommendations made in E 647 regarding threshold measurement is to follow the K-decreasing portion of the test with a K-increasing portion that covers the same segment of the da/dn curve in order to verify the results. While this may not be cost or time efficient in all cases, many of the anomalous crack growth thresholds would be detected early on if this recommendation were heeded. Attention to detail in designing experiments to measure thresholds is invaluable to eliminating extraneous influences due to the topics discussed in this paper.

References

- [1] Hudak, Jr., S. J., Saxena, A., Bucci, R. J., and Malcolm, R. C., "Development of Standard Methods of Testing and Analyzing Fatigue Crack Growth Rate Data-Final Report," *AFML TR 78-40*, Air Force Materials Laboratory, Wright Patterson Air Force Base, OH, 1978.
- [2] Bucci, R. J., "Development of a Proposed ASTM Test Method for Near-Threshold Fatigue Crack Growth Rate Measurement," *Fatigue Crack Growth Measurement and Data Analysis, ASTM STP 738*, S. J. Hudak, Jr., and R. J. Bucci, Eds., American Society for Testing and Materials, West Conshohocken, PA, 1981, pp. 5-28.
- [3] J. K. Donald, G. H. Bray, and R. W. Bush, "An Evaluation of the Adjusted Compliance Ratio Technique for Determining the Effective Stress Intensity Factor," *29th National Symposium on Fatigue and Fracture Mechanics, ASTM STP 1332*, edited by T. L. Panontin and S. D. Sheppard (American Society for Testing and Materials, West Conshohocken, PA, 1998).
- [4] G. H. Bray, and J. K. Donald, "Separating the Influence of K_{max} from Closure-Related Stress Ratio Effects Using the Adjusted Compliance Ratio Technique," *Advances in Fatigue Crack Closure Measurement and Analysis: Second Volume, ASTM STP 1343*, edited by R. C. McClung and J. C. Newman, Jr. (American Society for Testing and Materials, West Conshohocken, PA, 1998).
- [5] Hertzberg, R., Herman, W. A., Clark, T., and Jaccard, R., "Simulation of Short Crack and Other Low Closure Loading Conditions Utilizing K_{max} ΔK -Decreasing Fatigue Crack Growth Procedures," *Small Crack Test Methods, ASTM STP 1149*, Larsen, J. M. and Allison, J. E. eds., American Society for Testing and Materials, West Conshohocken, PA, 1991, pp. 197-220.
- [6] *Fatigue Crack Growth Under Spectrum Loads, ASTM STP 595*, American Society for Testing and Materials, West Conshohocken, PA, 1976.
- [7] Mills, W. J., "Load Interaction Effects on Fatigue Crack Growth in 2024-T3 Aluminum and A514F Steel Alloys," Ph.D. dissertation, Lehigh University, 1975.

- [8] Hopkins, S. W., Rau, C. A., Leverent, G. R., and Yeun, A., in *Fatigue Crack Growth Under Spectrum Loads, ASTM STP 595*, American Society for Testing and Materials, West Conshohocken, PA, 1976, pp. 125-141.
- [9] Miller, G. A., Hudak, S. J., Jr., and Wei, R. P., *Journal of Evaluation and Testing*, Vol 1, No. 6, 1973, pp. 524-530.
- [10] Paris, P. C., Bucci, R. J., Wessel, E. T., Clark, W. G., and Mager, T. R., "Extensive Study of Low Fatigue Crack Growth Rates in A533 and A508 Steels, Stress Analysis and Growth of Cracks," *Proceedings of the 1971 National Symposium on Fracture Mechanics, Part 1, ASTM STP 513*, American Society for Testing and Materials, West Conshohocken, PA, 1972, pp. 141-176
- [11] C. M. Hudson and S. K. Seward, "A Literature Review and Inventory of the Effects of the Environment on the Fatigue Behavior of Metals," *Engineering Fracture Mechanics*, 1976, Vol. 8, pp. 315-329.
- [12] Stanzl, S. E., Mayer, H. R., and Tschegg, E. K., "The influence of air humidity on near-threshold fatigue crack growth of 2024-T3 aluminum alloy," *Materials Science and Engineering*, A147, 1991, pp. 45-54.
- [13] Wei, R. P., Pao, P. S., Hart, R. G., Weir, T. W., and Simmons, G. W., "Fracture mechanics and surface chemistry studies of fatigue crack growth in an aluminum alloy," *Metallurgical Transactions A*, Vol 11A, January 1980, pp. 151-158.
- [14] Wei, R. P., "Some aspects of environment-enhanced fatigue-crack growth," *Engineering Fracture Mechanics*, Vol. 1, 1970, pp. 633-651.
- [15] Bretz, P. E., Vasudevan, A. K., Bucci, R. J., Malcolm, R. C., "Effect of Microstructure on 7xxx Aluminum Alloy Fatigue Crack Growth Behavior Down to Near-Threshold Rates," Final Report, U.S. Navy Contract N00019-79-C-0528, Naval Air Systems Command, Washington DC, 1981 October 30
- [16] Bretz, P. E., Bucci, R. J., Malcolm, R. C. and Vasudevan, A. K., "Constant-Amplitude Fatigue Crack Growth Behavior of 7xxx Aluminum Alloys," *Fracture Mechanics: Fourteenth Symposium - Volume II: Testing and Applications, ASTM STP 791*, American Society for Testing and Materials, West Conshohocken, PA, 1983, pp. II-67 - II-86.
- [17] Knott, J. F., and Pickard, A. C., *Metal Science*, Aug/Sept. 1979. pp. 399-404.
- [18] Bucci, R. J., "Effect of Residual Stress on Fatigue Crack Growth Rate Measurement," *Fracture Mechanics (13th Conference), ASTM STP 743*, 1981, pp. 28-47.
- [19] Bush, R. W., Bucci, R. J., Magnusen, P. E. and Kuhlman, G. W., "Fatigue Crack

- Growth Rate Measurements in Aluminum Alloy Forgings: Effects of Residual Stress and Grain Flow.” In *Fracture Mechanics: Twenty Third Symposium, ASTM STP 1189*, R. Chona, editor., American Society for Testing and Materials, West Conshohocken, PA, 1993, pp. 568-589.
- [20] Bucci, R. J. and Bush, R. W., “Purging Residual Stress Bias from Fracture Property Determinations on Incompletely Stress Relieved Parts” *AeroMat '96*, Dayton, Ohio, June 6, 1996.
- [21] Gao, M., Pao, P. S., and Wei, R. P., “Chemical and metallurgical aspects of environmentally assisted fatigue crack growth in 7075-T651 aluminum alloy,” *Metallurgical Transactions A*, Vol 19A, July 1988, pp. 1739-1750.
- [22] Radon, J.C., “Influence of environment on threshold in fatigue crack growth”, *Metal Science*, July 1979, pp. 411-419.
- [23] Nordmark, G.E. and Fricke, W.G., *Journal of Testing and Evaluation*, Vol. 6, No. 5, Sept. 1978, pp. 301-303.

Michael J. Caton,¹ J. Wayne Jones,¹ and John E. Allison²

Use of Small Fatigue Crack Growth Analysis in Predicting the S-N Response of Cast Aluminum Alloys

Reference: Caton, M. J., Jones, J. W., and Allison, J. E., "Use of Small Fatigue Crack Growth Analysis in Predicting the S-N Response of Cast Aluminum Alloys," *Fatigue Crack Growth Thresholds, Endurance Limits, and Design, ASTM STP 1372*, J. C. Newman, Jr. and R. S. Piascik, Eds., American Society for Testing and Materials, West Conshohocken, PA, 2000.

Abstract: The development of a material model to estimate the S-N response of a cast aluminum alloy is described. An important requirement of such a model is sensitivity to processing effects such as solidification time and subsequent material characteristics such as secondary dendrite arm spacing (SDAS), strength, and porosity. It has been speculated that the fatigue properties of aluminum castings are dominated by the propagation of cracks which initiate from microshrinkage pores ranging in size from ~ 10 to 1000 μm . A model was developed that calculates fatigue life based on small crack growth rates measured in cast 319 aluminum specimens with two different solidification times. Results from this small crack model are compared with predictions from a traditional LEFM model using long-crack data and measured thresholds.

Keywords: crack growth threshold, small fatigue cracks, cast aluminum, porosity, crack initiation, crack propagation, life prediction

Introduction

Over the past decade the automotive industry has increasingly employed cast aluminum alloys as a replacement for cast iron and steel components in order to achieve weight reduction and improved fuel efficiency. Cast aluminum is currently being used for wheels, transmission components, chassis and suspension components, and engine components. With the introduction of these alloys into structurally demanding applications there exists a need for a thorough understanding of their fatigue performance in order to ensure durability in the component design process. A traditional approach to incorporate the fatigue resistance of a material into the design of a component is the use of stress-life (S-N) curves. Such S-N curves are typically established experimentally with laboratory specimens and the influence of processing parameters on the fatigue

¹ Graduate Student and Professor, respectively, Department of Materials Science and Engineering, University of Michigan, 2300 Hayward Ann Arbor, MI 48109-2136.

² Senior Staff Technical Specialist, Ford Motor Company Scientific Research Laboratories, MD 3182 SRL, Dearborn, MI 48121-2053.

performance of a cast alloy is manifested by shifts in the S-N curves. However, experimentally determining S-N data for different variations in alloy, processing, and heat treatments can be expensive and time consuming. Even for a given alloy, heat treatment and casting process, variation in solidification condition in different regions of a component result in significant variations in fatigue properties. This substantially compounds database requirements and the ability to use general databases for component design. A material model capable of estimating the fatigue performance of cast alloys and indicating the influence of processing variables such as solidification time and the resulting strength and porosity distribution is preferred.

Numerous studies of cast aluminum alloys have reported that fatigue cracks initiate predominantly from pores which develop in the material during the solidification process [1-6]. Although porosity can result from entrapped gas, resulting in nearly spherical voids, in high quality casting it more typically results from a combination of volume contraction and failure of interdendritic feeding at the last stages of solidification, resulting in irregularly shaped voids termed "microshrinkage pores" [7]. Microshrinkage porosity is directly related to the solidification time in a given region of a casting and is generally considered a microstructural constituent of cast aluminum components. It is thought that microshrinkage pores located near the specimen surface are the most likely to result in the nucleation of a fatigue crack and therefore the most detrimental to fatigue performance [2, 8]. Figure 1 shows a typical microshrinkage pore on the fracture surface of a cast 319 aluminum fatigue specimen. A fatigue crack initiated at the $\sim 800 \mu\text{m}$ microshrinkage pore shown in Figure 1(b) and grew to a critical size resulting in fracture of the specimen. In general, pore sizes in cast aluminum alloys can range from ~ 10 to $1000 \mu\text{m}$.

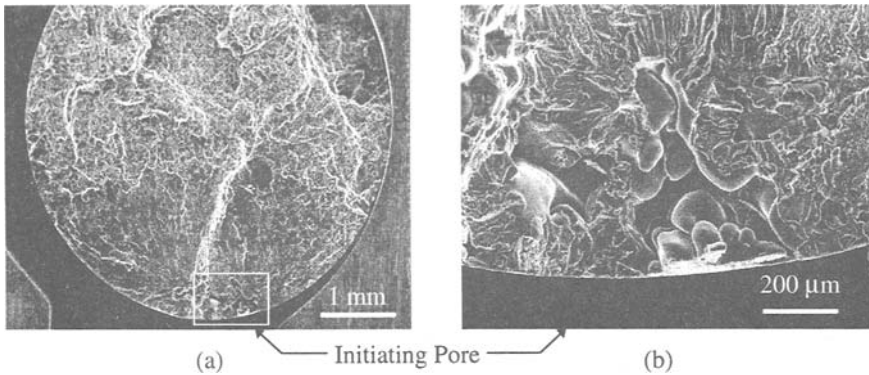


Figure 1 - Fracture surface of a W319-T7 Al fatigue specimen. (a) The fatigue crack initiated from the microshrinkage pore outlined in the white box. (b) The initiating pore is located at the specimen surface and has a maximum dimension of $\sim 800 \mu\text{m}$.

It is speculated that for a wide range of stress amplitudes, the number of cycles required to initiate a fatigue crack in a cast aluminum specimen is a negligible portion of the total fatigue life and that a fracture mechanics or crack growth type approach to

predicting fatigue performance is reasonable [1-3, 8, 9]. Several studies have predicted the fatigue performance of cast Al alloys based on fracture mechanics methods [1-3, 8, 9]. Most of this work has used a LEFM method coupled with fatigue crack growth constants acquired from long cracks. It is recognized, however, that a significant portion of fatigue lifetime can be spent propagating a small crack whose growth behavior is not accurately described by long crack data. For materials that exhibit a small crack effect, use of long crack data can lead to significantly non-conservative estimates of fatigue properties. This is because small cracks (typically of lengths less than ~1 to 2 mm) can propagate at significantly faster rates than long cracks under equivalent ΔK levels and at stress intensities less than the threshold stress intensity factor range, ΔK_{th} , measured for long cracks [10-12].

Several approaches have been used to modify long crack data in an attempt to estimate the behavior of small cracks when predicting fatigue performance. These approaches generally use closure-corrected, effective stress intensity factors to account for the reduced crack closure effects observed in small cracks. Couper et al. [1] determined the effective stress intensity factor range, ΔK_{eff} , for long cracks and used the Paris equation,

$$\frac{da}{dN} = C(\Delta K_{eff})^m \tag{1}$$

to predict the S-N behavior of an Al-7Si-0.4Mg casting alloy, where da/dN represents the rate of crack growth and C and m are constants determined empirically from the crack growth curve. Here, the effective driving force, ΔK_{eff} , is reduced by taking into account crack closure following Elber's approach [13] where $\Delta K_{eff} = U\Delta K$. In this case, a closure factor, U , of 0.5 is used for the fully reversed loading condition ($R = -1$). Reduced levels of crack closure are thought to be an important factor contributing to the accelerated growth of small fatigue cracks [13, 14]. The results of this approach were in reasonable agreement with experimental data but slightly non-conservative, especially at higher stresses. Skallerud et al. [2] also accounted for crack closure by using ΔK_{eff} in the following crack growth equation,

$$\frac{da}{dN} = C(\Delta K_{eff}^m - \Delta K_{th,eff}^m) \tag{2}$$

to predict the fatigue response of a cast A356 aluminum alloy. Here, $\Delta K_{th,eff}$ represents the threshold stress intensity range determined from long crack da/dN vs. ΔK_{eff} (closure corrected) data. This model is further modified by introducing an effective crack length, a_0 , which augments the stress intensity solution for small cracks as follows,

$$\Delta K_{eff} = \Delta \sigma_{eff} \cdot F \cdot \sqrt{\pi(a + a_0)} \tag{3}$$

where $\Delta \sigma_{eff}$ denotes the effective applied stress range, F is a correction factor, and a represents a measure of crack dimension. This is an approach proposed by El Haddad et al. [15] to correct for threshold behavior, where a_0 is a constant for a given material and

material condition determined from ΔK_{th} and the fatigue limit, $\Delta\sigma_c$. The predictions from this model were somewhat non-conservative for calculations omitting a_0 from Equation 3, and mostly conservative when a_0 was included in the calculations. Hinkle et al. [3] predicted the S-N response for a cast A356 aluminum alloy by using long crack data corrected for closure in a Forman crack growth equation,

$$\frac{da}{dN} = \frac{C(\Delta K_{eff})^m}{(1-R)K_{Ic} - \Delta K_{eff}} \quad (4)$$

where R is the stress ratio ($\sigma_{min}/\sigma_{max}$) and K_{Ic} represents the fracture toughness. In this model, small crack behavior is approximated by extrapolating the growth data beyond the threshold into the low ΔK regime and by using closure corrected, ΔK_{eff} long crack data. By using minimum and maximum observed pore sizes as an initial crack dimension, this model predicted reasonable bounds for the experimental data.

Relatively little work has been done to experimentally monitor the growth of small cracks in cast aluminum alloys. Gungor and Edwards [16] predicted the fatigue performance of a squeeze-cast aluminum alloy (6082-T6) by using measured small crack growth data (acquired at $R = 0.1$) in a Paris relation. The results were in very good agreement with experimental data at intermediate and low fatigue lifetimes but conservative at low stresses. The utility of this approach is enabled by the good correlation of small crack growth rates over a narrow range of stress amplitudes (40 to 57% σ_y) using a ΔK solution. However, other studies of small crack growth in cast aluminum alloys have shown that the applied stress level can significantly influence the da/dN vs. ΔK behavior [17, 18]. Such a stress level effect on small crack data significantly complicates the use of ΔK and a Paris relation for predicting S-N response. The values for C and m used in Equation 1 will change by an unknown amount as the applied stress amplitude changes, introducing error into the lifetime calculations. Shiozawa et al. [17] reported a stress level effect on small crack growth when using ΔK and employed an alternative crack driving force to estimate the S-N behavior of two squeeze-cast aluminum alloys (AC8A-T6 and AC4C-T6). In this case, the following crack growth relation proposed by Nisitani et al. [19] was used to successfully correlate the small crack data without any influence of stress level,

$$\frac{da}{dN} = C_1 \cdot \left(\frac{\sigma_a}{\sigma_t} \right)^n \cdot a \quad (5)$$

where σ_a is the applied stress amplitude, σ_t is the tensile strength, and C_1 and n are empirical constants. The S-N calculations determined by integrating Equation 5 were in good agreement with experimental data. Recently, Conley et al. [8] achieved good fatigue life predictions for a cast A356 alloy using a Paris relation and empirical constants (C and m in Equation 1) determined from small crack growth data reported by Seniw et al. [20]. However, the small crack measurements and the life predictions were only conducted for a single stress amplitude. If a stress level effect exists within this alloy, then this approach

will lead to inaccurate predictions for stress amplitudes that vary significantly from that used to acquire the small crack growth data.

In a study of small crack growth behavior in a cast 319 aluminum alloy, Caton et al. [18] reported not only a significant stress level effect, but also showed that the solidification time in a casting can significantly affect the growth behavior of small fatigue cracks. This represents an important consideration since different regions of a cast component can experience considerably different solidification times and therefore possess different microstructures, strengths, and fatigue characteristics. A small crack growth relation similar to Equation 5 was shown to uniquely define the growth of small cracks at two stress amplitudes in specimens of two different solidification times.

In the current paper, a model derived from this small crack relation is presented and used to estimate the S-N response of a cast 319-type aluminum alloy, a commercial Al-Si-Cu alloy used in casting automotive engine components (henceforth designated as W319). The results from this model are compared to those determined using a traditional LEFM model and long crack data. It will be shown that use of long crack data can result in considerable overestimates of the fatigue performance, particularly when threshold stress intensities are considered. The small crack model developed in this work greatly improves the accuracy of the stress-life calculations.

Experimental Methods

The material investigated in this study is a cast 319-type aluminum alloy whose nominal composition is (by weight %): 7.43 Si, 3.33 Cu, 0.22 Mg, 0.24 Mn, 0.38 Fe, 0.01 Ni, 0.12 Ti, 0.13 Zn, 0.03 Sr, 0.03 Cr, and balance Al. This alloy will be referred to as W319 throughout the paper. It has been shown that the solidification time significantly influences the tensile and fatigue properties of W319 [4]. The effect of solidification time on fatigue behavior is considered by examining specimens with solidification times of ~ 44 seconds and ~ 2603 seconds. The condition produced by the faster solidification will be referred to as the "Fine" condition due to its smaller secondary dendrite arm spacing (SDAS) while the condition produced by the slower solidification will be referred to as the "Coarse" condition. All of the specimens underwent a T7 heat treatment consisting of an 8 hour solution treatment at 495°C followed by a boiling water quench (~90°C) and 4 hours of aging at 260°C. A summary of the microstructural and tensile characteristics for the two material conditions are given in Table 1. The average grain sizes in these two microstructures do not differ greatly (~0.5 - 1.3 mm for the Fine condition and ~ 1.6 mm for the Coarse condition) [18].

The growth of small fatigue cracks (~ 17 μm to 2 mm) was monitored in uniaxial specimens taken from hot isostatically pressed (HIP) W319 aluminum using a replication technique. The 3 hour HIP procedure at 480°C and 105 MPa was applied to the small crack specimens prior to the T7 heat treatment and final machining and reduced the microshrinkage porosity to a negligible level. Eliminating the shrinkage porosity in these specimens increases the likelihood of surface initiation and facilitates the observation of naturally-initiated cracks from the earliest stages of propagation by means of replication. The tensile properties of the W319 alloy are changed only slightly by the HIP process and while the HIP procedure significantly alters the fatigue crack initiation in W319 Al [18],

Table 1 - *Tensile properties of the W319-T7 aluminum alloy as influenced by solidification time reported in [4].¹*

Material Condition	Average time for solidification	Average SDAS (μm)	Yield Strength (MPa)	Tensile Strength (MPa)
Fine	44 seconds	23	223	327
Coarse	2603 seconds	100	151	166

¹Data from specimens that did not undergo hot isostatic pressing.

it is suspected that the propagation behavior is not greatly influenced. Optical and SEM analyses indicated that there was no influence of the HIP procedure on any critical microstructural features other than porosity.

The small fatigue cracks were grown under constant amplitude, fully reversed loading ($R = -1$) and ΔK was determined using the solution presented by Newman and Raju [21] for a surface crack in a finite plate. The growth of long fatigue cracks (~ 10 to 25 mm) was measured in C(T) specimens at a stress ratio, R , of 0.1 and growth rates were determined as a function of ΔK and ΔK_{eff} . Testing was conducted at a commercial testing laboratory in accordance with ASTM Test Method for Measurement of Fatigue Crack Growth Rates (E 647-95). ΔK_{eff} was determined by the ASTM technique described in Donald [22]. More thorough details of the experimental procedures used to determine the long and small crack behavior are given in [18].

The samples for small crack growth testing were taken from the same starting material as castings that were used in a study of the fatigue behavior of W319 by Boileau et al. [4]. Stress-life data were established for the Fine and Coarse conditions of the W319 alloy which did not undergo the HIP process [4] using uniaxial, cylindrical specimens with a 5 mm gauge diameter and testing was conducted under fully reversed loads. The fracture surfaces of the failed specimens were examined using scanning electron microscopy and the number and sizes of the pores present on the surfaces were determined using an Oxford ISIS Imaging System [4].

Results and Discussion

As previously described, most of the models used to predict the fatigue performance of cast aluminum alloys have used closure-corrected long crack growth data. A considerable difference can exist between the behavior of fatigue cracks when they are small ($a < 1$ mm) and when they are long ($a > 5$ mm) and these models consequently possess some degree of error. This paper presents a comparison of stress-life calculations in W319 aluminum using both long and small crack growth data and therefore quantifies the degree of improvement that is achieved by using measured small crack growth data. This section first discusses the fatigue crack growth behavior in W319 and then presents two models that calculate the stress-life response. The first model is a traditional LEFM approach which uses long crack growth data and the second model is one based upon the measured growth behavior of the small fatigue cracks.

Crack Growth Behavior

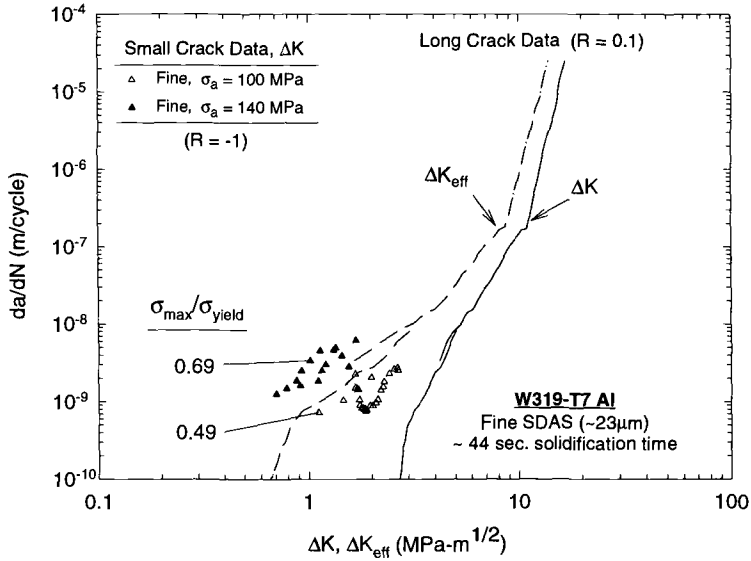
The crack growth data acquired for the Fine and Coarse SDAS conditions, originally reported in [18], are shown in Figure 2. Included in the plots are the long crack measurements (ΔK and ΔK_{eff}) obtained from C(T) specimens and small crack data measured at the stress amplitudes of 100 and 140 MPa. The small crack data in Figure 2 represent measurements from two to four cracks for each condition of microstructure and stress amplitude. The Paris constants, crack growth thresholds, and cyclic fracture toughness, K_Q , values determined from the long crack curves are given in Table 2. K_Q was taken as the maximum stress intensity at a growth rate of $\sim 1 \times 10^{-5}$ m/cycle. It can be seen from the plots in Figure 2 that there exists a significant small crack effect in this alloy for both solidification times. All of the measured small cracks experienced growth at stress intensities lower than the long crack threshold, ΔK_{th} . The closure-corrected long crack data (ΔK_{eff}) offers an improved approximation of the small crack behavior but still provides an inadequate estimate for a broad range of applied stress amplitudes.

It is evident from Figure 2 that the applied stress amplitude has a distinct effect on the small crack growth curves with application of higher stress amplitudes resulting in faster growth rates at equivalent ΔK levels for both microstructural conditions. The effect is more pronounced in the Coarse SDAS condition (Figure 2b) where the 100 and 140 MPa stress amplitudes represent a greater fraction of the strength. It is speculated that the observed stress level effect in this alloy is related to the varying degrees of plastic deformation attendant at the crack tip and violation of the small scale yielding assumption [18].

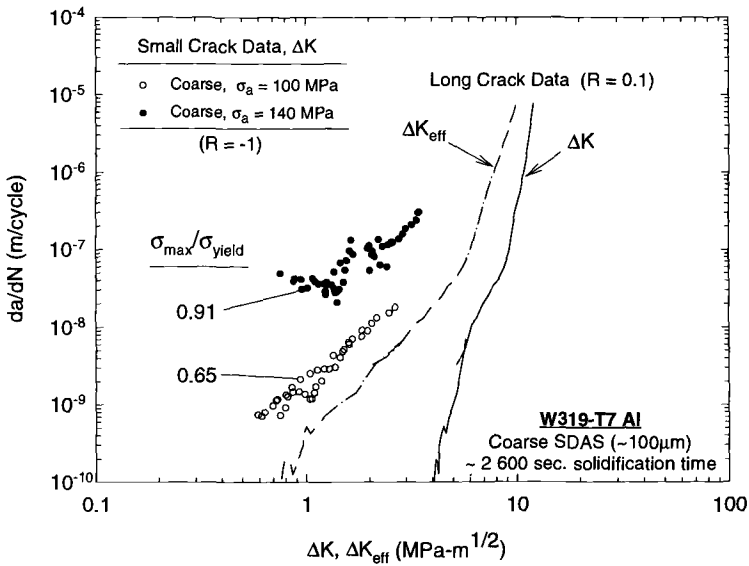
Table 2 - Paris constants, fatigue crack growth thresholds, and cyclic fracture toughness values calculated from the long crack growth curves in Figure 2 [18].

Material Condition	Testing Condition	C	m	Threshold (MPa-m ^{1/2})	Cyclic Toughness K_Q (MPa-m ^{1/2})
Fine (Fig. 2a)	Long Crack (ΔK)	4.82×10^{-12}	4.49	$\Delta K_{th} = 2.7$	16.72
Fine (Fig. 2a)	Long Crack (ΔK_{eff})	5.65×10^{-10}	2.59	$\Delta K_{th,eff} = 0.6$	13.9
Coarse (Fig. 2b)	Long Crack (ΔK)	2.44×10^{-15}	8.10	$\Delta K_{th} = 4.0$	13.24
Coarse (Fig. 2b)	Long Crack (ΔK_{eff})	3.46×10^{-10}	2.93	$\Delta K_{th,eff} = 0.8$	11.45

The solidification time also has a distinct effect on the growth behavior of the small fatigue cracks. Figure 3 shows the measured small crack growth data for the two different solidification times of ~ 44 seconds (Fine SDAS) and ~ 2603 seconds (Coarse SDAS) at stress amplitudes of 100 and 140 MPa. The curves indicate that faster growth occurs in the Coarse microstructure (slower solidification) for a given stress amplitude. It is speculated that the influence of solidification time is closely related to the significant differences in strength in these two conditions (see Table 1) [18].



(a)



(b)

Figure 2 - The long and small crack growth curves determined for (a) the Fine and (b) the Coarse microstructures of the W319-T7 alloy [18].

The influence of solidification time (microstructure) on the growth behavior of small cracks sheds some light on the factors responsible for observed differences in the fatigue properties of cast aluminum alloys. It has been shown that solidification time significantly alters the fatigue properties of the W319 alloy with faster solidification resulting in improved fatigue resistance [4]. While it is likely that the improved fatigue performance is due, in part, to reduction in pore size and quantity, the data in Figure 3 shows that this phenomenon is also due to differences in small crack growth behavior. Therefore, improved fatigue performance in a more quickly solidified alloy is not only a result of a smaller initial crack size (initiating from a smaller microshrinkage pore) but also results from slower crack propagation.

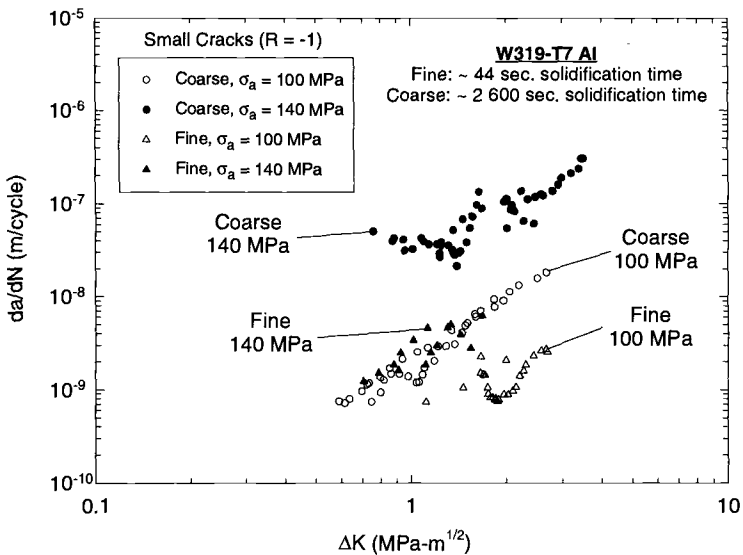


Figure 3 - The effect of solidification time and stress level on the da/dN vs. ΔK curves for small fatigue cracks in the W319-T7 alloy [18].

It has been recognized for some time that ΔK does not properly characterize the driving force behind the growth of small cracks and several more appropriate parameters have been proposed such as elastic-plastic parameters like ΔJ and ΔS [23]. Recent work by Edwards and Zhang [24, 25] demonstrates that the plastic zone size ahead of the crack tip serves as a good parameter to characterize the driving force of small crack growth in two 7000 series aluminum alloys. Nisitani et al. [19] have also proposed an alternative growth law for small cracks which is described by a relation like that given in Equation 5. As mentioned, Shiozawa et al. [17] have shown that Equation 5 works well in describing the growth of small cracks in two squeeze-cast aluminum alloys (AC8A-T6 and AC4C-T6).

In a previous study of W319-T7 aluminum [18], it was shown that a single growth relation, much like that proposed by Nisitani et al., works well in correlating the small

crack data for different solidification rates and at different stress amplitudes. The relation can be written as

$$\frac{da}{dN} = D \left[\left(\epsilon_{\max} \cdot \frac{\sigma_a}{\sigma_y} \right)^s a \right]^t \tag{6}$$

where ϵ_{\max} is the remote strain corresponding to the maximum stress in the load cycle, σ_a is the applied stress amplitude, σ_y represents the monotonic yield strength, and D , s , and t are empirical constants. The terms ϵ_{\max} and σ_y are introduced into the crack growth correlating parameter used in Equation 6 to allow for comparison of the propagation behavior in different materials as discussed in [18]. For a given applied stress amplitude, a material with lower yield strength (σ_y) will experience a greater degree of crack tip plasticity, and a material which experiences a greater remote strain (ϵ_{\max}) will encounter a greater contribution to crack tip opening displacement. Both of these phenomena contribute to faster propagation rates. Figure 4 shows a plot of the small crack data

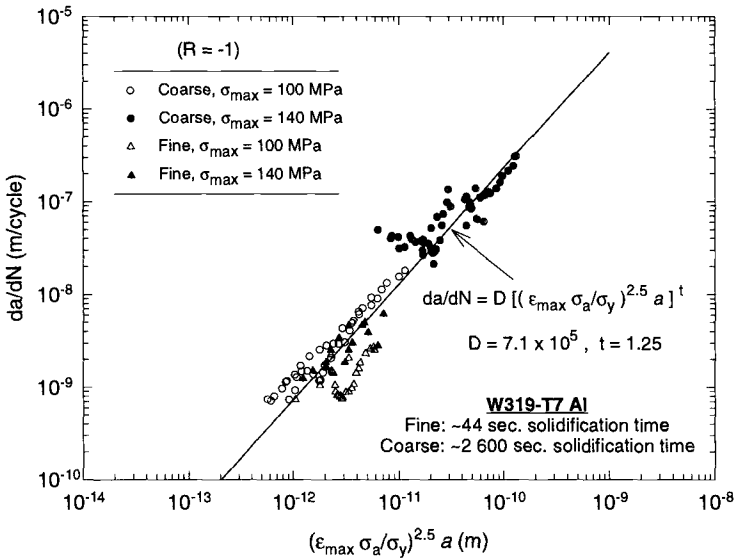


Figure 4 - The crack growth relation given in Equation 6 correlates the growth of small fatigue cracks in the W319-T7 alloy for two solidification times (~44 and ~2600 sec.) and at two stress amplitudes (100 and 140 MPa) [18].

measured in the W319-T7 alloy as a function of the correlating parameter $(\epsilon_{\max} \sigma_a / \sigma_y)^s a$. It can be seen that the growth data for the two different solidification rates and two different stress amplitudes can all be reasonably defined by the single expression given in Equation 6 where D , s , and t are determined to be 7.1×10^5 , 2.5, and 1.25, respectively.

The successful correlation of small crack data seen in Figure 4 suggests that data acquired at a limited number of stress amplitudes could be adequate to describe the growth behavior of small cracks for a wide range of untested stress levels. This enables a very straightforward calculation of the propagation life of a specimen, N_p , and the determination of S-N curves.

Stress-Life Modeling

Fatigue life calculations were conducted for the Fine and Coarse conditions of the W319-T7 alloy using the long crack growth data shown in Figure 2 in a LEFM method (Equation 2) and using a small crack model based on Equation 6. Results of the different methods of estimating fatigue life are compared to experimental data in Figure 5. The models used to estimate S-N response are described below.

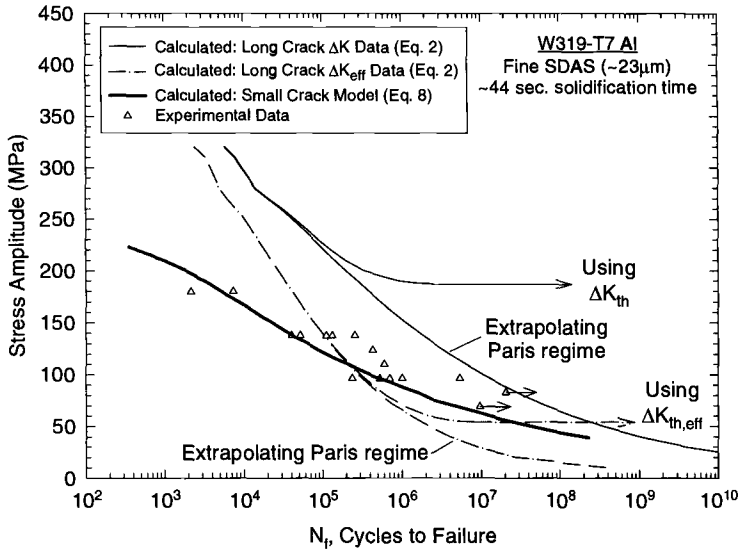
LEFM Model - The long crack growth data given in Table 2 were incorporated into a fatigue life prediction model described in [2]. This traditional LEFM model assumes a negligible initiation life and calculates the propagation life using the crack growth relation given in Equation 2. A computer program developed by Iveland and Odegard [2, 9] was used to calculate the fatigue lifetime based upon the following input parameters: yield strength (σ_y), tensile strength (σ_t), cyclic fracture toughness (K_Q), crack growth threshold (ΔK_{th} or $\Delta K_{th,eff}$), Paris' constant (C), Paris' exponent (m), plastic constraint factor (α), specimen radius (r), applied stress amplitude (σ_a), and stress ratio (R). The program is capable of predicting fatigue lifetime based upon crack initiation from several different pore configurations. The results given in Figure 5 are based upon initiation from a single pore modeled as a semi-circular surface crack. The K solution determined by the program for this crack configuration is outlined in [2]. The initial crack size was taken as the average equivalent pore diameter observed on the fracture surfaces of the W319-T7 fatigue specimens. Table 3 reports the pore size distribution which resulted from a study of the fracture surfaces of the fatigue specimens represented as experimental data in Figure 5 [4]. Therefore, the initial crack depth, b , and initial half crack length, a , were assigned values of 134 μm in the Fine condition and 526 μm in the Coarse condition. The model considers failure to occur when the stress intensity at the crack tip reaches the cyclic fracture toughness, K_Q . The fracture toughness values which were used in the program for the different material and testing conditions are given in Table 2.

Table 3 - Porosity distribution in the W319 aluminum alloy [4].¹

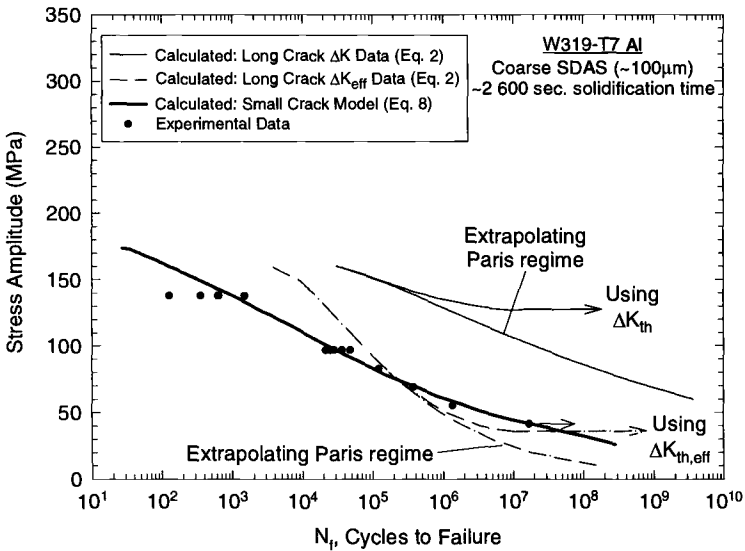
Material Condition	Equivalent Pore Diameter		
	Minimum (μm)	Average (μm)	Maximum (μm)
Fine (~ 23 μm SDAS)	20	134	278
Coarse (~ 100 μm SDAS)	156	526	1178

¹ Measured from fracture surfaces of fatigue specimens.

Figure 5 shows fatigue life calculations determined using crack growth parameters determined from the long crack ΔK data (lighter solid curves) and from the closure corrected ΔK_{eff} data (dash-dot curves). In both cases, the effect of considering crack growth thresholds is indicated. When the measured crack growth thresholds reported in



(a)



(b)

Figure 5 - S-N calculations are compared to experimental data for (a) the Fine and (b) the Coarse microstructures of the W319-T7 alloy.

Table 2 (ΔK_{th} or $\Delta K_{th,eff}$) are entered into the life calculation program, endurance limits are predicted. An alternative approach is to linearly extrapolate the Paris regime beyond the threshold into the low ΔK regime. This was implemented by selecting a sufficiently low threshold value in the program such that any applied stress amplitude will result in crack growth. In this case, no endurance limits are predicted as shown in Figure 5.

It can be seen in Figure 5 that the use of long crack ΔK data (lighter solid curves) results in substantial overestimates of the fatigue performance when compared to the experimental data for both the Fine and Coarse microstructures. The overestimates are particularly large when the measured ΔK_{th} values are used in the life calculation program. The experimental data shows failures at a stress level of ~ 96 MPa ($\sim 2 \times 10^5$ to 10^7 cycles) in the Fine microstructure, which is ~ 90 MPa less than the calculated endurance limit of 186 MPa. In the Coarse microstructure, a failure was observed experimentally at a stress amplitude of ~ 55 MPa ($\sim 10^6$ cycles) which is ~ 72 MPa less than the calculated endurance limit of 127 MPa. The calculations that were made using long crack ΔK data that was extrapolated beyond the measured thresholds show improvement, but are still non-conservative, particularly for the Coarse microstructure (Figure 5b).

The calculations in Figure 5 based upon the closure corrected long crack ΔK_{eff} data (dash-dot curves) show a marked improvement over those which did not consider crack closure. For the Fine microstructure (Figure 5a), the calculations based upon the ΔK_{eff} data correlate fairly well with experimental data, despite somewhat conservative estimations at low stress levels and significantly non-conservative estimation of the high stress level data. In the Coarse microstructure (Figure 5b), the calculations based upon the ΔK_{eff} data are non-conservative at intermediate to high stress levels. Recall that the long crack da/dN vs. ΔK_{eff} curve for the Coarse microstructure (Figure 2b) did not provide an adequate estimate of the small crack growth data tested at 100 MPa and 140 MPa stress amplitudes. The closure corrected long crack data provided a better estimate of the small crack growth in the Fine microstructure (Figure 2a) where the same applied stress levels represent a smaller fraction of the yield strength. It has been speculated that plasticity effects may contribute to faster growth rates at the higher stress levels and that the absence of crack closure cannot solely account for the small crack effect [18].

The S-N calculations from long crack ΔK_{eff} data provide good estimates of the fatigue performance at stress amplitudes where the da/dN vs. ΔK_{eff} curves are in close agreement with small crack growth curves. However, the effect of stress level on small crack behavior apparent in Figure 2 limits the stress amplitudes at which estimates of S-N from long crack ΔK_{eff} data are accurate. The primary objective of this work is to better understand and be able to better predict the fatigue performance of cast aluminum alloys as represented by the S-N data points in Figure 5. By observing the crack growth curves in Figure 2, it can be said that the long crack ΔK_{eff} curves do not describe the fatigue behavior which results in the S-N data in Figure 5. The long crack ΔK_{eff} curves only describe small crack behavior for a very limited range of stresses. Looking closely at the ΔK_{eff} calculations in Figure 5, it is for this limited stress range that the long crack ΔK_{eff} method provides accurate results. More accurate calculations over a wider range of applied stress amplitudes can be achieved from a knowledge of the small crack growth behavior and its dependence on stress level. The following model offers this improved accuracy.

Small Crack Model - The bold curves in Figure 5 represent fatigue life calculations determined using a small crack growth based model. Like the LEFM model described above, this model assumes a negligible initiation life and a pre-existing surface crack whose size, a_i , is equivalent to the average pore sizes reported in Table 3. The propagation lifetime is calculated by integrating Equation 6. First, it is recognized that the term $(\epsilon_{\max} \sigma_a / \sigma_y)^s$ is constant for a constant amplitude fatigue test. Then Equation 6 can be rewritten as

$$\frac{da}{dN} = D[Qa]^t = [DQ^t] a^t \quad (7)$$

where $Q = (\epsilon_{\max} \sigma_a / \sigma_y)^s$. Integration of Equation 7 then results in

$$N_f - N_i = N_p = \int_{a_i}^{a_f} \frac{1}{DQ^t} \cdot a^{-t} da \quad (8a)$$

$$N_p = \frac{1}{DQ^t} \cdot \frac{a_f^{-t+1} - a_i^{-t+1}}{-t+1} \quad (8b)$$

The critical crack size to cause failure, a_f , was assigned the value of 3 mm for all stress levels based upon experimental observations. It should be noted that the model is quite insensitive to variations in a_f , particularly for sizes greater than 2 mm.

The S-N calculations from this small crack model correlate well with the experimental data in Figure 5 and show a distinct improvement over the calculations from the LEFM model using both long crack ΔK and ΔK_{eff} data. In particular, a notable improvement can be seen at the high stress levels in both microstructures. Despite the improvements, however, the calculated curves resulting from the small crack model are at the high end of the experimental scatter for high stress amplitudes in the Coarse microstructure. For a 140 MPa stress amplitude applied to a specimen with the Coarse microstructure, the small crack model calculates a lifetime of ~ 1000 cycles. While a specimen was observed to fail at 1515 cycles under these conditions, another specimen was observed to fail at 130 cycles. In this case, the model gives a reasonable estimation for the longer life specimen, but overestimates the performance of the lower life specimen by approximately an order of magnitude. This calls into question the source of scatter in the experimental data and whether the degree of scatter can be estimated.

It is likely that the scatter in the S-N data is due in part to the variation of initiating pore size. Figure 6 compares the experimental data to the range in calculated fatigue life that results by using the minimum, average, and maximum pore sizes (see Table 3) as the initial crack size, a_i , in the small crack model. It can be seen that the range in lifetime resulting from variations in initiating pore size does not estimate the full range of the experimental data. In fact, the lowest bound of calculated lifetime for the Coarse condition at 140 MPa ($a_i = 1178 \mu\text{m}$, $N_p = 450$ cycles) overestimates the lowest experimental data point by $\sim 5x$ while the highest bound for the Fine condition at 100

MPa ($a_i = 20 \mu\text{m}$, $N_p = 10^6$ cycles) underestimates the highest experimental data point at this stress level by $\sim 5x$. In general, varying the initial crack size from $20 \mu\text{m}$ to $278 \mu\text{m}$ in the Fine microstructure or from $156 \mu\text{m}$ to $1178 \mu\text{m}$ in the Coarse microstructure results in approximately a $5x$ range in estimated cycles to failure. However, the experimental data for both solidification times can vary by more than an order of magnitude at a given stress amplitude.

The overestimation of fatigue performance in the Coarse microstructure at high stresses is thought to result from the oversimplified assumption of a single initiation site and a single propagating fatigue crack. In reality, there are likely multiple fatigue cracks propagating in a given specimen, particularly in the Coarse microstructure where the pores are much larger and represent a larger volume fraction of the microstructure [4].

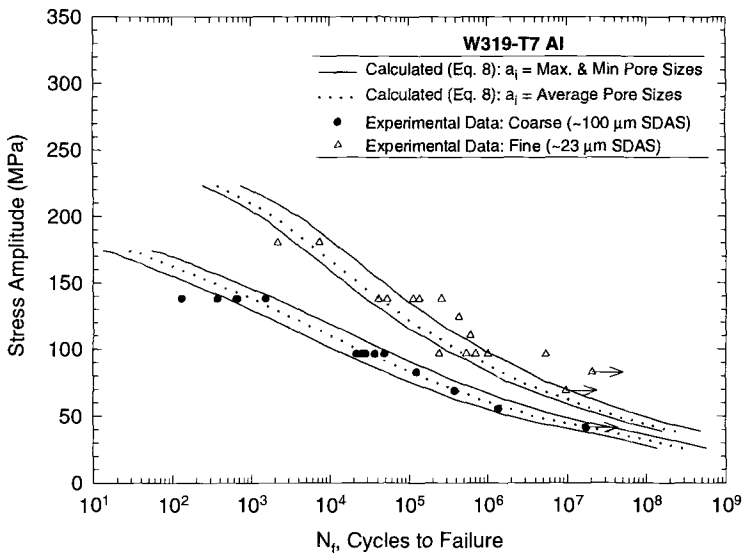


Figure 6 - The range in calculated S-N response obtained by varying the initial crack size from the minimum to maximum observed pore sizes (see Table 3) is compared to the scatter in experimental data.

Depending upon the proximity of initiating pores, propagating cracks can coalesce to form larger cracks which will quickly increase the propagation rate and decrease the number of cycles to reach a critical crack size. Odegard and Pederson [9] looked at the effect of considering multiple crack initiation sites on the estimated fatigue performance of a cast A356 aluminum alloy. They used the model described in [2] to calculate fatigue life for the two scenarios of initiation from a single pore and simultaneous initiation from three closely spaced pores. The scenario of closely spaced, multiple initiation sites resulted in lower calculated lifetimes which were in closer agreement with experimental results. The same approach can be taken with the small crack model. If we assume the simultaneous crack initiation from two near-surface pores located $500 \mu\text{m}$ apart from

each other, the small crack model gives reduced lifetimes as illustrated in Figure 7. If the two pores are assigned the average size for the Coarse condition ($a = 526 \mu\text{m}$), then the small crack model calculates a lifetime of ~ 600 cycles at a stress amplitude of 140 MPa. If the two pores are assigned the maximum size for this condition ($a = 1178 \mu\text{m}$) then a life of ~ 130 cycles is calculated at 140 MPa. These estimations based upon the scenario of multiple propagating cracks provide a much better approximation of the experimental data with the lowest lifetimes.

While multiple crack initiation can provide an explanation for the overestimation of fatigue performance in the Coarse condition, this cannot explain the underestimation of a few experimental points in the Fine microstructure. With smaller and less numerous pores present in the Fine microstructure, some fatigue specimens of this condition may not possess pores near the surface whose corresponding stress intensity is sufficient to

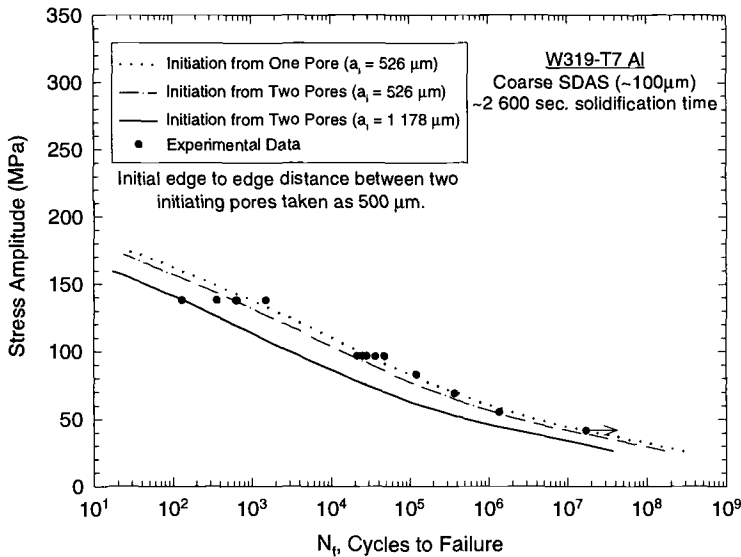


Figure 7 - The estimated influence of initiation at multiple pore sites on the S-N behavior is compared to experimental results for the Coarse microstructure of the W319-T7 alloy.

nucleate and grow a crack. In these cases, the assumption of a negligible initiation life is not correct. A significant number of cycles may be required to nucleate a crack from a small pore or a feature such as a Si particle or slip band. Also, the small crack model has not addressed the possibilities of crack deceleration or arrest due to microstructural barriers. This too would lead to conservative estimations of fatigue life.

The small crack model displays the ability to accurately estimate the influence of solidification time on fatigue performance in the W319-T7 alloy over a broad range of stress amplitudes. Such a capability is of great utility in the design process of castings. Since the local solidification condition significantly influences fatigue properties and can vary dramatically from one area of a casting to another, an accurate fatigue model can be

coupled with solidification models to optimize the component design and the casting process. A reliable predictive capability can also save the time and money required to experimentally establish an extensive stress-life database for a wide range of solidification conditions.

Summary

The following conclusions can be drawn from this study of methods for estimating the fatigue performance in the cast W319-T7 aluminum alloy:

- 1) A substantial small crack growth effect is observed in cast W319-T7, especially at slow solidification conditions (Coarse SDAS).
- 2) A significant stress level effect on the da/dN vs. ΔK behavior of small cracks in the W319-T7 alloy limits the applicability of a long crack LEFM approach to predict stress-life curves.
- 3) Use of long crack da/dN vs. ΔK data in a traditional LEFM model results in significant overestimates of fatigue performance, particularly when the crack growth threshold, ΔK_{th} , is taken into consideration. Use of closure-corrected long crack data (ΔK_{eff}) in this model results in a general improvement of the calculations, but still provides inaccurate estimates at certain stress levels.
- 4) A small crack growth relation that uses a correlating parameter written as $[(\epsilon_{max} \sigma_a / \sigma_y)^s a]$ is incorporated into a model that estimates fatigue life. This model is used for estimating the stress-life response of W319-T7 aluminum in two different microstructural conditions and provides a distinct improvement over the traditional LEFM approach using long crack data.
- 5) Future improvements to this approach include incorporation of multiple initiation sites and coalescing cracks.

Acknowledgments

The authors would like to express gratitude to J. M. Boileau, J. C. Newman, Jr., and P. C. Collins for their helpful discussions regarding this work, J. Odegard for supplying the LEFM algorithm, and K. Donald at Fracture Technology Associates for conducting the long crack testing and closure calculations. M. J. Caton and J. W. Jones also wish to express sincere appreciation to the Ford Motor Company for funding this project.

References

- [1] Couper, M. J., Neeson, A. E., and Griffiths, J. R., "Casting Defects and the Fatigue Behaviour of an Aluminum Casting Alloy," *Fatigue and Fracture of Engineering Materials and Structures*, Vol. 13, No. 3, 1990, pp. 213-227.
- [2] Skallerud, B., Iveland, T., Harkegard, G., "Fatigue Life Assessment of Aluminum Alloys with Casting Defects," *Engineering Fracture Mechanics*, Vol. 44, No. 6, 1993, pp. 857-874.

- [3] Hinkle, A. J., Brockenbrough, J. R., Burg, J. T., "Microstructural Material Models for Fatigue Design of Castings," *Proceedings from Developments in Aluminum Use for Vehicle Design*, Detroit, MI, 1996, SAE SP-1164, pp. 21-27.
- [4] Boileau, J. M., Allison, J. E., and Collins, P. C., "The Effect of Solidification Time and Heat Treatment on the Tensile and Fatigue Properties of a Cast 319 Aluminum Alloy," to be published in *Proceedings of the Fifth International Conference on Molten Metal Processing*, AFS Inc., Des Plaines, IL, 1998.
- [5] Boileau, J. M., and Allison, J. E., in *Fatigue '96*, Vol. 2, Elsevier Science, Inc., London, England, 1996.
- [6] Ting, C., "A Model for the Long-Life Fatigue Behavior of Small Notches," Ph.D. Thesis, University of Illinois at Urbana-Champaign, 1991.
- [7] Boileau, J. M., Zindel, J. W., and Allison, J. E., "The Effect of Solidification Time on the Mechanical Properties in a Cast A356-T6 Aluminum Alloy," *SAE Paper #970019*, SAE International, Warrendale, PA, 1997.
- [8] Conley, J. G., Moran, B., and Gray, J., "A New Paradigm for the Design of Safety Critical Castings," *Proceedings from SAE International Congress and Exposition*, Detroit, MI, 1998, SAE SP-1350, pp. 25-38.
- [9] Odegard, J. A. and Pedersen, K., "Fatigue Properties of an A356 (AlSi7Mg) Aluminum Alloy for Automotive Applications - Fatigue Life Prediction," *SAE Paper # 940811*, SAE, Warrendale, PA, 1994.
- [10] Larsen, J. and Allison, J. E., *Small-Crack Test Methods*, ASTM STP 1149, 1992.
- [11] Miller, K. J. and de los Rios, E. R., *The Behaviour of Short Fatigue Cracks*, Mech. Eng. Publishers, 1987.
- [12] Ritchie, R. O. and Lankford, J., *Small Fatigue Cracks*, The Metallurgical Society, Inc., 1986.
- [13] Elber, W., "The Significance of Fatigue Crack Closure," *Damage Tolerance in Aircraft Structures*, ASTM STP 486, 1971, pp. 230-242.
- [14] Suresh, S. and Ritchie, R. O., "A Geometric Model for Fatigue Crack Closure Induced by Fracture Surface Roughness," *Metallurgical and Materials Transactions A*, Vol. 13A, 1982, pp. 1627-1631.
- [15] El Haddad, M. H., Smith, K. H., and Topper, T. M., "Fatigue Crack Propagation of Short Cracks," *Journal of Engineering Materials and Technology*, Vol. 101, 1979, pp. 42-46.

- [16] Gungor, S. and Edwards, L., "Effect of Surface Texture on Fatigue Life in a Squeeze-Cast 6082 Aluminum Alloy," *Fatigue and Fracture of Engineering Materials and Structures*, Vol. 16, No. 4, 1993, pp. 391-403.
- [17] Shiozawa, K., Tohda, Y., and Sun, S-M., "Crack Initiation and Small Fatigue Crack Growth Behaviour of Squeeze-Cast Al-Si Aluminum Alloys," *Fatigue and Fracture of Engineering Materials and Structures*, Vol. 20, No. 2, 1997, pp. 237-247.
- [18] Caton, M. J., Jones, J. W., Boileau, J. M., and Allison, J. E., "The Effect of Solidification Rate on the Growth of Small Fatigue Cracks in a Cast 319-Type Aluminum Alloy," Submitted to *Metallurgical and Materials Transactions*, 1999.
- [19] Nisitani, H., Goto, M., and Kawagoishi, N., "A Small-Crack Growth Law and Its Related Phenomena," *Engineering Fracture Mechanics*, Vol. 41, No. 4, 1992, pp. 499-513.
- [20] Seniw, M. E., Fine, M. E., Chen, E. Y., Meshii, M., Gray, J., "Relation of defect size and location to fatigue failure in Al alloy A356 cast specimens," *Proceedings from High Cycle Fatigue of Structural Materials: Paul Paris Symposium*, Indianapolis, IN, 1997, pp. 1-9.
- [21] Newman, J. C., Jr. and Raju, I. S., "An empirical stress-intensity factor equation for the surface crack," *Engineering Fracture Mechanics*, Vol. 15, 1981, pp. 185-192.
- [22] Donald, K., "A Procedure for Standardizing Crack Closure Levels," *Mechanics Fatigue Crack Closure, ASTM STP 982*, J. C. Newman, Jr. and W. Elber, Eds., American Society for Testing and Materials, Philadelphia, PA, 1988, pp. 222-229.
- [23] Hudak, S. J., Jr. and Chan, K. S., "In Search of a Driving Force to Characterize the Kinetics of Small Crack Growth," *Small Fatigue Cracks*, R. O. Ritchie and J. Lankford, Eds., The Metallurgical Society, Warrendale, PA, 1986, pp. 379-405.
- [24] Edwards, L. and Zhang, Y. H., "Investigation of Small Fatigue Cracks - I. Plastic Deformation Associated with Small Fatigue Cracks," *Acta Metallurgica et Materiala*, Vol. 42, No. 4, 1994, pp. 1413-1421.
- [25] Edwards, L. and Zhang, Y. H., "Investigation of Small Fatigue Cracks - II. A Plasticity Based Model of Small Fatigue Crack Growth," *Acta Metallurgica et Materiala*, Vol. 42, No. 4, 1994, pp. 1423-1431.

Yoshiaki Akiniwa¹ and Keisuke Tanaka¹

Prediction of Fatigue Limits of Engineering Components Containing Small Defects

Reference: Akiniwa, Y. and Tanaka, K., “Prediction of Fatigue Limits of Engineering Components Containing Small Defects,” *Fatigue Crack Growth Thresholds, Endurance Limits, and Design*, ASTM STP 1372, J. C. Newman, Jr. and R. S. Piascik, Eds., American Society for Testing and Materials, West Conshohocken, PA, 2000.

Abstract: The propagation and arrest behavior of fatigue cracks under various stress ratios was investigated using structural carbon steel specimens having single edge or small surface pre-cracks with lengths ranging from 0.16 to 4.33 mm. The threshold condition of crack extension from pre-cracks was given by a constant value of the effective stress intensity range irrespective of pre-crack length and stress ratio, and the value was equal to the threshold value obtained for long cracks. Cracks extended from pre-cracks were arrested under low stress amplitudes because of the development of crack closure with crack growth. A cyclic resistance curve was constructed in terms of the maximum stress intensity factor which was the sum of the range of the threshold effective stress intensity and the crack opening stress intensity factor, and was used for predicting of fatigue thresholds. The predicted values of the fatigue limit for crack extension, the fatigue limit for fracture, and the length of non-propagating cracks agreed very well with the experimental results. The cyclic resistance-curve method was further applied to predict the effect of the mean stress on the endurance limit of smooth specimens. Haigh diagrams for the endurance limit were successfully derived from the arrest condition of nucleated small cracks in smooth specimens.

Keywords: fatigue, pre-crack, small crack, crack closure, stress ratio, mean stress, resistance-curve method, fatigue limit

Evaluation of the fatigue strength of structural components containing small defects is a classical subject for design engineers, because fatigue failures usually originates from those stress concentrations. The fatigue limit of engineering components is determined by the threshold condition of propagation of nucleated small cracks. An increasing number of studies have shown that the development of crack closure with crack propagation plays a key role in the propagation of small cracks [1-4]. The development of the crack closure with crack growth caused an increase of resistance for a crack to propagate.

Tanaka et al. [5] proposed a cyclic resistance-curve method to predict the fatigue limit of notched components. Fatigue limits for crack initiation, fracture, and non-

¹ Associate professor and professor, respectively, Department of Mechanical Engineering, Nagoya University, Furo-cho, Chikusa-ku, Nagoya 464-8603, Japan.

propagating crack length from a notch in various materials could be predicted by the method irrespective of notch geometry and loading condition [5,6]. Furthermore, Akiniwa et al. [7] successfully applied the method to the component containing crack-like defects.

Engineering components are often subjected cyclic loading under mean stresses in service. The effect of the mean stress has been discussed on the basis of the Haigh diagram [8]. Especially, the fatigue limit of smooth specimens has been evaluated by empirical relationships such as Goodman and Gerber curves. For specimens containing small defects, Murakami et al. [9] proposed the empirical equation to predict the fatigue limit on the basis of abundant experimental data. It is very useful for fatigue design, but underlying physical mechanisms are not clear.

In the present study, the propagation and non-propagation behavior of the fatigue cracks initiated from pre-cracks was investigated using structural carbon steel specimens with single-edge and small surface pre-cracks under several stress ratios. The crack closure behavior of the small surface cracks was dynamically measured at the same frequency of the fatigue tests by using an interferometric strain/displacement gage with a laser diode developed by Akiniwa et al. [10]. The cyclic resistance-curve method was extended to predict the fatigue strength of pre-cracked specimens under mean stresses.

Cyclic Resistance-Curve Method

A cyclic resistance-curve method was proposed in our previous papers [5,7]. The method applied to the crack extension from pre-cracks is briefly described below. In Fig. 1, the cyclic resistance-curve is indicated by the solid line. The maximum stress intensity factor (SIF), K_{\max} , is adopted to indicate the resistance of crack propagation. The threshold value, $K_{\max th}$, is given by the following equation as a function of the amount of crack extension, Δc :

$$K_{\max th} = K_{\text{opth}} + \Delta K_{\text{effth}} \quad (1)$$

where K_{opth} is the crack opening SIF at the threshold and ΔK_{effth} is the effective component of the SIF range. The value of ΔK_{effth} is constant and equal to the value obtained for long cracks, $\Delta K_{\text{effth}\infty}$ [1,5]. In the figure, c_1 is a pre-crack length. Crack closure is developed from $\Delta c=0$ and approaches the value for long cracks, $K_{\text{opth}\infty}$, at Δc_2 . The broken lines indicate the change of K_{\max} calculated for each applied stress. When K_{\max} is larger than $K_{\max th}$, a crack can grow. For the applied stress larger than σ_{w1} , the crack extends. It continues to propagate when the stress is larger than σ_{w2} . When the applied stress is between σ_{w1} and σ_{w2} , the crack ceases propagating at $\Delta c=\Delta c_{\text{np}}$. Namely, σ_{w1} and σ_{w2} are the fatigue limits of crack extension and of fracture, respectively.

The value of ΔK_{effth} is constant irrespective of crack length as described before. Once the change of the crack opening SIF at threshold as a function of the amount of crack extension from pre-cracks is established, σ_{w1} and σ_{w2} can be predicted by

$$\sigma_w = \frac{K_{\max th}}{\sqrt{\pi}(c_1 + \Delta c)F(c_1 + \Delta c)} \quad (2)$$

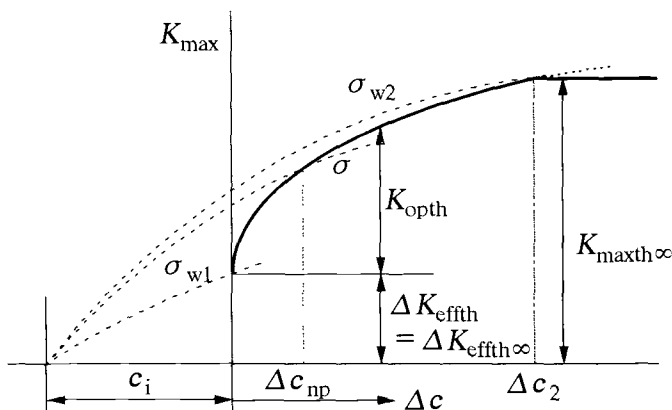


Figure 1 – Cyclic Resistance-Curve

Experimental Procedure

Material and Specimen

The material used in the experiments was a structural medium-carbon steel (JIS S45C) with the following chemical compositions in wt.%, 0.43 C, 0.19 Si, 0.81 Mn, 0.022 P, 0.02 S, 0.01 Cu, 0.02 Ni and 0.14 Cr. The material was annealed at 850°C for 1 h and cooled in the furnace. The ferrite grain size measured with the linear intercept method was 19 μm. The yield stress was $\sigma_y=316$ MPa, the tensile strength was $\sigma_B=612$ MPa, the true fracture stress was $\sigma_f=985$ MPa and the Vickers hardness was $H_v=124$.

Figure 2 shows a pre-cracked specimen with a thinned section at the center. The stress concentration factor is calculated to be 1.03. Surface pre-cracks with half lengths of 0.16, 0.38, 0.5 and 0.78 mm were introduced by fatigue. For the cases of 0.38, 0.5 and 0.78 mm, a starter notch with a diameter of 50 μm and a depth of 25 μm was drilled at the center of the specimen. For relatively long cracks, a single-edge-notched specimen was used. The notch depth was 0.75 mm. Through-thickness pre-cracks were introduced by fatigue. The total crack length including the notch depth was 2.23 and 4.33 mm. After pre-cracking, all the specimens were annealed at 650°C for 1 h to relieve the residual stress induced by pre-cracking.

Fatigue Tests

Fatigue tests were performed in a servo-hydraulic fatigue testing machine in air at room temperature under axial tension-compression. The loading frequency was 15 Hz. For the cases of the initial half crack length $c_i=0.16, 0.38, 0.78, 2.23$ and 4.33 mm, the stress ratio was $R=-1$. For the case of $c_i=0.5$ mm, the stress ratio was $R=-2, -0.5$ and 0 .

When the crack did not extend after stress cycles of 10^6 or arrested after a small amount of crack extension, the fatigue test was interrupted. The specimen was annealed again at 650°C for 1 h before subsequent fatigue tests to relieve the residual stress induced by preceding fatigue tests. The stress amplitude was raised step-wise until the crack propagated continuously. The initial pre-crack length becomes gradually larger during a series of the fatigue tests.

The crack length on the specimen surface was measured with a traveling microscope. Crack closure was determined by the unloading elastic compliance method [11]. For the case of surface cracks, an interferometric strain/displacement gage with a laser diode was used [10]. For the case of long through-cracks, the displacement signal adopted was the output of a strain gage glued on the front face or the back face of the notch. In both cases, the relation between the applied load and the crack opening displacement was measured dynamically at the same frequency of the fatigue tests.

The load shedding technique was adopted to investigate the near threshold propagation behavior of long fatigue cracks under $R=-2, -1, -0.5$ and 0 .

Stress Intensity Factor

For the surface cracks, the stress intensity factor was calculated by Newman and Raju's equation [12]. The aspect ratio used was calculated from the unloading elastic compliance on the basis of the surface crack length and the relation between the applied stress and the crack mouth opening displacement as reported by Ravichandran et al. [13].

Experimental Results and Discussion

Threshold Values for Long Cracks

The relation between the threshold SIF ranges of long cracks and the stress ratio is

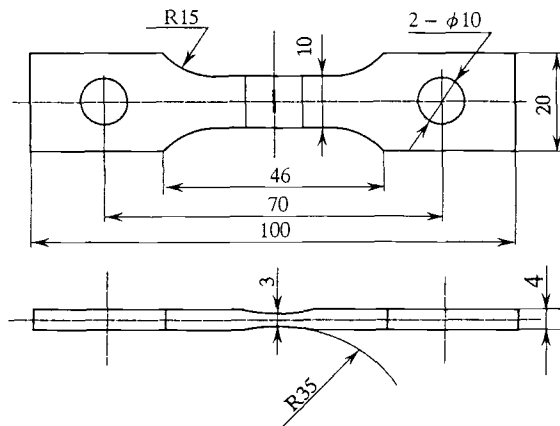


Figure 2 – Fatigue Specimen (dimensions in mm)

shown in Fig. 3. $\Delta K_{th\infty}$ decreases linearly with stress ratio, however $\Delta K_{effh\infty}$ remains constant. The threshold values are summarized in Table 1. From these results, $K_{maxh\infty}$ (MPa \sqrt{m}) can be approximated as follows:

$$\begin{aligned}
 K_{maxh\infty} &= 5.08 & R &\leq R_c \\
 &= 2.92 / (1 - R) & R &> R_c
 \end{aligned}
 \tag{3}$$

where $R_c=0.425$. When R is larger than R_c , $\Delta K_{th\infty}$ is equal to $\Delta K_{effh\infty}$.

Propagation Behavior From Pre-Cracks

Figure 4 shows an example of the relation between the crack propagation rate, dc/dN , and the SIF range, ΔK , obtained for the specimen with a pre-crack length of 0.5 mm for $R=0$. In the figure, the solid line indicates the relation obtained for long cracks. For the stress amplitude of 52.5 MPa, cracks did not extend. For the case of 89 MPa,

Table 1 – *Threshold SIF Ranges for Long Cracks and Fatigue Limit of Smooth Specimen*

Stress ratio R	$\Delta K_{th\infty}$ (MPa \sqrt{m})	$K_{maxh\infty}$ (MPa \sqrt{m})	$\Delta K_{effh\infty}$ (MPa \sqrt{m})	σ_w (MPa)
0	5.06	5.06	2.98	188
-0.5	7.55	5.03	3.00	205
-1	10.52	5.26	2.94	223
-1.5	—	—	—	224
-2	14.98	4.99	2.77	—

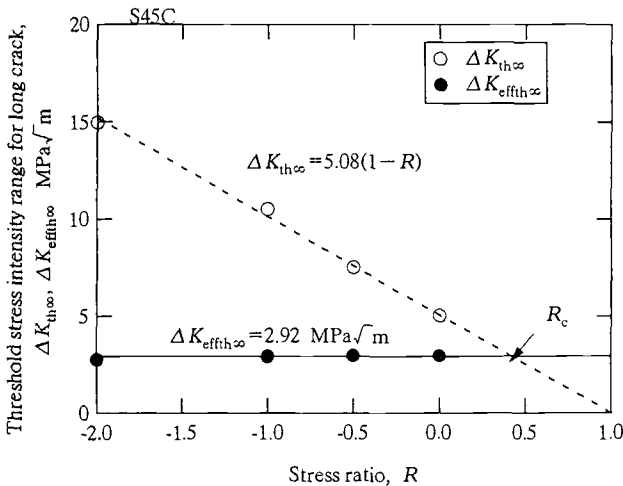


Figure 3 – *Relation between Threshold SIF Ranges and Stress Ratio for Long Cracks*

dc/dN accelerates along the solid line after taking a minimum value, and subsequently the specimen was broken. When the stress amplitude was between these values, the crack became non-propagating after a small amount of crack extension. The cracks can propagate even at ΔK below the threshold value for long cracks. Most of the propagation data of the small surface cracks lie above the relation for long cracks, when compared at the same ΔK . The threshold value, ΔK_{th} , increases with increasing stress amplitude.

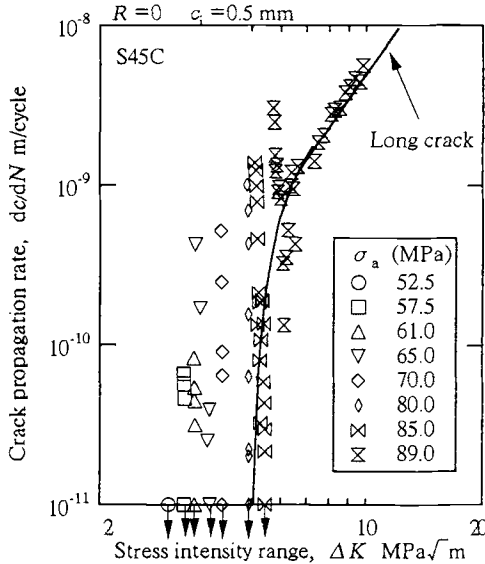


Figure 4 – Relation between Crack Propagation Rate and SIF Range

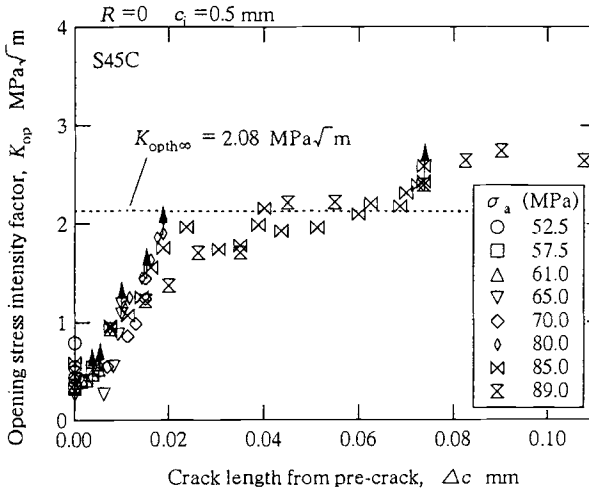


Figure 5 – Change of Crack Opening SIF at Threshold with Crack Growth

Crack Opening Behavior

Figure 5 shows the crack opening stress intensity factor, K_{op} , as a function of the increment of half crack length from a pre-crack, Δc . In the figure, the marks with the arrow indicate the arrest of surface cracks and the broken line means the threshold value for long cracks, $K_{opth\infty}$. The initial value of K_{op} at $\Delta c=0$ is close to zero irrespective of the stress amplitude. The value of K_{op} increases gradually with crack extension.

When dc/dN is plotted against ΔK_{eff} , a unique relation could be obtained between dc/dN and ΔK_{eff} irrespective of applied stress, and it agreed well with the relation for long cracks as reported in our previous paper [7]. Namely, the threshold condition is given by $\Delta K_{effth\infty}$. For other stress ratios and crack lengths, similar results were obtained.

Cyclic Resistance Curve

As described above, the change of the crack opening SIF at threshold as a function of the increment of crack extension from pre-cracks, Δc_{np} , is necessary for the resistance-curve method. For the case of small pre-cracks, a higher stress amplitude is necessary to extend the fatigue crack. Then the ratio of the maximum stress, σ_{max} , to the yield stress, σ_y , is also an important parameter for crack closure. In this study, we propose a following equation for the pre-cracked specimen.

$$K_{op} = \alpha \left(\frac{\sigma_{max}}{\sigma_y} \right)^{-1} \sqrt{\Delta c} + \gamma \tag{4}$$

where α and γ are parameters to be determined from the experimental results. All the

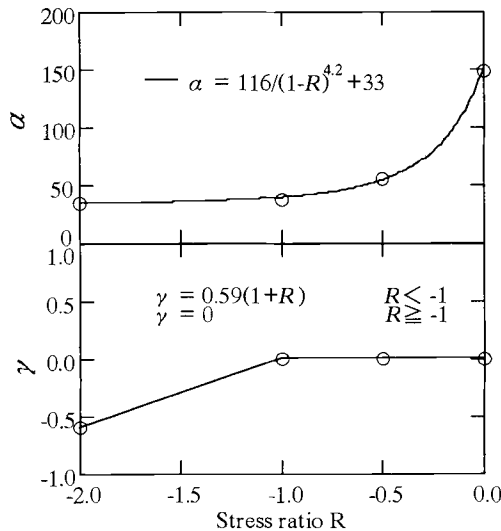


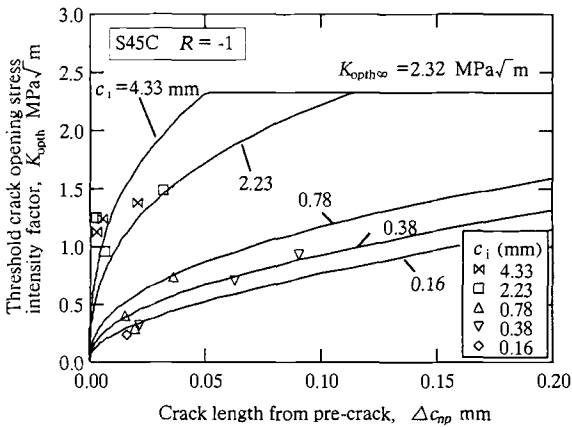
Figure 6 – Change of Coefficients of Resistance-Curve with Stress Ratio

experimental data were used to determine the optimized parameters, α and γ . Figure 6 shows the change of α and γ with stress ratio R . Although α increases with R , γ is nearly zero except for $R=-2$. The values of α and γ can be approximated as follows:

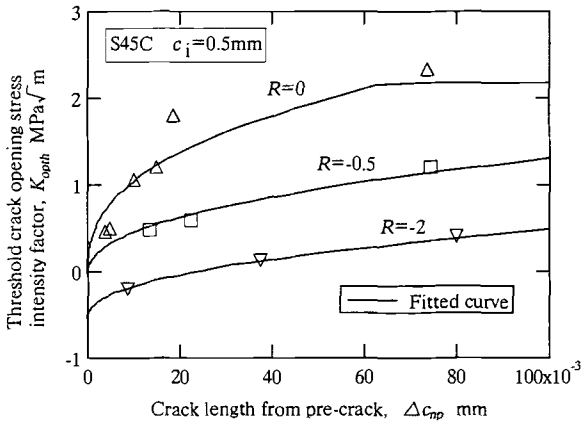
$$\alpha = 116 (1 - R)^{4.2} + 33 \tag{5}$$

$$\begin{aligned} \gamma &= 0 & R \geq -1 \\ &= 0.59 (1 + R) & R < -1 \end{aligned} \tag{6}$$

where γ is negative for $R < -1$.



(a)



(b)

Figure 7 – Change of Crack Opening SIF with Crack Extension
 (a) $R=-1$. (b) $R=0, -0.5$, and -2 .

Figures 7 (a) and (b) show the relation between K_{opth} and Δc_{np} . In the figures, the solid lines indicate the fitted lines calculated by Eqs 1 and 4. Very good fitting was obtained. It is possible to approximate the change of K_{opth} as a function of Δc_{np} and $\sigma_{\text{max}}/\sigma_{\text{y}}$.

According to the R-curve method, the condition of crack arrest can be described as follows.

$$K_{\text{max}} \leq K_{\text{maxth}} = \Delta K_{\text{effth}} + K_{\text{opth}} \tag{7}$$

where K_{opth} is given by Eq 4 as a function of Δc_{np} . The threshold stress can be evaluated from Eq 2.

The relation between the stress amplitude, σ_{th} , and the equivalent pre-crack length l ($=c_i F^2$) is shown in Fig. 8 for $R=0, -0.5$ and -2 . In the figure, the dotted line, the dot-dash-line and the double dot-dash-line correspond to the fatigue limits of smooth specimen, $K_{\text{max}} = \Delta K_{\text{effth}\infty} + \gamma$ and $K_{\text{max}} = K_{\text{maxth}\infty}$, respectively. The open, half-open and solid marks mean no growth, growth and arrest, and continuous growth, respectively.

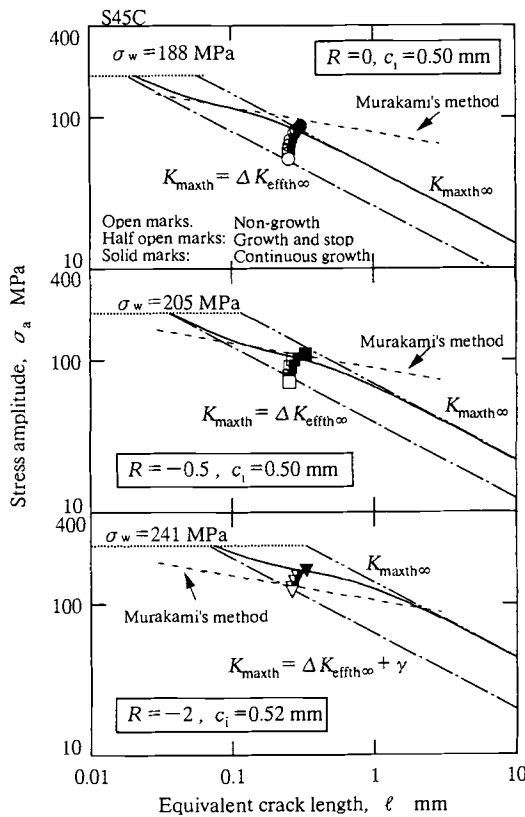


Figure 8 – Change of Threshold Stress with Pre-Crack Length

The solid line indicates the fatigue limit for fracture predicted by the resistance-curve method. For longer initial cracks, the predicted fatigue limit for fracture is given by the double dot-dash-line, i.e. $K_{max}=K_{maxth\infty}$. On the other hand, for smaller initial cracks, the threshold value is less than the double dot-dash-line, and is close to the dot-dash-line, i.e. $K_{max}=\Delta K_{effh\infty}+\gamma$. The solid line agrees very well with the experimental results. The condition of crack extension is given by $K_{max}=\Delta K_{effh\infty}+\gamma$. At the stress level between the dot-dash-line and the solid line, the crack arrests after a small amount of crack extension. In the figure, the broken lines indicate the prediction by Murakami's method [9]. The predicted value of $R=-2$ is lower than the experimental result. For the other two cases, a fairly good agreement is observed.

In Fig. 9, all the measured fatigue limits are summarized. In the figure, the bar-marks mean the experimental results connected between no-growth and continuous growth data. The experimental results agree very well with the solid lines predicted by the cyclic resistance-curve method. The threshold stress amplitude decreases with increasing stress ratio, when compared at the same crack length.

Even when the applied stress is lower than the fatigue limit of smooth specimens, non-propagating surface cracks can be observed in the smooth specimen. In Fig. 9, the relation between the applied stress and the maximum non-propagating crack length observed in the smooth specimen is also plotted by the open marks. The relation between the applied stress and the equivalent non-propagating crack length can be approximated by the linear relationship irrespective of stress ratio as indicated by the dot-dash-line. The fatigue limits of smooth specimens indicated by the dotted lines are identical to the intersection points between the solid line and the dot-dash-line. The crack length at the intersection point means the maximum non-damaging crack length. Once the relation of the dot-dash-line is known, the fatigue limit of smooth specimens under any mean stresses can be predicted as the intersection point.

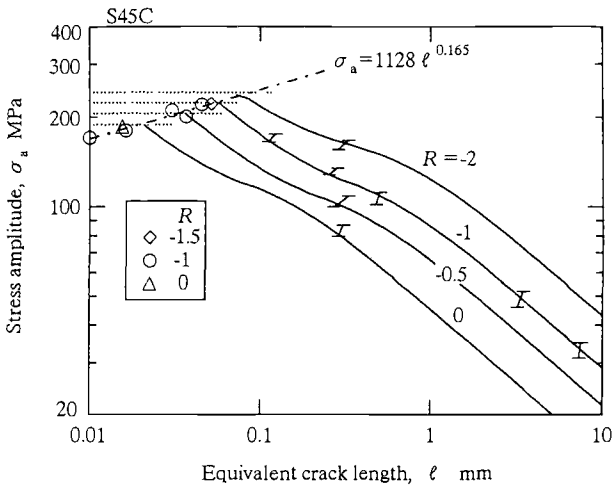
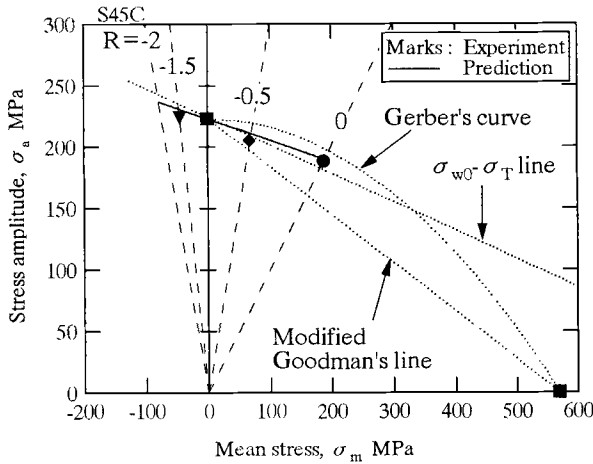
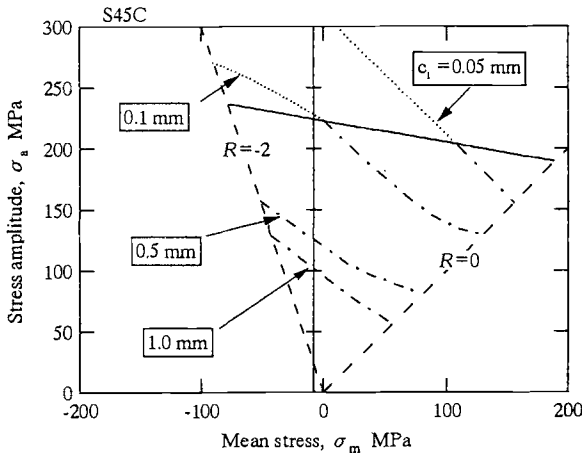


Figure 9 – Relation between Stress Amplitude and Pre-Crack Length and Non-Propagating Crack Length in Smooth Specimen

Figure 10(a) shows the Haigh diagram which is the relation between the stress amplitude and the mean stress at the fatigue limit. The solid marks indicate the measured fatigue limit of smooth specimen. The solid line is the above-mentioned prediction and lies between Gerber and Goodman lines, and is close to the relation between the fatigue limit under $R=-1$, σ_{w0} , and the true fracture stress, σ_T . Figure 10(b) shows the effect of initial defect size on the fatigue strength. The dot-dash lines are the predicted strength for each initial crack length, and the solid line is the prediction given in Fig. 10(a). When compared at the same mean stress, the fatigue limit for fracture decreases with the initial crack length. For the case of $c_i=0.05$ mm, when the mean



(a)



(b)

Figure 10 – Haigh Diagram. (a) Smooth Specimen. (b) Pre-Cracked Specimen

stress is larger than 100 MPa, the fatigue limit of cracked specimens is lower than that of smooth specimens. Namely, at mean stresses below 100 MPa, the non-damaging crack length is larger than 0.05 mm.

Simplified Method

Material parameters required for the resistance-curve method based on Eq 4 are $\Delta K_{th\infty}$, $\Delta K_{effth\infty}$ and σ_Y . Furthermore, the relation between the applied stress and the maximum non-propagating crack length is necessary to evaluate the fatigue limit of smooth specimens. In this study, a simplified method using only Vickers hardness, Hv , of the material will be proposed below.

The values of σ_B , σ_{w0} and σ_Y (MPa) are related to Hv as follows:

$$\sigma_B = 3.2 Hv \tag{8}$$

$$\sigma_Y = 2.8 Hv \tag{9}$$

$$\sigma_{w0} = 1.6 Hv \tag{10}$$

If $\Delta K_{effth\infty}$ is assumed to be constant (i.e. $3 \text{ MPa}\sqrt{\text{m}}$), the SIF range at threshold under $R=-1$, $\Delta K_{th\infty, R=-1}$, can be estimated from Hv [6]. Once $\Delta K_{th\infty, R=-1}$ is known, $\Delta K_{th\infty}$ under arbitrary stress ratio is given by the following equation as shown in Fig. 3.

$$\Delta K_{th\infty} = \Delta K_{th\infty, R=-1} (1 - R) / 2 \quad (\Delta K_{th\infty} \geq \Delta K_{effth\infty}) \tag{11}$$

As described before, the relation between the applied stress amplitude, σ_a , and the maximum non-propagating crack length, l , is expressed by

$$\sigma_a = m (l)^n \tag{12}$$

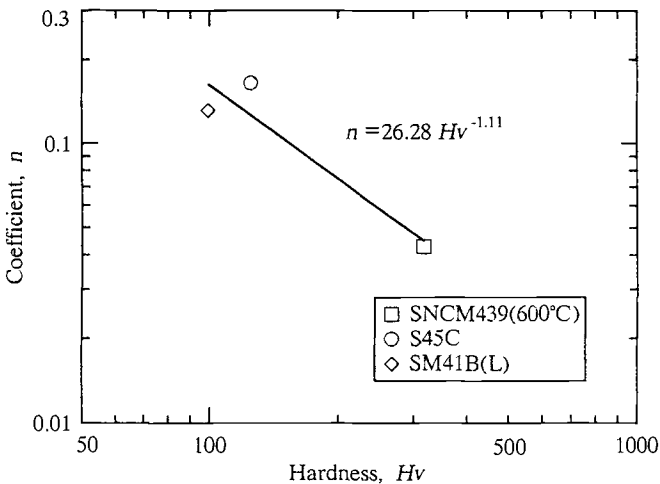


Figure 11 – Change of Coefficient n with Hardness

where m and n are material constants. Figure 11 shows the relation between n and Hv obtained for three materials. The relation can be approximated by

$$n = 26.3 Hv^{-1.11} \tag{13}$$

On the other hand, one fixed point in Eq 12 is given by an intersection point between the predicted line by the resistance-curve method (see the solid line in Fig. 9) and $\sigma_a = \sigma_{w0}$ ($=1.6Hv$) (see the dotted line in Fig. 9) for $R=-1$. Thus all the parameters used in this method are obtained from Hv .

Figure 12 shows the threshold relation between stress amplitude and amount of crack extension for $c_i=0.5$ mm. In the figure, the broken line and the solid line indicate the predicted value obtained by the resistance-curve method and the simplified method, respectively. Although the results for the simplified method (solid line) is slightly higher than the R-curve method (broken line), the predicted values agree well with the experimental data.

Figure 13 shows the change of the threshold stress amplitude with Hv for $R=-1$ for various crack lengths. When Hv is small, the fatigue strength, σ_w , is given by $1.6Hv$. The value of σ_w increases gradually with Hv for $c_i=0.05$ mm. On the other hand, for the case of $c_i=0.5$ mm, σ_w decreases with increasing Hv after taking a maximum value.

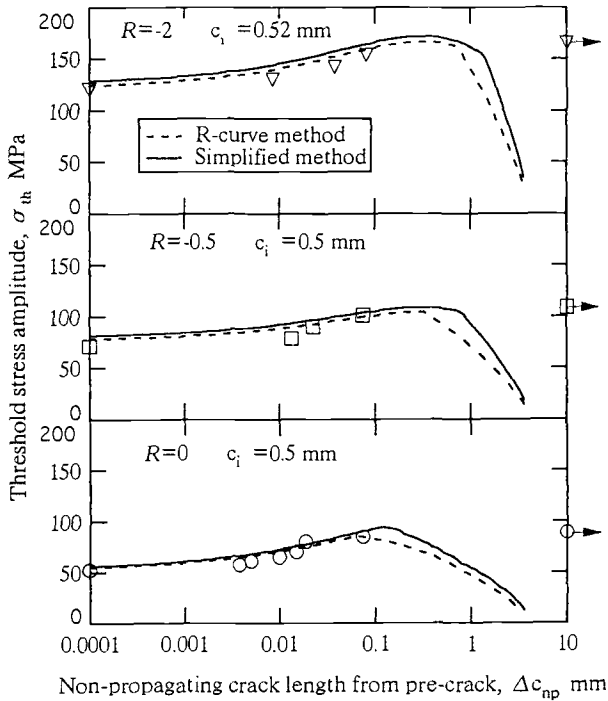


Figure 12 – Limiting Curves for Pre-Cracked Specimen

Conclusions

Specimens having various pre-cracks were fatigued. The propagation behavior of fatigue cracks initiated from pre-cracks was investigated on the basis of the measurement of crack closure. The cyclic resistance curve was determined experimentally to predict the fatigue strength for the components containing crack-like defects. The followings can be concluded:

1. The threshold of fatigue crack extension from pre-cracks was given by the condition that the initial maximum stress intensity factor was larger than the sum of the effective SIF range at the threshold for long cracks, $\Delta K_{\text{eff}\infty}$, and the initial crack opening SIF.
2. Since crack closure developed with crack growth, cracks initiated from pre-cracks were arrested under lower stress amplitudes. The threshold condition was given by $\Delta K_{\text{eff}} = \Delta K_{\text{eff}\infty}$.
3. The cyclic resistance curve method was used for predicting the fatigue threshold of cracked specimens for arbitrary stress ratio. The predicted values of the fatigue limits for crack initiation and fracture agreed very well with the experimental results.
4. A simplified method to determine the resistance-curve using hardness was proposed. A good agreement was obtained between the prediction and experiments.

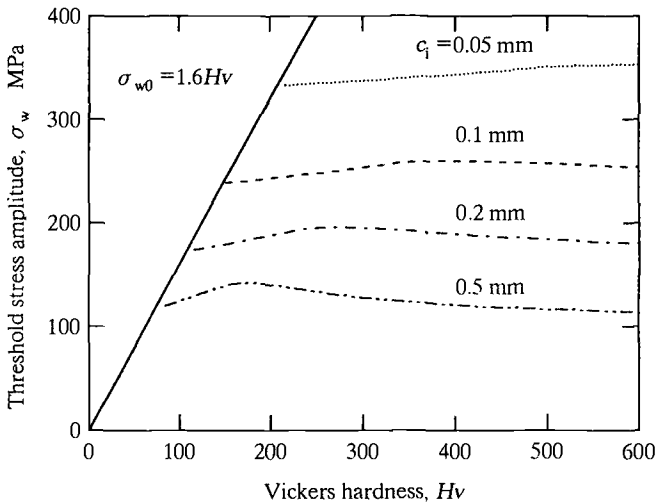


Figure 13 – Change of Fatigue Strength with Hardness

References

- [1] Tanaka, K. and Nakai, Y., "Propagation and Non-propagation of Short Fatigue Cracks at a Sharp Notch," *Fatigue of Engineering Materials and Structures*, Vol. 6, 1983, pp. 315-327.
- [2] Ogura, K., Miyoshi, Y., and Nishikawa, I., "Fatigue Crack Growth and Closure at Notch Root of SUS 304 Stainless Steel," *Proceedings, 26th Japan Congress on Materials Research*, 1983, pp. 91-96.
- [3] Sharpe, Jr., W. N., "Closure Measurements of Naturally Initiating Small Cracks," *Engineering Fracture Mechanics*, Vol. 30, 1988, pp. 275-294.
- [4] Tanaka, K., Akiniwa, Y., Nakao, M., and Kinefuchi, M., "Propagation Threshold and Crack Closure of Small Fatigue Cracks," *Transactions, Japan Society of Mechanical Engineers*, (in Japanese), Vol. 56, 1990, pp. 715-722.
- [5] Tanaka, K. and Akiniwa, Y., "Resistance-Curve Method for Predicting Propagation Threshold of Short Fatigue Cracks at Notches." *Engineering Fracture Mechanics*, Vol. 30, 1988, pp. 863-876.
- [6] Akiniwa, Y., Tanaka, K., and Zhang, L. M., "Prediction of Fatigue Thresholds of Notched Components based on Resistance-Curve Method," *Proceedings, 6th International Fatigue Congress*, 1996, pp. 449-454.
- [7] Akiniwa, Y., Zhang, L. M., and Tanaka, K., "Prediction of Fatigue Limit of Cracked Specimens Based on R-Curve Method," *Fatigue and Fracture of Engineering Materials and Structures*, Vol. 20, 1997, pp. 1387-1398.
- [8] Bannantine, J. A., Comer, J. J., and Handrock, J. L., "*Fundamentals of Metal Fatigue Analysis*," Prentice Hall, 1990, p. 5.
- [9] Murakami, Y. and Endo, M., "Quantitative Evaluation of Fatigue Strength of Metals Containing Various Small Defects or Cracks," *Engineering Fracture Mechanics*, Vol. 17, 1983, pp. 1-15.
- [10] Akiniwa, Y., Harada, S., and Fukushima, Y., "Dynamic Measurement of Crack Closure Behaviour of Small Fatigue Cracks in an Interferometric Strain/Displacement Gauge with a Laser Diode," *Fatigue of Engineering Materials and Structures*, Vol. 14, 1991, pp. 317-328.
- [11] Kikukawa, M., Jono, M., Tanaka, K., and Takatani, M., "Measurement of Fatigue Crack Propagation and Crack Closure at Low Stress Intensity Level by Unloading Elastic Compliance," *Journal of the Society of Materials Science, Japan*, (in Japanese), Vol. 25, 1976, pp. 899-903.
- [12] Newman, J. C., Jr. and Raju, I. S., "Stress-intensity Factor Equations for Cracks in Three-dimensional Bodies", *ASTM STP 791*, American Society for Testing and Materials, West Conshohocken, 1983, pp. 238-265.
- [13] Ravichandran, K. S. and Larsen, J. M., "An Approach to Measure the Shapes of Three-Dimensional Surface Cracks during Fatigue Crack Growth," *Fatigue and Fracture of Engineering Materials and Structures*, Vol. 16, 1993, pp. 909-930.
- [14] Akiniwa, Y. and Tanaka, K., "Micro Structural Effect on Propagation of Short Fatigue Cracks in Notched Components," *Proceedings, 4th International Conference on Fatigue and Fatigue Thresholds*, 1990, pp. 1121-1126.

E. J. Czyryca¹

Corrosion Fatigue Crack Growth Thresholds for Cast Nickel-Aluminum Bronze and Welds

Reference: Czyryca, E. J., “Corrosion Fatigue Crack Growth Thresholds for Cast Nickel-Aluminum Bronze and Welds,” *Fatigue Crack Growth Thresholds, Endurance Limits, and Design, ASTM STP 1372*, J. C. Newman, Jr. and R. S. Piascik, Eds., American Society for Testing and Materials, West Conshohocken, PA, 2000.

Abstract: Fatigue crack-growth rate tests of cast NAB and NAB weld metal specimens were conducted to determine the threshold for fatigue crack growth (ΔK_{th}). The tests were conducted in accordance with ASTM E 647, Standard Test Method for Measurement of Fatigue Crack Growth Rates, in artificial seawater at a cyclic frequency of 2 Hz at R-ratios of +0.05, +0.40, and +0.60. The specimens were machined from both poor and good quality, as-cast NAB. Production NAB weldments were used for NAB weld metal specimens.

The fatigue crack growth-rate curves for duplicate tests at each R-ratio of cast NAB in seawater were analyzed in the near-threshold regime to determine ΔK_{th} . With increasing stress intensity ratio (R), ΔK_{th} decreased. Compared to the values for cast NAB, higher ΔK_{th} and higher crack closure levels in NAB weld metal tests were noted, due to the residual stress in the weldment. The same fatigue crack growth-rate curve sets were corrected for crack closure, and the near-threshold stress intensity decreased significantly when the closure loads were deducted. The closure-corrected, near-threshold stress intensity, based on ΔK_{eff} , ranged from 4.4 to 6.1 MPa- \sqrt{m} for cast NAB versus 4.4 to 7.4 MPa- \sqrt{m} for NAB weld metal.

Keywords: nickel-aluminum bronze, fatigue crack growth rate, fatigue crack growth rate threshold, corrosion fatigue, seawater, crack closure

Nickel-aluminum bronze (NAB) is a copper-base alloy widely used for naval and commercial marine propellers. The nondestructive testing (NDT) methods available for the inspection of nickel-aluminum bronze propellers include dye penetrant testing, ultrasonic testing, eddy current testing, and radiographic testing. A sensitive NDT method and stringent accept/reject criteria can result in the detection and rejection of numerous indications of small casting defects and weld flaws. The subsequent repairs slow production and increase costs. Such repairs have been invoked to ensure that cracks

¹ Metallurgical Engineer, Naval Surface Warfare Center, Carderock Division, 9500 MacArthur Blvd., West Bethesda, MD 20817-5700.

and flaws do not propagate in service. Propellers are designed to operate under low-level cyclic stress in service. Thus, the flaw tolerance criteria should primarily be based on seawater corrosion fatigue crack growth.

Quantifying the propensity of pre-existing cracks to grow by fatigue (cyclic stresses) is derived through linear-elastic fracture mechanics, which provides the relationships among applied cyclic stress, crack size, and structural geometry [1]. In fracture mechanics, the crack-tip stress intensity factor for crack opening, K_I , is calculated to relate crack size, geometry, and load orientation, as follows:

$$K_I = F_{ab} \sigma \sqrt{\pi a} \quad (1)$$

where F_{ab} = geometry function, σ = stress, and a = crack length. In order to conduct an analysis to determine the flaw size which will not extend in service, using a fracture mechanics approach, the following information is required:

- (a) steady and cyclic stresses which act on the component,
- (b) typical inherent flaw sizes in the material (or the NDT detectability limits), and
- (c) the threshold for fatigue crack growth (ΔK_{th}) for the material in its operating environment.

Fatigue crack growth rates (da/dN) are expressed in terms of the stress intensity factor range (ΔK_I). The "threshold" stress intensity, ΔK_{th} , is the value where da/dN approaches zero, i.e. the stress intensity for "non-propagating" cracks under cyclic stress [1]. Thus, the threshold flaw size represents the smallest flaw under the service loading conditions, which must be repaired; smaller flaws will not propagate. Standard test methods have been developed for the determination of ΔK_{th} .

This paper presents the results of fatigue crack growth rate tests and the determination of the threshold for fatigue crack growth (ΔK_{th}) for Nickel-Aluminum Bronze (NAB) and NAB weld metal. A fracture mechanics analysis was conducted to conservatively estimate threshold flaw sizes for NAB and NAB weld metal with respect to cyclic loading conditions.

Materials Investigated

The casting used for this study was a propeller hub-blade segment of nickel-aluminum bronze to MIL-B-24480A (ASTM B 148, Alloy UNS C95800). The casting was sectioned to provide test coupons for fatigue crack growth specimens. Coupons were sectioned from both the blade portion (maximum thickness approximately 60 mm) and the hub portion (uniform thickness approximately 85 mm). Coupons were also cut from both portions for tensile tests. A weldment was fabricated to provide test specimens for fatigue crack growth rate testing of NAB weld metal. The weldment was a single-vee butt joint (60° included angle) of two pieces of 12.5 mm thick, rolled NAB plate to ASTM B 171, Alloy UNS C63200, with a similar piece as backing bar. The weldment was fabricated by gas metal-arc welding (GMAW) process with AMPCOTRODE® 46 NAB wire

electrode. A total of 75 mm weld length was produced. A single all-weld-metal tensile specimen, standard 6 mm diameter, was machined from the weldment.

Wet chemical check analyses were conducted using samples removed from all the NAB products in this study. The results are given in (Table 1) and show that all the NAB metals were within specified composition limits.

Table 1 - *Chemical composition of nickel-aluminum bronze metals used*

Chemical Composition (weight %)	Hub Area	Blade Area	Cast NAB MIL-B -24480A	Weld Metal	Weld Wire Ampcotrode 46 [2]	NAB Plate	NAB plate ASTM B171 C63200
Cu	80.3	81.4	Balance	81.3	balance	81.7	Balance
Mn	1.14	1.05	0.8-1.5	1.74	0.6-3.5	1.71	1.2-2.0
Ni	4.54	4.66	4.0-5.0	4.49	4.0-5.5	4.33	4.0-4.8
Fe	4.16	3.77	3.5-4.5	3.79	3.0-5.0	3.63	3.5-4.3
Al	9.46	8.99	8.5-9.5	8.59	8.5-9.5	8.54	8.7-9.5
Si	0.023	Nil	0.10 maximum	0.038	not specified	0.040	0.10 maximum

Tension tests of the NAB casting were conducted to ASTM E 8, using standard 12.5 mm diameter tensile specimens. The results of the tests are given in (Table 2). As shown in (Table 2), the tensile properties were below that specified by MIL-B-24480A for separately cast coupons. The fractures and test length of specimens cut from the hub portion showed extensive porosity and shrinkage cavities. Metallographic examination of samples from both blade and hub portions was conducted. (Figures 1 and 2) compare the microstructure of hub and blade, respectively. The microstructure of the NAB metal in the hub (Figure 1) shows the extensive porosity, a network of shrinkage along grain boundaries, and a dispersion of inclusions ("dirt") throughout the microstructure. However, the metal of the blade showed porosity, isolated shrinkage, and much lower inclusion volume in the microstructure (Figure 2).

The all-weld-metal properties resulting from the tensile test (6 mm diameter) are shown in (Table 2), where the strength and ductility exceeded the minimum properties specified for cast NAB and were similar to the producer's typical values. (Figure 3) shows fine-grained, defect-free microstructure of the weld deposit. In machining of specimens for fatigue crack growth tests, the notch was at the weld centerline.

Table 2 - Tensile properties of cast nickel-aluminum bronze propeller segment and nickel-aluminum bronze weld metal

Specimen No.	Yield Strength (MPa)		Tensile Strength (MPa)	Elongation in 4 diameters (%)	Notes
	0.2% offset	0.5% extension			
#1-hub	228.2	237.2	393.7	5.2	porosity
#2-hub	215.1	222.0	351.3	4.0	porosity
#3-blade	227.5	231.0	571.2	22.8	good ductility
weld metal	513.0	506.8	799.8	17.0	good ductility
Specifications					
MIL-B-24480A	not specified	241.3 minimum	586.0 minimum	15.0 minimum	for separately cast coupons
Ampcotrode 46 GMAW	406.8 (average)	-	717.0 (average)	23.5 (average)	[2]
ASTM B148 C95800	234.4 minimum	248.2 minimum	620.5 minimum	10.0 minimum	

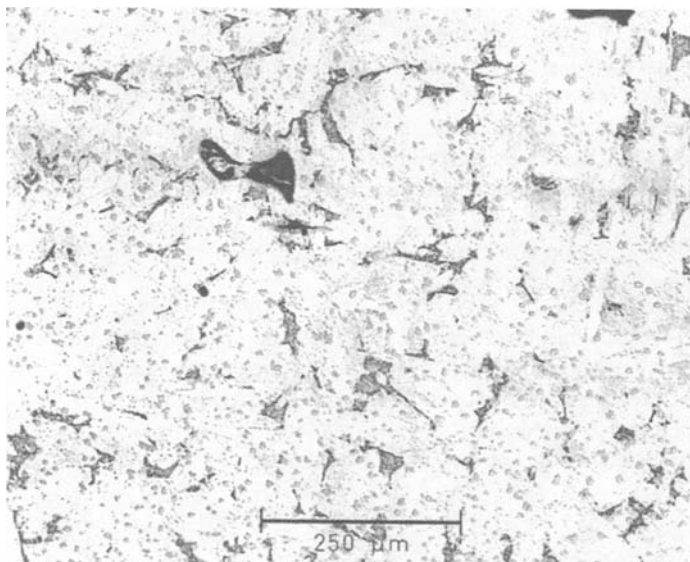


Figure 1 - Photomicrograph of cast NAB microstructure in hub section (100X)

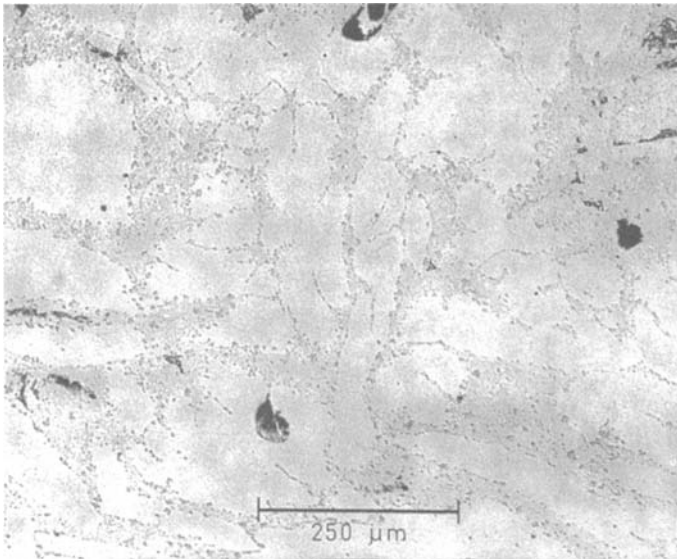


Figure 2 - Photomicrograph of cast NAB microstructure in blade section (100X)

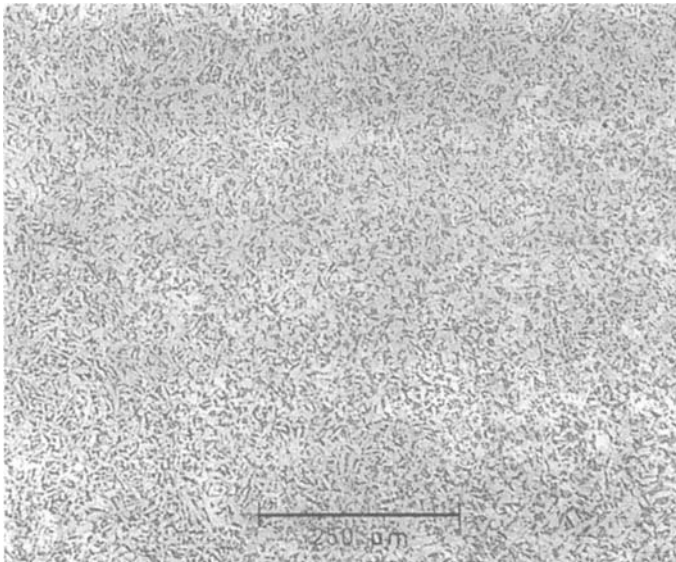


Figure 3 - Photomicrograph of as-deposited NAB weld metal microstructure (100X)

Experimental Methods

Fatigue crack growth rate (FCGR) testing of cast NAB and NAB weld metal specimens was conducted to determine the threshold for fatigue crack growth (ΔK_{th}) in seawater. The tests were conducted in accordance with ASTM Standard Test Method E 647-91, "Measurement of Fatigue Crack Growth Rates," with the following specific procedures:

- 1) The test specimens in all cases were standard compact specimens C(T), with the thickness dimension, $B = 12.5$ mm and the uncracked ligament length, $W = 50$ mm.
- 2) The continuous K-decreasing procedure of ASTM E 647-91 was followed for each test, and R ratio remained fixed during each test.
- 3) Once a growth rate of 10^{-7} mm/cycle or below was obtained, the test was continued using a K-increasing procedure to verify the lower portion of the fatigue crack growth rate curve and to generate additional data at the higher growth rates.
- 4) As a minimum, fatigue crack growth rates spanned the range of 2.5×10^{-4} mm/cycle to below 10^{-7} mm/cycle for each determination of threshold (ΔK_{th}).

Crack closure loads were monitored using the compliance methods described in ASTM E 647-91, 647, Standard Test Method for Measurement of Fatigue Crack Growth Rates, and an on-line, automated method of closure determination was used. Crack-mouth opening displacement (COD) versus applied load data were sampled each cycle to determine deviation from linearity as the closure load criterion. Since residual stress in cast metals and weldments, as well as pressure from accumulated corrosion products in corrosion fatigue tests can act against applied crack opening forces, determination of crack closure load is critical at the low-load amplitudes involved in ΔK_{th} determinations.

The test conditions for determining threshold for fatigue crack growth for both cast NAB and NAB weld metal were as follows:

- 1) Tests were conducted in ASTM artificial seawater at a cyclic frequency of 2 Hz with a sinusoidal waveform, and
- 2) Duplicate tests of each metal were conducted at stress intensity ratio, R of +0.05, +0.40, and +0.60.

The fatigue crack growth tests were conducted by Fracture Technology Associates, Bethlehem, PA, in a 20,000-pound (89 kN) capacity, servo-hydraulic test machine fitted with a 5,000-pound (22 kN) capacity load cell for best precision in low load measurement. Crack opening displacement was measured by a clip gage attached to the specimen notch-mouth, and crack length was monitored throughout the tests using the compliance measurement technique. Both the clip gage and compliance technique are described in ASTM E 647. The crack length measurement precision by this technique was ± 0.005 mm.

The tests were conducted in a horizontal load frame, such that the compact specimens had notch tip and crack immersed in circulating, aerated ASTM artificial seawater at room temperature (24 °C). Each test was conducted using a fresh 6 liter batch of seawater, which ranged from 8.25 to 8.50 in measured pH.

The cyclic, crack-tip stress intensity factor, ΔK , for the CT specimen was calculated by the equations given in ASTM E 647-91. The cyclic stress intensity for the CT specimen is calculated by the following equation:

$$\Delta K = \frac{\Delta P \left[f \left(\frac{a}{W} \right) \right]}{B \sqrt{W}} \tag{2}$$

where $f \left(\frac{a}{W} \right) = \frac{(2 + \alpha)}{(1 - \alpha)^{3/2}} (0.886 + 4.64\alpha - 13.32\alpha^2 + 14.72\alpha^3 - 5.6\alpha^4)$;

- and ΔP = maximum load - minimum load,
- a = crack length,
- W = specimen width,
- B = specimen thickness,
- α = a/W.

Under constant-amplitude loading (constant ΔP), as the crack length increases, ΔK also increases. Direct, visual measurement of crack length was not possible for tests conducted in the seawater environment, and crack length was indirectly measured via crack-mouth-opening displacement. The crack length was determined using the elastic relationship between specimen compliance (inverse of stiffness) and crack length which has been determined for the CT specimen [3]. Computation of fatigue crack growth rates used a modified secant method, where the crack growth at length a, was based on an increment of crack extension, Δa , and an increment of elapsed cycles of applied cyclic load, ΔN , between a_{i-1} and a_{i+1} .

In order to determine ΔK_{th} , the general procedure used initiates fatigue crack growth at a moderate level of ΔK and approach a target, low growth-rate by a series of load amplitude reductions, called the K-decreasing method [4]. To minimize any effects of crack growth retardation, the K-gradient for decrease is maintained to provide a fractional change in the plastic zone size at the crack tip, as crack length is increasing. The K-gradient procedures were conducted through automated load-shedding by a computer-controlled test system [5]. For the test results shown herein, a decreasing K-gradient of -0.16 mm^{-1} was used.

After initial crack growth progressed at a moderate rate, the target FCGR for threshold was approached by the K-decreasing sequence in accordance with ASTM E 647. After the target FCGR was established, the loading was switched to a K-increasing mode to generate supplemental crack growth-rate data. The overlap in data at the target FCGR or below, provides verification of the threshold determined by the K-decreasing technique. The software for data acquisition and analysis calculates a continuous slope for loading and unloading segments of the load cycle. From these data, an automated crack closure determination was made based on the change in slope, to separate from the total, applied stress intensity that portion “effective” in crack opening, which acts to extend the crack length [6] by simple subtraction:

$$\Delta K_{eff} = \Delta K_{app} - \Delta K_{cl} \tag{3}$$

- where ΔK_{app} = total, applied stress intensity range,
- ΔK_{cl} = crack closure portion of ΔK_{app} ,

ΔK_{eff} = effective stress intensity range for crack opening and growth.

Results

The fatigue crack growth-rate curves for duplicate tests of cast NAB in seawater are plotted in (Figure 4, R = +0.05), (Figure 5, R = +0.40), and (Figure 6, R = +0.60) on the basis of ΔK_{app} . The differences crack growth rates at higher stress intensities between the duplicate tests at R = +0.05 (Figure 4) and R = +0.60 (Figure 6) may have been due to porosity which was noticeable on the post-test crack surfaces, as well as on the machined faces of the specimens. The porosity and shrinkage cavities may act to blunt the progressing crack front, leading to slower growth at a given stress intensity. However, their influence was not significant in the threshold regime. All the results are compared in (Figure 7), where the effect of R on fatigue crack growth rates near threshold are notable. All FCGR data shown in these and subsequent figures included only the K-decreasing portion of the tests. The complete FCGR curves for each test, K-decreasing and K-increasing, were used as data sets for curve fit by log-log linear regression analysis to determine ΔK_{th} and the parameters to the linear, Paris Law crack growth regime [1] for each test. These values from the FCGR tests of cast NAB are summarized in (Table 3).

Table 3 - Results of fatigue crack growth rate tests of NAB in seawater

Test Code	Stress Intensity Ratio	FCGR Threshold		Paris Law Parameters	
		(ksi-√in)	(MPa)		
GKR-2	+0.05	8.48	9.32	1.513 X 10 ⁻¹⁴	6.599
GKR-5	+0.05	8.75	9.61	1.881 X 10 ⁻¹²	4.809
GKR-4	+0.40	6.32	6.94	2.153 X 10 ⁻¹¹	4.375
GKR-6	+0.40	5.98	6.57	2.488 X 10 ⁻¹¹	4.338
GKR-1	+0.60	4.99	5.48	1.323 X 10 ⁻¹²	5.771
GKR-3	+0.60	4.60	5.05	1.939 X 10 ⁻¹¹	4.617
	R	ΔK_{th}		C	n

The fatigue crack growth-rate curves for duplicate tests of NAB weld metal in seawater are plotted in (Figure 8) for the condition R = +0.40 on the basis of ΔK_{app} . At each stress intensity ratio, there was reasonable agreement between the duplicate tests. The results for all of the NAB weld metal tests (R = +0.05, +0.40, & +0.60) are compared in (Figure 9), where the effect of R on fatigue crack growth rates near threshold again was significant.

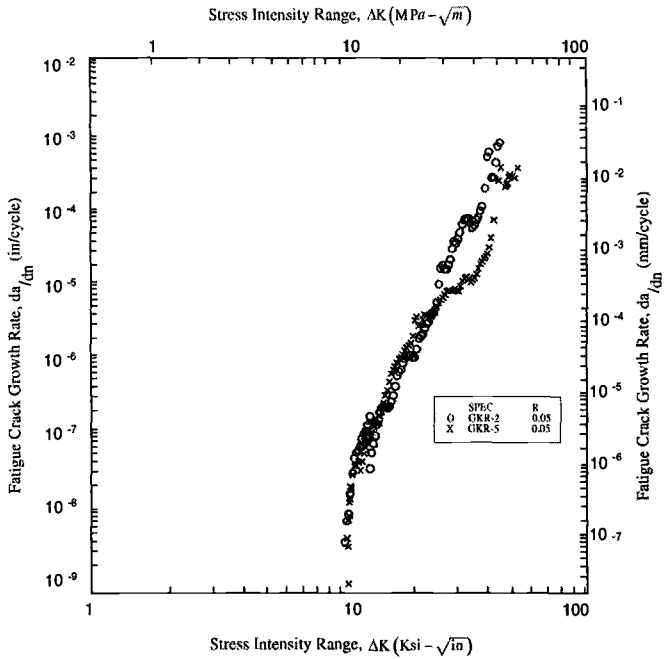


Figure 4 - Plot of fatigue crack growth rates for NAB in seawater at $R = +0.05$

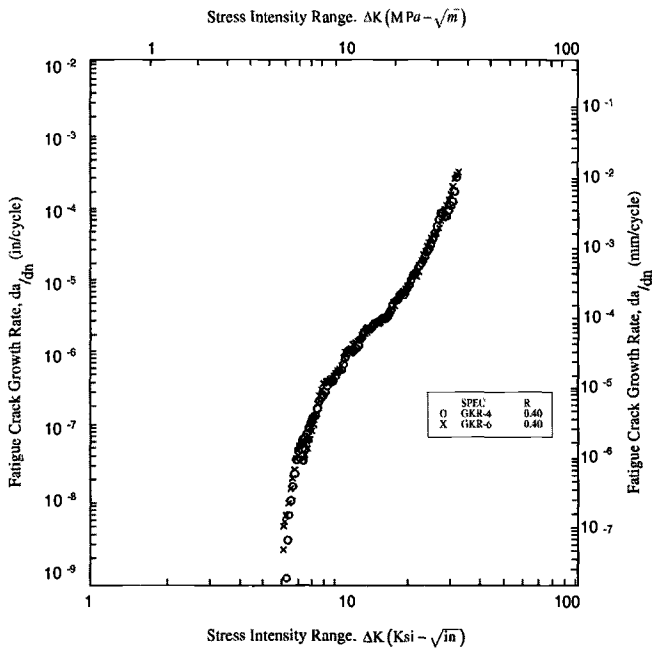


Figure 5 - Plot of fatigue crack growth rates for NAB in seawater at $R = +0.40$

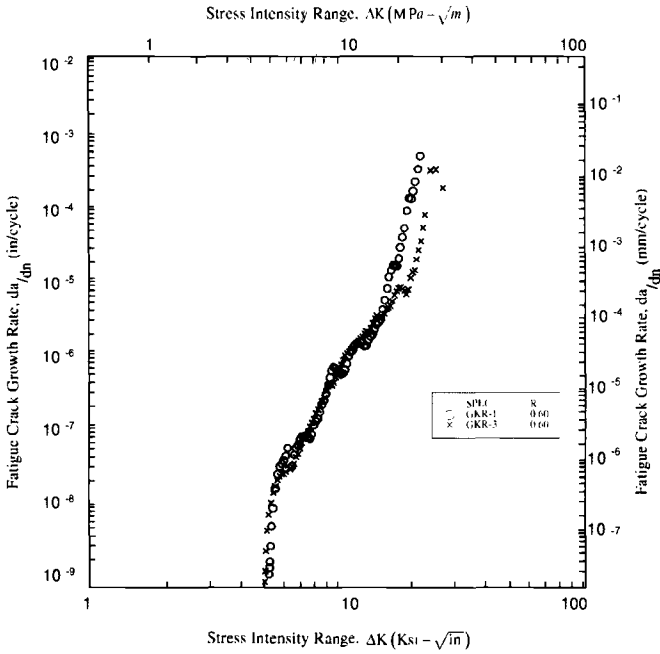


Figure 6 - Plot of fatigue crack growth rates for NAB in seawater at $R = +0.60$

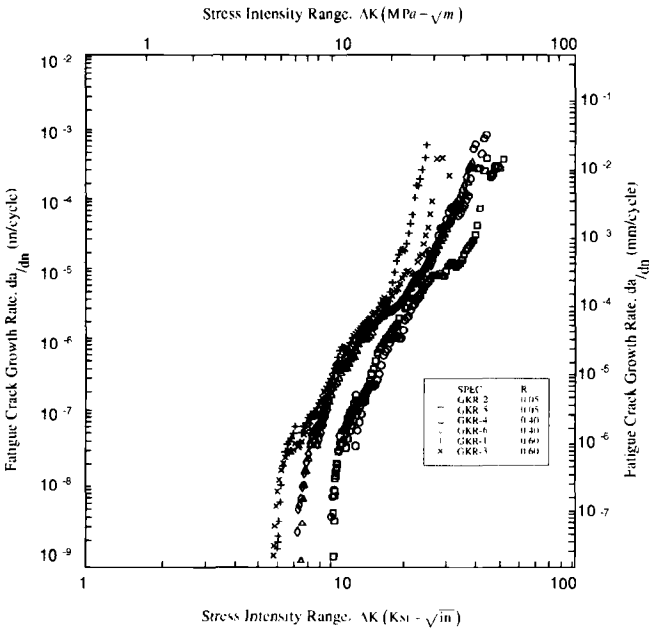


Figure 7 - Comparison of fatigue crack growth rates for NAB in seawater at three stress ratios based on applied stress intensity-range

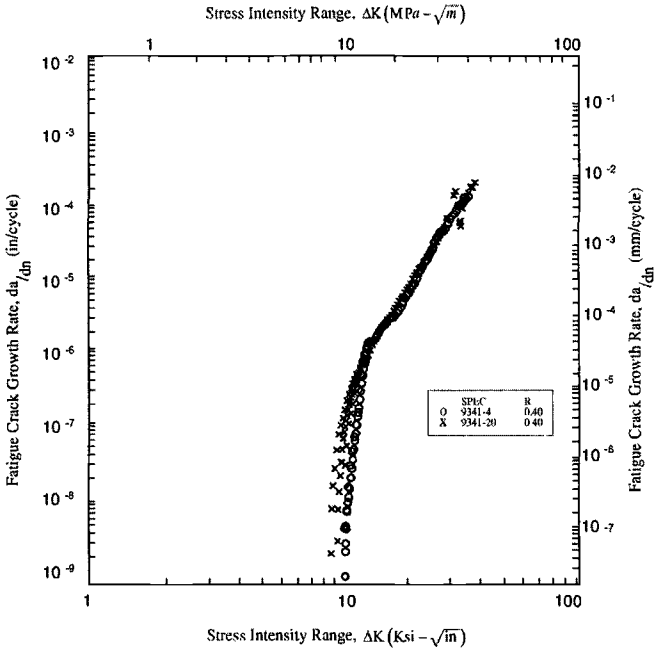


Figure 8 - Plot of fatigue crack growth rates for NAB weld metal in seawater at $R = +0.40$

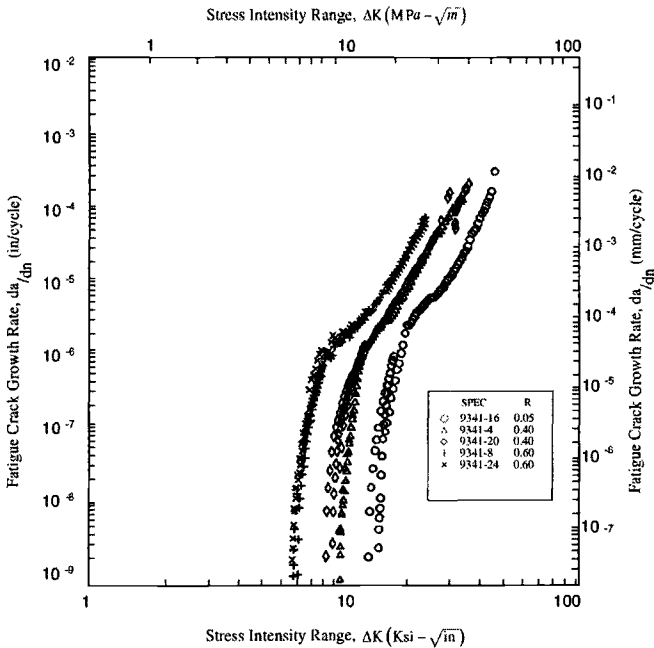


Figure 9 - Comparison of fatigue crack growth rates for NAB weld metal in seawater at three stress ratios based on applied stress intensity-range

Again, the FCGR data shown in (Figure 8) and (Figure 9) included only the K-decreasing portion of the tests. The complete FCGR curves for each test of NAB weld metal, K-decreasing and K-increasing, where curve fit (log-log linear regression analysis) to determine ΔK_{th} and the parameters to the linear, Paris Law crack growth regime for each test. These values from the FCGR tests of NAB weld metal in seawater are summarized in (Table 4). Note again that increasing the stress intensity ratio, R (high mean stress), decreased ΔK_{th} for NAB weld metal in seawater.

Table 4 - Results of fatigue crack growth rate tests of NAB weld metal in seawater

Test Code	Stress Intensity Ratio	FCGR Threshold		Paris Law Parameters	
		(ksi- $\sqrt{\text{in}}$)	(MPa)		
9341-12	+0.05	7.37	8.10	poor correlation	poor correlation
9341-16	+0.05	16.35	17.97	4.107×10^{-15}	6.204
9341-4	+0.40	12.10	13.30	3.121×10^{-14}	6.262
9341-20	+0.40	10.43	11.46	3.009×10^{-13}	5.538
9341-8	+0.60	7.72	8.48	7.017×10^{-12}	4.932
9341-24	+0.60	7.54	8.28	1.349×10^{-11}	4.727
	R	ΔK_{th}		C	n

The same fatigue crack growth-rate curve sets for the duplicate tests of cast NAB in seawater are plotted in (Figure 10) for the condition $R = +0.05$ to compare results based on ΔK_{app} with data corrected for crack closure, i.e. on the basis of ΔK_{eff} . Note that the near threshold stress intensity is significantly decreased when the closure loads are deducted. A summary of the results for cast NAB based on ΔK_{eff} for all loading conditions ($R = +0.05, +0.40, \& +0.60$) is plotted in (Figure 11). Similarly, fatigue crack growth-rate curve sets for the duplicate tests of NAB weld metal in seawater are plotted in (Figure 12) ($R = +0.60$) to compare results based on ΔK_{app} with data corrected for crack closure (ΔK_{eff}). Near-threshold stress intensity was decreased when the closure loads were deducted, and the magnitude of the correction was greater for the weld metal than for the cast NAB. A summary of the results for all tests of NAB weld metal ($R = +0.05, +0.40, \& +0.60$) based on ΔK_{eff} is plotted in (Figure 13).

The values of ΔK_{th} determined from the FCGR tests of cast NAB and NAB weld metal in seawater are summarized in (Table 5). The fatigue crack growth-rate curves for duplicate tests of cast NAB in seawater were analyzed in the near threshold regime to determine ΔK_{th} on the basis of ΔK_{app} . Note that increasing stress intensity ratio, R (high mean stress) decreased ΔK_{th} for NAB and NAB weld metal in seawater. Compared to the values for cast NAB in (Table 5), NAB weld metal tests exhibited higher ΔK_{th} values. The higher crack closure levels in NAB weld metal tests were due to the residual stress in the weldment. When the data were corrected for crack closure, i.e. on the basis of ΔK_{eff} , the near threshold stress intensity decreased. It has been shown that increasing load ratio R

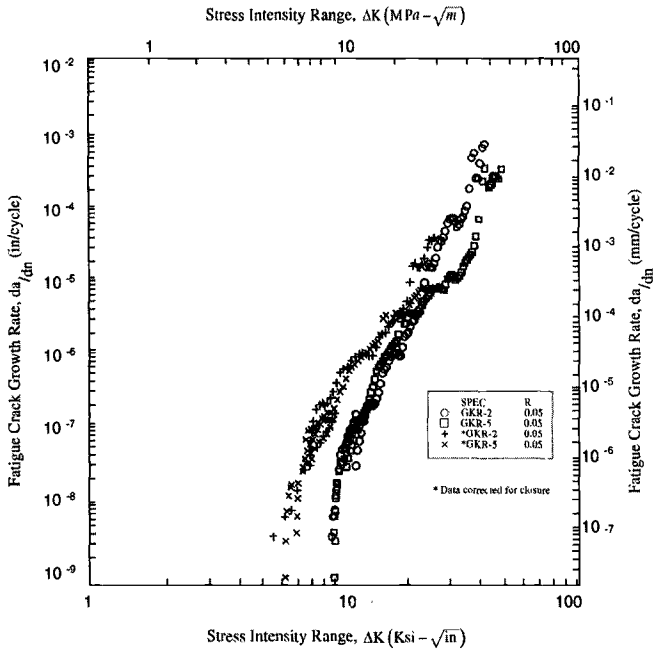


Figure 10 - Plot of fatigue crack growth rates for NAB in seawater at $R = +0.05$ comparing results based on applied stress-intensity versus effective stress-intensity

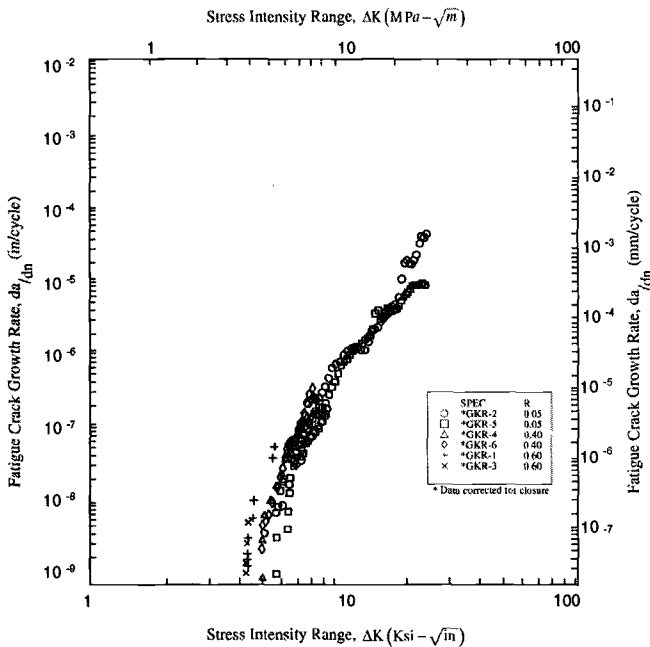


Figure 11 - Comparison of fatigue crack growth rates for NAB in seawater at three stress ratios based on effective stress-intensity range

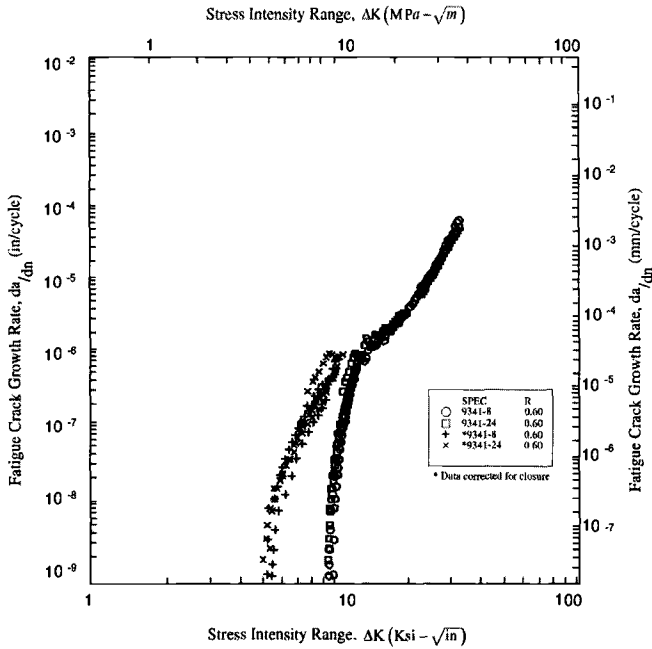


Figure 12 - Plot of fatigue crack growth rates for NAB weld metal in seawater at $R = +0.60$ comparing results based on applied stress-intensity versus effective stress-intensity

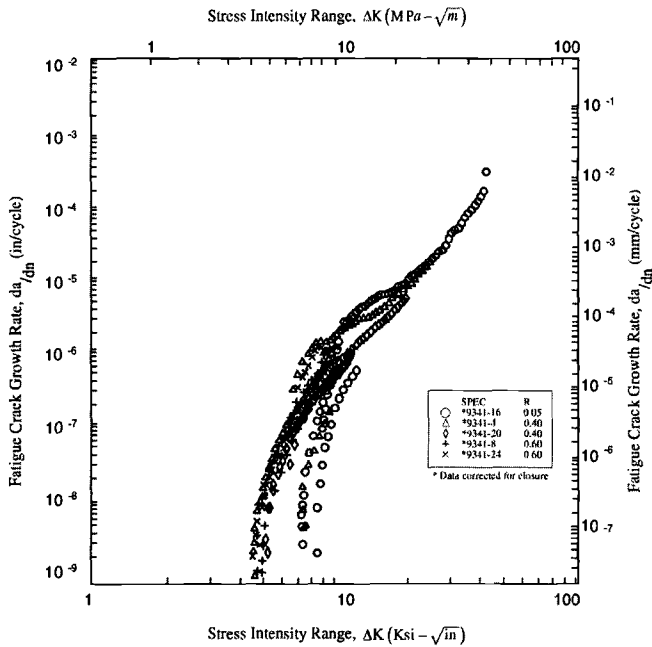


Figure 13 - Comparison of fatigue crack growth rates for NAB weld metal in seawater at three stress ratios based on effective stress-intensity range

reduces $(\Delta K_{th})_{app}$ to a level approaching $(\Delta K_{th})_{eff}$ the “intrinsic” ΔK_{th} of the material [7,8]. Fatigue cycling at high mean load (high R) keeps the crack mouth open and minimizes the factors causing closure effects. It should be noted that the closure-corrected, near-threshold stress intensity, based on ΔK_{eff} , ranged from 4.4 to 6.0 MPa- \sqrt{m} for cast NAB versus 4.4 to 7.5 MPa- \sqrt{m} for NAB weld metal.

Table 5 - Summary of results for fatigue crack growth rate tests of NAB and NAB weld metal in seawater

Test Code	Test Material	Stress Intensity Ratio	Applied FCGR Threshold (MPa- \sqrt{m})	Effective FCGR Threshold (MPa- \sqrt{m})
GKR-2	casting, blade	+0.05	9.32	5.44
GKR-5	casting, hub	+0.05	9.61	6.16
GKR-4	casting, blade	+0.40	6.94	5.06
GKR-6	casting, hub	+0.40	6.57	5.11
GKR-1	casting, blade	+0.60	5.48	4.35
GKR-3	casting, blade	+0.60	5.05	4.27
9341-12	weld metal	+0.05	8.10*	5.63*
9341-16	weld metal	+0.05	17.97	7.48
9341-4	weld metal	+0.40	13.30	5.55
9341-20	weld metal	+0.40	11.46	4.91
9341-8	weld metal	+0.60	8.48	4.61
9341-24	weld metal	+0.60	8.28	4.36

Note: * = Invalid test data due to uneven crack front.

Discussion

NAB Fatigue Crack Growth Rate Database

Ships’ propellers are high-value machinery items. Consequently, studies to determine the corrosion fatigue crack growth properties of NAB alloy have been conducted as the fracture mechanics approach to fatigue crack growth and flaw tolerance developed in order to provide a basis for inspection. Several studies [9-13] presented da/dN versus ΔK data for NAB. However, these did not provide experimental data to specifically determine ΔK_{th} , and the effects of crack closure on ΔK_{th} were not addressed. The results tended to over-estimate values of ΔK_{th} at low R-values. (Table 6) summarizes these data, indicating an estimated ΔK_{th} by extrapolation of the data and the lowest fatigue crack growth rate for which data were plotted.

Table 6 - Summary of estimated and measured fatigue crack growth rate threshold values, ΔK_{th} , for cast nickel-aluminum bronze and weld metal

NAB Casting Type	Test Medium	Cyclic Frequency (Hz)	Load Ratio R	Estimated ΔK_{th} (MPa \sqrt{m})	Lowest da/dN Value Measured (mm/cycle)
cast plate [9]	air	18.3	0.0	8.79	5.0×10^{-9}
prop blade, 0.5R [10]	air	5.0	0.0	8.35	2.0×10^{-8}
prop blade, 0.5R [10]	synthetic seawater	5.0	0.0	7.76	2.0×10^{-8}
cast block [10]	synthetic seawater	5.0	0.0	7.76	1.0×10^{-7}
prop blade, 0.3R [11]	synthetic seawater	6.0	0.0	5.89	2.5×10^{-8}
prop blade, 0.3R [11]	synthetic seawater	1.5	+0.4	5.58	2.0×10^{-8}
prop blade, 0.3R [11]	synthetic seawater	6.0	+0.4	5.58	5.0×10^{-8}
prop blade, 0.6R [12]	synthetic seawater	6.0	+0.4	5.58	2.5×10^{-8}
prop blade, 0.9R [12]	synthetic seawater	6.0	+0.4	7.13	1.3×10^{-8}
cast plate [12]	air	50.0	+0.10	8.49	2.5×10^{-8}
cast plate [12]	air	50.0	+0.28	7.00	7.5×10^{-8}
cast plate [12]	air	50.0	+0.50	6.00	1.0×10^{-7}
cast plate [13]	air	-	+0.20	8.00	-
cast plate [13]	air	-	+0.50	6.00	-

The database for NAB fatigue crack growth rate threshold provides some information regarding the influence of microstructure, cyclic frequency, environment, and mean stress (R-ratio). For comparable FCGR test conditions, threshold values for specimens sectioned from cast plates [9,12,13] were higher than those measured for specimens sectioned from thick cast blocks [10] and from near the root (0.3R) or mid-chord (0.5R to 0.6R) of full-size propeller blades [10,11]. Threshold values for specimens sectioned from near the propeller tip (0.9R) were higher than those for tests of specimens from root or mid-chord from the same propeller [11]. The present studies also suggest the threshold values for specimens sectioned from the blade area were higher than for specimens sectioned from the hub. From these results it may be inferred that the smaller grain size and lesser propensity for casting defects in thinner sections, where cooling rates are greater, increases FCGR threshold of NAB, as with most metals [8].

In those studies where FCGR was measured in air versus seawater [10,12] and the effect of cyclic frequency in the environment was examined [10-12], these factors had greatest influence in Region 2 (power law region), with only a minor effect on threshold values. The effect of frequency on fatigue strength and FCGR was negligible in the frequency range for commercial vessel propeller revolution speeds [11]. The effect of stress ratio on FCGR threshold in seawater was, however, a significant factor identified in most of the experiments [11-13], as well as in the tests of the present study.

Applications of Fracture Mechanics to Propellers

Early applications of fracture mechanics analysis were applied in studies of the fatigue failure of highly loaded propellers. It was shown that fatigue crack growth rates in the full-scale test of a manganese bronze aircraft carrier propeller could be modeled as a semi-elliptical surface crack on the tension side of a plate in bending [9], and showed that very small surface cracks would propagate under the stress measured in at-sea stress trials in the blade root area (0.3R). The measured stresses in the root full-ahead on straight course were 8.5 ksi (58.6 MPa) steady stress \pm 4.25 ksi (\pm 29.3 MPa) alternating stress (or \pm 50% of the mean).

A fracture mechanics analysis was conducted to estimate the crack propagation life in service of a highly-loaded container ship NAB propeller [10], again modeling the propeller blade as the growth of a semi-elliptical, surface crack in a plate bending. In this case, failure occurred from a known initial flaw (6 mm deep by 13 mm long) mid-chord at the root (0.3R), where a stress amplitude = 54.9 MPa at a stress ratio, $R = +0.40$, was estimated for cruising speed. The predicted life of 2 years, 1 month, compared to actual service life of 2 years, 8 months, was good considering the estimations used and the sparse database [10]. For the analysis, ΔK_{th} measured for NAB in seawater of 7.7 MPa- \sqrt{m} at $R = 0$ was reduced by 30% to account for an increased stress ratio of $R = +0.4$ for operating propellers. A value of $\Delta K_{th} = 5.4$ MPa- \sqrt{m} was used, which agreed with values subsequently measured at $R = +0.40$ [11]. The shape of fatigue cracks, tracked by beach marks on the fracture surface of NAB blades which failed in service, showed that the aspect ratio for flaw growth changed from near semi-circular for shallow, near surface flaws to semi-elliptical for deep cracks [10]. The fracture mechanics analyses were extended to provide accept/reject criteria for ultrasonic inspection of ships' propeller blades [14]. For use as UT criteria, the flaw size calculations were used to determine critical flaw detection areas, which were dependent on propeller design, vessel, and design condition [14], since the flaw size calculation was most sensitive to cyclic stress range and blade thickness.

A study on the growth of fatigue cracks from casting defects in NAB [12], showed that defects act as crack initiation sites in sizes as small as 100 μm . Shrinkage cavities were most common in sizes up to 3 mm, but defects smaller than 250 μm being common throughout the casting (see Figures 1 and 2). Cracks deeper than 300 μm were found to obey the same fatigue propagation laws as long, through-cracks [12]. A $\Delta K_{th} = 4.6$ MPa- \sqrt{m} at $R = +0.50$ was determined by reducing data for the effects of frequency

and seawater corrosion, which predicted a smooth bar S-N corrosion fatigue curve for NAB, assuming a flaw of 0.5 mm. Using the same $\Delta K_{th} = 4.6 \text{ MPa}\sqrt{\text{m}}$ at $R = +0.50$ and a “realistic” defect size of 1 mm, a maximum safe operating stress range of 75 MPa for NAB ships’ propellers was suggested [12]. With no safety factors applied, the calculation converted to a maximum stress = 149.6 MPa, mean (steady) stress = 112.4 MPa, and cyclic stress amplitude = $\pm 37.2 \text{ MPa}$ (33% of the mean).

Defect Tolerance Analysis

A fracture mechanics analysis, using the FCGR thresholds of this study, was conducted to determine the propensity for pre-existing casting defects in NAB propellers to propagate by fatigue under cyclic stress in service. Details of the analysis are beyond the scope of this paper, but salient points are summarized in the following.

Propeller Operating Stress and Residual Stress

Steady and alternating stress data for naval and commercial ships’ propellers have been obtained from at-sea trials with instrumented propellers. These are usually conducted to validate loads modeling and new designs, and to investigate service problems [9,10]. In at-sea trials, unsteady stress measurements for commercial vessels [10] ranged from $\pm 29\%$ (tanker) to $\pm 84\%$ of steady stress (cargo ship which experienced two propeller failures).

Propeller design is an iterative process, where an optimization of blade section for propulsive efficiency (thinner blade) and adequate strength (thicker blade) is conducted. For structural design of the propeller blade, the allowable stress used by classification societies (American Bureau of Shipping, Det Norske Veritas, etc.) is based on the minimum tensile strength and density of the propeller material [15]. Fatigue, per se, is not part of the design criteria.

Navy propeller blade design limits the blade stress (mean stress at the full-power ahead, zero-rudder condition) to 12,500 psi (86.2 MPa) for NAB propellers. Although the value of 12,500 psi (86.2 MPa) approximates the seawater corrosion fatigue strength of NAB at 10^8 cycles [16], its use as a design criterion does not directly consider propeller fatigue performance. Service experience with NAB propellers indicates that blade fatigue life is unlimited if the maximum blade steady stress is not more than 12,500 psi (86.2 MPa). The design of Navy propellers has an aim of $\pm 20\%$ of steady stress. However, higher values of unsteady stress magnitude may occur due to greater disturbance to inflow to the propeller than anticipated in design. Although commercial and naval propellers are both designed for a condition of full-power ahead, the usage factors are different. The commercial vessel spends a majority of its total time at sea and at full power in commerce transit. In general, the missions of a naval vessel, especially in peace-time, require infrequent full-power operation.

In the production of large-diameter propellers, the thick sections experience uneven solidification patterns and cooling rates, which may result in residual stresses of significant magnitude. Weld repairs are common on large, rough propeller castings prior to finishing, and stress relief is not required after welding NAB. Residual stress influences crack growth rates and the threshold for crack growth in metals. However, residual stress will be relieved by the application of an external load if local plastic flow ensues. NAB typically exhibits a rounded stress-strain curve with a proportional limit well below the yield strength [17], where local inelastic strain relieves and redistributes residual stress. Experimental studies were conducted on the effects of plug weld repairs on the corrosion fatigue properties of large cast NAB specimens [17]. It was shown that tensile residual stress equivalent to yield occurred in the vicinity of the weld repairs. However, no reduction in fatigue strength due to the weld repairs was found. The applied cyclic stress conditions (patterned after propeller stress conditions), in combination with the high residual stress from welding, caused a “shakedown” effect, wherein the mean stress was reduced to that of the applied condition.

Fracture Mechanics

The analysis considered ΔK_{th} values corrected for crack closure, i.e. on the basis of ΔK_{eff} . This allows the use of a single intrinsic value for the FCGR threshold for any combination of mean stress (R-value) or residual stress. For the analysis, a single conservative value of $(\Delta K_{th})_{eff} = 4.4 \text{ MPa}\sqrt{\text{m}}$ was used. The value was similar to that used in other studies [11,12].

Simplifying assumptions were made to focus on threshold aspects. The stresses on propeller blades are predominantly generated by the bending moment from developed thrust and centrifugal force due to rotational speed on the blade mass. The highly-stressed areas (i.e. the blade root at mid-chord) are thick (15 to 30 cm). A small defect at or near the surface (where the highest stress intensities occur) is essentially in a uniform, tensile stress field, rather than the case for a large, deep crack where the bending case might be more appropriate. Small defects deep in the blade section approach the neutral axis and are much less susceptible to growth. The growth of fatigue cracks in propeller blades, as observed from service failures or controlled laboratory tests, showed initial growth at the surface near the same as into the depth of the blade (semi-circular shape as in a uniform stress field) [10,11]. The types of defects that may occur in propeller castings and weld repairs are as follows: porosity (spherical holes), inclusions, dross or trapped slag (sharp, linear, flake-like defects), and cracks (hot tears, shrinkage cracks, hot shorts, etc.). Defects like shrinkage cavities, slag, and hot tears can have very irregular shapes. In the analysis, handbook stress intensity solutions [18] for four general types of flaws were used: (1) surface-breaking, semi-circular crack (plane strain, tension), (2) surface-breaking, semi-elliptical crack (10 to 1 aspect ratio), (3) embedded circular crack (uniform tension), and (4) embedded elliptical crack (uniform tension).

The results of the fracture mechanics showed that smaller surface-breaking flaws than embedded flaws were required for growth by fatigue. In general, the results show that large surface breaking flaws (easily detectable by NDT methods) are not likely to grow by fatigue if the allowable design conditions of 12,500 psi \pm 20% (86.2 MPa \pm 20%) are not exceeded. Conversely, at higher cyclic stress amplitudes and mean stress, very small flaws, such as those typically present in a large propeller casting, can be expected to propagate by fatigue crack growth. Essentially, ΔK_{eff} for cast NAB was used as the crack-tip stress intensity factor, K_I in the crack models. Computations, then, are of the form of equation (1), with the critical crack size for fatigue crack growth, a , being inversely proportional to the square of the cyclic stress amplitude ($\Delta\sigma$). Thus, unsteady stress amplitude mapping of the propeller was used to generate critical flaw size mapping for NDT. NDT methods and indication accept/reject criteria based on flaw tolerance limit intensive NDT to critical locations. Visual inspection and the good workmanship criteria apply in other areas.

Summary

Fatigue crack growth rate thresholds were determined for cast NAB & weld metal in seawater at cyclic frequency related to ships' propeller operation. Increasing stress intensity ratio, R (high mean stress) decreased ΔK_{th} for NAB and NAB weld metal in seawater. Both cast NAB and NAB weld metal showed large closure loads, particularly at $R = +0.05$. The higher ΔK_{th} and higher crack closure levels in NAB weld metal tests at all test conditions were due to the residual stress in the weldment. When corrected for crack closure effects, the effective ΔK_{th} was reduced. Closure corrected values suggested an "intrinsic" ΔK_{th} of 4.4 to 5.5 MPa- $\sqrt{\text{m}}$.

The results of the NAB corrosion fatigue crack growth rate thresholds were used to conduct a fracture mechanics-based analysis for the defect/flaw tolerance of NAB propellers related to propeller design stress and measured operating stresses.

References

- [1] Underwood, J.H., and W.W. Gerberich, "Concepts of Fracture Mechanics," Chapter 2, *Application of Fracture Mechanics for Selection of Metallic Structural Materials*, J.C. Campbell, W.W. Gerberich, and J.H. Underwood (eds.), American Society for Metals, Metals Park, OH, 1982.
- [2] *AMPCO® Copper and Copper Alloy Weldrod Products*, Bulletin W17-371, Ampco Metal Division, Milwaukee, WI, 1971.
- [3] Saxena, A., and S.J. Hudak, Jr., "Review and Extension of Compliance Information for Common Crack Growth Specimens," *International Journal of Fracture*, Vol. 14, No. 5, October 1978.

- [4] Bucci, R.J., "Development of a Proposed ASTM Standard for Near-Threshold Fatigue Crack Growth Rate Measurement," *Fatigue Crack Growth Rate Measurement and Data Analysis*, ASTM STP 738, S.J. Hudak, Jr., and R.J. Bucci (eds.), American Society for Testing and Materials, Philadelphia, PA, 1981, pp.5-28.
- [5] Donald, J.K., and D.W. Schmidt, "Computer-Controlled Stress Intensity Gradient Technique for High Rate Fatigue Crack Growth Rate Testing," *Journal of Testing and Evaluation*, vol. 6, no. 3, May 1978, pp. 167-174.
- [6] Donald, J.K., "A Procedure for Standardizing Crack Closure Levels," *Mechanics of Fatigue Crack Closure*, ASTM STP 982, J.C. Newman, Jr., and W. Elber (eds.), American Society for Testing and Materials, Philadelphia, PA, 1988, pp. 222-229.
- [7] Taylor, D., *Fatigue Thresholds*, Butterworths & Co., Ltd., London, U.K., 1989, p.43.
- [8] Taylor, D., and L. Jianchun, *Sourcebook on Fatigue Crack Propagation: Thresholds and Crack Closure*, Engineering Materials Advisory Services, Ltd., London, U.K., 1993.
- [9] Gatzoulis, J., W. Werchniak, and E. Czyryca, "Fatigue Behavior of Large Propellers," *Naval Engineers Journal*, October 1974, pp. 65-77.
- [10] Tokuda, S., Y. Okuyama, H. Inoue, and S. Denho, "Fatigue Failure in Marine Propeller Blades," *Propellers '78*, Paper No. 5, The Society of Naval Architects and Marine Engineers, New York, NY, 1979.
- [11] Denho, S., K. Morimoto, I. Nakano, and K. Moriya, "Fatigue Strength in Marine Propeller Blades, Part I. Fatigue Strength of Propeller Materials," *Bulletin of the Marine Engineering Society of Japan*, Vol. 9, No. 2, June 1981, pp. 103-113.
- [12] Taylor, D., and J.F. Knott, "Growth of Fatigue Cracks from Casting Defects in Nickel-Aluminum Bronze," *Materials Technology*, Vol. 9, June 1982, pp. 221-228.
- [13] Pickard, A.C., PhD Thesis, University of Cambridge, 1977.
- [14] Nakano, I., M. Oku, N. Gotoh, K. Moriya, S. Denho, and Y. Sasaki, "Fatigue Strength in Marine Propeller Blades, Part II. Allowable Flaw Size in Propeller Blades," *Bulletin of the Marine Engineering Society of Japan*, Vol. 9, No. 2, June 1981, pp. 114-205.
- [15] Schoenherr, K.E., "Formulation of Propeller Blade Strength," *Transactions of the Society of Naval Architects and Marine Engineers*, Vol. 71, 1963, pp.81-119.

- [16] Czyryca, E.J., and R.B. Niederberger, "Mechanical, Fatigue and Corrosion Properties of Propeller Bronzes," *Propellers '75*, Paper no. 8, Technical & Research Symposium S-4, The Society of Naval Architects and Marine Engineers, New York, NY, 1976.
- [17] Sasaki, Y., N. Hayami, and K. Moriya, "Effects of Welding Repairs on Fatigue Strength of Marine Propellers," *Bulletin of the Marine Engineering Society of Japan*, Vol. 12, No.1, March 1984, pp. 1-12.
- [18] *Stress Intensity Factors Handbook*, Murakami, Y., editor, 2 vols., Pergamon Books, Ltd. Oxford, U.K., 1987.

C. Sarrazin-Baudoux,¹ Y. Chabanne,¹ and J. Petit¹

Mean Stress and Environmental Effects on Near-Threshold Fatigue Crack Propagation on a Ti6246 Alloy at Room Temperature and 500°C

REFERENCE: Sarrazin-Baudoux, C., Chabanne, Y., and Petit, J., “Mean Stress and Environmental Effects on Near-Threshold Fatigue Crack Propagation on a Ti6246 Alloy at Room Temperature and 500°C,” *Fatigue Crack Growth Thresholds, Endurance Limits and Design, ASTM STP 1372*, J.C. Newman, Jr. and R.S. Piasick, Eds., American Society for Testing and Materials, Philadelphia, 2000.

ABSTRACT : The cracking behavior of a Ti6246 alloy under cyclic loading superimposed to different levels of mean stress is studied, with special attention to the near-threshold fatigue crack propagation regime, and to possible coupled effects of corrosion and creep. Tests were conducted at room temperature and 500°C in selected environmental conditions (high vacuum, controlled atmospheric leak low pressure, controlled partial pressure of water vapor in pure argon) and at different frequencies. The near-threshold crack propagation at low K_{max} (i.e. low R ratio) is shown to be highly sensitive to the environment, and a predominant detrimental influence of water vapor is observed, even under very low partial pressure. Conditions for the occurrence of an abnormal behavior consisting in the disappearance of the threshold for sufficiently high K_{max} level, are discussed from tests performed at various constant K_{max} levels in ambient air, high vacuum and humidified argon. This effect is observed in air and in vacuum for K_{max} higher than 52 MPa√m, and is related to an intrinsic creep damage process which appears more efficient at room temperature than at 500°C and more accentuated in air than in vacuum. The origin of this abnormal near-threshold behavior is discussed in comparison with a similar behavior described in the literature at room temperature on another type of Ti6246 alloy and at 120°C on an IMI834. Additional experiments conducted at 500°C in humidified argon have shown a critical K_{max} level reduced to 22 MPa√m. This behavior is suspected to be related to a contribution of stress corrosion cracking induced by water vapor when some conditions favoring a localization of the deformation and the attainment of a critical embrittlement are fulfilled.

KEYWORDS: fatigue, titanium alloys, environment, corrosion, temperature, mean stress crack propagation threshold

¹ Chargée de Recherche CNRS, Research scientist, Directeur de Recherche CNRS, Laboratoire de Mécanique et de Physique des Matériaux - UMR CNRS n° 6617 ENSMA - B.P. 109 - Chasseneuil de Poitou - 86960 Futuroscope Cedex-France

Failure of structural materials operating in various environments due to cracking remains a safety and economic problem despite the effort that has been devoted to understand the phenomena of fatigue, stress corrosion and creep. Titanium alloys are interesting to aerospace designers because of their corrosion resistance, high specific strength and low density. They are often used under cyclic conditions in aggressive environments such as moist air at elevated temperature (up to 600°C). They can also be submitted to the superposition of a constant loading and small amplitude perturbations inducing a too soon fracture of some critical pieces at relatively low K_{\max} levels. Then a detailed characterization of these alloys is required in order to ensure a good damage tolerance during their operational life. Recently a perplexing near-threshold behavior has been reported in the literature for several titanium alloys when the K_{\max} -constant test method [1,2] is used. This experimental procedure is valuable when one wants to determine the threshold value of the effective stress intensity factor range in condition eliminating the contribution of crack closure. The maximum stress intensity factor, K_{\max} , is kept constant, while the minimum, K_{\min} , is gradually increased until the threshold is reached. But when the value is sufficiently high and the fatigue amplitude, ΔK , becomes sufficiently small, the IMI834 tested at 120°C by Marci [1] was found not to exhibit an effective threshold. More recently, similar effect has been observed for Ti-6Al-6V-2Sn, IMI685 and Ti-6Al-2Sn-4Zr-6Mo [2] at room temperature. It is noticeable that this kind of effect has not been detected at room temperature on a nickel-based super alloy IN100 and a 7475 T7351 Al alloy [2] and has been up to now only observed on titanium alloys. In the context of another study of the fatigue crack growth behavior of titanium alloys at elevated temperature, a no threshold effect has been detected by Sarrazin-Baudoux et al. [3] on a Ti6246 alloy tested at 500°C in moist environments evoking a possible interaction between fatigue creep and stress corrosion cracking (SCC) coupled with a detrimental action of water vapor. This last phenomenon refers to ripple loading [4], leading to fracture of structural materials at stress intensity levels very much lower than the static K_{ISCC} threshold.

This paper deals with new developments on the study of the near-threshold fatigue crack growth behavior of Ti6246 alloy under high mean stress levels at room temperature and 500°C, with a special care to potential effects of environment.

Material and Experimental Procedures

The Ti6246 alloy (5.68 Al, 1.98 Sn, 3.96 Zr, 6.25Mo) used in this investigation is β -forged at 950°C. The heat treatment consists of 930°C for two hours, followed by water quenching, aged at 900°C for one hour and air cooled, held at 595°C for a total aging time of eight hours and air cooled.

The alloy contains 75% of α grains and displays a Widmanstätten structure, consisting of intermeshing colonies of α platelets contained in large prior β grains (300 μm), the size of the actual α grains not exceeding 50 μm . The chemical composition and mechanical properties are given in Table 1.

Fatigue crack growth experiments are carried out on Compact Tension C(T) specimens (10 mm thick and 40 mm wide) in accordance with ASTM Test Method for Measurements of Fatigue Crack Growth Rates (E 647-88) using a servo-hydraulic machine equipped with an environmental chamber and a furnace allowing testing in

ambient air, high vacuum (3×10^{-4} Pa) and controlled atmospheres such as humidified argon with controlled partial pressure of water vapor, at temperatures ranging up to 500°C . Crack lengths are tracked using a DC (electrical) potential drop technique [9]. Precracking for all specimens is carried out at room temperature at $R = 0.1$. The crack propagation rate is determined using a shedding procedure of the load which is decreased by steps of 8% down to the threshold, the average crack advance being of 0.1mm. For tests performed at increasing ΔK after threshold, the load is progressively increased by steps of 3 to 5 %. The specimens are submitted to sinusoidal loading at frequencies varying from 35 Hz to 10^{-3} Hz with a load ratio (R) of 0.1 or at variable R. Crack closure is detected using a capacitive displacement gauge and determined by means of the offset compliance technique [5,6]. K_{\max} -constant tests for near threshold propagation are conducted at increasing steps of K_{\min} , the decreasing steps of ΔK being similar as for the constant R tests. However, it should be noticed that each shed portion was R constant, K_{\max} variations being lower than ± 1.0 %. In such condition, K_{\min} is at any time higher than the stress intensity level for crack closure and so closure is eliminated in all the explored range. Some additional dwell waveforms are used at 500°C in air with 10 seconds rise and fall time and hold periods of 90 seconds and 180 seconds or without hold time (triangular signal of 10s-10s).

The environmental effect is studied with complementary experiments performed in various gaseous atmospheres controlled by mean of a mass spectrometer and high performance hygrometers. On one hand, the partial pressure of water vapor can be lowered by reducing the total pressure : high vacuum, medium vacuum I; on the other hand, an atmospheric environment saturated with water vapor and with a very low amount of oxygen is obtained by mean of a controlled leak connecting the chamber to an input of humidified argon containing water vapor at a partial pressure around 100 Pa.(medium vacuum II). For the different environmental conditions used, the partial pressures of oxygen and water vapor are given in Table 2.

Table 1 – Mechanical properties of Ti6246

Temperature	σ_y (Mpa)	σ_u (Mpa)	A%	K_{IC} (Mpa $\sqrt{\text{m}}$)	E (Gpa)
Room T	987	1098	10.2	75	122
425°C	727	859	14.6	–	106
500°C	680	800	–	–	102

Table 2 – Environmental conditions for propagation tests

Environments	Partial pressure	Partial pressure	Partial pressure	Total pressure(Pa)
	H ₂ O (Pa)	O ₂ (Pa)	N ₂ (Pa)	
Ambient air	1300	2×10^4	8×10^4	10^5
Humidified argon I	1300	< 1	–	10^5
Humidified argon II	3000	< 1	–	10^5
Medium vacuum I	1	–	–	1.33
Medium vacuum II	100	–	–	133
High vacuum	$< 2 \times 10^{-4}$	$< 10^{-6}$	–	3×10^{-4}

Influence of Environment at Low Mean Stresses.

A conventional approach of the study of the near-threshold fatigue crack propagation (FCP) is based on experiments conducted at $R=0.1$, and the effective propagation is determined by mean of closure correction. More recently, K_{max} constant tests have been recommended to reach directly the effective behavior without closure correction which can be more or less controversial [7], especially when interaction can occur between closure and environment, for example when there exists a competitive influence of closure induced by oxide wedging and a limitation of the access of the embrittling species (i.e. water vapor molecules) up to the crack tip by oxide deposits [8], or an activation of environmental embrittlement by rupture of the oxide film induced by closure as observed on Ti alloys at 500°C [9]. However, as mentioned here above, when K_{max} becomes too high, some abnormal behavior can occur. Hence, in this section, are considered effective data provided by tests with closure correction where closure-environment interaction are not observed, or by tests performed at sufficiently low K_{max} level to avoid any influence of mean stresses.

The da/dN vs ΔK_{eff} diagram plotted in Figure 1a for tests performed at room temperature at a frequency of 35 Hz shows that for tests run at K_{max} lower than $47 \text{ MPa}\sqrt{\text{m}}$ there is no influence of the mean stress level on the effective behavior and that data provided by K_{max} -constant tests or obtained after closure correction from tests at $R=0.1$ are comparable. This validate the compliance offset technique used to detect closure. To illustrate the influence of environment on the fatigue crack propagation

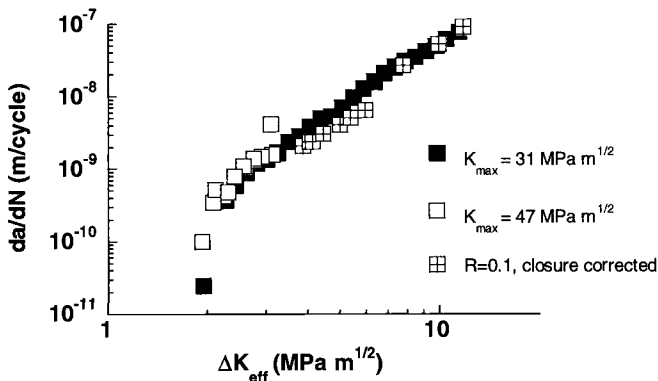


Figure 1a – da/dN vs ΔK_{eff} relation in ambient air at room temperature at 35 Hz.

behavior at room temperature, (da/dN) is plotted with respect to ΔK_{eff} in Figure 1b for tests performed at constant $K_{max} < 47 \text{ MPa}\sqrt{\text{m}}$ at room temperature in air, high vacuum and humidified Argon I which contains a same partial pressure of water vapor of 1.3 kPa as that in air (see Table 2). The test frequency is 35 Hz. In all the explored range, the propagation rates in ambient air and in humidified Argon are similar and are four times faster than in high vacuum at a given ΔK_{eff} range, supporting a comparable effect of both gaseous environments. This effect has been related to a detrimental effect of water vapor as evoked in the literature[11].

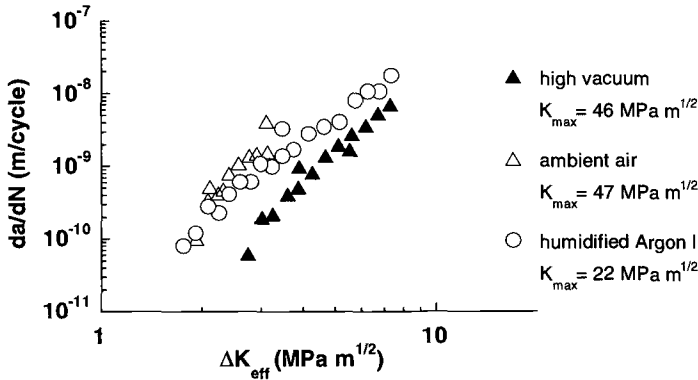


Figure. 1b – da/dN vs ΔK_{eff} relation in high vacuum, ambient air and humidified argon I at room temperature at 35 Hz.

Results of tests performed at 500°C are shown on Figure 2 where data in moist argon II are compared to those obtained in air and high vacuum. The propagation is shown to be slightly faster in moist Argon than in air, and, in comparison to high vacuum, both environments exhibit a huge enhancement of the growth rates especially in the near-threshold domain, i.e. below a plateau range which is absent in high vacuum. These observations are in accordance with a great sensitivity of the response of the material to the environment at 500°C [9] and support a predominant effect of water vapor. The

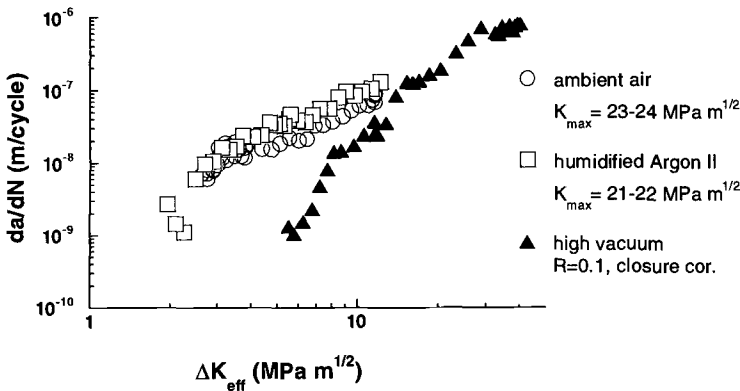


Figure 2 – Effective fatigue crack propagation in Ti6246 alloy at 500°C in air, high vacuum and humidified Argon II (35 Hz).

influence of the test frequency was explored in air, by mean of tests performed in condition without closure (constant K_{max} tests, $30 \text{ MPa}\sqrt{\text{m}}$) at frequencies ranging from 35 Hz to 0.1 Hz (Figure 3). Only a slight acceleration is observed at 3.5 Hz while the growth rates reach an order of magnitude of acceleration at 0.5 Hz and 0.1 Hz. Crack

growth data with a triangular loading at 0.05 Hz and trapezoidal loading with dwells of 90 s and 180 s support a saturation of the effect of environment for frequencies lower than 0.5 Hz. Such environmentally assisted crack propagation regime can be described by a relation in accordance with the following model initially proposed by McClintock [10]:

$$da/dN = 0.5 \Delta CTOD$$

where $\Delta CTOD$ is the crack tip opening displacement range. Such behavior is in accordance with the saturation of the process and is more consistent with a corrosion-fatigue mechanism than a creep-fatigue mechanism.

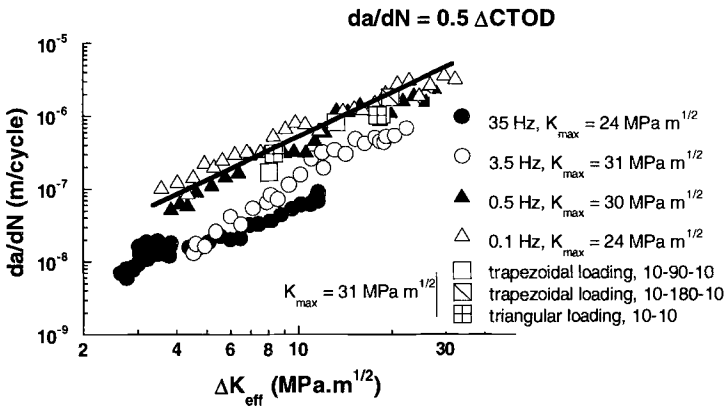


Figure 3 – Influence of test frequency and of dwell time on effective crack propagation in air at 500°C.

To explore more precisely the kinetics of the effect of water vapor, tests were run under low pressure and at very low frequencies (Figure 4). A first experiment was

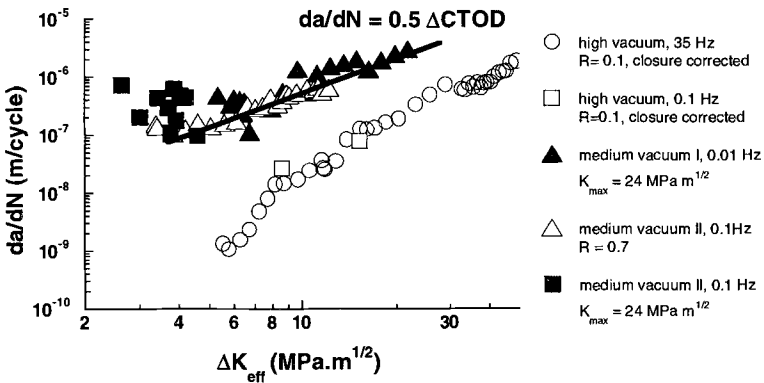


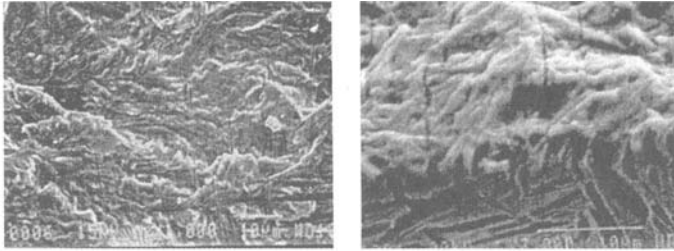
Figure 4 – Influence of low pressure of water vapor and test frequency on effective fatigue crack propagation at 500°C.

performed under a low vacuum obtained by mechanical pumping giving a total pressure of 1.3 Pa. The partial pressure of oxygen was below the detection threshold of the analyzer while that of water vapor was of 1 Pa. The data of the test performed at 0.01 Hz fall within the scatterband of the tests in air at 0.5 Hz and 0.1 Hz and appear to be consistent with the saturated corrosion-fatigue mechanism described above. In contrast, a frequency of 0.1 Hz has no effect on the propagation in high vacuum. Another test was performed in medium vacuum II (total pressure of 133 Pa, partial pressure of water vapor of about 100 Pa and oxygen not detectable). The tests performed at a stress ratio R of 0.7 (no closure) and at 0.1 Hz give the same result as under a pressure of 1.3 Pa at 0.01 Hz (medium vacuum I, see Fig. 4) and in air at frequency lower than 0.5 Hz (Fig. 3). These two experiments are very convicting for the detrimental effect of water vapor which is shown to be active even under very low partial pressure and in absence of any detectable traces of oxygen. This effect of water vapor has also been reported in the literature for titanium alloys, but only at room temperature [11,12]. The critical exposure as previously defined [11] can be estimated about 10^{-2} Pa.s and the substantial enhancement of the growth rates of the saturated regime can be attributed to the adsorption of water vapor on freshly created surfaces at the crack tip [13-15] followed by an unknown embrittling mechanism.

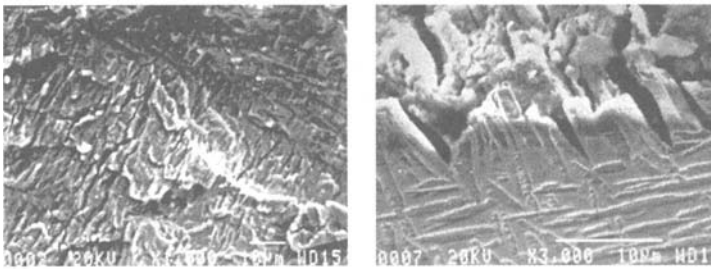
The test in medium vacuum II ($P_{H_2O}=100$ Pa) was continued at a constant K_{max} of 24 $MPa\sqrt{m}$ in view of an evaluation of the threshold for crack propagation. Exploring the ΔK range from 4 $MPa\sqrt{m}$ to 2 $MPa\sqrt{m}$, a substantial scatter in the rate measurements was observed, but no threshold was attained, and even without clean cut evidence, the crack growth seemed to become independent on the ΔK range. Such behavior could be in accordance with the predominance of a mechanism of propagation controlled by K_{max} instead of ΔK which could be controlled by a creep or a stress corrosion cracking process. This aspect is explored and discussed in the following.

The fracture surfaces given in Figure 5 are representative of the corrosion-fatigue process found on the Ti6246 in humidified argon II, air and medium vacuum I. For the three environments, FCP produces flat surfaces corresponding to a transgranular stage II propagation and numerous. Microcracks, which are present in all the cases, seem associated to the coupled action of temperature [16] and water vapor. The most significant feature is the difference of the microcracks morphology with respect to environment. In medium vacuum I, the microcracks are parallel to the propagation direction while they are perpendicular in humidified argon and in air. Specimen have been sectioned, parallel to the propagation direction, to reveal the correlation between the microstructural features and the subsurface microcracks (Figure 5). In air, the section plane shows that microcracking proceeds along α laths and seems to be associated with oxidation, while in humidified argon, the microcracks have a more brittle appearance and seem to be independent on microstructure. In medium vacuum I, microcracks can not be observed because they are parallel to the section plane. In humidified argon and in air, both surfaces are respectively covered with blue and yellow oxide layers but are generally free of oxide debris. In medium vacuum I, little oxide is present. But whatever these differences in the surface morphology, the FCP rates are quite similar (especially in medium vacuum I and in air). This is consistent with previous studies [17] which establish that surface oxide films are not damaging. All these results support that, as compared to high vacuum, even if fracture surfaces have a typical morphology for each

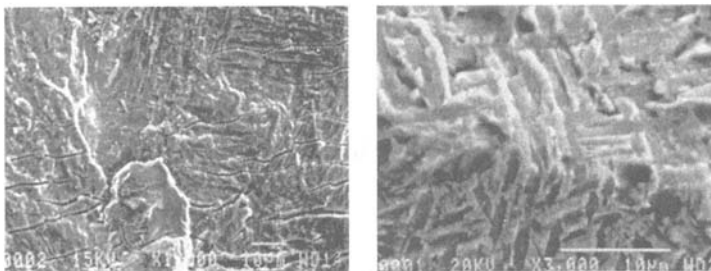
environment, water vapor constitutes the active specie that is responsible for the great enhancement of growth rates observed in the mid-rate range.



(a) Humidified Argon II



(b) Ambient air



(c) Medium vacuum I

Figure 5 – Microfractographic aspect of cracked surfaces at 500°C in the corrosion-fatigue regime : (a) Humidified Argon (0.1 Hz), (b) Ambient air (0.1 Hz), (c) Medium vacuum I (0.01 Hz). The crack propagation direction is from the left to the right

Influence of the mean stress on the FCP behavior

Room temperature

Crack growth data for tests conducted at room temperature in ambient air and in high vacuum are given in Figures 6a and 6b respectively. Five K_{max} levels were tested in air and three levels in high vacuum. For stress intensity factor ranges, ΔK , higher than 3 $\text{MPa}\sqrt{\text{m}}$ in air (Figure 6a) and 5 $\text{MPa}\sqrt{\text{m}}$ in vacuum (Figure 6b), the crack growth rate da/dN appears independent on K_{max} and all data fall within the same scatter band. At lower ΔK ranges and for K_{max} levels lower than 47 $\text{MPa}\sqrt{\text{m}}$, a threshold is obtained with a value close to 2 $\text{MPa}\sqrt{\text{m}}$ in air and 3 $\text{MPa}\sqrt{\text{m}}$ in vacuum. But above $K_{max} = 52 \text{ MPa}\sqrt{\text{m}}$,

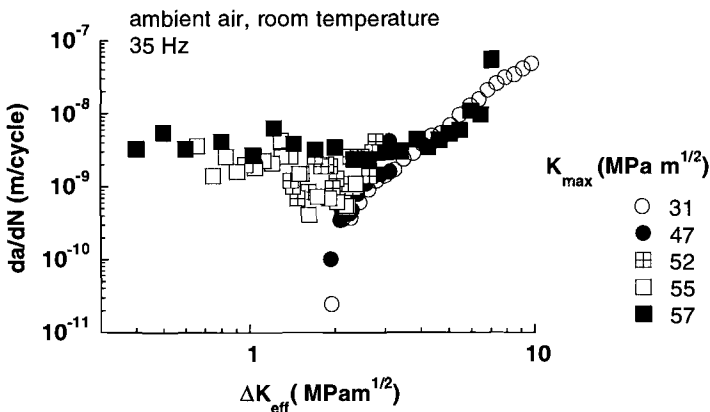


Figure 6a – Fatigue crack propagation in ambient air at room temperature for different K_{max} levels (35 Hz).

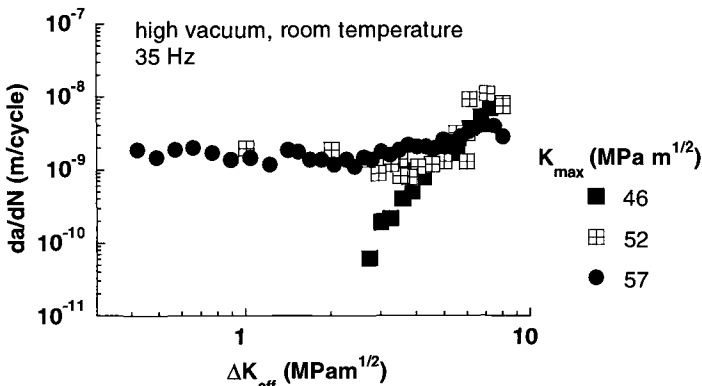


Figure 6b – Fatigue crack propagation curves in high vacuum at room temperature for different K_{max} levels (35 Hz).

an abnormal near-threshold behavior is observed, and, in both environments, the growth rate becomes independent on ΔK and lays around 3×10^{-9} m/cycle in air and 10^{-9} m/cycle in vacuum. These results confirm the existence in ambient air of an abnormal near-threshold behavior as recently detected by Marci [1] and Larsen and co-authors [2]. In the figure 7 are compared data exhibiting this abnormal behavior in different Ti alloys. It is of importance to notice the similitude of the response of the different materials but also the difference in the K_{max} levels at which this phenomenon is observed. Furthermore, data in high vacuum also demonstrate its existence in an inert environment, supporting that this phenomenon is associated with an intrinsic governing mechanism. In Figure 8, data in air and in vacuum are compared at two K_{max} levels of 46–47 MPa \sqrt{m} and 57 MPa \sqrt{m} . At 47 MPa \sqrt{m} , where a threshold is obtained, the effect of environment leads to crack propagation rate in air which can be one order of magnitude higher than in high vacuum for a same fixed ΔK_{eff} . The threshold value close to 2 MPa \sqrt{m} in air is lower than that in high vacuum which is of 2.8 MPa \sqrt{m} . At $K_{max} = 57$ MPa \sqrt{m} , where the steady regime is established, the growth rate appears to be slightly faster in air than in vacuum, which indicates a lower assistance of environment to the cracking process.

- Ti6246, 47 MPa m^{1/2}
- Ti6246, 57 MPa m^{1/2}
- ▲ IMI 834, 32 MPa m^{1/2}, Ref. (1)
- △ IMI 834, 28 MPa m^{1/2}, Ref. (1)
- Ti-6Al-6V-2Sn, 32 MPa m^{1/2}, Ref. (1)
- ▣ Ti-6Al-6V-2Sn, 28 MPa m^{1/2}, Ref. (1)
- Ti-6Al-6V-2Sn, 25 MPa m^{1/2}, Ref. (1)
- ▽ IMI 685, 46 MPa m^{1/2}, Ref. (1)
- ▼ IMI 685, 48 MPa m^{1/2}, Ref. (1)
- + Ti6246, 22 MPa m^{1/2}, Ref. (2)

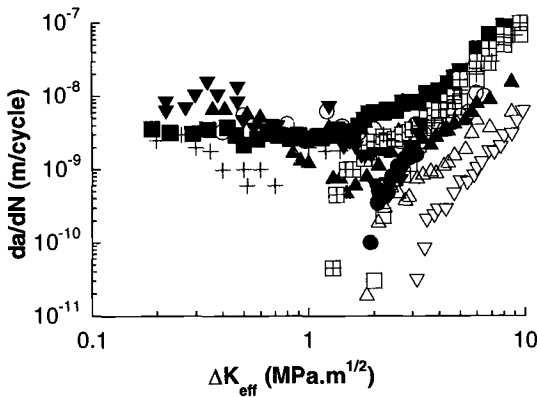


Figure 7 – Comparison of fatigue crack propagation rates in titanium alloys presenting the abnormal near-threshold behavior at room temperature in ambient air.

In all cases, including literature, the abnormal crack growth effect occurs roughly around 70% of the fracture toughness. As it has been evoked, the explanation of this

abnormal behavior could be related to room temperature creep which is a well-known phenomenon in titanium alloys [2].

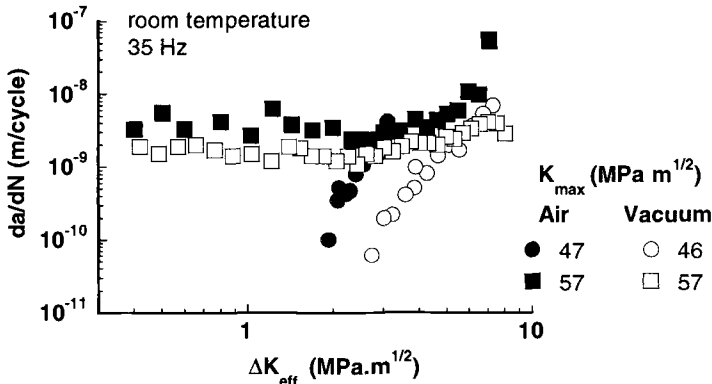


Figure 8 – Comparison of crack propagation curves in air and high vacuum at room temperature for $K_{max} = 46-47 \text{ MPa}\sqrt{\text{m}}$ and $57 \text{ MPa}\sqrt{\text{m}}$ (35 Hz).

The potential influence of creep has been investigated by performing K-constant test without cycling between two steps of ΔK shedding, the sustained stress intensity factor being equal to the K_{max} level of the former fatigue step. When such constant loading sustain is applied during testing in the mid ΔK range, the crack does not propagate. But when it is applied below a critical ΔK range, (which means when the so called abnormal behavior is reached), it results in a crack advance which was recorded along an extension of about 0.1 mm. Measurements of the propagation rate with respect to time, da/dt , are plotted in Figure 9 for tests conducted in air and in high vacuum. An example of recording of the evolution of the potential drop corresponding to the crack advance is presented in Figure 10. It can be clearly observed that the growth rate during the period of cycling and during the period of constant K sustain is comparable. These observations demonstrate that below a certain ΔK range and for a given environment, the crack advance becomes only controlled by the maximum level of the stress intensity factor and hence results mainly from a creep damage process. Lang et al. [2] have investigated a series of tests with intermittent unloading cycles ($K=0 \text{ MPa}\sqrt{\text{m}}$) during the K_{max} -constant test in order to see if once the abnormal occurs, the crack growth rate interacting with plasticity decreases or even stops. They have shown that, introducing single or multiple unloading cycles does not affect the propagation which continues approximately at the previous growth rate. Then, these tests support that the abnormality does not depend on the loading history characteristic of the K_{max} -constant test when the process is initiated. Their conclusions are in contradiction with the present results which show a load history dependence with a critical ΔK range in addition to a critical K_{max} level.

However, at such low ΔK ranges and low growth rate, the real influence of single or few underloads is not obvious and an increment of crack advance could be required to have a substantial load history effect which means the application of a much larger number of underloads.

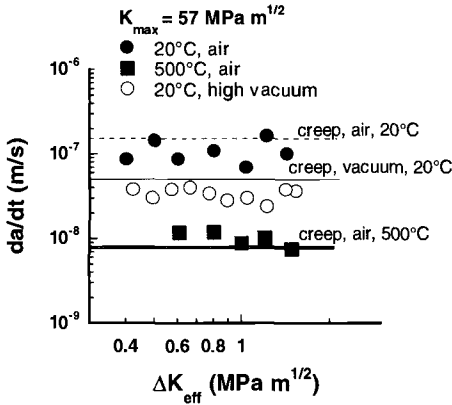


Figure 9 – Comparison of growth rates (in meter per second) at $K_{max} = 57 \text{ MPa}\sqrt{\text{m}}$ in fatigue at ΔK lower than $1.5 \text{ MPa}\sqrt{\text{m}}$ and under sustained loading.

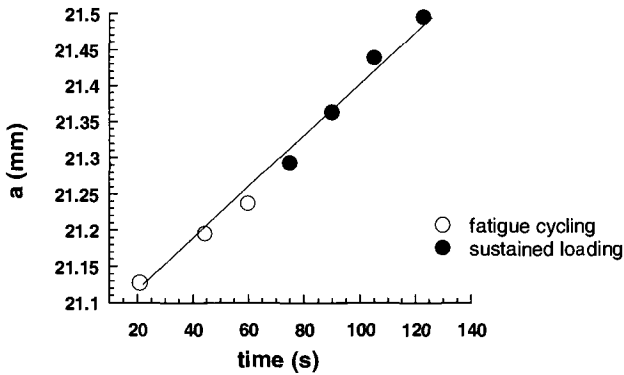


Figure 10 – Evolution of crack advance versus time during cyclic and sustained loading for a test run at in high vacuum at room temperature and at $K_{max} = 57 \text{ MPa}\sqrt{\text{m}}$.

It can be observed in the Figure 11 a that the crack path is not the same for the creep-fatigue regime and the pure creep regime. In the first case, the crack develops continuously in the plane normal to the loading axis. When cycling is stopping, the development of two wings corresponding to the monotonic plastic deformation is observed, and then the crack is growing within one of the two wings hence following the zone where shearing is assumed to be maximum. So, when the test is switching from one regime to the other, some transitional local retardation or acceleration can be observed

when the crack tends to change from one kind of path to the other, even if the average growth rate is not substantially affected.

The morphology of the fracture surfaces of the specimen of figure 11a is shown in figure 11b fatigue regime, and in figure 11c for the abnormal regime. The fatigue crack path is very flat and corresponds to a transgranular faceted cracking process typical of a stage II regime which is poorly sensitive to microstructure. Conversely, the fracture surface of the abnormal regime is mixing transgranular and intergranular cracking (fig. 11c), and is characterized by the formation of dimples shown at higher magnification (fig. 11d) typical of a process of static rupture and supporting a predominant creep mechanism.

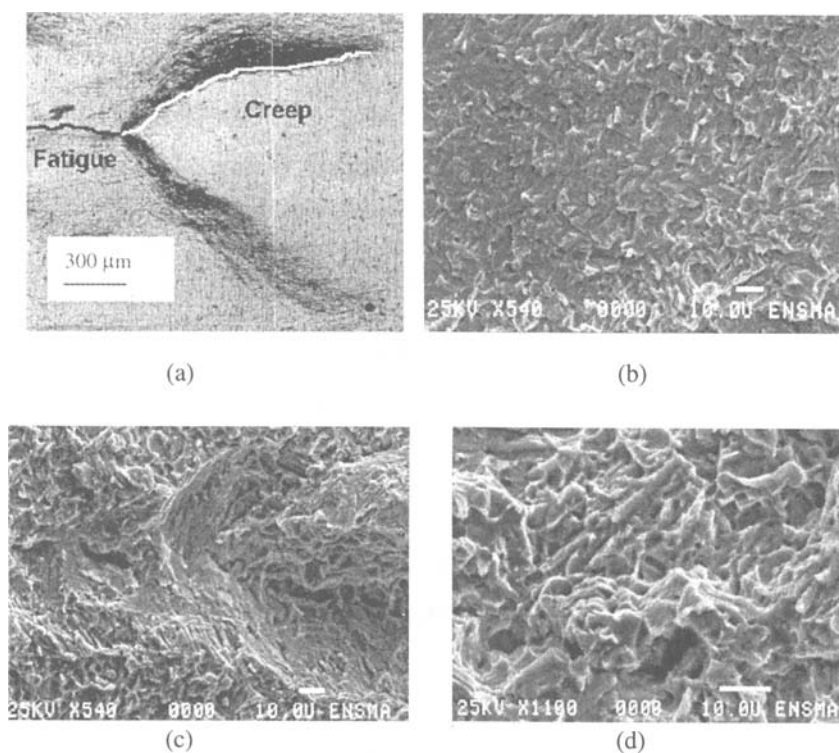


Figure 11 – (a) *Photography of the surface of a specimen tested in air at room temperature at $K_{max} = 55 \text{ MPa}\sqrt{\text{m}}$, comparing the crack path in fatigue ($\Delta K = 2.0 \text{ MPa}\sqrt{\text{m}}$) and under sustained loading.* (b) *Microfractographic aspect of the fracture surface in the fatigue regime of Figure 11a.* (c) *Microfractographic aspect of the fracture surface in the creep regime of Figure 11a.* (d) *: magnification of Figure 11c) showing dimples associated to constant $-K$ loading. The crack propagation direction is from the left to the right.*

High temperature

Figure 12 shows the da/dN - ΔK data of the tests conducted at 500°C in air and in high vacuum with $K_{max} = 46, 55$ and $57 \text{ MPa}\sqrt{\text{m}}$. In high vacuum, no K_{max} effect is observed and the propagation curves are very similar with a threshold ranging about $3 \text{ MPa}\sqrt{\text{m}}$. In ambient air, for K_{max} ranging up to $55 \text{ MPa}\sqrt{\text{m}}$, crack growth rates are comparable, and hence independent on K_{max} . A substantial effect of environment is observed especially in the low ΔK range with rates of two orders of magnitude higher than those in high vacuum (at $\Delta K_{eff}=3.5 \text{ MPa}\sqrt{\text{m}}$, $da/dN=10^{-10} \text{ m/cycle}$ in vacuum and 10^{-8} m/cycle in air), and a much lower threshold value close to $2 \text{ MPa}\sqrt{\text{m}}$. Such enhancement of the propagation in air at 500°C has been related to an environmental effect very much more pronounced at elevated temperature than at room temperature [9]. The abnormal behavior is detected in air and at K_{max} of $57 \text{ MPa}\sqrt{\text{m}}$ with a steady crack growth ranging about 3 to $4 \times 10^{-9} \text{ m/cycle}$. A comparison of the response of the material at room temperature and 500°C, in air and high vacuum at $K_{max} = 57 \text{ MPa}\sqrt{\text{m}}$ is shown in Figure 13. The surprising result is related to the steady crack growth in air at 500°C of $4 \times 10^{-9} \text{ m/cycle}$ which is much lower than the rate measured at room temperature as well in air as high vacuum in the same loading conditions.

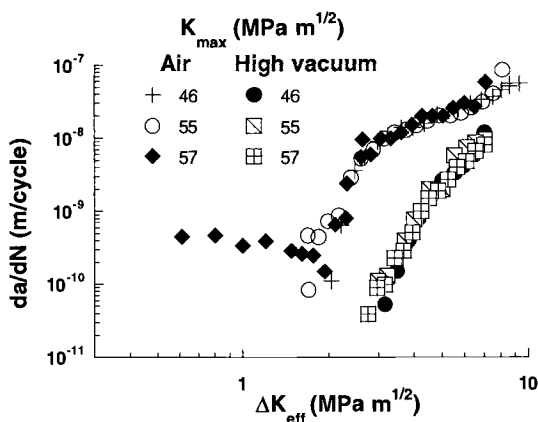


Figure 12 – Comparison of crack propagation curves at 500°C in air and in high vacuum and for K_{max} ranging from $46 \text{ MPa}\sqrt{\text{m}}$ to $57 \text{ MPa}\sqrt{\text{m}}$ (35 Hz).

It is difficult to explain a less accentuated abnormal behavior at 500°C than at room temperature since an enhanced creep contribution would be expected at elevated temperature. However such behavior could result from a shearing process of the α phase as evoked for fatigue dwell effect [17] at low temperature, and the contribution of this mechanism could be reduced at elevated temperature with increasing ductility.

In the upper ΔK range, temperature does not significantly affect the crack propagation in high vacuum but induces a substantial enhancement of the rates in air. Such detrimental effect has been related to a water vapor assistance to the propagation mechanism [3,8,18].

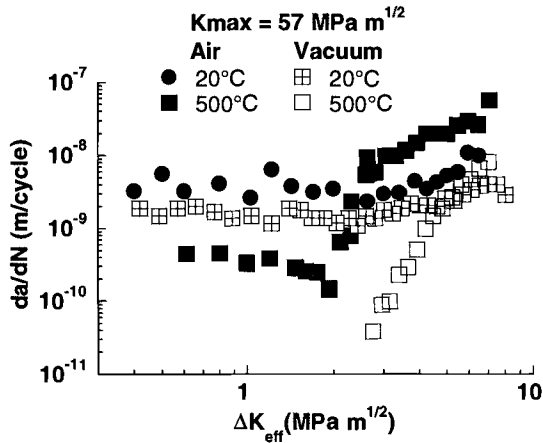


Figure 13 – Comparison of crack propagation curves in air and in high vacuum at room temperature and 500°C and for $K_{max} = 57 \text{ MPa}\sqrt{m}$ (35 Hz).

Humidified Argon.

To investigate a possible detrimental effect of water vapor on the mean stress effect, tests were performed in humidified argon I. Corresponding crack growth data are compared to those in air at room temperature and 500°C in Figure 14. For tests run at

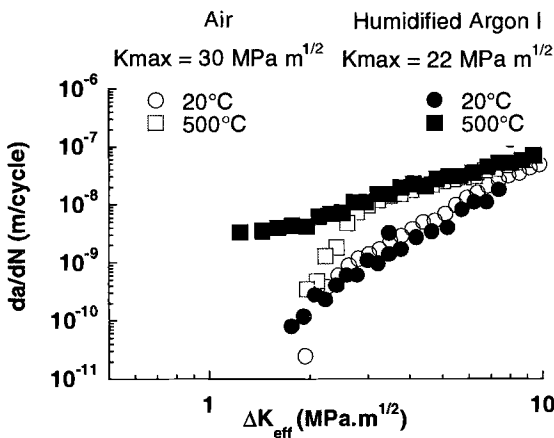


Figure 14 – Comparison of fatigue crack propagation in air and in humidified Argon I at low K_{max} levels, at room temperature and 500°C (35 Hz).

room temperature at relatively low K_{max} levels, both environments give similar crack growth data with an effective threshold ranging about 1.8 to 2 MPa \sqrt{m} , which is consistent with a comparable detrimental effect of water vapor in both environments. At

500°C, a comparable behavior is again observed in both environments for ΔK above 2 MPa√m, but for lower ΔK range, an abnormal behavior is detected in moist Argon I at a critical K_{max} level which is only of 22 MPa√m and is characterized by a sustained crack growth rate greater than 2×10^{-9} m/cycle. It is of importance to notice that the partial pressure of water vapor in the argon gas filling the chamber is comparable to that of laboratory air (see Table 2). So, the same amount of water vapor in a neutral gas appears to be much more detrimental than in air. This would support that oxygen contained in air is more preventing the detrimental effect of water vapor than being a detrimental gaseous specie.

In Figure 15 are collected all data obtained at 500°C in the three test environments : three K_{max} levels in air, two K_{max} levels in high vacuum and K_{max} of 22 MPa√m in humidified argon II. This diagram clearly shows that in humidified argon and at a very much lower K_{max} value than in air, an abnormal behavior is detected with a sustained crack growth rate which is of one order of magnitude higher than in air at 57 MPa√m.

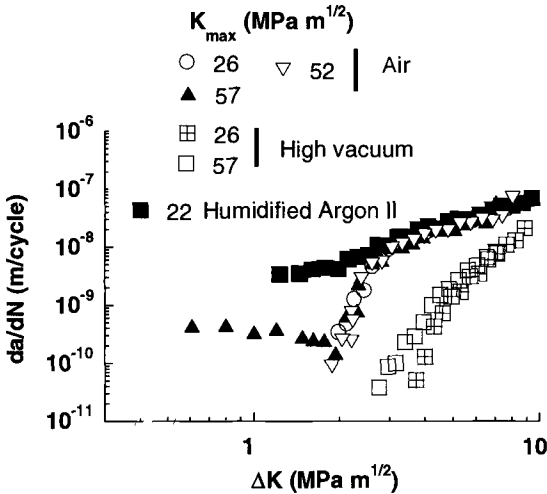


Figure 15 – Influence of environment on the occurrence of the abnormal near threshold behavior at 500°C (35 Hz).

Such an effect is associated to a mechanism which should be different from the creep process operating in air and in high vacuum. It could be a stress corrosion cracking mechanism induced by water vapor which appears much more enhanced in the absence of oxygen. To reinforce this assumption, tests were conducted in argon containing a great amount of water vapor (humidified argon II, see Table 2), the partial pressure of water vapor being 3 kPa. Figure 16 gives an illustration of the response of the material submitted to different loading conditions. A threshold test run at 35 Hz and a constant K_{max} of 21 MPa√m seems to lead to a threshold for a stress intensity factor range at about 2.3 MPa√m. But further steps in the decreasing of ΔK do not confirm the existence of a threshold and even more, exhibit a re-acceleration of the crack propagation. Such a behavior is comparable to that described in the above section and is

consistent with a substantial K_{max} effect. In the same figure, are compared crack growth data obtained at 0.1 Hz and at a R ratio of 0.1 (very low K_{max} ranging from 6 to 12 MPa√m), and at R=0.9 (high K_{max} ranging from 21 to 55 MPa√m). Crack growth rates for the tests conducted at R of 0.1 and at 0.1 Hz follow the saturated fatigue corrosion regime previously identified. But, operating at higher R ratio, which means much higher mean stress levels, a substantial acceleration is detected. These results also demonstrate a huge influence of the mean stress and suggest the existence of an additional mechanism of stress corrosion cracking at $K_{max} < 57 \text{ MPa}\sqrt{\text{m}}$.

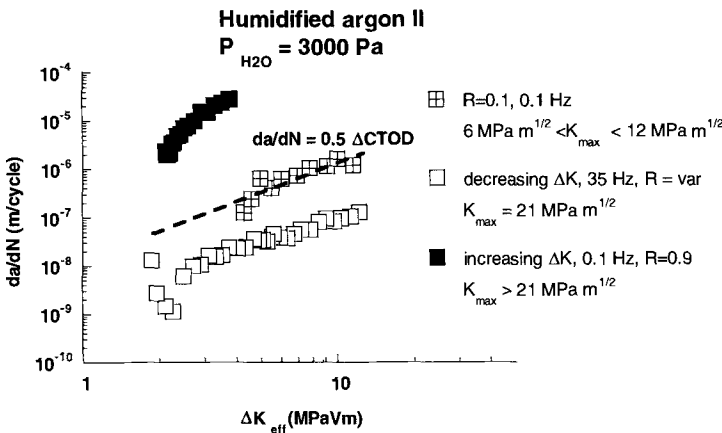


Figure 16 – Influence of loading conditions on the effective crack propagation at 500°C in humidified argon II

Figures 17a and b show crack profiles obtained in humidified argon II. On the first hand is illustrated a situation when fatigue-corrosion cracking is dominating (Figure 17a, R=0.1, 0.1 Hz), and on the second hand when stress corrosion cracking is expected (Figure 17b, R=0.9, K_{max} =21-24 MPa√m). In the former case, the crack path is mainly flat without secondary cracking,

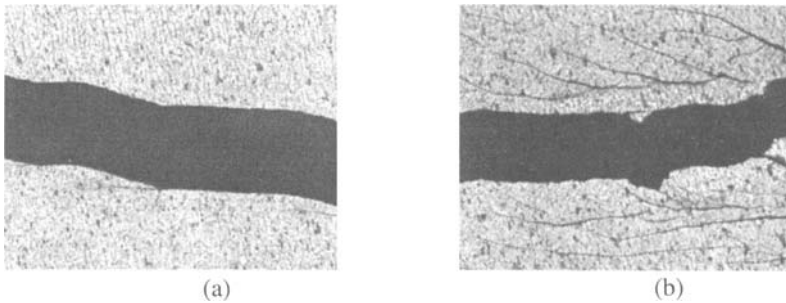


Figure 17 – Crack profiles in humidified Argon at 500°C II : (a) fatigue corrosion cracking, (b) stress corrosion cracking.

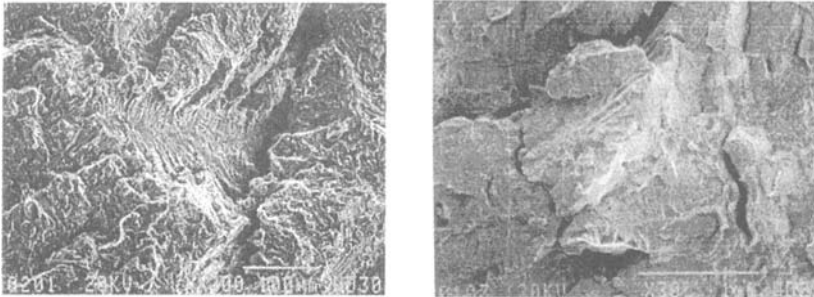


Figure 18 – Cracked surfaces for stress corrosion cracking in humidified argon II at 500°C.

while in the second case, the crack path is very tortuous with the presence of numerous secondary cracks and related branching supporting a huge embrittlement induced by water vapor [20,21]. The cracked surface corresponding to stress corrosion cracking process (Figure 18) shows very rough areas with intergranular decohesion at the prior- β grains which might be in accordance with a strong embrittlement of grain boundaries by water vapor which is not observed in air (i.e. in presence of oxygen).

Conclusions

The following conclusions can be drawn from this study of the fatigue crack growth behavior of the Ti6246 alloy :

- A substantial crack growth rate enhancement is obtained in air versus high vacuum in the near-threshold range and appears more pronounced at 500°C than at room temperature. From tests performed in controlled environments, the loss of crack propagation resistance in air has been attributed to a deleterious effect of water vapor.
- At 500°C, by mean of tests at various frequencies and under different partial pressures of water vapor, a corrosion-fatigue crack propagation regime has been identified. At saturation of the effect of water vapor, this regime can be approximated by the relation : $da/dN = 0.5 \Delta CTOD$.
- A near-threshold abnormal behavior consisting in the disappearance of the threshold and resulting in a constant crack growth rate independent on ΔK is observed at room temperature as well in high vacuum as in ambient air, when two conditions are fulfilled : 1) K_{max} higher than a critical level about 52 MPa \sqrt{m} which means around 70% of the fracture toughness. 2) Superposition of cycling loading at ΔK lower than some 3 MPa \sqrt{m} .
- This phenomenon is also observed at 500°C in air, but not in high vacuum, and the rate of the steady propagation in air is about ten time slower than at room temperature.

- The corresponding mechanism is assumed to be controlled by a creep damage process which appears more efficient at room temperature than at 500°C and more accentuated in air than in vacuum.
- In humidified argon, at 500°C, a comparable abnormal behavior is detected but at a much lower critical K_{max} of 22 MPa√m. The sustained crack growth rate is about 2×10^{-9} m/cycle which is of about an order of magnitude higher than that in air at $K_{max} = 57$ MPa√m. This phenomenon refers more to stress corrosion cracking, than to creep contribution as in air or vacuum. Such behavior is consistent with previous observations made on fatigue crack propagation in similar environmental conditions supporting a more detrimental effect of water vapor in an inert gas than in air.

On the practical side, these results are very important. For example, the case of a turbine disc containing a crack, subjected to constant stress of the same order as that one sufficient stress corrosion cracking with additional very small cycling loading can be encountered and can lead to unexpected component failure. A conservative evaluation of the critical size of the defect must be done on the base of the above mentioned critical stress intensity level instead of the fracture toughness which is more than two times higher. On going studies will give a complete description and modelling of such a critical behaviour for titanium alloys and will be explored on some other metallic materials.

References

- [1] Marci, G., "Failure Mode Below 390 K with IMI 834" *Fatigue 96*, G. Lütjering et al. Eds. Pergamon Press, Vol. 1, 1996, pp. 493-498.
- [2] Lang, M., Hartman, G.A and Larsen, J.M., "Investigation of an Abnormality in Fatigue Crack Growth Curves - The Marci Effect", *Scripta Materialia*, No. 12, 1998, pp.1803-1810.
- [3] Sarrazin-Baudoux, C., Chabanne, Y. and Petit, J., "Corrosion Fatigue Behaviour of Ti6246 alloy at 500°C", *Engineering Mechanics*, 3, No. 5, 1998, pp.193-197.
- [4] Pao, P. S., Meyn, D.A., Bayles, R.A., Feng, C.R. and Yoder, G.R., "Effect of ripple loads on sustained-load cracking in Titanium alloys", *Scripta Metallurgica et Materialia*, 33; 1995, pp. 497-501.
- [5] Elber, W., "The Significance of Crack Closure" *Damage Tolerance in Aircraft Structures, ASTM STP 486*, 1971, pp.230-242.
- [6] Kikukawa, M., Jono, M. and Mikami, S., "Fatigue Crack Propagation and Crack Closure Behavior under Stationary Varying Loading-Test Results on Aluminum Alloy", *Journal of the Society on Materials Science Japan*, 31, 1982, pp.438-487.
- [7] Sarrazin, C., Lesterlin, S. and Petit, J., "Atmospheric influence on fatigue crack propagation in titanium alloys at elevated temperature", *Elevated temperature effects on fatigue and fracture, ASTM STP 1267*, Ed. R.S. Piasick, R.P. Gangloff and A. Saxena, (ASTM,1997), 1997, pp. 117-139.
- [8] Kwon, J.H., "Influence de l'Environnement sur le Comportement en Fatigue d'un Acier E460 et d'un Alliage léger 7075 près du Seuil de Fissuration", Doctorate Thesis, University of Poitiers, France, 1985.

- [9] Lesterlin, S., "Influence de l'Environnement et de la Température sur la Fissuration par Fatigue des Alliages de Titane", Doctorate Thesis, University of Poitiers, France, 1996.
- [10] J. McClintock, "Plasticity aspects of fracture", *Fracture*, an advance treatise, H. Leibewitz Ed., 1968, pp. 48.
- [11] Gao, S.J., Simmons, G.W., and Wei, R.P., "Fatigue Crack Growth and Surface Reactions for Titanium Alloys Exposed to Water Vapor", *Mat. Sc. and Engng.*, Vol. 62, 1984, pp. 65-78.
- [12] Wanhill, R.J.H., "Environmental Fatigue Crack Propagation in Ti-6Al-4V Sheet", *Metallurgical Transactions*, 7A, 1976, pp.1365-1373.
- [13] Langmuir, I., "The Adsorption of Gases on Plane Surfaces of Glass, Mica and Platinum", *Journal of American Chemical Society*, No. 40, 1918, pp. 1361-1403
- [14] Rehbinder, P.A., "Les phénomènes de surface dans la déformation et la fracture des solides", Séminaire de mécanique des surfaces, ISMCM, 1971.
- [15] Piascik, R.S. and Gangloff, R.P., "Environmental Fatigue of an Al-Li-Cu Alloy: Part I. Intrinsic Crack Propagation in Hydrogenous Environments", *Metallurgical Transactions*, Vol. 22A, 1991, pp. 2415-2428.
- [16] Foerch, R., Madsen, A. and Ghonem, H., "Environmental Interactions in High Temperature Fatigue Crack Growth of Ti-1100", *Metallurgical Transactions*, Vol. 24A, 1993, pp.1321-1332.
- [17] Allison, J.E., Williams, J.C., "Near-threshold fatigue crack growth phenomena at elevated temperature in titanium Alloys", *Scripta Metallurgica et Materialia*, No. 19, 1985, pp.773-778.
- [18] Faber, R., Kassner, M.E., Kosada, K., Bristow, B., Reichman S.H. and Hall, J.A., TMS'98 Fall Meeting, 11-15 October 1998, Chicago, Illinois, USA, to be published.
- [19] Sarrazin-Baudoux, C.S.B., Chabanne, Y. and Petit J., "Fatigue crack growth behaviour at elevated temperature of Titanium alloys", *Fracture from defects*, Eds. M.W. Brown, E.R. de los Rios and K.J. Miller, 1998, pp.315-320.
- [20] Mankowski, G., "Corrosion sous contrainte et fragilisation par l'hydrogène des alliages de Titane et de Zirconium", *Corrosion sous contrainte-Phénoménologies et mécanismes*, Les éditions de physique, Eds. D. Desjardins and R. Oltra, 1990, pp.645-684.
- [21] Dickson, J.I., Li, S.Q. and Bailon, J.P., "Aspects fractographiques de la corrosion sous contrainte", *Corrosion sous contrainte-Phénoménologies et mécanismes*, Les éditions de physique, Eds. D. Desjardins and R. Oltra, 1990, pp.425-464.

David Taylor¹ and Ge Wang¹

Component Design: The Interface Between Threshold and Endurance Limit

Reference: Taylor, D. and Wang, G., “**Component Design: The Interface Between Threshold and Endurance Limit,**” *Fatigue Crack Growth Thresholds, Endurance Limits, and Design, ASTM STP 1372*, J. C. Newman, Jr. and R. S. Piascik, Eds., American Society for Testing and Materials, West Conshohocken, PA, 2000.

Abstract: This paper discusses the use of methods derived from fracture-mechanics for the assessment of stress concentrations in components. It is known that some sharp notches can be modelled as cracks, their fatigue limits corresponding to the threshold value for a crack of the same length. Using this methodology for the assessment of components gives rise to two problems. The first problem concerns geometry: real stress concentrations have complex shape and cannot be modelled as notches of simple profile. The second problem concerns notch size: can short notches be modelled in the same way as short cracks? An approach has been developed which is an extension of the well-known critical-distance concept. It can be applied to both cracks and notches and takes into account the size effect. This has been tested using data from specimens containing short cracks and circular notches of various sizes; it has also been successfully applied to the analysis of a component in service.

Keywords: Thresholds, notches, components, endurance limit, short cracks.

Introduction

The aim of recent research in our laboratory has been to develop methods of analysis for the prediction of high cycle fatigue behaviour in engineering components. In particular, we have tried to predict endurance limits for cases where failure occurred from geometrical features (stress concentrators) of complex shape, in components which did not contain pre-existing cracks. Despite this we attempted to use the methods of linear elastic fracture mechanics (LEFM) because it had previously been shown that many geometric features, such as sharp notches [1] and small surface defects [2], can be analysed by modelling them as cracks of the same

¹Associate Professor and research scientist, respectively, Mechanical Engineering Department, Trinity College, Dublin 2, Ireland.

depth. Since most components are now designed using finite element (FE) analysis, we sought to use linear elastic FE stress data, aiming to generalise the LEM solutions to the point where they could be applied to stress data taken from a body of any shape, thus making them independent of geometric parameters such as notch depth, which are not always defined for a component. Some success was achieved using a method by which an equivalent stress intensity was estimated for the notched (uncracked) body or component [3,4,5]. Having obtained this K value by examination of the local stress field, the fatigue limit could be predicted by setting $\Delta K = \Delta K_{th}$: the conventional threshold parameter. The method was called "Crack Modelling"; it was shown that components such as automotive crankshafts and other complex shapes could be successfully analysed in this way, predicting fatigue limits with errors of less than 10%. Problems were encountered when the method was applied to physically small notches which, like short cracks, display anomalous behaviour which cannot simply be predicted from material data obtained from larger features.

In this paper we present a new method which approaches the problem from the opposite end. Instead of beginning with a fracture mechanics approach and adapting this for notches, we start with a well-known method of notch analysis and try to apply this to the behaviour of cracked bodies. The aim is to develop a general solution, applicable to cracks, notches and plain specimens, which takes account of size effects in an intrinsic fashion.

Outline of the Theory

Background to Critical-Distance Approaches

The present methodology is based on the so-called "critical distance" theories which have been used in the analysis of notches and plain specimens for several decades, since the work of Peterson [6], Neuber [7], Siebel and Stieler [8] and others. The basic idea here is to examine the stresses not only at the notch tip (the "hot spot") but also within a certain volume of material surrounding the notch. It is assumed that fatigue failure will occur if the average cyclic stress within this volume exceeds some given value. For a plain specimen in tension, for which the stress is the same everywhere, this value is necessarily the fatigue limit, $\Delta\sigma_0$. For a plain specimen in bending, and also for a notch, a stress gradient is set up so that the stress, when averaged over some distance from the hot-spot, is lower than the hot-spot value. If the notch is large and blunt this effect will be negligible and the hot-spot stress will still equal $\Delta\sigma_0$ at the fatigue limit; for sharp notches, or for relatively thin bending beams, the hot-spot stress will be significantly higher. This methodology has been realised in various different ways which are all essentially the same. For example, Siebel and Stieler [8] expressed their predictions in terms of the normalised stress gradient at the notch, whereas Peterson [6] used the notch root radius as the determining parameter. Usually the stress field is approximated in some way so as to simplify the calculations. For example, Peterson assumed a linear stress-distance variation (i.e. a constant stress gradient) so that the average stress over a certain distance could be

approximated by the stress at a given point. In what follows we will consider four possible ways of obtaining the stress value, which will be referred to as the *point*, *line*, *area* and *volume* methods, depending on whether the stress at a fixed point is used, or whether the stress is found by averaging over a given line, area or volume. In each case the region concerned will commence at the hot spot and end at some fixed distance from it. The major weakness of all of these critical-distance approaches is the choice of the distance parameter. In practice, the correct distance (i.e. the one which gives the best predictions) varies considerably from one material to another, tending to be larger in materials of low strength, when it can exceed 1mm, and much smaller (less than 0.1mm) in high-strength materials. Up to now the appropriate distance has been found from experimental data. Peterson developed an empirical relation between this distance and the UTS in steels, by analysing a large amount of test data, and his results are widely used in industry. However, the accurate determination of this parameter is a major problem because small variations in the distance chosen can lead to large errors, especially for sharp notches. Additional errors arise from other simplifying assumptions such as the assumption of constant stress gradient and the reliance on root radius as the only relevant geometric parameter.

Our Approach to Finding the Critical Distance

We commence by stating a hypothesis which is somewhat unusual. It is proposed that the fatigue limit of cracked bodies and of uncracked bodies can be predicted using the same theory. Mechanistically, this amounts to saying that the processes of crack initiation and short-crack growth which are necessary precursors to the failure of uncracked bodies, are not fundamentally different from the process of crack extension which is necessary for the failure of a body containing a long crack. Historically, cracked and uncracked bodies have been considered using different theories, based on ΔK for the former and $\Delta\sigma$ (or $\Delta\epsilon$) for the latter. If the present hypothesis is correct, then methods of analysis which work for plain and notched bodies, such as the critical-distance approach, will also work for cracked bodies.

Consider the application of a simple critical-distance approach to a long crack, for which the local stress field can be approximated by...

$$\sigma(r) = \sigma(a/2r)^{1/2} \quad (1)$$

...where $\sigma(r)$ is the stress at a distance r ahead of a centre crack of half-length a under a remote applied stress σ . The simplest approach is the *point* method; equation (1) can be used to find the critical distance, r_c , for which an applied stress range of $\Delta\sigma$ gives rise to the fatigue limit stress range, $\Delta\sigma_o$. The result is:

$$r_c = (\Delta\sigma/\Delta\sigma_o)^2.(a/2) \quad (2)$$

Since the stress intensity for this crack is...

$$\Delta K = \Delta\sigma(\pi a)^{1/2} \quad (3)$$

...then equation (2) can be rewritten as:

$$r_c = (\Delta K/\Delta\sigma_o)^2.(1/2\pi) \quad (4)$$

By definition, at the fatigue limit of this cracked body, $\Delta K = \Delta K_{th}$. If we substitute this into equation (4) we find an interesting result: the value of r_c is equal to $a_o/2$, where a_o is the parameter defined by ElHaddad et al [9] in their work on short cracks. Specifically, ElHaddad proposed a modification to the conventional long-crack equation to allow prediction of short-crack fatigue limits, as...

$$\Delta K_{th} = \Delta\sigma[\pi(a+a_o)]^{1/2} \quad (5)$$

...which leads to the result that, for a plain specimen ($a=0$)...

$$a_o = (\Delta K_{th}/\Delta\sigma_o)^2.(1/\pi) \quad (6)$$

Equation (6) is directly comparable with equation (4). ElHaddad's equation was purely empirical, and the parameter a_o was not given any physical significance. The above analysis implies that: (a) the critical-distance approach can be used to predict the fatigue limit of a cracked body, and (b) the physical significance of the a_o parameter is that it is directly related to this critical distance.

The above analysis has shown that the *point* method - the simplest type of critical distance method - can be used to predict the fatigue limit in the presence of a long crack. This supports the hypothesis stated above - that cracks, notches and plain specimens can be analysed using one common approach. It has also allowed us to identify the relevant critical distance, which can be calculated knowing the long-crack threshold and plain specimen fatigue limit, thus removing the empiricism inherent in earlier critical-distance methods. The next section considers whether this same approach can be applied to short cracks.

Application to the Short-Crack Problem

It is well known that short cracks grow more easily than long cracks at the same ΔK , and that the fatigue limit stress range for a short crack is lower than would be predicted using the conventional long-crack equation (eqn.3). This fatigue limit will tend to the plain-specimen value, $\Delta\sigma_o$, as the crack length tends to zero. Taylor and O'Donnell [10] examined a wide range of data from the literature and concluded that ElHaddad's empirical equation (eqn.5) was able to predict the effect of crack length on the fatigue limit with reasonable accuracy. Normally the experimentally-measured fatigue limit stress was within 15% of the predicted value: in some cases the error was larger, up to 30%, but these larger errors were always conservative, the experimental value being higher than the predicted one, and generally occurred in high-strength

materials for which the physical crack sizes were very small. Such experiments are relatively inaccurate owing to the difficulties of measuring short-crack growth rates, so an experimental error of at least 20% is expected. Thus equation (5) describes the effect of crack length on the fatigue limit with reasonable accuracy.

The present critical-distance theory can be used to predict the fatigue limits of short cracks, using the approach outlined above: the applied stress is found which gives rise to a value of $\Delta\sigma_c$ at a distance $a_c/2$ from the crack tip. However, for a valid analysis it is not sufficient to describe the stress field with equation (1) because this equation is only valid for distances $r \ll a$. As the crack length becomes small, with respect to a_0 , equation (1) will tend to underestimate the stress at the critical distance. Instead it is necessary to use a more accurate estimate of $\sigma(r)$, such as that developed by Westergaard [11]:

$$\sigma(r) = \sigma/[1-(a/(a+r))^2]^{1/2} \tag{7}$$

This will lead to a prediction of $\Delta\sigma$ for the fatigue limit of the cracked body which

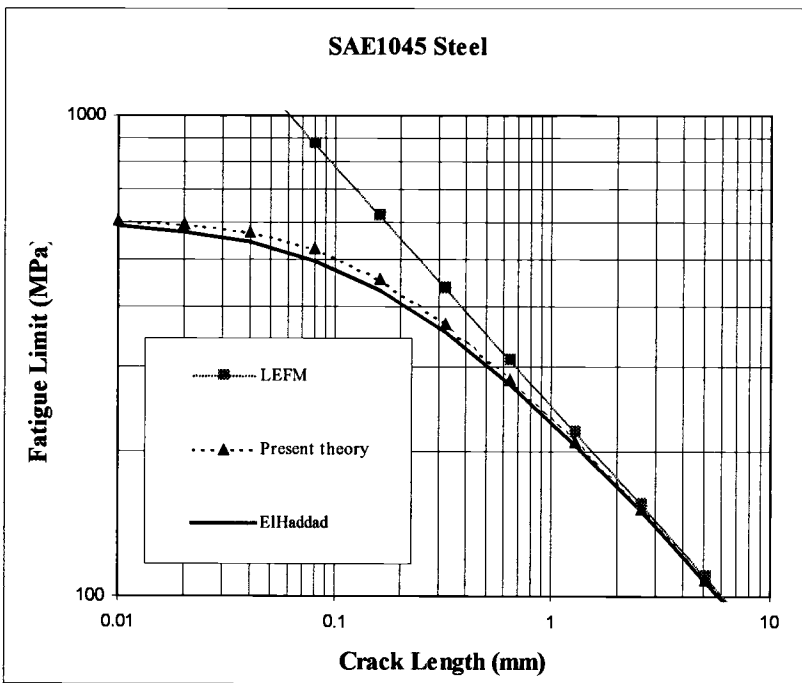


Figure 1 - Predictions of the short crack effect, comparing the present theory to that of ElHaddad et al [9].

is identical to the above prediction when the crack is long, but becomes less than the long-crack crack prediction as a decreases. When the crack length becomes much less than a_0 the stress range at the critical distance tends to become constant, equal to the applied stress range: the crack no longer has any significant effect on the fatigue limit.

Fig. 1 is a plot of the fatigue limit (applied remote stress) as a function of crack length, comparing the ElHaddad equation with predictions from the present theory. The long-crack prediction (labelled "LEFM") is shown for comparison. The constants used in making these predictions are typical for steel: they are actually the properties of an SAE1045 steel, results from which will be shown below. It is clear that the present approach gives predictions which are close to those of ElHaddad et al, implying that it will also be a good predictor of the experimental data. To confirm this, fig. 2 shows the results of applying the method to short-crack data for various materials including low-strength and high-strength steels, and copper [12-15]. The error in estimating the fatigue limit is plotted, with positive values implying a conservative error, as a function of crack length, normalised as a/a_0 . Prediction errors are very acceptable considering the experimental methods involved. The greatest errors occur for the high-strength materials at low a : errors are almost always conservative.

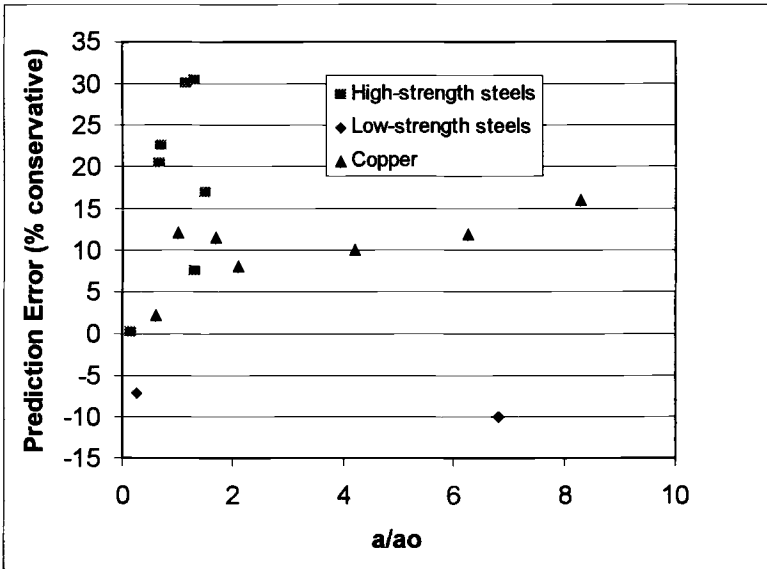


Figure 2 - Accuracy of fatigue-limit predictions for various sets of experimental data from the literature [12-15].

Thus it has been shown that this critical distance method is applicable to short cracks as well as to long cracks. This implies that both short and long cracks obey the same basic criterion as regards their fatigue limits: that the stress at a certain distance from the crack tip must be equal to a fixed value, $\Delta\sigma_0$. It is not clear how this criterion relates to the known propagation behaviour of short cracks, which is complex, especially for microstructurally short cracks which may initially grow but then become non-propagating. A consideration of this mechanism of fatigue failure is beyond the scope of the present paper. In the next stage we will attempt to apply the same theory to notches, and in particular to investigate the size effect in notches.

Large and Small Notches

In what follows we shall consider one simple notch geometry: a circular hole in a large plate, for which the stress field is given by Airy's equation...

$$\sigma(R) = (\sigma/2)[2+(a_n/R)^2 + 3(a_n/R)^4] \tag{8}$$

...where a_n is the size of the notch (i.e. the hole radius) and R is the distance measured from the centre of the hole. If the same critical-distance approach is used, examining the stress range at a distance $R=a_n+a_o/2$, then it is found that there are three regimes of behaviour, depending on the size of the notch. For very large notches ($a_n \gg a_o/2$) the

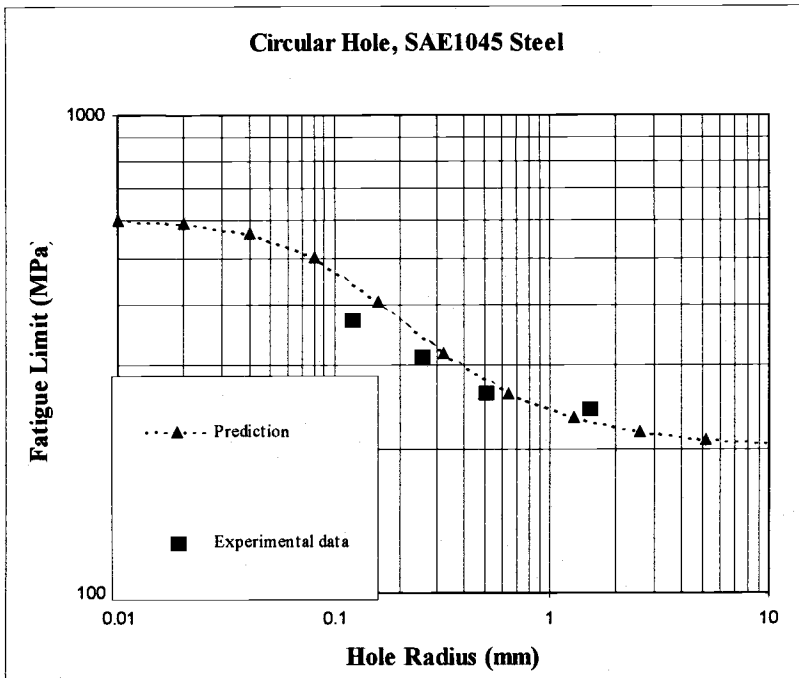


Figure 3 - The effect of hole size on the fatigue limit: experimental data from DuQuesnay et al [16].

stress at the critical distance is equal to three times the applied stress, independent of notch size, so the fatigue limit of these large notches is constant. For very small notches the stress at the critical distance is also constant, equal to the applied remote stress, so the notch has no effect on $\Delta\sigma_o$. For intermediate sizes, where a_n is of the same order of magnitude as a_o , the fatigue limit is dependent on notch size, varying gradually between the two extreme values noted above. Fig.3 shows predictions, comparing them with experimental data for SAE 1045 steel taken from DuQuesnay et

al [16]. Fig.4 shows similar predictions for an aluminium alloy (2024) with data from the same source [16]. Prediction errors are small, in most cases less than 10%, which is better than the expected experimental error, and most of the predictions are conservative. The worst prediction, which was about 15% conservative, occurred for the smallest of the holes in the steel.

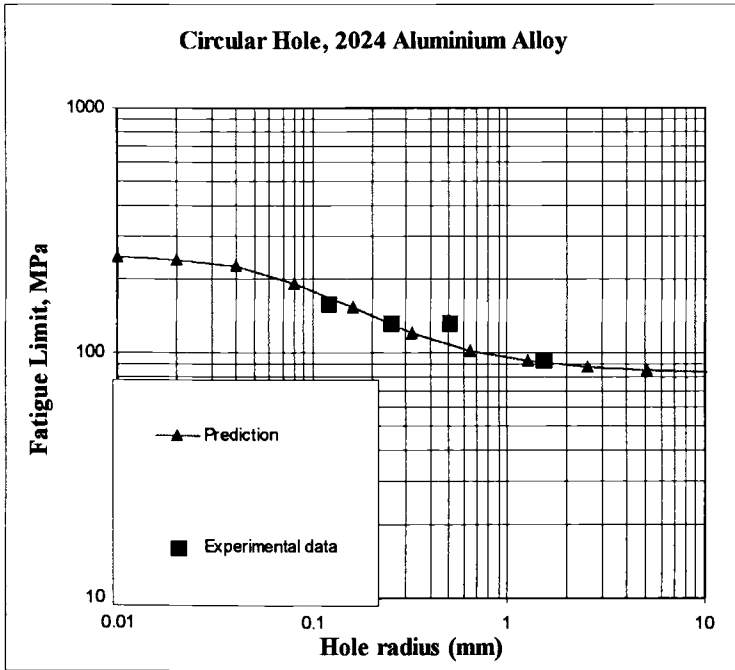


Figure 4 - *The effect of hole size on fatigue limit: experimental data from DuQuesnay et al [16] for an aluminium alloy.*

This demonstrates that the method also works for notches, and predicts accurately the notch size effect. The next section considers its use for an engineering component.

Application of the Method to a Component in Service

In a previous paper [3] we examined the failure of a large casting in a component made from grey cast iron. In service this component had failed by fatigue; cracking initiated from a right-angle corner which had a fillet radius of 0.3mm. In an attempt to prevent fatigue, this radius was increased by a factor of 10, to 3.18mm, but unfortunately failures continued to occur. An alternative approach, in which the original small fillet radius was unchanged but the service loads were reduced, was successful in preventing fatigue. Fig.5 shows the stress as a function of distance from the hot spot for these three design conditions: S1 refers to the original design; S2

refers to the increased root radius and C shows the reduced loading conditions on the original radius. The stress value which is plotted is the greatest principal stress at the point of maximum load in the cycle. Also shown on the graph is the critical distance $a_o/2$, which was calculated to be 1.9mm, based on measurements of the fatigue limit and threshold [3]. The graph also shows two horizontal lines representing the plain-

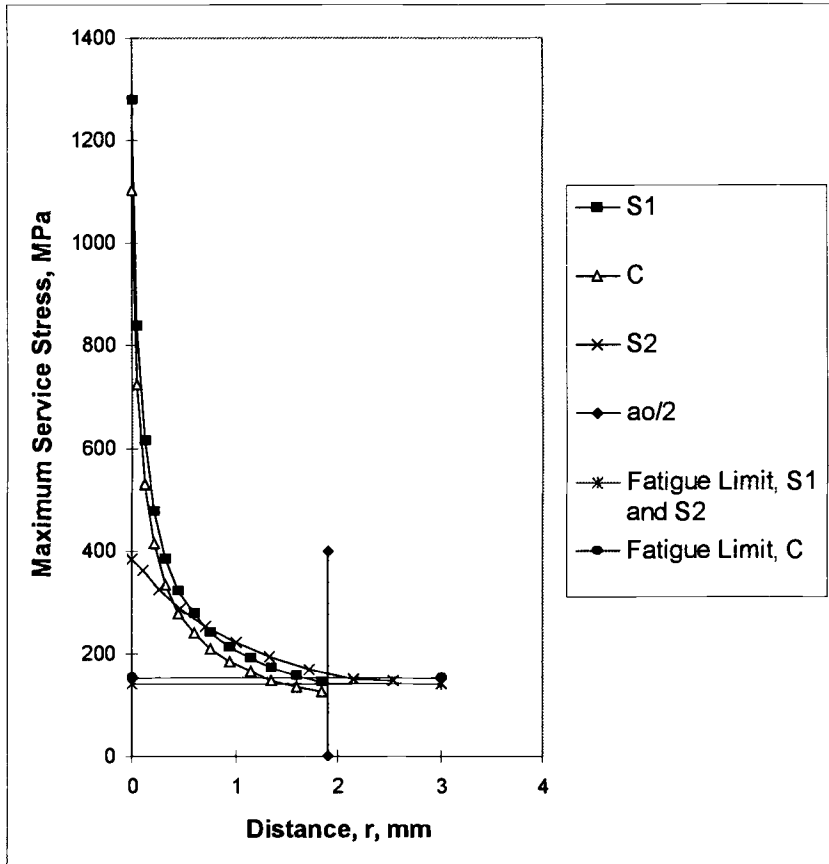


Figure 5 - Stress-distance plots for the component in the S1, S2 and C designs, showing also the critical distance ($a_o/2$) and relevant fatigue limits.

specimen fatigue limit. This varied slightly because of a change in R ratio: designs S1 and S2 experienced stresses with $R=0.56$, but the reduced stresses of design C had a slightly different R of 0.65. The relevant $\Delta\sigma_o$ values were deduced from experimental tests at a range of R ratios up to 0.7. They were 62.4MPa at $R=0.56$ and 53.4MPa at $R=0.65$, giving maximum stress values of 142MPa and 153MPa respectively.

It can be seen from the figure that the critical distance method predicts the in-service behaviour of this component very well. The S1 and S2 conditions have stress levels which lie above their fatigue limit value, whilst the stress at $a_o/2$ in the C

condition lies below its fatigue limit. This is very much in contrast to the behaviour of the hot-spot stress, which is much lower in the S2 condition due to the larger root radius. Clearly this blunting of the corner, which would normally be considered good design practice, is ineffective in this case, largely due to the material having a very high a_0 value of 3.8mm.

Such behaviour is well known to designers, who would describe cast iron as having a low notch-sensitivity. Normal design practice would be to calculate a notch-sensitivity index using an empirical equation such as Peterson's in which the critical distance would be estimated from the material's UTS. This critical distance is then used to estimate a fatigue strength reduction factor, K_f , based on the K_t value of the stress concentration. To use this approach a K_t value has to be estimated for the feature - a procedure which is very imprecise for any real component geometry and loading pattern. K_t is only strictly defined for simple geometries such as a notch under uniform tension or bending, for which a unique nominal stress can be defined. Given the popularity of finite element methods in engineering design, it is more appropriate to use approaches which take advantage of the detailed stress analysis of the feature that can be provided by these methods.

The above predictions have all been made using the simplest type of critical-distance method: the *point* method. It is assumed that the controlling parameter is really the average elastic stress over a volume surrounding the crack, and that the single-valued stress at this critical point is an approximation to this average stress. In the next section we consider other ways of estimating this average stress.

Critical-Distance Approaches Using Line, Area or Volume Averages

The same approach can be used in conjunction with other methods of determining this average stress. Thus, starting from the equation for a long crack (equation (1)) we can find a critical length, area or volume over which the average stress range is equal to $\Delta\sigma_0$, and we can relate this critical dimension to the ElHaddad constant a_0 . The detailed mathematics will not be presented in this paper (they are outlined in more detail in another publication [17]; we will instead confine ourselves to stating some interesting results.

Firstly, regarding the *line* method, it can be shown that, when a long crack is loaded to its threshold stress intensity, then the average stress is equal to $\Delta\sigma_0$ over a distance of $2a_0$: exactly four times as large as the critical distance for the *point* method. It can also be shown that the application of this method to short cracks gives a prediction of the fatigue limit which is, mathematically, exactly the same as ElHaddad's equation.

Regarding the *area* method, a choice arises concerning the exact shape of the area over which one should average the stress. For example, if one chooses an area in the form of a semi-circle centered on the crack tip, then the critical radius of this semi-circle is found to be approximately a_0 . The result is approximate because, in fact, if the radius a_0 is used it is found that the average stress within this area is $1.1\Delta\sigma_0$: 10% larger than required. This means that the use of a_0 as the distance here will give slightly conservative predictions.

So far we have not attempted a *volume* method, but given the availability of FE stress data for a component, it is not particularly difficult to find the average stress within any given volume. However, this method presents us with even more choice regarding the appropriate shape of the volume: possible shapes include a hemi-sphere centred on the hot spot or a prismatic shape formed by extruding the semi-circular area. The latter seems more appropriate for straight-fronted cracks or notches, being simply an extension of the area method into three dimensions, but this will not be appropriate for all possible geometries.

Another piece of work which is planned for the near future is the consideration of notches of different shapes. So far we have only analysed circular holes; it is assumed that, as one considers sharper notches with higher K_t values, then the local stress field will become more and more crack-like as K_t increases, so that the case of a sharp crack will gradually be approached. Hopefully it will be possible to predict results such as those of Smith and Miller [1], who showed that a critical K_t value existed for any given notch depth, beyond which the notch could be described as a crack.

It should be noted that the theoretical model used here is not a mechanistic one. It does not consider explicitly the processes of crack initiation and growth, which we know take place during fatigue. Our sole aim has been to predict the fatigue limit, using information about the stress field; we have demonstrated that the method works in a number of cases, but we have not considered why it works. This aspect is considered in a recent publication [17] and is being further developed in a paper currently in preparation. It is important to point out that the fatigue limit stress is not the same as the stress needed to cause crack propagation, because there are many cases of crack growth occurring below the fatigue limit, giving rise to non-propagating cracks. Examples are microstructurally-short cracks and cracks growing from sharp notches.

Conclusions

- 1) Critical-distance analysis, which is conventionally used to predict the fatigue limits of notched bodies, can also be applied to bodies containing long, sharp cracks. In this case the critical distance can be found analytically, as a function of the material's threshold and plain-specimen fatigue limit. Using the simplest type of critical-distance approach - the *point* method - this distance parameter is found to be $a_0/2$, where a_0 is the ElHaddad constant used in short-crack analysis.
- 2) Using the same method with the same distance constant, short-crack effects can be predicted. The variation of the fatigue limit with crack length is found to be similar to that in ElHaddad's equation. Experimental data can be predicted with reasonable accuracy in this way.
- 3) The same method can also be used to predict the behaviour of notches: analysis of data on circular holes in two different materials gave accurate predictions of their fatigue limits as a function of hole size.

4) The theory can also be applied to more complex shapes, such as stress concentrations in components. The in-service fatigue behaviour of a component was analysed, predicting successfully the behaviour of three different designs.

5) The *point* method is only an approximate estimate of the stresses in the critical volume. More accurate methods, in which the stress is averaged over a given line, area or volume, should be investigated. Initial results show that the *line* method is feasible, and gives identical predictions to ElHaddad's equation. *Area* and *volume* methods require some decisions regarding the shape of the area or volume: these have not yet been considered in detail.

Acknowledgements

We are grateful to Rover, UK for continued funding of this work, and also to Materials Ireland for providing support for one of the authors (G.Wang).

References

- [1] Smith RA and Miller KJ "Prediction of Fatigue Regimes in Notched Components," *Int.J.Mech.Sci.*, 20, 1978, 201-206.
- [2] Murakami Y and Endo M "Quantitative Evaluation of Fatigue Strength of Metals Containing Various Small Defects or Cracks," *Engineering Fracture Mechanics*, 17, 1983, 1-15.
- [3] Taylor D "Crack Modelling: a Technique for the Fatigue Design of Components," *Engineering Failure Analysis*, 3, 1996, 129-136.
- [4] Taylor D Ciepalowicz AJ Rogers P and Devlukia J "Prediction of Fatigue Failure in a Crankshaft using the Technique of Crack Modelling," *Fatigue and Fracture of Engineering Materials and Structures*, 20, 1997, 13-21.
- [5] Taylor D and Lawless S "Prediction of Fatigue Behaviour in Stress-Concentrators of Arbitrary Geometry," *Eng.Fract.Mechanics*, 53, 1996, 929-939.
- [6] Peterson RE "Notch Sensitivity," *Metal Fatigue* (Ed. G.Sines & J.L.Waisman) McGraw Hill (New York), 1959, 293-306.
- [7] Neuber H *Theory of notch stresses*, Publ. Springer, Berlin, 1958.
- [8] Siebel E and Stieler M "Dissimilar Stress Distributions and Cyclic Loading," *Z.Ver.Deutsch.Ing.*, 97, 1955, 121-131.

- [9] ElHaddad MH Dowling NF Topper TH and Smith KN. "J Integral Applications for Short Fatigue Cracks at Notches," *Int.J.Fract*, 16, 1980, 15-24.
- [10] Taylor D and O'Donnell M "Notch Geometry Effects in Fatigue: a Conservative Design Approach," *Engineering Failure Analysis*, 1, 1994, 275-287.
- [11] Westergaard HM "Bearing Pressures and Cracks," *J.Appl.Mech. A*, 1939, 49-53.
- [12] Frost NE Marsh KJ and Pook LP *Metal Fatigue*, Publ.Oxford University Press(UK), 1974.
- [13] Usami S *Soc.Mater.Sci.Japan*, 1985, 101-111.
- [14] Lankford J *International Journal of Fatigue*, 16, 1980, 7-17.
- [15] James MN. PhD Thesis, University of Cambridge, 1984.
- [16] DuQuesnay DL, Topper TH and Yu MT "The Effect of Notch Radius on the Fatigue Notch Factor and the Propagation of Short Cracks," In *The Behaviour of Short Fatigue Cracks*, EGF Publication 1 (Eds K.J.Miller & E.R.de los Rios). Mechanical Engineering Publications, London, 1986 323-335.
- [17] Taylor D Geometrical Effects in Fatigue: a Unifying Theoretical Model. *Int.J.Fatigue* 1999 (In Press).

Pedro Albrecht¹ and William J. Wright²

Near-Threshold Fatigue Strength of a Welded Steel Bridge Detail

Reference: Albrecht, P. and Wright, W. J., “Near-Threshold Fatigue Strength of a Welded Steel Bridge Detail,” *Fatigue Crack Growth Thresholds, Endurance Limits, and Design*, ASTM STP 1372, J. C. Newman, Jr. and R. S. Piascik, Eds., American Society for Testing and Materials, West Conshohocken, PA, 2000.

Abstract: This paper consists of three parts. First, fatigue test data are presented for a tensile specimen with transverse stiffeners, a typical steel bridge detail. The specimens were tested under variable-amplitude fatigue for up to 250,000,000 cycles of loading proportional to the gross vehicle weight distribution of 27,000 trucks weighed on highways. Few and, in some cases, no stress ranges exceeded the endurance limit in the longest life tests. It took up to nine months to test the longest-life specimens.

Second, the variable-amplitude S-N life is predicted with an equivalent stress range model in which stress ranges smaller than the fatigue limit are assumed not to contribute to fatigue damage. A simplified S-N model is proposed for determining the fatigue life of existing bridges. The variable-amplitude fatigue limit is shown, both experimentally and analytically, to be a function of the constant-amplitude fatigue limit and the ratio of root-mean-cube stress range to maximum stress range of the variable-amplitude load spectrum.

In the third part of the paper, the variable-amplitude fatigue lives of the transverse stiffener specimens are predicted with a fracture mechanics model of crack growth.

Keywords: Fatigue, highway bridges, variable amplitude, fatigue limit, steel, design, testing, specifications, overload, stiffeners, welds

Introduction

Fatigue under repeated truck loading is a common and critical problem in highway bridges. Fatigue cracks initiate mostly at details of high stress concentration located in areas of high stress range. The cracks propagate until they reach a critical crack size at which the member then fractures.

Highway bridges are designed for fatigue to the requirements of the Bridge Design Specifications issued by the American Association of State Highway and Transportation Officials (AASHTO). These specifications have two shortcomings.

¹ Prof., Dept. of Civ., Engrg., Univ. of Maryland, College Park, MD 20742.

² Turner-Fairbank Highway Research Center, Federal Highway Administration, 6300 Georgetown Pike, McLean, VA 22101.

First, the specifications are based on constant-amplitude test data while in reality highway bridges are subjected to randomly ordered truck loading. As several studies have noted, the fatigue behavior under variable-amplitude loading differs from that under constant-amplitude loading. To improve the specifications, fatigue test data are needed for weldments subjected to variable-amplitude stress range histories corresponding to the actual distribution of gross vehicle weights.

Second, the Bridge Design Specifications are largely based on fatigue test data in the finite life regime, that is, at stress ranges greater than the fatigue limit for constant-amplitude loading. Little data are available on long-life variable-amplitude fatigue when only few stress ranges are greater than the constant-amplitude fatigue limit.

Objective

The objective of the present study is to determine both experimentally and analytically the fatigue life of a typical welded bridge detail subjected to variable-amplitude stress cycling near the fatigue limit.

Experimental Work

Specimens

The long-life fatigue behavior of a typical steel weldment was determined in the present study with constant-amplitude and variable-amplitude fatigue tests of the transverse stiffener detail shown in Fig. 1. All dimensions are in mm.

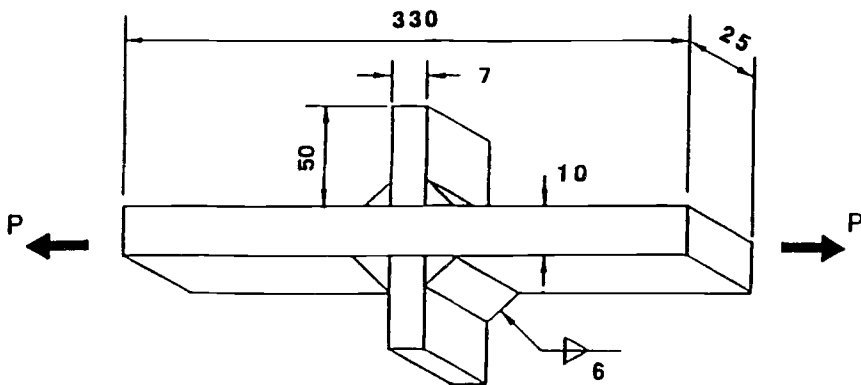


Figure 1 — *Steel Stiffener Specimen*

The steel for the stiffener specimens satisfied the requirements of the ASTM Specification for High-Strength, Low-Alloy Structural Steel with 345 N/mm² Minimum Yield stress to 100 mm Thick (A 588). The 10-mm-thick main plate was made of Grade A steel with 482 N/mm² yield strength and 655 N/mm² tensile strength. The 7-mm-thick

stiffener plate was made of Grade B steel with 406 N/mm^2 yield strength and 556 N/mm^2 tensile strength. The Charpy V-notch energy of the main plate was 200 J.

The rolling direction of the main plate was parallel to the longitudinal axis and loading direction of the specimen. All welds were placed manually with 1.6-mm-diameter Lincoln E-8018-C3 electrodes. Figure 2 shows the polished and etched longitudinal section of a specimen.

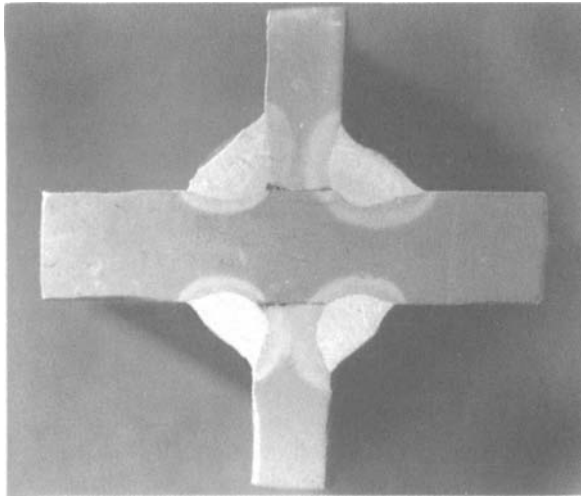


Figure 2 — Polished and Etched Longitudinal Section of Specimen

Test Matrix

Twenty-nine specimens were tested under constant amplitude loading with stress ranges of 90 to 290 N/mm^2 . Twenty-six specimens were tested at variable-amplitude loading with seven levels of equivalent stress range:

$$f_{re} = \left(\frac{\sum_{i=1}^k n_i f_{ri}^m}{\sum_{i=1}^k n_i} \right)^{1/m} = \left(\sum_{i=1}^k \gamma_i f_{ri}^m \right)^{1/m} \quad (1)$$

where

k = index for peak stress range, the highest stress range of the spectrum

n_i = number of cycles of i -th stress range in spectrum

n = total number of cycles in spectrum

$\gamma_i = n_i/n$ = frequency of occurrence of i -th stress range

f_{ri} = i -th stress range

The minimum stress was 3 N/mm^2 in the constant amplitude tests and 14 N/mm^2 in the variable amplitude tests; both give low load ratios.

Load Spectrum

The variable-amplitude fatigue tests were performed with a spectrum of stress ranges proportional to the gross vehicle weight (GVW) distribution of trucks. Although there are many more automobiles than trucks on the highways, automobiles are too light to cause fatigue damage and were therefore excluded from the GVW distribution.

The GVW distribution chosen for testing the specimens under variable-amplitude fatigue came from a weigh-in-motion (WIM) study by Snyder et al [1]. In that study, a total of 27,513 trucks were weighed on 31 Interstate, U.S., and State route bridges located in seven States. Figure 3 shows the probability density function for GVW ranging from 2.8 to 100% or, in terms of GVW, from 25 to 890 kN. In comparison, the design truck for highway bridges weighs 325 kN.

For an equal number of trucks, the equivalent GVW is defined as the weight that produces the same amount of fatigue damage as is done by all trucks of the GVW distribution. It is calculated from

$$W_e = \left(\frac{\sum n_i W_i^m}{\sum n_i} \right)^{1/m} \quad (2)$$

where

W_i = i -th gross vehicle weight

n_i = number of trucks of weight W_i

$m = 3$ = rounded value of slope of log-log S-N lines for welded details

The equivalent GVW for the 27,513 trucks is $W_e = 239 \text{ kN}$. This value is about the same as the weight of the fatigue truck in the Bridge Design Specifications, which was obtained by multiplying the 325-kN GVW of the design truck for static loading by the normalized equivalent GVW to arrive at the fatigue truck:

$$W_f = \phi_e W_{\max} = 0.75 \cdot 326 = 244 \text{ kN} \quad (3)$$

where

W_f = weight of fatigue design truck

$\phi_e = 0.75$ = normalized equivalent weight of fatigue truck

W_{\max} = weight of design truck for static loading

The probability density corresponding to a bar of the histogram is defined as the frequency of occurrence divided by the width of the bar. These values were plotted at normalized GVWs corresponding to the mid-widths of the bars. The points were then connected with straight lines, giving a probability density function (PDF) for GVW.

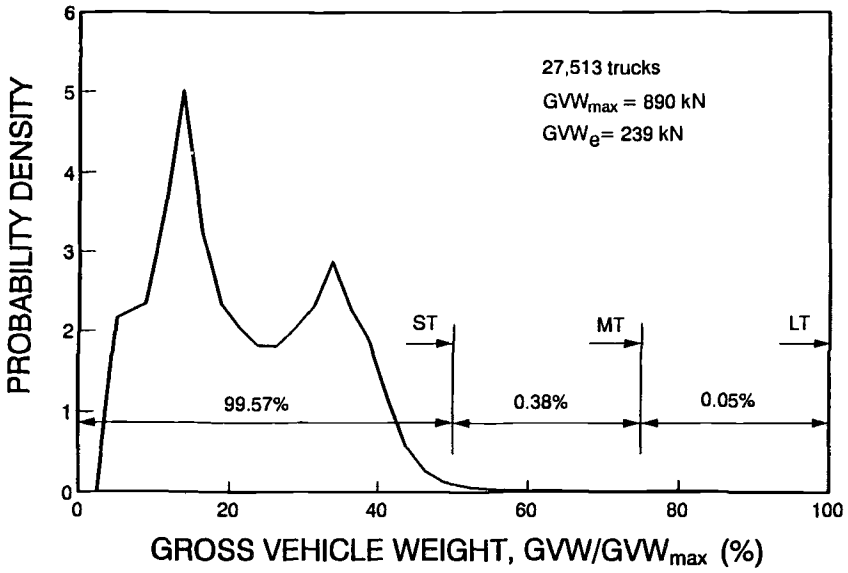


Figure 3 — Probability Density Function for GVWs

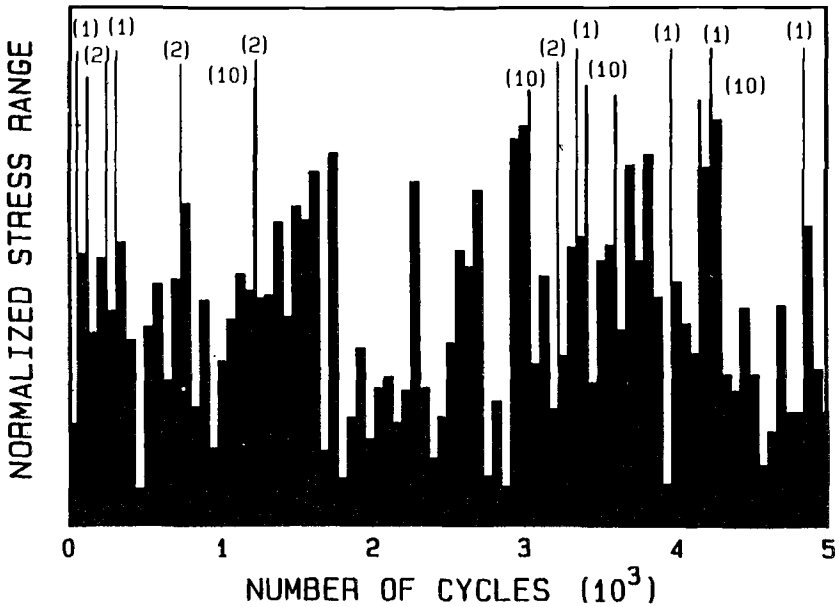


Figure 4 — One-half of Random-order 10 000-cycle Load Spectrum

The area under the PDF is equal to one. The probability density is very small for the upper half, $GVW/GVW_{\max} > 50$ percent.

All specimens were subjected to medium-tail (MT) spectrum loading, from 2.8 to 75% of GVW_{\max} or 25 to 668 kN GVW. The very few trucks with GVW greater than 668 kN were left out because these overloads would have prolonged the fatigue life [2]. Retaining them in the loading spectrum to be applied on the specimens would have masked the true effect of variable amplitude fatigue.

The PDF was subdivided into $N = 10,000$ areas of equal frequency of occurrence $1/N$ but of different widths. These 10,000 cycles were then grouped in 197 blocks of 1, 2, 10 and 60 cycles of constant amplitude. This was done so that during a test, the feedback signal from the load cell could be identified from one block to another, allowing the value of each feedback signal to be checked for accuracy against the corresponding command signal. Combining individual cycles into blocks of at most 60 cycles has no effect on fatigue life. This is apparent from the work by Albrecht and Yamada who showed that more than 300 cycles can be combined into one block without delaying the rate of crack growth in high-low stress range sequences [3].

The 197 blocks of the 10,000-cycle spectrum were arranged in random order to simulate trucks crossing a bridge in service. The spectrum was repeatedly applied until the specimen failed. Figure 4 shows one-half of the load spectrum.

Test Results

Crack Initiation And Propagation

Of the 24 specimens that failed under variable-amplitude cycling, 22 exhibited multiple crack initiation and 2 single crack initiation. More cracks initiated along the weld toe line than at a corner (23 versus 1). Clearly the specimens were well aligned.

Multiple cracks propagating through the thickness of the main plate coalesced and formed a long, shallow, half-tunnel-like crack across the width of the specimen. The specimen eventually failed when the crack front approached the back face of the plate, causing the net ligament to rupture in a ductile mode at a mean net section stress about equal to the tensile strength of the base metal.

Constant-amplitude Tests

The data for the 29 specimens tested under constant-amplitude fatigue are plotted with square symbols in Fig. 5. Twenty-four specimens were tested in the finite life regime at stress ranges of $f_r = 97$ to 290 N/mm^2 . The mean S-N line for these specimens was determined from regression analysis performed on the logarithms of N and f_r giving:

$$N = \frac{10^b}{f_r^m} = \frac{10^{12.4266}}{f_r^{3.008}} \quad (4)$$

where b and m are the intercept and inverse slope of the log-log mean S-N line. The value of f_r in Eq. 4 must be substituted in units of N/mm^2 . The lower-bound S-N line is located at two standard deviations ($s = 0.1180$) on the logarithm of life to the left of the mean S-N line:

$$N = \frac{10^{b-2s}}{f_r^m} = \frac{10^{12.1906}}{f_r^{3.008}} \tag{5}$$

Three of the five specimens tested at the lowest stress range of $f_r = 90 \text{ N/mm}^2$ were runouts at 10 million cycles. The fatigue limit for constant-amplitude cycling (CAFL) — the upper dashed line in Fig. 5 — was estimated to lie at [4]:

$$F_{\text{CAFL}} = 81 \text{ N/mm}^2 \tag{6}$$

Variable-amplitude Tests

Twenty-six specimens were tested at seven equivalent stress ranges and minimum stress of $f_{\text{min}} = 14 \text{ N/mm}^2$.

Figure 5 compares the variable-amplitude fatigue data (triangular symbols) with the constant-amplitude data. The data points for the eight specimens tested in the finite life regime fell to the right ($f_{re} = 152 \text{ N/mm}^2$) and along ($f_{re} = 103 \text{ N/mm}^2$) the mean S-N line

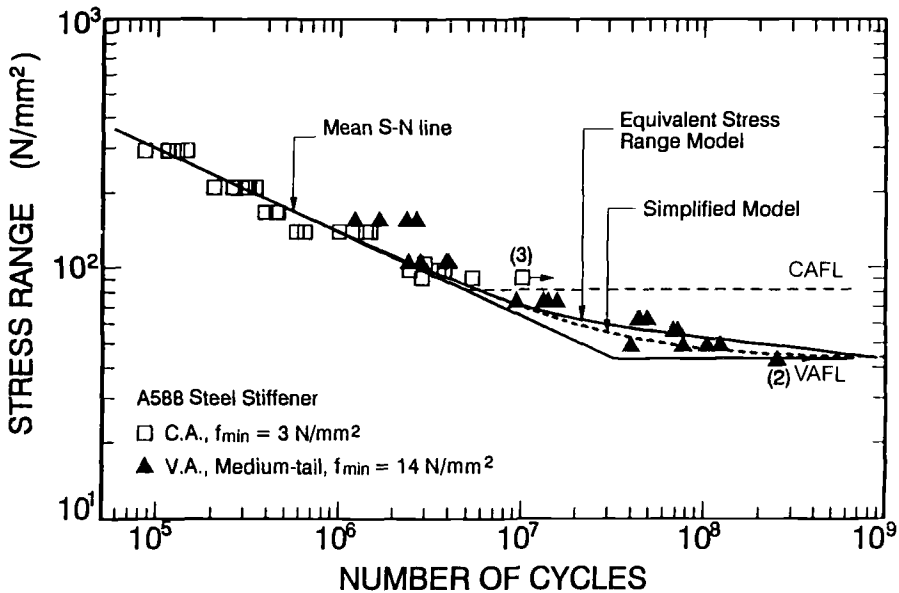


Figure 5 — Constant-amplitude and Variable-amplitude Fatigue Test Data; Comparison with Equivalent and Simplified Stress Range Models

for constant amplitude. The data points for the 18 specimens tested at $f_{re} = 72$ to 48 N/mm^2 fell well below the CAFL, $F_{\text{CAFL}} = 81$ N/mm^2 from Eq. 6. Finally, two specimens tested at the lowest equivalent stress range of $f_{re} = 42$ N/mm^2 did not fail after 250 million cycles of loading at which time the tests were ended.

With decreasing equivalent stress range, fewer cycles had stress ranges that exceeded the CAFL, and the data points fell increasingly to the right of the extended straight S-N line. This runout trend with decreasing exceedence level was originally reported by Albrecht and Friedland [5].

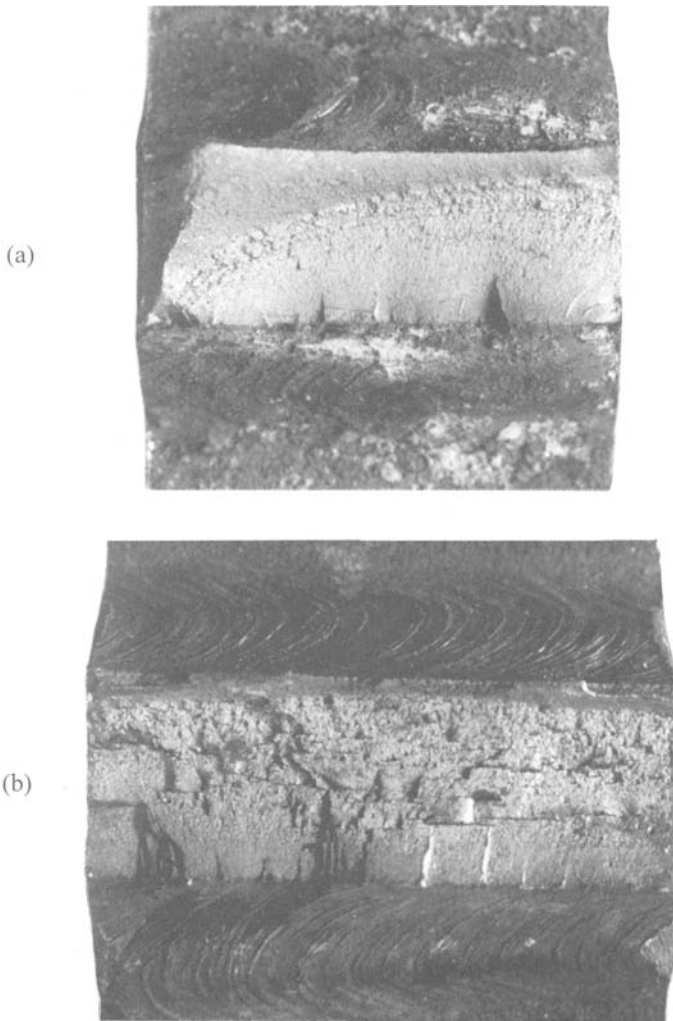


Figure 6 — Typical Crack Surfaces (a) Without Inclusions and (b) with Inclusions

Effect of Inclusions

The main plate contained 0.032% sulfur by weight. While this value is lower than the 0.05% max allowed by the specification, elongated and flattened manganese sulfide inclusions still formed in the center half of the plate thickness during rolling. Wilson previously reported this phenomena, known to occur in A588 weathering steel [7].

Figure 6(a) shows a typical crack surface of a stiffener specimen without inclusions. The surface had a fine texture as the crack grew through the first 15% of the main plate thickness. This corresponds to the extent of the fine-grained, heat-affected zone at the weld toe in Fig. 2. The morphology became slightly coarser when the crack entered the base metal, and much coarser yet when the net ligament began to yield.

Manganese sulfide inclusions were visible on the fatigue crack surface of some specimens as shown in Fig. 6(b). Layers of steel between flattened inclusions contracted transversely at fracture, causing the inclusions to open and making them easily visible. These inclusions, oriented parallel to the loading direction and normal to the crack plane, acted as obstacles and forced the crack to propagate around them.

Figure 7 groups the variable-amplitude data by the presence (solid triangles) or absence (open triangles) of inclusions. Clearly, inclusions prolonged fatigue life at high stress ranges at which fatigue life consists of a relatively short crack initiation phase and a long crack propagation phase.

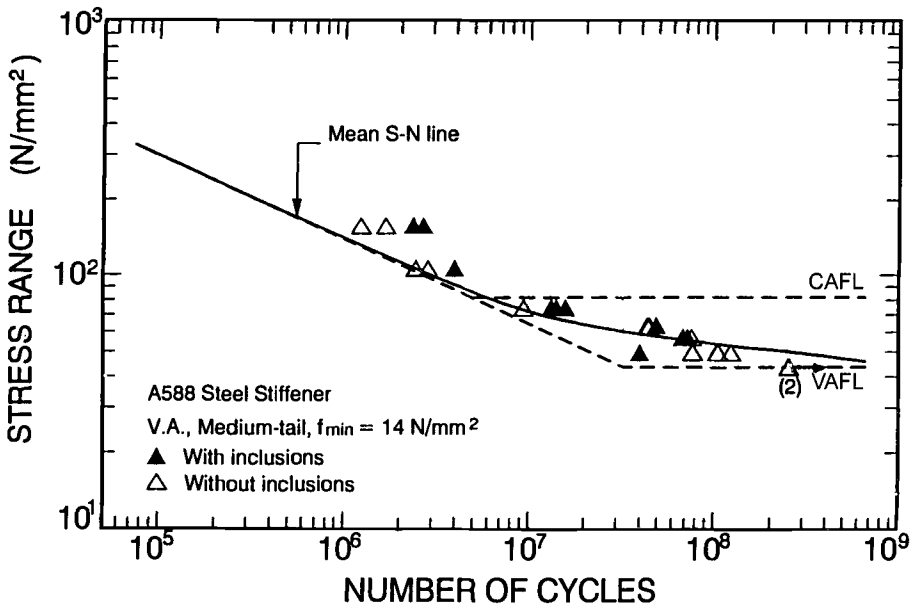


Figure 7 — *Effect of Inclusions on Fatigue Strength*

Inclusions did not noticeably delay crack growth at low stress ranges, $f_{re} \leq 55$ N/mm², where crack initiation consumes a greater part of the total fatigue life than does crack propagation.

Straight-line Extension Model

The straight-line extension model extends the mean S-N line (Eqs. 4 and 11) down to the VAFL in Fig. 5. It increasingly underestimates fatigue life, the more the equivalent stress range is lower than the CAFL; it is used hereafter only as a reference line against which the models presented in the following are compared.

Equivalent Stress Range Model

Separate equations are needed to predict the variable amplitude fatigue life depending on whether all, some, or no stress ranges of the spectrum are higher than the CAFL. The three conditions are illustrated in Fig. 8 where the horizontal line through the CAFL divides the schematic histograms into light and shaded portions of stress ranges greater and smaller than the CAFL.

All Stress Ranges Greater than CAFL

When all stress ranges are greater than the CAFL, the histogram can be replaced by the equivalent stress range, f_{re} , of Eq. 1, meaning that a given number of cycles of

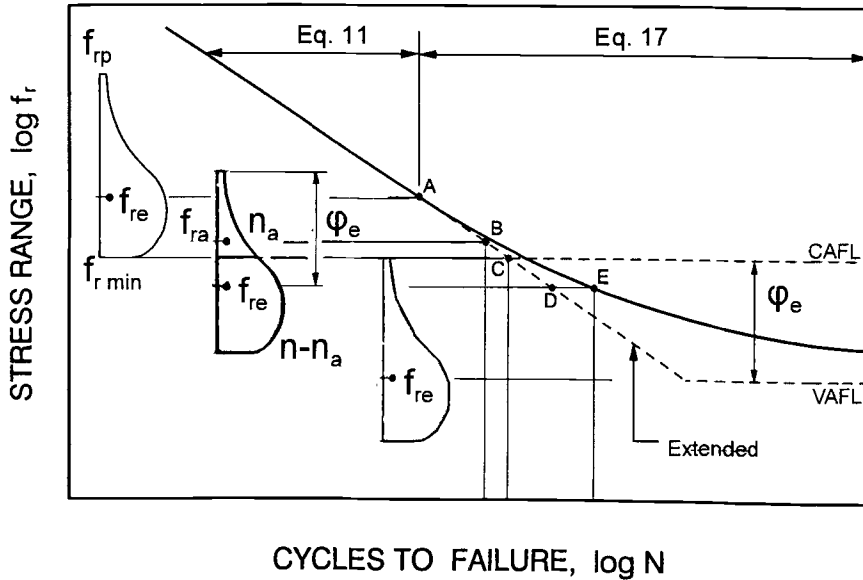


Figure 8 — Equivalent Stress Range Model

variable-amplitude stress ranges causes the same fatigue damage as an equal number of cycles of equivalent constant-amplitude stress range. Normalizing the individual stress ranges by the peak stress range of the spectrum leads to

$$f_{re} = \left(\sum_{i=1}^k \gamma_i \phi_i^m \right)^{1/m} f_{rp} \tag{7}$$

where

$$\phi_i = \frac{f_{ri}}{f_{rp}} \tag{8}$$

and

ϕ_i = i -th normalized stress range
 f_{rp} = peak stress range in spectrum

For convenience, Eq. 7 can be written as

$$f_r = \phi_e f_{rp} \tag{9}$$

where the normalized equivalent stress range

$$\phi_e = \left(\sum_{i=1}^k \gamma_i \phi_i^m \right)^{1/m} \tag{10}$$

depends only on the frequency of occurrence and distribution of the variable-amplitude stress ranges.

Therefore, when all stress ranges are greater than the CAFL, the fatigue life may be calculated with any of the following expressions:

$$N = \frac{10^b}{\left(\sum_{i=1}^k \gamma_i \phi_i^m \right) f_{rp}^m} = \frac{10^b}{\sum_{i=1}^k \gamma_i f_{ri}^m} = \frac{10^b}{f_{re}^m} = \frac{10^b}{(\phi_e f_{rp})^m} \tag{11}$$

The left-most stress range spectrum in Fig. 8 shows the lowest position for which Eq. 11 is still valid; that is, when the smallest stress range is just equal to the CAFL and all other stress ranges are greater than the CAFL. At this position, the equivalent stress range, f_{re} , is the ordinate of point A. Eq. 11 is valid to the left of point A.

Some Stress Ranges Greater than CAFL

Albrecht and Friedland proposed a numerical method of calculating the variable-amplitude fatigue life when only some stress ranges in the spectrum are greater than the CAFL [5]. The method assumes that only the stress ranges greater than the CAFL propagate the crack. On that basis, they predicted the variable-amplitude fatigue life of transverse stiffeners with good success.

In the present study the authors derived the closed-form equation for the Albrecht and Friedland model. According to Eq. 1, the equivalent stress range for the stress ranges greater than the CAFL (the upper portion of the center spectrum in Fig. 8) is

$$f_{ra} = \left(\frac{\sum_{i=a}^k n_i f_{ri}^m}{\sum_{i=a}^k n_i} \right)^{1/m} = \left(\frac{\sum_{i=a}^k \frac{n_i}{n} f_{ri}^m}{\sum_{i=a}^k \frac{n_i}{n}} \right)^{1/m} = \left(\frac{\sum_{i=a}^k \gamma_i f_{ri}^m}{\sum_{i=a}^k \gamma_i} \right)^{1/m} \tag{12}$$

where

a = index for stress range equal to CAFL
 $f_{ri} = F_{CAFL}$ for $i = a$, and $f_{ri} = f_{rp}$ for $i = k$.

The numerator and denominator in the second term of Eq. 12 should be divided by n_a (number of cycles in spectrum greater than the CAFL) instead of n . However, since the dividers are constant and cancel out, either one can be used. The value n was chosen to keep the same definition of frequency, $\gamma_i = n_i/n$, as in Eq. 1. As a result, the sum of the frequencies of occurrence in Eq. 12 is $\sum \gamma_i < 1$, for $i = a$ to k , whereas the sum in Eq. 1 is $\sum \gamma_i = 1$, for $i = 1$ to k . Plotted on the horizontal line through point B in Fig. 8 is the equivalent stress range f_{ra} for the cycles with stress ranges greater than the CAFL. The corresponding fatigue life is

$$N_a = \frac{10^b}{f_{ra}^m} \tag{13}$$

where f_{ra} = equivalent stress range for cycles with stress ranges greater than the CAFL.

Although the cycles with stress ranges smaller than the CAFL (the lower portion of the center spectrum in Fig. 8) are assumed to not contribute to crack growth, they must still be counted. Adding them to N_a from Eq. 13 gives the total fatigue life:

$$N = N_a + \frac{n - n_a}{n_a} N_a = \frac{N_a}{n_a/n} \tag{14}$$

where

n = total number of cycles in spectrum

n_a = number of cycles with stress ranges greater than the CAFL.

The term n_a/n is the sum of the frequencies of occurrence of the cycles with stress ranges greater than the CAFL

$$\frac{n_a}{n} = \sum_{i=a}^k \gamma_i \quad (15)$$

Inserting the values of N_a from Eq. 13 and n_a/n from Eq. 15 into Eq. 14 gives

$$N = \frac{10^b}{f_{ra}^m \sum_{i=a}^k \gamma_i} \quad (16)$$

Finally, noting that the denominator of Eq. 15 is equal to the numerator of the right-hand side of Eq. 12 leads to the following equation for predicting the fatigue life when some, but not all, stress ranges are greater than the CAFL:

$$N = \frac{10^b}{\sum_{i=a}^k \gamma_i f_{ri}^m} = \frac{10^b}{\left(\sum_{i=a}^k \gamma_i \Phi_i^m \right) f_{rp}^m} \quad (17)$$

Equation 17 is drawn as a solid curve in Fig. 8, beginning at point A and curving down and to the right. The abscissa of point E on this curve is the fatigue life for a spectrum with some stress ranges greater than the CAFL; the ordinate of point E is the equivalent stress range for the full spectrum. If the fatigue-limit effect were neglected, the fatigue life would be calculated with Eq. 11, yielding point D on the dashed straight-line extension of Eq. 11. The distance between points D and E is the increase in fatigue life that comes from assuming that only stress ranges greater than the CAFL cause the crack to grow.

No Stress Ranges Greater than CAFL

When the peak stress range is lowered to the CAFL ($f_{rp} = F_{CAFL}$ and $a = k$ in right spectrum in Fig. 8), the denominator in Eq. 17 is zero and the equivalent stress range of the full spectrum becomes the variable-amplitude fatigue limit (VAFL):

$$F_{VAFL} = \Phi_e F_{CAFL} \quad (18)$$

where ϕ_e is the normalized equivalent stress range (Eq. 9). Thus the variable-amplitude fatigue life is infinite when $f_{re} \leq F_{VAFL}$. The relationship between the CAFL and VAFL is shown with the right spectrum in Fig. 8.

Variable-Amplitude Fatigue Limit

According to Eq. 18, the VAFL should be $F_{VAFL} = \phi_e F_{CAFL} = 0.361 \cdot 81 = 29 \text{ N/mm}^2$ for the stiffener specimen of Fig. 1, where $\phi_e = 0.361$ for the MT spectrum (Fig. 3). On the other hand, there are very few cycles — 0.38% in Fig. 3 — between the short-tail (ST) and MT spectra. While these cycles have a negligible effect on the calculation of the equivalent stress range, retaining the peak stress range of the MT spectrum reduces unreasonably the equivalent stress range. To counter this imbalance, the VAFL in Fig. 5 was set at the value for the ST spectrum:

$$F_{VAFL} = \phi_e f_{CAFL} = 0.536 \cdot 81 = 43.4 \text{ N/mm}^2 \quad (19)$$

where $\phi_e = 0.536$ is the normalized equivalent stress range of the ST spectrum. Additional tests in which specimens were subjected to MT and ST spectrum loading confirmed that the chosen value of ϕ_e is reasonable [4].

Furthermore, the two specimens tested at $f_r = 42 \text{ N/mm}^2$ endured 250 million cycles of loading without failing, a good indication that the VAFL given by Eq. 19 is reasonable. To determine whether cracks had initiated in these specimens, the weld toes were brushed with Dykem steel blue; testing was then resumed at a higher equivalent stress range of $f_{re} = 103 \text{ N/mm}^2$. One specimen failed after an additional 1.8 million cycles, which is 56% of the mean fatigue life ($N_{\text{mean}} = 3.2 \cdot 10^6$) of the four regular specimens tested at the same equivalent stress range. The fracture surface contained a marked crack about 2.5 mm deep and 11.5 mm long. Initiation and growth of a crack to that size consumes about 44% of the expected life of the specimen [6]. It would have taken about 600 million cycles to fail the specimen had the test been continued.

The second specimen failed after 4.35 million cycles of $f_{re} = 103 \text{ N/mm}^2$ equivalent stress range, which is 136% of the mean fatigue life of the other four specimens tested at the same equivalent stress range. Since the fracture surface did not contain any markings indicative of a change in stress range, this test was indeed a runout at $f_{re} = 42 \text{ N/mm}^2$.

Predicted Fatigue Lives

The predicted variable-amplitude fatigue lives are shown in Fig. 5 as a solid curve, emanating from the constant-amplitude mean S-N line and approaching asymptotically the VAFL at extremely long lives of 10^9 cycles. It was calculated with the equivalent stress range model (Eq. 17), using the mean S-N line ($b = 12.4266$, $m = 3.008$) and the CAFL ($F_{CAFL} = 81 \text{ N/mm}^2$). The predicted S-N curve correlated reasonably well with the data although more points fall to the left than to the right of the predicted curve. Table 1 compares the predicted lives with the mean log-mean fatigue lives of the test specimens

at each equivalent stress range. Clearly, the lower the equivalent stress range, the more the model overestimates fatigue life.

Principles of fracture mechanics help to explain this observation. During the initial stages of growth, when the crack is still short, the combination of crack length and variable-amplitude stress range produces only a few ranges of stress intensity factor greater than the threshold, $\Delta K > \Delta K_{th}$. As the crack grows longer, more ΔK values exceed ΔK_{th} . Accordingly, the behavior gradually changes from few to many stress ranges causing fatigue damage during the long life of the specimen. But since most of the life is spent growing the crack while it is still short, the equivalent stress range model predicts fatigue life more accurately than does the straight-line extension. In summary, stress ranges smaller than the CAFL cause some damage, but not as much as the straight-line extension nor as little as the equivalent stress range model predict (Table 1).

The equivalent stress-range model assumes that stress ranges smaller than the fatigue limit cause no fatigue damage. This renders the calculation of fatigue life difficult because the summation in Eq. 17 must be determined anew for each value of equivalent stress range between $F_{CAFL} < f_{re} < F_{VAFL}$.

Table 1 — Comparison of Measured and Predicted Variable-amplitude Fatigue Life of Stiffener Detail

Equivalent Stress Range f_{re} (N/mm ²)	Fatigue Life (No. of cycles)				
	Measured Log-Mean	Straight-Line Extension Model Eqs. 4 and 11	Equivalent Stress Range Model Eq. 17	Simplified Stress Range Model Eq. 21	Fracture Mechanics Eq. 29
152	1,890,000	730,000	746,000	747,000	616,000
103	3,200,000	2,355,000	2,546,000	2,544,000	2,428,000
72	12,810,000	6,914,000	9,092,000	8,846,000	8,677,000
61	46,900,000	11,380,000	23,330,000	17,780,000	16,782,000
55	72,410,000	15,540,000	57,280,000	30,540,000	28,376,000
48	79,150,000	23,410,000	288,200,000	89,830,000	86,975,000
43.4 ^a	Not tested	31,700,000	Infinite	Infinite	Infinite ^c
42	250,000,000 ^b	Infinite	Infinite	Infinite	Infinite ^c

Notes: ^a VAFL. ^bRunout. ^c All values of ΔK at the initial crack length are smaller than ΔK_{th} .

Simplified Stress Range Model

Analogy Between S-N Curve and da/dN Curve

Fatigue life prediction would be greatly simplified if the summation in the denominator of Eq. 17 could be avoided. An idea from the fracture mechanics literature yields an elegant simplification. In one of several available models, the gradual transition between the crack growth equation and the threshold value of the stress intensity factor range is given as

$$\frac{da}{dN} = C (\Delta K^n - \Delta K_{th}^n) \quad (20)$$

where

da/dN = crack growth rate

a = crack length

ΔK = stress intensity factor range

ΔK_{th} = threshold value of stress intensity factor range

C, n = material constants

The corresponding model for S-N data, herein called the *simplified stress range model*, is given by:

$$N = \frac{10^b}{f_{re}^m - F_{VAFI}^m} \quad (21)$$

where f_{re} = equivalent stress range for full spectrum.

Predicted Fatigue Lives

The simplified model (dashed curve) is compared in Fig. 5 with the straight-line extension model and equivalent stress range models (solid curve). The simplified model has three important advantages over the others:

1. It predicts the mean trend of the test data more accurately than does the straight-line extension and equivalent stress range model (Table 1).
2. The closed-form Eq. 21 is valid in both the finite (above CAFL) and infinite (below CAFL) life regimes.
3. Eq. 21 is easy to use because the equivalent stress range is that of the full spectrum and does not change with stress level as is the case in the equivalent stress range model.

Fracture Mechanics Model

While S-N data are needed for designing structures, they are purely experimental, apply only to the specific specimen being tested, and are not based on principles of mechanics. Also, the measured fatigue life is the sum of two inseparable parts — the crack initiation life and the crack propagation life.

In contrast to the S-N approach, linear elastic fracture mechanics models the physical phenomena of crack extension at the leading edge and can predict the fatigue life of structural components subjected to constant- and variable-amplitude loading.

The variable-amplitude fatigue life of the stiffener is calculated with a fracture mechanics model that includes the threshold effect. The results are compared with those from the S-N curve approach.

Stress Intensity Factor

Figure 9 shows a part-through crack of semi-elliptical shape at the weld toe of the transverse stiffener. Stress intensity factors for this type of crack were calculated with the Newman and Raju [8] and Albrecht and Yamada [9] equations. The former is given by:

$$K = f \sqrt{\pi \frac{a}{Q}} F_s \left(\frac{a}{c}, \frac{a}{t}, \frac{c}{b}, \varphi \right) \tag{22}$$

for $0 \leq a/c \leq 2$, $c/b < 0.5$, and $0 \leq \varphi \leq \pi$. In equation 22,

- a = length of crack, in thickness direction of plate
- c = half-width of crack, in width direction of plate
- b = half-width of cracked plate

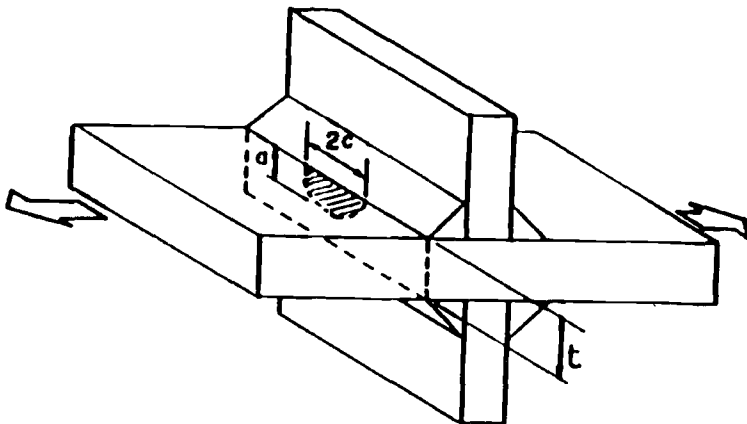


Figure 9 — *Part-through Crack at Weld Toe in Calculation of Stress Intensity Factor*

t = thickness of plate
 Q = shape factor for elliptical crack, equal to complete elliptical integral of second kind
 φ = parametric angle of ellipse
 F_s = boundary-correction factor for surface crack in plate
 f = uniform stress applied remotely

To account for the effect of a nonuniform stress field caused by the geometrical discontinuity at the weld toe, Newman and Raju's tension solution was multiplied by Albrecht and Yamada's stress gradient factor, f_g :

$$K = f \sqrt{\pi \frac{a}{Q}} F_s \left(\frac{a}{c}, \frac{a}{t}, \frac{c}{b}, \varphi \right) f_g \tag{23}$$

where

$$f_g = \frac{2}{\pi} \sum_{i=1}^n \frac{f_{bi}}{f} \left(\arcsin \frac{b_{i+1}}{a} - \arcsin \frac{b_i}{a} \right) \tag{24}$$

and

f_{bi} = normal stress at i -th element obtained from finite element analysis of uncracked plate
 b_{i+1} , b_i = distance from crack origin to near and far sides of i -th finite element.

Albrecht and Yamada also proposed a simple method of calculating the stress intensity factor for a semi-elliptical crack growing from a weld toe in a nonuniform stress field. Their equation consists of Irwin's solution for the semi-elliptical crack in a finite width plate under remote tension multiplied by the stress gradient factor of Eq. 24.

$$K = f \sqrt{\pi \frac{a}{Q}} \left(1.12 - 0.12 \frac{a}{c} \right) \sqrt{\frac{2t}{\pi a} \tan \frac{\pi a}{2t}} f_g \tag{25}$$

Figure 10 compares the normalized stress intensity factors calculated according to Newman and Raju, without and with f_g (dotted and solid curves), as well as Albrecht and Yamada (dashed curve). The two solutions differ by less than 5% for $a/t < 0.3$ and less than 10% for $a/t < 0.6$, with the Newman and Raju solution yielding higher values. Since most of the fatigue life is spent growing a crack while it is still short, these small differences in K values have a minor effect on predicting fatigue life. Therefore, Albrecht and Yamada's method was used in the present study because it is simple and f_g was available from a previous study.

Fatigue Life Prediction Model

Generally, the fatigue process may be divided into the two stages of crack initiation and propagation. But since welded details have severe stress concentrations and crack-like flaws, the number of cycles in the crack initiation stage is small. Most of the fatigue

life is spent growing a short crack at small stress ranges. Therefore, the following two assumptions were made in calculating fatigue life: (1) the crack initiation life is negligible, and (2) the propagation life lasts from an inherent initial crack length to a final crack length.

The threshold ΔK is to variable-amplitude crack growth rate as the CAFL is to variable-amplitude fatigue life. The similarities are apparent from Figs. 8 and 11. Therefore, three loading conditions were modeled: constant-amplitude loading, variable-amplitude loading with all stress intensity factor ranges greater than the threshold, and variable-amplitude loading with some stress intensity factor ranges greater than the threshold. For each loading condition, the fatigue life prediction consists of defining the crack growth rate model and integrating the crack growth rate equation from the inherent initial crack length to the final crack length. The following equations are used.

For constant-amplitude loading:

$$\frac{da}{dN} = C(\Delta K)^n \tag{26}$$

where ΔK = constant-amplitude stress intensity factor range. The fatigue life equation

$$N = \frac{1}{C f_r^n} \int_{a_i}^{a_f} \frac{1}{[F(a) \sqrt{\pi a}]^n} da \tag{27}$$

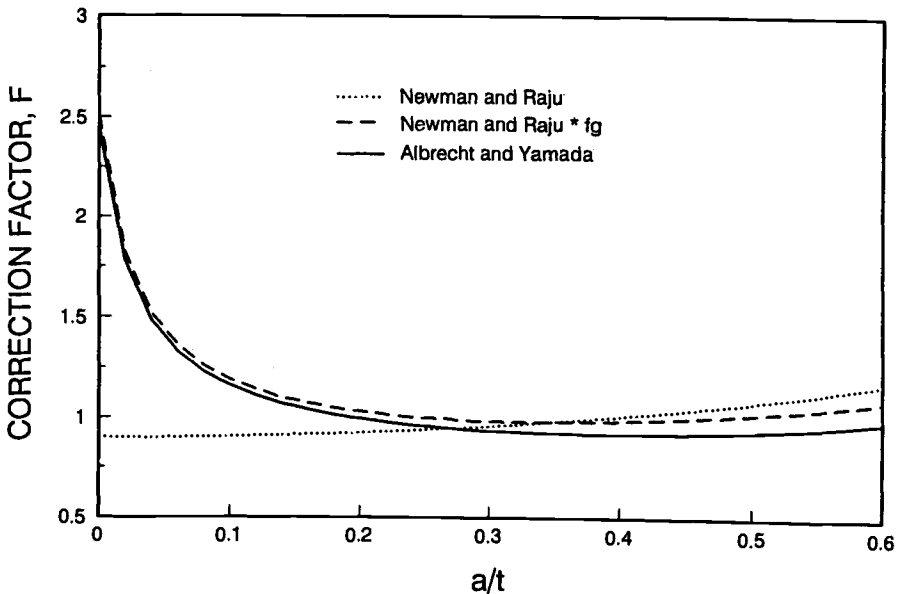


Figure 10 — Normalized Stress Intensity Factor; Comparison of Newman and Raju's Solution [8] with Albrecht and Yamada's Solution [9]

is solved numerically with 32-point Gaussian quadrature.

For variable-amplitude loading with all stress intensity factor ranges greater than the threshold:

$$\frac{da}{dN} = C(\Delta K_e)^n \tag{28}$$

where ΔK_e = equivalent stress intensity factor range for the full spectrum. The fatigue life equation

$$N = \frac{1}{C f_{re}^n} \int_{a_i}^{a_f} \frac{1}{[F(a) \sqrt{\pi a}]^n} da \tag{29}$$

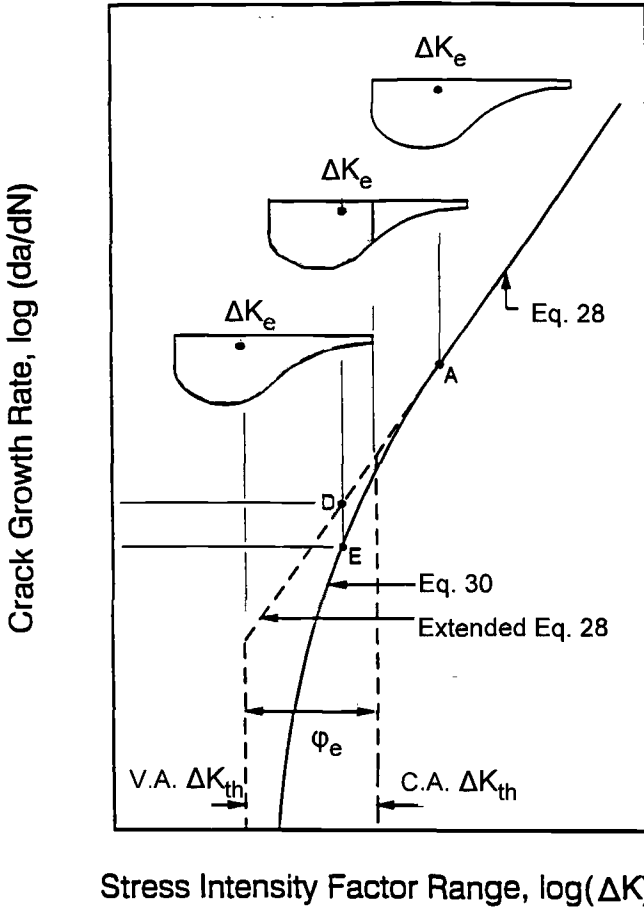


Figure 11 — Fatigue Crack Growth Rate under Variable Amplitude Loading; Equivalent Stress Intensity Factor Model

is again solved numerically with 32-point Gaussian quadrature.

For variable-amplitude loading with some stress intensity factor ranges greater than the threshold:

$$\frac{da}{dN} = C \left(\sum_{i=a}^k \gamma_i (\Delta K_i)^n \right) \quad (30)$$

The fatigue life is obtained by solving the equation with the Runge-Kutta method.

Inherent Initial Crack Length

The fatigue life was assumed to consist of the crack propagation life from an inherent initial crack length to a final crack length. Since constant-amplitude fatigue test data were available for each detail, the inherent initial crack length at each stress range at which tests were performed was calculated with Eq. 27, beginning with the final crack length and integrating backward over the mean fatigue life at that stress range. The resulting initial crack length was $a_i = 0.567$ mm for the stiffener shown in Fig. 1. The inherent initial crack length, a measure of existing flaws in a detail, is related to weld quality.

Final Crack Length

Since fatigue life varies little with final crack length, the latter was determined with a simple, approximate method. Analysis of fracture surfaces showed that the specimens failed when the average stress on the net ligament reached the tensile strength of the steel. Crack initiation at multiple sites, followed by crack coalescence, led to nearly straight crack fronts at failure of many specimens. Therefore, the final crack length was assumed to occur when the net ligament ruptured.

$$A_{net} = (t - a_f)w = \frac{P_{max}}{F_u} \quad (31)$$

where

t = thickness of main plate

a_f = final crack length

w = width of main plate

P_{max} = maximum applied load

F_u = tensile strength of steel.

The final crack length for each specimen is then given by

$$a_f = t - \frac{P_{max}}{F_u w} = t \left(1 - \frac{f_{max}}{F_u} \right) \quad (32)$$

where f_{\max} is the maximum applied stress.

Material Constants in Crack Growth Rate Model

Yazdani and Albrecht [10] performed an extensive analysis of crack growth rate data for mild high-strength low-alloy (HSLA) and quenched and tempered (QT) structural steels cycled in air, water, and saltwater. Over 3,500 data points for both constant-amplitude and variable-amplitude loading were analyzed and compared. The following equation for mild and HSLA steels in air was used herein:

$$\frac{da}{dN} = 1.537 \cdot 10^{-12} \Delta K^{3.344} \quad (33)$$

where da/dN and ΔK are in units of m/cycle and $\text{MPa}\sqrt{\text{m}}$, respectively.

Crack Growth Rate Threshold

The threshold was inferred from the CAFL of the stiffener detail tested in the present study. Assuming the inherent initial crack length and a stress range equal to the CAFL determined from tests, $f_r = F_{\text{CAFL}}$, gives the threshold:

$$\Delta K_{th} = F(a_i) F_{\text{CAFL}} \sqrt{\pi a_i} = 4.5 \text{ MPa}\sqrt{\text{m}} \quad (34)$$

This value lies well within the 3.5 to 5.5 $\text{MPa}\sqrt{\text{m}}$ range reported by Reynolds and Todd [11]; it was retained for the subsequent analyses.

Crack Aspect Ratio

The ratio of length to half-width of the crack, a/c , is needed to calculate the stress intensity factor range for a part-through crack. Available data on crack aspect ratios for cover plates and transverse stiffeners, summarized in [4], are widely scattered and cannot be represented by a single equation. Therefore, referring to the values used in previous studies, a constant aspect ratio of $a/c = 0.5$ was assumed for the stiffener specimen.

Predicted Fatigue Lives

There is excellent agreement between the fatigue lives predicted with the fracture mechanics and simplified stress range models, both above and below the CAFL $F_{\text{CAFL}} = 81 \text{ N/mm}^2$ from Eq. 6 (Table 1). In a way this might be expected because the inherent initial crack length was calculated from the constant-amplitude test data. On the other hand, no attempt was made to match the crack aspect ratio in the fracture mechanics model to that of each specimen separately. Nor was crack growth delay from delaminations included in the fracture mechanics model.

Both models yield fatigue lives shorter than the log-mean lives of replicate specimens. The biggest mismatch occurs in the finite life regime at $f_{re} = 152 \text{ N/mm}^2$, mostly a result of delaminations caused by the manganese sulfide inclusions that delayed crack growth in the specimens.

In the infinite life regime where the equivalent stress range is smaller than the CAFL, $f_{re} < F_{CAFL}$, the fracture mechanics and the simplified stress range models still predict comparable fatigue lives at equivalent stress ranges of $f_{re} = 48$ and 72 N/mm^2 . In between, at $f_{re} = 55$ and 61 N/mm^2 , the agreement is not as good, presumably because only two specimens were tested at each stress range, a number too small to capture the variability inherent in fatigue tests at very low stress ranges.

Finally, the fracture mechanics model predicts shorter fatigue lives in the infinite regime than does the equivalent stress range model, because the contributions of the small stress ranges to crack growth are not neglected.

Conclusions

Specimens tested under GVW spectrum loading failed at equivalent stress ranges much lower than the CAFL.

As the number of stress ranges greater than the CAFL decreased, the data points fell increasingly to the right of the straight-line extension of the S-N line.

When the highest stress range in the spectrum is just equal to the CAFL and all others are lower, the equivalent stress range of the entire spectrum becomes the VAFL. The VAFL is located below the CAFL by a factor equal to the ratio of the equivalent stress range to the highest stress range of the spectrum (Eq. 19).

Specimens tested at an equivalent stress range $f_{re} = 42 \text{ N/mm}^2$ slightly below the VAFL $f_{VAFL} = 43.4 \text{ N/mm}^2$ survived 250,000,000 cycles of loading without failing. These tests lasted about eight months. The number of cycles corresponds to an average daily truck traffic of 9,100 in one direction during a 75-year service life span, a value typical of truck traffic on I-495, the Beltway around Washington, D.C. Each truck crossing a grade separation bridge at a highway intersection produces one major stress range cycle.

The straight-line extension model (Eq. 4) increasingly underestimates fatigue life, the more the equivalent stress range approaches the VAFL.

The equivalent stress range model (Eq. 17) overestimates fatigue life because none of the stress ranges lower than the CAFL are assumed to cause damage irrespective of crack length.

The simplified model (Eq. 21) is preferred over the straight-line extension and the equivalent stress range models for the following reasons: (1) it predicts best the mean trend of the data, (2) is easy to use, and (3) yields fatigue life from the finite life regime to the VAFL with one simple, closed-form equation.

The fracture mechanics model correlates very well with the simplified stress range model; both predict fatigue lives comparable to those measured in the tests. But fracture mechanics models are too complex for use in ordinary design of highway bridges.

Application to Steel Highway Bridges

Structural details on steel highway bridges are designed for fatigue in accordance with the bridge specifications [12], using the following equation written in the nomenclature of this paper:

$$f_{re} \leq F_r \quad (35)$$

where

f_{re} = equivalent stress range at structural detail calculated with beam theory
 F_r = allowable stress range

The allowable S-N line for a given detail is taken as the lower-bound S-N line at two standard deviations to the left of the mean S-N line (Eq. 5). Setting $m = 3$, substituting A for 10^{b-s} and F_r for f_r , and solving Eq. 5 for F_r , gives the expression for the allowable stress range in the bridge specifications [12]:

$$F_r = \left(\frac{A}{N} \right)^{1/3} \geq 0.5 F_{CAFL} \quad (36)$$

Values of the constant A and the CAFL are listed in the bridge specifications for each type of detail.

Eq. 36 is conservative in two ways: (1) the model consists of extending the lower-bound S-N line as a straight line down to the VAFL, and (2) the VAFL is set at a lower value, that is, $0.5 F_{CAFL}$ versus $0.536 F_{CAFL}$ in the present study (Eq. 19). This added conservatism may be justified for new bridges because projections of GVWs and average daily truck traffic 75 years (design fatigue life) into the future is at best imprecise.

But straight-line extension is too conservative a model for estimating the fatigue life of an existing bridge for which information on past loading history may exist in the form of traffic counts and weighing station records, and fatigue-critical details can be inspected for cracks with non-destructive methods. For these reasons, an extra safety margin is not needed, and the simplified stress range method should be used instead for estimating the remaining life of an existing bridge. Substituting A for 10^{b-s} and setting $m = 3$ in Eq. 21 gives the fatigue life of an existing bridge:

$$N = \frac{10^4}{f_{re}^3 - F_{VAFL}^3} \quad (37)$$

where f_{re} must be calculated for all past and future GVWs and their frequency of occurrence.

In summary, the authors recommend designing new bridges with the straight-line extension model, Eq. 36, as is done in the bridge specifications, and existing bridges with the simplified model, Eq. 37.

References

- [1] Snyder, R. E., Likins, G. E. and Moses, F., *Loading Spectrum Experienced by Bridge Structures in the United States*, Report No. FHWA-RD-85-012, Federal Highway Administration, McLean, VA, 1985.
- [2] Abtahi, A., Albrecht, P. and Irwin, G. R., "Fatigue of Periodically Overloaded Stiffener Detail." *Journal of the Structural Division*, American Society of Civil Engineers, Vol. 102, ST11, November, pp. 2103-2119, 1976.
- [3] Albrecht, P. and Yamada, K., "Simulation of Service Fatigue Loads for Short-Span Highway Bridges," *ASTM STP 671, Symposium on Service Fatigue, Loads Monitoring, Simulation and Analysis*, American Society for Testing and Materials, Philadelphia, PA, 155-277, 1979.
- [4] Albrecht, P., Lu, H. Y., Jung, K. S., Liu, H. J. and Cheng, J. G., "*Long-Life Variable-Amplitude Fatigue Strength of Welded Steel Bridge Details*." Report No. FHWA-RD-94-108, Federal Highway Administration, McLean, Virginia, 1994.
- [5] Albrecht, P. and Friedland, I. M., "Fatigue-Limit Effect on Variable-Amplitude Fatigue of Stiffeners," *Journal of the Structural Division*, American Society of Civil Engineers, Vol. 105, No. ST12, 2657-2675, 1979.
- [6] Sahli, A. H. and Albrecht, P., "Fatigue Life of Welded Stiffeners with Known Initial Cracks," *ASTM STP 833, Fracture Mechanics: Fifteenth Symposium*, American Society for Testing and Materials, Philadelphia, PA, pp. 193-217, 1984.
- [7] Wilson, A. D., "Influence of Inclusions on the Fracture Properties of A588A Steel," *ASTM STP 833, Fracture Mechanics: Fifteenth Symposium*, American Society for Testing and Materials, Philadelphia, PA, 1984, pp. 412-435.
- [8] Newman, J. C. and Raju, I. S., "Stress-Intensity Factor Equations for Cracks in Three-Dimensional Finite Bodies," *ASTM STP 791, Fracture Mechanics: Fourteenth Symposium Volume I: Theory and Analysis*, American Society for Testing and Materials, Philadelphia, PA, 1983.
- [9] Albrecht, P. and Yamada, K., "Rapid Calculation of Stress Intensity Factors," *Journal of the Structural Division*, American Society of Civil Engineers, Vol. 103, No. ST2, pp. 377-389, 1977.

- [10] Yazdani N. and Albrecht, P., "Crack Growth Rates of Structural Steels in Air and Aqueous Environments." *Journal of Engineering Fracture Mechanics*, Vol. 32, No. 6, pp. 997-1007, 1989.
- [11] Reynolds, G. H. and Todd, J. A., "Threshold Corrosion Fatigue of Welded Shipbuilding Steels," *Technical Report No. SSC-366*, Ship Structure Committee, U.S. Coast Guard, Washington, D.C., 1992.
- [12] Bridge Design Specifications — LRFD , First Edition, American Association of State Highway and Transportation Officials, Washington, D.C., 1994.

Rune Lindström,¹ Per Lidar,¹ and Bo Rosborg¹

Fatigue Crack Growth Thresholds Measurements in Structural Materials

Reference: Lindström, R., Lidar, P., and Rosborg, B., “Fatigue Crack Growth Threshold Measurements in Structural Materials,” *Fatigue Crack Growth Thresholds, Endurance Limits, and Design, ASTM STP 1372*, J. C. Newman, Jr. and R. S. Piascik, Eds., American Society for Testing and Materials, West Conshohocken, PA, 2000.

Abstract: Fatigue crack growth thresholds and da/dN -data at low ΔK_I -values (<10 MPa \sqrt{m}) have been determined for type 304 stainless steel, nickel-base weld metal Alloy 182, nickel-base metal Alloy 600, and low-alloy steel in air at ambient temperature and in high-temperature water and steam. The stainless alloys have been tested in water with 0.2 ppm O₂ at 288°C and the low-alloy steel in steam at 286°C. The fatigue crack growth threshold was defined as the ΔK_I -value resulting in a crack growth rate of 10⁻⁷ mm per cycle. The measured fatigue crack growth thresholds (at frequencies from 0.5 to 20 Hz) are quite similar independent of the material and the environment.

A relatively inexpensive and time-saving method for measuring fatigue crack growth thresholds, and fatigue crack growth rates at low ΔK_I -values, has been used in the tests. The method is a ΔK_I -decreasing test with constant K_I^{Max} .

Keywords: fatigue crack growth rates, fatigue crack growth thresholds, DC potential drop, type 304 stainless steel, Alloy 182, Alloy 600, low-alloy steel, air, high-temperature water

Introduction

Crack growth due to vibrations and pressure variations in pipes and pressure vessels in nuclear power plants can lead to downtime costs and safety risks. It is therefore of interest to determine fatigue crack growth threshold (ΔK_{th}) and fatigue crack growth rate (da/dN) data in the threshold region for different material - environment systems. These data are needed to estimate the remaining life of components, to determine the time between inspections, and for safety analysis.

Factors that can have an influence on the measured ΔK_{th} for a specific material are the environment, load frequency, load ratio ($R = K_I^{Min}/K_I^{Max}$), and rate of ΔK_I -reduction in the test [1-5].

Measuring crack growth rates in the “near threshold region” and determining fatigue crack growth thresholds can be time consuming and thus expensive. To measure the

¹Researcher, section head, and technical director, Studsvik Material AB, SE-611 82 Nyköping, Sweden.

crack growth on-line with a sensitive method during the test can reduce the time and number of specimens needed to determine the threshold value. A number of test methods have been proposed for determining fatigue crack growth thresholds. The most widely used is the ΔK_I -decreasing method, where ΔK_I can be decreased step-wise at selected crack lengths, or decreased in a continuous manner until crack arrest occurs. Other methods involve combinations of ΔK_I -decreasing and ΔK_I -increasing methods, where ΔK_I is increased or decreased according to a "test scheme" depending on the measured fatigue crack growth rates [6-8].

This work deals with fatigue behavior in the "near threshold region" for relatively long cracks in structural materials. Short cracks and crack initiation have not been addressed. The objective of the work was to estimate fatigue thresholds values and fatigue crack growth rates at low ΔK_I for structural materials in light water reactor environments. On the whole (except regarding the ΔK_I reduction rate for some specimens) the recommendations in the ASTM standard E647-95a have been followed.

Experimental Procedure

Material and Specimens

The materials used were type 304 stainless steel, nickel-base weld metal Alloy 182, nickel-base metal Alloy 600, and low-alloy steel (LAS). Table 1 shows the chemical composition of the materials, and Table 2 shows the mechanical properties.

Table 1 – Chemical Composition in Weight %

Material	C	Si	Mn	P	S	Cr	Ni	Mo	N
	Cu	Al	V	Fe	Ta	Co	Nb	Ti	
Type 304 SS	.044	.50	1.0	.025	.025	18.5	10.5	.45	.088
	.3	.02	.07	bal.	–	–	–	–	
Alloy 182	.04	.46	7.24	.011	.004	13.9	68.3	–	–
	.01	–	–	7.86	.01	.02	1.70	.44	
Alloy 600	.072	.35	.19	–	.003	14.65	74.94	–	–
	.3	–	–	9.16	–	.33	–	–	
LAS	.16	.46	1.54	.012	.005	.03	.05	–	.006
	.02	.037	–	bal.	–	–	.03	–	

Table 2 – Mechanical Properties at Room Temperature

Material	$R_{p0.2}$ (MPa)	R_m (MPa)
Type 304 SS	296	595
Alloy 182	376	641
Alloy 600	248	683
LAS	368	545

The specimens were standard 25 mm wide compact tension (CT) specimens with a Chevron notch and 2.5 mm side-grooves on each side. Figure 1 shows the geometry of the CT-specimens. The crack plane orientation and heat treatment for the specimens are listed in Table 3. After heat treatment the specimens were fatigue pre-cracked in air at room temperature to a crack length of about 25 mm. The maximum K_I during the pre-fatigue was lower than the maximum K_I in the following test.

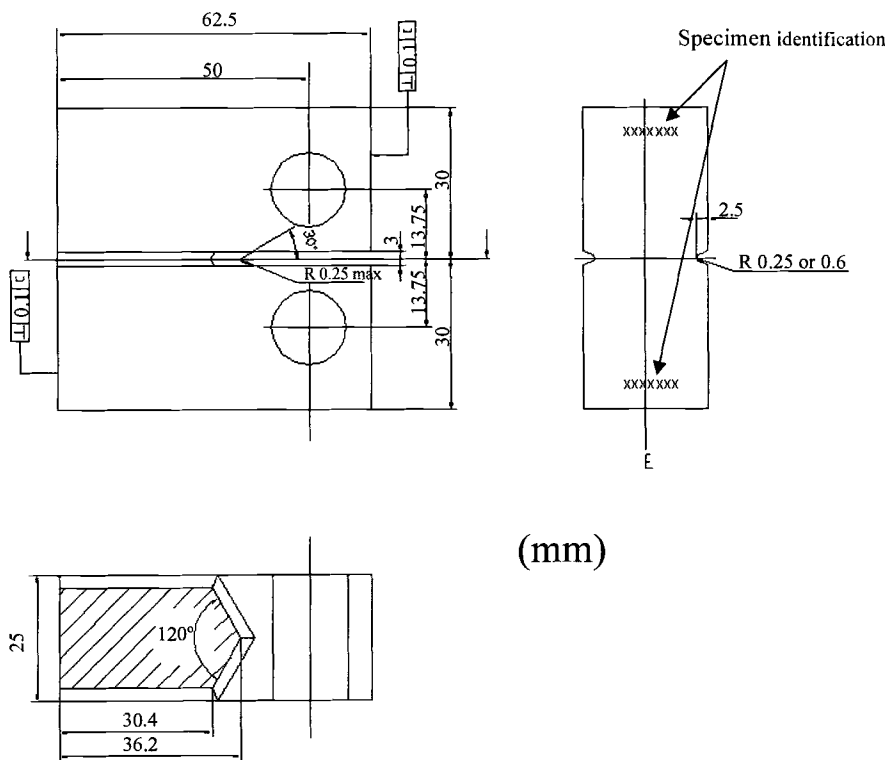


Figure 1 – Geometry of the CT-specimens.

Table 3 – Crack Plane Orientation and Heat Treatment for the CT-specimens

Material	Orientation*	Heat treatment
Type 304 SS	L-S	1050°C/20 min/oil quenched (oq)+ 680°C/1 h/oq + 500°C/24 h/air cooled
Alloy 182	see Figure 2a	as welded
Alloy 600	see Figure 2b	1050°C/30 min/oq + 600°C/24 h/air cooled
LAS	L-S	none

* Orientation according to ASTM Test Method for Plane-Strain Fracture Toughness of Metallic Materials (E 399-90).

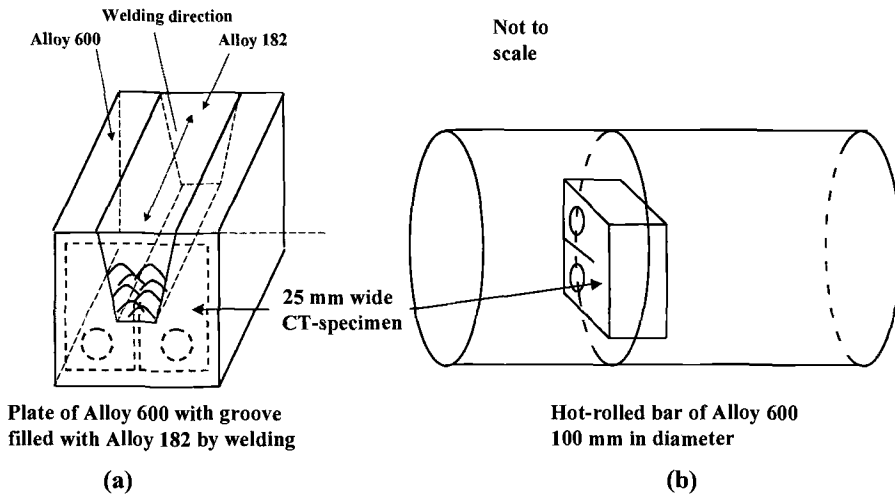


Figure 2 – Orientation of the Alloy 182 and Alloy 600 Specimens.

The Alloy 182 material was welded according to nuclear practice using \varnothing 4 mm weld electrodes. The weld passes were oriented in such a way that the crack plane could be oriented parallel with the weld dendrites.

Test Equipment and Test Environments

All tests were performed in a computer controlled servohydraulic materials testing machine. In this equipment fracture mechanics specimens can be tested under constant stress intensity or constant stress intensity factor range. The K_I and ΔK_I levels can also be changed automatically during a test.

The crack growth in the specimen was measured on-line during the tests using both DC Potential Drop (DCPD) and compliance techniques. Current reversals and an experimentally determined calibration curve for transforming the DCPD-signal to crack growth were used. The compliance of the specimen was measured using a Linear Voltage Differential Transducer (LVDT) attached to the front face of the specimen. The specimens were galvanically insulated from the autoclave system, grips, and loading pins.

Boiling water reactor environments – For the tests in simulated boiling water reactor (BWR) environments the materials testing machine was equipped with an autoclave. The autoclave system was a once-through flow system with a volume of 6.7 l water with the specimen mounted, and the flowrate through the autoclave was about 8 l/h. The temperature was 288°C and the pressure 9 MPa. The conductivity at room temperature of the inlet and the outlet water was monitored during the tests and the typical outlet conductivity was less than 0.25 μ S/cm. Air- or oxygen-saturated water was added to pure water to reach a level of about 0.2 or 0.5 ppm oxygen in the outlet water. The corrosion potential of the specimen was monitored during the test using a silver - silver chloride reference electrode.

Secondary-side pressurized water reactor environment – The secondary-side pressurized water reactor (PWR) environment was simulated using pure water with 50 ppb hydrazine. In this test the upper half of the autoclave contained water-saturated steam and the lower half water. The temperature was 286°C and the pressure 7.1 to 7.2 MPa. A differential pressure transmitter was used to control the amount of water flowing into the autoclave to maintain a constant water level. The specimen was mounted in the steam above the water level.

Air at room temperature – The tests in air at room temperature were performed in the same or similar type of equipment as used for the tests in high-temperature water and steam.

Test Procedure

Most of the tests were performed similarly: After the specimen had been pre-exposed to the environment for about a week (either unloaded or with only a small load applied) a fatigue load with constant ΔK_I was applied. When the crack had propagated a certain distance (usually 1 mm for the first “step” and for every following step the distance was decreased by about 5 %), ΔK_I was decreased while maintaining a constant K_I^{Max} ; thus, the R-value was increased. This procedure was automatically repeated until the fatigue crack growth rate (da/dN) reached very low values (below 10^{-7} mm per cycle). The shedding of ΔK_I was performed using the formula for the normalized K-gradient (C) according to ASTM Test Method for Measurement of Fatigue Crack Growth Rates (E 647-95a), but with ΔK_I instead of K_I .

$$C = \frac{1}{\Delta K_I} \cdot \frac{d\Delta K_I}{da} \quad (1)$$

where a is the crack length and $d\Delta K_I/da$ is the slope of the ΔK_I versus a curve. In step-wise ΔK_I -decreasing tests, as in this work, the next ΔK_I is then calculated according to following equation:

$$\Delta K_I = \Delta K_I^{\text{old}} \cdot e^{(C \cdot \Delta a)} \quad (2)$$

where Δa is the crack advance since the previous decrease of ΔK_I .

The value of C was in most of the tests close to -0.1 mm^{-1} , but in some exceptional cases it was as low as -0.3 mm^{-1} . The R-value was higher than 0.8 at the end of all tests.

The load waveform was triangular and the frequency was 20 Hz for testing in simulated BWR environments. For the tests in simulated PWR environment the frequency was in the range 0.5 to 20 Hz. The tests in air were performed with a frequency of 5 to 20 Hz depending on the test equipment used. From an environmental influencing point of view, the frequencies used were relatively high, thus any large effect of the environment on the fatigue crack growth rates and threshold values was not expected.

After testing the specimen was cooled in liquid nitrogen, broken into two pieces, and the fracture surfaces were examined in a scanning electron microscope. The true crack lengths were measured on the fracture surface and the measured crack growth was corrected. For every ΔK_I -level the corresponding da/dN -value was estimated by fitting a straight line to the data points (crack length versus number of cycles).

Results

The results from the different tests are compiled in Figures 3a-c, which show the fatigue crack growth rate versus ΔK_I for the different material - environment combinations. Table 4 summarizes the estimated fatigue crack growth thresholds (ΔK_{th}). The threshold values were estimated by fitting a curve (third-order polynomial) to the data points and calculate its intersection with the $da/dN=10^{-7}$ mm per cycle line.

The fracture surfaces showed transgranular (transdendritic for Alloy 182) cracking. They were quite similar for tests in the high-temperature environments and in air at room temperature.

Table 4 – Measured Fatigue Crack Growth Thresholds

Material/ environment	ΔK_{th} (MPa \sqrt{m})
Type 304 SS/air	4.7
Type 304 SS/BWR	4.2
Alloy 182/air	5.0
Alloy 182/BWR	4.9
Alloy 600/BWR	5.4
LAS/air	4.3

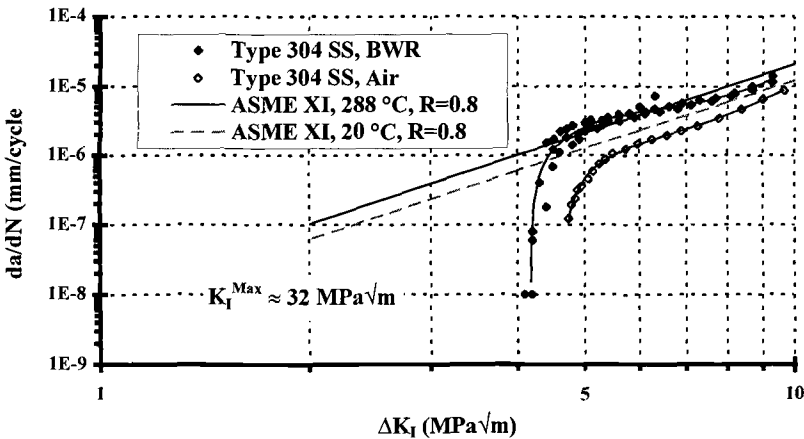


Figure 3a – Fatigue Crack Growth Rate versus ΔK_I for Type 304 Stainless Steel in Simulated BWR Environments and in Air.

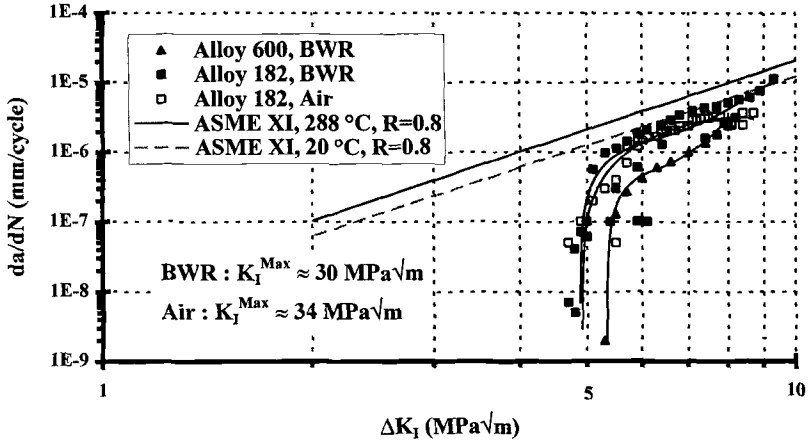


Figure 3b – Fatigue Crack Growth Rate versus ΔK_I for Ni-base Alloy 182 and Alloy 600 in Simulated BWR Environments and in Air.

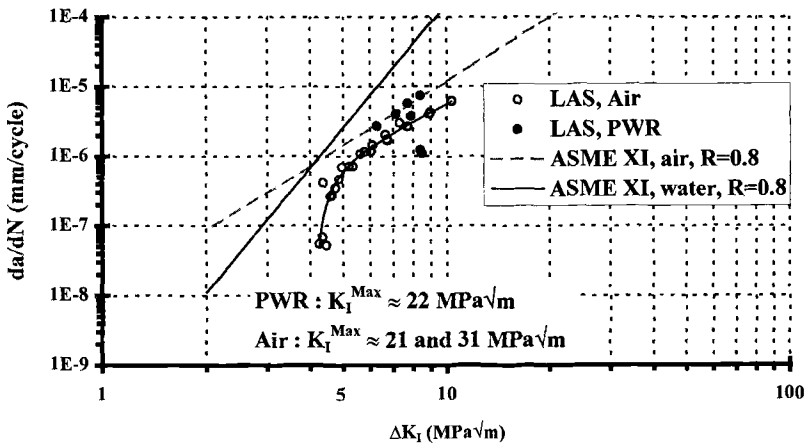


Figure 3c – Fatigue Crack Growth Rate versus ΔK_I for LAS in a Simulated PWR Environment and in Air.

Discussion

Test Technique

The tests to estimate fatigue crack growth thresholds were performed with decreasing ΔK_I in order to avoid long initiation times until crack propagation starts and to be able to perform the pre-cracking with a reasonably high ΔK_I . A constant C-value according to Equation 1 was used for the step-wise shedding of ΔK_I in order to use the specimens as efficiently as possible (large span of ΔK_I). To minimize problems with crack closure, a constant K_I^{Max} (that is an increasing R-value) was maintained during the tests.

Keeping K_I^{Max} constant should make it possible to relax the demand on C being greater than -0.08 mm^{-1} as stated in ASTM E 647. One possible disadvantage of using constant K_I^{Max} is that changing the R-value may effect da/dN (especially at low ΔK_I) and the threshold value [1].

Hysteresis of the load can be a problem when performing tests in a pressurized autoclave with the load cell placed outside the autoclave at atmospheric pressure. If the force on the pull rod from the pressure seal is not sufficiently small compared to the load amplitude on the specimen the hysteresis has to be compensated for. Another possible problem in fatigue testing at relatively high frequencies using servohydraulic machines is that above a certain frequency (depending on actuator type, oil flow, weight of grips and the specimen, or type and condition of the servovalve) the load amplitude decreases with increasing frequency even if the demand signal is unchanged. In the tests reported here the amplitude was automatically compensated for both the hysteresis and the frequency effect to achieve the correct load amplitude on the specimen.

The present tests have shown that da/dN -data at low ΔK_I and fatigue crack growth thresholds can be determined in a reasonably inexpensive and time-saving way. A good crack growth measurement technique, computer controlled test equipment, and software for automatic control of ΔK_I and R-value are needed.

Fractography

The fracture surfaces showed transgranular or transdendritic (Alloy 182) cracking. The fact that the fracture surfaces from the tests in the high-temperature environments were similar to those from the tests in air at room temperature is not surprising since the frequencies used during the testing were relatively high. The environmental contribution to the cracking usually decreases with increasing load frequency [3, 5, 9, 10].

For the tests in simulated BWR environments a transition from fatigue cracking to stress corrosion cracking (SCC) in the end of the tests, when the R-value was high enough, could be anticipated (see Figure 4). This should be manifested by an increasing amount of intergranular cracking on the fracture surfaces. However, the anticipated transition in crack mode at the end of the tests did not appear in any of the tests. The reason may be that the tests were interrupted before any initiation of intergranular cracking could be observed.

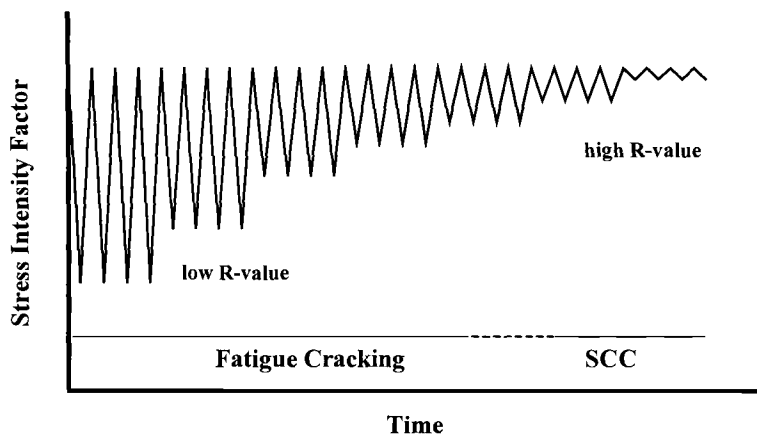


Figure 4 – Schematic Diagram of the Change in K_I during a Typical Test.

Threshold Values and da/dN

A threshold value was found for all material - environment combinations in this work except for LAS in simulated secondary-side PWR environment. The threshold values fall within the rather narrow range of 4.2 to 5.4 $\text{MPa}\sqrt{\text{m}}$. Comparing type 304 stainless steel and Ni-base alloys in air at room temperature and in the simulated BWR environments (Figures 3a-b) shows that stainless steel in the simulated BWR environments has the highest da/dN -values and the lowest fatigue crack growth threshold, and that Alloy 600 has the lowest da/dN -values and the highest threshold.

In Figures 3a through 3c reference lines according to the American Society of Mechanical Engineers (ASME) Boiler and Pressure Vessel Code, Section XI, are also shown. The data for the stainless alloys are compared with the reference curve for austenitic stainless steel in air (Article C-3000, Fig. C-3210-1) and the LAS data is compared with the reference curves for carbon and low-alloy ferritic steel in air (Article A-4000, Fig. A-4300-1) and in water environments (Article A-4000, Fig. A-4300-2). The fatigue crack growth rates according to ASME are slightly higher than the data points from the present study for all materials except for stainless steel in the simulated BWR environment, where the data points fall on both sides of the ASME line. Since the ASME guidelines do not use any threshold values they are very conservative at low ΔK_I -levels near and below $\Delta K_{I,th}$.

The reason for not being able to measure a fatigue crack growth threshold for LAS in simulated secondary-side PWR environment was that the crack stopped long before the crack growth rate was lowered to 10^{-7} mm per cycle. The lowest ΔK_I where crack growth was observed was higher than 6 $\text{MPa}\sqrt{\text{m}}$ and da/dN was then higher than 10^{-6} mm per cycle. When comparing with the results from tests in air of the same material it was obvious that the effective ΔK_I on the specimen for some reason was lower than the measured ΔK_I . The reason for the smaller effective ΔK_I is not known, however, it is probably not

malfunction of the specimen or the test equipment, since this phenomenon was not observed when testing in air at room temperature using the same specimen and test equipment. A range of phenomena can cause crack arrest at nominally "high" ΔK_I -values, such as, an overly high rate of ΔK_I -reduction, surface roughness induced crack closure, crack closure due to corrosion products on the crack surfaces, and test interruptions [2].

An important question is whether a true threshold or merely an apparent threshold has been measured. Therefore, a recommended procedure after testing with decreasing ΔK_I is to increase ΔK_I again to check the validity of the measurements [2]. In the tests reported here an increase in ΔK_I was not done due to lack of time. However, since the R-values were rather high (>0.8) in the end of the tests, and ΔK_{th} usually decreases with increasing R-value [1, 4, 7, 8, 11], the threshold values measured in the tests should be conservative in most cases with relatively high (higher than about 1 Hz) load frequencies or in non-aggressive environments.

Even if the obtained threshold and da/dN -values are conservative as to the R-value, they are probably not conservative with respect to the frequency. The tests were all performed at relatively high frequencies considering any environmental influence. Fatigue crack growth rates in water environments usually increase with decreasing frequency due to the larger environmental contribution to the cracking at lower frequencies [3, 5, 9, 10].

Conclusions

A relatively inexpensive and time-saving method to measure da/dN -data at low ΔK_I -levels and determine fatigue crack growth thresholds in light water reactor environments at frequencies in the order of 20 Hz has been demonstrated. The method is based on a ΔK_I -decreasing test with constant K_I^{Max} (on the whole following the recommendations in the ASTM standard E647-95a). A further improvement of the method would be to incorporate a ΔK_I -increasing test in the end, when a threshold value has been reached, to check the validity of the measurements.

The method has been applied on type 304 stainless steel, nickel-base weld metal Alloy 182, and nickel-base metal Alloy 600 in a simulated BWR environments, and on a low-alloy steel in a simulated secondary side PWR environment, and also in air at ambient temperature. A threshold value was found for all material - environment combinations except for the low-alloy steel in the simulated secondary-side PWR environment. All threshold values fall within the rather narrow range of 4.2 to 5.4 $MPa\sqrt{m}$.

The measured fatigue crack growth rates fall below or on the ASME XI reference lines.

Acknowledgments

This work has been sponsored by Vattenfall AB Ringhals, Forsmarks Kraftgrupp AB, Barsebäck Kraft AB, OKG Aktiebolag, and Studsvik AB. The contribution to the work and the assistance from colleagues from all sponsoring organizations is gratefully acknowledged.

References

- [1] Amzallag, C., Rabbe, P., Bathias, C., Benoit, D., and Truchon, M., "Influence of Various Parameters on the Determination of the Fatigue Crack Arrest Threshold," *Fatigue Crack Growth Measurement and Data Analysis, ASTM STP 738*, S. J. Hudak, Jr., and R. J. Bucci, Eds., American Society for Testing and Materials, 1981, pp. 29-44.
- [2] Bucci, R. J., "Development of a Proposed ASTM Standard Test Method for Near-Threshold Fatigue Crack Growth Rate Measurement," *Fatigue Crack Growth Measurement and Data Analysis, ASTM STP 738*, S. J. Hudak, Jr., and R. J. Bucci, Eds., American Society for Testing and Materials, 1981, pp. 5-28.
- [3] Bamford, W. H., "Application of Corrosion Fatigue Crack Growth Rate Data to Integrity Analyses of Nuclear Reactor Vessels," *Journal of Engineering Materials and Technology*, vol. 101, 1979, pp. 182-190.
- [4] Radon, J. C., "Fatigue Crack Growth in the Threshold Region," *Fatigue Thresholds – Fundamentals and Engineering Applications*, J. Bäcklund, A. F. Blom, and C. J. Beevers, Eds., Engineering Materials Advisory Services Ltd., 1982, vol. I, pp. 113-132.
- [5] Achilles, R. D. and Bulloch, J. H., "The Near-Threshold High R-Ratio Fatigue Crack Growth Characteristics of SA508 cl III Reactor Pressure Vessel Steel," *International Journal of Pressure Vessels and Piping*, vol. 35, 1989, pp. 363-382.
- [6] Bailon, J. P., Chappuis, P., and Masounave, J., "A Rapid Experimental Method for Measuring the Threshold Stress Intensity Factor," *Fatigue Thresholds – Fundamentals and Engineering Applications*, J. Bäcklund, A. F. Blom, and C. J. Beevers, Eds., Engineering Materials Advisory Services Ltd., 1982, vol. I, pp. 77-98.
- [7] Cadman, A. J., Brook, R., and Nicholson, C. E., "Effect of Test Technique on the Fatigue Threshold ΔK_{th} ," *Fatigue Thresholds – Fundamentals and Engineering Applications*, J. Bäcklund, A. F. Blom, and C. J. Beevers, Eds., Engineering Materials Advisory Services Ltd., 1982, vol. I, pp. 59-75.
- [8] Döker, H., Bachmann, V., and Marci, G., "A Comparison of Different Methods of Determination of the Threshold for Fatigue Crack Propagation," *Fatigue Thresholds – Fundamentals and Engineering Applications*, J. Bäcklund, A. F. Blom, and C. J. Beevers, Eds., Engineering Materials Advisory Services Ltd., 1982, vol. I, pp. 45-57.
- [9] Scott, P. M., "Corrosion Fatigue in Pressure Vessel Steels for Light Water Reactors," *Metal Science*, vol. 13, 1979:7, pp. 396-401.
- [10] Hishida, M., Saito, M., Hasegawa, K., Enomoto, K., and Matsuo, Y., "Experimental Study on Crack Growth Behavior for Austenitic Stainless Steel in High Temperature Water," *Journal of Pressure Vessel Technology*, vol. 108, 1986, pp. 226-233.
- [11] Vasudeven, A. K., Sadananda, K., and Louat, N., "A Review of Crack Closure, Fatigue Crack Threshold and Related Phenomena," *Materials Science and Engineering*, Elsevier Sequoia, 1994, pp. 1-22.

Gary Marquis,¹ Roger Rabb,² and Laura Siivonen¹

Endurance Limit Design of Spheroidal Graphite Cast Iron Components Based on Natural Defects

Reference: Marquis, G., Rabb, R., and Siivonen, L., “Endurance Limit Design of Spheroidal Graphite Cast Iron Components Based on Natural Defects,” *Fatigue Crack Growth Thresholds, Endurance Limits, and Design*, ASTM STP 1372, J. C. Newman, Jr. and R. S. Piascik, Eds., American Society for Testing and Materials, West Conshohocken, PA, 2000.

Abstract: Cast irons are used extensively in the production of large diesel engines for power generation or oceangoing ships. One current trend is to replace grey iron with spheroidal graphite (SG) iron for fatigue critical components. In order to take advantage of the higher fatigue strength of SG iron and ensure the reliability of a design, better understanding of the typical defects for these large castings and the relationship between these defects and the endurance limit fatigue strength have been studied. Testing included uniaxial constant amplitude, constant amplitude torsion, and simple variable amplitude loading sequences in the long-life regime. Defects in several thick wall castings have been statistically evaluated. A fracture mechanics based model involving matrix hardness and $\sqrt{\text{area}}$ successfully related the defect size to the experimentally observed fatigue limit. For ferritic-pearlitic SG iron, the hardness of the tougher pearlite phase was used in the model. The model also correlated the torsion and tension endurance limits. Endurance limit as a function of mean stress is presented in the form of Haigh diagrams.

Keywords: fatigue, nodular cast iron, spheroidal graphite cast iron, GRP 500, endurance limit, nonpropagating cracks, fatigue threshold, casting defects, shrinkage pores

Introduction

Spheroidal graphite (SG) cast iron is used extensively in the production of large diesel engines for power generation. Casting provides an economical advantage over other production methods by offering significant freedom in geometrical shaping for functionality and material utilisation. When compared to grey iron, SG cast irons have significantly higher fatigue strengths that can be used to great advantage in the design of rotating or reciprocating machinery. Rigid quality control during the casting operation

¹Researcher, VTT Manufacturing Technology, P.O. Box 1704, FIN-02044 VTT, Finland

²Section Manager, Wärtsilä NSD Corp., P.O. Box 244, FIN-65101 Vaasa, Finland

can eliminate the relatively large defects often associated with complex castings, but small microstructural irregularities can never be completely eliminated for large thick-section castings. These shrinkage pores, inclusions, and other types of naturally occurring defects have a controlling effect on the endurance limit strength.

Diesel engines used in conjunction with electrical generators must often operate continuously for many tens of thousands of hours. Design optimisation for long-lives requires an understanding of the high cycle fatigue behaviour of the cast material. Loading is primarily constant amplitude, but start-up and other transient events can result in occasional overloads which are known to greatly effect the fatigue performance of materials. Fatigue lives are typically computed even in billions of load cycles.

The current paper describes an experimental program to measure the constant amplitude endurance limit of a SG cast iron at various stress ratios. Results are presented in the form of Haigh diagrams for long life design. The role of casting defects has been evaluated via examination of the fracture surfaces and identifying the defect from which the failure crack initiated. The $\sqrt{\text{area}}$ parameter developed by Murakami, Endo and co-workers is examined as a means of quantitatively correlating the defect size and endurance limit. Nonpropagating surface cracks at the endurance limit were investigated on highly polished specimens. Torsion tests and several long-life uniaxial variable amplitude tests are also reported.

The $\sqrt{\text{area}}$ Model

Murakami, Endo and co-workers [1-6] have made extensive studies of the constant amplitude long life fatigue strength of materials containing small cracks, holes, inclusions, porosity and other inhomogeneities. They show that the fatigue limit is not the critical stress for crack initiation but the threshold stress for propagating a crack which emanates from the original defect. Many of these flaws are irregularly shaped and they proposed using the $\sqrt{\text{area}}$ as a measure of the flaw size. For an arbitrary three dimensional flaw, the $\sqrt{\text{area}}$ is measured by projecting the flaw onto a plane normal to the principal normal stress direction as illustrated in Fig. 1.

This model is based on the experimental observation that cracks may nucleate at small stress concentrations early in fatigue but do not propagate if the loading amplitude remains constant. The fatigue limit is related to the size of the notch, $\sqrt{\text{area}}$, and is less dependent on notch shape or stress concentration. Two flaws producing the same stress intensity will not always have the same fatigue limit because of the size dependence of ΔK_{th} . In defining $\sqrt{\text{area}}$, the additional size contribution from the small crack that forms at the edge of the hole or defect is small and is ignored.

The threshold stress intensity, ΔK_{th} , for the material is a critical factor in determining if flaws will result in fatigue failure. Experimentally, it has been found to be a function of both material strength and flaw size. The resulting relation for surface breaking defects for fully reversed loading is

$$\sigma_{\text{fl R}=-1} = \frac{1.43(\text{Hv} + 120)}{(\sqrt{\text{area}})^{1/6}} \quad (1)$$

where Hv is the Vickers hardness. Stress ratio effects are considered with the relation

$$\sigma_{flR} = \sigma_{flR=-1} \left[\frac{1-R}{2} \right]^\alpha \quad (2)$$

$$\alpha = 0.226 + Hv \times 10^{-4}$$

The units are ΔK_{th} : $MPa\sqrt{m}$, σ_{fl} : MPa , Hv : kgf/mm^2 , and \sqrt{area} : μm . A precise definition of \sqrt{area} is unnecessary because it is raised to the power $1/6$ to obtain the fatigue limit. This exponent means that a 50% increase in the \sqrt{area} parameter will result in only a 7% decrease in the fatigue limit.

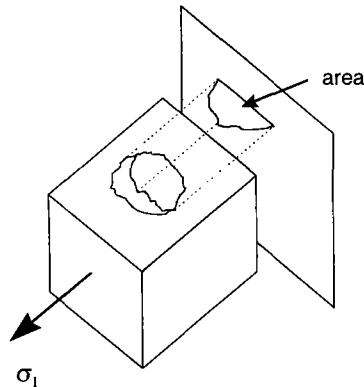


Figure 1 - Definition of area in the \sqrt{area} Parameter [4].

In torsion, fatigue cracks in some materials nucleate at defects along tensile planes oriented 45° from the applied shear stresses. Crack growth is controlled by the mode I stress intensity. The mode I stress intensity factor is higher in torsion than in tension for a small crack emanating from a hole or volumetric defect. This means that the nominal stress required to propagate a crack in torsion near a notch or defect will be lower in torsion than in tension. Based on the \sqrt{area} model, $\sigma_n / \tau_n \approx 1.25$ [5].

The \sqrt{area} parameter has been verified for a variety of metallic materials and a wide range of different defects and surface features. It has been used to correlate fatigue reduction for many naturally occurring defects including non-metallic inclusions, second phase particles and spheroidal graphites [6]. Beretta et al. [7] successfully applied the method to cast connecting rods and specimens from three different nodular irons with relatively large defects. Cast irons, like those used in the current study are of particular interest because of their complex non-homogeneous microstructure which consists of graphite nodules in a dual ferritic-pearlitic matrix.

Haigh Diagram

In high cycle fatigue design, the endurance limit stress amplitude as a function of mean stress is often presented in the form of a Haigh diagram. Construction of the diagram requires two monotonic constants, R_m and $R_{p0.2}$ and two fatigue values, typically $\sigma_{fl R=0}$ and $\sigma_{fl R=-1}$. The relation between stress amplitude and mean stress is considered linear along the line A-B in Fig 2. This is the region between tensile and compressive yielding.

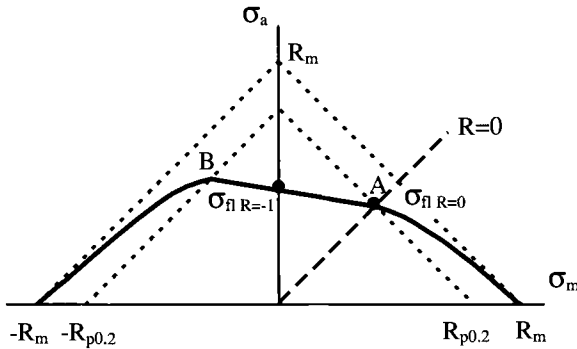


Figure 2 - Haigh Diagram.

As the mean stress is reduced past that at point B, the allowable stress amplitude gradually reduces to zero at the compressive ultimate strength. Similarly, as the mean stress increases past that at point A, the allowable stress amplitude smoothly reduces to zero at the ultimate strength in tension. For materials like cast iron, the ultimate strength in compression is not necessarily the point of fracture, but may correspond to a specified degree of gross deformation. The curve of the diagram between the yield and ultimate strengths can be used only in the case where elastic shakedown occurs, i.e., plastic strain is in one direction only without reverse yielding. It should be noted, however, that the effect on mean stress and especially compressive mean stress on materials like nodular cast iron are poorly documented in the available literature and it is difficult to propose design curves with any certainty.

Experiments

Test Material

Test bars were cut from 100 x 100 x 300 mm ingots and from the cylinder head of a Wärtsilä 64 medium speed diesel engine. The cylinder head is a complex casting with outside dimensions of approximately 750 x 1000 x 1400 mm. Material from both the ingots and cylinder head were nominally identical, GRP 500/ISO 1083 nodular cast iron, but were received from two different foundries.

Material taken from the cylinder head is hereafter designated as batch 1 and material taken from the ingots is designated batch 2. Average tensile properties for the two

batches of material are $R_{p0.2} = 307$ MPa and $R_m = 517$ MPa for batch 1 and $R_{p0.2} = 340$ MPa and $R_m = 620$ MPa for batch 2.

Figure 3 shows micrographs from the two materials. Both show approximately the same distribution of nodular graphites and a dual ferritic-pearlitic matrix. Material from batch 1 (Fig. 3a) is approximately 50% pearlite, 40% ferrite and 10% graphite and material from batch 2 (Fig. 3b) is 77% pearlite, 10% ferrite and 13% graphite.

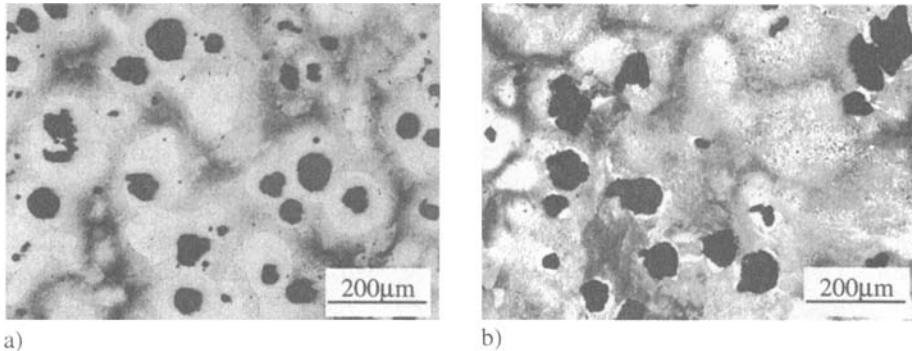


Figure 3 - Microstructure of a) Batch 1 and b) Batch 2 GRP 500 Nodular Iron.

Microhardness measurement of the different phases were made. For batch 1, the ferrite phase had a mean hardness of $H_v = 170$ (200 g) and the pearlite phase $H_v = 235$ (200 g). The corresponding values for batch 2 material were $H_v = 225$ (10 g) and $H_v = 300$ (200 g). Because of the very small ferrite fraction in batch 2, only a 10 g weight could be applied while in other cases a 200 g weight was used. Due to the highly non-homogenous microstructure, microhardness measurements were difficult and standard deviation in hardness was about 25% for batch 1 and 10% for batch 2.

Fatigue Testing

The majority of fatigue testing was accomplished on a computer controlled resonant type test machine manufactured by Rumul. Test frequency was nominally 160 Hz. Axial test specimens were 12 mm dia. with a 30 mm gage section and 50 mm transition radius. Torsion testing was performed using tubular specimens, 20 mm ID x 25 mm OD with a 10 mm gage section and 35 mm transition radius. Specimens were polished with emery paper and diamond paste so that no scratches or machining marks perpendicular to the loading direction were visible under x20 magnification. Axial testing was performed using several stress ratios while $R=0$ was used for torsion testing.

The cutoff limit in the constant amplitude tests to establish the endurance limit was 1×10^7 cycles. The staircase test strategy [8] was followed and the median endurance limit and variance were computed using the simplified maximum likelihood estimation method developed by Dixon and Mood [9]. For analysis purposes, the fatigue strength of a population of specimens was assumed to be normally distributed. In most cases 15 specimens were used to determine a single endurance limit value. The computed standard

deviation in fatigue strength for all test series was 8 - 15 MPa. All values reported in this paper, however, are median values.

For observing nonpropagating fatigue cracks at the endurance limit, eight rectangular cross section specimens were tested in four-point bending. The cross section was 20 x 20 mm and the highly stressed region between the two inner rollers was 20 mm long. The stress amplitude in these tests was 90% of the measured endurance limit stress amplitude in bending, $R=0.05$.

In addition to the approximately 120 specimens tested using constant amplitude loading, five specimens were tested using a variable amplitude load history. The variable amplitude load history consisted of a block of 220,000 cycles at a stress amplitude of 83.5 MPa and mean stress of 260 MPa. This stress combination did not cause failure under constant amplitude loading within 1×10^7 cycles. After the low amplitude cycles, one single cycle with maximum and minimum stress of 343.5 MPa and 10 MPa was applied. Maximum stress in both the small amplitude cycles and the single underload cycle were identical. It can be noted that the minimum nominal stress in each underload cycle was less than the minimum stress of the small amplitude cycles but remained tensile, the term "tensile underload" is, therefore, used to describe the nature of the event. The variable amplitude history is illustrated in the insert in Fig. 4.

Because resonant testing was used, short transients occur both before and after the application of each underload event. Prior to the underload, the resonance excitation is removed causing a gradual decrease in cyclic amplitude lasting several seconds. Similarly, after the underload, the resonant excitation is renewed and the amplitude gradually increases to the reported value of 83.5 MPa. Because of the high frequency, both transients occupy 500 - 800 fatigue cycles. This, however, represents less than 1% of the total cycles in the load history. During the short transients the mean stress remained constant at 260 MPa. Underloads were achieved by quasi-statically altering the mean load on the specimen in the absence of resonance.

Results

Figure 4 shows finite life and run outs for batch 2 material at two values of mean stress. Also shown in this figure are results from the five variable amplitude tests. The small amplitude cycles in the variable amplitude tests had a mean stress of 260 MPa as did the solid diamond symbols in this figure. The single largest cycle in the variable amplitude history had approximately the same mean stress as the square symbols and, according to Fig. 4, the stress amplitude of 167 MPa would result in a fatigue life of around 4×10^5 cycles to failure. Scatter in the failure lives of the variable amplitude loaded specimens was greater than that observed for the constant amplitude loaded specimens. The number of tensile underloads required to cause failure ranged from only 10 to 227.

Haigh Diagram

Endurance limit values for the GRP 500 are here presented in the form of Haigh diagrams, see Fig. 5. Results in this case are mean experimental fatigue strengths and not design values. The form of the curve, however, is suitable for long-life design if material

scatter and batch to batch variation are considered. Each point on the Haigh diagram is determined by 6-25 long-life fatigue tests. Yield and ultimate strength values were found using 10 specimens in tension. The yield and tensile strength for cast iron in compression may be different than that in tension, but in this figure only the more conservative tensile values are used.

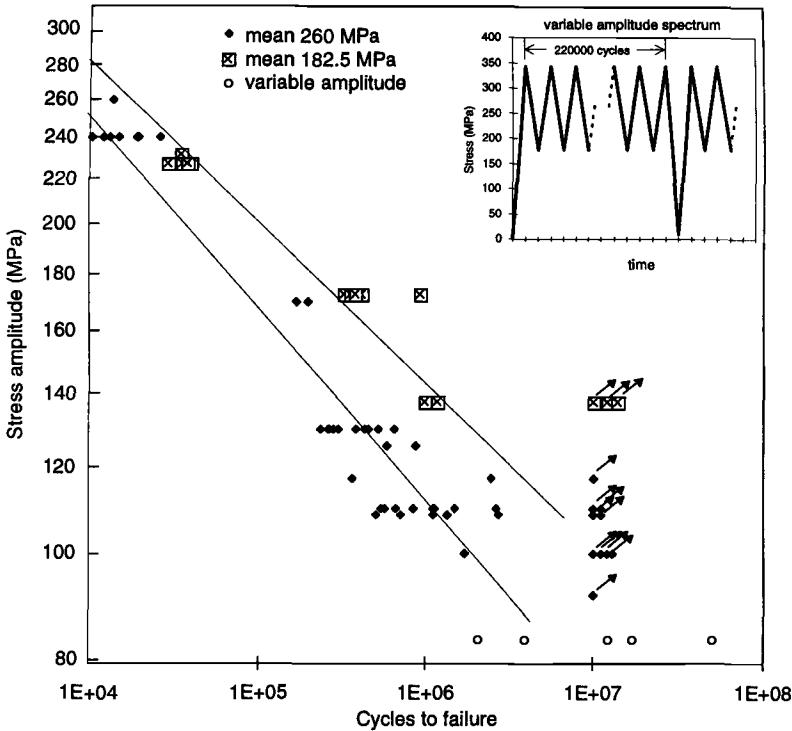


Figure 4 - Constant and Variable Amplitude Finite Life and Constant Amplitude Endurance Limit Fatigue Data for GRP 500 SG Iron.

Figure 5a shows the predicted effect of mean stress for batch 1 based on equation 2. The line was forced to pass through the point $\sigma_{fl, R=-1}$. This figure also shows the predicted mean stress effect of a Smith, Watson and Topper (SWT) based parameter [10]. For high cycle fatigue this parameter can be expressed as.

$$\sigma_{fl, R} = \sigma_{fl, R=-1} \sqrt{\frac{1-R}{2}} \tag{3}$$

The Goodman mean stress correction factor found in many fatigue textbooks predicts data to follow a straight line between R_m and $\sigma_{fl, R=-1}$ [11]. This is also shown in

Fig. 5a. The limited variety of stress ratios for the batch 2 material did not make it possible to evaluate possible R ratio correction equations. In addition to the uniaxial endurance limit results, Fig. 5b also shows the result from torsion fatigue tests at R=-1 and R=0.

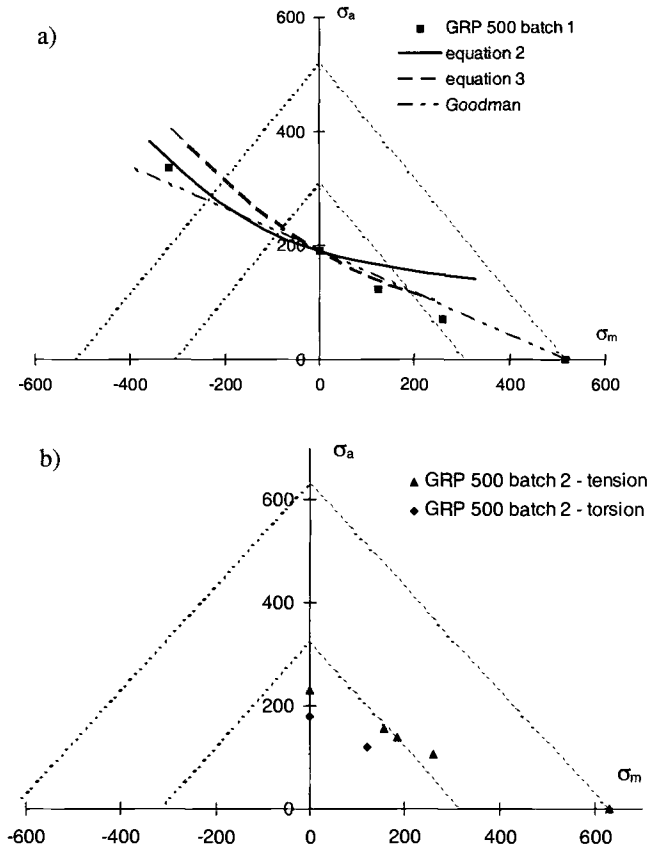


Figure 5 - Haigh Diagrams for GRP 500 SG Iron.

Defect Distributions

Following fatigue failure the fracture surfaces were examined with a SEM to locate the point of crack initiation and to observe the defect type and size that caused initiation. Sizes were approximated as the area of the smallest ellipse or semi-ellipse that would completely enclose the defect. Ellipses were used for internal defects while semi-ellipses were used for the more common surface breaking defect. As mentioned earlier, the

expected endurance limit is dependent only on the approximate size, so this method was deemed adequate even for defects of highly irregular shape.

Defects were of two types, inclusions and shrinkage pores. Shrinkage pores tended to be larger than the inclusions. Figure 6 shows a typical near surface shrinkage pore and an inclusion which resulted in fatigue failure.

Figure 7 shows the distribution of defects from the two batches of specimens. Because high cycle fatigue is characterized by only a small number of crack initiation sites and little or no crack linking, the observed defects are assumed to be the most severe for the volume of material near the specimen surface. Approximately 90% of all fatigue initiation sites were surface defects and in no cases did cracks initiate from defects at depths greater than 0.5 mm from the free surface. Figure 7 shows that the defect sizes can be reasonably well described by the Type I extreme value distribution. Batch 2 material had both a smaller mean defect size and smaller variation as compared to batch 1 material.

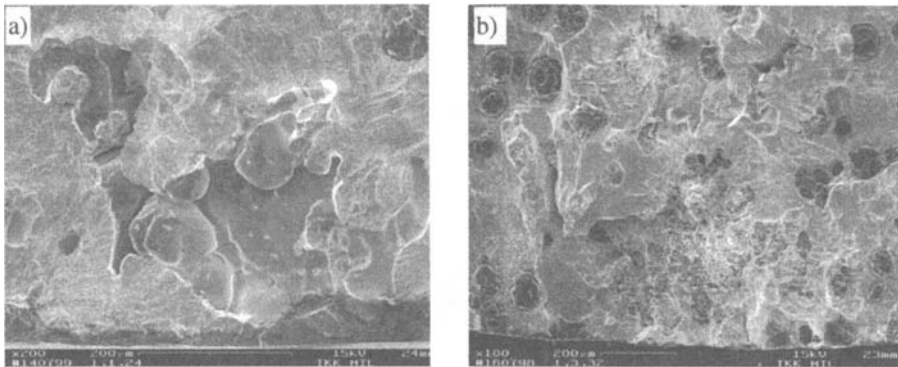


Figure 6 - Examples of Defects Leading to Failures: a) Shrinkage Pore and b) Inclusion.

Nonpropagating Cracks

Figure 8 shows a nonpropagating crack observed in a four-point bend specimen after 5×10^6 fatigue cycles. Etching was performed after fatigue cycling and reveals the complex ferritic-pearlitic microstructure. This crack has a surface length of approximately 260 μm but the majority of observed nonpropagating cracks were of length 50-150 μm . The defect from which the crack initiated cannot be seen, but further polishing revealed a shrinkage pore just below the surface. The density of nonpropagating fatigue cracks observed was 5-10 / cm^2 .

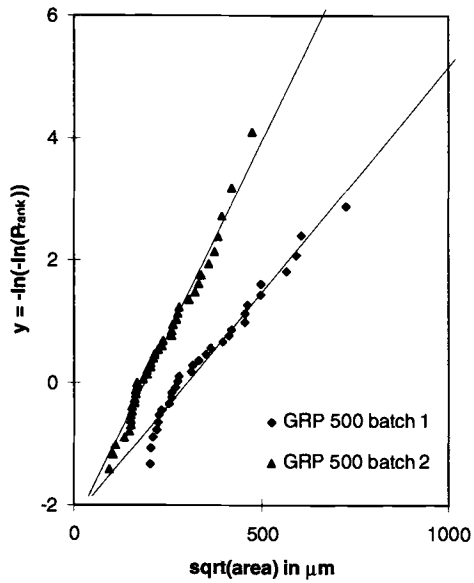


Figure 7 - Defect Size Distributions for the Two Batches of Material.

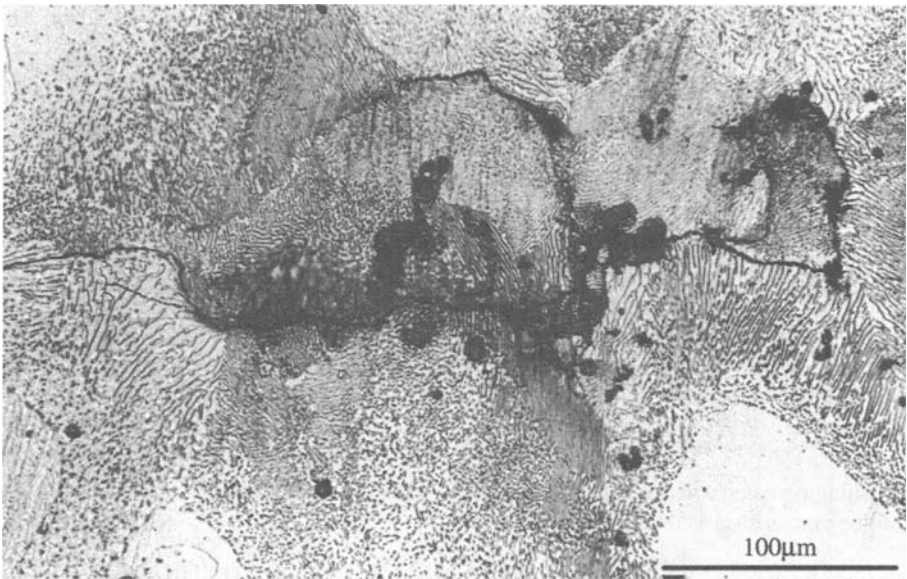


Figure 8 - Nonpropagating fatigue crack after 5×10^6 cycles near the endurance limit.

Discussion

Mean Stress Effects

As seen by the two curves in Fig. 5, Equation 2 tends to underpredict the reduction in endurance limit with increasing mean stress for GRP 500 SG iron. The SWT parameter has been found to be suitable for materials like cast iron that fail by mode I crack growth [12] and predicts better than Eq 2 the harmful effects of tensile mean stress. Equation 3 more closely follows the data but still under predicts the damaging effect of tensile mean stress.

The Goodman mean stress correction was very similar to Eq 3 for tensile mean stresses, but was better than either Eqs 2 or 3 for the single compressive mean stress data point. This single data point corresponds to high compressive loads such that general yielding has occurred and other stress states with less negative stress ratios should be investigated.

Fatigue Strength in Torsion

Many early studies in fatigue were devoted to determining the ratio of tensile and torsion fatigue limits, σ_f / τ_f , for different materials. Published values of σ_f / τ_f range from 0.9 to 2.7. Static yield criteria which are often used to relate fatigue data obtained from different stress states predict constant σ_f / τ_f ratios for any material. For example, the maximum shear stress theory predicts $\sigma_f / \tau_f = 2.0$, the octahedral shear stress theory, 1.73, and maximum principal stress theory, 1.0. As mentioned earlier, the $\sqrt{\text{area}}$ model which is based on the growth of cracks from small naturally occurring defects predicts $\sigma_f / \tau_f = 1.25$. This is in very good agreement with experiments for GRP 500 at $R=0$ which showed $\sigma_f / \tau_f = 148 \text{ MPa} / 120 \text{ MPa} = 1.23$. At $R=-1$ the respective values were $230 \text{ MPa} / 182 \text{ MPa} = 1.26$. Figure 5b shows the torsion endurance limit values and their relation to the tension value.

Nonpropagating Cracks

Contrary to what is sometimes presented in the literature, the endurance limit does not commonly represent a stress level where cracks do not initiate. Instead, it represents a stress level where initiated cracks become nonpropagating [13]. Murakami and Endo [1-6] have observed this in a variety of metallic materials and Clement et al. [14] and Palin-luc et. al. [15] have shown this to be the case for nodular cast irons.

The density of nonpropagating fatigue cracks observed was only $5-10 / \text{cm}^2$ which is far less than the density observed by Palin-luc et. al., but it should be noted that their test specimens were taken from relatively small crank shafts and initiation was due to graphite nodules. Material in the current study was intentionally taken from heavy section castings where shrinkage pores are more likely to be present. The significantly lower endurance limit stress in the current series, 192 MPa as compared to 268 MPa for Palin-luc et. al., can be partially accounted for in that crack initiation was due to shrinkage pores or inclusions which are several times larger than the nodules. The current

test series involved axial testing while Palin-luc et. al. employed fully reversed bending; bending produces less driving force for crack growth into the specimen thickness and results in a slightly higher endurance limit strength.

For the crack shown in Fig. 8, the bending stress amplitude was 150 MPa which translates to a threshold stress intensity of $4.3 \text{ MPa}\sqrt{\text{m}}$. This value is close to measured threshold stress intensity values for short cracks [14,16] or closure-free long cracks in nodular cast iron [17-18].

Variable Amplitude Loading

Figure 4 shows data obtained for five tensile underload tests using specimens identical to those used for the constant amplitude tests. The amplitude of small cycles in the spectrum was approximately three standard deviations below the measured endurance limit stress of 105 MPa, so failure would not be expected for such a small test series in the absence of the large underload cycles. As few as 10 tensile underload cycles were required to cause failure and the mean (geometric) number of underloads was only 54. Under constant amplitude cycling at the larger amplitude, fatigue life would be approximately $N_f = 400,000$. The damage fraction caused by the larger cycles was therefore only in the range of 0.01%. The greatly increased damage of small cycles observed here is even greater than that observed by Rabb [19] for grey cast iron using simple variable amplitude load histories.

During constant amplitude loading at 130 MPa the difference in fatigue lives between the shortest and longest of ten tests was a factor of about 2.5. The load history consisting of many small amplitude cycles with single underloads resulted in a difference of more than 20 between the shortest and longest of five tests. This increased scatter is in contrast to experimental results for welds and some wrought materials which show that variable amplitude loading normally produces less scatter than does constant amplitude loading.

The number of tensile underload cycles required to cause failure in the variable amplitude test ranged from only 10 to 227. This number was several times smaller than expected based on the experimental results for grey iron [19] or from theoretical predictions based on the Haibach principle [20]. It is significant because it shows that *even the small number of underload cycles that may result from transporting or overhauling a piece of machinery will destroy the fatigue limit and dramatically reduce the allowable operating stresses.*

Simple fracture mechanics arguments can not easily account for the additional damage produced by the tensile underload cycles. For example, if it is assumed that the nonpropagating crack size due to constant amplitude loading is the same as the measured defects $\sim 500 \mu\text{m}$, the stress intensity due to low amplitude cycling would be $3.4 \text{ MPa}\sqrt{\text{m}}$. The larger underload cycles produce stress intensities approximately twice this value. By using average crack growth properties measured for SG iron [14,16-18], the crack growth extension due to the relatively small number of tensile underloads is expected to be only several microns. It is unlikely that small cycles would suddenly become damaging only due to this small increment in crack length. A more likely explanation can be found in research work on smooth and notched steel and aluminum specimens by Topper and co-workers [21-23]. Tensile underloads cause local plasticity near the small defects which

reduce closure resulting in greater effective stress ranges for the small cycles. Further experimentation on the role of tensile underloads including smaller amplitude cycling, varying block sizes and longer fatigue lives is continuing.

Defects and Fatigue Strength

As seen in Fig. 7, material in batch 1 had a mean defect size of 330 μm while batch 2 had a mean defect size of only 220 μm . The variation in defect sizes was also significantly greater for the batch 1 material implying a significantly greater scatter in material properties. In batch 1, approximately 80% of fatigue failures initiated from shrinkage pores. In batch 2 the size of shrinkage pores was reduced so that the smaller inclusions began to control fatigue crack initiation. Only 45% of the failures for batch 2 initiated at shrinkage pores.

Based on the mean defect size and mean hardness measurements for batch 1, the value of $\sigma_{fR=1}$ based on Eq 1 is 159 MPa if the ferrite phase is considered and 193 MPa if the pearlite phase is considered. It is reasonable to consider the higher value more accurate since the weaker ferrite phase is always surrounded by a tougher pearlite phase. Both phases must fracture if fatigue failure is to occur. This higher value is close to the measured endurance limit of 192 MPa. For batch 2 the fatigue strength based on the mean defect size 205 μm and the hardness of the pearlite phase using Eq 1 gives $\sigma_{fR=1} = 247$ MPa. This again is close to the experimentally measured value of 230 MPa. The increased matrix hardness of the pearlite phase between the two batches of material provides a predicted increase in strength of 19% while the smaller defect size provides the remaining 9%. It should be noted, however, that the measured hardness of the different phases varied even within a single specimen. This should be studied further.

In the current test series, approximately 90% of all fatigue initiation sites were surface defects and in no cases did cracks initiate from defects at depths greater than 0.5 mm. Because specimens were cut from random internal locations within the ingots and cylinder head, defects would be expectedly be evenly distributed throughout the specimen volume. Murakami et. al. [2] have estimated that surface defects are more severe than internal defects of equal size. The computed difference in stress intensity factor is about 9% which means that, e.g., a surface defect $\sqrt{\text{area}} = 300 \mu\text{m}$ would be equally severe as an internal defect $\sqrt{\text{area}} = 500 \mu\text{m}$. This does not fully explain, however, the absence of internally initiated failures.

Conclusions

Long life experimental fatigue studies have been done on GRP 500 spheroidal graphite cast iron specimens obtained from thick section castings. Constant amplitude endurance limit tests at several stress ratios, torsion tests and simple variable amplitude tests were performed. Endurance limit values are presented in the form of Haigh diagrams. Statistics on defects leading to failure for two batches of nominally identical material have been obtained. The following conclusions can be made:

1. For the ferritic-pearlitic SG cast iron tested, the $\sqrt{\text{area}}$ parameter could be used to predict the mean endurance limit strength when the hardness value of the tougher pearlite phase was used. However, microhardness measurements of the non-homogenous microstructure were difficult and showed significant scatter.
2. The $\sqrt{\text{area}}$ model accurately predicted the relationship between the torsion and tensile fatigue limit.
3. Mean stress corrections developed by Murakami, SWT and Goodman have been evaluated. Goodman's correction provided the best fit while the others underestimated the strength reduction with increasing mean stress.
4. Nonpropagating cracks several grain sizes in length were observed in non-failed specimens cycled near the fatigue limit. The density was 5-10 / cm² and the sizes were typically 50-150 μm .
5. The load history which contained cycles smaller than the constant amplitude endurance limit and periodic underloads produced more scatter than did finite life constant amplitude loading above the endurance limit. Single underload cycles themselves caused an insignificant amount of damage but greatly increased the damaging effect of the smaller cycles.

Additional work with variable amplitude spectra and using simple notched specimens is continuing. Statistics relating the variation in defect sizes and material hardness to variation in the endurance limit strength should also be studied.

Acknowledgements

Work reported here was performed as part of the Finnish research project SCILLED funded by The Technology Development Centre of Finland (TEKES), Wärtsilä NSD, Valmet Corp., and VTT Manufacturing Technology.

References

- [1] Murakami, Y. and Endo, T., "Effects of Small Defects on Fatigue Strength of Metals," *International Journal of Fatigue*, Vol. 2, No. 1, 1980, pp. 23-30.
- [2] Murakami, Y. Kodama, S. and Konuma, S. "Quantitative Evaluation of Effects of Non-metallic Inclusions on Fatigue Strength of High Strength Steels. I: Evaluation of Correlation Between the Fatigue Fracture Stress and the Size and Location of Non-metallic Inclusions," *International Journal of Fatigue*, Vol. 11, No. 5, 1989, pp. 291-298.
- [3] Murakami, Y. and Endo, T., "Effects of Hardness and Crack Geometries on ΔK_{th} of Small Cracks Emanating from Small Defects," *The Behaviour of Short Fatigue Cracks EGF 1*, K. J. Müller and E. R. de los Rios, Eds., 1986, pp. 275-293.
- [4] Murakami, Y. and Endo, M., "Effects of Defects, Inclusions and Inhomogeneities on Fatigue Strength," *International Journal of Fatigue*, Vol. 16, 1994, pp. 163-182.
- [5] Endo, M. and Murakami, Y., "Effects of an Artificial Small Defect on Torsional Fatigue Strength of Steels," *ASME Journal of Engineering Materials and Technology*, V. 109, 1986, pp 124-129.

- [6] Endo, M., "Fatigue Threshold for Small Cracks in Spheroidal Graphite Cast Iron," *Proceedings of Fatigue 90*, H. Kitagawa and T. Tanaka, Eds., MCE Pub. Ltd., Birmingham, UK, 1990, pp. 1357-1362.
- [7] Beretta, S. Blarasin, A. Endo, M. and Murakami, Y., "Defect Tolerant Design of Automotive Components," *International Journal of Fatigue*, Vol. 19, No. 4, 1997, pp. 319-333.
- [8] Little, R.E., *Manual on Statistical Planning and Analysis, ASTM STP 588*, American Society for Testing and Materials, West Conshohocken, PA, 1975, 149 p.
- [9] Dixon, W.J., and Mood, A. M., "A Method for Obtaining and Analyzing Sensitivity Data," *J. Am. Stat. Assoc.*, Vol. 43, 1948, pp. 109-126.
- [10] Smith, R. N. Watson, P. and Topper, T. H., "A Stress-Strain Parameter for the Fatigue of Metals," *Journal of Materials*, Vol. 5, No. 4, 1970, pp. 767-778.
- [11] Bannantine, J. Comer, J. and Handrock, J., *Fundamentals of Metal Fatigue Analysis*, Prentice-Hall, Englewood Cliffs, NJ, 1990, 273 p.
- [12] Socie, D., "Critical Plane Approaches for Multiaxial Fatigue Damage Assessment," *Advances in Multiaxial Fatigue, ASTM STP 1191*, D. L. McDowell and R. Ellis, Eds., American Society for Testing and Materials, Philadelphia, 1993, pp. 7-36.
- [13] Miller, K. J., "Metal Fatigue - Past, Current, and Future," 27th John Player Lecture, *Proc. Inst. Mech. Eng*, 1991, 14 p..
- [14] Clement, P. Angeli, J. P. and Pineau, A., "Short Crack Behaviour in Nodular Cast Iron," *Fatigue and Fracture of Engineering Material and Structures*, Vol. 7, 1984, pp. 251-265.
- [15] Palin-luc, T. Lasserre, S. and Bérard, J.-Y., "Experimental Investigation on the Significance of the Conventional Endurance Limit of a Spheroidal Graphite Cast Iron," *Fatigue and Fracture of Engineering Material and Structures*, Vol. 21, 1998, pp. 191-200.
- [16] Yaacoub Agha, H. Béranger, A.-S. Billardon, R. and Hild, F., "High-cycle Fatigue Behaviour of Spheroidal Graphite Cast Iron," *Fatigue and Fracture of Engineering Material and Structures*, Vol. 21, 1998, pp. 287-296.
- [17] Ogawa, T. and Kobatashi, H., "Near Threshold Fatigue Crack Growth and Crack Closure in a Nodular Cast Iron," *Fatigue and Fracture of Engineering Material and Structures*, Vol. 10, 1987, pp. 273-280.
- [18] Tokaji, K. Ogawa, T. and Shamato, K., "Fatigue Crack Propagation in Spheroidal Graphite Cast Irons with Different Microstructures," *International Journal of Fatigue*, Vol. 16, 1994, pp. 344-350.
- [19] Rabb, R., "Fatigue Life Evaluation of Grey Cast Iron Machine Components," *Fatigue Design and Reliability*, G. Marquis and J. Solin, Eds., ESIS Publication 23, Elsevier Science, Ltd, Amsterdam, 1999, pp. 51-63.
- [20] Haibach, E., "Modifizierte lineare Schadensakkumulations - Hypothese zur Berücksichtigung des Dauerfestigkeitsafalls mit fortschreitender Schädigung," Darmstadt: LBF, Technische Mitteilung TM 50/70, 1970.
- [21] Pompetzki, M. A. Topper, T. H. and DuQuesnay, D. L., "The Effect of Compressive Underloads and Tensile Overloads on Fatigue Damage Accumulation in SAE 1045 Steel," *International Journal of Fatigue*, Vol. 12, 1990, pp. 207 - 213.

- [22] MacDougall, C. and Topper, T. H., "The Influence of Variable Amplitude Loading on Crack Closure and Notch Fatigue Behaviour," *International Journal of Fatigue*, Vol. 19, 1997, pp. 389-400.
- [23] DuQuesnay, D. L. MacDougall, C. Dabayeh, A. and Topper, T.H., "Notch Fatigue Behaviour as Influenced by Periodic Overloads," *International Journal of Fatigue*, Vol. 17, 1995, pp. 91-99.

Author Index

- | | |
|-------------------------|------------------------------|
| A | N |
| Akiniwa, Y., 304 | Newman, J. A., 63 |
| Albrecht, P., 374 | Newman, J. C., Jr., 227 |
| Allison, J. E., 285 | |
| | O |
| B | Ohashi, M., 123 |
| Bathias, C., 135 | |
| Bucci, R. J., 269 | P |
| Bush, R. W., 269 | Petit, J., 3, 341 |
| | Piasek, R. S., 63, 109 |
| C | Pippan, R., 96, 252 |
| Caton, M. J., 285 | Powell, P., 96 |
| Chabanne, Y., 341 | |
| Czyryca, E. J., 319 | R |
| | Rabb, R., 411 |
| D | Riddell, W. T., 63 |
| DeCarmine, A., 123 | Riemelmoser, F. O., 252 |
| Donald, J. K., 269 | Rosborg, B., 400 |
| | |
| G | S |
| Garr, K. R., 155 | Sarrazin-Baudoux, C., 3, 341 |
| | Schindler, H.-J., 46 |
| H | Shover, R., 123 |
| Hadrboletz, A., 31 | Siivonen, L., 411 |
| Henaff, G., 3 | Smith, S. W., 109 |
| Hresko, G. C., III, 155 | Stephens, R. R., 175 |
| | Stickler, R., 31 |
| | |
| J | T |
| Jones, J. W., 285 | Tabernig, B., 96 |
| | Tanaka, K., 304 |
| L | Taylor, D., 361 |
| Lidar, P., 400 | Topper, T. H., 192 |
| Liknes, H. O., 175 | |
| Lindström, R., 400 | V |
| | Varvani-Farahani, A., 192 |
| M | |
| Marci, G., 81 | W |
| Marquis, G., 411 | Wang, G., 361 |
| McClung, R. C., 209 | Weiss, B., 31 |
| McEvily, A. J., 123 | Wright, W. J., 374 |

Subject Index

A

Adsorption, 3
 Aircraft applications, advanced, 123
 Aluminum alloys, 3, 81
 cast, 285
 endurance limits, 135
 nickel aluminum bronze, 319
 particle reinforced, 96
 stress intensity factor effects, 63
 thin sheet, 227
 Amplitude, variable, 374
 ASTM standards
 E 647, 269, 319

B

BCS model, 252
 Biaxial fatigue, 192
 Biaxiality ratio, 155, 175
 Bridges, highway, 374
 Bronze, nickel aluminum, 319

C

Castings, wall, 411
 Closure effects, 31
 Closure-free fatigue life, 192
 Compressive overstrain, periodic, 192
 Compressor disk titanium alloys, 81
 Constant amplitude fatigue limit, 192
 Constant amplitude loading, 227
 Constant amplitude torsion, 412
 Constraint, 155, 227
 Copper, 31
 copper-base alloy, 319
 Corrosion, 341
 fatigue, 319
 Crack closure, 46, 209
 aluminum alloy, 31, 227
 cast nickel-aluminum bronze, 319
 fatigue limit prediction, 304
 nickel-based superalloy, 155
 steel, 31
 titanium alloy, 109, 123, 175
 Crack growth, near threshold, 3, 63
 Crack growth rate, 192, 252, 400
 Crack initiation, 285
 Crack length, 269
 Crack, nonpropagating, 411
 Crack opening displacement, 227
 Crack opening levels, 209

Crack opening stress measurements, 192
 Crack propagation, 285, 341
 aluminum alloys, 96
 mechanisms and modeling, 3
 nickel alloy, 135
 nickel based superalloy, 155
 titanium alloys, 81
 Cracks, short, 361
 Crack, surface, 123
 Crack tip process zone damage
 mechanisms, 63
 Crack tip shielding, 46
 Creep damage process, 341
 Critical distance concept, 361
 Cut compliance method, 46
 Cyclic loading, 341
 Cyclic resistance curve method, 304

D

Damage mechanisms, 63
 Deformation, 341
 Dislocation configuration, 31
 Dislocation mechanics, 252
 Dislocation model, discrete, 252

E

Electron channeling contrast imaging
 technique, 31
 Endurance limits, 135, 361, 411

F

FASTRAN strip yield model, 209
 Fatigue limit, 135, 374
 Fatigue limit prediction, 96, 304
 Finite element model, 209
 Fractography, 63

G

Gigacycle fatigue, 135

H

Haigh diagrams, 304, 411
 High Speed Civilian Transport, 123
 Highway bridges, 374

I

Incubation phenomenon, 135
 Intrinsic threshold, 31, 46
 Iron
 nodular cast, 411
 spheroidal graphite cast, 411

K

Kitagawa diagram, 96

L

Load history, 175
 Loading, biaxial fatigue, 192
 Loading, cyclic, 81, 374
 Load ratio, 63, 175
 Load reduction, 175, 227
 Load shedding, 175, 209

M

Material flow strength, 209
 Mean stress, 304, 341, 411
 Microstructure, 3
 Models and modeling
 BCS model, 252
 crack closure, 227
 discrete dislocation model, 252
 fatigue life calculation, 285
 finite element, 209
 near-threshold fatigue crack propagation,
 3
 short notches, 361
 stress-life, for life prediction, 374
 strip yield model, 209

N

Nickel alloys, 135
 Nickel aluminum bronze, 319
 Nickel-based superalloy, 155
 Nickel-base metal, 400
 Nickel-base weld metal, 400
 Notches, 361

O

Overload, 123, 374

P

Plastic deformation, 252
 Plasticity, 227

Plasticity-induced closure, 209
 Plastic strain amplitude, 31
 Plastic zone size, overload, 123
 Porosity, 285

R

R-curve, 96
 R-effect, 46
 Residual stress, 269
 Resistance curves, 96
 method, 304

S

Scanning electron microscope, 31
 Scanning laser microscopy technique,
 confocal, 192
 Seawater, 319
 Secondary dendrite arm spacing, 285
 Shear strain, 192
 Shielding, crack tip, 46
 Spheroidal graphite cast iron, 411
 Steam testing, 400
 Steel, 135, 374
 stainless, 400
 Stiffeners, 374
 Strain intensity factor, 192
 Stress amplitude, 304
 Stress concentration assessment, 361
 Stress corrosion cracking, 341
 Stress crack propagation threshold, 341
 Stress intensity, 319
 Stress intensity factor, 81, 135, 227
 cyclic, 63
 effective, 3
 effect on fatigue crack growth rate, 109
 initial, 209
 range, 96, 269
 Stress life curves, 285
 Stress ratio, 304
 effects, 109
 Stress, residual, 46
 Strip yield model, 209
 Surface crack, 123

T

Tensile specimen, 374
 Thin foils, 31
 Titanium alloys, 3, 81, 109, 175
 cracking behavior, 341
 overload effects on crack growth
 behavior, 123

Transverse stiffener specimens, 374
T stress, 155, 175

U

Ultrasonic vibratory effort, 135

V

Vacuum, 3
Variable amplitude loading, 411
Void production, 63

W

Water testing, 400
Water vapor, 3, 341
Weld, 374
metal, 319, 400

Y

Yield strength, 123
Yield stress, 252

ISBN 0-8031-2624-7